



Università degli studi di Catania

Dipartimento di Scienze Biologiche, Geologiche e
Ambientali

Corso di Dottorato di Ricerca in Scienze Geologiche, Biologiche e
Ambientali - XXX Ciclo

Innovative numerical petrological methods for
definition of metamorphic timescale events of
southern European Variscan relicts via
thermodynamic and diffusion modelling of zoned
garnets

Tesi di Dottorato di Ricerca di
Roberto Visalli

Tutor
Prof. Rosolino Cirrincione

Coordinatore
Prof.ssa Agata di Stefano

Co-Tutor
Prof. Gaetano Ortolano

Anno Accademico 2016/2017

List of Contents

ABSTRACT	12
RIASSUNTO	13
1. INTRODUCTION	17
1.1 Aims.....	24
2. “PETROMATICS” AND NUMERICAL PETROLOGY SUPPORTED BY IMAGE ANALYSIS... 26	
2.1 General outlines	26
2.2 Grain Size Detection (GSD): a new ArcGIS® toolbox to construct grain size distribution by drawing mineral grain boundaries on thin section scans	28
2.2.1 Pre-edge detection filter phase.....	31
2.2.2 Edge detector	33
2.2.3 Grain polygons creator.....	36
2.2.4 Final remarks	38
2.3 Quantitative X-ray Map Analyser (Q-XRMA): A new GIS-based statistical approach for Mineral Image Analysis.....	38
2.3.1 Algorithms.....	41
2.3.1.1 First cycle: pre-calibration procedure.....	45
2.3.1.2 Second cycle: calibration algorithm.....	47
2.3.1.3 Second cycle: maps calibration (data setting and outputs).....	52
2.3.1.4 Third cycle: mineral end-member maps.....	56
2.3.2 Case study	58
2.3.2.1 Garnet.....	59
2.3.2.2 Plagioclase	60
2.3.2.3 Biotite	62
2.3.3 Final Remarks	63
2.4 Mineral Grain Size Distribution (Min-GSD): a useful tool to display the grain size frequency distribution of each rock-forming mineral	64
3. THE DIFFUSION MODELLING TOOL APPLIED FOR DISCOVERING TIMESCALES AND RATES OF GEOLOGICAL PROCESSES	70
3.1 General Outlines.....	70
3.2 Diffusion mechanisms.....	74
3.3 Element diffusion coefficients.....	76
3.3.1 Factors affecting diffusion coefficient measurements.....	79
3.3.2 Diffusion coefficient map creator (DCMC): A Q-XRMA image-processing add-on for creating map of various kinetic coefficients in a Local Information System (LIS)	81

3.4	Mathematics of diffusion	87
3.4.1	Basics of diffusion laws.....	87
3.4.2	Solutions of diffusion equations.....	91
3.4.2.1	Initial condition.....	92
3.4.2.2	Boundary conditions.....	93
3.4.2.3	Numerical solution: The finite-difference explicit method	96
4.	CASE STUDIES	99
4.1	General outlines	99
4.2	First case study: Timescale of Late-Variscan static event constrained by garnet multicomponent diffusion modelling: new insights from the Serre Massif (Southern Calabria, Italy) 103	
4.2.1	Introduction.....	103
4.2.2	Geopetrological background	107
4.2.3	Methodology	110
4.2.4	Petrography and mineral chemistry.....	111
4.2.5	Image-assisted thermodynamic modelling	115
4.2.5.1	Quantitative image processing.....	117
4.2.5.2	Thermobaric constraints.....	122
4.2.6	Diffusion modelling	128
4.2.6.1	Image-assisted diffusion modelling.....	129
4.2.6.2	Sources of uncertain	136
4.2.7	Final Remarks	137
4.3	Second case study: Timescale and cooling of the Calabria continental lower crust inferred via garnet diffusion modelling: An example from the Sila Piccola Massif	139
4.3.1	Introduction.....	140
4.3.2	Geological Background.....	141
4.3.3	Mesostructural features.....	143
4.3.4	Petrography and mineral chemistry.....	146
4.3.4.1	Methods	146
4.3.4.2	Petrographic description	146
4.3.4.3	Garnet-biotite-sillimanite paragneiss – CEL1B sample	149
4.3.5	Image-assisted thermodynamic modelling	151
4.3.5.1	Quantitative image processing and thermobaric constraints	152
4.3.6	Diffusion modelling	154
4.3.7	Final remarks	156
5.	CONCLUSIONS	161
	ACKNOWLEDGEMENTS	166
	BIBLIOGRAPHY	168
	APPENDICES	187
	APPENDIX A1 – Grain size detection of thin sections	187
	APPENDIX B1 – Quantitative X-ray Map Analyser User’s Guide	190

APPENDIX B2 – EMP analyses of the investigated phases.....	220
APPENDIX B3 – X-ray maps of the studied example domain.....	235
APPENDIX B4 – Input control spot analysis.....	236
APPENDIX B5 – Summary report of the multilinear regressions	246
APPENDIX B6 – EMP/Q-XRMA comparisons	269
APPENDIX C1 – EMP analyses of Serre Massif rocks	275
APPENDIX C2 – X-ray maps of garnet microdomains from Serre Massif rocks	301
APPENDIX C3 – XRF composition	302
APPENDIX C4 – Sample locations.....	302
APPENDIX C5 – Isopleth intersections	303
APPENDIX C6 – X-ray maps of a zoom in a garnet rim.....	304
APPENDIX C7 – Sequence of calculation adopted in the MATLAB scripts.....	304
APPENDIX D1 – EMP analyses of Sila Piccola rocks	305

List of Figures

Fig. 1.1 - Schematization of the sequential steps adopted to achieve the aims of the PhD project	25
Fig. 2.1 - Effect of the pre-processing phase on the input thin section scan.....	29
Fig. 2.2 - Screenshot of the routine composing the Grain Size Detection toolbox	30
Fig. 2.3 - Flow chart of the Pre-edge detection filter phase routine	31
Fig. 2.4 - Schematic representation of the low filter principle used in the procedure.....	31
Fig. 2.5 - Schematization of the single steps of the Pre-edge detection routine.....	32
Fig. 2.6 - Schematic representation of the high filter principle used in the procedure	33
Fig. 2.7 - Flow chart of the Edge detector filter phase routine	34
Fig. 2.8 - Schematization of the single steps of the Edge detector routine.....	35
Fig. 2.9 - Flow chart of the Grain polygons creator routine	36
Fig. 2.10 - Schematization of the single steps of the Grain polygons creator routine.	36
Fig. 2.11 - Difference between a smoothed vs. a non-smoothed polyline feature.....	37
Fig. 2.12 - Effect of a non-completed boundary regarding the creation of polygon features.....	37
Fig. 2.13 - Simplified flow charts of the GIS-based image-processing procedure	41
Fig. 2.14 - Flow chart of the first cycle of the geoprocessing procedure.....	43
Fig. 2.15 - Flow chart of the second cycle of the geoprocessing procedure.....	44
Fig. 2.16 - Flow chart of the third cycle of the geoprocessing procedure	45
Fig. 2.17 - Example of schematic 3D representation of the decorrelation function.....	46
Fig. 2.18 - Example of possible relationship between dependent and explanatory variables	49
Fig. 2.19 - Difference between heteroscedasticity vs. Homoscedasticity distribution of the residuals.....	51
Fig. 2.20 - Effect of outliers on the regression results (i.e., R^2 values).	52
Fig. 2.21 - Point coordinates conversion spreadsheets	54
Fig. 2.22 - PtAnls.xlsx file used by the Python code to create an ArcGIS® point shapefile	55
Fig. 2.23 - Editing step of the ArcGIS® shapefile for removing points close to the edge mineral zones.....	55
Fig. 2.24 - Summary results of the calibration procedure using iron as a dependent variable.....	56
Fig. 2.25 - Window shell of the third analytical cycle.....	57
Fig. 2.26 - Output of the first analytical cycle	58
Fig. 2.27 - Outputs of the second and third analytical cycles for garnet.....	59
Fig. 2.28 - Outputs of the second and third analytical cycles for plagioclase	61
Fig. 2.29 - Outputs of the second and third analytical cycles for biotite.....	62
Fig. 2.30 - Grain size distribution derivation	65
Fig. 2.31 - Thin Section X-ray map array.	66
Fig. 2.32 - Mineral classification of the entire thin section via Q-XRMA.....	67
Fig. 2.33 - Flow chart of the Mineral Grain Size Distribution toolbox	67
Fig. 2.34 - Grain size distribution distinct for each thin section-forming mineral.....	68
Fig. 3.1 - Schematic example of how diffusion works in a liquid.....	70
Fig. 3.2 - Schematization of particle diffusion between two solids in contact along their faces	71
Fig. 3.3 - Schematic representation of the proceeding of diffusion	73
Fig. 3.4 - Schematic representation of the main crystal lattice defects.....	75
Fig. 3.5 - Schematization of the various intergranular diffusion mechanisms.....	75
Fig. 3.6 - Different crystallographic structures influencing diffusion	80
Fig. 3.7 - Windows shell of the DCMC add-on showing the initial prompts.....	82
Fig. 3.8 - Windows shell of the DCMC tool showing the sequential operative step.	83
Fig. 3.9 - Flow chart of the DCMC geoprocessing procedure	84
Fig. 3.10 - Input data of the DCMC add-on	85
Fig. 3.11 - Temperature and Pressure maps derived by the DCMC.....	85
Fig. 3.12 - Windows shell of the three-different diffusion coefficient calculations.....	85
Fig. 3.13 - Mineral component concentration maps from the third analytical cycle of the Q-XRMA	86
Fig. 3.14 - Matrix of diffusion coefficients computed for garnet	86
Fig. 3.15 - Illustration of Fick's first law	87

Fig. 3.16 - Nomenclature for the mass balance of fluxes in a rectangular solid	89
Fig. 3.17 - Different cases of pre-diffusion initial condition	93
Fig. 3.18 - The diffusion process graphically illustrated for a half grain of a single phase	94
Fig. 3.19 - Visualization of the discretization of time and space used in finite difference algorithms	96
Fig. 3.20 - Example of a loop structure built in a MATLAB® script	98
Fig. 4.1 - Distribution of the Alpine and Pre-Alpine Basement in Western Europe.	99
Fig. 4.2 - Sketch of the possible configuration of Variscan Western Europe in Late Carboniferous	100
Fig. 4.3 - Geological map representations of the Calabria-Peloritani Orogen).	102
Fig. 4.4 - Geological framework of the Serre Massif.....	107
Fig. 4.5 - Garnet porphyroblasts showing different steps of the metamorphic evolution	113
Fig. 4.6 - Mineral chemistry of the samples investigated	114
Fig. 4.7 - Thin section classification.....	117
Fig. 4.8 - Three-selected investigated domains via Q-XRMA image processing procedure	121
Fig. 4.9 - Pseudosections computation supported by image analysis.....	123
Fig. 4.10 - New image-assisted PT-path of the Serre Massif.....	127
Fig. 4.11 - Mineral grain size distribution of the MA271 sample	130
Fig. 4.12 - Schematic image-processing sequence to derive diffusion coefficient maps via DCMC	131
Fig. 4.13 - Diffusion modelling results obtained by using image-assisted thermodynamic modelling	133
Fig. 4.14 - Diffusion modelling results.....	135
Fig. 4.15 - Temperature-time diagram of the Upper Crust (Serre Massif).....	138
Fig. 4.16 - Geo-structural map of the crystalline basement of the Sila Piccola.....	144
Fig. 4.17 - Mesostructural features in orthogneiss and metapelites of the Castagna Unit rocks	145
Fig. 4.18 - Observed microstructures representing two opposite sense of shear	148
Fig. 4.19 - CEL1B sample features	150
Fig. 4.20 - X-ray maps of the selected garnet domain from the CEL1B metapelite sample.....	151
Fig. 4.21 - Definition of the effective reactant volume (ERV) by image analysis	153
Fig. 4.22 - PT pseudosection of the syn-mylonitic assemblage for the CEL1B sample.	154
Fig. 4.23 - Diffusion model of the garnet retrograde zoning	156

List of Tables

Tab. 1.1 – Summary of the tools developed.....	21
Tab. 2.1 – Output of the 1st cycle for the selected domain in the Q-XRMA.....	58
Tab. 3.1 – Datasets of diffusion data reported in the literature.....	81
Tab. 4.1 – Thin section 1st cycle output for the first case study.....	119
Tab. 4.2a – Domain 1st cycle output for the first case study.....	120
Tab. 4.2b – Garnet 2nd cycle output for the first case study.....	121
Tab. 4.3 – Calculation of oxide amounts to be fractionated from garnet porphyroblasts.....	126
Tab. 4.4 – Calculation of the effective bulk composition from the effective reactant volume.....	127
Tab. 4.5 – Reconstruction of garnet overgrowing stages.....	128
Tab. 4.6 – Summary of diffusion coefficient expressed as a function of T and P.....	134
Tab. 4.7 – Summary of the blasto-deformational events for the second case study.....	159

List of Equations

Eq. 1	Generic diffusion equation when D is constant
Eq. 2	Interdependent multilinear regression algorithm
Eq. 3	Conversion of the analytical device X -coordinate when $X > 0$
Eq. 3b	Conversion of the analytical device X -coordinate when $X < 0$
Eq. 3c	Conversion of the analytical device Y -coordinate when $Y > 0$
Eq. 3d	Conversion of the analytical device Y -coordinate when $Y < 0$
Eq. 4	Calculation of the interdiffusion coefficient
Eq. 5	Matrix of diffusion coefficients
Eq. 6	Calculation of the element of the diffusion matrix
Eq. 7	Effective binary diffusion coefficient calculation
Eq. 8	Calculation of diffusion coefficient as a function of T and P
Eq. 9	Fick's first law of diffusion
Eq. 10	Expression of the diffusion tensor for anisotropic medium
Eq. 11	Diffusion equation in presence of crystal growth/dissolution
Eq. 12a	One-dimension fluxes in a n -multicomponent system
Eq. 12b	Fick's first law for a n -multicomponent system
Eq. 13a	One-dimensional flux within a small solid volume
Eq. 13b	One-dimensional compositional changes in a small solid volume
Eq. 13c	Continuity equation
Eq. 14	Limit of the continuity equation
Eq. 15	Fick's second law of diffusion
Eq. 16a	Fick's second law of diffusion when D is constant
Eq. 16b	Fick's second law of diffusion when D is not constant
Eq. 17	Compositional change along the spatial coordinate
Eq. 18a	Forward difference scheme for the spatial coordinate
Eq. 18b	Compositional change along the time coordinate
Eq. 19	Forward difference method when D is constant
Eq. 20	Forward difference method when D is not constant
Eq. 21	Characteristic temperature of diffusion

List of Symbols

$\llbracket \]$	Discretized positive value of a map's pixel
$\llbracket C_i \rrbracket$	The absolute and discretized concentration of the element i computed for each pixel
$\llbracket GV_i \rrbracket_0^{255}$	The discrete pixel-intensity values of the $i, j, k \dots n$, one-channel elemental maps
$\alpha_{1; 2; 3; \dots n}$	Regression coefficients between the measured concentration value of the elements and the corresponding pixel intensity value of the original X-ray raster images at the same point
β_i	Value of the intercept for the element i
C	Generic chemical concentration
C_i, C_1	Concentration of the component i
\mathbf{C}	A column vector of the concentrations of $n - 1$ independent components in an n -component system
D	Generic diffusion coefficient
D_0	Pre-exponential factor (i.e., the self- or tracer coefficient)
D_i, D_1	Diffusion coefficient of an element i
D_{i-j}	Interdiffusion coefficient
\mathbf{D}	Matrix of diffusion coefficients
D_{ij}, D_{11}	Element of the \mathbf{D} -matrix
$D(EB)$	Effective binary diffusion coefficient
$D(P, T)$	Diffusion coefficient expressed as a function of temperature and pressure
ΔV	Activation volume of diffusion
δ_{ij}	Kronecker delta
fO_2	Oxygen fugacity
J_i, J_1	Flux of a component i
J_i^x, J_i^y, J_i^z	Flux of a component i in a three-dimensional space
\mathbf{J}	A column vector of the fluxes of $n - 1$ independent components in an n -component system
P	Pressure
Q	Activation energy of diffusion
R	Gas constant
R^2	Measure of the model performance
T	Temperature
T_{peak}	Temperature at metamorphic peak conditions
T_{ch}	Characteristic temperature of diffusion
t	Variable of time
v	Crystal growth/dissolution rate
x	Variable of space

X	Generic atomic fraction
X_i	Atomic fraction of the element i
Xp_{GIS}, Yp_{GIS}	Spatial xy -coordinates of a point within the ArcGIS® reference system
Xp_{LAB}, Yp_{LAB}	Spatial xy -coordinates of a point within the analytical device reference system
Xm_{GIS}, Ym_{GIS}	Spatial xy -coordinates of an X-ray map within the ArcGIS® reference system
Xm_{LAB}, Ym_{LAB}	Spatial xy -coordinates of an X-ray map within the analytical device reference system
γ_i	Residuals of the element i

List of Abbreviations

AICc	Corrected akaike's information criterion
a.p.f.u	Atomic per formula unit
CPO	Calabria-Peloritani orogen
DCMC	Diffusion coefficient map creator
Dfr	Diffusion along fractures
DGb	Diffusion along grain boundaries
DsGb	Diffusion along subgrain boundaries
Dv	Volume diffusion
DV(s)	Dependent variable(s)
EBC(s)	Effective bulk rock composition(s)
EBDC, EB	Effective binary diffusion coefficient
EDS	Energy dispersive spectroscopy
EMP	Electron microprobe
EOS	Equation of state
ERV(s)	Effective reactant volume(s)
EV(s)	Explanatory variable(s)
FEC	Fixed edge compositions
GIS	Geographic information system
GSD	Grain size detection
LIS	Local information system
L.O.I.	Loss of ignition
MetPetIS	Metamorphic petrology information system
Min-GSD	Mineral grain size distribution
MLC	Maximum likelihood classification
MPC	Mammola Paragneiss Complex
PCA	Principal component analysis
PC(s)	Principal component(s)
PFZ	Pollino Fault Zone
Q-XRMA	Quantitative X-ray map analyser
ROI(s)	Region(s) of interest
SQL	Structured query language
SPM	Sila Piccola Massif
TL	Taormina Line
VEC	Variable edge composition
VIF	Variance inflation factor
XRF	X-ray fluorescence spectroscopy
WDS	Wave-length dispersive spectroscopy

Abstract

Innovative numerical petrology methods have been developed using several computer programming languages, to investigate chemical-physical properties of metamorphic rocks at the microscale. These methods can help users to analyse the final aspect of the metamorphic rocks, which derives from the counterbalancing factors controlled by deformation vs. recovery processes, through a better quantification of the rock fabric parameters (e.g., grain and mineral size distribution) as well as of the rock volumes and the specific compositions that take part in the reactions during each metamorphic evolutionary stage.

In this perspective, a grain boundary detection tool (i.e., **Grain Size Detection - GSD**) was created to draw grain boundary and create polygon features in a **Geographic Information System (GIS)** platform using thin section optical scans as input images. Such a tool allows users to obtain several pieces of information from the investigated samples such as grain surfaces and sizes displayed as derivative maps. These maps have been then integrated with the mineralogical distribution map of the entire thin section classified from the micro X-ray maps. This step has been made to enhance the grain size distribution analysis by associating a mineral label to each polygon feature, by developing a further tool called **Min-GSD** (i.e., **Mineral-Grain Size Distribution**).

The image analysis of rocks at the microscale was further improved by introducing a new multilinear regression technique within a previous image analysis software (i.e., **X-ray Map Analyser - XRMA**), with the aim to calibrate X-ray maps per each classified mineral of the selected thin section microdomain. This enhancement (called **Quantitative X-ray Map Analyser - Q-XRMA**) allowed to compute: (a) the elemental concentration within a single phase expressed in a.p.f.u; (b) maps of the end member fractions defining the potential zoning patterns of solid solution mineral phases.

Moreover, the classification through this new method of one or several microdomains per thin section, able to describe the potential sequence of recognized metamorphic equilibria, has been here used to a better definition of the effective bulk rock chemistries at the base of a more robust thermodynamic modelling, providing more reliable thermobaric constraints.

These thermobaric constraints were here converted for the first time into **Pressure-Temperature (PT)** maps by the development of an add-on (i.e., **Diffusion Coefficient Map Creator - DCMC**) of the previous tool (Q-XRMA), for creating maps of compositionally-dependent diffusion coefficients, by integrating diffusion data from the literature. As a result, an articulated **Local Information System (LIS)** for the investigated mineral, involving data on composition, grain size, modal amounts and kinetic rates, is created and potentially useful for detailed investigations as, for instance, the determination of the timescales of metamorphic events.

All of these methods mentioned above can be considered part of “**the Petromatics**” discipline, here for the first time defined as the science which integrates new computers

technologies with different techno-scientific sectors related to the detection and handling of spatial minerochemical data characterising rocks at the microscale.

Furthermore, the quantification of the rock parameters at the microscale laid the groundwork for the development of an innovative numerical petrological workflow here called **Metamorphic Petrology Information System (MetPetIS)**. The latter is a new LIS able to store, manage and elaborate multidisciplinary and multiscale data collection from metamorphic basement rocks within a unique cyber-infrastructure.

As an application, two case studies have been selected for testing the methodologies described above, with the aim to derive the timescales of specific metamorphic events. In particular, paragneisses from the Serre and Sila Massifs (Calabria, Italy) were investigated applying models of compositional changes due to diffusion which are preserved in the mineral chemical profiles, by creating LISs for millimetre almandine-rich garnets. The diffusion equation solvers were developed by coding scripts in MATLAB languages using the forward finite-difference method, obtaining timescale of 1-5 Ma and fast cooling rates for the last thermal metamorphic overprint experienced by the Serre Massif rocks, whereas a timescale > 5 Ma and the slower cooling rates were obtained for the Sila Massif ones.

Riassunto

In questo lavoro sono stati sviluppati e applicati a due casi studio dei metodi innovativi di petrologia numerica, utilizzando diversi linguaggi informatici di programmazione (Model Builder; Python; Matlab), con l'intento di studiare le proprietà chimico-fisiche delle rocce metamorfiche alla microscala. Tali metodi si sono rivelati utili per analizzare l'aspetto finale delle rocce metamorfiche, che sono spesso il risultato dei fattori di contro bilanciamento tra i processi di deformazione e di "recovery", attraverso una migliore quantificazione dei parametri che definiscono la "struttura" della roccia (ad esempio, distribuzione delle dimensioni dei grani e dei minerali) così come dei volumi di roccia e delle composizioni specifiche effettivamente reagenti durante ogni fase dell'evoluzione metamorfica.

In questa prospettiva, è stato creato uno strumento di rilevamento dei bordi dei grani (cioè, **Grain Size Detection - GSD**) per tracciare automaticamente i confini dei grani e creare oggetti poligonali all'interno di una piattaforma GIS (ossia un **Geographic Information System**), utilizzando scansioni ottiche dell'intera sezione sottile come immagini di input. Tale strumento permette agli utenti di ottenere diverse informazioni dai campioni esaminati, come le superfici e le dimensioni dei grani visualizzate come mappe derivate. Queste mappe sono state poi integrate con le mappe di distribuzione mineralogica dell'intera sezione sottile classificate a partire dalle mappe a raggi X degli elementi, al fine di migliorare l'analisi della distribuzione dei grani suddividendoli per tipologia di minerale, sviluppando un ulteriore tool chiamato Min-GSD (**Mineral-Grain Size Distribution**).

L'analisi delle immagini delle rocce alla microscala è stata ulteriormente migliorata introducendo una nuova tecnica di regressione multilineare all'interno di un precedente software di analisi delle immagini (cioè, **X-ray Map Analyser - XRMA**), al fine di calibrare le mappe a raggi X per ogni minerale identificato all'interno del micro dominio selezionato dalla sottile sezione. Questo miglioramento (chiamato **Quantitative X-ray Map Analyser - Q-XRMA**) ha permesso di calcolare: (a) la concentrazione elementare in una singola fase espressa in a.p.f.u; (b) le mappe delle frazioni dei componenti mineralogici che definiscono le potenziali zonature all'interno dei minerali che presentano soluzioni solide.

Inoltre, la classificazione attraverso questo nuovo metodo di uno o più micro domini per sezione sottile, in grado di descrivere la potenziale sequenza degli equilibri metamorfici riconosciuti, è potenzialmente utilizzabile per una migliore definizione delle composizioni di equilibrio che stanno alla base di una più robusta modellizzazione termodinamica, fornendo vincoli termobarici più affidabili.

Questi vincoli termobarici sono stati qui convertiti per la prima volta in mappe *PT* (Pressione-Temperatura) mediante lo sviluppo di un componente aggiuntivo (cioè, **Diffusion Coefficient Map Creator - DCMC**) del software precedente di analisi di immagine (Q-XRMA), al fine di generare mappe dei coefficienti di diffusione dipendenti dalla composizione, integrando i diversi dati sperimentali di diffusione conosciuti in letteratura. Di conseguenza, è stato creato un **Sistema Informativo Locale completo (LIS)** per ogni minerale esaminato, che coinvolge i dati composizionali, le dimensioni dei grani, le quantità modali e i tassi cinetici, tutti potenzialmente utili per la determinazione delle durate degli eventi metamorfici.

Tutti questi metodi sopra descritti possono essere considerati parte di una nuova disciplina "**La Petromatica**", qui definita per la prima volta come la scienza che integra nuove tecnologie informatiche con diversi settori tecno-scientifici atti alla rilevazione e alla gestione di dati mineralogici-spaziali che caratterizzano le rocce alla microscala.

Inoltre, la quantificazione dei parametri di roccia alla microscala ha posto le basi per lo sviluppo di un innovativo flusso di lavoro per lo sviluppo di dati petrologici quantitativi, qui chiamato **Metamorphic Petrology Information System (MetPetIS)**. Quest'ultimo è un nuovo LIS in grado di memorizzare, gestire ed elaborare la raccolta di dati multidisciplinari e multiscalarari provenienti da rocce metamorfiche, all'interno di un'unica infrastruttura dati informatica.

Per testare le metodologie sviluppate, sono stati infine selezionati due casi studio allo scopo di derivare le durate di specifici eventi metamorfici. In particolare sono stati selezionati alcuni campioni di paragneiss dei Massicci delle Serre e della Sila (Calabria, Italia), applicando modelli di variazioni composizionali dovuti a diffusione preservati nei profili chimici dei minerali zonati, strutturando diversi LIS per i granati millimetri almandinici. I metodi di risoluzione delle equazioni di diffusione sono stati sviluppati codificando script nel linguaggio MATLAB usando il metodo delle differenze finite, ottenendo come risultato tempi di 1-5 Ma e un tasso di raffreddamento rapido per la

sovraimpronta metamorfica termica registrata dalle rocce del Massiccio delle Serre, mentre una scala temporale > 5 Ma e un tasso di raffreddamento più lento è stato ottenuto per quelle del Massiccio della Sila.

*“We can set up deliberately designed
and automated programs that work
on their own to handle boring
repetitive tasks, thus releasing our
minds to do more interesting and
creative things”*

Grinder J. & Bandler R.

1. Introduction

The birth, evolution and the gravitational collapse of the collisional belts are the core processes of any geological study designed to understand the geological-geodynamic evolution of our planet.

The reconstruction of such a history spans macro scale investigation (e.g., field, structural and hand specimen analyses), microscale observations (e.g., optical, chemical and X-ray image analyses), pressure and temperature estimates to outline *PT*-paths of rocks (e.g., conventional geothermobarometry and thermodynamic modelling) and the determination of geochronological constraints (e.g., isotopic dating or diffusion modelling).

In this view, petrographic and microstructural study of basement rocks plays a key role in understanding these processes as it can numerically fix some essential parameters for the reconstruction of the geologic and geodynamic evolution, such as Pressure and Temperature of the recognised paragenetic equilibria (e.g., [Spear & Selverstone, 1983](#); [Spear & Peacock, 1989](#); [Caddick & Thompson, 2008](#) and references therein), as well as the different Strain Rate encountered during the single evolutionary steps of the orogenic processes (e.g., [Handy, 1994](#); [Tullis, 2002](#); [Gueydan et al., 2005](#); [Cirrincione et al., 2009, 2010](#) and references therein). Recently, these studies have also been accompanied by an analysis of diffusion processes of zoned minerals (e.g., garnet), constrained by the analytical study of diffusion profiles. This approach allows to constrain the timescale of the metamorphic events ([Elliott, 1973](#); [Lasaga, 1979, 1983](#); [Zhang, 1994](#); [Ganguly, 2002](#); [Chakraborty, 2006, 2008](#); [Costa et al., 2008](#); [Ganguly, 2010](#); [Zhang, 2010](#)) as well as to give an indirect measure of the preservation of thermodynamic equilibria.

These results are all the more suitable, the more an appropriate choice of representative paragenetic equilibria have been carried out, permitting in turn to reconstruct increasingly reliable *PT* trajectories (e.g., [Stüwe & Ehlers, 1996](#); [Evans, 2004](#); [Fiannacca et al., 2012](#); [Ortolano et al., 2014a](#)).

It is evident, therefore, that geosciences are experimenting in the last years a further strong evolution to the quantification of petrological parameters such as the definition of a robust **Effective Bulk rock Chemistry (EBC)** for the single metamorphic events (e.g.,

Stüwe & Ehlers, 1996; Evans, 2004; Zuluaga et al., 2005; Zeh, 2006; Fiannacca et al., 2012; Ortolano et al., 2014a), as well as a better quantification of rock fabric parameters (e.g., grain size and mineral size distribution, Cashman & Ferry, 1988), which together numerically define the final aspect of a rock sample.

In the metapelite system, for instance, garnet represents one of the best pressure-temperature-time recorder used to infer the tectono-metamorphic history of a crystalline basement, as it forms porphyroblasts which are particularly suitable for electron or ion microprobe analyses, and for its chemical stability in a wide range of *PTX* conditions (e.g., Ganguly & Saxena, 1984; Spear, 1991, 1993; Ganguly & Tirone, 1999; Spear, 2004; Dasgupta et al., 2004, 2009; Tirone & Ganguly, 2010; Spear, 2014). For these reasons, compositional zoning in garnet is widely used by petrologists to depict thermobaric and compositional variations experienced by the rocks, and this is also possible as the slow cationic diffusion characterising garnet allows maintaining its original zoning pattern. Indeed, the slower the cationic motions, the higher the probability that garnet preserves its growth or reaction compositional zoning potentially linked with different metamorphic events. It is worth noting that a complete knowledge of how diffusion works in minerals, under different *PTX* conditions, becomes crucial in dealing with any attempt of tectono-metamorphic reconstruction based on the chemical compositions. Diffusion mechanisms are governed by the Fick's laws describing the variation in concentration owing to cationic movements. These mechanisms play a fundamental role in the development of the compositional pattern in solid solutions like garnets, as they could homogenise the compositional distribution formed during the mineral growth. As an alternative, diffusion processes could also affect an original zoning by inducing a new one along the edges of crystals, in response of a changing in the environmental variables (i.e., T , P , fO_2 , μH_2O , μSiO_2). Therefore, the magnitude of the compositional readjustment occurred due to diffusion could be used for retrieving information about the timescales of the metamorphic processes such as heating and cooling histories, from which infer the burial and exhumation rates, respectively (Chakraborty, 2006, 2008; Ganguly, 2010; Ague et al., 2013).

In the case of garnet, the determination of the timescales of geological processes could be considered easier, by the isotropic structure of the mineral itself allows treating

diffusion as an isotropic phenomenon as well. However, there are some difficulties correlated, just to mention a few, with: (i) the multicomponent character of garnet, involving diffusion up to four different components (e.g., almandine, grossular, pyrope, and spessartine); (ii) the uncertain in measuring correct diffusion coefficients linked with the uncertain of temperature and pressure estimations of particular metamorphic events; and (iii) the high compositional dependence of kinetic coefficients which forces more elaborate treatments of diffusion problems.

As garnet is affected by slow cationic diffusion rates, the choice of an appropriate Fick's equations solver represents another complication. Indeed, diffusion modelling requires huge iterative steps which can't be executed using a conventional spreadsheet (e.g., Excel) but involve more complex computer scripting through more sophisticated programming languages and software (e.g., MATLAB, Fortran, R, and similar). Moreover, there are also several hindrances beyond the issues associated with the mineralogical phase investigated, as for instance, the availability, the type and the amounts of minerals providing nutrients for the diffusive exchange (e.g., biotite or clinopyroxene for a diffusive exchange with garnet) or thin section cuts which could conceal the real chemical composition of a mineral if the latter is not cut from its centre.

Keeping in mind all of these clues, a full understanding of how the diffusion works in minerals could be inadequate without the application of a multidisciplinary approach based on a rigorous scientific investigation protocol supporting researchers in reaching their geological conclusions. In this view, the use of quantitative petrography represents an important aspect of constraining phenomena numerically, and computer science applied in geology is nowadays one of the best "partner" to obtain this purpose.

For all of the reasons above, one of the aims of this PhD work is the development of an investigation protocol based on a multidisciplinary approach allowing to determine all of the parameters required in the diffusion modelling, such as mineral grain size, composition and diffusion coefficients, to obtain the timescales of metamorphic events, using image analysis.

To acquire pieces of information about the mineral grain sizes, in this thesis has been developed an ArcGIS® toolbox (i.e., the Grain Size Detection – GSD) able to draw grain boundaries from a thin section optical scan, from which derives grain polygon features

representative of the grain surfaces (Tab. 1.1). These latter are used, then, in conjunction with another developed ArcGIS® toolbox (i.e., the Mineral Grain Size Distribution – Min-GSD) able to provide a specific mineral name per each polygon created. These pieces of information are fundamentals to choose suitable crystals, where applying diffusion modelling and to correctly setup the models to be used. For instance, the results of the thin section image processing can show a remarkable amount and distribution of an appropriate diffusive partner with garnet. If this last condition is verified, a model of a garnet fixed edge composition (i.e., the FEC model of Chakraborty & Ganguly, 1991) is suggested on the more complex variable edge composition one (i.e., the VEC model of Chakraborty & Ganguly, 1991). In both of the toolboxes created, a visual programming language integrated within the ArcGIS® software, namely the Model Builder, is used for building workflows (Tab. 1.1). This language is used for creating, managing and automatizing sequences of geoprocessing tools implemented within ArcGIS®, which are required to obtain the outputs.

With the aim to determine the chemical concentrations of the element of interest, has been developed an image analysis software (i.e., Quantitative X-ray Map Analyser) allowing to convert a qualitative raster grid image (i.e., 8 bits monochromatic image with 256 different intensities) into a quantitative format one (i.e., an array of equally sized square grid points storing an absolute numeric value). In this case, the single pixel is compared to a container inside which storing all the relevant mineral information such as composition, potential sub-phases occurrences (as in the case of zoned minerals), temperature and pressure reached by the rock, and specific kinetic coefficients related to the mineralogical phase under examination. With this purpose, Python programming knowledge, acquired during the PhD, the period is used to modify an existing image processing tool package (i.e., the X-ray Map Analyser of Ortolano et al., 2014b) interfaced with ArcGIS® (Tab. 1.1).

The maps calibrated for the elements concentrations have been further used to derive additional maps concerning the mineral components concentrations, the element diffusion coefficients computed as a function of temperature and pressure as well as the matrix of the diffusion coefficients (D) for garnet (Tab. 1.1). The usefulness of having maps containing these pieces of information consists in the possibility to draw transects

directly on the ArcGIS® project and extract all the necessary information without passing through further micro probe laboratory analyses. In this way, it is possible to extract and use different profiles from the same mineral to study the variations arising from the acting diffusion processes in a fairly straightforward and fast way.

Then, profiles extracted through this methodology can be used as inputs to define the initial and boundary conditions characterising the diffusion models to be applied. Model calculations are subsequently performed creating scripts using the MATLAB computer language (Tab. 1.1), learnt during the doctorate period, as particularly suitable for iteratively processing considerable amounts of data. Moreover, the use of multiple profiles from the same mineral allows sharpening better the timescales of metamorphic investigated events computed by diffusion modelling, spanning results to a range of values as probable as possible.

Tab. 1.1 - Summary of the tools developed

<i>Name</i>	<i>Abbreviation</i>	<i>Development Platform</i>	<i>Programming Language</i>	<i>Applications</i>
Grain Size Detection	GSD	ArcGIS®	Model Builder	
Mineral Grain Size Distribution	Min-GSD	ArcGIS®	Model Builder	
Quantitative X-ray Map Analyser	Q-XRMA	Python for ArcGIS®	Python 2.7	Every specimen of geoscientific interest
Diffusion Coefficient Map Creator	DCMC	Python for ArcGIS®	Python 2.7	
Diffusion modelling scripts		MATLAB®	MATLAB	

Once calculated the timescales associated with specific metamorphic events, assumptions can be made inherent to the geodynamic models of burial/exhumation in different tectono-metamorphic environments, defining the evolution of a crystalline basement bracketed within a specific geological time.

In this perspective, are analysed garnets from two different case studies considered representative of many geological setting and most suitable for diffusion investigations. The first one comes from the Serre Massif (Southern Calabria - Italy), located in the central portion of the Calabria-Peloritani Orogen (CPO). In this case, are investigated millimetre almandine-rich garnet crystals from several micaschists samples, showing a relict inclusion-rich core rimmed by an inclusion-poor overgrowth (Angi et al., 2010). These rocks highlight a multi-stage metamorphic evolution consisting of an orogenic cycle partly overprinted by a thermal one, both of them ascribable to the Hercynian

orogenesis. In particular, a prograde low amphibolite facies history followed by a retrograde “quasi”-adiabatic decompression and evolving towards a retrograde deep-seated shearing stage, is responsible for the development of the garnet relict core. The subsequent post-tectonic progressive emplacement of huge masses of granitoid bodies gave rise to a gradually distributed thermal metamorphic overprint which led to the formation of the static garnet overgrowth. This last evolutionary stage is followed by a low-pressure cooling path consistent with the final unroofing stage of the ancient crystalline basement complex (Caggianelli, et al., 2000a, 2000b; Caggianelli & Prosser, 2002; Caggianelli et al., 2007; Angi et al., 2010; Langone et al., 2014; Fiannacca et al., 2016).

In this tangled scenario, relaxation of garnet zoning profiles is modelled to estimate the timescales of the static event registered by the upper crust section of the southern Variscan European Belt, by quantifying the duration of the thermal perturbation.

The timescale of this specific metamorphic event is particularly constrainable by studying garnet compositional relaxation, as the high-temperature experienced by the rocks during the thermal metamorphism facilitated the occurrences of volume diffusion (i.e., intracrystalline diffusion, Watson & Baxter, 2007; Chakraborty, 2008), in opposition to the lower temperatures of the regional one. Furthermore, the presence of a static overgrowth on a relict core allows examining all of the aspects of the multicomponent diffusion (e.g., Lasaga, 1979; Loomis et al., 1985; Chakraborty & Ganguly, 1991; Kress & Ghiorso, 1993; Trial & Spera, 1994; Kress & Ghiorso, 1995; Cussler, 1997; Liang et al., 1997; Mungall et al., 1998; Costa et al., 2008; Ganguly, 2010; Zhang, 2010) without concealing any details about the shape changes of concentration profiles (i.e., the preservation of the kinetic window condition, Chakraborty, 2008).

The second case study comes from the Sila Massif (Northern Calabria - Italy) and, in particular, from a portion of the Calabria crystalline basement known in the literature as “Castagna Unit” (Dubois & Glangeaud, 1965). This unit represents a pervasively mylonitized horizon located within the Calabride continental crust involving greenschist to amphibolite facies metamorphic rocks intruded by late-Hercynian granitoids (Amodio-Morelli et al., 1976; Colonna & Piccarreta, 1977; Graeßner & Schenk, 2001).

Such a Unit registered distinct mylonitic events ascribable to the latest extensional stages of the Hercynian orogeny ([Sacco, 2011](#)).

In this case, are investigated millimetre almandine-rich garnet crystals from different mylonitic gneiss samples exhibiting garnets with a “*quasi*”-absent crystal zoning, probably reflecting a long residence time at high depths. A flat compositional profile in garnet is not an appropriate condition for applying diffusion models, as no kinetic information is preserved. However, a retrograde zoning along the crystal edges attributable to the late-Variscan exhumation steps is recognised, constituting a suitable example for retrieving the cooling rates by using diffusion modelling.

Furthermore, the peculiar development of this garnet zoning allows treating compositional changes as a result of an efficient binary interdiffusion with an appropriate mineral phase, rather than a more complex n -multicomponent one. Such a condition permits to calculate a single diffusion coefficient (i.e., an effective binary diffusion coefficient - EBDC) avoiding to simultaneously compute nine different ones implying considerable saving of computational resources.

Since both the first and the second case studies constitute different portions of the same orogen, yielded results of the timescales of the specific metamorphic events contribute at defining a clear temporal framework of the tectono-metamorphic evolution of the investigated crystalline basement, which represents a relict of the original southern European Variscan belt.

Finally, the applied multidisciplinary protocol was standardized within a GIS software platform to manage and store all the dataset collection, laying the groundwork for the development of a new **Local Information System** (LIS - i.e., an information system accompanied by specific toolkits). This latter was designed primarily to support some capabilities of **Geographic Information Systems** (GIS), although their primary function is the reporting of statistical data rather than the analysis of geospatial ones ([Oakford & Williams, 2011](#)). This new LIS, named **Metamorphic Petrology Information System** (MetPetIS), has the aim to structure a database queryable and potentially interoperable for more fruitful comparisons among metamorphic petrology data collection carried out in different parts of the world.

1.1 Aims

The main goals of this work are:

- Create a first image analysis tool able to construct grain boundary maps and combine them with mineral classification maps for extracting both grain and crystal size distribution information (i.e., GSD and Min-GSD in [Tab. 1.1](#)) useful to set up each diffusion model properly ([Fig. 1.1](#)).
- Create further image analysis tools (i.e., Q-XRMA and DCMC in [Tab. 1.1](#)) able to define a petrological database through the derivation of mineral maps, storing all relevant information such as atomic composition, end-member concentration, temperature and pressure experienced by the rock, and specific element diffusion coefficients ([Fig. 1.1](#)).
- Use the mineral maps of the petrological database created to extract all of the pieces of information required to make diffusion model calculation scripts ([Tab. 1.1](#)) by using the MATLAB programming language ([Fig. 1.1](#)).
- Define a replicable investigation protocol applicable in all fields of petrological interest.
- Apply the developed tools on different case studies to (a) determine the timescales of metamorphic events, (b) to unravel the geological history and (c) to reconstruct the geodynamic evolution of a crystalline basement ([Fig. 1.1](#)).
- Construct a new LIS (MetPetIS) able to store, manage and elaborate multidisciplinary and multiscale data collection from metamorphic basement rocks through a unique cyber infrastructure ([Fig. 1.1](#)).

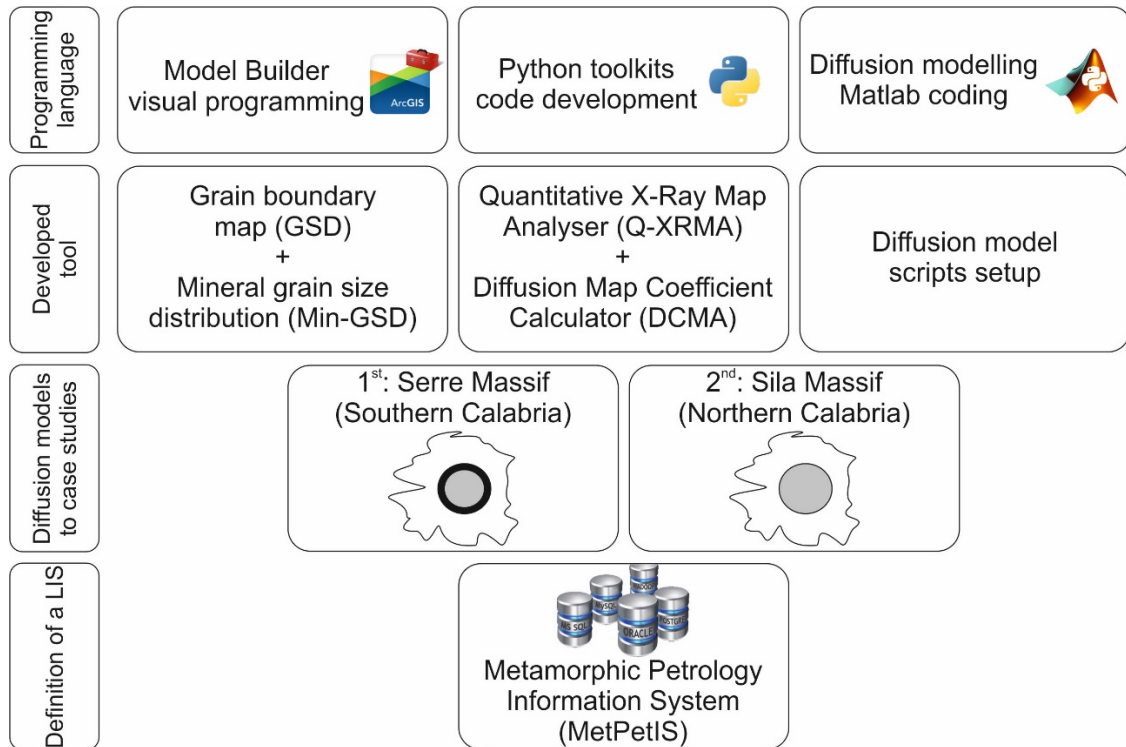


Fig. 1.1 - Schematization of the sequential steps adopted to achieve the aims of the PhD project.

2. “Petroomatics” and numerical petrology supported by image analysis

2.1 General outlines

The magnitude of the compositional readjustment recorded by minerals, as a result of diffusion mechanisms acting during a change in the intensive variables or as a long residence time at specific high PT conditions, is controlled by several factors inherent to the mineral itself such as initial compositional gradient, grain size and the element kinetic diffusion coefficients. It is worth noting that to deduce the timescales at which these mineral compositional variations occurred at specific metamorphic events, all of the factors mentioned above must be known.

Indeed, the diffusion equation explaining the compositional changes over time within a mineral can be expressed in a general form as follow:

$$\text{Compositional readjustment} \left(\frac{\partial C}{\partial t} \right) = D \left(\frac{\partial^2 C}{\partial x^2} \right) \quad (\text{Eq. 1})$$

Diffusion coefficient
Chemical gradient

Where C is the element concentration, D is the kinetic diffusion coefficient of an element, x is the space coordinate for the specific mineral grain size and t is time. It follows from *Eq. 1*, that the compositional changes are as effective as the smaller the size of the mineral grains, the faster the cationic diffusion motion and the larger the chemical gradient. Since time represents the unknown variable to be unraveled, the quantification of mineral composition, mineral grain size and element diffusion coefficients was the focus of the first part of this work.

With the advent of the digital era and increasingly performing computers, the ability to quickly obtain and quantify these parameters through the iterative execution of numerous and complex calculations has become increasingly larger. In particular, in recent years, the use of image processing techniques for studying rocks, has played a key role in the field of metamorphic petrology and all of the disciplines of geosciences in the broadest sense (e.g., [Launeau et al., 1994](#); [Gu, 2003](#); [Coutelas et](#)

al., 2004; Tinkham & Ghent, 2005; Friel & Lyman, 2006; Tarquini & Favalli, 2010; Ortolano et al., 2014a, 2014b; Belfiore et al., 2016).

In this view, the quantitative extraction of the grain size distribution through the image analysis of thin sections optical scans was one of the goals of this research. For this purpose, the Model Builder integrated within the ArcGIS® software, equipped with ArcInfo license and supporting spatial analyst and data management extensions, has been chosen as the visual programming language to design workflows and create, manage and automatize sequence of operations, by the development of a specific Arc Toolbox (namely the Grain Size Detection.tbx, see below). As a result, this tool led obtaining grain boundary and grain polygon maps from which derive grain size frequency classes.

The next step was based on the extrapolation of mineral compositional data through the image processing of the elemental X-ray maps. With this aim, the Python code at the base of an image analysis software (i.e., the X-ray Map Analyser of Ortolano et al., 2014b), primarily developed to construct mineral maps and to highlight potential mineral sub-phases using some functions built-in ArcGIS®, was modified and enhanced in order to insert new analytical cycles allowing, respectively: a) to calibrate and convert qualitative element raster grid images per detected mineral phase (i.e., 8 bits images with 256 intensity levels) into qualitative format ones, where each pixel (i.e., the grid point) stores the concentration as an absolute numeric value (expressed in atomic per formula unit); b) to obtain mineral component maps, as in the case of a solid solution, showing the reciprocal distribution within each detected mineral sub-phases. In this way, every segment drawn on the map with the use of the ArcGIS® functions can be considered as the same of a microprobe transect, without passing through further laboratory analyses. Both of these image analytical methods mentioned above will be described below, and they could be considered as a part of the "***Petromatics***", here defined for the first time as *the science which promotes an integrated multidisciplinary systematic approach to develop tools and techniques for detecting, handling, integrating, processing, analyzing, archiving and distributing textural-related spatial*

minerochemical data characterising rocks at the micro scale with continuity and in a digital format.

2.2 Grain Size Detection (GSD): a new ArcGIS® toolbox to construct grain size distribution by drawing mineral grain boundaries on thin section scans

In recent years, geographic information systems (GISs) have been increasingly found a wide variety of applications in solving various geoscientific problems (e.g., [Li et al., 2008](#); [DeVasto et al., 2012](#); [Ortolano et al., 2014a, 2014b](#); [Belfiore et al., 2016](#); [Fiannacca et al., 2017](#)). The strength of a GIS relies on the possibility to manage and overlap big data structured in database potentially interoperable and in the capability to integrate different spatial information. Moreover, a GIS is fully implemented with several tools and scripts for spatial and image analysis allowing users to investigate data in many different ways. For all of the reasons above, the use of GIS is particularly indicated for extrapolating, handling, and analysing fabric information from deformed rocks. In literature, there are many examples of tool used to quantify rock fabric characteristics through the automatic images digitalization (e.g., [Sardini et al., 1999](#); [Perring et al., 2004](#); [Martínez-Martínez et al., 2007](#); [Beggan & Hamilton, 2010](#); [Berger et al., 2010](#)), but most of these constrain the users to apply specific laboratory equipment or owner codes.

Instead, the use of an accessible development platform as the Model Builder of the ArcGIS® software, where the user can further edit and manipulate every sequence of operation as a function of the specific needs, can help to overcome these hindrances. For instance, [Li et al. \(2008\)](#) addressed the construction of mineral grain size distribution maps on quartz arenite samples, by developing an ArcGIS® toolbox which requires three different-oriented optical thin sections input images, to detect grain boundaries. Such a choice has been made by the authors to highlight the contrast between the edges of neighbouring grains. However, the operative sequence developed by [Li et al. \(2008\)](#) well works with optical images characterised by big grains of one mineral type with evident and sharp boundaries but fails when thin section scans are composed prevalently of tiny and polymineralic grains.

[DeVasto et al. \(2012\)](#) reduced the number of the input thin section images required by the tool described above, to achieve the grain detection result also on

polymineralic rock samples. Such a reduction was possible thanks to a preprocessing image phase realised by the application of the Adobe Creative Suite® packages (i.e., Photoshop®, Illustrator® and Bridge®). Nevertheless, despite the lesser number of input images required to execute the tool, the obtained results are not advantageous when the input thin section scan is composed of tiny grains. This effect is because the toolbox developed by Li et al. (2008) was primarily designed and tested on quartz arenite samples where crystals are characterised by sharp and evident contacts each other.

In this thesis, the construction of the grain boundary maps is based on the acquisition of high-resolution thin section optical scans. For this purpose, an Epson V750 Pro dual lens system scanner at the Geoinformatics and Image Analysis Lab of the Biological, Geological and Environmental Sciences of Catania University was used. The choice of the scan resolution was made taking into account the image quality and the related processing time. Indeed, high-resolution scans (e.g., 9600 dpi) highlights straight grain boundaries better than lower ones but requires big hard drive space on a computer and more elaboration time as the pixel matrix could be huge (e.g., 15000 x 9300 pixels). Counterwise, low-resolution images (e.g., 300 dpi) could homogenise small neighbouring grains in a unique one saving image processing time as the smaller pixel matrix (e.g., 680 x 375).

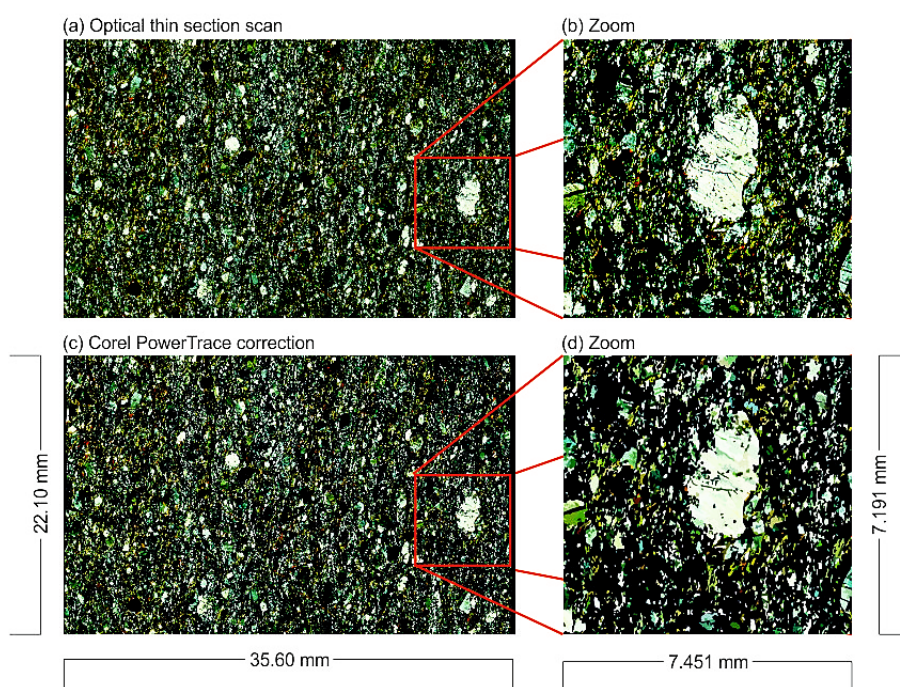


Fig. 2.1 - Effect of the pre-processing phase on the input thin section scan of a paragneiss sample: (a) original optical thin section; (b) zoom of an area containing a large plagioclase crystal; (c) result of the PowerTrace Function of Corel Draw® Software; (d) same zoom as in b.

Keep in mind all of these reasons, the input images (usually 38.4 x 20.6 mm in size) used to construct mineral grain size maps were acquired with a resolution of 4200 dpi (e.g., Fig. 2.1a, b), because considered a good compromise between image quality and hard drive space allocation on a common personal computer.

Such a choice was made after several attempts of different scanner setting based on a population of 100 samples where the procedure described below has been applied (some examples are shown in APPENDIX A1). Every thin section scan was successively subjected to a preliminary pre-processing phase through the Corel Graphic Suite® software, to highlight grain boundaries better (Fig. 2.1c, d). This step usually consists on brightness and contrast corrections followed by the application of the PowerTrace function of the Corel Draw® which allows reducing noise background as well.

Once the thin section scan has been subjected to this preliminary step, the output was used as input image of the developed **Grain Size Detection (GSD)** toolbox. The latter is subdivided into three different analytical routines (Fig. 2.2): (i) a pre-edge detection filter phase, able to distinguish grains from boundary lines which are identified with several colors as a consequence of an iso-cluster unsupervised classification; (ii) an edge detection phase, able to select and refine grain boundaries; (iii) a grain polygons creator, able to make polygons features with specific areas and perimeters. In the next sections will be presented the sequential operative steps to be followed for obtaining the outputs.

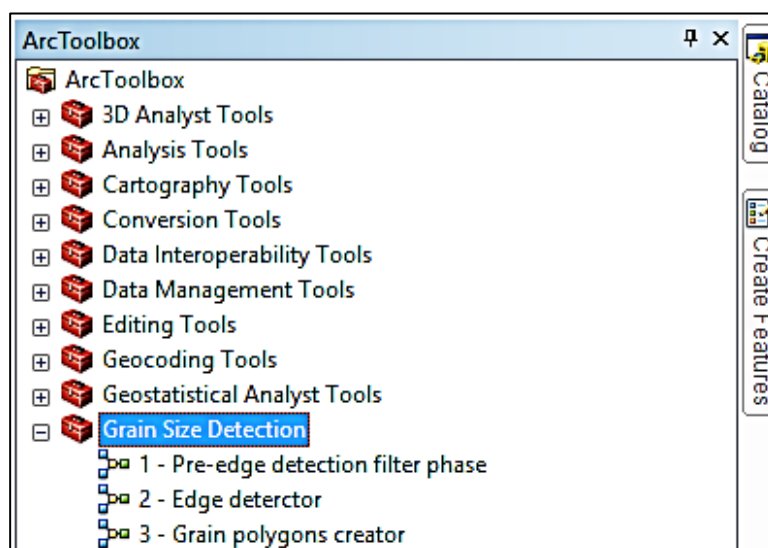


Fig. 2.2 - Screenshot of the routine composing the Grain Size Detection toolbox.

2.2.1 Pre-edge detection filter phase

This preliminary filter phase is applied to identify and successively isolate grains and boundary lines. It is subdivided in a sequence of different steps (Fig. 2.3) passing through a first low-pass filter consisting of a rectangular 3-by-3 cell smoothing on a raster, which reduces the significance of abnormal cell values (i.e., the pixels).

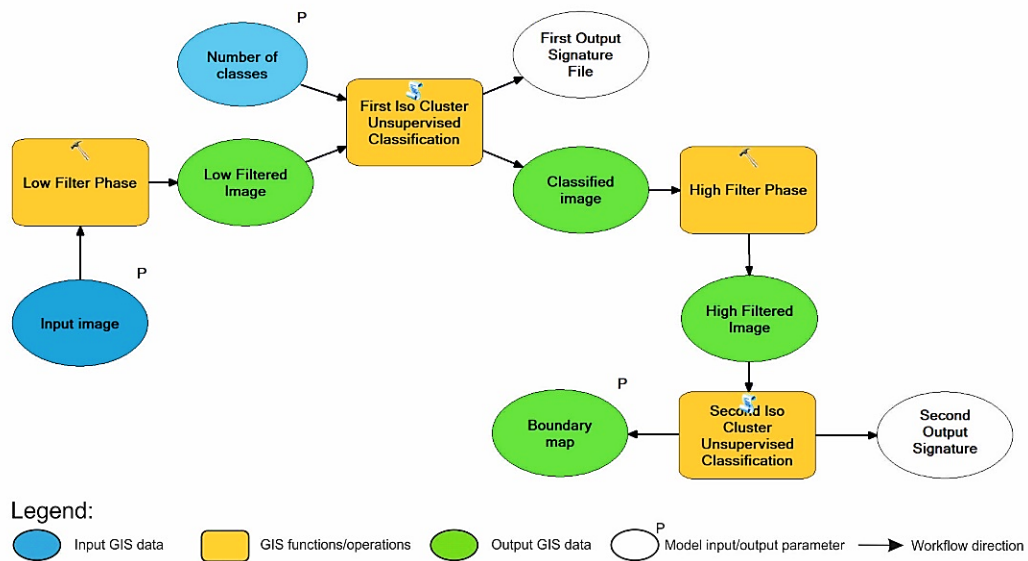


Fig. 2.3 - Flow chart of the Pre-edge detection filter phase routine.

In the whole, the filtering procedure calculates new cell values over every input pixel (Richards, 1986). A low filtering phase smooths the input data (Fig. 2.4, Fig. 2.5a) by reducing local variation and eliminating noise, by calculating the mean value for each 3x3 neighbourhood (Fig. 2.4, Fig. 2.5b). In such a way, the higher and lower values enclosed in each neighbourhood will be averaged, decreasing the extreme values in the data (Fig. 2.4).

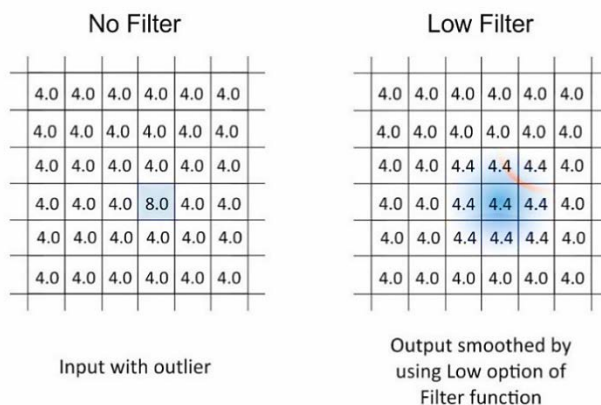


Fig. 2.4 - Schematic representation of the low filter principle used in the procedure: a circle geometry with 3*3 cells per side where any cells whose centre falls inside the radius of the circle will be included in processing neighbourhood. Since the mean is being calculated from all the input values, the highest value in the list, which is the value 8 of the processing cell, is averaged out.

After this step, an iso-cluster unsupervised classification is used to determine the characteristics of the natural groupings of cells in a multidimensional attribute space (Fig. 2.5c). By default, the number of grouping classes is ten because it results in the best number to identify all of the boundary lines and grains. However, users can define their own classes number. The classified image obtained is successively subjected to a high pass filter (Fig. 2.6) allowing to enhance the edges of the subdued features in a raster (Fig. 2.5d). The high filter function identifies the edge zones marked by a sharp contrast between a cell's values and its neighbours within a raster pixel matrix, weighting these values to remove low-frequency variations and highlights the boundary between different regions (Richards, 1986).

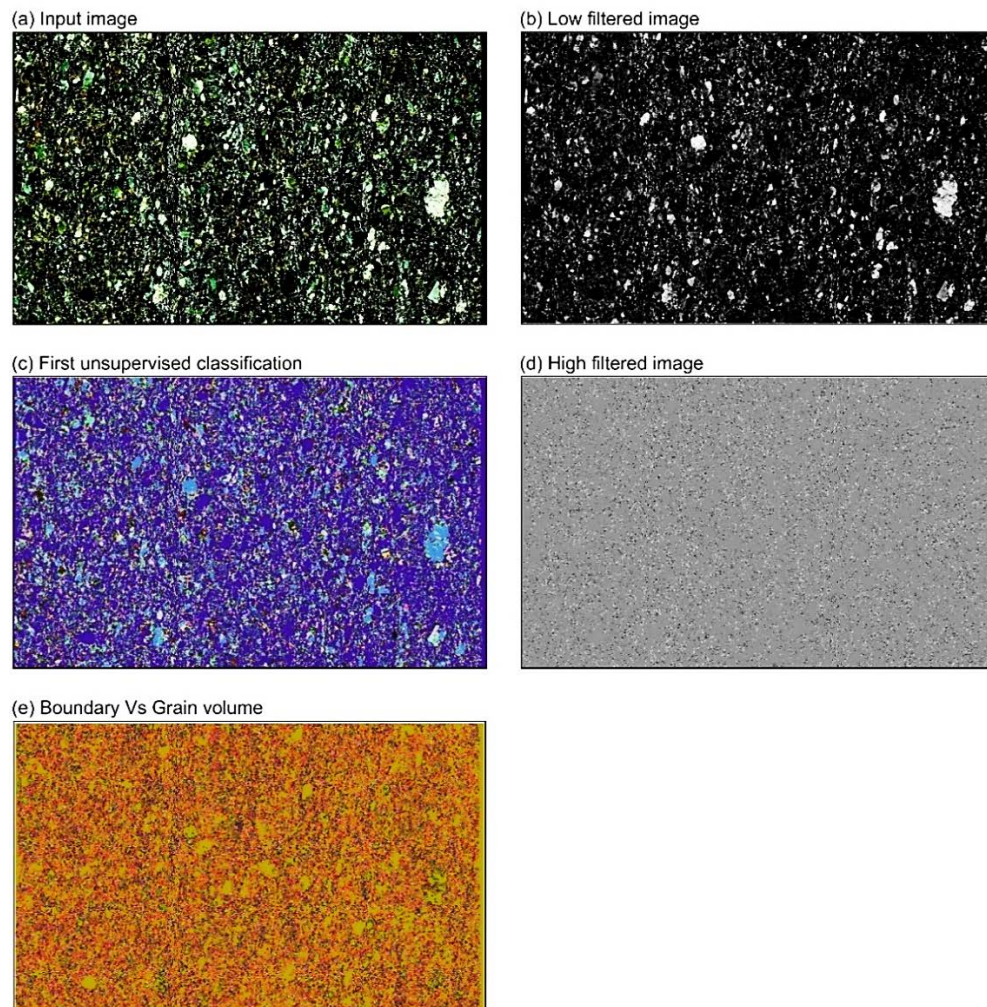


Fig. 2.5 - Schematization of the single steps of the Pre-edge detection routine: (a) pre-processed input thin section scan; (b) low filtered image; (c) the unsupervised classified image; (d) high filtered image; (e) the final output of the tool distinguishing grain boundary lines with different color from the grain background, represented by a unique colour (i.e., yellow).

After the edge- enhancement filter, a second iso-cluster classification is applied for grouping each grain in a unique background class, whereas all of the boundary lines will be consolidated in the remaining ones. The obtained output (i.e., boundary map in Fig. 2.3), showing grain edge contacts emphasised with respect the grain background (Fig. 2.5e), is successively used as the input file of the second analytical routine.

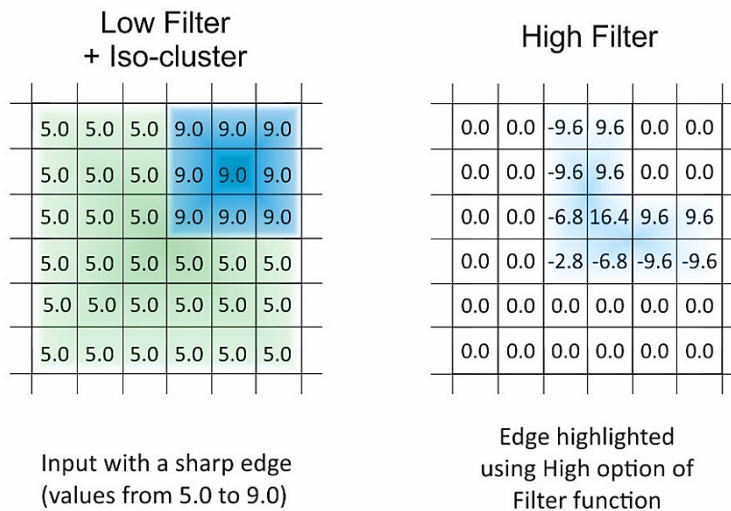


Fig. 2.6 - Schematic representation of the high filter principle used in the procedure: the input z-values of the straight contrast identified along the edge zones are weighted to remove low frequency variations and highlights the boundary between different regions. By giving negative weights to its neighbours, the filter accentuates the local detail by pulling out the differences or the boundaries between objects.

2.2.2 Edge detector

The second analytical routine consists in the making of a single feature class representing grain boundary lines, through the use of five different sub-procedures (Fig. 2.7) from which successively derive grain polygons.

It can be summarised by a first reclassification of the classes identified in the first analytical routine (Fig. 2.8a). In other words, this step is made to group every class representing boundary lines in a unique one (e.g., if the classes identifying grain boundaries are 1, 2, 3, 4, 6, 7, 8, 9, 10, all of this value will be substituted by the same number representing a unique class as, for instance, 1, 1, 1, 1, and so on). Indeed, the reclassify function updates the cell values in a raster, through the definition of a remap table that controls how the values will be reclassified, by the substitution of the old cell values with new ones. As a result, a raster with only two

classes (i.e., the boundary class and the grain background class) is obtained (Fig. 2.8b).

The second step is used to extract only the class representing the grain boundaries (Fig. 2.8c) by selecting it with a specific Structured Query Language (SQL) statement in the extraction tool. Since the obtained output consists in significantly large boundaries due to the overlapping pixels primarily forming different classes, a focal variety filter performed with a rectangular shape on a 3x3 pixel neighbourhood and a thinning line function are executed.

The focal variety statistics is used to homogenise boundaries (Fig. 2.8d) where missing data occurs (e.g., a missing pixel which interrupts the continuity of a line), calculating for each input cell location the number of unique values within the specified neighbourhood around it.

Whereas, the role of the thinning function consists of thin linear features by reducing the number of pixels representing the width of the boundary lines. The output thinned image contains, once again, the boundaries class and a grain background one (Fig. 2.8e).

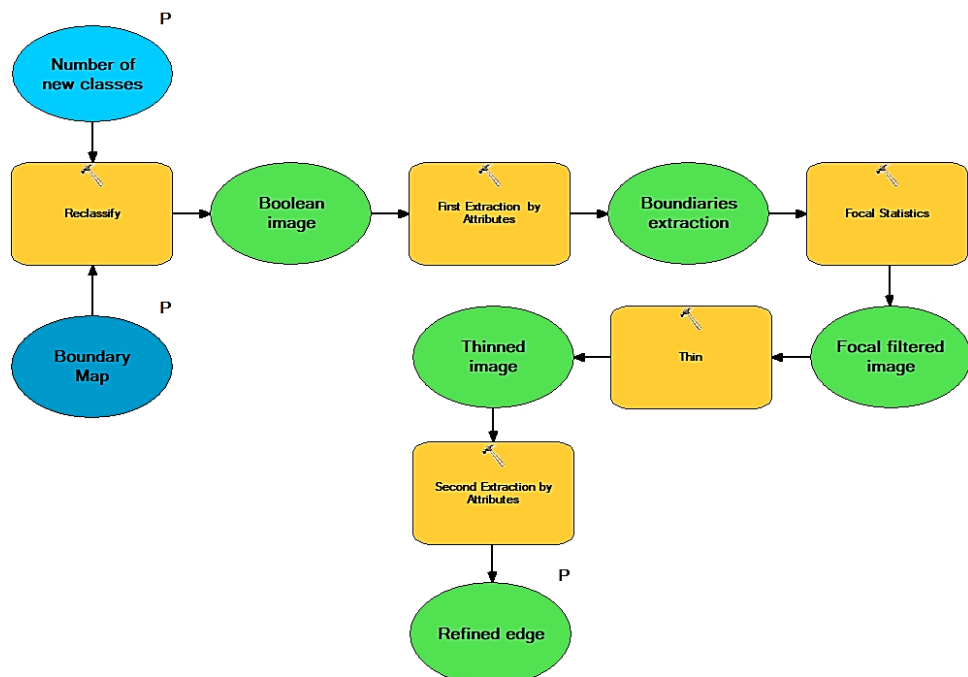


Fig. 2.7 - Flow chart of the Edge detector filter phase routine. Legend as in Fig. 2.3.

For this reason, the final step of this analytical routine consists of a second extraction of the class of interest (i.e., that related to the grain boundaries) using an SQL statement similar to the first extraction. The final output image (Fig. 2.8f) is a raster where the lines representative of the grain boundaries are highlighted as a result of the sequential operative steps of the second analytical routine.

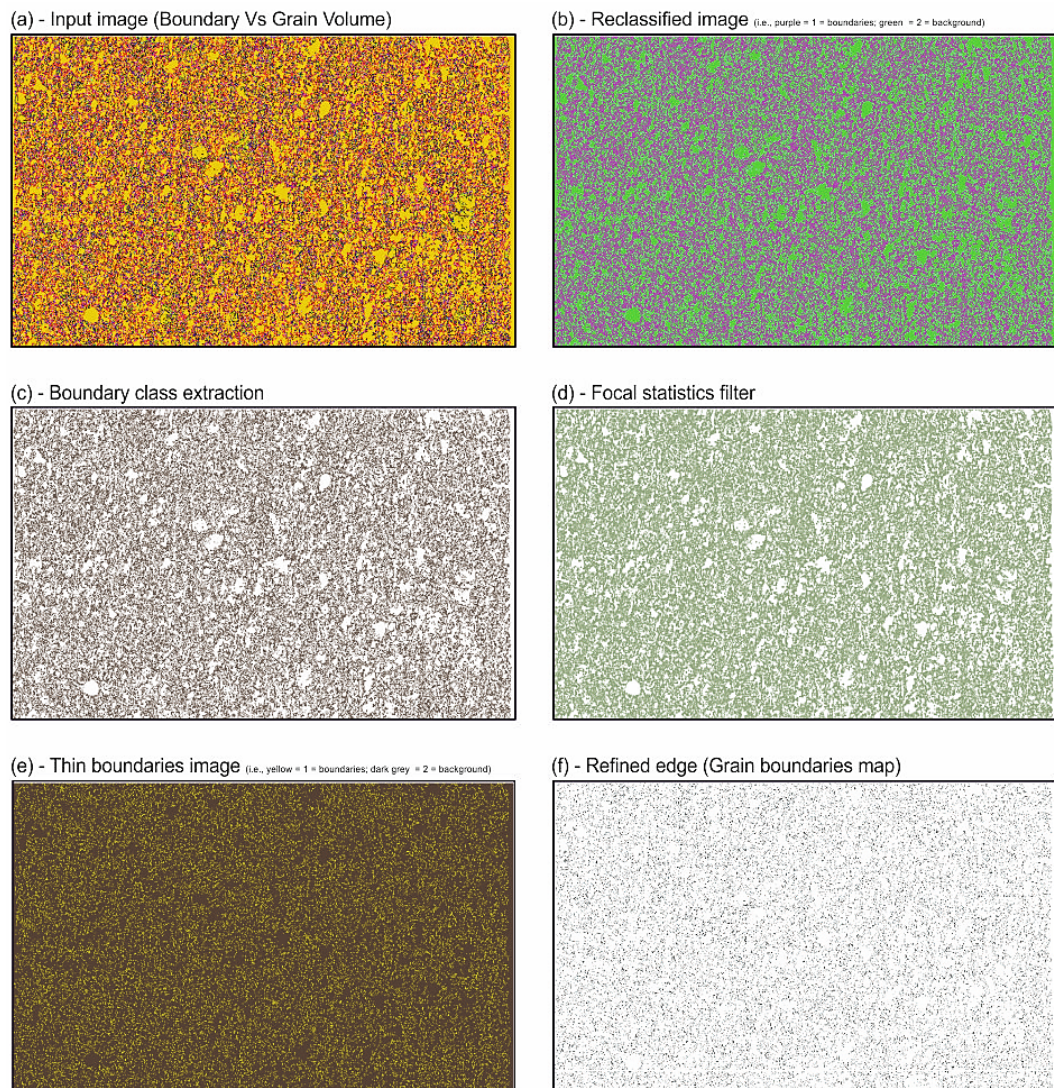


Fig. 2.8 - Schematization of the single steps of the Edge detector routine: (a) input image obtained as the output of the Pre-edge detection routine; (b) reclassified Boolean image; (c) extraction of the boundary class; (d) focal variety filtered image; (e) boundary image after the application of the thin function for reducing the thickness of the focal variety filtered image; (f) the output image obtained via the extraction of the boundary class.

2.2.3 Grain polygons creator

The last analytical routine can be summarised in two basic steps (Fig. 2.9). The first one consists of a raster conversion function which takes the grain boundaries map as the input data (Fig. 2.10a), to derive a shapefile which spatially describes boundary line features (Fig. 2.10b).



Fig. 2.9 - Flow chart of the Grain polygons creator routine. Legend as in Fig. 2.3.

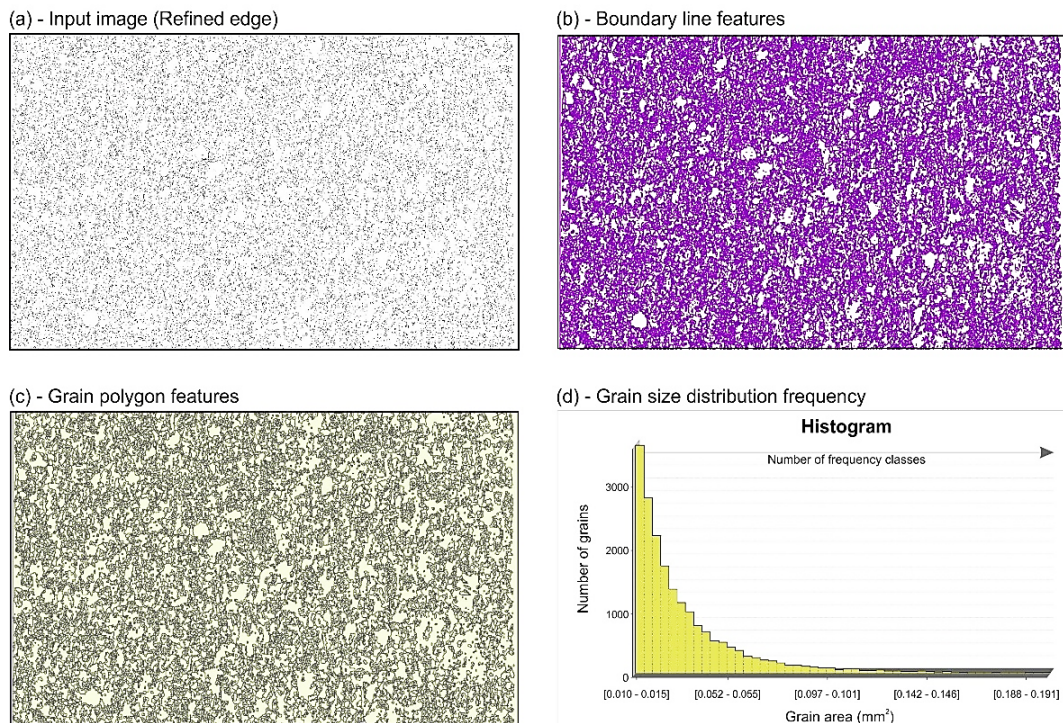


Fig. 2.10 - Schematization of the single steps of the Grain polygons creator routine: (a) input image obtained as the output of the Edge detector routine; (b) Grain boundary polyline shapefile; (c) polygon shapefile created via a feature to polygon conversion; (d) histogram of the grain polygon as a function of their shape area.

Such a function allows to simplify the output line features by smoothing corners or not (Fig. 2.11). In the GSD toolbox, the default option is not to simplify features to preserve, as much as possible, the real shape of the grain boundaries.

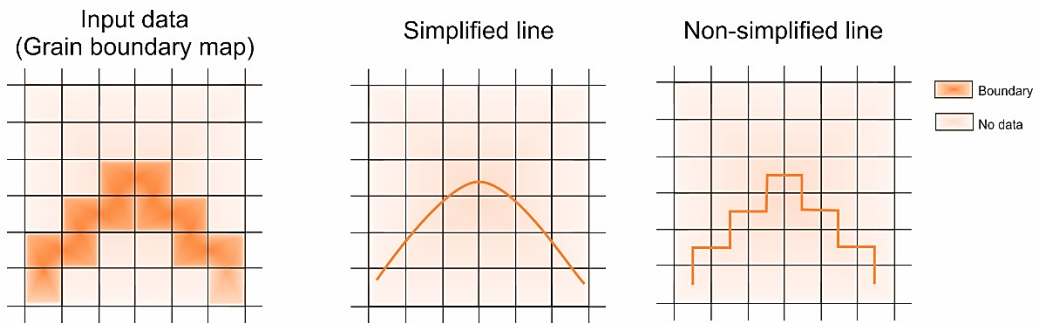


Fig. 2.11 - Difference between a smoothed (i.e., simplified) vs. a non-smoothed (i.e., non-simplified) polyline feature.

The second one, creates a new feature class containing polygons (Fig. 2.10c) derived where the boundary lines enclose an area (Fig. 2.12). However, a very poor homogenization in the real number of grains can affect the output where the boundary lines have no intersections able to define an area (Fig. 2.12), as probably due to a not perfect ab-initio image contrast correction. Despite this, results obtained from a population of 100 samples (see APPENDIX A1), highlights that the number of the missing polygons representative of the real grains are lesser than 1-2 % of the total thin sections-forming crystals.

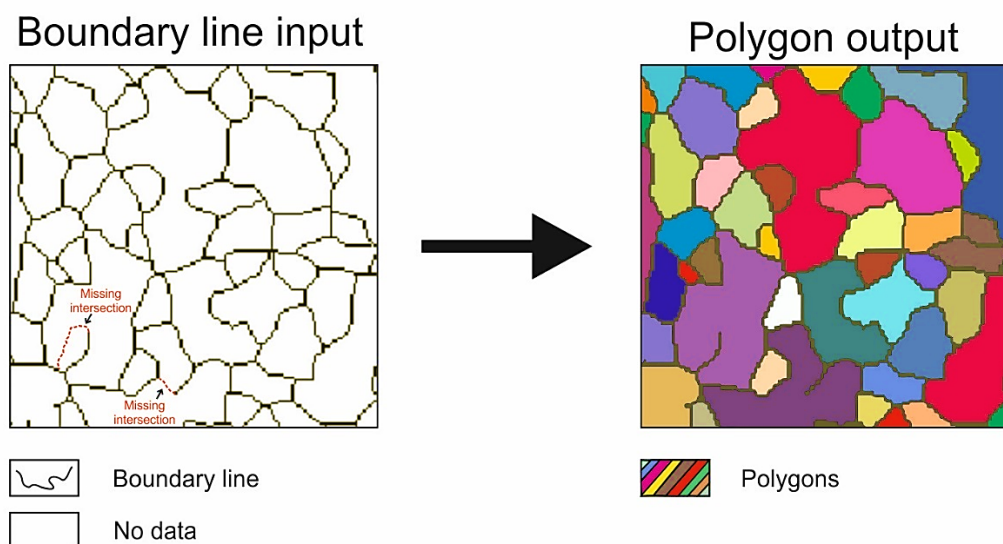


Fig. 2.12 - Effect of a non-completed boundary regarding the creation of polygon features

Once polygons are created, a measure of their area and perimeter is stored in the associated attribute table and then, can be used to build a grain size frequency diagram. Figure 2.10d shows the result obtained by the developed tool in the form

of the grain size distribution frequency, using [figure. 2.1c](#) as the input image. The distribution takes into account fifty grain size classes based on the area enclosed inside the polygons, highlighting as the investigated sample is prevalently constituted by tiny grains (i.e., class 1 in [Fig. 2.10d](#)) with an area ranging from 0.01 to 0.015 mm², whereas the larger grains (i.e. 0.10 to 0.19 mm²) are clearly lesser in number.

2.2.4 Final remarks

The developed GSD toolbox represents a valuable asset for investigating the fabric characterising deformed rocks, especially those formed by many tiny grains. Indeed, the tool permits to detect boundaries of all the grains having an area < 0.01 mm² as well. This result represents a significant improvement in the quantitative determination of the rock fabric information by the automatic digitalization of optical images.

As to the topic of diffusion, such a result is advantageous to a priori select the appropriate grains where study the elements diffusion behaviour if other conditions are satisfied (e.g., if mineral can be considered cut from its centre). Indeed, according to [Caddick et al. \(2010\)](#), smaller grains change their core composition faster than the larger ones when diffusion proceeds, losing any information about the original growth chemical history. Therefore, studying the diffusive element behaviour on several grains with different grain sizes and compositions can improve any thermobaric reconstruction as well as the timescale determination of geological events.

2.3 Quantitative X-ray Map Analyser (Q-XRMA): A new GIS-based statistical approach for Mineral Image Analysis

The second fundamental parameter that must be known to apply diffusion modelling is the chemical composition of the mineral components along different potential mineral sub-phases, where chemical gradients could exist and therefore be modified by diffusion. On the whole, microprobe spot analyses are performed to find out these pieces of information, but recently, it is getting more use of software treating X-ray elemental maps as containers of chemical data stored as absolute

values within each image-forming pixel. Indeed, the increasingly requested application of numerical petrology in the field of geosciences answers to the growing need to support qualitative geological and petrographic observations with a series of quantitative information. The acquisition and analysis of X-ray elemental maps, in particular, can be helpfully applied in the field of the mining industry, cultural heritage, forensic geology and even more in the field of basic scientific research, allowing, in turn, more fruitful comparisons among data collection carried out in different parts of the world from similar lithotypes, or from the same area, after the use of the various data acquisition methods.

In this view, several manufacturers of micro analytical devices have invested a great deal in the development of increasingly powerful software packages with the aim to obtain quantitative chemical information based on assigning numerical values to interdependent variables, by attempting to replicate the reality mathematically. Nevertheless, these new tools are dedicated to specific devices, and the generated output files are often characterised by proprietary formats that limit their use, making them difficult to be processed for additional purposes.

In this perspective, a new ArcGIS®-based tool has been developed in Python programming language with the aim: a) of acquiring quantitative information of petrological interest; b) to overcome the limits mentioned above using a device-independent stepwise controlled procedure. Moreover, the use of ArcGIS® permits to flexibly manage a large number of data also through the overlaying of data from different sources, allowing at the same time their potential storage in an interoperable data infrastructure (e.g., [Ortolano & Zappalà, 2012](#)).

In general, image processing in material science is mainly based on multivariate statistical analysis of EDS/WDS X-ray multispectral images, whose channels are raster images (typically, 8-bits images with 256 intensity levels) that record the distribution of chemical elements. It is one of the main techniques routinely applied for the interpretation of many geo-petrological processes (e.g., [Coutelas et al., 2004](#); [Ortolano et al., 2014a](#); [Belfiore et al., 2016](#)). The extensive use of such a technique is also due to the development of several semi-automatised tools classifying mineral phases and quantifying modal parameters from selected thin

section micro-domains (e.g., [Launeau et al., 1994](#); [Gu, 2003](#); [Tinkham & Ghent, 2005](#); [Friel & Lyman, 2006](#); [Tarquini & Favalli, 2010](#); [Ortolano et al., 2014b](#)).

Others tools also use a very efficient clustering algorithm (i.e., K-means), with the aim to obtain several homogeneous groups of pixels automatically bounded by a mask (e.g., [Cossio et al., 2002](#); [Lanari et al., 2014](#)). Specifically, software such as Petromod ([Cossio et al., 2002](#)) and XMapTools ([Lanari et al., 2014](#)) treat, indeed, each of these groups of pixels as an X-ray spectrum intensity array, representative of a single mineral phase, where the element pixel array is a function of its chemical concentration. These software are focusing on linear regression functions allowing to obtain new sets of calibrated X-ray images, converting a qualitative raster image into a calibrated grid format (i.e., an array of equally-sized square grid points storing the concentration as an absolute numeric value) ([Cossio & Borghi, 1998](#); [Togami et al., 2000](#); [Cossio et al., 2002](#); [De Andrade et al., 2006](#); [Lanari et al., 2014](#)).

It is evident that in this view, the used calibration techniques represent a crucial aspect of the quantification processes of the raster images. Therefore, these methods require a careful control of each prediction model for obtaining physically significant results.

In this new developed ArcGIS®-based image processing tool, called **Quantitative X-ray Map Analyser** (i.e. Q-XRMA), the calibration procedure relies on a multilinear regression technique that mirrors the interdependent element relationship constrained by the stoichiometry of the minerals. The procedure requires an appropriate number of control spot analyses (i.e., internal standards) providing several test indexes that allow a fast check of the calibration reliability. The code is based on an earlier image-processing tool (i.e., X-ray Map Analyser, [Ortolano et al., 2014b](#); [Zappalà, 2014](#)) primarily designed for classifying the minerals from X-ray element maps through two analytical cycles. The native Python code has been here deeply revised and subdivided in three different cycles ([Fig. 2.13](#)), now embedding: (a) a new second analytical cycle based on a multilinear regression algorithm allowing obtaining X-ray grid images for each single recognised mineral phase; (b) a third analytical cycle that uses calibrated maps for the extraction of potential zoning patterns of complex solid solution mineral phases.

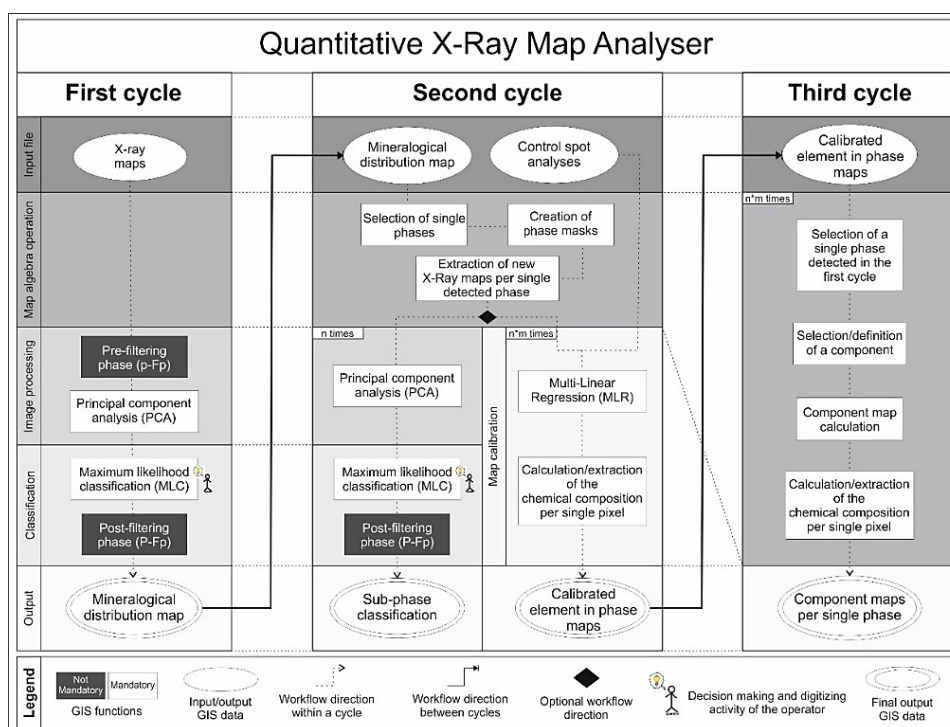


Fig. 2.13 - Simplified flow charts of the GIS-based image-processing procedure (from Ortolano et al., under review).

The assisted semi-automated procedure allows, in turn, the extraction of a huge amount of data automatically stored within queryable tables.

As a test, the new tool was applied to amphibolite-facies garnet-bearing micaschists, by calibrating X-ray maps for both anhydrous (i.e., garnet and plagioclase) and hydrous (i.e., biotite) phases. Comparing calibration results with electron microprobe analyses performed at the same spot, a good fit with a satisfactory average standard deviation of about 2% was obtained. This new GIS-based software can thus be usefully applied in many fields of petrological and material science investigations. Moreover, the enormous quantitative data extraction opens new perspectives for the development of a thin section micro-chemical database that, integrated within a GIS platform, can be linked with the others main geoscientific international databases.

2.3.1 Algorithms

Ortolano et al. (2014b) developed in Python programming language a semi-automated image processing procedure based on several functions implemented in ArcGIS®. Such a procedure, relied on multivariate statistical analysis of X-ray maps, was designed for classifying chemically homogeneous zones as well as for

extracting quantitative information, such as mineral modes, from high-contrast pseudo-coloured images (e.g., [Ortolano et al., 2014a](#); [Belfiore et al., 2016](#)).

The Python code of this procedure was implemented with two analytical cycles: (a) the first one able to classify all the recognizable phases within the entire selected domain ([Fig. 2.13](#)); (b) the second one useful to deepen the analysis of the previously recognised phases, emphasizing potential sub-phases occurrence, such as those related to mineral zoning ([Fig. 2.13](#)). Both cycles use **Principal Component Analysis (PCA)** together with **Maximum Likelihood Classification (MLC)** algorithm to generate several outputs required for obtaining graphical results.

Despite a significant amount of information obtained with this image processing procedure, it lacked an algorithm able to transform the derived qualitative raster X-ray image for classified phase, into a quantitative format one.

Therefore, a new Python code has been here implemented with the main aim to cyclically calibrate sets of X-ray maps for each classified phase using the ArcGIS® licensed software available at the Geoinformatics and Image Analysis Lab of the Biological, Geological and Environmental Sciences of Catania University.

In this view, the first cycle ([Fig. 2.14](#)) remained unchanged, with the aim to use the classification of the entire selected domain for obtaining new sets of the original X-ray maps filtered per detected mineral phase.

The second cycle ([Fig. 2.15](#)) was instead deeply modified, introducing a multilinear regression technique with the aim to predict the element concentration value per each pixel (expressed in atom per formula unit – a.p.f.u) within a specific phase, by using some control spot analyses for the calibration.

This step was crucial to implement in turn, a third analytical cycle ([Fig. 2.16](#)) with the aim to derive maps of mineral end-members potentially highlighting quantitative chemical variation within the investigated phases.

In the following sections, will be described the main steps of the three analytical cycles, with particular attention to the adopted multilinear regression technique (see [section 2.3.1.2](#)).

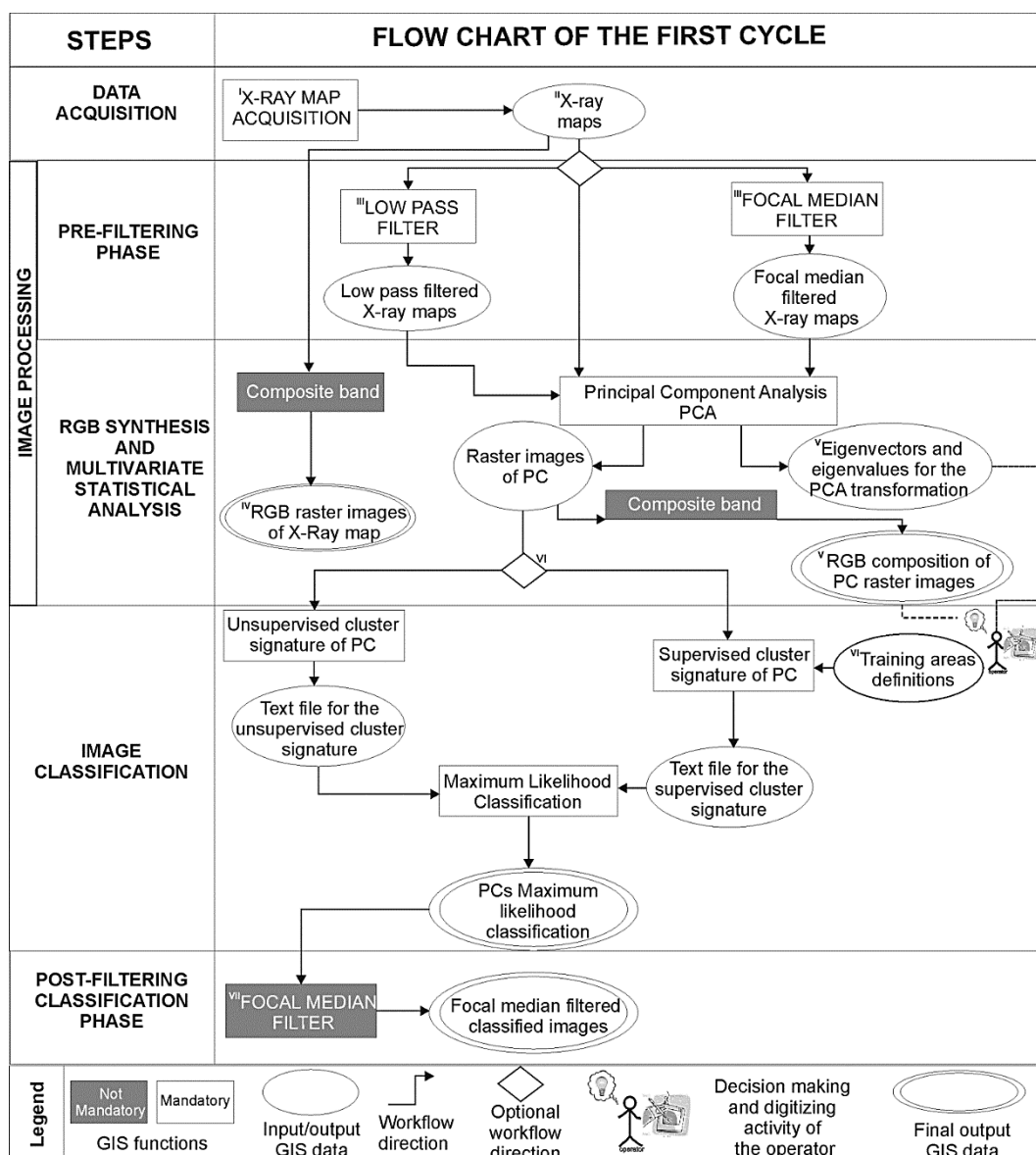


Fig. 2.14 - Flow chart of the first cycle of the geoprocessing procedure. Details of the procedure: I) SEM magnification has to be set in order to obtain a pixel dimension close to the double size of the beam radius of the used microprobe; II) the total number and dimension of the X-ray maps can be freely set; III) pre-classification filtering stage is an optional operation, useful for minimising the potential background noise of X-ray maps. A low-pass filter calculates the average value for a pixel centered around eight immediate neighbours. A focal median filter allows to replace the original pixel values calculated as the median of the pixel-values around a rectangular or circular perimeter of arbitrary dimension; IV) the procedure allows one optionally to compose all the possible RGB combinations with or without permutations of the original element channels; V) the analysis of the eigenvector matrix obtained from PCA transformation permits to easily analyze the variance of the multidimensional space represented by PCA analysis, allowing the operator to choose the best RGB combination for discrimination of the constituent phases; VI) after the decorrelation of the original X-ray maps and subsequent combination of the new PCs, it is possible to choose an unsupervised and/or supervised classification procedure. The first one is based upon an automated iso-cluster approach. The second one upon a semi-assisted procedure working by means of the definition of polygonal training areas digitized by the operator, characterised by an ascertained classification; VII) classified images can be successively filtered to enhance the segmentation (from [Ortolano et al., 2014b](#)).

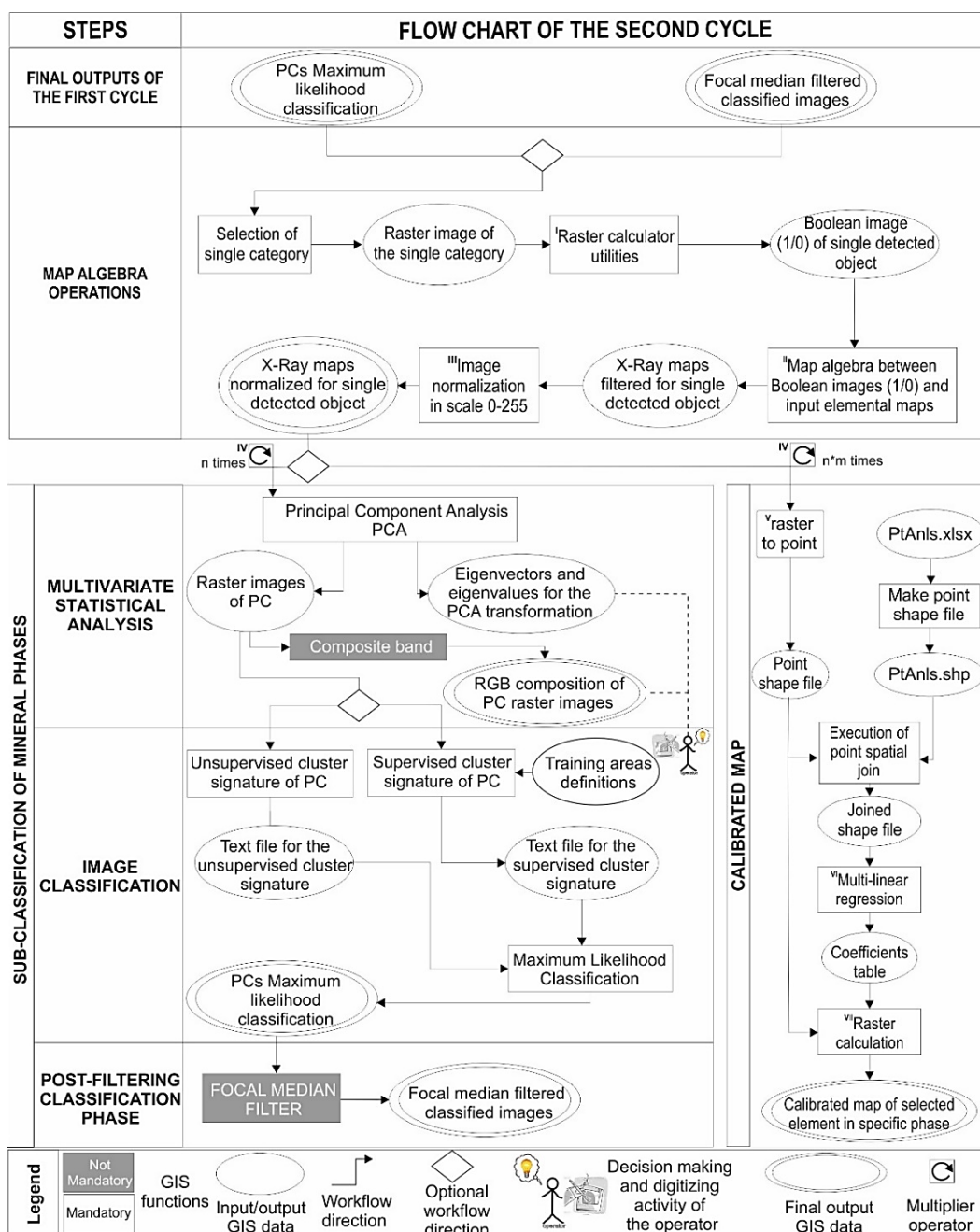


Fig. 2.15 - Flow chart of the second cycle of the geoprocessing procedure. Details of the procedure: I) the raster calculator utilities are a pixel-based tools package useful to manage raster images. These were here used for the calculation of a series of Boolean images (i.e., composed only of pixels with a value of one or zero) aiming to obtain new sets of the original X-ray maps filtered and normalized per detected class (e.g. mineral phase); II) the application of a multilinear regression algorithm between normalized image per detected class and laboratory control spot analyses to obtain new sets of calibrated X-ray maps. The procedure permits one to choose the type of primary X-ray maps (i.e., Original; Low Pass filtered; Focal median Filtered); III) the procedure can be potentially repeated n times for the second cycle of classification or $n*m$ times for the calibration procedure within the single mineral phase, where n is the number of phases classified in the first cycle, and m is the number of elements of the original X-ray map; IV) input data set for calibration provides the preliminary transformation of the original pixels to a point vector file containing as information the pixel value; V) multilinear regression calculates regression coefficients for the element investigated a table format where store results.; VI) map algebra operation between coefficients calculated and the pixel intensity values of the original X-ray maps (from [Ortolano et al., under review](#)).

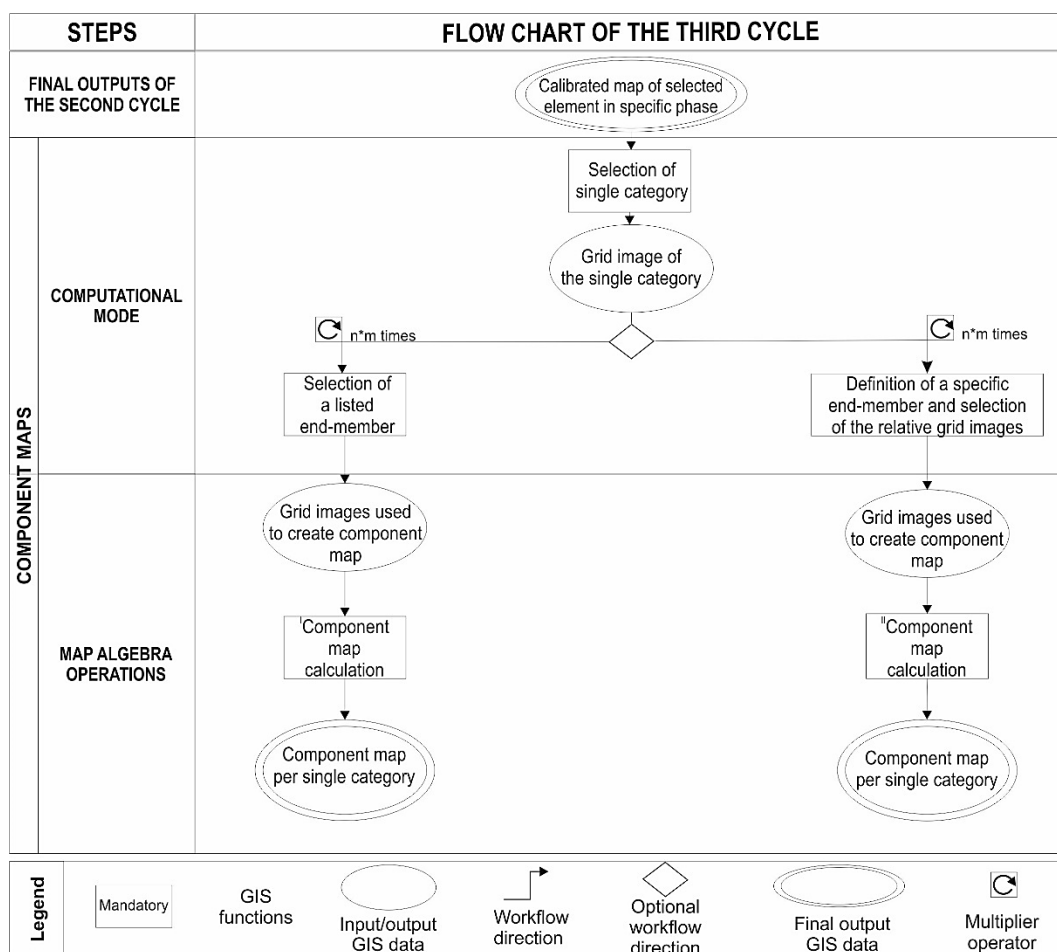


Fig. 2.16 - Flow chart of the third cycle of the geoprocessing procedure. Details of the procedure: I) the component map calculation specific for an end-member proposed by the tool per single detected class; II) the component map calculation characteristic for an end-member defined by the user by choosing specific calibrated X-ray maps (from [Ortolano et al., under review](#)).

2.3.1.1 First cycle: pre-calibration procedure

As a preliminary operation at the beginning of the first cycle ([Fig. 2.14](#)), an optional focal median filter is applied to the native X-ray raster images with the aim to reduce the common background noise of the EDS images (see [Ortolano et al., 2014b](#) for details). The use of the EDS detector is here preferred because it has the advantage of detecting and displaying X rays over a large energy range (e.g., 0–20 keV) within which can be selected Regions of Interest (ROIs) corresponding to specific spectral windows adequately chosen around each analytical peak. This choice permits to obtain integrated counts within the window to modulate pixel intensities in a single element map.

After the filtering phase, a PCA of the original set of the X-ray maps is executed. In general outlines, the application of the PCA on a multiband image raster set, each

of them representative of a specific channel characterising one or more chemical parameter expressed by means of a numeric value (i.e., the digital number of the pixel) within a 0-255 scale, means to analyse the covariance relationships between the different channels composing the investigated monochrome image array. This analysis is used to transform the data attributes of an original multiband raster, such as the X-ray map array, from the input multivariate attribute space to a new multivariate attribute space characterised by a rotation of the axis concerning the original one (see [Ortolano et al., 2014b](#) - Fig. 2.17). In this way, the PCA makes a new multiband raster displaying the same number of bands like the original raster (i.e., one band per axis in the new space), where the first principal component is characterised by the greatest variance, the second will show the most variance not described by the first, and so on ([Ortolano et al., 2014b](#)).

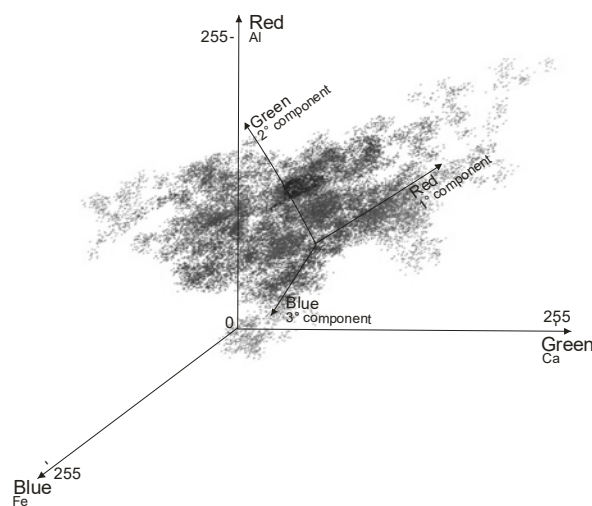


Fig. 2.17 - Example of schematic 3D representation of the decorrelation function known as principal component analysis, useful to re-project pixel values variability into a new coordinate system given by the axes of the principal components. This new coordinate system is able to minimize the redundancy (i.e., the superposition) of the original distribution, emphasizing class separability (from [Ortolano et al., 2014b](#))

The transformation of the original data distribution shown in the n -elemental space in a new multi-dimensional one represented by PCA is made: a) to compress data by eliminating redundancy; b) to emphasise the variance within the bands of a raster, and c) to make the data more interpretable. This analysis can help the operator in discovering the potential interdependence (e.g., the specific covariance) between elemental variability related, for instance, with the recognition of the mineral phases ([Ortolano et al., 2014b](#)).

After the application of the PCA, the procedure allows the user to classify all of the recognisable classes present in a selected micro-domain through an unsupervised

or a supervised MLC. The first one performs an automatic classification of the chosen X-ray map set if the number of principal component images to be used in the calculation and the approximate number of the expected classes (e.g. mineral phases) are given (Ortolano et al., 2014b). The second one requires the drawing of some training areas by the user, with the aim to provide a partial mineral pre-recognition. These training areas are then used by the signature function to prepare a text file used by the MLC algorithm, identifying each spectral class as a specific mineral phase.

This first analytical cycle then permits to classify the minerals, by deriving a mineralogical distribution map of a selected micro domain. This first output allows selecting the single classified mineral phases during the second cycle map algebra operations (Fig. 2.15) and generating at the same time new sets of X-ray maps for each single detected object (Fig. 2.15). These new sets of X-ray maps are then used as input for the calibrating procedure.

2.3.1.2 Second cycle: calibration algorithm

The multilinear regression algorithm (e.g., Marquardt, 1980; Hosmer & Lemeshow, 1989; Neter et al., 1996) has been here chosen as considered the most suitable approach to take into account the natural compositional constraints existing within each mineral due to its stoichiometry. This choice was also useful to overcome the hindrances due to the different potential relationships (e.g., linear, exponential, logarithmic) existing between the element concentration and the correspondent pixel intensity. The concentration-element/pixel-value relationship can be affected for instance: (a) from the ab-initio selection of the setting parameters of the used device, or (b) using data carried out by different acquisition instruments. The use of a multilinear regression allows, indeed, to derive for each pixel the absolute concentration of an element (i.e., the **Dependent Variable - DV**) in a specific mineral phase, taking into account the weight of all of the other elements as well (i.e., the **Explanatory Variables - EVs**), in order to ensure the stoichiometry preservation.

Usually, one of the main issues in adopting a multilinear regression approach is in finding the correct explanatory variables helping to explain the potential

interdependent variation of a parameter of interest. To settle this question, we selected as explanatory variables, the pixel intensities for major elements constituting most of the common minerals (i.e., Al, Ca, Fe, K, Mg, Mn, Na, Si, Ti). The calibration procedure is based on the application of the following interdependent multilinear regression equation:

$$[[C_i]] = [(\alpha_1 [[GV_i]]_0^{255}) + (\alpha_2 [[GV_j]]_0^{255}) + (\alpha_3 [[GV_k]]_0^{255}) + \dots + (\alpha_n [[GV_n]]_0^{255})] + \beta_i + \gamma_i \quad (Eq. 2)$$

Where:

- $[[\quad]]$ = discretized positive value;
- i represents the element whose concentration is to be predicted;
- $j, k, l \dots n$ represent the other elements;
- $[[C_i]]$ = the absolute and discretized concentration of the element i computed for each pixel; this variable is dependent of the explanatory variables;
- $\alpha_{1; 2; 3; \dots n}$ = the calculated coefficients of the regression between the measured concentration value of the elements stored in the control spot analysis, and the corresponding pixel intensity value of the original X-ray raster images at the same point;
- $[[GV_i]]_0^{255}; [[GV_j]]_0^{255} \dots [[GV_n]]_0^{255}$ = the discrete pixel-intensity values of the $i, j, k \dots n$, one-channel elemental maps; they are independent explanatory variables;
- β_i = value of the intercept for the element i , that is the expected value of the dependent variable ($[[C_i]]$) if all the independent (explanatory) variables ($[[GV]]$) are zero;
- γ_i = random error for the element i , defined by the difference between the measured and predicted values.

The adopted calibration procedure also provides a regression report printed on the screen, filled with several statistical parameters allowing to assess model performance and to evaluate the reliability of the predicted results. These parameters can be summarised as follows:

- a) *Regression coefficients (α_n)*: the coefficient calculated for each explanatory variable ($[[GV_n]]$) depicts the type of relationship (i.e., negative, positive or no relationship – Fig. 2.18) between explanatory and dependent variables. In other words, to predict, for instance, the Ca content in plagioclase ($[[C_{Ca}]]$), it would be expected a negative relationship (i.e., $\alpha_{Na} < 0$) with the Na pixel values ($[[GV_{Na}]]$). If during the calibration procedure an unexpected positive coefficient for the above-mentioned relationship occurs, attention should be made before to proceed.

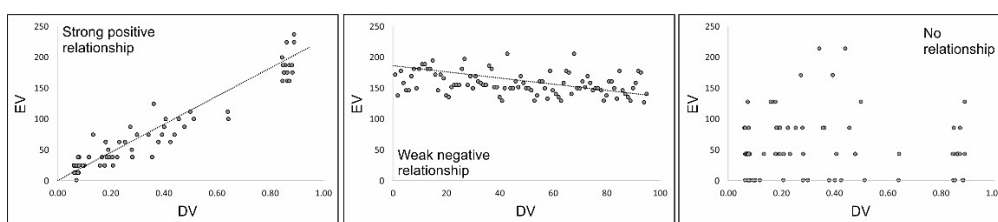


Fig. 2.18 - Example of possible relationship between dependent and explanatory variables

- b) *Probability*: this parameter allows checking if every regression coefficient of the EVs is near or equal to zero. The smaller probability value is, the smaller the possibility that the coefficient is equal to zero, and the higher the correlation between the dependent and explanatory variables. This probability implies that those specific coefficients are relevant for the regression model. By contrast, EVs with coefficients showing high probability values should be removed from the regression equation. In the developed ArcGIS®-based image processing procedure, when the probability is lower than 0.01, an asterisk close to the value will appear on the regression report alerting that the coefficient of those specific EVs is consistent with the prediction model. Nevertheless, some explanatory variables could be considered good predictors as well from a theoretical point of view (e.g., for stoichiometry preservation), although showing regression coefficients with

high probability values. This assumption is statistically permitted, verifying the consistency of other test indexes (i.e., *Joint F-Statistic and Joint Wald Statistic*), highlighting the mutual interdependence relationship between the regression coefficients.

- c) *Variance inflation factor (VIF)*: the VIF is a check parameter that depicts the weight of the redundancy among the EVs. It is an index that measures how much the multicollinearity (i.e., a situation in which two or more explanatory variables in a multiple regression model have linear relationships each other) affects the variance values. If the explanatory variables assume VIF values larger than about 7.5, the variance increase because of collinearity and, then, the model is not good. As a rule of thumb, the EVs should be removed from the regression model, however, an alternative strategy could be the increase of the number of the control spots.
- d) *R-Squared (R^2) and Corrected Akaike's Information Criterion (AICc)*: the R^2 values are measures of model performance ranging from 0.0 to 1.0 and explaining the variation in the dependent variable. For instance, an R^2 value of 0.8 means that the EVs explain 80 percent of the variation in the dependent variable. The AICc is used to compare different models performed about the same dependent variable (e.g., increasing or decreasing of control spot analysis). By comparing different calibration models, the model with a lower AICc is to be preferred.
- e) *Joint F-Statistic and Joint Wald Statistic*: These test indexes are used to verify the overall model statistical significance since they assess the regression coefficient relationships simultaneously. As a consequence, these tests measure the statistical meaning of the multilinear regression models, even when one or more of the single coefficients result statistically meaningless (i.e., with a probability value > 0.01). In particular, these tests compare a model with no explanatory variables (i.e., an intercept-only model) to the user-specified model. When the values are lower than 0.01 (i.e., marked with an asterisk by the tool on the regression report), the user-specified model

provides a better fit than the intercept-only one and, consequently, the set of the explanatory variables improved the fit. Therefore, when such a result is achieved, the applied multiple regression models can be considered reliable if the value associated with the Koenker (BP) statistic test (see below) is higher than 0.01.

- f) *The Koenker (BP) Statistic*: It is a test to determine whether the EVs in the model have a consistent relationship to DV across the entire study area. If such a test shows a value lower than 0.01, the EVs vs DV relationships are non-stationary or heteroscedastic (i.e., characterised by a not uniform variance distribution). Heteroscedasticity provides information about the error between data sets, such as the observed and predicted values for a specific DV, and can be considered as a deviation measure of data from the mean value. Figure 2.19 shows an example of heteroscedastic vs homoscedastic variance distribution.

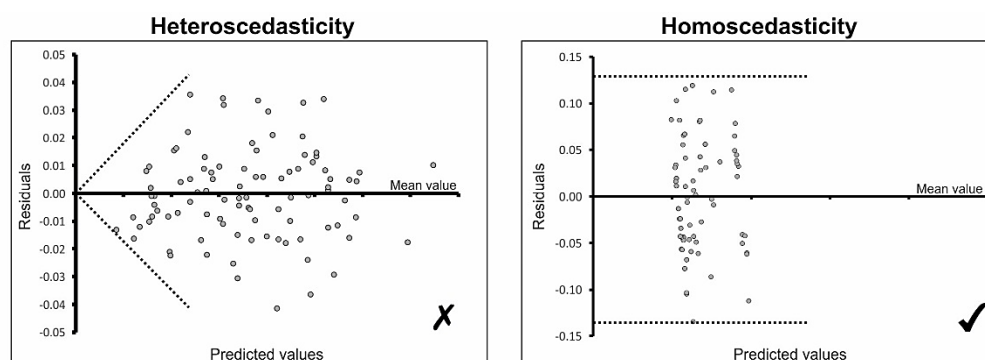


Fig. 2.19 - Difference between heteroscedasticity vs. Homoscedasticity distribution of the residuals.

When an asterisk marks the Koenker (BP) test, a heteroscedastic distribution as that shown in figure 2.19a is obtained. As the Q-XRMA software writes test and regression results in specific folders and tables, the heteroscedastic/homoscedastic condition can be easily verified by constructing scatter plots between estimated/predicted values vs. residuals (i.e., the observed dependent variable values minus the predicted ones).

- g) *The Jarque-Bera statistic*: It is a test to assess whether the residuals are normally distributed according to a Gaussian distribution. When the result of

this test gives a value lower than 0.01, the residuals are not normally distributed, indicating the occurrence of a probable bias, which can influence the reliability of the predictions. This bias could be due, for instance, to the presence of outliers in the control spot analyses. These latter can affect the modelled regression relationship producing a non-best fit, biasing regression coefficient (Fig. 2.20). A possible solution could be removing the outliers, restarting the procedure.

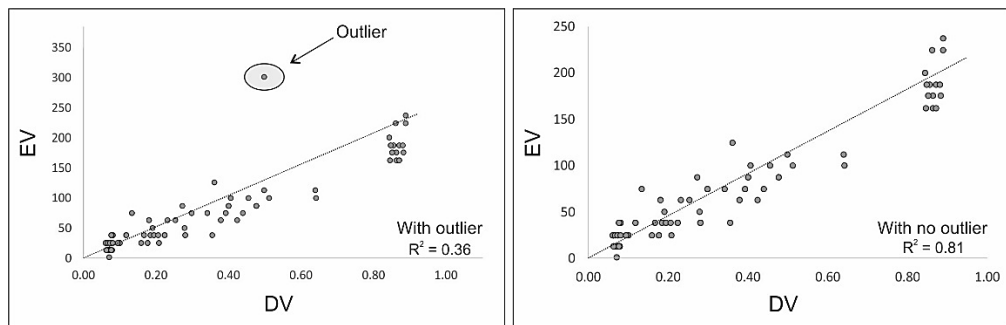


Fig. 2.20 - Effect of outliers on the regression results (i.e., R^2 values).

During the calibration procedure, the new tools package displays on the screen the results of each of these tests, alerting the user with an asterisk when they give values smaller than 0.01. This warning provides the user with a fast way to check the reliability of its model. Moreover, model results are saved in specific folders as output tables.

2.3.1.3 Second cycle: maps calibration (data setting and outputs)

To preserve the interdependence relationship between the explanatory variables (i.e., the pixel values of selected major elements), the calibration procedure works for one identified mineral phase per time, previously classified and bracketed during the first cycle of analysis (see above). To run the calibration procedure, all of the selected EVs are needed (i.e., Al, Ca, Fe, K, Mg, Mn, Na, Si, Ti X-ray maps), and two spreadsheets must be set as well. This operation has to be repeated whenever users wish to investigate a new mineralogical phase.

The first spreadsheet (i.e., Q-XRMA point coordinate conversion tool – Fig. 2.21) is used to ensure the correct location of the control spot analyses within the map,

converting the original device coordinates of each spot into the ArcGIS® coordinate system, according to the following equations:

$$Xp_{GIS} = \frac{(Xp_{LAB} - Xm^c_{LAB})}{|(Xm^l_{LAB} - Xm^r_{LAB})|} * |(Xm^l_{GIS} - Xm^r_{GIS})| + Xm^c_{GIS} \quad (Eq. 3a)$$

- If $Xp_{LAB} > 0$

$$Xp_{GIS} = \frac{(Xm^c_{LAB} - Xp_{LAB})}{|(Xm^l_{LAB} - Xm^r_{LAB})|} * |(Xm^l_{GIS} - Xm^r_{GIS})| + Xm^c_{GIS} \quad (Eq. 3b)$$

- If $Xp_{LAB} < 0$

$$Yp_{GIS} = \frac{(Yp_{LAB} - Ym^c_{LAB})}{|(Ym^t_{LAB} - Ym^b_{LAB})|} * |(Ym^t_{GIS} - Ym^b_{GIS})| + Ym^c_{GIS} \quad (Eq. 3c)$$

- If $Yp_{LAB} > 0$

$$Yp_{GIS} = \frac{(Ym^c_{LAB} - Yp_{LAB})}{|(Ym^t_{LAB} - Ym^b_{LAB})|} * |(Ym^t_{GIS} - Ym^b_{GIS})| + Ym^c_{GIS} \quad (Eq. 3d)$$

- If $Yp_{LAB} < 0$

Where Xp_{GIS} is the calculated ArcGIS® X coordinate of the spots, Xp_{LAB} is the equivalent analytical device X coordinate, Xm_{LAB} and Xm_{GIS} are, respectively, the device X coordinate of the X-ray map and its equivalent on the ArcGIS® reference system, whereas l, c and r apices stand for the left corner, the centre and the right corner of the map along X , respectively (Fig. 2.21). Likewise, the same thing applies to the Y -coordinate where b, c and t stand for the bottom corner, the centre and the top corner of the X-ray map along Y (Fig. 2.21).

Such a coordinate conversion spreadsheet can be used in two different cases: (a) when X-ray maps and control spot analyses have been carried out with the same device (Fig. 2.21a); (b) when X-ray maps and control spot analyses have been carried out with different devices (Fig. 2.21b). In the first case, the device coordinates of the X-ray maps and their equivalents on ArcGIS® coordinate system are required as input information, together with the device coordinates of each single control spot. The ArcGIS® $X - Y$ map coordinates can be easily obtained by

using the extent information in the layer properties menu of the loaded map on the ArcGIS® project (see APPENDIX B1 for further discussion).

In the second case, it is necessary to provide: (a) the device $X - Y$ coordinates of at least two control spot analyses and their equivalent on ArcGIS® coordinate system; (b) the sizes of the X-ray maps; (c) the ArcGIS® coordinates of the X-ray maps; and (d) the device coordinates of each single control spot. After entering all the input values, the ArcGIS® $X - Y$ coordinates are automatically calculated for each single control spot and then can be successively inserted in the second spreadsheet.

Quantitative-X-ray Maps Analyser - Point coordinates conversion tool

Map XY coordinates	Device coordinates	ArcGIS® coordinates	Y	0.00	0.00	0.00	0.00	
x_left			0	Map coordinates				0.00
x_right			0					
y_bottom			0					
y_top				0	0	0	0	X
x_center	0	0.00						
y_center	0	0.00						

Quantitative-X-ray Maps Analyser - Point coordinates conversion tool for different acquisition devices

Map XY coordinates	Device coordinates	ArcGIS® coordinates	Y	0.00	0.00	0.00	0.00	
x_left	#DIV/0!		#DIV/0!	Map coordinates				0.00
x_right	#DIV/0!		#DIV/0!					
y_bottom	#DIV/0!		#DIV/0!					
y_top	#DIV/0!		#DIV/0!	#DIV/0!	#DIV/0!	#DIV/0!	#DIV/0!	X
x_center	#DIV/0!	0.00						
y_center	#DIV/0!	0.00						

Map resolution

Map resolution	Column	Rows	X position in the map	Y position in the map
			#DIV/0!	#DIV/0!
			#DIV/0!	#DIV/0!

Device (e.g. EMPA, SEM) and ArcGIS® coordinates of two control points

Device X coordinate	Device Y coordinate	ArcGIS® X	ArcGIS® Y
Point 1			
Point 2			

DataSet/Point

DataSet/Point	X	Y	ArcGIS® X coordinate	ArcGIS® Y coordinate
			#DIV/0!	#DIV/0!
			#DIV/0!	#DIV/0!
			#DIV/0!	#DIV/0!
			#DIV/0!	#DIV/0!
			#DIV/0!	#DIV/0!
			#DIV/0!	#DIV/0!
			#DIV/0!	#DIV/0!
			#DIV/0!	#DIV/0!
			#DIV/0!	#DIV/0!

ArcGIS® coordinate point projections

Copy and paste the computed ArcGIS® X and Y coordinates within PtAnls.xlsx file!!! (i.e. into POINT_X and POINT_Y columns)

Copy and paste the computed ArcGIS® X and Y coordinates within PtAnls.xlsx file!!! (i.e. into POINT_X and POINT_Y columns)

Fig. 2.21 - Point coordinates conversion spreadsheet used to automatically calculate the correct location of the control spot analyses converting the device coordinates into their equivalents on the ArcGIS® loaded maps: (a) point and X-ray maps acquired with the same device; (b) point and X-ray maps acquired with different devices (Ortolano et al., under review).

The second spreadsheet (PtAnls.xlsx, Fig. 2.22) contains all the information about the sample location, mineral phases, subphases of the mineral investigated, number of analyses, chemical compositions and the ArcGIS® X-Y coordinates.

A	B	C	D	E	F	G	H	I	J	K	L	M	N	O	P	Q	R	S	T		
ID	ID SAMPLE	LOCATION	MINERAL	SUB_PHASE	DOMAIN	ANALYSIS	POINT	AI	Ca	Fe	K	L	Mg	Mn	Na	O	P	Si	Ti	POINT_X	POINT_Y
2	1	MA271	MPC	Grt-I	IC	10	9415		1,95	0,84	1,68	0,00	0,05	0,43	0,01	0,00	2,97	0,01	2,14	2,64	
3	2	MA271	MPC	Grt-I	IC	10	9415		1,98	0,86	1,70	0,00	0,05	0,43	0,01	0,00	2,98	0,01	2,15	2,63	
4	5	MA271	MPC	Grt-I	IC	10	9415		1,94	0,84	1,70	0,00	0,05	0,46	0,00	0,00	2,99	0,01	2,16	2,61	
5	6	MA271	MPC	Grt-I	IC	10	9415		1,97	0,86	1,68	0,00	0,05	0,44	0,01	0,00	2,99	0,01	2,17	2,59	
6	8	MA271	MPC	Grt-I	IC	10	9411		1,94	0,87	1,71	0,00	0,05	0,44	0,00	0,00	2,99	0,01	2,18	2,58	
7	9	MA271	MPC	Grt-I	IC	10	9412		1,94	0,88	1,69	0,00	0,05	0,44	0,00	0,00	2,99	0,01	2,18	2,57	
8	10	MA271	MPC	Grt-I	IC	10	9418		1,93	0,86	1,69	0,00	0,05	0,46	0,00	0,00	2,93	0,01	2,20	2,54	
9	12	MA271	MPC	Grt-I	IC	10	9420		1,95	0,88	1,71	0,00	0,05	0,46	0,01	0,00	2,97	0,01	2,21	2,53	
10	13	MA271	MPC	Grt-I	IC	10	9411		1,94	0,89	1,66	0,00	0,05	0,46	0,01	0,00	2,97	0,01	2,25	2,46	
11	14	MA271	MPC	Grt-I	IC	10	9414		1,96	0,87	1,73	0,00	0,05	0,43	0,01	0,00	2,98	0,01	2,26	2,44	
12	15	MA271	MPC	Grt-I	IC	10	9418		1,93	0,87	1,70	0,00	0,05	0,47	0,01	0,00	3,00	0,01	2,27	2,42	
13	17	MA271	MPC	Grt-I	IC	10	9411		1,95	0,85	1,68	0,00	0,05	0,46	0,01	0,00	2,96	0,01	2,28	2,40	
14	18	MA271	MPC	Grt-I	IC	10	9412		1,98	0,88	1,67	0,00	0,05	0,44	0,01	0,00	3,00	0,01	2,28	2,40	
15	19	MA271	MPC	Grt-I	IC	10	9413		1,95	0,89	1,67	0,00	0,05	0,48	0,01	0,00	2,97	0,01	2,29	2,39	
16	22	MA271	MPC	Grt-I	IC	10	9418		1,96	0,89	1,65	0,00	0,05	0,48	0,01	0,00	2,99	0,01	2,31	2,36	
17	23	MA271	MPC	Grt-I	IC	10	9415		1,93	0,88	1,68	0,00	0,05	0,47	0,01	0,00	2,99	0,01	2,33	2,32	
18	24	MA271	MPC	Grt-I	IC	10	9413		1,96	0,87	1,70	0,00	0,05	0,42	0,00	0,00	2,97	0,01	2,36	2,27	
19	27	MA271	MPC	Grt-I	IC	10	9416		1,95	0,87	1,74	0,00	0,05	0,42	0,00	0,00	2,99	0,01	2,37	2,25	
20	29	MA271	MPC	Grt-I	IC	10	9416		1,96	0,85	1,70	0,00	0,05	0,43	0,00	0,00	2,97	0,01	2,38	2,24	
21	31	MA271	MPC	Grt-I	MNT	10	9416		1,94	0,36	2,16	0,01	0,13	0,39	0,01	0,00	2,97	0,01	2,40	2,20	
22	32	MA271	MPC	Grt-I	MNT	10	9412		1,96	0,41	2,16	0,00	0,12	0,38	0,00	0,00	2,98	0,01	2,42	2,16	
23	36	MA271	MPC	Grt-I	MNT	10	9416		1,95	0,50	2,11	0,00	0,13	0,32	0,00	0,00	2,97	0,01	2,44	2,12	
24	40	MA271	MPC	Grt-I	MNT	10	9416		1,98	0,22	2,37	0,00	0,18	0,32	0,00	0,00	2,96	0,00	2,48	2,06	
25	42	MA271	MPC	Grt-I	MNT	10	94102		1,96	0,27	2,31	0,00	0,17	0,32	0,00	0,00	2,96	0,01	2,49	2,04	
26	43	MA271	MPC	Grt-I	MNT	10	94104		1,96	0,34	2,27	0,00	0,16	0,32	0,00	0,00	3,00	0,01	2,50	2,03	
27	44	MA271	MPC	Grt-I	MNT	10	94105		1,94	0,38	2,20	0,00	0,14	0,30	0,01	0,00	2,94	0,00	2,50	2,03	
28	47	MA271	MPC	Grt-I	MNT	10	94113		1,96	0,44	2,24	0,00	0,16	0,25	0,00	0,00	2,98	0,01	2,53	1,98	
29	48	MA271	MPC	Grt-I	MNT	10	94115		1,95	0,31	2,30	0,01	0,19	0,26	0,01	0,00	3,00	0,01	2,53	1,97	
30	49	MA271	MPC	Grt-I	MNT	10	94117		1,96	0,34	2,28	0,00	0,19	0,22	0,00	0,01	2,98	0,00	2,54	1,96	
31	51	MA271	MPC	Grt-I	MNT	10	94120		1,94	0,23	2,46	0,00	0,21	0,20	0,00	0,00	3,01	0,00	2,55	1,94	

Fig. 2.22 - PtAnls.xlsx file used by the Python code to create an ArcGIS® point shapefile. POINT_X and POINT_Y fields are filled with the data obtained by the specific conversion coordinates spreadsheet (Fig. 2.21) (Ortolano et al., under review).

These coordinates are read by the software to automatically create a point shapefile subsequently required for the execution of the calibration steps. To avoid unexpected calibration results, it is important verifying that the points created by the software are not located close to other mineral phases or fractures. Otherwise, it is recommended removing these points by editing the shapefile mentioned above (Fig. 2.23).

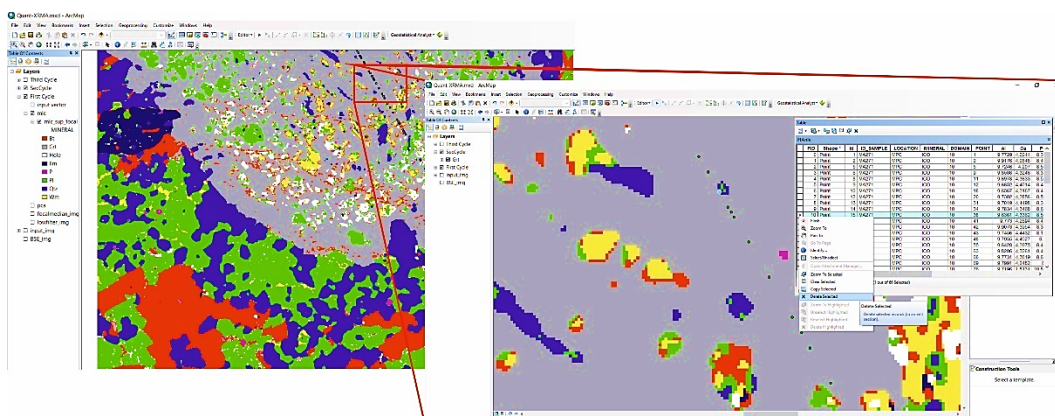


Fig. 2.23 - Editing step of the ArcGIS® shapefile for removing points close to the edge mineral zones (Ortolano et al., under review).

Once the input files have been correctly set, the calibration of the X-ray maps can be performed. During the execution of the calibration procedure, the software verifies the statistical meaning of each used calibration model, applying the statistical tests mentioned above.

Variable	Coefficient [a]	StdError	t-Statistic	Probability [b]	Robust_SE	Robust_t	Robust_Pr [b]	VIF [c]
Intercept	13,274252	1,382174	9,603894	0,000000*	1,473262	9,010112	0,000000*	-----
GRID_CODE	0,002146	0,011805	0,181826	0,856595	0,013321	0,161128	0,872767	1,628925
GRID_COD_1	-0,017011	0,002109	-8,065452	0,000000*	0,002056	-8,271844	0,000000*	2,190415
GRID_COD_2	0,002545	0,003198	0,795870	0,430582	0,002507	1,015193	0,315826	1,264814
GRID_COD_3	0,003140	0,003590	0,874774	0,386671	0,002627	1,195552	0,238578	1,098248
GRID_COD_4	0,004387	0,003158	1,389432	0,172024	0,002790	1,572601	0,123316	1,487331
GRID_COD_5	-0,005368	0,001712	-3,136069	0,003124*	0,002139	-2,509583	0,016031*	1,317592
GRID_COD_6	0,001241	0,005502	0,225456	0,822720	0,005095	0,243477	0,808823	1,158494
GRID_COD_7	-0,012900	0,008281	-1,557831	0,126778	0,007942	-1,624372	0,111780	1,127337
GRID_COD_8	0,003331	0,009676	0,344238	0,732386	0,010331	0,322401	0,748750	1,249212

OLS Diagnostics			
Input Features:	grt_gj.shp	Dependent Variable:	FE
Number of Observations:	52	Akaike's Information Criterion (AICc) [d]:	141,088583
Multiple R-Squared [d]:	0,844137	Adjusted R-Squared [d]:	0,810738
Joint F-Statistic [e]:	25,274127	Prob(>F), (9,42) degrees of freedom:	0,000000*
Joint Wald Statistic [e]:	498,363806	Prob(>chi-squared), (9) degrees of freedom:	0,000000*
Koenker (BP) Statistic [f]:	11,480331	Prob(>chi-squared), (9) degrees of freedom:	0,244215
Jarque-Bera Statistic [g]:	2,356136	Prob(>chi-squared), (2) degrees of freedom:	0,307873

Fig. 2.24 - Summary results of the calibration procedure using iron as a dependent variable. Test results (red areas) suggest that the applied statistical model can be considered reliable for the calibration (Ortolano et al., under review).

As shown in the red areas of figure 2.24, presented as an example of the iron calibration within garnet, statistical test results (e.g., VIF, Joint F- and Wald-Statistics, Koenker and Jarque-Bera statistics) suggest that the applied calibration model can be considered reliable for the investigated dependent variable (C_{Fe}).

Once the calibration of the selected elements has ended, new calibrated X-ray maps are obtained. These maps can be potentially used, in turn, as input files of the third analytical cycle (Fig. 2.16) useful to derive mineral end-member fraction maps.

2.3.1.4 Third cycle: mineral end-member maps

The main advantage resulting from the calibration procedure is the possibility to combine the calibrated elemental maps, aiming to obtain maps of mineral end-members. In this view, the software has been implemented with a third analytical cycle subdivided into two different computational modes. With the first one (blue area in Fig. 2.25), it is possible to automatically obtain different end-member maps defined for a set of common minerals, using as mask file a specific phase identified during the first analytical cycle (green area in Fig. 2.25).


```

This application allows to classify mineral phases by means of statistical data process of X-Ray Map

Please select one of the procedures listed below
1 - First cycle
2 - Second cycle
3 - Third cycle
4 - Exit
Please, choose one procedure to execute:
3

This is the third round of your analysis

I have found these workspace in your data:
CAGEO_2017
Please, select a folder listed above or digit a new workspace (Case Sensitive):
CAGEO_2017

Grt
Qtz
Pl
Bt
P
Ilm
Wm
Hole
Please, choose one class detected in the 1st cycle listed above (Case Sensitive):
Grt
You have selected Grt

1 - Alm, Grs, Prp, Sps
2 - Pheng
3 - Ab, An
4 - Di, Hed
5 - Fo, Fa
6 - Other
Please, choose the corresponding number listed above for your component calculation:

```

Fig. 2.25 - Window shell of the third analytical cycle. The green-delimited area displays the mineral phases already identified and classified during the first analytical cycle. These are used as masks to derive calibrated maps. The latter maps can display either mineral end-members (blue-delimited area; first computational mode) or arithmetic combinations of elements (red-delimited area; second computational mode) (Ortolano et al., under review).

With the second one (red square in Fig. 2.25), it is possible to manually select which elements have to be used within a raster calculator, which allows to create and execute a map algebra expression, for creating a specific end-member fractions map for a mineral phase detected during the first cycle (green area in Fig. 2.25), by choosing "other" as computational mode. In this latter case, the user must define the name of the output map, the number of the elements to be used and the correct expression for deriving graphical outputs.

In both computational modes, the graphical outputs and the relative normalised end-member concentration for each pixel are stored within database format tables potentially queryable for further purposes.

2.3.2 Case study

As an example, it has been investigated a garnet-plagioclase-biotite-bearing micro domain from a metapelite sample (Fig. 2.26). In order to test the applied methodology accurately, it has been used data input from two different laboratories, taking care to properly locate the control spot analysis within the pixel matrix of the corresponding EDS X-ray maps.

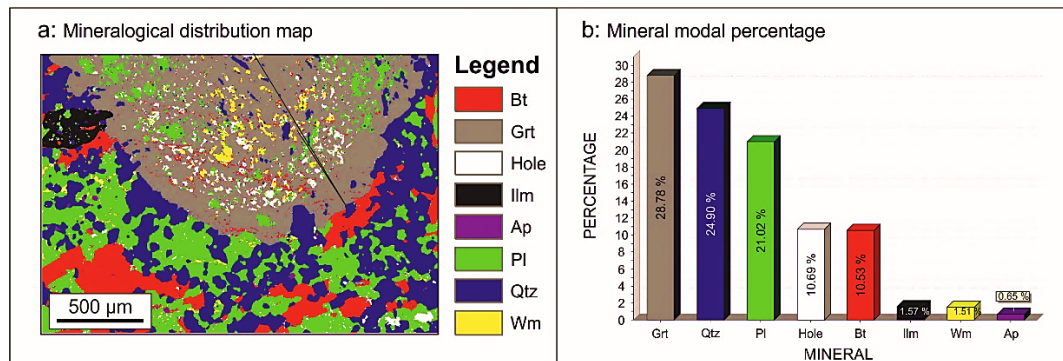


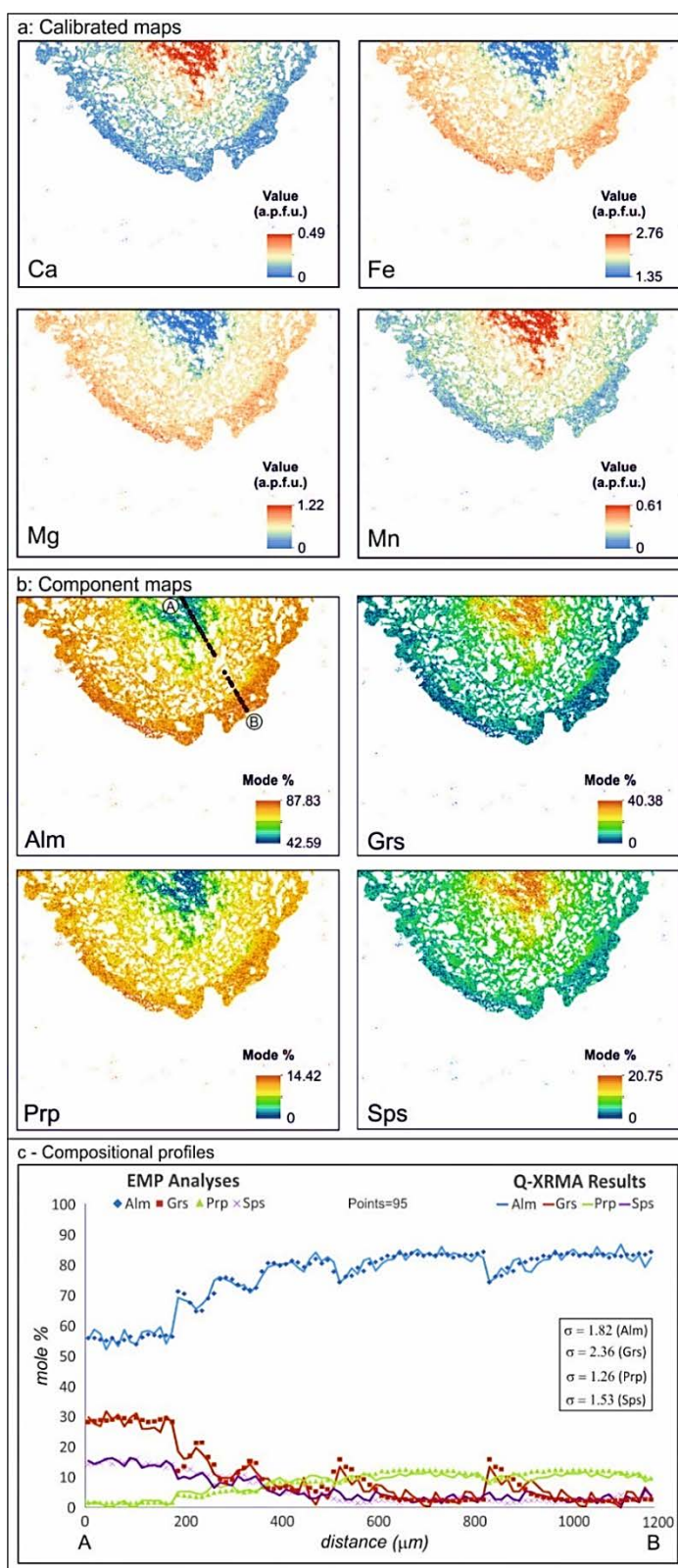
Fig. 2.26 - Output of the first analytical cycle. (a) mineralogical distribution map resulting from the classification; (b) histogram of the mineral modal percentages (Tab. 2.1) (Ortolano et al., under review).

Tab. 2.1 - Domain 1st cycle output

Mineral	Pixel count	Modal %
Pl	207510	19.21
Wm	9202	0.85
Bt	105842	9.80
Grt	311455	28.84
Qtz	266625	24.69
Ilm	16744	1.55
Hole	157542	14.59
Ap	5080	0.47
Chl	0	0.00
Total	1080000	100

Control spot analyses used for calibrating images were performed by a Cameca SX-FIVE electron microprobe (EMP) equipped with five WDS spectrometers at the Camparis laboratory in Paris, under the following operating conditions: ~ 1- μ m beam diameter; 15-kV accelerating voltage; and 10-nA beam current. Natural minerals and synthetic oxides were used as standards. Used mineral abbreviations are from Siivola & Schmid, (2007), whereas mineral formulae were calculated using MINPET 2.02 software (Richard, 1995). All mineral analyses and structural formulae are given in APPENDIX B2. EDS elemental maps, available in APPENDIX

B3, were acquired using a Tescan Vega-LMU scanning electron microscope equipped with an EDAX Neptune XM4-60 micro-analyser operating by energy-dispersive system characterised by an ultra-thin Be window coupled with an EDAX WDS LEXS (wavelength-dispersive low-energy X-ray spectrometer) calibrated for light elements, located at the Department of Biological, Geological and Environmental Sciences, University of Catania. The operating conditions were: 20-kV accelerating potential; dwell time of 500 ms and 128 frames; resolution of 1200×900 pixels, corresponding to a square pixel of about $2\text{-}\mu\text{m}$ side.



2.3.2.1 Garnet

With the aim to highlight the maximum range of

Fig. 2.27 - Outputs of the second and third analytical cycles for garnet: (a) Ca, Fe, Mg and Mn calibrated images expressed in a.p.f.u.; (b) almandine, grossular, pyrope and spessartine component maps expressed as mole percentage; (c) comparison of the compositional profiles obtained by EMP analyses (dots) and by the software (continuous lines) (Ortolano et al., under review).

composition variability of the selected zoned garnet porphyroblast, 95 control spot analyses (APPENDIX B4) were used for the calibration procedure following a core to rim transect, by using as control spot locator the available specific spreadsheet for the device vs ArcGIS® coordinate conversion (see section 2.3.1.3 for details).

The results are in agreement with garnet structural formula (i.e., $X_3Y_2[ZO_4]_3$) as emphasised by the sum of cations occupying the *X*, *Y* and *Z* sites, calculated per each pixel.

This evidence was further testified by the statistically meaningful results for each considered element consistent with the test indexes automatically calculated by the procedure (APPENDIX B5).

Results of the calibration process for divalent cations (i.e., Ca, Fe, Mg and Mn maps) are shown in figure 2.27a, where it is possible to observe the concentric garnet zonation.

Subsequently, the third analytical cycle was executed to derive end-member maps of almandine, grossular, pyrope and spessartine (Fig. 2.27b), which permitted to compare the EMP control spot analyses with the calibrated output of the software (Fig. 2.27c). Such a comparison highlights that the obtained compositional profiles extracted from the pixels of the calibrated images are very similar to the EMP patterns, considering a standard deviation of about 2% (APPENDIX B6).

2.3.2.2 Plagioclase

Following the same procedure used for garnet, elemental maps specific for plagioclase were calibrated by using 20 control spot analyses (APPENDIX B4) located on different grains, to point out and quantify compositional variations potentially linkable to various growth stages. The stoichiometry of the obtained results is consistent with plagioclase structural formula (i.e., $X[Z_4O_8]$), as further supported by reliable test index outcomes of the calibration procedure (APPENDIX B5).

The calibrated map of calcium (Fig. 2.28a) highlights a higher Ca content in those grains enclosed within garnet (i.e., 0.44 a.p.f.u), whereas the calibrated map of sodium (Fig. 2.28a) shows a higher Na content in the matrix grains (i.e., 0.92 a.p.f.u.), thus inciting to the distinction between different plagioclase generations. In this view, the third analytical cycle was used to derive albite and anorthite component maps (Fig. 2.28b). These two last outputs were used with the aim of conducting a comparison between EMP spot analyses, and component calibrated results, as displayed on the ternary feldspar classification diagram of Figure 2.28c. Such a comparison highlights that the calibration procedure improved the compositional characterization of the mineral phase increasing the number of compositional data available (i.e., 170854 calibrated pixels, Fig. 2.28c), thus integrating chemical information also where not directly controlled by EMP spot analyses (APPENDIX B6).

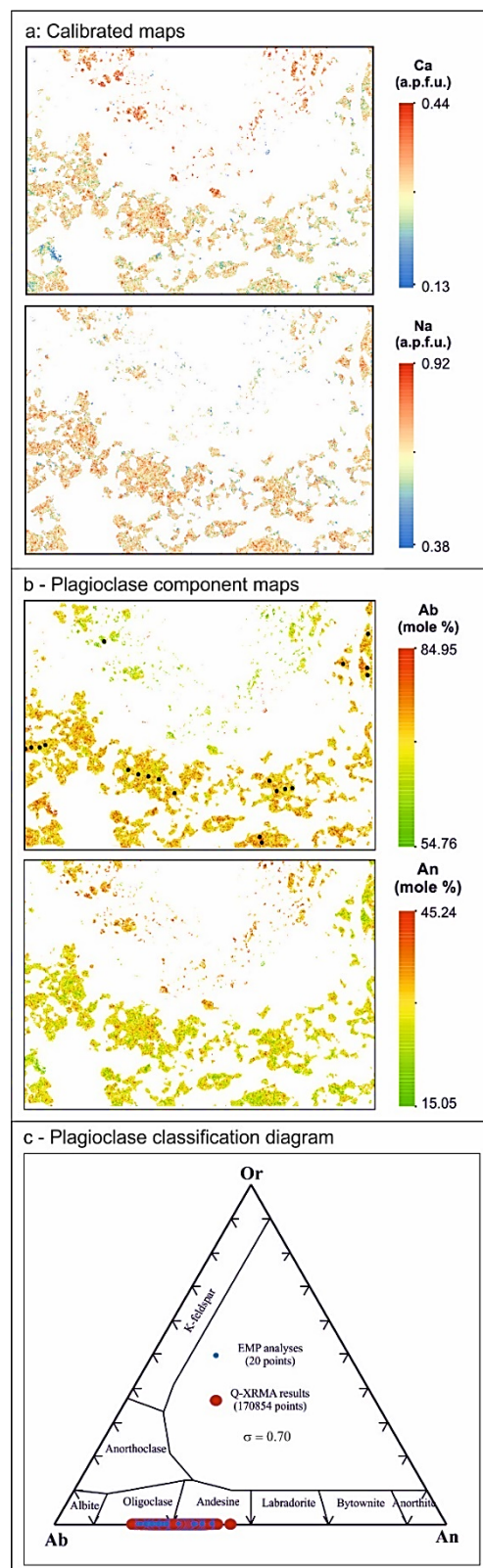


Fig. 2.28 - Outputs of the second and third analytical cycles for plagioclase: (a) Ca and Na calibrated images expressed in a.p.f.u.; (b) albite and anorthite component maps expressed as mole percentage; (c) comparison of the analyses obtained by EMP and the software in the feldspar ternary diagram (Ortolano et al., under review).

2.3.2.3 Biotite

Finally, to test the calibration procedure also for a hydrous mineralogical phase, 22 control spot analyses randomly distributed on several biotite crystals (APPENDIX B4) were used to set up the calibration models correctly. As the same for the anhydrous phases, the weight of each cation obtained for each pixel by the maps calibration procedure appears to be consistent with biotite structural formula (i.e., $WY_3[Z_4O_{10}](OH)_2$). Low values encountered for the Joint test indexes (see section 2.3.1.2 together with other satisfying statistical test results, confirmed the accuracy of the calibration models used per single investigated element (see APPENDIX B5). Calibrated maps of divalent cations (i.e., Fe and Mg) occupying the Y site in biotite are shown in Figure 2.29a, where it is possible to observe a higher iron content when in contact with garnet. This iron increase in biotite grains close to garnet was probably due to the iron/magnesium diffusive exchange occurring between the two mineralogical phases mentioned above, promoting at the same time, a magnesium increase in garnet.

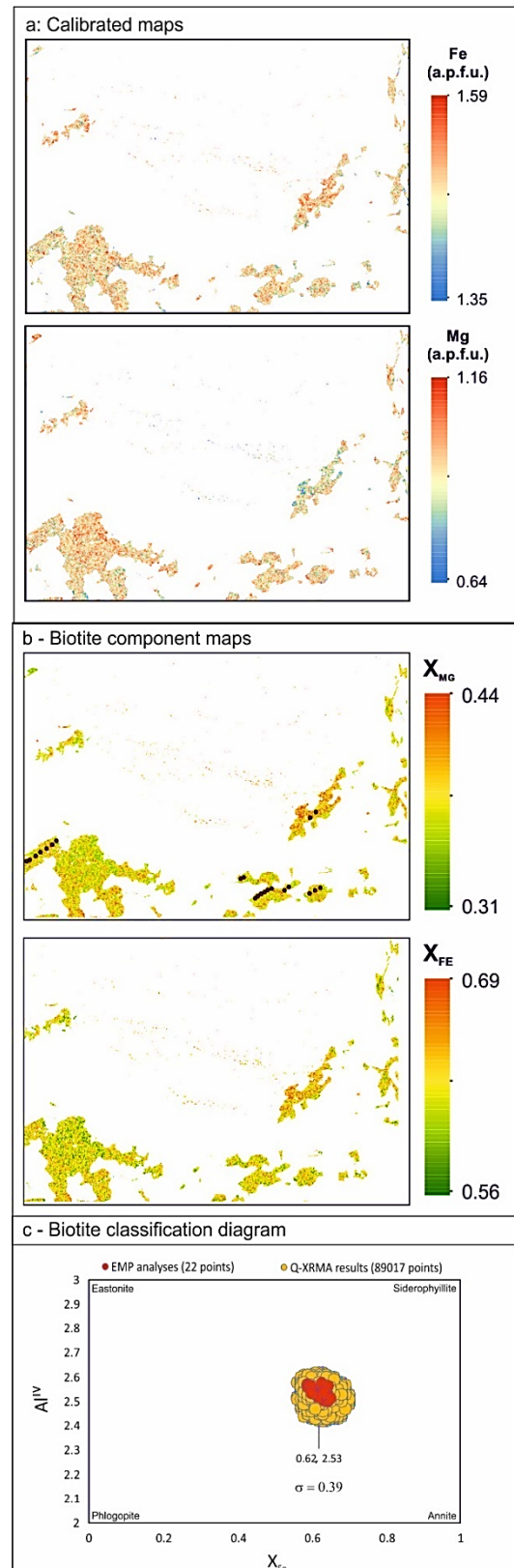


Fig. 2.29 - Outputs of the second and third analytical cycles for biotite: (a) Fe and Mg calibrated images expressed in a.p.f.u.; (b) X_{Fe} and X_{Mg} component maps expressed as mole fractions; (c) comparison of the analyses obtained by EMP and the software within the biotite-classification diagram (Ortolano et al., under review).

Subsequently, biotite X_{Fe} and X_{Mg} maps (Fig. 2.29b) were computed by using the raster calculator (i.e., second computational mode of the third cycle; see [section 2.3.1.4](#)), to emphasise possible chemical variations linkable to different metamorphic evolutionary stages. In this view, the calibrated results for X_{Fe} and X_{Mg} were compared with the EMP analyses ([APPENDIX B6](#)) and plotted on the biotite classification diagram (Fig. 2.29c). The significant increase in the chemical dataset available obtained by the calibration procedure (i.e., 89017 calibrated pixels), confirms a quite homogeneous biotite composition (i.e., Al^{IV} : 2.42–2.63; X_{Fe} : 0.55–0.70) within the biotite classification plot.

2.3.3 Final Remarks

Q-XRMA is a deeper enhanced version of a previous GIS-based image-processing procedure by [Ortolano et al. \(2014b\)](#), whose Python code structure has been modified. The new procedure is now subdivided in three sequential cycles that allow: (a) the mineral classification of the investigated micro domain; (b) the search for potential sub-phases within a previously-classified mineral phase; (c) calculating the concentration of an element by calibrating the native qualitative X-ray maps; (d) evidencing the distribution of end-members within solid-solution mineral phases.

The main aim of this new procedure is the quantitative calibration of element maps, expressed in a.p.f.u, computed for previously-classified mineral phases, to obtain several types of mineral end-member maps. EDS or WDS X-ray maps are calibrated using control spot analyses performed with the same or another device, taking care to preserve the connexion of each spot with the corresponding pixel in the map. This purpose can be reached using a spreadsheets package that converts the device coordinates into the ArcGIS® ones.

The calibration procedure applies a multilinear regression technique that mirrors the stoichiometry-controlled natural interdependence of the elements within a specific mineral. It permits to extract quantitative chemical information in a few minutes without passing through additional laboratory analyses. Owing to the intrinsic complexity of the applied multilinear regression approach, the software

provides some control parameters that allow testing the accuracy of the statistical models computed for a specific element.

The selected case study used to illustrate the methodology was carried out on an amphibolite-facies garnet micaschists characterised by the occurrence of bell-shaped zoned garnet associated with biotite and compositionally-heterogeneous plagioclase. Standard deviation values range from 0.39% to 2.36% (for biotite and garnet end-members, respectively). These results can be regarded as satisfactory, considering that the technique is easy to implement, relatively fast and low-cost. Moreover, several upgrades of the code have introduced the following improvements: (a) a better partition of the output results in specific folders referring to the used cycle, allowing an easier recognition of all files; (b) a saving of all the output files in database format tables potentially queryable; (c) the compatibility with 9.x and later versions of ArcGIS®; and, (d) the option of restarting a new round of analysis without exiting the program.

Finally, this new GIS-based software can be usefully applied to obtain an assisted semi-automated sequential image processing procedure applicable in many fields of petrological investigations. This new procedure minimises the bias influence consequent to the spot location decision-making activity, highlighting, in turn, quantitative distribution maps able to unravel complex or hidden paragenetic equilibria of petrological interest.

2.4 Mineral Grain Size Distribution (Min-GSD): a useful tool to display the grain size frequency distribution of each rock-forming mineral

An important consequence coming from the development of both the GSD toolbox and the Q-XRMA image processing software described previously is the possibility to obtain the grain size frequency distribution categorised per single mineral, by labelling and classifying each grain polygon with an appropriate mineral name. The use of the GSD toolbox alone does not permit any distinction between grains of different minerals unless the user manually renames each polygon. This last option can be tedious and time-consuming, especially when the investigated sample is characterised by small grains. However, combining classification results performed by the Q-XRMA software on X-ray maps from an entire thin section,

and the grain polygon features created by the GSD toolbox with the same software architecture (i.e., the ArcGIS®) in the same thin section, a diagram of the grain size frequency distribution specific for the single mineral class, can be obtained automatically. As an example, we investigated a paragneiss sample with a mineralogical assemblage represented by garnet, biotite, plagioclase, white mica and quartz with minor chlorite and secondary ilmenite and apatite. With the aim to construct the frequency distribution diagram, firstly, a thin section optical scan of c. 38 x 20 mm in size (Fig. 2.30a) was used as an input image in the GSD toolbox to derive the grain polygon map (Fig. 2.30b) and the associated grain size distribution (Fig. 2.30c). The analysed sample is prevalently constituted by small grains (i.e., 0.01 – 0.015 mm², corresponding to grains with a diameter of c. 100-125 µm if they can be assumed to be spheric) as

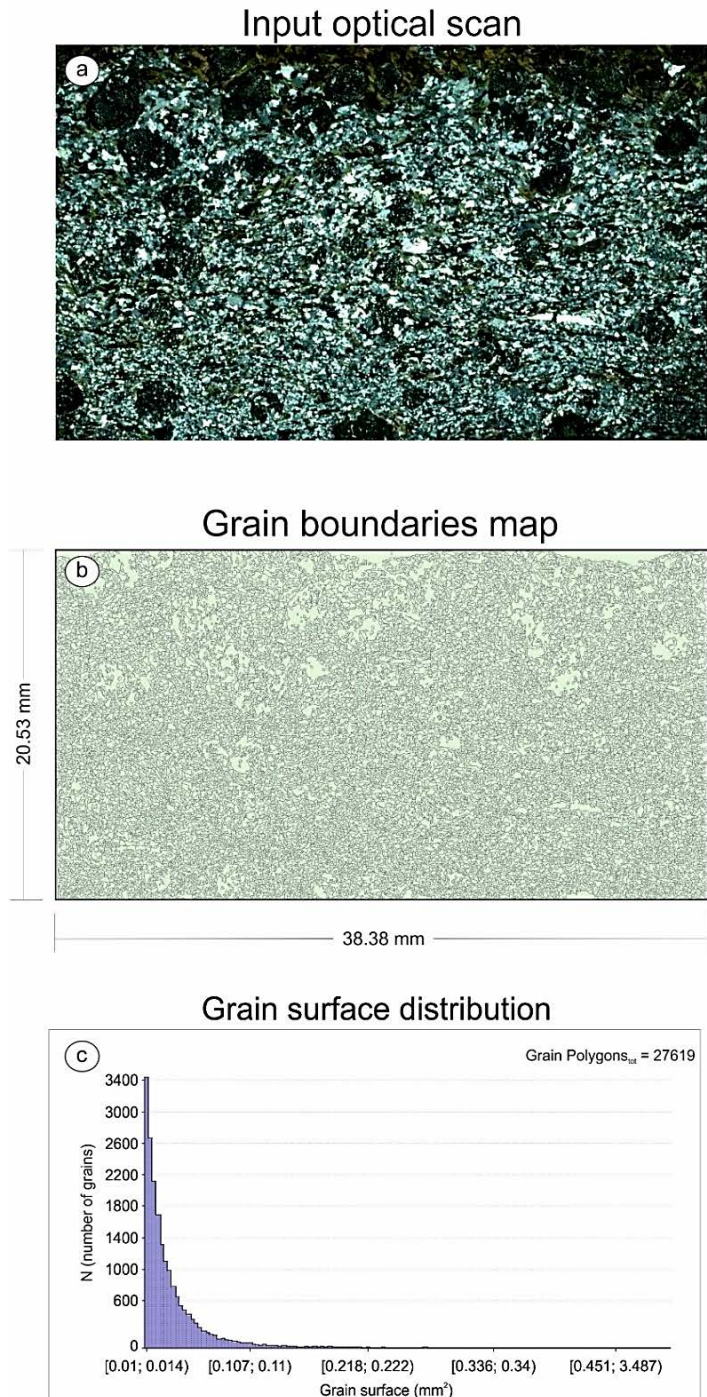


Fig. 2.30 - Grain size distribution derivation: (a) input pre-processed thin section optical scan; (b) grain polygon map derived via the Grain Size Detection toolbox; (c) histogram of grain size frequency.

highlighted in figure 2.30c, although larger grains (e.g., from 0.3 to 3 mm²) are also present.

Qualitative major element X-ray maps (Fig. 2.31) of the entire thin section (c. 38 × 20 mm) were then acquired using a μ -XRF Eagle III-XPL spectrometer equipped with an EDS Si(Li) detector and with an Edax Vision32 micro analytical system, located at the Department of Earth Sciences, University of Torino. The operating conditions were 400 ms counting time, 40 kV accelerating voltage and a probe current of 800 μ A. A spatial resolution of about 65 μ m in both x and y directions was used; the spot size was c. 30 μ m.

μ -XRF maps

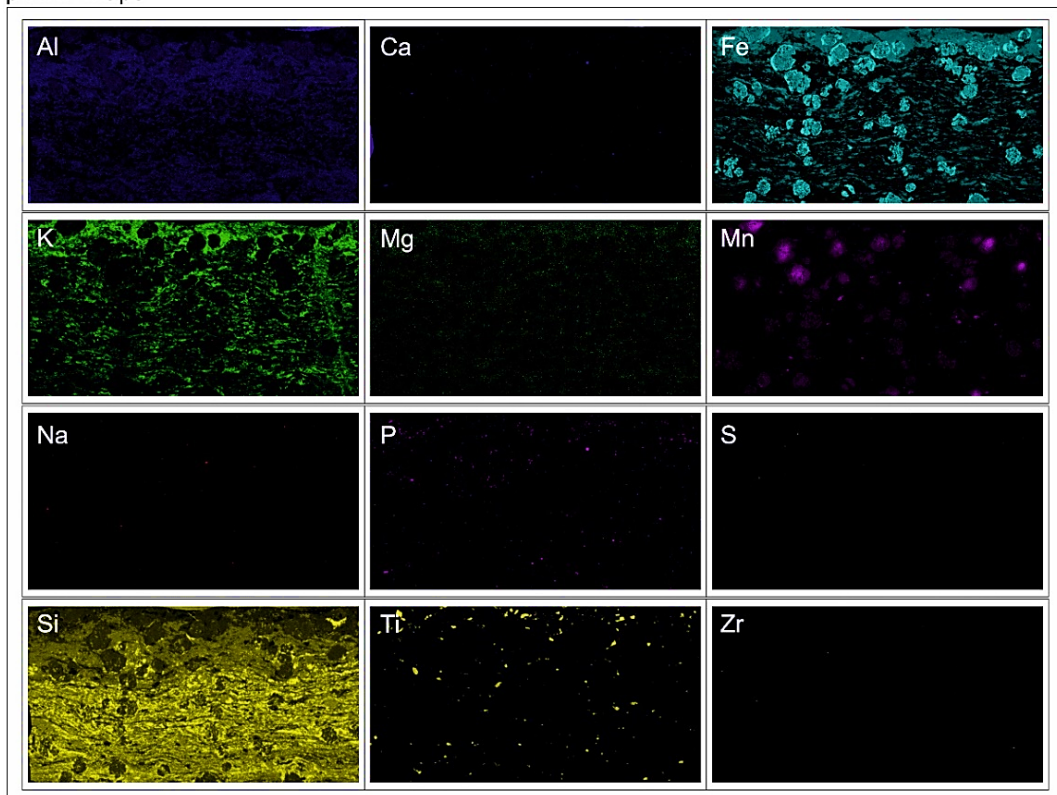


Fig. 2.31 - Thin Section X-ray map array (same scale of Fig. 2.30).

Such an X-ray map array was successfully processed by the Q-XRMA software, to obtain a thin section mineral map where each mineral is identified by a unique colour (Fig. 2.32a). As shown in figure 2.32b, plagioclase is the main mineralogical phase constituting the investigated sample, counting for the 33.26 % of the rock, followed by garnet (18.45 %), white mica (18.44 %), biotite (17.01 %) and quartz (10.05 %).

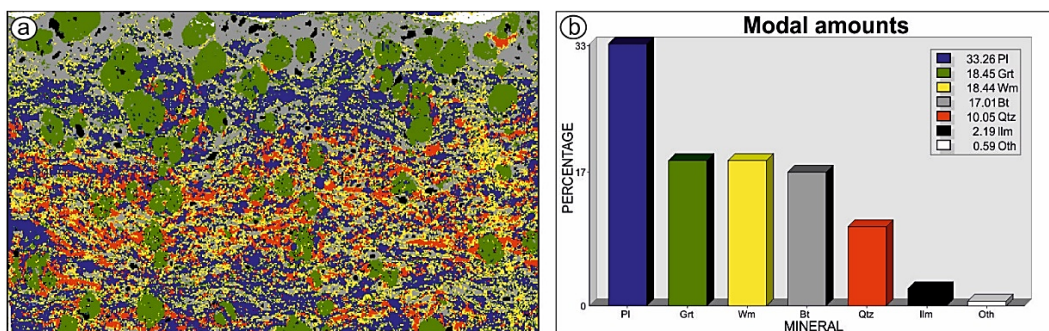


Fig. 2.32 - Mineral classification of the entire thin section via Q-XRMA: (a) mineralogical distribution map (same scale of Fig. 2.30); (b) histogram of mineral modal percentages.

Combining this output (Fig. 2.32a) with the grain polygon one (Fig. 2.30b), it is possible to distinguish the grain size distribution characterising every mineral. As a preliminary operation, a georeferencing of the maps under process has to be executed to ensure a perfect overlap between the two images. After that, the sequence of the operative steps summarises in fig. 2.33 must be followed.

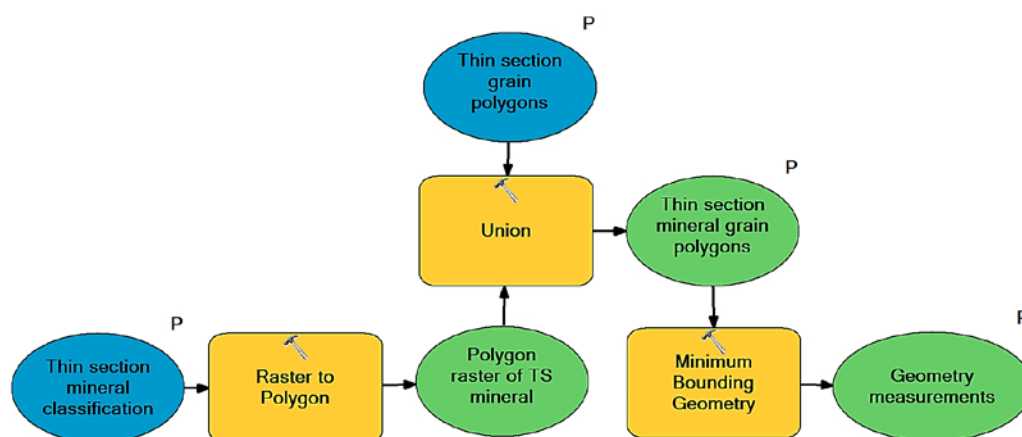


Fig. 2.33 - Flow chart of the Mineral Grain Size Distribution toolbox. Legend as in Fig. 2.3.

Such a sequence provides a first raster conversion of the thin section classification, obtained by the Q-XRMA, in polygon features where each polygon represents a specific mineral phase. Because of the different pixel matrix dimension of the input images and the effect linked with the georeferencing stretch, it is necessary to delimit the area enclosed within each polygon feature. This goal can be achieved adopting a union function which requires that the inputs not to be raster files, explaining, in this way, the reason of the initial raster to polygon conversion. This step is followed by a minimum bounding geometry operation which allows to

obtain pieces of information about the orientation of the single grains and the short and the long axis of each polygon, updating the attribute information stored in the table associated with the grain polygon map. In such a way, a final updated output is obtained, where each grain polygon can be now displayed with the associated mineral name (Fig. 2.34a).

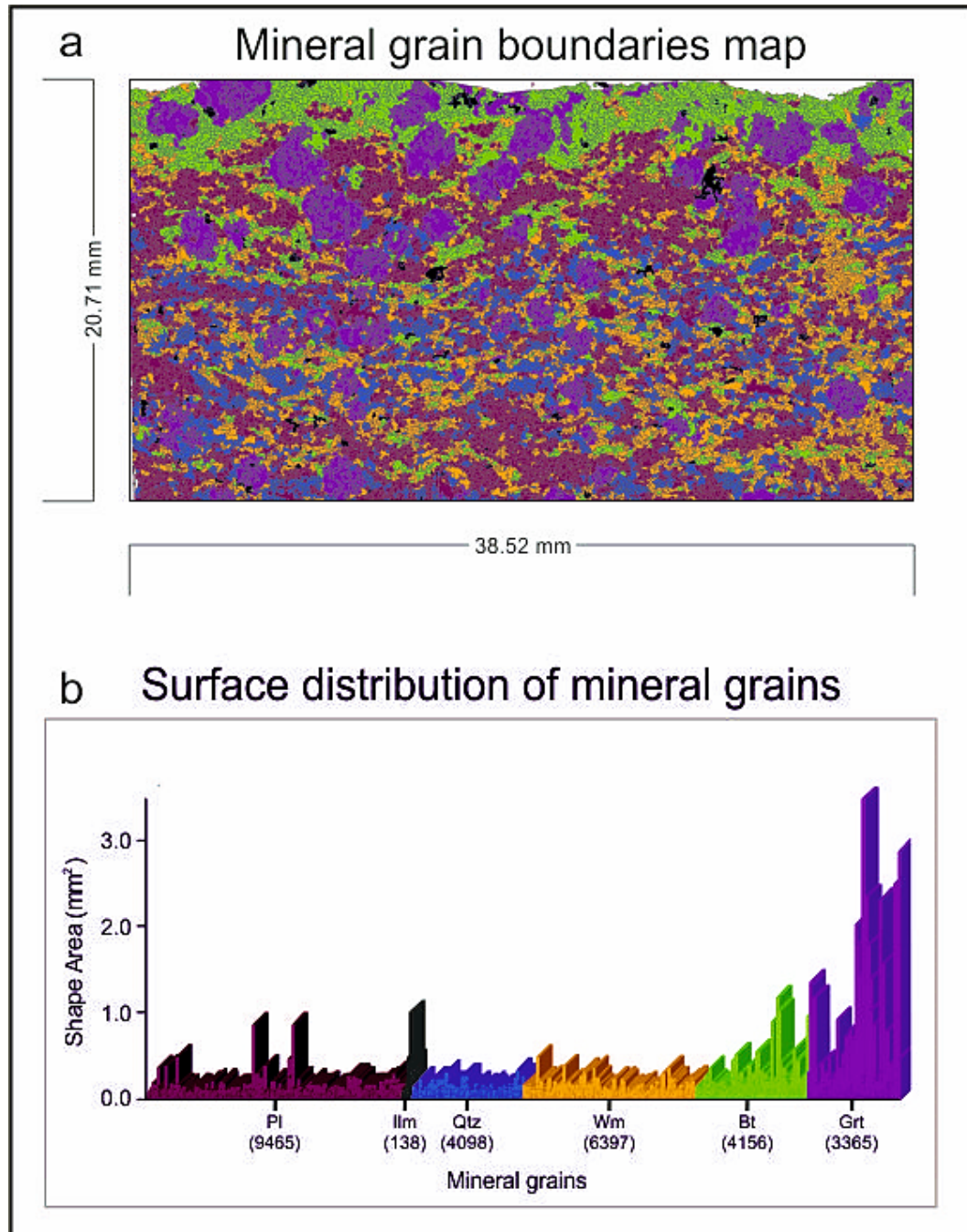


Fig. 2.34 - Grain size distribution distinct for each thin section-forming mineral: (a) mineral grain size polygon map. All of the polygons constructed by the GSD toolbox are labelled with the appropriate mineral name classified via the Q-XRMA; (b) histogram of grain size frequencies distinct for each mineral.

The latter can then be used to construct the diagram of the mineral grain size distribution as that shown in Fig. 2.34b, where the number of specific mineral grains is plotted vs their shape areas. Figure 2.34b shown as garnet and biotite together with some plagioclase crystals represent the mineralogical phases with larger grains. In particular, garnet shows three different grain size clustered at c. 0.5 mm^2 , 1.5 mm^2 and 3 mm^2 and a lesser grains number with respect to the white mica. Despite this, as shown in figure 2.32b, both garnet and white mica are characterised by almost the same modal abundance due to the porphyroblastic feature of garnet. Such a result can be advantageous in the view of diffusion studies, as the compositional variability observed within several crystals, could be strictly connected to different diffusive relaxation effectivenesses at various grain sizes. Therefore, the combined use of the GSD toolbox and the Q-XRMA software provides valuable information about the composition and the mineral grain sizes that must be taken into account in the choice of the crystals to be investigated, as well as minimising the user decision-making activity.

The other main parameter to be known for applying diffusion studies is the kinetic element coefficients characterising the cationic motion in a mineral. The quantitative determination of this parameter represents the topic of the following sections, where a brief description of diffusion concepts and the fundamental factors affecting cationic motion rates will be given.

3. The diffusion modelling tool applied for discovering timescales and rates of geological processes

3.1 General Outlines

Recently, one of the most challenging topics faced by geologists consists in unravelling the timescales of deep tectono-metamorphic processes which driven the Earth orogenic dynamics. The discovery of ultra high metamorphic rocks cropping out on the Earth surface, suggests that such processes can be “fast” enough to preserve mineral assemblages and compositionally-zoned solid solutions, recording their progressive growth history typical of higher thermobaric conditions (e.g., [Duchene et al., 1997](#); [O’Brien, 1997](#); [Perchuk & Philippot, 1997](#); [Oelker et al., 2003](#); [Li et al., 2008](#); [Zhang et al., 2010](#)). As a counterpart, prolonged processes can destroy any proof of the *PT* path followed by the rocks, by flattening first chemical gradients established in zoned minerals during their growth stages as a consequence of the metamorphic evolution (e.g., [Anderson & Olimpo, 1977](#); [Woodsworth, 1977](#); [Spear, 1988, 2014](#)). In this view, finding a tool capable of outlining and quantifying temperature-pressure-time history of rocks, would constitute a major step-ahead for unveiling how our dynamic planet evolves. In the last decades, concentration gradients modelling, altered by diffusion mechanisms, turned out to be a useful and versatile tool able to constrain the geological event timescale ([Elliott, 1973](#); [Lasaga, 1979, 1983](#); [Zhang, 1994](#); [Ganguly, 2002](#); [Chakraborty, 2006, 2008](#); [Costa et al., 2008](#); [Ganguly, 2010](#); [Zhang, 2010](#)).

Diffusion is a natural process involving a transport of matter from one region to another where chemical gradients exist, as a result of the Brownian motions of ions, atoms and molecules. The effect of this transport can be assimilated to what happens when a drop of coloured ink is placed on a glass of water (Fig. 3.1a).

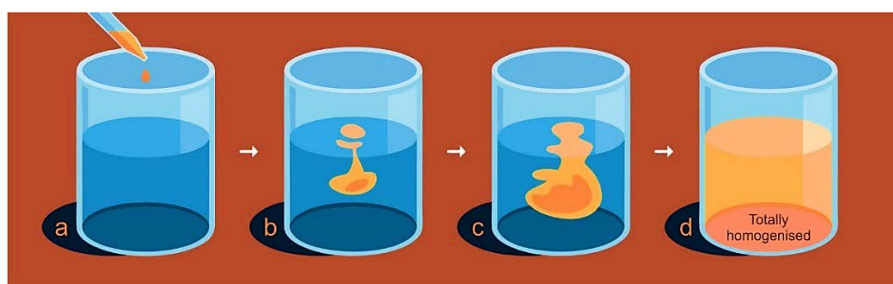


Fig. 3.1 - Schematic example of how diffusion works in a liquid

At first, the drop will be highly concentrated where it encounters the water molecules (Fig. 3.1b). After a specific time, as a function of the specific molecular interaction, the coloured ink drop will penetrate inwards (Fig. 3.1c) until diffusion homogenises the concentrations totally, completing the mixing (Fig. 3.1d). The described phenomenon is specific for liquids, but analogously mechanisms are typical in gases and solids. As can be seen from figure 3.1, the advance of diffusion takes place over a period which can be deduced if some fundamental parameters are known (e.g., the composition of the medium and the diffusing substance, the rate of diffusion and the distance covered).

Specifically, solid-state diffusion constitutes the main focus of petrologists as rocks are mainly composed of minerals. The topic of diffusion in solids was firstly addressed in detail by studying the behaviour of alloys under high-temperature conditions (Callister, 1985; Stalker & Morral, 1990; Mehrer, 2007 and references therein). It can be schematized using a diffusion couple constituted by two different bars of metals joined along a direct contact of their faces (Fig. 3.2a). In this case, the atom locations of both of the bars (Fig. 3.2b) define a sharp contrast in the chemical compositions across the interface (Fig. 3.2c). If an increase in temperature occurs over time, the atoms will migrate (Fig. 3.2d) between the crystalline structures of the two metals (Fig. 3.2e), modifying their original compositions (Fig. 3.2f) until the cooling at room temperature.

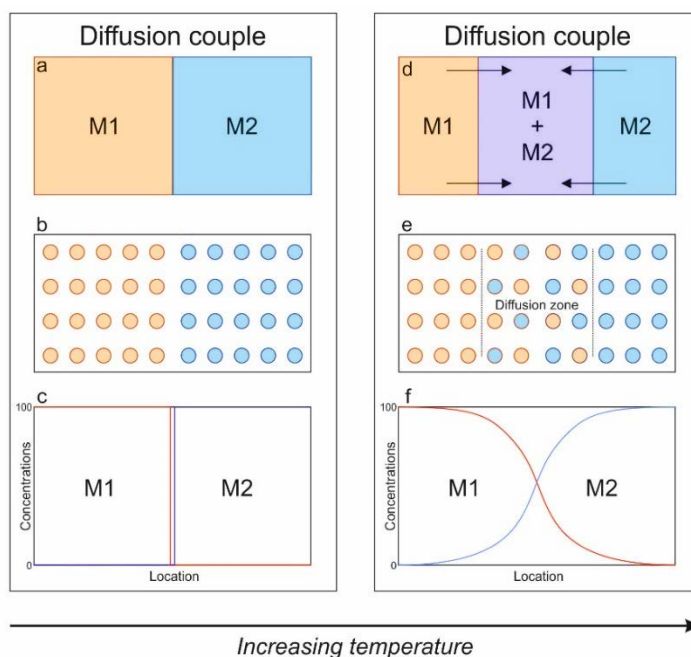


Fig. 3.2 - Schematization of particle diffusion between two solids in contact along their faces: (a) pre-diffusion initial condition; (b) atomic view; (c) concentration profiles; (d) post-diffusion condition; (e) atomic migration; (f) modified concentration profiles.

The result of this process is known as interdiffusion and it well-explains the behaviour of two diffusing species. A typical example of interdiffusion in natural samples is found in olivine, where the Fe-Mg exchanges can modify the original mineral chemistry. Such a modification is often modelled by petrologists, for instance, to derive timescales of various magmatic processes such as magma mixing, degassing, transport and fractionation or residence time in a magmatic chamber (e.g., [Costa et al., 2008](#) and references therein), which usually take place in hours, days or weeks.

When the fluxes involved in the diffusive exchanges are more than two, the diffusion process is multicomponent. One of the best examples of this kind of material transport is represented by garnet, where such a mechanism usually regards the fluxes of four principal components (i.e., almandine, grossular, pyrope and spessartine). Garnet is one of the best recording minerals of thermal and dynamic histories of a large variety of crustal and mantle rocks. This peculiarity is due to its high stability in a wide range of *PT* conditions as well as its slow cationic diffusion rates, which allow preserving traces of the growth evolution in the form of chemical zonings. Moreover, the porphyroblastic features typical of garnets permits an easy measure of these zonings using common ion, proton or electron microprobes. For all of the reasons above, garnet is also one of the most used minerals in diffusion studies, for unravelling timescales of metamorphic processes such as heating and cooling phenomena from which infer burial and exhumation rates, respectively. These rates can be obtained because diffusion tends to erase the original chemical gradients by homogenising the compositions (e.g., after long residence time under high temperature) born from fractionation processes during the garnet growth, or inducing new compositional zonings as a result of a change in temperature, pressure, fluid compositions or reaction rates (e.g., retrograde zonings along the edges of garnet crystals). Therefore, knowing cationic diffusion rates (namely the element diffusivity) represents a corner stone for evaluating the period at which the extent of the compositional readjustments occurs, as a consequence of specific triggering geological processes. In the last years, several efforts have been made to constrain the diffusivity of major cations in garnet (i.e.,

Ca, Fe, Mg and Mn) by using different experimental types of equipment (e.g., piston cylinder apparatus in talc-glass pressure cells within a graphite furnace – Elphick & Ganguly, 1985; Loomis et al., 1985; Chakraborty & Ganguly, 1992; Ganguly et al., 1998; Carlson, 2006; Perchuk et al., 2009; a mixed-gas vertical-tube furnace – Schwandt et al., 1995, 1996; or silicate thin film by pulsed laser deposition – Dohmen et al., 2002; Jackson, 2005), and several critical reviews of these data followed (Korolyuk & Lepezin, 2008; Perchuk et al., 2009; Brady, 2010; Chu & Ague, 2015). However, despite the huge amount of data produced, a potential innovation would come from the knowledge of the diffusivity of other elements as well (e.g., REEs), that could provide more robust assumptions about the evolution and timescales of geological processes if combined with those obtained from the major cations, but this is beyond the scope of this work.

It is important to point out, that any diffusion study aimed to acquire timescale of geological events requires that the “kinetic window condition” (Chakraborty, 2008) has to be satisfied. This last request is verified if exists an intermediate state (Fig. 3.3b) between an initial condition (Fig. 3.3a), where there is no diffusion in the system (e.g., as a consequence of fast geological events or residence at too low temperatures), and a final state (Fig. 3.3c) where diffusion have homogenised the system totally, reaching equilibrium (e.g., as a consequence of long residence time at high temperatures).

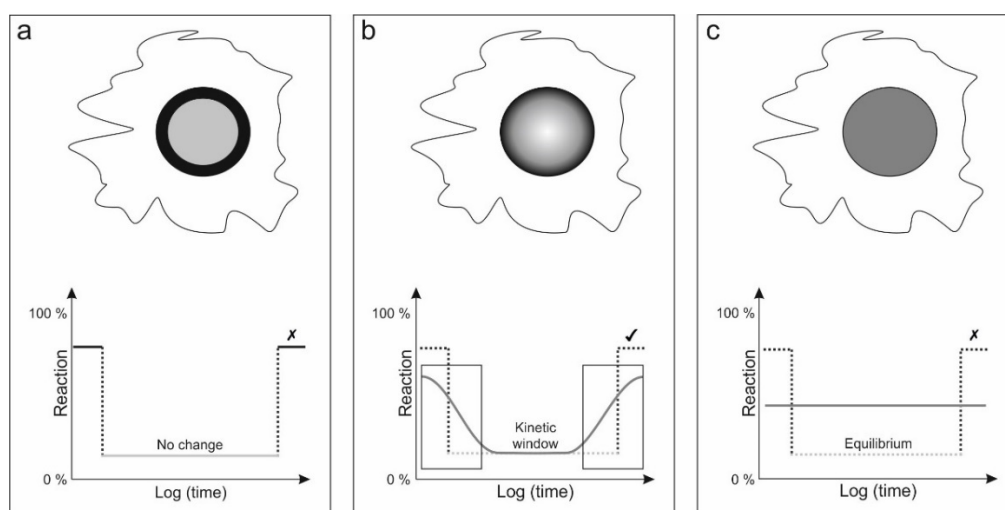


Fig. 3.3 - Schematic representation of the proceeding of diffusion: (a) no-diffusion condition with original sharp compositional contrast between two distinct chemical zones; (b) diffusional changes occurred after a lot of time; (c) equilibrium steady-state with no diffusion evidence

In the following sections, a discussion about the cationic migration mechanisms in solids, on the nomenclature of kinetic coefficients with a description of the main affecting-factors of the cationic motion rates, on the main physical laws governing diffusion and on the possible analytical and numerical solutions, will be made. Moreover, two different cases studies are here presented to highlight the potential contribution provided by the diffusion modelling in the $PT\Delta t$ -path reconstruction of metamorphic rocks, using the methodological approach developed and described in the [chapter 2](#).

Although the diffusion topic is here addressed to derive the duration of metamorphic processes, there are many other fields where this approach can be applied. For instance, diffusion modelling also finds application in the area of geomorphology to quantify how landforms (e.g., hillslopes) are smoothed over time ([Pelletier, 2008](#)). Indeed, in this case, the diffusional process tends to homogenise elevation at the same manner of chemical gradients in minerals, helping to determine the temporal evolution of well-dated shoreline scarps and volcanic cones, if a constrained topography of the past is available.

Another application is represented by the elemental diffusion in semiconductors like Si, and Ge employed in high-tech devices development (e.g., [Shaw, 1973](#); [Willoughby, 1978](#); [Tan & Gosele, 2005](#); [Mehrer, 2007](#)) such as memory and processors chips used by smartphones and computers or solar cells in photovoltaic equipment. In this case, solid-state diffusion is closely connected to the manufacturing process of electronic devices, as it governs the conductivity type of the material and the impurity gettering formed during crystal growth. These examples highlight how the diffusion topic finds a wide range of application in every field of scientific research, providing information that can be used to improve the knowledge of electronic and earth materials.

3.2 Diffusion mechanisms

The diffusion process can be considered as a result of two main mechanisms, identified in the intragranular diffusion and intergranular diffusion.

The first one is also known as volume diffusion (Dv), and it can be defined as the atoms migration within the crystalline lattice ([Chakraborty, 2008](#)). Such a

phenomenon affects the development of mineral compositional zonings, the atomic order in the mineral crystallographic sites, the formation and progressive growth of the exsolution lamellae as well as the maintenance of the isotopic features used as a quantitative clock of their own thermic and growth history. A fundamental condition required to have particles migration is the existence of lattice defects as vacancies, interstitial atoms or impurities (Fig. 3.4). In this way, atoms can move by a substitution of their original lattice location, migrating towards a vacancy or an interstitial position, if they are not already occupied by other atoms.

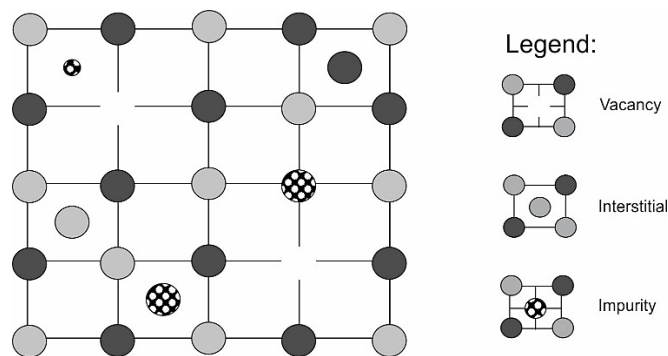


Fig. 3.4 - Schematic representation of the main crystal lattice defects

In the case of the intergranular diffusion, atoms can migrate along grain boundaries (DGb) of two different crystals or sub-grain contacts ($DsGb$) and fractures (DFr) within the same crystal (Fig. 3.5).

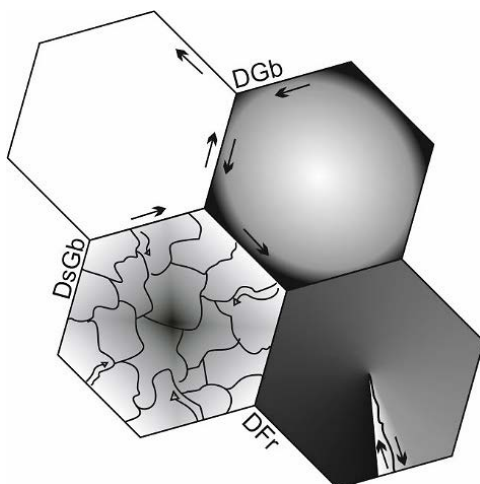


Fig. 3.5 - Schematization of the various intergranular diffusion mechanisms. The $DsGb$ shows as the more the sub-grains are, the more pronounced will be the effect of diffusion with respect to the diffusion along a unique grain boundary (DGb) or along a fracture (DFr).

The volume diffusion is more efficient at high temperatures and coarse grain sizes, as the activation energy, linked with the atoms migration from one crystallographic site to another one, is greater than the inter-granular diffusion (i.e., $QDv > QGb >$

$Q_{sGb} > Q_{Fr}$), as the thickness of the grain boundary is smaller with respect the entire clast (Chakraborty, 2008). Therefore, it is evident that: (a) the completeness of the material transport depends on both on the diffusion rates (i.e., the magnitude of the diffusion coefficients) and the availability of diffusion paths (i.e., the concentration of defects); (b) the temperature plays a crucial role in the specifically-acting diffusion mechanism.

The contribution of temperature and the other specific environmental variables, are fundamental to determine how fast atoms can diffuse and they will be treated in details in the following sections.

3.3 Element diffusion coefficients

The most important parameter to know is the diffusivity of a specific parameter governing the rates at which diffusion can obliterate and re-equilibrate an initial gradient. Such a diffusivity can describe the element exchanges in a wide range of diffusive conditions.

After a deep review of the existing literature, various definitions have emerged on the nomenclature of the kinetic coefficients (denoted as D) identifying different types of diffusive transport (e.g., Watson & Baxter, 2007; Ganguly, 2010; Zhang, 2010) and therefore, it was considered useful to summarize the most adopted ones. Overall, any definition can be grouped into two main categories, that is: (a) the self-diffusion, describing the transport of matter in the absence of a chemical gradient, but just due to the particle Brownian motions (Watson & Baxter, 2007); (b) the chemical diffusion, describing the particle fluxes occurring in presence of a chemical potential gradient (Watson & Baxter, 2007).

The first category (a) includes those coefficients derived by experimental laboratory measurements, such as:

- *Tracer diffusion coefficient*: is related to an isotope of an element describing its flux in the presence of the specific isotopic concentration gradient in a chemically homogeneous medium (Ganguly, 2010; same of the self-diffusion coefficient in Zhang, 2010). In other words, this condition is possible if the

isotope diffuses by exchanging position with another isotope of the same element.

- *Self-diffusion coefficient*: is associated with the flux of an element solely due to its concentration gradient. When all the isotopes of the element have the same diffusivity, tracer and self-diffusion coefficients could be considered the same quantity. According to [Ganguly, \(2010\)](#), this approximation could be regarded as suitable for most addressed geological problems.

The second one (b), can be subdivided in:

- *Interdiffusion coefficient*: is used to describe the ionic fluxes of two elements (e.g., Fe-Mg in olivine or MgO-SiO₂ diffusion in binary melts) expressed as the weighted average of two self-diffusion coefficients. In the case of two equally-charged species which diffuse in a fixed molar volume, the interdiffusion is expressed as:

$$D_{i-j} = \frac{D_i D_j}{D_i X_i + D_j X_j} \quad (\text{Eq. 4})$$

Where $D_i X_i$ denotes the self diffusion and molar fraction of the element i and $D_j X_j$ are the same for the element j .

- *Matrix of diffusion coefficients*: explains the fluxes of more than two components in a chemical system (e.g., [Lasaga, 1979](#); [Loomis et al., 1985](#); [Chakraborty & Ganguly, 1991](#); [Kress & Ghiorso, 1993](#); [Trial & Spera, 1994](#); [Kress & Ghiorso, 1995](#); [Cussler, E. L. \(1997\)](#); [Liang et al., 1997](#); [Mungall et al., 1998](#); [Costa et al., 2008](#); [Ganguly, 2010](#); [Zhang, 2010](#)). In a multicomponent system with n components (i.e., $n \geq 3$), there are $(n - 1)$ independent components, as the flux of the $n - th$ component (selected according to convenience, [Ganguly, 2010](#)) is fixed by those of the other $(n - 1)$ components as a function of the stoichiometric constraint ($\sum X_i = 1$) ([Ganguly, 2010](#)). Then, the flux of each component is controlled not only from its own concentration gradient but from the concentration gradients of all

other independent components as well. In this case, the mutual component interchanges are expressed by an $(n - 1) \times (n - 1)$ matrix of diffusion coefficients (\mathbf{D}) usually referred as a \mathbf{D} -matrix:

$$\mathbf{D} = \begin{bmatrix} D_{ij} & \dots & D_{i(n-1)} \\ \vdots & \ddots & \vdots \\ D_{(n-1)j} & \dots & D_{(n-1)(n-1)} \end{bmatrix} \quad (\text{Eq. 5})$$

Every element of the \mathbf{D} -matrix is computed according to the formulation of Lasaga, (1979), as follow:

$$D_{ij} = D_i \delta_{ij} - \frac{D_i X_i}{\sum_{K=1}^n D_K X_K} (D_i - D_n) \quad (\text{Eq. 6})$$

Where δ_{ij} is the Kronecker delta (i. e., $\delta_{ij} = 1$ when $i = j$ and $\delta_{ij} = 0$ when $i \neq j$), X_i and D_i are, respectively, the mole fraction and the self diffusion coefficient of the species i , and the n^{th} component (D_n) is treated as dependent. Since the complexity of the multicomponent diffusion, usually are applied some simplifications, as the concept of the effective binary diffusion coefficients described below.

- **Effective binary diffusion coefficient:** is used when a multi component system can be treated as a binary mixture where a diffusing species is the solute, and the rest of the solution represents the solvent (Cooper, 1968). The last statement means that or all other species are treated as a combined component or the cross diffusivities in the multicomponent diffusion matrix are ignored because of a no-significant contribution in the diffusive changes (Chakraborty & Ganguly, 1992; Ganguly, 2010; Zhang, 2010). From a mathematical point of view, the effective binary diffusion coefficient (denoted as $EBDC$ or $D(EB)$) can be calculated as follow:

$$D(EB) = D_{11} + D_{12} \frac{\partial C_2}{\partial C_1} + \dots + D_{1(n-1)} \frac{\partial C_{(n-1)}}{\partial C_1} \quad (\text{Eq. 7})$$

Where all the compositional dependence, and even dependence on concentration gradients, are enclosed in this one term. It is also worth noting that the *EBDC* of every component in a multicomponent system may be different as depending on the spatial gradient, and therefore it cannot be used to model different crystals of similar composition.

3.3.1 Factors affecting diffusion coefficient measurements

The diffusive flux of an element exists in the presence of a concentration gradient, which is in turn controlled by several factors such as partition coefficients, availability of reactant nutrients and mineral modal abundances (Chakraborty, 2008). All of these factors are further governed by the element concentrations, mineral crystallographic structure and several environmental variables such as temperature, pressure and fugacity of specific species.

Temperature has the strongest effect on the dependence of the kinetic coefficients as diffusion is a thermally activated process. Whereas, pressure and composition also affect the elemental kinetic rates but in a lesser measure. The equation most commonly used to calculate diffusion coefficients from experimental data, explaining the temperature and pressure dependencies of D , is an Arrhenius-type equation defined as:

$$D(P, T) = D_0 \exp\left(\frac{-Q - \Delta VP}{RT}\right) \quad (\text{Eq. 8})$$

where $D(P, T)$ is the diffusion coefficient expressed as a function of temperature and pressure, T is the absolute temperature in Kelvin, P is the pressure in bar, D_0 is the pre-exponential factor (i.e., the tracer- or self- D), derived experimentally, representing the diffusion coefficient at infinite temperature and atmospheric pressure (Chakraborty, 2008), Q is the activation energy at 1 bar, ΔV is the activation volume of diffusion and R is the gas constant. The influence of fugacity (e.g. f_{O_2} , f_{H_2O}) and composition are usually bracketed in the pre-exponential factor (e.g., Dohmen & Chakraborty, 2007; Hier-Majumder et al., 2005; Costa & Chakraborty, 2008). Another parameter influencing diffusion coefficients is the

crystal symmetry, as in the case of olivine where diffusion is anisotropic and D along the c -axis = $6 \times D$ along the a - and b -axes (Fig. 3.6a), in opposite to garnet, where the isotropic character of the mineral can explain the same D value in each crystallographic direction (Fig. 3.6b). In the case of an anisotropic medium, using an erratic value of D could result in an underestimation of the timescale of the linked geological event.

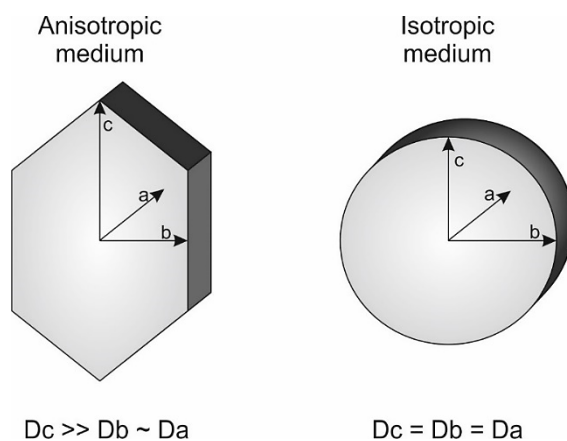


Fig. 3.6 - Different crystallographic structures influencing diffusion: (a) the anisotropic medium has a fast diffusion along c -axis rather than a - and b -axes (e.g., olivine); (b) the isotropic medium has the same diffusion in all of the directions (e.g., garnet).

Overall, if temperature and pressure are known (e.g., as a result of a thermodynamic modelling), the $D(P, T)$ of an element can be obtained applying Eq. 8, by using experimental data of D_0 , Q and ΔV . As an example, in Tab. 3.1 are reported some of the garnet element diffusion datasets acquired experimentally and most used for deriving $D(P, T)$.

Such datasets are here implemented in a new image-processing tool described below, able to calculate maps and create databases of $D(P, T)$ values automatically, and further used to derive the different chemical diffusion coefficients described in section 3.3.

Tab. 3.1 - Datasets of diffusion data reported in literature

Element	D_0 (m ² /s)	Q (kcal/mol)	ΔV^\ddagger (m ³ /mol)	Activation energy (kJ/mol)	Experimental conditions	D (m ² /s) at T = 530 °C and P = 4.2 kbar	D (m ² /s) at T = 670 °C and P = 6.1 kbar	Study
<i>Fe</i>	3.10E-09	61.3		256.48 ± 35.56		6.47E-25	1.94E-22	
<i>Mg</i>	2.00E-09	59.9		250.62 ± 33.05	T = 1300 - 1500 °C; P = 40 kbar	1.00E-25	2.64E-23	Loomis et al. (1985)
<i>Mn</i>	2.20E-09	48.1		201.25 ± 33.05		1.79E-22	1.57E-20	
<i>Ca</i>	1.55E-09							
<i>Fe</i>	6.40E-08	65.8	5.60E-06			5.52E-26	2.31E-23	
<i>Mg</i>	1.10E-07	68.0	5.30E-06		T = 1300 - 1480 °C; P = 14-35 kbar	2.48E-26	1.28E-23	Chakraborty & Ganguly (1992)
<i>Mn</i>	5.10E-09	60.6	6.00E-06			1.15E-24	2.95E-22	
<i>Ca</i>	3.20E-08							
<i>Fe</i>	2.19E-08	63.2	1.36E-05			5.80E-26	1.7E-23	
<i>Mg</i>	2.17E-09	58.4	8.57E-06			1.66E-25	3.33E-23	Carlson (2006)
<i>Mn</i>	2.23E-08	63.2	9.63E-06			7.71E-26	2.39E-23	
<i>Ca</i>	1.57E-10	55.1	9.80E-06			8.58E-26	1.25E-23	

3.3.2 Diffusion coefficient map creator (DCMC): A Q-XRMA image-processing add-on for creating map of various kinetic coefficients in a Local Information System (LIS)

A new Python code has been here implemented as an ArcGIS®-based add-on of the Q-XRMA image analysis software, with the aim to create diffusion coefficient maps (*D*-maps) of selected minerals from an investigated thin section domain. In this view, all of the three cycles of the Q-XRMA (see [section 2.3](#)) have to be executed before using the new tool. This latter allows to derive *D*-maps for garnet, but it could be extended potentially to other mineralogical phases as, for instance, olivine and plagioclase (red area on [Fig. 3.7](#)), if experimental diffusion data are available. The creation of garnet *D*-maps relies on three different experimental diffusion datasets (see [Tab. 3.1](#); green area on [Fig. 3.7](#)). The choice of these datasets comes from: (a) the chance to investigate results carried out with old experimental data (e.g. [Loomis et al., 1985](#)), by comparing them with the more recent ones (e.g., [Carlson, 2006](#)); (b) using the most applied data sets in literature (i.e., [Carlson, 2006](#); [Chakraborty & Ganguly, 1992](#)); (c) applying diffusion data obtained by different experimental determinations.

```

D:\Q-XRMA\prog\cmd.exe - D:\Q-XRMA\prog\plug-in\DCMA.py
DIFFUSION COEFFICIENT MAPS ANALYZER V. 1.0 (R01) 03/05/2017 devolper: RV

Hello v_rob!
You are working on Windows_NT 6.2.9200
This application is a plugin of the Quantitative X-Ray Map Analyser (Ortolano et al., submitted 2017) allowing to derive diffusion
coefficient maps

I have found these workspaces in your data path:

Old_elaborations
PROVA
Please, select a folder listed above or digit a new workspace:
PROVA

1 - Garnet
2 - Olivine
3 - Plagioclase
Please, select a phase listed above by selecting the relative number:
1
You have selected: Garnet

1 - Loomis et al., 1985
2 - Chakraborty & Ganguly, 1992
3 - Carlson, 2006
Please, select a diffusion coefficient dataset listed above by selecting the relative number:
2
You have selected: Chakraborty & Ganguly, 1992
DCa: 0.00032    cm^2/s
DFe: 0.00064    cm^2/s
DMg: 0.0011    cm^2/s
DMn: 0.00051    cm^2/s

```

Fig. 3.7 - Windows shell of the DCMC add-on showing the initial prompts. Red area encloses three mineralogical phases where execute the calculation potentially. Green area delimits the three-different diffusion dataset from the literature, implement for garnet.

By default, these data are expressed in cm^2/s but a conversion in m^2/s , mm^2/s and $\mu\text{m}^2/\text{s}$ is possible as well (red area on Fig. 3.8).

As a priori condition, a domain (green area on Fig. 3.8) and a mineral sub-phase classification (blue area on Fig. 3.8), which can be obtained by using, respectively, the first and second cycle of the Q-XRMA software (see Fig. 2.14, 2.15), are required (Fig. 3.9). The domain mineral classification (e.g., Fig. 3.10a) is necessary to select a mineralogical phase to be used as a mask where execute the calculations (in this case, garnet). Whereas, the mineral sub-phases identification (e.g., the garnet mantle = MNT and the garnet static rim = SR, in Fig. 3.10b) is used to associate, one-by-one, temperature and pressure values linked to each sub-phases growth stage (e.g., Fig. 3.11), which is required to solve Arrhenius Eq. 8 in the calculation of D (Fig. 3.9).

Indeed, the add-on asks users to provide temperature and pressure information specific for every mineral sub-phase identified (yellow area on Fig. 3.8). As a result, maps of D expressed as a function of temperature and pressure (i.e., $D(P, T)$ -maps), are obtained (Fig. 3.9).

Furthermore, since the strong dependence of the element diffusivity from the mineral compositions, the add-on permits to derive maps of the chemical diffusion coefficients summarised in section 3.3 (red area on Fig. 3.12). These outputs are

obtained solving Eq. 4, Eq. 6 or Eq. 7, by using the absolute value stored in each pixel of the $D(P, T)$ -maps and the mineral component ones (Fig. 3.9), the latter derived executing the third analytical cycle of the Q-XRMA (see Fig. 2.16 and Fig. 3.13 as an example).

```

D:\Q-XRMA\prog\cmd.exe - D:\Q-XRMA\prog\plug-in\DCMA_theisgy
Do you want change unit of measure? Y/N
y
1 - m^2/s
2 - mm^2/s
3 - Åµm^2/s
Please, select an unit of measure listed above:
3
Your dataset now is: Chakraborty & Ganguly, 1992
DCa: 31800.0 Åµm^2/s
DFe: 63600.0 Åµm^2/s
DMg: 111000.0 Åµm^2/s
D'n: 51500.0 Åµm^2/s
Bt
Qtz
Pl
Ilm
Hbl
Grt
Alm
An
Please, select a class listed above to be used as a mask (Case Sensitive):
Grt
You have selected Grt
I found this subphase: COR within Grt
Please, insert a temperature value (A°C) for COR: 495
Please, insert a pressure value (bar) for COR: 4400
Computing diffusion coefficients for COR per single pixel...
  
```

Fig. 3.8 - Windows shell of the DCMC tool showing the sequential operative steps. Red area encloses three possibilities of unit conversion. Green area delimits the mineral classes identified by the first cycle of the Q-XRMA (mineral abbreviations are from Siivola & Schmid (2007)). Blue area shows the mineral sub-phase classified during the second cycle of the Q-XRMA (e.g., the garnet core = COR), where executing the calculation. Yellow area brackets the PT prompts asked the users.

Then, for every potential mineral investigated it is possible to obtain a database of specific D -values expressed as a function of temperature, pressure and chemical composition, which represent the input parameters applied in diffusion modelling. The possibility to have chemical diffusion coefficient maps represents the main advantage characterising the new Q-XRMA add-on, as the compositional dependence of the kinetic coefficients requires that a new value of D be calculated for each value of chemical concentration. Such a calculation would be an extensive time-consuming if done manually, especially in the case of a multicomponent diffusion typical of garnet, where nine coefficients must be computed at the same spot. Figure 3.14 shows an example of a D -matrix constructed for a garnet at the contact between its rim (SR) and mantle (MNT) zones, highlighting as faster diffusion coefficients are localised where the garnet sub-phase grew at higher temperatures.

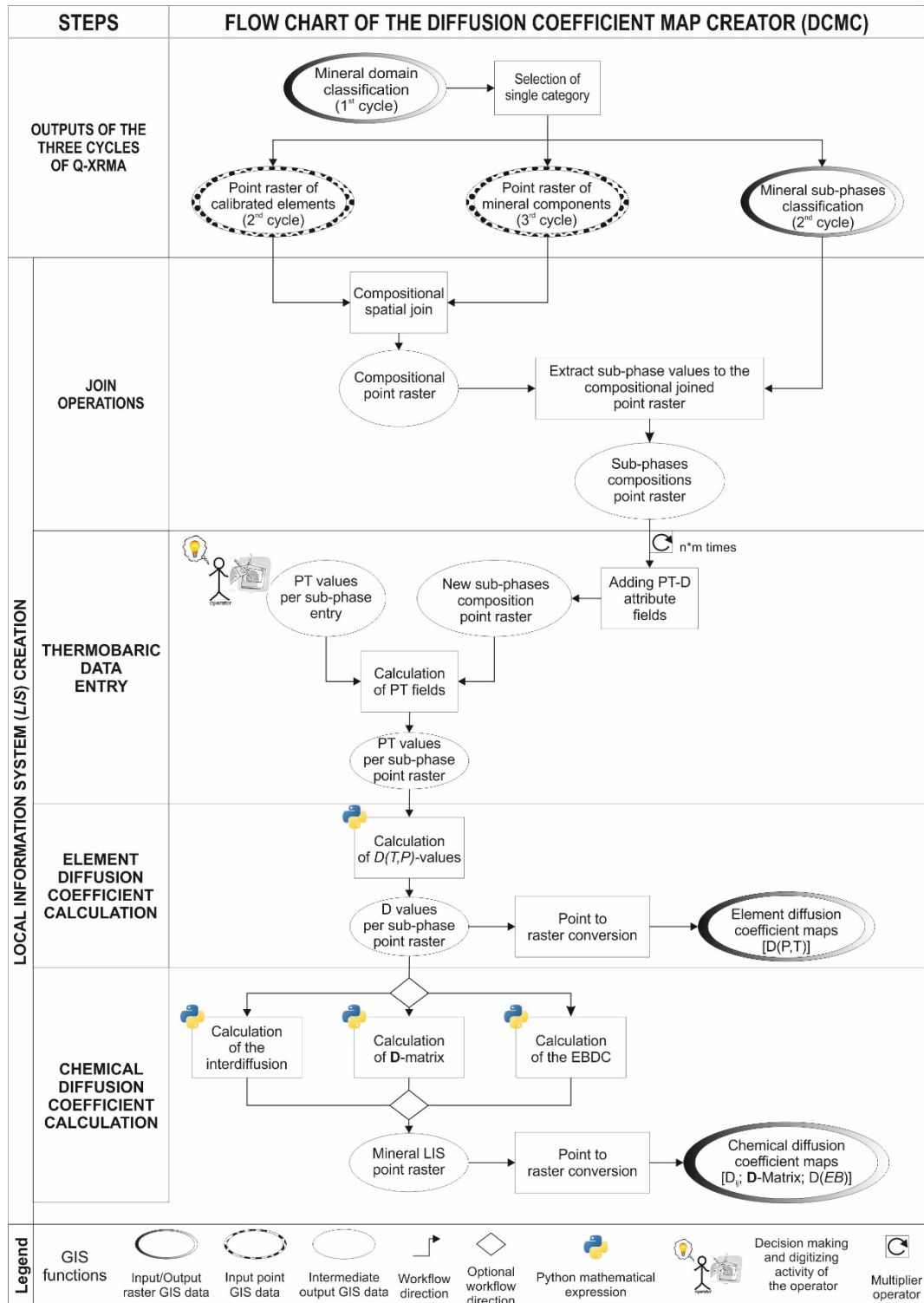


Fig. 3.9 - Flow chart of the DCMC geoprocessing procedure. The *D* coefficient calculations are marked by the Python icons. The input point shapefiles are marked by bubble-ellipses, whereas raster input/output image is shown with grey-scale ellipses. User icon marks the request by the add-on of sub-phases' thermobaric data entries.

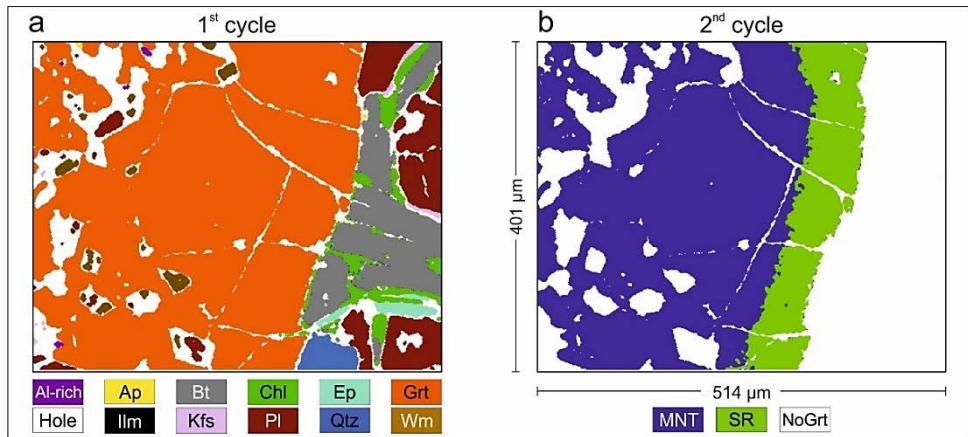


Fig. 3.10 - Input data of the DCMC add-on: (a) mineralogical distribution map obtained by the first cycle classification of the Q-XRMA (mineral abbreviations are from *Siivola & Schmid (2007)*); (b) mineral sub-phase distinctions obtained by the second cycle classification of the Q-XRMA. MNT = garnet mantle; SR = garnet static rim; NoGrt = No garnet phase.

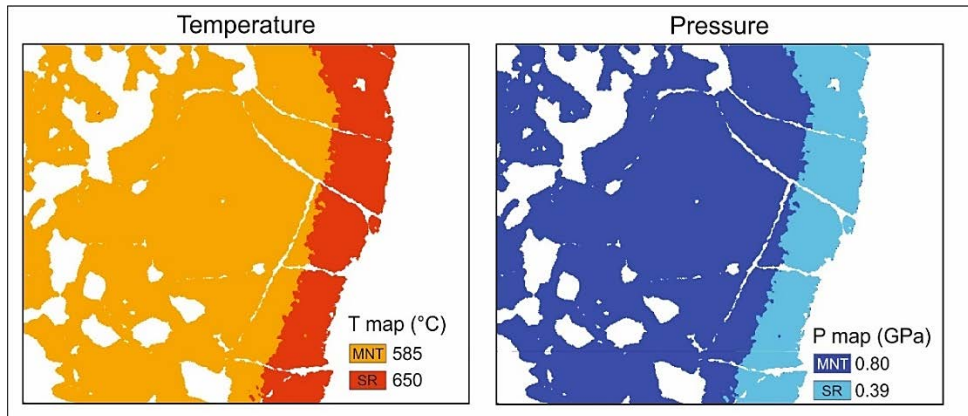


Fig. 3.11 - Temperature and Pressure maps derived by the DCMC.

```

D:\Q-XRMA\prog\andase - D:\Q-XRMA\prog\plug-in\DCMA_deskuy
Ap
Please, select a class listed above to be used as a mask (Case Sensitive):
Grt
You have selected Grt

I found this subphase: COR within Grt
Please, insert a temperature value (Å°C) for COR: 495
Please, insert a pressure value (bar) for COR: 4400
Computing diffusion coefficients for COR per single pixel...

I found this subphase: MNT within Grt
Please, insert a temperature value (Å°C) for MNT: 570
Please, insert a pressure value (bar) for MNT: 7200
Computing diffusion coefficients for MNT per single pixel...

I found this subphase: SRIM within Grt
Please, insert a temperature value (Å°C) for SRIM: 650
Please, insert a pressure value (bar) for SRIM: 3900
Computing diffusion coefficients for SRIM per single pixel...

I found this subphase: NO within Grt
Please, insert a temperature value (Å°C) for NO: 0
Please, insert a pressure value (bar) for NO: 0
Computing diffusion coefficients for NO per single pixel...

1 - Interdiffusion coefficient
2 - Multicomponent diffusion (D-Matrix)
3 - Effective binary diffusion coefficient
Please, select a chemical diffusion coefficient listed above you want calculate, by selecting the relative number:
2
Executing calculation of the D-matrix...

```

Fig. 3.12 - Windows shell of the three-different diffusion coefficient calculations.

Definitely, the DCMC tool permits the user to derive a unique mineral map accompanied by an attribute table containing each information subdivided per sub-phase, such as: (a) atomic and component composition; (b) modal abundances; (c) temperature and pressure; (d) element diffusion coefficient (expressed as a function of T and P); and (e) the derived chemical diffusion coefficient.

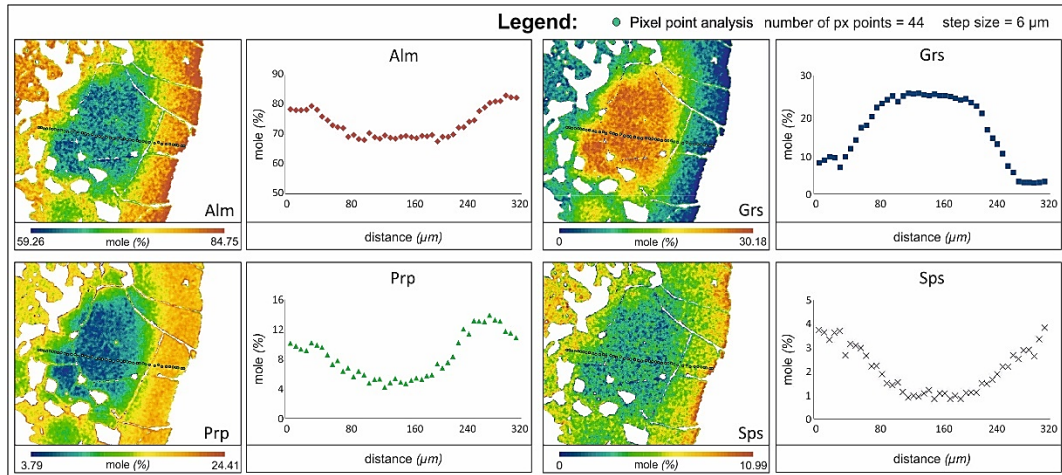


Fig. 3.13 – Mineral component concentration maps from the third analytical cycle of the Q-XRMA used by the DCMC to calculate a map of diffusion coefficients. In the figure are shown garnet component maps and a compositional transect extracted from them for a total of forty-four-point pixels. The step size is 6 μm .

This database-format table can be considered as a part of the Local Information System (LIS) stated, in a GIS-statement similar sense, as a system designed to store, manipulate, analyse, manage, and present spatial micro petrographic data.

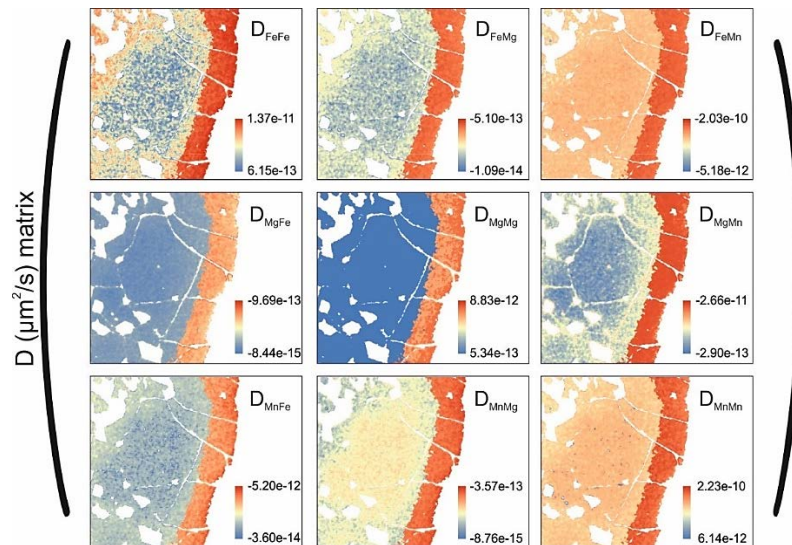


Fig. 3.14 - Matrix of diffusion coefficients computed for garnet. Every map of the matrix element is computed according to Eq. 6.

3.4 Mathematics of diffusion

3.4.1 Basics of diffusion laws

The mathematical formulations of diffusion were developed for the first time by [Fick \(1855\)](#). He applied the theory derived by [Fourier \(1822\)](#), about heat transfer by conduction due to the random molecular motions, to the transfer rate of substances due to diffusion. He observed that the flux of a species J_i (i.e., the matter transfer per unit) was proportional to the concentration gradient of i ($\partial C_i / \partial x$), representing the driving force of this transport, through a proportionality constant D_i :

$$J_i = -D_i \frac{\partial C_i}{\partial x} \quad (\text{Eq. 9})$$

Such a relationship is also known as Fick's first law (Fig. 3.15) and it is analogous to other laws describing various kind of fluxes in the presence of a driving force, such as the Ohm's law (i.e., electrical current to electrical potential gradient) or Fourier's Law (i.e., heat flux to the temperature gradient).

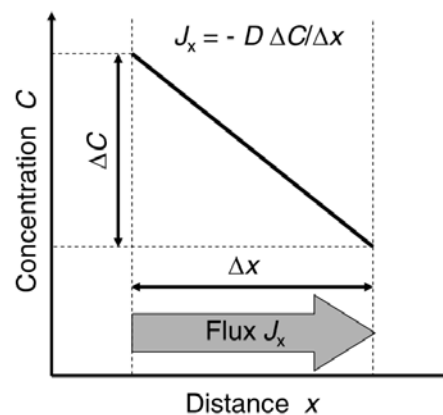


Fig. 3.15 - Illustration of Fick's first law (from [Mehrer, 2007](#)).

The negative sign in Eq. 9 arises because diffusion occurs in the direction opposite to that of increasing concentration ([Crank, 1975](#)). It is important to note that Eq. 9 is consistent only for isotropic media (e.g., garnet in natural samples), whose diffusion properties in the neighbourhood of any point are the same relative to all directions ([Crank, 1975](#)). In the case of an anisotropic medium, (e.g., a non-cubic

crystal), the total flux along a specific direction (i.e., x , y , or z) is the result of the sum of three different terms according to the form of Eq. 9:

$$\begin{aligned} J_i^x &= -D_i^{xx} \frac{\partial C_i}{\partial x} - D_i^{xy} \frac{\partial C_i}{\partial y} - D_i^{xz} \frac{\partial C_i}{\partial z} \\ J_i^y &= -D_i^{yx} \frac{\partial C_i}{\partial x} - D_i^{yy} \frac{\partial C_i}{\partial y} - D_i^{yz} \frac{\partial C_i}{\partial z} \\ J_i^z &= -D_i^{zx} \frac{\partial C_i}{\partial x} - D_i^{zy} \frac{\partial C_i}{\partial y} - D_i^{zz} \frac{\partial C_i}{\partial z} \end{aligned} \quad (\text{Eq. 10})$$

Eq. 10 can be simplified, by transforming the axes x , y , z into the principal axis of a diffusion tensor (see Ganguly, 2002 for further details), which can coincide with the crystallographic symmetry axes in some crystal classes, as is the case for orthorhombic olivine (Costa et al., 2008).

A complication in solving Eq. 9, comes from crystal growth or dissolution phenomena, which involve moving boundary problem. In such a case, Eq. 9 becomes:

$$J_i = -D_i \frac{\partial C_i}{\partial x} + v * C_i \quad (\text{Eq. 11})$$

Where the flux of a species J_i depends from diffusion plus the flux linked to the growth or dissolution of a crystal in a surrounding medium (e.g., a melt), acting at the surface of the growing/dissolving crystal with a specific rate v . This situation could be the case, for instance, of a Mn back-diffusion in garnets, occurred as a consequence of a symplectite formation in high-grade metamorphic rocks.

An evolution of the Fick's first law was developed intuitively by Onsager, (1945), to describe the coupling fluxes of different species in a n -multicomponent system, expressed in one-dimension as:

$$\begin{aligned} J_1 &= -D_{11} \left[\frac{\partial C_1}{\partial x} \right] - D_{12} \left[\frac{\partial C_2}{\partial x} \right] \dots - D_{1(n-1)} \left[\frac{\partial C_{(n-1)}}{\partial x} \right] \\ J_2 &= -D_{21} \left[\frac{\partial C_1}{\partial x} \right] - D_{22} \left[\frac{\partial C_2}{\partial x} \right] \dots - D_{2(n-1)} \left[\frac{\partial C_{(n-1)}}{\partial x} \right] \end{aligned} \quad (\text{Eq. 12a})$$

$$\vdots$$

$$J_{n-1} = -D_{(n-1)1} \left[\frac{\partial C_1}{\partial x} \right] - D_{(n-1)2} \left[\frac{\partial C_2}{\partial x} \right] \dots - D_{(n-1)1(n-1)} \left[\frac{\partial C_{(n-1)}}{\partial x} \right]$$

That in matrix notation is:

$$\mathbf{J} = -\mathbf{D} \frac{\partial \mathbf{C}}{\partial x} \quad (\text{Eq. 12b})$$

Where \mathbf{J} and \mathbf{C} are $(n - 1)$ column vector and \mathbf{D} is the $(n - 1) \times (n - 1)$ matrix of diffusion coefficients as defined by Eq. 5 and Eq. 6. In his work, Onsager highlighted as Eq. 12b fulfils some thermodynamic criteria, and further experimental studies demonstrated as these relationships can adequately describe diffusion in multicomponent system (e.g., Cooper, 1968; Chakraborty & Ganguly, 1992; Liang et al., 1997).

Fick's first law explains the diffusive flux as a function of the concentration gradient, but in diffusion studies, is often required to determine how a concentration profile would evolve with time, starting from an initial concentration distribution. With this purpose, a mass balance is introduced in Eq. 9 (Crank, 1975; Mehrer, 2007; Costa et al., 2008).

Let consider a small volume of a solid with incrementally small lengths (i.e., dx , dy and dz) per each side (Fig. 3.16), and let suppose, for simplicity, that the flux of particles occurs along x -direction.

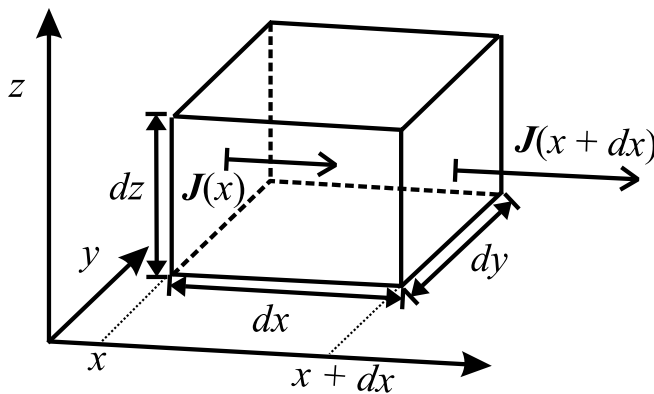


Fig. 3.16 - Nomenclature for the mass balance of fluxes in a rectangular solid. The volume of a rectangular parallelepiped with each side characterised by incrementally small lengths (e.g., dx , dy , dz). $J(x)$ and $J(x + dx)$ are the flux parallel to the x -direction at positions x , and $x + dx$, respectively (from Costa et al., 2008).

Since the number of particles that came into the solid ($J(x)$) is different from that which left ($J(x + dx)$) (Fig. 3.16), the total number of particles which crossed the solid side by side is:

$$(J(x + dx) - J(x)) * dy * dz = \frac{\partial J}{\partial x} * dx * dy * dz \quad (\text{Eq. 13a})$$

Considering an infinitesimal time interval dt , the number of particles in the incremental volume dv (i.e., $dx * dy * dz$), defined as $C(x, t)$, changes to $C(x, t + dt)$ according to:

$$C(x, t + dt) - C(x, t) = -\frac{\partial J}{\partial x} * dt \quad (\text{Eq. 13b})$$

Which can be rewritten as:

$$\frac{\partial C(x, t)}{\partial t} = -\frac{\partial J}{\partial x} \quad (\text{Eq. 13c})$$

Because of the:

$$\lim_{dt \rightarrow 0} \left(\frac{C(x, t + dt) - C(x, t)}{dt} \right) = \frac{\partial C}{\partial t} \quad (\text{Eq. 14})$$

Eq. 13c is also known as continuity equation, and replacing J in this equation with Eq. 9, it is possible to obtain the corresponding time dependent equation:

$$\frac{\partial C(x, t)}{\partial t} = \frac{\partial}{\partial x} \left(D \frac{\partial C}{\partial x} \right) \quad (\text{Eq. 15})$$

Also known as Fick's second law. If D is constant (i.e., independent of C and x), which is the case for tracer or self diffusion in chemically homogenous systems, then Eq. 15 can be written as:

$$\frac{\partial C(x, t)}{\partial t} = D \frac{\partial^2 C(x, t)}{\partial x^2} \quad (\text{Eq. 16a})$$

Otherwise, it assumes the following expanded form:

$$\frac{\partial C(x, t)}{\partial t} = \frac{\partial D}{\partial x} * \frac{\partial C(x, t)}{\partial x} + D \frac{\partial^2 C(x, t)}{\partial x^2} \quad (\text{Eq. 16b})$$

Which is particularly useful to model compositional changes, occurred over time, of natural samples, as diffusion coefficients often vary as a function of C and x . Then, *Eqs. 16* help to model the evolution of the specific concentration distribution (i.e., the mineral concentration profile to be modelled), C , at any point of time, t , and of spatial coordinates, x , after the beginning of diffusion. With this purpose, a pre-diffusion initial condition, together with the boundary conditions governing particle fluxes at the boundary of the system (i.e., the mineral), must be specified. In the following section, a brief summary of different initial and boundary conditions and of solutions of diffusion laws will be given.

3.4.2 Solutions of diffusion equations

This section aims to provide the reader with some key points about how to set up diffusion models for solving the Fick's law, specific for different conditions and crystalline geometries (e.g., diffusion in a plane sheet, cylinder or a sphere). Depending on whether we are dealing with a compositionally-independent diffusion coefficient or not, we can adopt different solutions. In the first case, analytical solutions (e.g., [Crank, 1975](#); [Shewmon, 1989](#)) have been provided for a wide range of initial and boundary conditions to solve [Eq. 16a](#). Such solutions generally incorporate Gaussians error functions and related integrals, or they are given in the form of Fourier series ([Crank, 1975](#)). These last are not particularly indicated to model diffusion in natural samples, since often we are dealing with compositionally-dependent diffusion coefficient and, therefore, only solutions of [Eq. 16b](#) will be treated below. In this last case, numerical methods are necessary to solve diffusion equation ([Crank, 1975](#)). These methods have the advantage of being more adaptive to geometries and initial conditions inherent to specific systems ([Chakraborty, 2006](#)). Furthermore, they can be performed by specific mathematical software (e.g., Mathematica[®], MATLAB[®], R[®] and others), if some of

the computer programming knowledge is a user skill, and if initial and boundary conditions of the system to be modelled are known. Different examples of these conditions, which can be considered representative of most of the natural system, will be presented below.

3.4.2.1 Initial condition

Defining the initial conditions of a system means seeking the shape of an original concentration distribution of a mineral before diffusion alters it. This step represents, perhaps, one of the most hardly-constrainable points of the modelling process and it requires all of the standard petrographic skills. There is no single way to overcome such a hindrance, as it depends on the mineral, but some potentially initial distributions have been provided in the literature, which could explain common chemical zonings in minerals (Costa et al., 2008). Figure 3.17 shows four different initial concentration distributions which can characterise some of the natural samples and the diffusion-modified ones. In particular, it is possible to distinguish four different conditions (Costa et al., 2008), such as (a) a gradual chemical zoning (e.g., a commonly bell-shaped growth zoning typical of garnet); (b) a sharp chemical contrast (e.g., characteristic of a mineral overgrowth); (c) a homogeneous condition with a flat profile (e.g., leading to diffusional changes in retrograde rims); and (d) an oscillatory zoning (e.g., in the case of magmatic plagioclase).

As an alternative, in the case of metamorphic minerals like garnets, the initial shape of the compositional profile can be derived by the investigation of lower grade rocks, where the same mineral can be probably unmodified by diffusion at the lower temperature (Chakraborty, 2006). Another solution could be using, for instance, chemical profiles within minerals of the same thin section where no diffusion occurred due to local unavailability of a diffusion exchange partner (e.g., Hauenberger et al., 2005). A combination of all of these approaches to constrain the initial profile shape is preferred. However, the change of different initial profile shapes according to the petrographic observation provides various modelling results that should be checked before tracking any temporal-evolution of a rock.

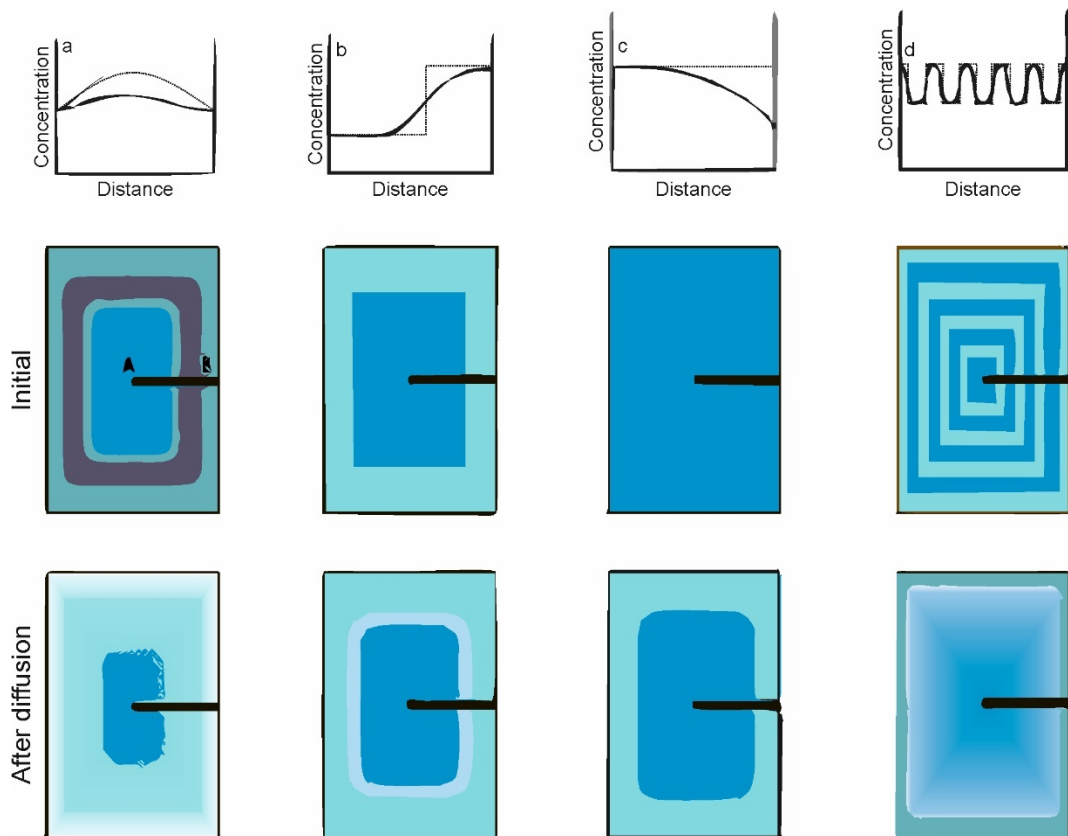


Fig. 3.17 - Different cases of pre-diffusion initial condition: (a) growth zoning; (b) overgrowth; (c) retrograde zoning; (d) oscillatory zoning (redrawn from DMG Shortcourse / MSA Workshop Aug 25, 2015 – Bochum).

3.4.2.2 Boundary conditions

The boundary conditions describe the nature of the elements exchanges occurring at the border of the crystal with its surrounding matrix. Concentrations at the grain boundary are set when a local and instantaneous equilibrium between the mineral surface and the matrix is achieved (e.g., [Dohmen & Chakraborty, 2003](#)). Defining boundary conditions requires, firstly, finding samples where crystal growth or dissolution phenomena associated with diffusion was insignificant ([Chakraborty, 2006](#)), to avoid moving grain boundary problems. When this condition is satisfied, the remaining boundary conditions can be grouped, by a petrological point of view, in two main classes: the Fixed Edge Composition (FEC) and the Variable Edge Composition (VEC) models ([Chakraborty & Ganguly, 1991](#)). The first one can be compared to an effectively infinite reservoir where the element partitioning of the mineral is maintained by the continuous supply of nutrients from the diffusing partner (e.g., closed system on [Fig. 3.18](#)).

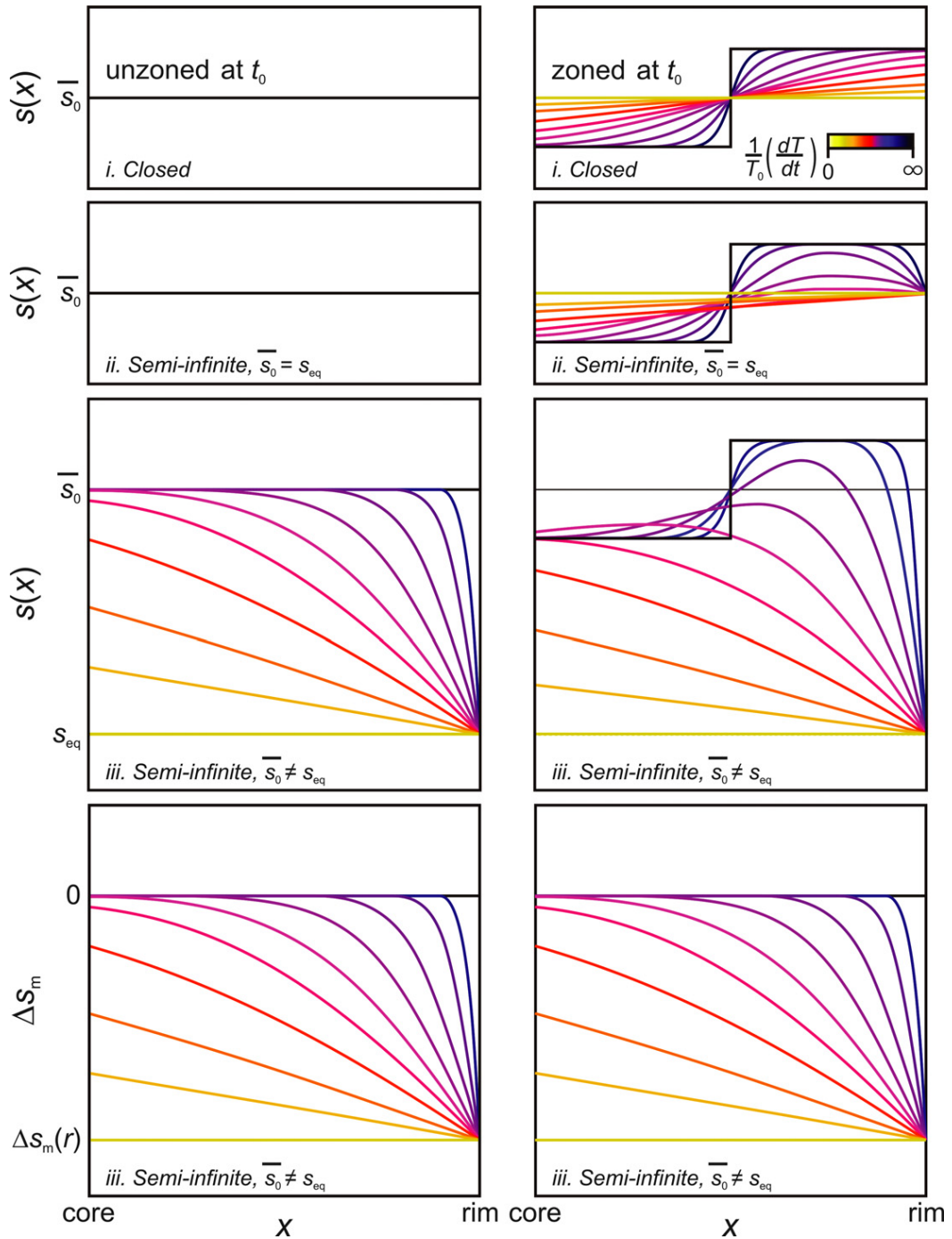


Fig. 3.18 - The diffusion process graphically illustrated for a half grain of a single phase that is initially homogeneous (a) and one that is heterogeneous, exhibiting a step-function elemental distribution (b). The matrix borders the grain at the rim. The concentration of s after cooling as a function of x is shown for different $T^{-1}dT / dt$ (measure for the extent of diffusion). Three scenarios are illustrated: (i) a closed system; (ii) an open (semi-infinite) system in which the equilibrium concentration of s (s_{eq}) is equal to the average concentration; and (iii) an open (semi-infinite) system in which s_{eq} is not equal to the average concentration (from [Smith et al., 2013](#)).

The second one, requires more information to be applied, such as the effective volume of the exchanging medium, its initial concentration, the distance covered

along the diffusion path and so forth. Then, it is evident that when the FEC model may be applied the following modelling is simpler with respect the VEC one. However, it is important keeping in mind that an effectively infinite medium condition also depends on the element exchange capability of the medium itself (Chakraborty, 2006). For instance, a diffusion couple consisting of pyroxene-garnet could not be a FEC condition for Fe-Mg diffusion in garnet, because element diffusion coefficients in pyroxene are similar or slower than the garnet ones (Chakraborty, 2006). A simple strategy to test if a FEC situation is applicable in the modelled system, is to measure the compositions at all garnet (i.e., the mineral of interest) grain boundaries to verify if they are the same in a given thin section, irrespective of the phase it is in contact with (e.g. quartz, biotite, pyroxene) (Chakraborty, 2006).

A particular situation in defining initial and boundary conditions is the case of mineral overgrowths (e.g., due to a static metamorphic overprint) on an existing crystal (e.g., garnet on garnet or successive plagioclase growth zones) during a later stage of the rock evolution (e.g., Ganguly, 1996; O'Brien, 1997; Datch & Proyer, 2002; Faryad & Chakraborty, 2005; Angi et al., 2010). Such a situation, indeed, can provide information on the initial shape of the compositional profile if compositional measurements are carried out far from the diffusion zone, the latter being strictly limited to the overgrowth interface (Chakraborty, 2006). However, it should be petrographically verified that the overgrowth is not the result of a substitution of the old crystal proceeded from outside inward, as that characterising atoll-shaped garnet formation (Ortolano et al., 2014a).

Once both initial and boundary conditions are set, numerical methods can be applied to solve Eq. 16b. In the case of a multicomponent diffusion, characterising metamorphic garnets, computer scripts are required to solve the diffusion equation iteratively, as nine diffusion coefficient equation must be solved simultaneously at any point of concentration and at any value of dt considered. For these reasons, the MATLAB® software was chosen as the mathematical platform to develop diffusion modeling scripts, by using a finite-difference explicit numerical method.

3.4.2.3 Numerical solution: The finite-difference explicit method

The best choice to solve Eq. 16b useful to describe diffusion in garnet is the application of a forward difference scheme. It involves a discretization of the space and time coordinates to make a grid where a step size Δx characterises the spatial coordinate, whereas a step size Δt subdivides the time coordinate (Fig. 3.19).

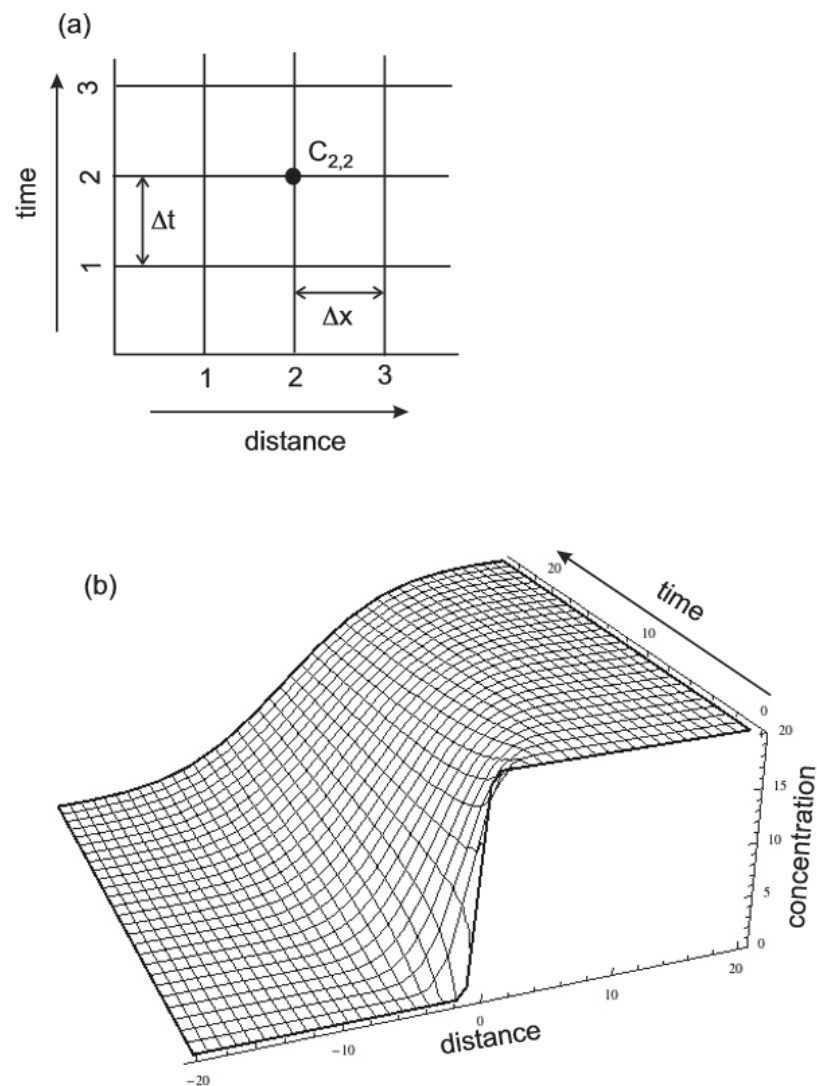


Fig. 3.19 - Visualization of the discretization of time and space used in finite difference algorithms. (a) There is a value of concentration associated with each point in space and time. (b) Three-dimensional visualization of how the concentration changes due to diffusion using the discretization of space and time (from Costa et al., 2008).

Below of these step size, a computer cannot recognise any other smallest variation (e.g., if $\Delta x = 6 \mu\text{m}$ and $\Delta t = 100$ years, neither distances $< \Delta x$ nor time scales $< \Delta t$ cannot be resolved by the numerical calculation) (Costa et al., 2008). Subsequently, the differential equations are converted into discrete forms by

applying the Taylor series approximation carried out in a forward difference scheme (see Crank, 1975 for a detailed discussion), which means:

$$\frac{\partial C}{\partial x} = \frac{C_{i+1,j} - C_{i,j}}{\Delta x} \quad (\text{Eq. 17})$$

Where subscripts i and j are related, respectively, to the space and time grid points (i.e., $C_{2,2}$ is the grid points at $2 \Delta x$ and $2 \Delta t$, Fig. 3.19a).

Such a forward modelling allows transforming a complex differential expression in an easier algebraical one, which can be handled with simple addition and multiplication rules.

For instance, in the case of the space coordinate (i.e., the right side of Eq. 16a):

$$\frac{\partial^2 C}{\partial x^2} = \frac{\partial}{\partial x} \left(\frac{\partial C}{\partial x} \right) = \frac{1}{\Delta x} \left(\left(\frac{C_{i+1,j} - C_{i,j}}{\Delta x} \right) - \left(\frac{C_{i,j} - C_{i-1,j}}{\Delta x} \right) \right) = \frac{C_{i+1,j} - 2C_{i,j} + C_{i-1,j}}{\Delta x^2} \quad (\text{Eq. 18a})$$

Whereas, in the case of the time coordinate (i.e. the left side of Eqs. 16):

$$\frac{\partial C}{\partial t} = \frac{C_{i,j+1} - C_{i,j}}{\Delta t} \quad (\text{Eq. 18b})$$

Then, putting together Eqs. 18a and 18b and using algebra fundamentals, Eq. 16a can be written as:

$$C(x, t) = C_{i,j+1} = D\Delta t \left(\frac{C_{i+1,j} - 2C_{i,j} + C_{i-1,j}}{\Delta x^2} \right) + C_{i,j} \quad (\text{Eq. 19})$$

Where $C_{i,j+1}$ represents the new concentration computed at a space grid point i for any time step $j + 1$ and $C_{i,j}$ represents the old concentration value (i.e., the initial concentration) at $t = 0$. Eq. 19 is iterated during the calculation, shifting i by the Δx step size over all grid points, with the aim to obtain a complete concentration profile at $t = j + 1$ ($j = 0$ at $t = 0$). The new concentration values are then used to repeat the calculation at $t = j + 2$ for obtaining, again, new concentration values which will be used to a new calculation at $t = j + 3$ and so on (Costa et al., 2008). Such a procedure is known in literature as explicit finite-difference numerical method.

However, as we dealt with compositionally-dependent diffusion coefficients, we need to solve Eq. 16b, that in finite difference scheme is:

$$C_{i,j+1} = D\Delta t \left(\frac{C_{i+1,j} - 2C_{i,j} + C_{i-1,j}}{\Delta x^2} \right) + \Delta t \left(\frac{D_{i+1,j} - D_{i,j}}{\Delta x} \right) \left(\frac{C_{i+1,j} - C_{i,j}}{\Delta x} \right) + C_{i,j} \quad (\text{Eq. 20})$$

It is important to highlight that solution of Eq. 20 is stable if the so called Dirichlet boundary condition (Cheng & Cheng, 2005), which requires that $D\Delta t/\Delta x^2 < 0.5$, is satisfied (e.g., Crank, 1975). As D and Δx are usually constrained, the choice of Δt is controlled by the Dirichlet condition. Such a limit explains the reason of using high-performing mathematical software, since the enormous iterative steps required in the case of a mineral with very slow D (e.g., garnet) or small grain sizes. This latter statement justifies the choice to make MATLAB® scripts, which use loop structures to iterative execute the calculation. Basically, a loop structure merely repeats the same calculation for a range of grid points, starting from the first until the last one. Figure 3.20 shows an example of a loop structure built in a MATLAB® script, where new concentration values are iteratively calculated at each grid point (excluded the first one set as fixed) for a specific Δt . The *acoeff* on Fig. 3.20 contains the expression of the Dirichlet condition.

```
%now calculate new concentration values for the current timestep
for k=2:nodes-1           %start spatial loop over inner nodes
    conc(k)=c_old(k)+(acoeff*(c_old(k-1)-(2*c_old(k))+c_old(k+1)));
end;                       %end spatial loop over inner nodes
```

Fig. 3.20 - Example of a loop structure built in a MATLAB® script. New concentration values (i.e. *conc(k)*) are computed along the distance covered from the diffusion interface to the outer rim (i.e. $k=2:nodes-1$) by solving Equation 20.

Such a method, in combination with the image analysis procedure developed in chapter 2, is applied to investigate garnet compositional changes due to diffusion, from two different case study. In the first case study, a Variscan static garnet overgrowth grew on the regional garnet, giving rise to a condition similar that shown in figure 3.17b. Therefore, modelling diffusional compositional changes could lead to valuable information about the later thermal event. In the second one, a quasi-flat zoning garnet shows diffusion effects at the grain boundaries reflecting a retrograde diffusive condition as that shown in figure 3.17c. Therefore, also, in this case, modelling diffusional compositional changes could allow deriving the cooling rate at which the basement exhumed.

4. Case studies

4.1 General outlines

The choice of the case studies has been made taking into account the possibility to investigate minerals able at: (a) keeping track of their compositional changes due to diffusion; (b) representing different initial conditions of the investigated system as those shown on [figure 3.17](#); (c) giving back reliable timescales of the different metamorphic evolutionary stages.

Following these guidelines, the case studies have been selected from two different sectors of the Calabria-Peloritani Orogen (CPO). The latter is constituted by a puzzle of Variscan terranes ([Cirrincione et al., 2015](#)) locally replaced by an early Alpine strike-slip tectonics ([Ortolano et al., 2013](#)). Finally, the CPO was involved into the Alpine-Apennine thrust sheet system before the opening of the Tyrrhenian basin, which controlled in turn the extensional collapse of the present-day belt ([Ortolano, et al., 2005](#)) (Fig. 4.1).

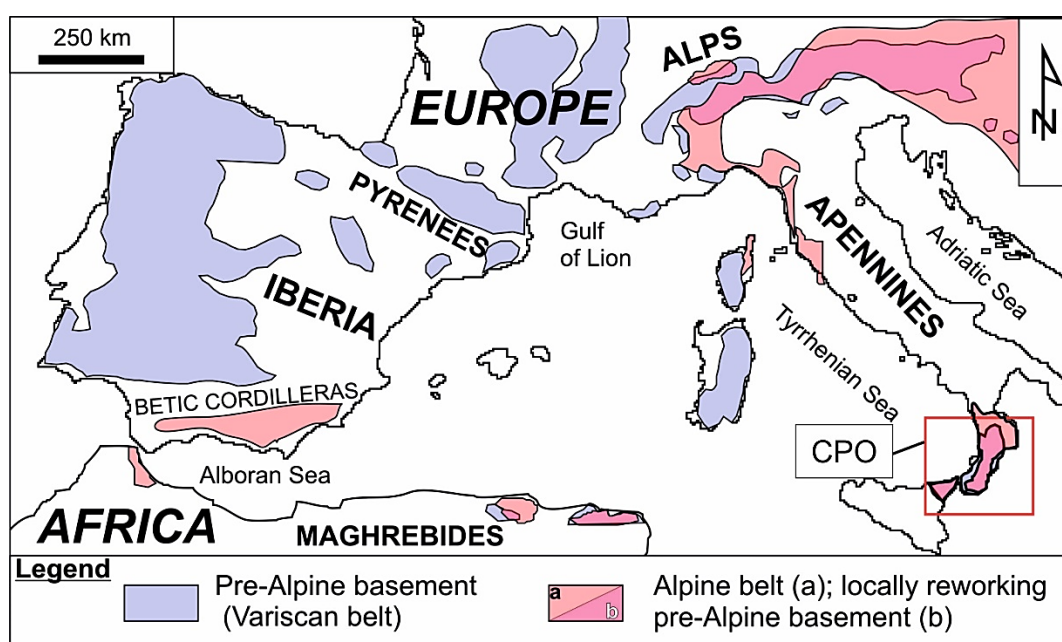


Fig. 4.1 - Distribution of the Alpine and Pre-Alpine Basement in Western Europe (from [Cirrincione et al., 2015](#)).

The present-day structural configuration of the CPO can be described as a thrust building, overlapping the underlying units of the Adrian domain, extending from the northern Calabria, delimited by the Pollino Fault Zone (PFZ), up to the north-

eastern part of Sicily (Cirrincione et al., 2008; Fazio et al., 2008; Cirrincione et al., 2012), bounded by the Taormina Line (TL) (Cella et al., 2004; Cirrincione et al., 2015) (Fig. 4.3). In this scenario, CPO can be separated in different orographic domains known as Coastal Chain, Sila, Serre and Aspromonte Massifs in Calabria, and the Peloritani Mountains in Sicily (e.g., Ortolano et al., 2014a; Cirrincione et al., 2015). Before the Alpine dismembering tectonics, the Variscan belt in Europe, which extended from southern Iberia to Poland, was interpreted as the reassembling of a series of specific terranes (i.e., the Armorican, Gondwana, Laurentia and Avalonia, Fig. 4.2, Padovano et al., 2012) merged during Devonian-Carboniferous times (e.g., Matte, 2001; Von Raumer et al., 2003; Marotta & Spalla, 2007; Compagnoni & Ferrando, 2010). Within this geodynamic framework, the CPO was probably localized along the snake-shaped crustal scale strike-slip system of the Eastern Variscan Shear Zone (EVSZ in Fig. 4.2) in late Carboniferous time (e.g., Padovano et al., 2012).

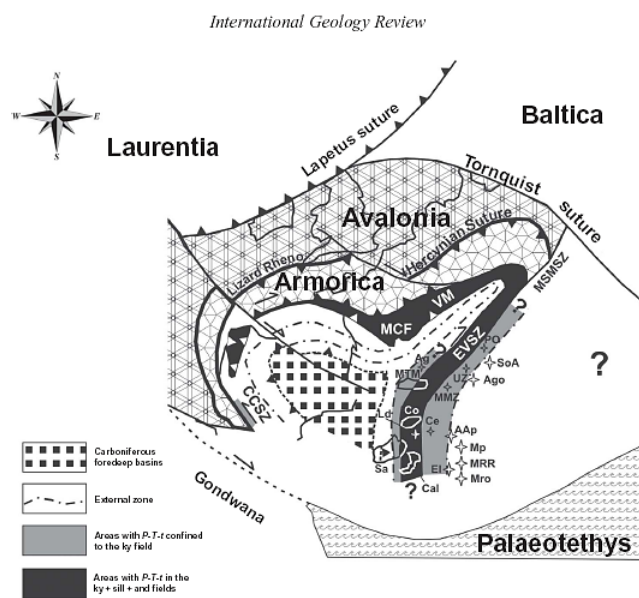


Fig. 4.2 - Sketch of the possible configuration of Variscan Western Europe in Late Carboniferous time (from Padovano et al., 2012, not to scale). CCSZ, Coimbra–Cordoba Shear Zone; EVSZ, East Variscan Shear Zone; MSMSZ, Moldanubian–Stare Mesto Shear Zone; MCF, French Massif Central; VM, Vosges Massif; Ag, Argentera Massif; MTM, Maures–Tanneron Massif (Western and Eastern); Sa, Sardinia (HGMC, Posada Valley Zone, Nappe Zone, and External Zone); Cal, Calabria–Peloritani Massif, Co, Corsica; El, Elba Island; Ld, Larderello/Travale geothermal areas; Ce, Cerreto area; SoA, Southern Alps; Ago, Agordo area; PO, Pohorje Massif; UZ, Ulten Zone; MMZ, Monte Muggio Zone; AAp, Apuan Alps; Mp, Monti Pisani area; MRR, Monticiano-Roccastrada Ridge; Mro, Monti Romani.

This evidence implies as the likely driving forces that controlled the exhumation of the basement rocks were mechanisms of tranpression vs. transtension developed along the last stages of the EVSZ activity, with northern Calabria affected by transtensional kinematics (e.g., Festa et al., 2004; Padovano et al., 2012) and the southern Calabria located in a transpressional domain (e.g., Cirrincione et al., 2015).

In particular the first case study come from the Mammola Paragneiss Complex (MPC). MPC constitutes the deeper part of the upper level of the Serre Massif (Acquafredda et al., 2008; Angi et al., 2010), an almost continuous continental crustal section of a segment of the original southern European Variscan Belt. This is nowadays surfacing after an Alpine age tilting, which led the lowermost portion to emerge to the northern part of the Massif and the uppermost one surfacing to the south (Cirrincione et al., 2015) (Fig. 4.3).

The second case study belongs to the upper part of the deepest levels of the Sila Massif which is constituted by remnants of an almost complete crustal section of the original southern European Variscan margin. This section is currently overlapped on the Alpine oceanic derived units of the Liguride complex. Such a contact is marked, in the deepest part of the Sila crustal section, by the mylonitic horizon of the Castagna Unit. This mylonitic horizon was interpreted as a result of a late Variscan shearing zone activity, probably connected with the EVSZ, belatedly reworked during a Europe-vergent early-Alpine tectonics (Cirrincione et al., 2015). Selected samples belong to low-strain domains within these mylonites preserving memories of the original Variscan metamorphic equilibria.

Pressure-temperature estimates followed by timescale determinations of the late Variscan metamorphic evolution, have been carried out with the aim to open new interpretations about this relic sector of the original southern European Variscan chain.

Specifically, the used investigated samples, selected with the aim to retrieve the timescale of the Variscan metamorphic events, come from the Serre (southern Calabria) and Sila Massif (northern Calabria), where different exhumation mechanisms occurred.

In the first case (i.e., Serre Massif, Fig. 4.3), garnets show a static overgrowth rimming the relict cores formed as a consequence of a contact metamorphism, where diffusional compositional changes can be modelled considering a pre-diffusion condition analogously to that shown in figure 3.17b.

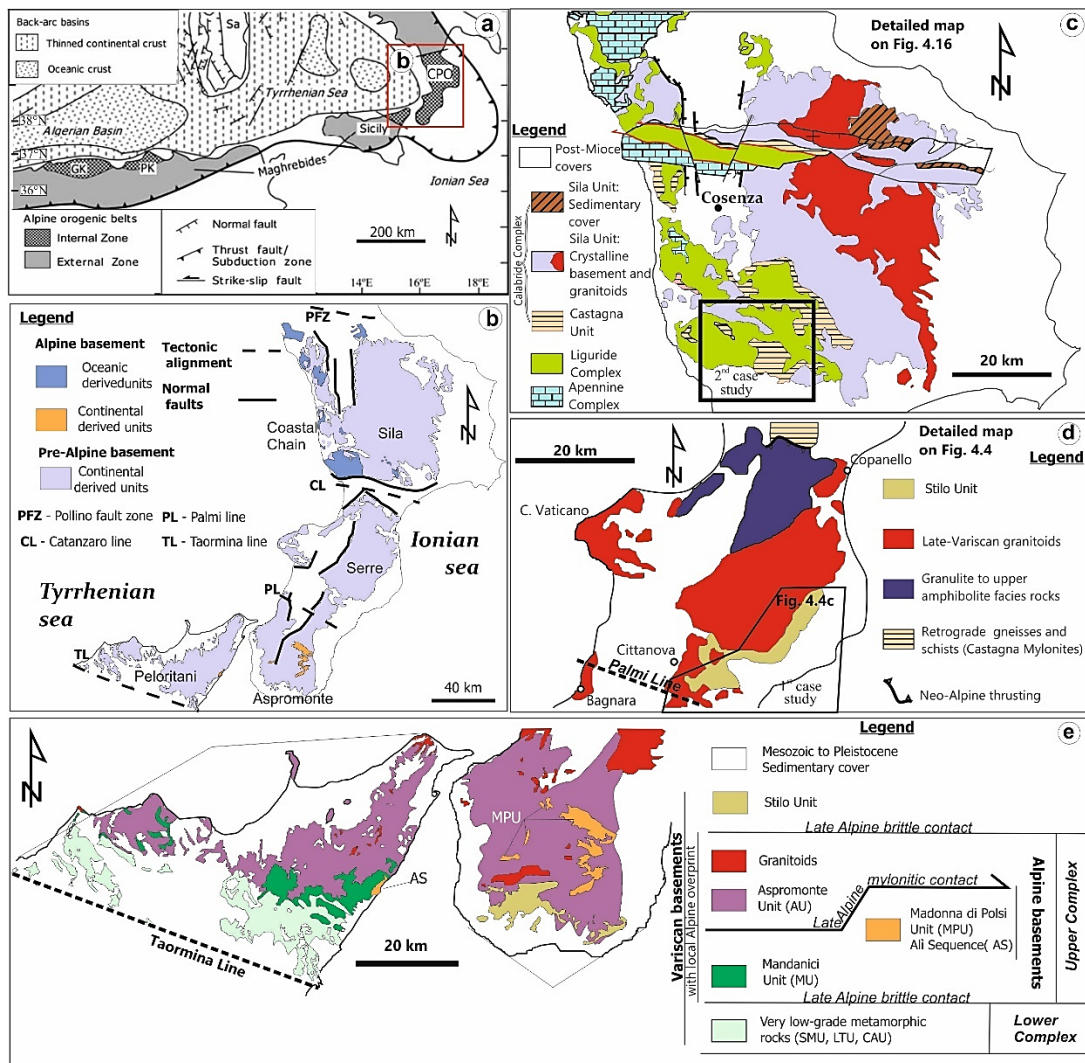


Fig. 4.3 - Geological map representations of the Calabria-Peloritani Orogen: (a) Schematic map of the Alpine belt in the southern Mediterranean area (GK = Grande Kabylie; PK = Petit Kabylie; Sa = Sardinia; CPO = Calabrian Peloritani Orogen); (b) Geological sketch map of the Calabria-Peloritani Orogen with distribution of its massifs and related Alpine and pre-Alpine basement rocks (modified after Angi et al. 2010); (c) Geological sketch map of the Sila and Coastal Chain Massifs; (d) Geological sketch map of the Serre Massif; (e) Geological sketch map of the Aspromonte Massif and Peloritani Mountain Belt (from Cirrincione et al., 2015).

In the second case (i.e., Sila Massif, Fig 4.3c), garnets are characterised by a flat compositional profile except for the outermost edges, where a net retrograde diffusive exchange with the surrounding matrix occurred, as highlighted by a depletion in magnesium and an iron-enrichment. Here, diffusional compositional changes can be modelled considering a pre-diffusion condition analogously to that shown in figure 3.17c.

In both cases, diffusive alteration of the original garnet chemical zonings was modelled with the support of the numerical petrology (e.g., the new image processing tools described previously), and they will be focussed in detail in the following sections.

4.2 First case study: Timescale of Late-Variscan static event constrained by garnet multicomponent diffusion modelling: new insights from the Serre Massif (Southern Calabria, Italy)

Millimetre almandine-rich garnet crystals from garnet-micaschists of the Mammola Paragneiss Complex (Serre Massif – southern Calabria, Italy) have been investigated to estimate the timescale of the last metamorphic event registered in the upper crust section of the Variscan European belt. With this aim, the extent of the relaxation of the garnet growth zoning was modelled via a forward finite-difference numerical method supported by a detailed and innovative image analysis. The investigated rocks highlighted a multistage metamorphic evolution consisting of an orogenic cycle partly overprinted by a thermal one, both of them ascribable to the Variscan orogenesis. In particular, a prograde low amphibolite facies evolution ($P = 5.5\text{--}8.5$ Kbar; $T = 500\text{--}600$ °C) followed by a retrograde stage ($P = 4$ Kbar; $T = 500$ °C) are recognised. The subsequent post-tectonic emplacement of granitoid bodies gave rise, then, to a gradually distributed thermal metamorphic overprint ($P = 4$ Kbar; $T = 670$ °C), followed by a low-pressure cooling path ($P = 2.9$ Kbar; $T = 500$ °C) consistent with the final unroofing stage of the former crystalline basement. In this tangled scenario, the relaxation of the garnet zoning profiles was modelled using the diffusion data of [Chakraborty, & Ganguly, 1992](#)). Obtained results highlighted a timescale of 2 ± 3 Ma for the last thermal metamorphic overprint experienced by the Serre Massif metapelite rocks. This result suggests a faster heating/cooling rate linked with a rapid exhumation of the upper crust of this southern European Variscan relict.

4.2.1 Introduction

Tectono-metamorphic evolution of metamorphic basement rocks reflects the dynamic journey faced during their burial evolution into the deep crust up to exhumation upon surface, passing, potentially, through one or more static metamorphic stages due to local thermal rising. This implies a continuous changing in the intensive variables (e.g., T, P, fO_2) through several types of dP/dT gradient for different precursor rocks, as highlighted by the peculiar continuous adjustment of the mineral assemblages as well as of the solid solution

compositions (e.g., [Spear & Selverstone, 1983](#); [Spear & Peacock, 1989](#); [Caddick & Thompson, 2008](#) and references therein). In the metapelite system, for instance, garnet is the solid solution mineral that best records these changes, since its common porphyroblastic fabric and its slow cationic diffusion rates, making it one of the mineral most commonly used as a tracer of the *PT* trajectories of metamorphic basements ([Caddick & Thompson, 2008](#) and references therein). The significant advantage of using garnet as a recorder of changes of the metamorphic conditions comes from the peculiar diffusive behaviour of its constitutive elements. In fact, garnet is characterised by diffusion rates slower than rates of syn-metamorphic growth/dissolution processes ([Chakraborty, 2006](#)). This means that at low temperature and/or short time it can preserve its growth chemical zoning, whereas with increasing temperature and/or time solid state diffusion tends to partially homogenise the original zoning, providing information on the duration of metamorphic episodes ([Florence & Spear, 1993](#); [Ehlers et al., 1994](#); [Spear & Parrish, 1996](#); [Spear, 2004](#); [Storm & Spear, 2005](#); [Chakraborty, 2006, 2008](#); [Ague et al., 2013](#); [Spear, 2014](#)). Static events, for instance, often produce well-developed idiomorphic overgrowths, which can be trace of the thermal rising due to neighbouring pluton emplacement, which can be driven from different emplacement mechanisms evolving for a considerable time.

The time duration of these events is hardly constrainable and can be defined studying the growing evolution of some time-sensitive minerals in the plutonic rocks (e.g., zircon – [Fiannacca et al., 2016](#)) as well as in the host ones (e.g., monazite – [Langone et al., 2014](#)) through detailed in situ isotopic investigations. The latter can be integrated with detailed geothermobarometric constraints normally fixed using *PT*-sensitive minerals in plutonic rocks (e.g., conventional amphibole geothermobarometer – [Perchuk & Lavrent'yeva, 1990](#)) as well as in the metamorphic host ones (e.g., garnet isopleths geothermobarometers – [Gaidies et al., 2006](#); [Zeh, 2006](#); [Cirrincione et al., 2008](#)).

Nevertheless, in situ isotopic investigations shown some disadvantages associated with laboratory analyses. As an example, laser ablation ICP mass spectrometers used for U/Th-Pb dating of many accessory minerals can measure 5 µm spots in

monazite and 15 μm spots in zircon, but the pits deep (8 μm) affects the degree of uncertainty of the obtained results. Whereas, sensitive high-resolution ion microprobe used principally for U-Pb dating of zircons, although measuring 20 x 0.5 μm spots, it is characterised by a very time-consuming sample preparation as well as by \sim 15 minutes for each analysis. Moreover, to avoid an unreliable reset of the isotopic clock, the temperature of the studied event has to be close to the closure temperature of the analysed isotopic system (Ganguly & Tirone, 1999; Chakraborty, 2006).

As an alternative solution, in recent years, modelling concentration gradients modified by cationic diffusion processes has become an increasingly used geochronometry tool to constrain durations of thermal events, if temperature, pressure and element diffusion coefficients are known and if kinetic window condition is verified (Chakraborty, 2008). Since the pioneering works of Dodson (1973, 1976, 1986), Lasaga (1979, 1983), Lasaga et al. (1977) and Loomis (1978a, 1978b), indeed, many authors used the diffusion clock for obtaining timescales and rates of several geological processes (e.g., Ganguly, 1996; Spear, & Parrish, 1996; Duchene et al., 1977; Ganguly et al., 2000; Fernando et al., 2003; Spear, 2004; Faryad & Chakraborty, 2005; Storm & Spear, 2005; Hallett & Spear, 2011; Spear, 2014). One of the main pitfalls encountered in the application of diffusion modelling and solution of diffusion laws is represented by the correct determination of kinetic coefficients, especially in a multicomponent system like garnet involving simultaneous fluxes of more than two components. In this case, the diffusive flux for each element depends on the potential chemical gradient of all elements and therefore it is commonly necessary to calculate the $(n - 1) \times (n - 1)$ matrix of diffusion coefficients (D) (Lasaga, 1979; Chakraborty & Ganguly, 1992; Ganguly, 2002), described in section 3.3.

To obtain a set of reliable input variable values (e.g. T, P, X) useful to extrapolate the kinetic element information, a quantitative representation of the single overgrowing stages of each metamorphic event have been suggested.

According to Fiannacca et al. (2012) and Ortolano et al. (2014a) the use of quantitative image analysis of X-ray maps opens new perspectives for a more

correct definition of the effective bulk rock chemistries (EBCs) (Evans, 2004; Stüwe & Ehlers, 1996) as well as of the effective reactant volumes (i.e., the real reacting volumes of each recognised metamorphic equilibria - ERVs) acting during the single equilibration steps of the entire metamorphic evolution. In this view, the multivariate statistical analysis of X-ray maps followed by a quantitative calibration procedure (e.g., Cossio et al., 2002; Lanari et al., 2014; Ortolano et al., under review), have been here used: a) to identify the main parageneses linked to the metamorphic growth stages (e.g., by Q-XRMA); b) to quantify the modal percentage involved in the potential fractionation processes, minimising the subjectivity of the operator in the definition of the ERVs (e.g., by Q-XRMA); c) to obtain, for the first time, a map set representative of the input parameters useful to solve diffusion equations (i.e., T , P , X images) (e.g., by Min-GSD and DCMC).

With the aims mentioned above, we depth the investigations of the millimetre almandine-rich garnet crystals from amphibolite facies garnet-micaschists of the Mammola Paragneiss Complex (Serre Massif - Southern Calabria) already studied by Angi et al. (2010). These rocks, characterised by a multistage metamorphic evolution, experienced an orogenic cycle partly overprinted by a thermal one. Such an evolution locally led to the fractionation of the garnet core porphyroblasts that driven the continuous change of the EBCs of the system stepwise controlled by the ongoing variation of the ERVs. In this view, the image-assisted analysis thermodynamic modelling applied here permitted to extrapolate a correct definition of the ERVs and then of the EBCs to be used in the pseudosection computation, integrating the PT constraints previously obtained by Angi et al. (2010).

This procedure permitted then to transform each calibrated elemental map into real PT maps highlighting the pressure and temperature conditions of each syn-metamorphic growing stages, which were potentially useful in turn to calculate different kinetic coefficients operating during each single metamorphic stage.

In particular, the focus was on the thermal cycle due to the reaching of a peak temperature which favoured the diffusion triggering. This evidence permitted to estimate the timescale of the static event linked to the final emplacement of the

Southern Variscan plutonic complexes, probably driven by the development of the snake-shaped East Variscan shear-zone (Padovano et al., 2012; 2014; Cirrincione et al., 2015), and to deduce the associated cooling rate.

4.2.2 Geopetrological background

The Serre Massif is located in the central portion of the CPO (Fig. 4.4a). It represents a continental crustal section formed by three different horizons (Rottura et al., 1990; Del Moro et al., 1994; Fornelli et al., 1994; Caggianelli et al., 2000a, 2000b; Festa et al., 2003; Angi et al., 2010; Cirrincione et al., 2015; Fiannacca et al., 2015, 2016) (Fig. 4.4b).

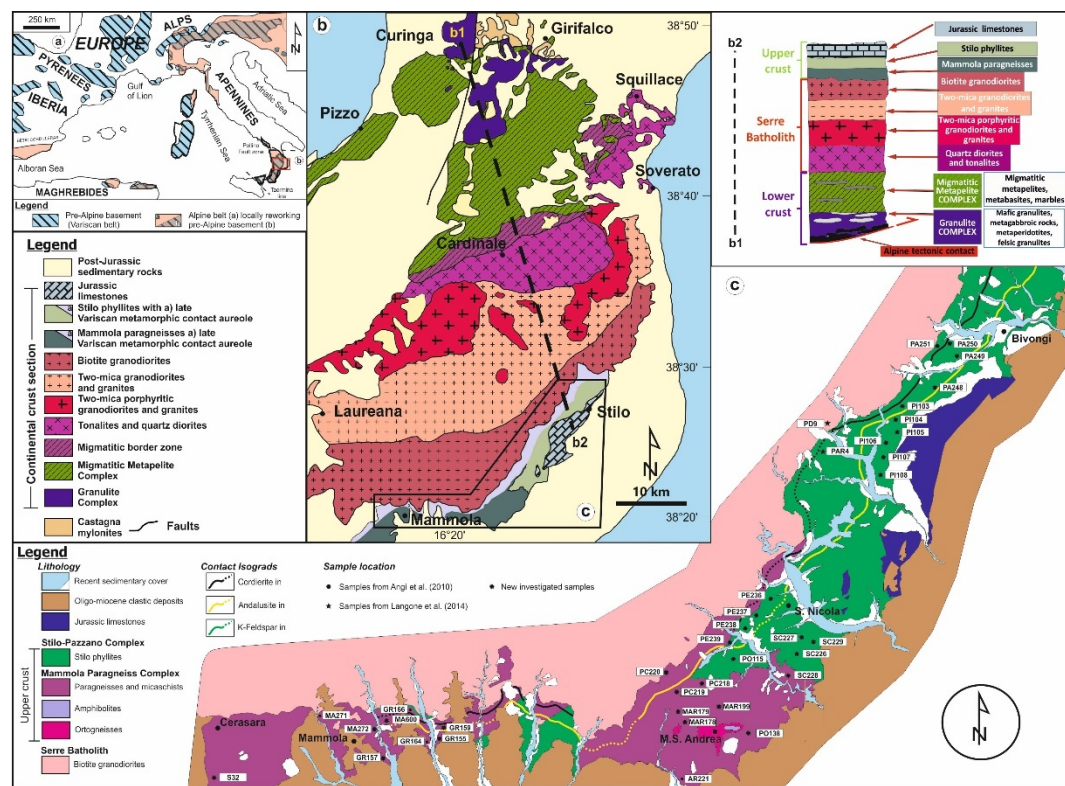


Fig. 4.4 - Geological framework of the Serre Massif: (a) distribution of Pre-Alpine vs. Alpine terranes; (b) geological map of the Serre Massif. In yellow the crustal column is shown on the top-right of the figure; (c) petrography-based lithological map of the investigated area (i.e., Mammola). K-Feldspar, andalusite and cordierite isograds are located parallel to the primary contact with the top of the Serre batholith.

The deepest horizon (i.e., Granulite Complex), consists of mafic granulites, metagabbros and felsic granulites underlying the Migmatitic Metapelite Complex (Maccarrone et al., 1983; Schenk, 1984, 1989; Fornelli et al., 2002, 2004; Acquafredda et al., 2006, 2008; Cirrincione et al., 2015; Fiannacca et al., 2016) (Fig. 4.4b). The latter, essentially constituted by migmatitic paragneisses and minor

felsic granulites, is also intruded by mafic dykes ranging in composition from quartz monzogabbro to quartz monzodiorite (Schenk, 1980; Fornelli, et al., 2011). According to Acquafredda et al. (2006, 2008), mafic granulites have been subjected to different decompression steps at *PT* conditions passing from 1.1 GPa – 900 °C to 0.7/0.8 GPa – 650/700 °C, whereas the Migmatitic Metapelite Complex has been affected by an amphibolite facies metamorphism at 0.8 GPa – 700 °C *PT* conditions.

The middle horizon is represented by the large emplacement of the Serre Batholith at depths ranging from c. 23 to c. 6 Km (Caggianelli et al., 2000a; Festa et al., 2013; Langone et al., 2014; Fiannacca et al., 2015, 2016) (Fig. 4.4b). It appears lithologically zoned passing through quartz diorites and tonalites at the bottom (Fiannacca et al., 2016), two-mica porphyritic granodiorites and monzogranites at the intermediate level of the batholith (Del Moro et al., 1994; Fiannacca et al., 2015), till the shallowest portion constituted by granodiorites and granites grading to biotite ± amphibole peraluminous granites with a predominant isotropic fabric (Fornelli et al., 1994; Caggianelli et al., 2000b; Fiannacca et al., 2016). In contact with lower crustal wall rocks, batholith emplacement produced a migmatitic border zone (Rottura et al., 1990; Langone et al., 2014), whereas in the upper crustal ones has led to the development of contact aureoles with a maximum thickness of 1800 m (Angi et al., 2010; Festa et al., 2013) (Fig. 4.4c). The first appearance of biotite, andalusite and cordierite generated by contact metamorphism testifies the preservation of the primary contact between granitoids and the upper host rocks. According to Fiannacca et al. (2016), the development of the batholith occurred by incremental multipulse overaccretion in a time period of 5.1 ± 4.0 Ma, from 297.3 ± 3.1 Ma up to 292.2 ± 2.6 Ma, while, for Langone et al., (2014), the emplacement of the top of the batholith postdates by about 10 Ma the emplacement of the lower one. Furthermore, Langone et al. (2014) obtained a weighted average age of 292 ± 4 Ma for the contact metamorphism linked to the intrusion of the shallowest portion of the batholith, based on the dating of metamorphic monazite from hornfels of the upper crust (Stilo-Pazzano Complex).

Finally, the upper crustal horizon localised in the south-eastern part of the Serre Massif consists of two different metamorphic complexes assembled during Variscan tectonics along a low-angle detachment (Colonna et al., 1973; Angi et al., 2010; Festa et al., 2013) (Fig. 4.4c). This contact separates the hanging wall complex (i.e., Stilo-Pazzano Complex, Angi et al., 2010) in which low greenschist facies metapelites together with quartzites, marbles and metavolcanic levels occur, from the higher metamorphic footwall complex (i.e., Mammola Paragneiss Complex, Angi et al., 2010) characterised by amphibolite facies paragneisses with minor leucocratic gneisses and amphibolites (Fig. 4.4b, c). According to Angi et al. (2010), this portion of the Serre Massif followed an early tectono-metamorphic history similar to the lower crustal segment, characterised by a crustal thickening evolution (*PT* peak conditions: 0.9 GPa – 530 °C) and a subsequent fast exhumation along a predominant extensional shear zone (Angi et al., 2010). Nevertheless, the occurrence of widespread distributed sub-vertical Mylonitic shear zones, partly recovered by the late- to post-kinematic thermal rise due to the plutonic intrusion, recently led to consider an alternative exhumation mechanism, probably controlled by a transpressional related strike-slip tectonics, consistent with the involvement of the CPO in the late-Variscan snake-shaped East Variscan shear zone (Padovano et al., 2012, 2014; Cirrincione et al., 2015).

It is worth noting that in both complexes are recognisable effects related to a pervasive static overprint induced by the intrusion of the Late-Variscan granitoids (Bonardi et al., 1987; Rottura et al., 1990; Angi et al., 2010; Cirrincione et al., 2012; Festa et al., 2013) at about 670 °C and 0.3 GPa (Angi et al., 2010). Such effects are testified by the blastesis of large crystals of biotite together with andalusite and cordierite, especially close to the main plutonic body. In the Mammola Paragneiss Complex, the Late-Variscan static overprint is also highlighted by a garnet sub-euhedral overgrowth rimming the Variscan garnet core (Angi et al., 2010). According to the thermal model proposed by Caggianelli & Prosser, 2002) about the heat dissipation of a large tabular magmatic body in a continental crust, the granitoids emplacement induced a significant increment in temperature of about 250 °C near the primary contact with the upper crustal level. Such an increase in

temperature led the upper crust to achieve peak conditions relatively faster (i.e., ~ 1 Ma) than the lower one (i.e., ~ 4 , Ma).

In this case study, the main focus was on the last garnet overgrowing stage (Fig. 4.5 – samples MA271 and S32), with the aim to estimate the duration of the thermal event via diffusion modelling. With this purpose, a quantitative image-assisted thermodynamic modelling has supported here the routinely petrographic and chemical analytical approach. This method allowed the extraction of numerical parameters useful to constrain the sequence of the EBCs of the single metamorphic evolutionary stages. These EBCs were then used to compute very reliable PT pseudosections, useful for constraining a new set of pressure-temperature estimates. These latter were also used to obtain the input parameters necessary to set up the diffusion models to evaluate the timescale of the investigated metamorphic stage.

4.2.3 Methodology

Previous microprobe analyses (Angi et al., 2010) were here integrated with new ones (i.e., APPENDIX C1), performed by a Cameca SX-FIVE electron microprobe (EMP) equipped with four WDS spectrometers at the Camparis laboratory in Paris, under the following operating conditions: ~ 1 μm beam diameter, 15 kV accelerating voltage, and 10 nA beam current. Natural minerals and synthetic oxides were used as standards. Used mineral abbreviations are from Siivola & Schmid (2007), whereas mineral formulae were calculated using MINPET 2.02 software (Richard, 1995) (i.e., APPENDIX C1).

Qualitative EDS elemental maps (APPENDIX C2) were acquired using a Tescan Vega-LMU scanning electron microscope equipped with an EDAX Neptune XM4-60 micro-analyzer operating by energy dispersive system characterised by an ultra-thin Be window coupled with an EDAX WDS LEXS (wavelength dispersive low energy X-ray spectrometer) calibrated for light elements, located at the Department of Biological, Geological and Environmental Sciences, University of Catania. The operating conditions were a 20-kV accelerating potential, a dwell time of 500 ms per 128 frames (corresponding to an acquisition time of ~ 4 h,

including a detector dead time $\sim 35\%$) and a resolution of 512×400 pixels or 1200×900 in which each pixel corresponds to about $2 \mu\text{m}$ per side.

Qualitative major element X-ray maps of the entire thin section ($\sim 38 \times 20 \text{ mm}$) were acquired using a $\mu\text{-XRF}$ Eagle III-XPL spectrometer equipped with an EDS Si(Li) detector and with an Edax Vision32 microanalytical system, located at the Department of Mineralogical and Petrological Sciences, University of Turin. The operating conditions were 400 ms counting time, 40 kV accelerating voltage and a probe current of $800 \mu\text{A}$. A spatial resolution of about $65 \mu\text{m}$ in both x and y directions was used, while the spot size was c. $30 \mu\text{m}$.

Quantitative atomic concentrations and modal amounts of each mineral phase were obtained by processing the X-ray maps with the software program Q-XRMA (Ortolano et al., under review) developed at the Geoinformatics and Image Analysis Lab of the Biological, Geological and Environmental Sciences of Catania University. The sequence of the EBCs, used to construct the different pseudosections representative for each metamorphic stage, was computed by combining the mineral proportions obtained from the modal estimate of the $\mu\text{-XRF}$ maps with the mineral chemistry.

Bulk rock chemistry (i.e., APPENDIX C3) was obtained by XRF on pressed powder pellets using a Philips PW 2404 spectrometer equipped with a Rh anticathode at the Department of Biological, Geological and Environmental Sciences of Catania University. $\text{FeO}/\text{Fe}_2\text{O}_3$ ratio was determined by titration with KMnO_4 , whereas H_2O was measured as weight loss on ignition (L.O.I.) and was determined by standard gravimetric procedures, after heating the powder at $\sim 900 \text{ }^\circ\text{C}$ for about 6 h.

4.2.4 Petrography and mineral chemistry

The investigated metapelite samples belong to the Mammola Paragneiss Complex (MPC) and represent the bottom of the upper crustal segment of the Serre Massif (Fig. 4.4c). This portion of the original Variscan crustal section is presently surfacing in a longitudinal branch after the tilting linked to the final exhumation stages occurred during the local activity of the Alpine orogenesis (Festa et al., 2003; Angi et al., 2010; Festa et al., 2013).

According to Angi et al. (2010), MPC rocks have been affected by a multi-stage metamorphic evolution subdivided in an orogenic cycle, characterised by a prograde metamorphic path, ranging from $T = 500\text{ °C} - P = 0.59\text{ GPa}$ to $T = 530\text{ °C} - P = 0.90\text{ GPa}$, testified by well-preserved zoned garnets (Grt I, Fig. 4.5) with evident Mn bell-shaped profiles (Fig. 4.6). The prograde stage is followed by a retrograde one, mostly testified by the peripheral local resorption of the previous garnet porphyroblasts (i.e., sample AR221 in Fig. 4.5) highlighted by a Mn-enrichment along the grain boundaries (Fig. 4.5b, Fig. 4.6).

Such an evidence allowed to constrain the retrograde trajectory linked with a steep exhumation path at PT values of $T = 470\text{ °C}$ and $P = 0.30\text{ GPa}$ (Angi et al., 2010). Both the euhedral and the deeply resorbed garnets are characterised by a well-developed static overgrowth (Grt II, Fig. 4.5b, c) marked by an increase in the iron and magnesium contents (Fig. 4.6). Such an overgrowth is linked with the thermal rise connected to the late- to post-orogenic emplacement of the granitoids, which mark the final stages of the Variscan orogenesis.

In order to constrain the timescale of the thermal event by modelling garnet multicomponent diffusion, the MA271 sample has been selected starting from 37 specimens (see Fig. 4.4c and APPENDIX C4 for sample location). This sample has been chosen since its neighbourhood distance from the primary contact (i.e., not affected nor by brittle tectonics nor by resorption effects) from the adjoining pluton and for the occurrence of well-preserved static overgrowing coronas in several garnets.

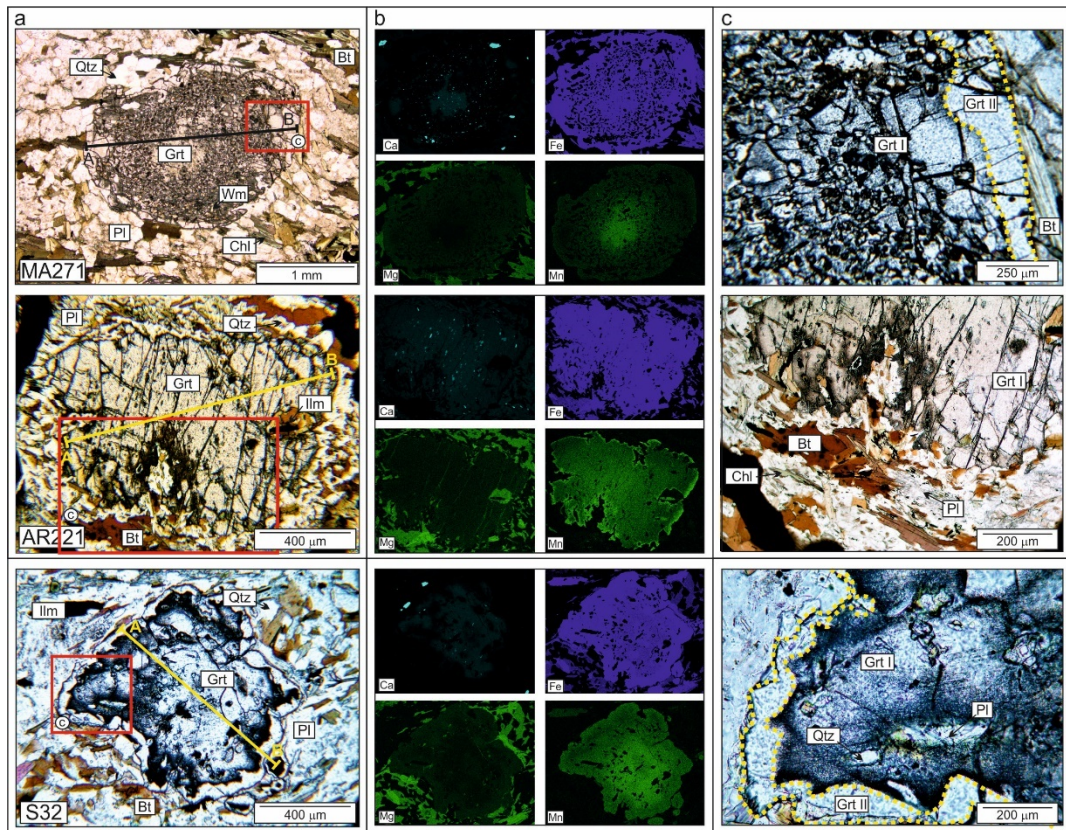


Fig. 4.5 – Garnet porphyroblasts showing different steps of the metamorphic evolution: (a) Nicols // optical photos showing garnet static overgrowths as bright inclusion-poor rims (i.e., MA271 and S32), and retrograde effects as dark thin resorbed rims (AR221); (b) qualitative elemental X-ray maps; (c) zoom on the garnet outer rims. The figure shows how the static rim overgrowths (Grt II) are very small in size (i.e., ~ 100 μm) with respect the regional garnet (Grt I) (i.e., ~ 2000 μm).

In this sample, main mineralogical phases are garnet, biotite, plagioclase and quartz with minor white mica and chlorite and secondary ilmenite and apatite.

Garnet porphyroblasts (up to 3 mm in size) are usually zoned.

These grains are characterised by syn-tectonic garnet growing stages, followed by a syn-granite emplacement static one. The syn-tectonic garnet (Fig. 4.6, Grt I) consists of a spessartine-rich core (COR: $Alm_{50-63} Grs_{24-30} Prp_{1-2} Sps_{12-20}$), embedding tiny zoisite grains, evolving to a zoisite inclusion-free mantle (MNT: $Alm_{66-82} Grs_{5-20} Prp_{4-10} Sps_{4-12}$) linked with the achieving of the orogenic peak metamorphic conditions as highlighted by a decrease in Mn and Ca contents (Angi et al., 2010).

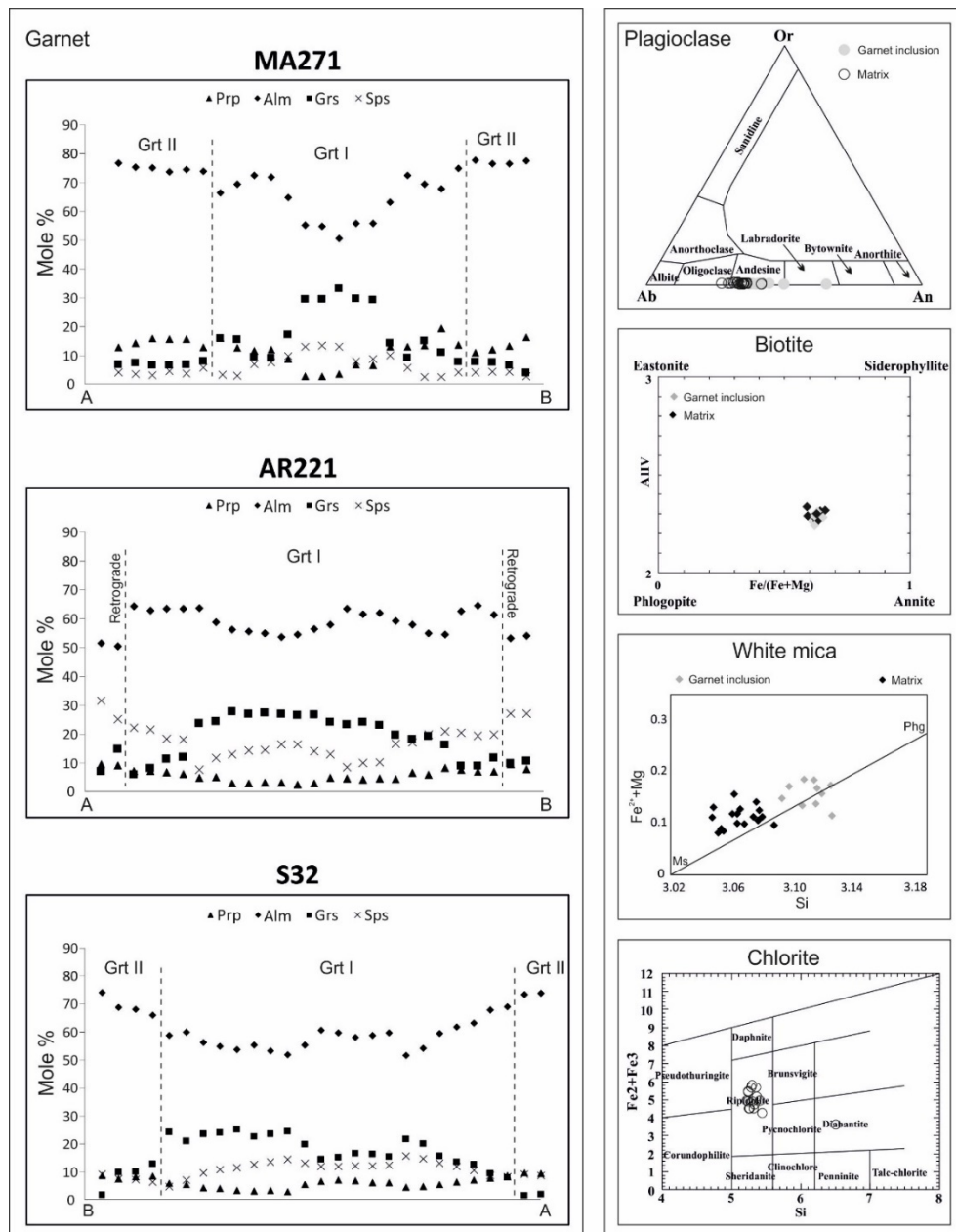


Fig. 4.6 - Mineral chemistry of the samples investigated. GRT I is characterised by an earlier metamorphic history determining the development of a growth zoning. Whereas, GRT II is characterised by a sharp compositional contrast with respect GRT I, setting a chemical gradient which could give diffusion. Feldspars and Micas show compositional differences between regional and static generations.

The syn-granite emplacement garnet (Fig. 4.6, Grt II) is highlighted by a static euhedral almandine-rich overgrowth (SR: $Alm_{82-86} Grs_{2-5} Prp_{10-13} Sps_{2-4}$) with an average thickness of $\sim 100 \mu m$, rimming the syn-tectonic grains (Fig. 4.5c). According to the isotopic dating reported in the literature for the contact metamorphism, Grt II was formed during the early Permian (292 ± 4 Ma, Langone

et al., 2014). Unlike the Grt I, Grt II shows a higher content of Mg and Fe than Ca and Mn (Fig. 4.6).

Biotite grains can be found both as relict inclusion into garnet porphyroblasts both as decussate-structure laminae grew up during the thermal event in equilibrium with Grt II. In both cases, great compositional variations are not observed and all grains group close to the annite zone ($Al^{IV} = 2.20 - 2.40$; $X_{Fe} = 0.59-0.65$) in the Al^{IV} vs $Fe^{2+} / (Fe^{2+} + Mg)$ diagram (Fig. 4.6).

Plagioclase in equilibrium with Grt II shows a higher andesine content ($An = 0.35 - 0.41$) (Fig. 4.5) compared to plagioclase in equilibrium with Grt I ($An = 0.21 - 0.30$). White mica can be found as inclusions in Grt I whereas, in other samples (e.g., S32 – Fig. 4.5) as static-growth crystals in equilibrium with Grt II as well. In the first case, white mica shows a higher phengite content with respect to the second generations as shown in figure 4.6 (Wm I: $Si = 3.10 - 3.14$, $Fe^{2+} + Mg = 0.13 - 0.19$ a.p.f.u.; Wm II: $Si = 3.04 - 3.09$, $Fe^{2+} + Mg = 0.07 - 0.15$ a.p.f.u.).

Chlorite occurs as a matrix mineral and in some case, is found as a replacement product of garnet, showing a predominant ripidolite composition in the Si vs. Fe_{tot} diagram ($Si = 5.24 - 5.43$; $Fe_{tot} = 4.51 - 5.79$) (Fig. 4.6).

4.2.5 Image-assisted thermodynamic modelling

Thermodynamic modelling of metamorphic rocks, nowadays routinely supported by several analytical techniques (e.g., SEM and EMP analysis), became in the last years the most efficient tool to quantify the $PTXt$ evolution of the orogenic processes. This is true thanks to the advent of ever more efficient and user-friendly phase diagram computing systems (i.e., Perplex – Connolly & Petrini, 2002; Connolly, 2005; or Thermocalc – Holland & Powell, 1998), stepwise controlled by the calculation of quantitative effective bulk rock chemistry (e.g., Stüwe & Ehlers, 1996; Evans, 2004; Zuluaga et al., 2005; Zeh, 2006; Fiannacca et al., 2012; Ortolano et al., 2014a). This last concept is at the base of quantifying the robustness of the modelled systems and then its relation to the real petrogenetic processes, which depend on the “objective” interpretation of textural equilibria. The choice of the most simplified chemical system capable of describing all observed paragenetic equilibria, the most appropriate solid solution models and the most meaningful

effective bulk rock chemistry is at the base of the pseudosection computation method. The sources of uncertainty in such a method can derive from: a) intrinsic limits such as the propagation of the uncertainty in the thermodynamic data used for compilation of the database and in the solid solution models, or the effects of the pseudocompound approximation used, for instance, in the perplex algorithm for Perplex users; b) extrinsic measurable parameters such as the influence of potential chemical fractionation induced by mineral phases, that, reaching a specific critical size, are potentially able to extract a specific percentage of constituents oxides from the effective bulk-rock chemistry.

A useful methodological approach for obtaining more reliable “a priori” information for the *PT*-pseudosection calculation as well as “a posteriori” check on the model robustness can be reached from the numerical extraction of petrological data, such as those derived from the calibration of the X-ray maps. Maps calibration consists in the conversion of a qualitative raster image into a grid format (e.g., an equally-sized image where each pixel stores the absolute chemical concentration of an element) and can be obtained from the use of last generation device software such as: (a) ℓ 1-SPIRiT ([Murphy et al., 2012](#)); (b) Labspec (www.horiba.com/scientific/products/raman-spectroscopy/software/), and (c) Pathfinder (www.thermofisher.com/it/en/home/industrial/spectroscopy-elemental-isotope-analysis/microanalysis-electron-microscopy/pathfinder-X-ray-microanalysis-software.html); or using post-processing X-ray map classification tools such as: (a) Petromap ([Cossio & Borghi, 1998](#)); (b) XMapTools ([Lanari et al., 2014](#)) and (c) Q-XRMA ([Ortolano et al., under review](#)).

In this work, the multilinear regression algorithm of Q-XRMA software is here applied to extrapolate the compositional variation of the analysed mineral equilibria. This step permitted to highlight the potential chemical fractionation occurring during metamorphic history, the critical size and mode percentage of critically sized grains (e.g., garnet) potentially able to yield fractionation process, also emphasising the presence/absence of compositional changes within zoned phases. All of these parameters are to be taken into careful attention to obtain reliable constraints in pseudosection *PT* space as reported in several scientific

papers (e.g., Connolly & Petrini, 2002; Evans, 2004; Zuluaga et al., 2005; Fiannacca et al., 2012; Ortolano et al., 2014a).

4.2.5.1 Quantitative image processing

Numerical elaboration of major elements X-ray map (see 2.4) of the entire MA271 thin section (600x320 pixels with 30 μm pixel size) (Fig. 4.7) supported by others three opportunely selected garnet micro-domains (512*400 pixels for the first domain, 1200*900 pixels for the other ones, with 2 μm pixel size) (Fig. 4.8) have been here integrated to extrapolate the effective bulk compositions

(EBCs) operative during the

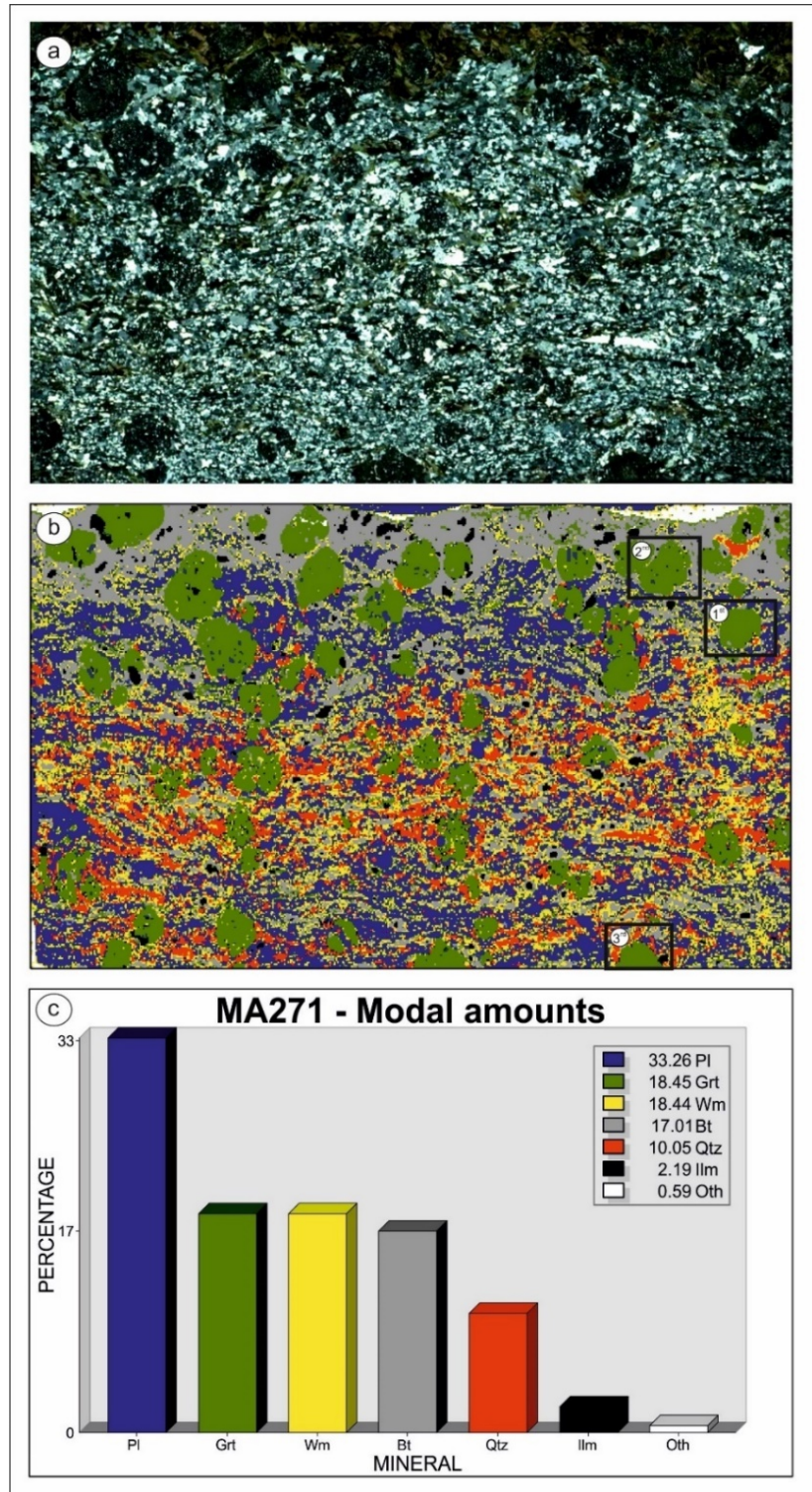


Fig. 4.7 - Thin section classification: (a) pre-processed optical thin section scan; (b) mineralogical distribution map of the entire thin section (first cycle of the Q-XRMA); (c) histogram of the mineral modal percentages for the analysed sample.

different steps of the regional metamorphism as well as during the quasi-static thermal rise.

According to [Ortolano et al. \(2014b\)](#) a semi-automated classification technique based on the sequential use of the Principal Component Analysis (PCA) and of the supervised Maximum Likelihood Classification (MLC) algorithms were applied to the major elements X-ray map of the entire thin section, with the aim to extrapolate modal percentages (Table 4.1) of the representative rock-forming minerals ([Fig. 4.7b, c](#)). Obtained mineral amounts were used in turn to verify the presence of potentially fractionating porphyroblasts (i.e., able to stepwise modify the EBCs of the metamorphic stages) by using the spreadsheet of [Zuluaga, et al., 2005](#)) modified after [Fiannacca et al. \(2012\)](#) (see [section 4.2.5.2](#)).

As shown in [figure 4.7](#), plagioclase represents the major mineral component of the MA271 sample constituting 33.26 % of the rock, followed by garnet that instead accounts for 18.45 %, displaying most of the large porphyroblasts (up to 4 mm in size) in correspondence of a biotite-rich layer (top of [Fig. 4.7a, b](#)).

Both white mica and biotite show very similar modal amounts, accounting for 18.44 % and 17.01 % of the rock-forming minerals, respectively.

Tab. 4.1 - Thin section 1st cycle output

Mineral	Pixel count	Modal %
Pl	59673	31.08
Wm	37594	19.58
Bt	32244	16.79
Grt	30357	15.81
Qtz	27711	14.43
Ilm	3081	1.60
Hole	1340	0.70
Ap	0	0.00
Chl	0	0.00
Total	192000	100

As shown in [figure 4.7a, b](#), white mica is mostly found as a mineral matrix and rarely included into garnet grains. Analogously, biotite could be found either as the inclusion within garnet or as large dark-brown matrix grains, grown statically as a result of the thermal rise (top of [Fig. 4.7a, b](#)). Finally, quartz represents the last significant mineral of the rock in terms of modal amounts, accounting for

10.01 % of the whole sample and aligned together with white mica and biotite parallel to the main foliation (Fig. 4.7a, b). The remaining 2.78 % includes the secondary minerals mostly constituted by ilmenite (2.19 %) and others unclassifiable phases accounting for 0.59 %, because below the used pixel size detection limits of 30 μm .

Modal and composition numerical extrapolation of the single metamorphic equilibria was then carried out on the major elements X-ray maps (APPENDIX C2) of the three-selected garnet microdomains (i.e., a garnet-plagioclase-rich, a garnet-biotite-rich and a garnet-quartz-rich domain. See 2.3.2 for the latter) (Fig. 4.8), which were considered representative of the main parageneses (Table 4.2a). Adopted image processing procedure consists of three various analytical steps, allowing to obtain: a) a mineralogical distribution map of the selected domain (Fig. 4.8a); b) a sub-phases subdivision within zoned minerals (Fig. 4.8b) and the calibration of the native X-ray elemental images; c) quantitative mineral end-member maps showing compositional changes within zoned crystals (Fig. 4.8c). Figure 4.8a shows the main assemblage characterising the MA271 specimen obtained as a result of the first analytical step. In all of the three microdomains, such an assemblage is given by $\text{Grt} + \text{Pl} + \text{Bt} + \text{Qtz} + \text{Wm} \pm \text{Ilm} \pm \text{Chl} \pm \text{Ap}$.

Tab. 4.2a – Domain 1st cycle output

Mineral	1 st Domain		2 nd Domain		3 rd Domain		Average
	Pixel count	Modal %	Pixel count	Modal %	Pixel count	Modal %	Modal %
Pl	51469	25.13	235201	21.78	207510	19.21	22.04
Wm	8924	4.36	61446	5.69	9202	0.85	3.63
Bt	18442	9.00	207229	19.19	105842	9.80	12.66
Grt	99518	48.59	412720	38.21	311455	28.84	38.55
Qtz	9496	4.64	14819	1.37	266625	24.69	10.23
Ilm	11933	5.83	5658	0.52	16744	1.55	2.63
Hole	0	0.00	78950	7.31	157542	14.59	7.30
Ap	960	0.47	11510	1.07	5080	0.47	0.67
Chl	4058	1.98	52467	4.86	0	0.00	2.28
Total	204800	100	1080000	100	1080000	100	100

Tab. 4.2b – Garnet 2nd cycle output

	1 st Domain		2 nd Domain		3 rd Domain		Average
	Pixel count	Modal %	Pixel count	Modal %	Pixel count	Modal %	Modal %
Sub Phases							
COR	7350	3.59	27016	2.50	35099	3.25	3.11
MNT	39790	19.43	86059	7.97	43137	3.99	10.46
SR	55198	26.95	190414	17.63	342467	31.71	25.43
No Garnet	102462	50.03	776511	71.90	659297	61.05	60.99
Total	204800	100	1080000	100	1080000	100	100

Garnet is the prevalent phase, ranging from about 29 to 50 %, plagioclase accounts for the 22 % averagely, whereas biotite is the third predominant phase observed, with a domain modal amount ranging from 7 to 19 %. White mica is not particularly abundant accounting only for 0.8 - 5.7 % alike chlorite, observed only for 3.6 – 4.8 % as a result of biotite or garnet breakdown. Quartz is found in small percentages as well (1.4 – 4.9 %) especially in the domains 1 and 2 (Fig. 4.8a – Table 4.2a), whereas the domain 3 shows a larger quartz amount of about 25 %. Secondary phases like apatite and ilmenite can be found as inclusions in garnet in very minimum quantities (0.4 – 1.17 % and 0.5 – 1.55 % respectively – Table 4.2a).

The second analytical step of the image analysis permitted to depict the presence of garnet sub-phases.

This investigation allows quantifying the modal amount of garnet core fractionation, permitting the computation of the peak and retrograde metamorphic EBCs. In each domain, garnet shows three distinct sub-zones (Fig. 4.8b – Table 4.2b), namely: a) a quasi-isodiametric relict core with an average diameter of 500 μm accounting for ~ 8 % of total of the garnet grains; b) an inclusion-rich mantle with a thick up to 1000 μm and a modal percentage ranging from 10 % to 40 %; and c) an inclusion-poor euhedral rim of about 100 μm of thickness and 55 % to 80 % as modal amounts.

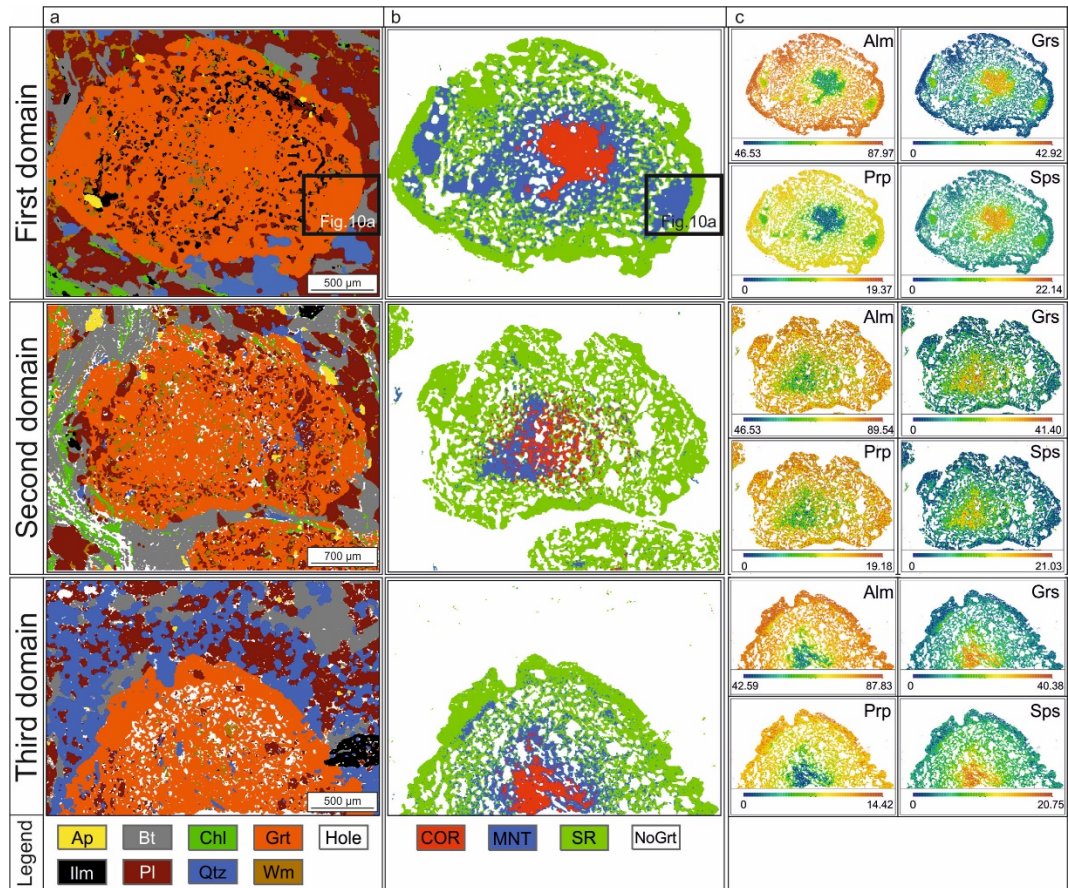


Fig. 4.8 – Three-selected investigated domains via Q-XRMA image processing procedure: (a) mineralogical distribution maps (first cycle classification); (b) garnet sub-phases identification (second cycle classification) highlighting regional metamorphism core (COR) and mantle (MNT) rimmed by a contact metamorphism static overgrowth (SR); (c) garnet component maps (third cycle classification) highlighting an enrichment in almandine and pyrope towards the rim accompanied by a depletion in grossular and spessartine.

Figure 4.8c shows the outputs of the third image processing step regarding the end-member maps displaying compositional variation observed through each sub-phase which characterise garnet porphyroblasts.

As already indicated by mineral chemistry, the calibrated end-member maps (Fig. 4.8c) confirm a higher spessartine (20.75 – 22.14 mole %) and grossular (40.38 – 42.92 mole %) content into the relict core, that decrease towards the static rim where an opposite trend in the almandine (87.83 to 89.54 mole %) and pyrope (14.42 to 19.37 mole %) one is clearly observed.

All of these pieces of information are then averaged for all three selected microdomains and subsequently used in combination with the mineral modes of the entire thin section with the aim to define thermodynamic models properly.

4.2.5.2 Thermobaric constraints

To constrain the PT values representative of the recognised metamorphic equilibria three different pseudosections have been calculated, taking care into account the EBCs as well as the specific system parameters to be set out for each metamorphic stage. In this view, the first pseudosection was calculated using the XRF composition representing the effective bulk rock chemistry involved in the growth of the garnet core (Fig. 4.9a), whereas the others two PT pseudosections (Fig. 4.9b, c) were calculated using data extrapolated from the X-ray map image processing of the three selected micro-domains. Perple_X software package (updated to November 2016, www.perplex.ethz.ch) has been chosen as the phase diagram computing system (Connolly 1990a; Connolly & Petrini, 2002; Connolly, 2005). The computed pseudosections span a PT range of $T = 450\text{--}700$ °C and $P = 0.3\text{--}0.9$ GPa, as considered suitable to enclose the PT constraints of the observed parageneses. MnO-Na₂O-K₂O-FeO-MgO-Al₂O₃-SiO₂-H₂O (MnNKFMAsh) system was used. SiO₂ and H₂O have been considered in excess, and the CORK fluid equation of state (EOS) of Holland & Powell (1998) was chosen to model the fluid phase behaviour.

The applied solid solution models were: (a) Ti-Fe-Mg-Mn biotite of Powell & Holland (1999) extended to cover Fe and Mn-solution; (b) a quaternary garnet model of Holland & Powell (1998); (c) the white mica model of Holland & Powell (1998) valid for Na-poor compositions; (d) the chlorite model extended from Holland et al. (1998); (e) a binary plagioclase solid solution (Newton et al., 1980). According to Evans (2004) and Cirrincione et al. (2008), to derive suitable PT constraints, the intersections of at least three isopleths per time were checked from the different garnet compositions, texturally constrained using the image processing.

Mineral isopleths computed per each pseudosection are in APPENDIX C5. The PT conditions of the various garnet growth stages were calculated considering an average estimated error of ± 30 °C and ± 0.1 GPa (e.g., Cirrincione et al., 2008), stepwise verifying the Effective Reactant Volume (ERV) operating during the different evolutionary stages of the metamorphic history.

The first pseudosection (Fig. 4.9a) permitted to obtain isopleth garnet core intersections ($Alm_{55-65}Grs_{26-32}Prp_{1-3}Sps_{10-15}$) depicting a PT interval of $T = 490-520$ °C and of $P = 0.51-0.57$ GPa (Fig. 4.8a), very close to the PT constraints previously defined by Angi et al. (2010) at 500 °C and 0.59 GPa.

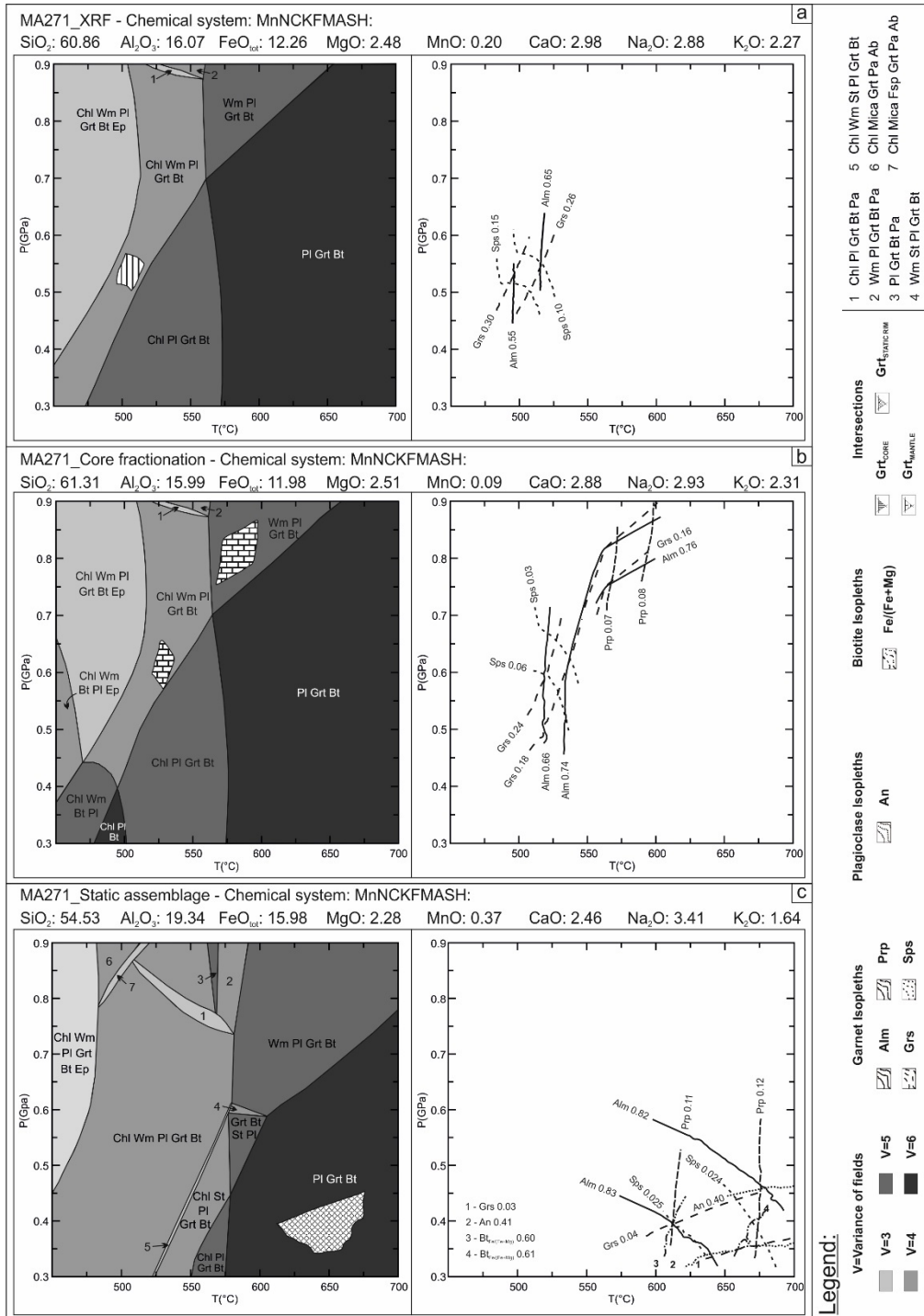


Fig. 4.9 – Pseudosections computation supported by image analysis: (a) first pseudosection, computed using XRF analysis, permitted to constraint PT condition of the garnet core (COR); (b) second pseudosection, computed fractionating the COR, allowed to define the PT evolution of the garnet mantle (MNT); (c) third pseudosection, computed by isolating the static equilibrium assemblage, defined the PT values of the garnet static overgrowth (SR).

The compositional range of the mantle garnet overgrowth not permitted any reliable intersection in this pseudosection PT space due to the fractionation effects of the garnet cores, already mentioned by Angi et al. (2010) that obtained through garnet isopleths thermobarometer a large PT range spanning from T of 520 to 545 °C and P ranging from 0.7 to 1.0 GPa.

For this reason, a second pseudosection (Fig. 4.9b) was constructed fractionating the garnet core using a modified version of the spreadsheet of Zuluaga et al. (2005) to compute the effective bulk composition (Table 4.3).

Table 4.3 - Calculation of amount of oxides to be fractionated from garnet porphyroblasts using Q-XRMA image analysis software

Garnet density (Kg/m ³)	Rock density (Kg/m ³)	Density ratio	Garnet amounts							
			Domains	COR Sub- Phase	Thin section	COR % in thin section	To be fractionated			
4060	2830	1.43	Averaged pixel count	99515	7857	30357	2397	1.28		
			Averaged modal %	38.55	3.11	15.81	1.28			
Oxides	SiO ₂	TiO ₂	Al ₂ O ₃	FeO	MgO	MnO	CaO	Na ₂ O	K ₂ O	Total
Garnet inner core composition (wt %)	37.67	0.00	21.03	27.76	0.73	6.01	8.74	0.16	0.07	102.18
Normalized to 100	36.86	0.00	20.58	27.17	0.71	5.89	8.56	0.16	0.07	100.00
Fractionated garnet deduction (mode adjustment ratio)	0.68	0.00	0.38	0.50	0.01	0.11	0.16	0.00	0.00	1.83
Bulk rock chemistry (wt %)	60.86	0.00	16.07	12.26	2.48	0.20	2.98	2.88	2.27	100.00
Normalized to 100	60.86	0.00	16.07	12.26	2.48	0.20	2.98	2.88	2.27	100.00
Bulk rock chemistry (wt %) normalized to 100 - fractionated garnet deduction	60.18	0.00	15.69	11.76	2.47	0.09	2.82	2.88	2.27	98.17
Normalized to 100	61.31	0.00	15.99	11.98	2.51	0.09	2.88	2.93	2.31	100.00

In this case, the isopleths intersections (i.e., $Alm_{66-74}Grs_{18-24}Prp_{3-5}Sps_{3-6}$) and ($Alm_{76-78}Grs_{16-18}Prp_{7-8}Sps_{1-2}$) of the garnet mantle sub-phase determine two distinct areas located at $T = 515-535$ °C, $P = 0.55-0.63$ GPa and $T = 570-600$ °C, $P = 0.75-0.85$ GPa respectively (Fig. 4.9b), indicating a prograde evolution towards the upper-amphibolite facies reaching the thermobaric peak of the regional metamorphism more reliable than those previously calculated in the Angi et al. (2010).

Finally, to estimate the PT conditions associated with the static metamorphic event responsible for the garnet rim overgrowth, a representative portion of the relative equilibrium volume has been used to derive ERV and, as a consequence, to obtain the EBC adopted in the pseudosection computation.

Tab. 4.4 - Calculation of the effective bulk composition from the effective reactant volume of the static assemblage by Q-XRMA

	Garnet		Plagioclase		Biotite		Quartz		Total	
	Domain	ERV	Domain	ERV	Domain	ERV	Domain	ERV	Domain	ERV
Average Percentage	32.26	5.10	20.81	6.47	15.90	2.67	1.86	1.86	70.83	16.10
Percentage normalized to 100	45.55	7.20	29.38	9.13	22.45	3.77	2.63	2.63	100.00	22.73
Garnet										
Reacted mode %	7.20									
Oxides	<i>SiO₂</i>	<i>TiO₂</i>	<i>Al₂O₃</i>	<i>FeO</i>	<i>MgO</i>	<i>MnO</i>	<i>CaO</i>	<i>Na₂O</i>	<i>K₂O</i>	<i>Total</i>
Average Composition (Wt%)	37.15	0.00	21.07	38.09	3.07	1.14	0.86	0.00	0.01	101.39
Normalized to 100	36.64	0.00	20.78	37.57	3.03	1.13	0.85	0.00	0.01	100.00
Oxide amounts of the reacted mode %	2.64	0.00	1.50	2.71	0.22	0.08	0.06	0.00	0.00	7.20
Plagioclase										
Reacted mode %	9.13									
Oxides	<i>SiO₂</i>	<i>TiO₂</i>	<i>Al₂O₃</i>	<i>FeO</i>	<i>MgO</i>	<i>MnO</i>	<i>CaO</i>	<i>Na₂O</i>	<i>K₂O</i>	<i>Total</i>
Average Composition (Wt%)	62.32	0.01	23.98	0.06	0.01	0	5.45	8.42	0.12	100.37
Normalized to 100	62.09	0.01	23.89	0.06	0.01	0.00	5.43	8.39	0.12	100.00
Oxide amounts of the reacted mode %	5.67	0.00	2.18	0.01	0.00	0.00	0.50	0.77	0.01	9.13
Biotite										
Reacted mode %	3.77									
Oxides	<i>SiO₂</i>	<i>TiO₂</i>	<i>Al₂O₃</i>	<i>FeO</i>	<i>MgO</i>	<i>MnO</i>	<i>CaO</i>	<i>Na₂O</i>	<i>K₂O</i>	<i>Total</i>
Average Composition (Wt%)	35.17	2.86	17.53	22.71	7.45	0.06	0.01	0.10	9.03	94.93
Normalized to 100	37.05	3.02	18.47	23.92	7.85	0.07	0.01	0.11	9.51	100.00
Oxide amounts of the reacted mode %	1.40	0.11	0.70	0.90	0.30	0.00	0.00	0.00	0.36	3.77
Quartz										
Reacted mode %	2.63									
Oxides	<i>SiO₂</i>	<i>TiO₂</i>	<i>Al₂O₃</i>	<i>FeO</i>	<i>MgO</i>	<i>MnO</i>	<i>CaO</i>	<i>Na₂O</i>	<i>K₂O</i>	<i>Total</i>
Average Composition (Wt%)	100.00	0.00	0.00	0.00	0.00	0.00	0.00	0.00	0.00	100.00
Normalized to 100	100.00	0.00	0.00	0.00	0.00	0.00	0.00	0.00	0.00	100.00
Oxide amounts of the reacted mode %	2.63	0.00	0.00	0.00	0.00	0.00	0.00	0.00	0.00	2.63
Effective Bulk Composition (EBC) of the Effective Reactant Volume (ERV)										
Oxides	<i>SiO₂</i>	<i>TiO₂</i>	<i>Al₂O₃</i>	<i>FeO</i>	<i>MgO</i>	<i>MnO</i>	<i>CaO</i>	<i>Na₂O</i>	<i>K₂O</i>	<i>Total</i>
ERV Bulk Composition (Wt%)	12.33	0.11	4.37	3.61	0.52	0.08	0.56	0.77	0.37	22.73
Normalized to 100	54.25	0.51	19.24	15.90	2.27	0.37	2.45	3.39	1.63	100.00
ERV Bulk Composition (Wt%) with no TiO ₂ used to construct the new pseudosection	54.53	0.00	19.34	15.98	2.28	0.37	2.46	3.41	1.64	100.00

This last step was possible isolating from the three selected domains the portion representative of the static assemblage, using ArcGIS® raster analysis (Dainelli et al., 2010) and using a modified version of the spreadsheet of Ortolano et al. (2014a). Once the modal amount of the new phases and their compositions were known, the bulk composition of this volume was determined (Tab. 4.4) and the relative phase diagram section constructed (Fig. 4.9c).

In this case, the isopleths intersections of the static minerals (i.e., Grt: $Alm_{82-83}Grs_{3-4}Prp_{11-12}Sps_2$; Pl: An_{40-41} ; Bt: $Fe/(Fe + Mg)_{60-61}$) define a PT range of $T = 625-675$ °C and $P = 0.35-0.43$ GPa (Fig. 4.9c), very similar to those obtained by Angi et al. (2010) at T of 685°C and 0.3 GPa on another sample.

Tab. 4.5 – Reconstruction of garnet overgrowing stages

Sample		MA271		
Pseudosection: Fig. 4.7		Observed assemblages*	Constraining phases and P-T estimates	Pseudosection computation method
Orogenic cycle	Garnet Core	Grt _I + Pl _I + Bt _I + Wm + Chl + Ep + Qtz	Garnet core isopleths: ($Alm_{55-65}Grs_{26-32}Prp_{1-3}Sps_{10-15}$) 0.54 ± 0.03 GPa 505 ± 15°C	Bulk rock chemistry (XRF)
	Garnet Mantle (MNT)	Grt _I + Pl _I + Bt _I + Wm + Chl + Qtz	Garnet inner mantle isopleths: ($Alm_{66-74}Grs_{18-24}Prp_{3-5}Sps_{3-6}$) 0.59 ± 0.04 GPa 525 ± 10°C	EBC from garnet core composition fractionation (Zuluaga et al., 2005 modified)
		Grt _I + Pl _I + Bt _I + Wm + Qtz	Garnet outer mantle isopleths: ($Alm_{76-78}Grs_{16-18}Prp_{7-8}Sps_{1-2}$) 0.80 ± 0.05 GPa 585 ± 15°C	
Thermal metamorphism	Garnet Static Rim (SR)	Grt _{II} + Pl _{II} + Bt _{II} + Qtz	Garnet static rim isopleths: ($Alm_{82-83}Grs_{3-4}Prp_{11-12}Sps_2$) Static plagioclase isopleths: (An_{39-41}) Static biotite isopleths: ($Fe/(Fe+Mg)_{59-61}$) 0.39 ± 0.04 GPa 650 ± 25°C	EBC of the ERV of the static assemblages (Ortolano et al., 2014a modified)

* Observed mineral assemblages have been recalculated: a) Garnet, considering all iron as FeO (i.e., on the basis of Alm-Sps-Grs-Prp end-members); b) White mica, considering the $Si_{a.p.f.u.}$, variable from 3.0 (i.e., Muscovite) to 4.0 (i.e., Celadonite), expressed as phengite content; c) Chlorite and biotite was expressed as $Fe^2/(Fe^2+Mg)$ ratio.

The new obtained PT path partly adjust those previously achieved by Angi et al. (2010) given the most suitable compositional mineral dataset and for the

possibility to compute stepwise the EBCs operative during the evolution of the metamorphic evolutionary stages as traced by the recognised garnet overgrowing stages (Tab. 4.5).

This new obtained *PT* path was then compared with the path of [Acquafredda et al. \(2006\)](#) representative for the top of the lower crust of the Serre (Fig. 4.10), highlighting as both of them shared the same burial history up to the maximum depth. Beyond this point, the upper crust followed a retrograde path connected with a deep-seated shearing stage ([Angi et al., 2010](#)) and was affected by the subsequent post-tectonic progressive emplacement of huge masses of granitoid bodies. Finally, a low-pressure cooling path is consistent with the final unroofing stage of the ancient crystalline basement complex ([Angi et al., 2010](#)).

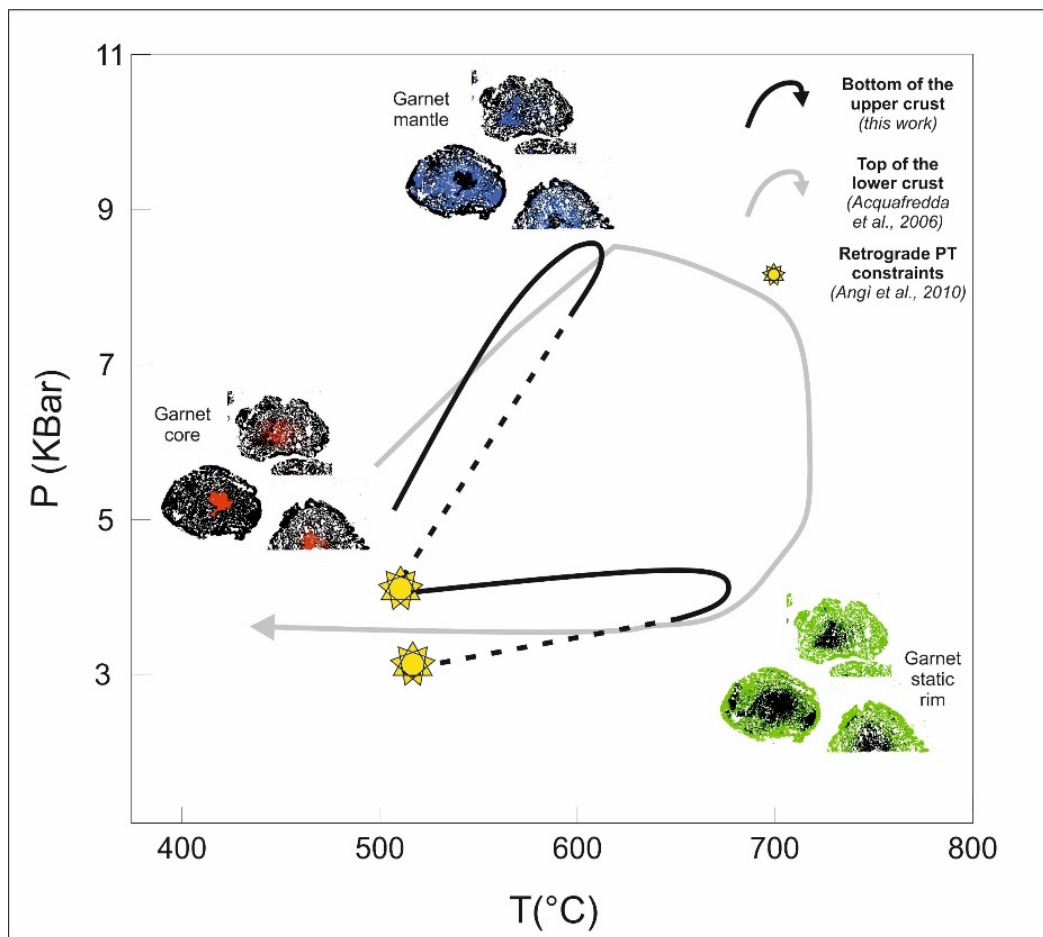


Fig. 4.10 – New image-assisted *PT*-path of the Serre Massif. Red, blue and green zones of garnets represent the COR, MNT and SR used to constraint thermobaric conditions of the upper crust of the Serre Massif (black path). Yellow stars marks the retrograde conditions constrained by [Angi et al. \(2010\)](#). In grey the *PT*-path of [Acquafredda](#), highlighting similar regional peak temperatures between the top of the lower crust and bottom of the upper one.

4.2.6 Diffusion modelling

Diffusion modelling of major elemental compositional zonings is arising as a valuable tool to quantify how long a zoned mineral can resist in chemical disequilibrium with the surrounding matrix at high temperature before the pre-existing composition is modified by the triggering of the diffusion phenomena (Ague et al., 2013). This approach has been used here to derive the timescales of the static metamorphic event, providing information about the heating and cooling history of the investigated samples. Such a geological timescale estimation is possible by studying concentration gradients set in solid mineral solutions between old (i.e. theoretical) compositions and newly formed ones. These chemical variations evolve as a consequence of the mineral-chemical adjustment due to the continuous changes of the intensive variables (e.g., T , P , $X_{\text{H}_2\text{O}}$, X_{CO_2} , $f\text{O}_2$), and tend to be preserved if the diffusive fluxes have not act for a long time. As shown in 3.3, one of the most important parameters to be know is the diffusion coefficient, which can be defined, in the broadest sense, as the transfer rate of a particle within a homogeneous medium (with the dimension of L^2/t), although more detailed diffusion coefficient distinctions have been made (e.g., Ganguly, 2002; Watson & Baxter, 2007; Ganguly, 2010). Acquiring diffusion coefficient datasets for specific minerals represents a fundamental aspect in modelling compositional changes, and numerous efforts have been made in such a direction. For instance, Chakraborty & Ganguly (1992) derived experimental data on the diffusion of garnet cations using an almandine-spessartine diffusion couple under 14-35 Kbar and 1100-1200 °C experimental PT conditions, integrating data obtained previously by Loomis et al. (1985). Chakraborty & Rubie (1996) obtained the magnesium diffusion coefficients from pyrope-almandine diffusion couples at 1 bar - 750–850 °C and 85 Kbar - 1300 °C, as well as Ganguly et al. (1998) derived divalent cations diffusion properties from almandine-pyrope natural couples at 22-40 Kbar, 1057-1400 °C using a piston-cylinder apparatus. Other experiments have been carried out by Freer & Edwards (1999) for obtaining the pseudobinary interdiffusion coefficients of Ca-(Fe, Mg). Whereas Carlson (2006) extrapolated the diffusion coefficients at 3.0-5.3 Kbar and 600-900 °C considering the dimension

of the unit cell as a further parameter to be used in the calculation of the cation kinetic values. A brief detailed review of the experimental determinations of cation diffusion coefficients in garnet can be found in [Chu & Ague \(2015\)](#), where statistical simulations have been made to analyse the kinetic coefficient data and the related uncertainties reported in the literature.

In this case study, the integration of thermodynamic modelling with an advanced quantitative image analysis of specific equilibrium microdomains (e.g., classified garnet sub-phases), permitted to derive, for the first time, a multidimensional chemical-physical dataset, such as map sets of temperature, pressure and cation diffusion coefficients using the experimental data of [Chakraborty & Ganguly \(1992\)](#). In particular, we focussed our attention on the garnet thermal overgrowth (SR: $\sim 100\text{-}200\ \mu\text{m}$) in contact with the earlier regional one (MNT) and modelling garnet compositional changes due to the propagation of diffusion mechanisms. With this aim, it was assumed that the garnet overgrowth rate was higher (i.e., as instantaneous) in comparison with the diffusion rate (e.g., see [Fig. 3.17b](#), [Ganguly et al., 1996](#)). Such a hypothesis is supported by crystal growth rate studies conducted on metapelites, which given garnet fast growth rate also of $\sim 1\ \text{mm/Ma}$ during regional metamorphism ([Cashman & Ferry, 1988](#); [Christensen et al., 1989](#)).

4.2.6.1 *Image-assisted diffusion modelling*

The use of the image processing has been revealed helpful for choosing garnet grains to be used for diffusion modelling. The criteria applied for such a choice can be summarised as follows: a) identify those minerals cut probable for their centre; b) select those grains showing an appropriate size able to develop and highlight compositional zonings; c) choose those crystals as near as possible to the matrix minerals suitable for the cationic diffusive exchange (e.g., biotite for iron and magnesium diffusion). In the first case, the $\mu\text{-XRF}$ maps and especially the manganese one (see [Fig. 2.31](#)) allowed to individuate the garnet grains with noticeable Mn-rich cores typical of a bell-shaped growth zoning, likely indicative of a cut passing through the crystal centre.

Once this first sorting is done, the granules with the highest surface area were selected after the construction of the grain boundary map of the entire thin section (Fig. 4.11a), using the GSD ArcGIS® toolbox (see section 2.2) developed at the Geoinformatics and Image Analysis Lab of the Biological, Geological and Environmental Sciences of Catania University. The input image (38.4 x 20.6 mm) was acquired with a resolution of 4200 dpi using an Epson V750 Pro dual lens system scanner and successively subjected to a preprocessing phase to make straight evident boundaries. Results of this analytical step show as the 99.25 % of the rock-forming grains (i.e., 27414) have a surface area ranging from 0.01 mm² (corresponding averagely to a crystal with a diameter of 100 μm in size) and 0.22 mm² (i.e., a crystal with about 500 μm in diameter) (Fig. 4.10).

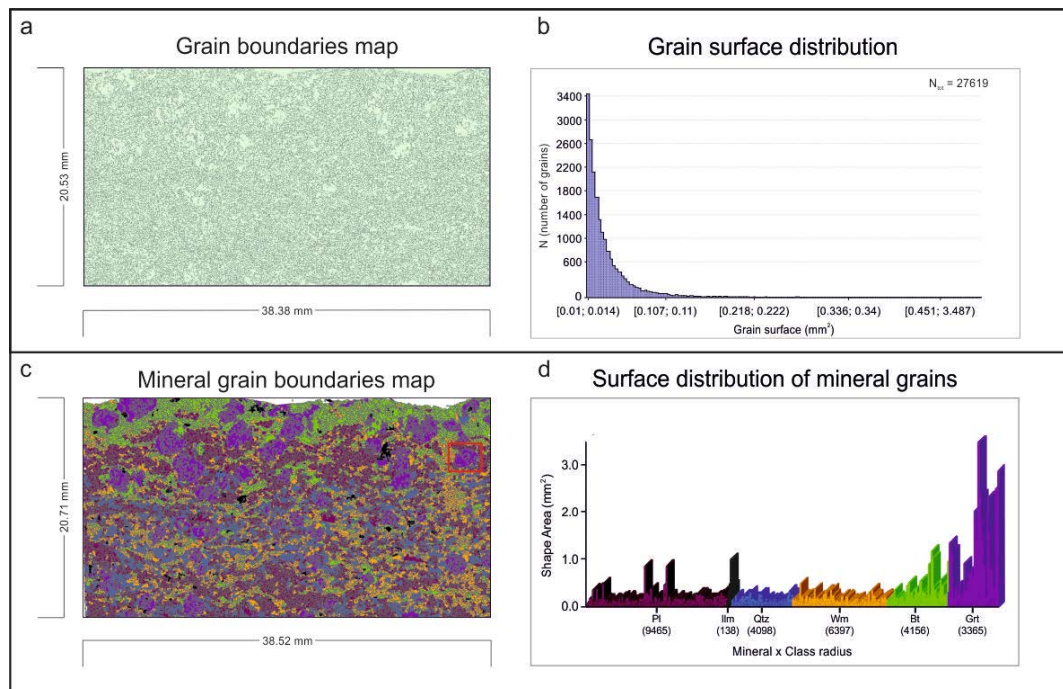


Fig. 4.11 - Mineral grain size distribution of the MA271 sample (for the sake of clarity in the current discussion, this figure combines Fig. 2.30 and Fig. 2.32): (a) ArcGIS® polygon grain map constructed by the GSD tool; (b) size frequency distribution; (c) same as in (b), but subdivided per each rock-forming mineral; (d) grain sized frequency per each detected mineral.

While the 0.75 % of the remaining grains, mainly represented by garnet porphyroblasts, are lesser in number (i.e., 205 grains on a total of 27619) but higher in size (i.e., with a surface area between 0.33 and 3.48 mm²) (Fig. 4.11b).

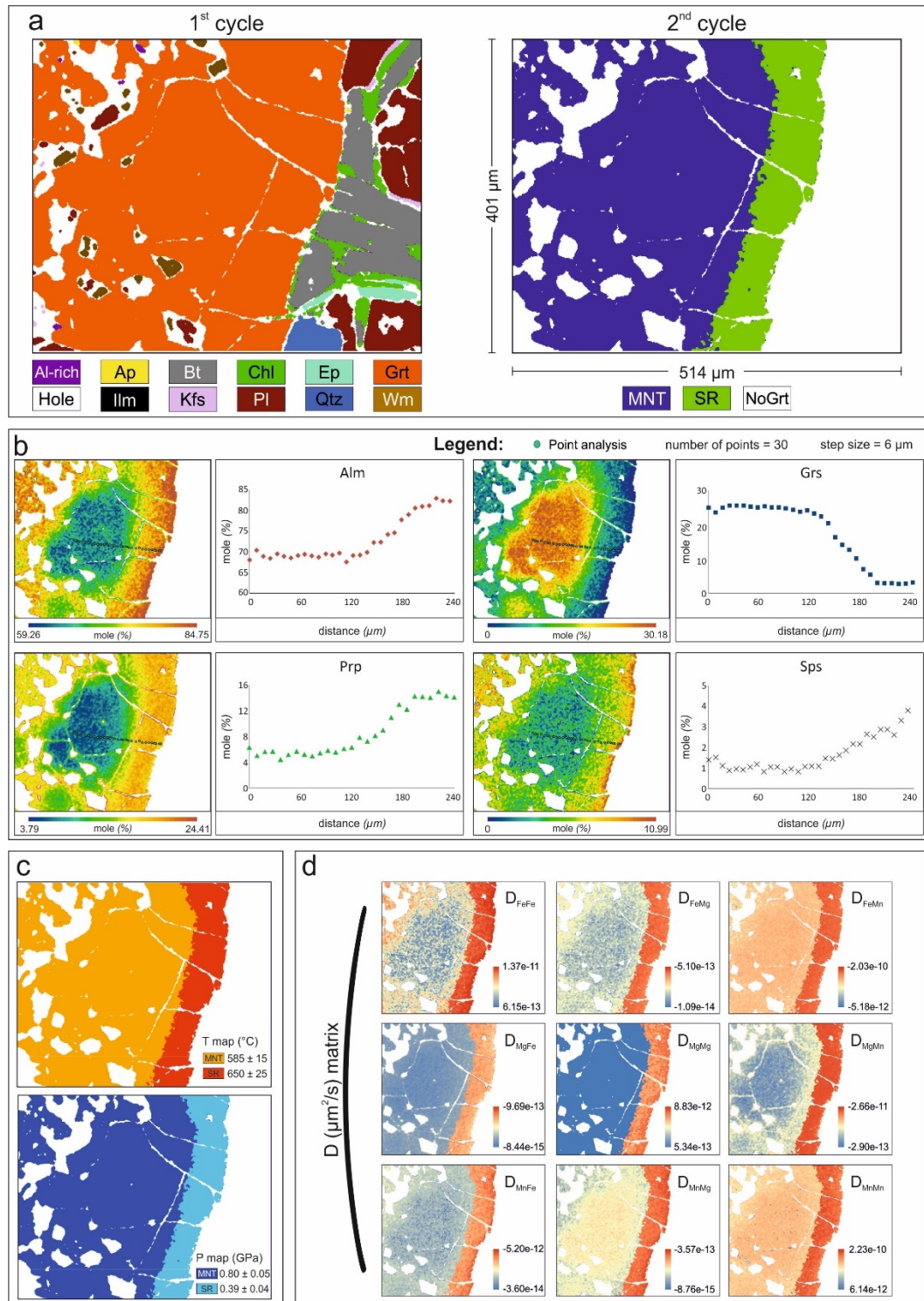


Fig. 4.12 - Schematic image-processing sequence to derive diffusion coefficient maps via DCMC (for the sake of clarity in the current discussion, this figure combines Fig. 3.10, Fig. 3.11, Fig. 3.13 and Fig. 3.14): (a) first and second cycle classification (Q-XRMA); third cycle quantification (Q-XRMA). A transect focussed on garnet-garnet (i.e., MNT-SR) diffusion couple was derived from the maps; (c) temperature and pressure maps highlighting different sub-phases' values; (d) an example of a matrix of diffusion coefficients highlighting the effect of the temperature- and compositional-dependence of the kinetic coefficients.

Combining this output map with the mineral distribution one of the Fig. 4.7 using the Min-GSD described in section 2.4, all grains were clustered as a function of each rock-forming mineral (Fig. 4.11c, d).

In such a way, has been possible to select, as a target to make diffusion studies, those garnet crystals with a diameter ranging from 1.0 to 2.0 mm (corresponding to a surface area between 1.0 and 4.0 mm²) (Fig. 4.11d).

Within this cluster, was selected the larger garnet grain located near the biotite-rich matrix (red square on Fig. 4.11c) focusing the investigation on the static rim overgrowth (SR) (Fig. 4.12a) by acquiring a new set of X-ray maps (APPENDIX C6) subsequently processed by image analysis. Results of the image processing (Fig. 4.12a) highlighted a static rim (SR), measuring ~ 100 μm in size, enriched in almandine and pyrope (Fig. 4.12b), whereas compositional gradients relaxed due to diffusion can be observed along the contact between the mantle and rim garnet zones (Fig. 4.12b). To model this diffusional compositional relaxation, the information obtained from thermodynamic modelling have been used to construct temperature and pressure maps specifically for each garnet sub phase (Fig. 4.12c) by using the DCMC tool described in section 3.3.2.

The T and P values stored in every pixel of the relative map have been successively used to compute the garnet element diffusion coefficients (Tab. 4.6) according to Eq. 8, which relates the element pre-exponential factor (i.e., the self/tracer-diffusion coefficient), with the activation energy, the activation volume of diffusion and the gas constant.

Tab. 4.6 – Summary of diffusion coefficient expressed as a function of T and P

	630 °C - 3500 Kbar	650 °C - 3700 Kbar	670 °C - 4000 Kbar
Tch	584.84	603.84	622.84
D _{Fe} (mm ² /s)	8.30E-19	1.90E-18	4.16E-18
D _{Mg} (mm ² /s)	4.05E-18	9.52E-17	2.15E-16
D _{Mn} (mm ² /s)	3.48E-18	7.68E-18	1.62E-17
D _{Ca} (mm ² /s)	4.15E-19	9.49E-19	2.08E-18

Since the PT range obtained for the static event spans from 0.35 GPa and 630 °C to 0.40 GPa and 670 °C, mean values of P and T (i.e., $P = 0.37$ GPa – $T = 650$ °C) were used in the numerical models, to bracket the timescale of the thermal event as close to reality as possible (Fig. 4.13). Nevertheless, the highest and lowest PT

values (i.e., $P = 0.40 \text{ GPa} - T = 670 \text{ }^\circ\text{C}$ and $P = 0.35 \text{ GPa} - T = 630 \text{ }^\circ\text{C}$) were used to investigate the maximum range of timescales related to the thermal event (Fig. 4.14), comparing results with the PTt history known in literature (e.g., Caggianelli et al., 2000a; Caggianelli & Prosser, 2002; Festa et al., 2003, 2013; Langone et al., 2014).

According to Faryad & Chakraborty (2015), the temperature value used in Eq. 8 for calculating the element diffusion coefficients was corrected using the characteristic temperature of diffusion:

$$T_{ch} = 0.95 * T_{peak} \quad (\text{Eq. 21})$$

where T_{peak} is the temperature of the Late-Variscan thermal peak and T_{ch} (i.e., the characteristic diffusion temperature) is a constant value. Such equation is here adopted for treating and simplifying the non-isothermal path, linked with the emplacement and cooling of the top of the Serre Batholith (i.e., delimited by yellow stars on Fig. 4.10, from heating to cooling), as an isothermal one. In such a way, the duration obtained by the isothermal diffusion modelling at this characteristic temperature could be assumed the same as that of a non-isothermal one.

$T = 650 \text{ }^\circ\text{C} - P = 3700 \text{ Kbar} - D(\text{mm/s}^2) \text{ Fe} = 1.90\text{e-}18; \text{ DMg} = 9.52\text{e-}17; \text{ DMn} = 7.68\text{e-}18; \text{ DCa} = 9.49\text{e-}19;$

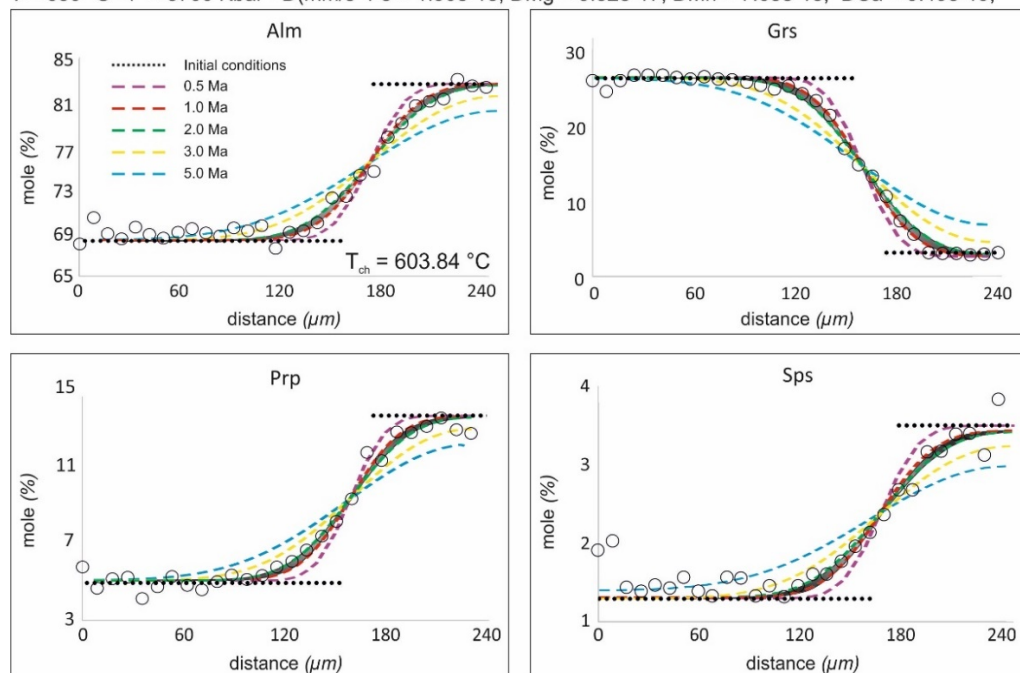


Fig. 4.13 - Diffusion modelling results obtained by using image-assisted thermodynamic modelling. Modelled garnet component profiles highlight compositional changes occurred in a period of 1-2 Ma during the contact metamorphism using mean PT values constrained in Fig. 4.8c.

The obtained kinetic coefficient values were then used to study the garnet multicomponent diffusion (Lasaga, 1979; Chakraborty & Ganguly, 1991), by deriving representative maps of the compositionally-dependent interdiffusion coefficients of the \mathbf{D} -matrix (Fig. 4.12d), applying Eq. 5 and Eq. 6. In this case, calcium was treated as the dependent component (i.e., $X_{Ca} = 1 - X_{Fe} + X_{Mg} + X_{Mn}$) and, according to Chakraborty & Ganguly (1992), the relative D was assumed $\sim 0.5 D(P, T)_{Fe}$. Pre-diffusion Initial condition was set using the composition along the flat profiles at both sides of the diffusion zone (i.e., the interface between garnet SR and MNT sub-phases) (e.g., Chakraborty, 2006).

This choice was further supported by intersecting isopleths of garnet components and those relative to the modal percentage of the overgrowth (APPENDIX C5), whose averaged values were derived via image analyses (see Tab. 4.2b). Since the compositional dependence of the interdiffusion coefficients, Eq. 20 was numerically solved applying a finite-difference forward modelling (see section 3.4.2.3) implemented in a MATLAB® script, on the base of an initial compositional profile shape as that shown in Fig. 3.17 and considering diffusion in a semi-infinite medium as the boundary conditions (see Fig. 3.18). Such an approach was repeated as long as there was a good match between the shape of the simulated compositional profiles and the measured ones. The complete sequence of the calculations is in APPENDIX C7.

Figure 4.13 shows the diffusion modelling results of compositional changes recorded by garnet, highlighting a timescale of around 1-2 Ma for the thermal event consequent to the Late-Variscan granitoid emplacement. Such a timescale highlights a relatively fast heating/cooling of rocks (~ 65 °C/Ma) of the upper crust of the Serre Massif, as similarly emphasised in the works of Caggianelli et al. (2000a), Caggianelli & Prosser (2002) and Caggianelli et al. (2007) where a pre-intrusion temperature of the host rocks of ~ 400 °C was assumed. However, a shorter or longer timescale could be obtained if lower or higher temperatures are assumed in the models for calculating \mathbf{D} . As shown in figure 4.14, a timescale of ~ 1 Ma is derived if the upper limit of PT condition (i.e., $PT = 4000$ Kbar at 670 °C) shown in Fig. 4.9 is used in the modelling. Whereas a timescale of $\sim 3-5$ Ma is

obtained if the lower limit of PT condition (i.e., $PT = 3500$ Kbar at 630 °C, Fig. 4.9) is used for computing diffusion coefficients.

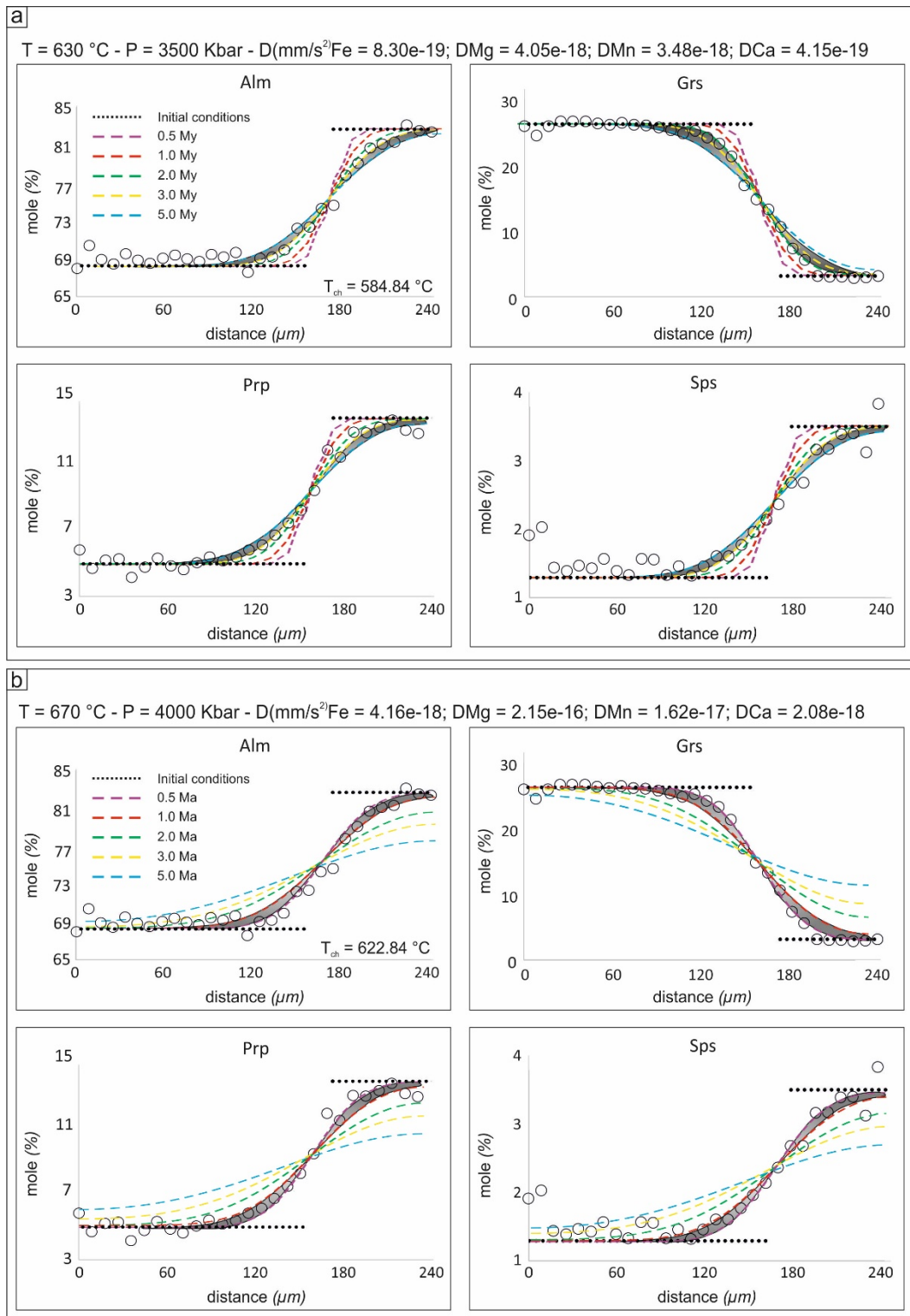


Fig. 4.14 - Diffusion modelling results obtained by using the minimum and maximum PT ranges from Fig. 4.8c. In this case, modelling garnet component provides a timescale interval of 1 to 5 Ma for the contact metamorphism. Such a range come from the strong temperature-dependence of the garnet kinetic coefficients.

4.2.6.2 Sources of uncertain

The main source of uncertain leading to the difference in the timescale obtained is because diffusion coefficients in garnets have activation energy very sensitive to the changes in temperature (see Eq. 8). This effect implies that small variations in the temperature values involve large errors in the calculation of D and, hence, of the Δt (Dodson, 1973; Ganguly et al., 1996; Chakraborty, 2006; Ganguly, 2010). Another hitch encountered in the correct estimation of the timescale of geological processes derives from the low-temperature extrapolation of the diffusion experimental data, as a change in the diffusion mechanism could occur (Ganguly et al., 1996). However, comparing studies (e.g., Chakraborty & Ganguly, 1991; Ganguly et al., 1996) between lower temperature experimental data of the ^{27}Mg tracer (i.e., until 750 °C) and the lower temperature Arrhenian extrapolation from higher temperature values (i.e., ~ 1300 °C), have shown a good agreement if both datasets are normalised to the same P and fO_2 conditions (e.g., Chakraborty & Ganguly, 1991; Chakraborty & Rubie, 1996; Ganguly et al., 1996). These results suggested the authors that a change in the diffusion mechanism (e.g., from intra- to intergranular diffusion) not occur at this range of temperature. However, any information about the possibility of a change in the diffusion mechanism at temperatures below 750 °C is not available, as due to the very slow diffusion processes at these temperatures difficult to reproduce at the time of laboratory experiments. At any case, if a change in the diffusion mechanism occurs, this would improve the extension of kinetic compositional relaxation leading to an overestimation of the Δt (Ganguly et al., 1996). On the other hand, same result would be achieved if sectioning effects affect the mineral investigated, as an artificial extension of the diffusion profile would result.

In summary, there can be several sources of uncertain, but the difference in the temperature of the rocks represent the most influencing factor. Keeping in mind all of these aspects, a timescale of 3 ± 2 Ma could be considered reasonable for the contact metamorphism reflected by the garnet static overgrowth.

4.2.7 Final Remarks

Innovative numerical petrology methods supported by image analysis were here applied to model the *PT* conditions and the timescale of a late Variscan static garnet overgrowth stage, by deriving quantitative maps able in turn to extrapolate the effective bulk compositions to be used in the pseudosection construction. A total of three pseudosection were calculated and the mineral isopleths intersections were carried out on a garnet micaschist sample (i.e., MA271). *PT* constraints permitted to draw a *PT* -path integrating and improving the previously defined one (i.e., Angi et al., 2010), which was affected by missing application of garnet fractionation techniques and, as a consequence, by missing of specific reliable isopleth intersections. The new *PT* values were, then, used in conjunction with the garnet component compositions obtained by the Q-XRMA, with the aim to acquire a suitable dataset of kinetic data to be used into the diffusion modelling. This latter was addressed via a finite-difference numerical solution as the huge number of calculations required to model very slow cationic motions characterising garnet.

Results of modelled profiles (Fig. 4.13, Fig. 4.14) show a good fit between observed and predicted concentration values defining timescales ranging from 1 to 5 Ma for the Late-Variscan contact metamorphism. Such a result testifies relatively very fast heating/cooling rates (e.g., averagely from 40 °C/Ma to 150 °C/Ma) affecting the upper crustal rocks of the Serre Massif. These rates are in a good agreement with the thermal model proposed by Caggianelli et al. (2000a) and Caggianelli & Prosser (2002) for the same investigated region if a higher temperature isotherm perturbation is considered (i.e., 400 °C in Fig. 4.15). These authors, modelled the thermal perturbation induced by large hot bodies (i.e., the granitoid) surrounded by more colder ones (i.e., the Mammola paragneiss host rocks), deriving a significant initial heating increase of 250 °C/Ma, followed by a relatively slower cooling rate of 30-40 °C/Ma for at least 5 Ma.

As the strong dependence from temperature of the diffusion coefficients, and the limit in detecting absolute values of temperature conditions, a timescale of 3 ± 2 Ma is constrained for the last metamorphic event affecting the bottom part of the

upper crustal rocks of the Serre Massif, experiencing a probable faster heating/cooling rate from the lower crust of the same metamorphic basement.

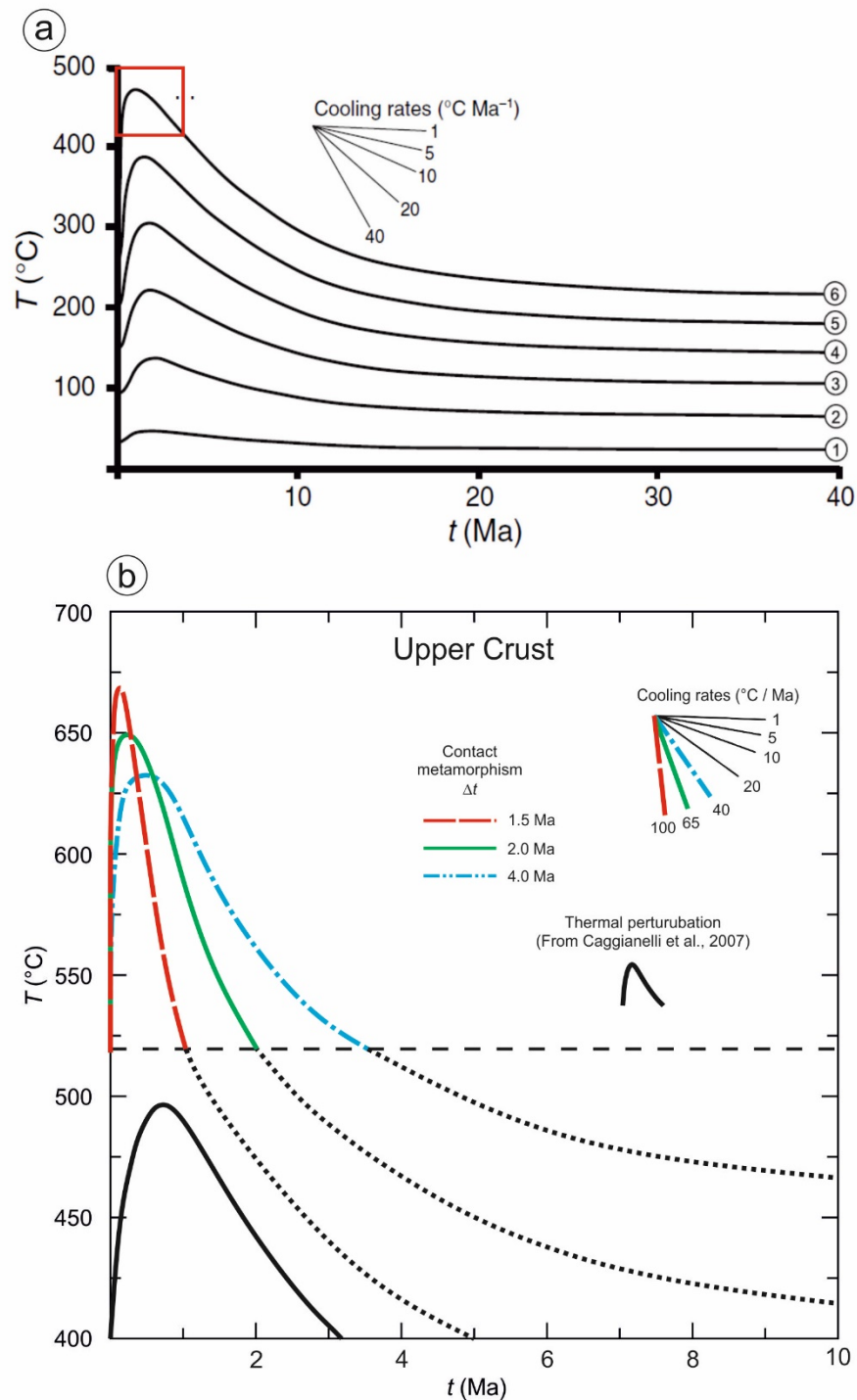


Fig. 4.15 - Temperature-time diagram of the Upper Crust (Serre Massif): (a) T-t diagram showing the recovery of the thermal perturbation induced by the Late-Variscan granitoid emplacement, at different upper crust levels of the Serre Massif. Numbers in circles increase as a function of the crust depth (from Caggianelli et al., 2007); (b) T-t diagram derived from the diffusion modelling results of this work, highlighting faster cooling rates of the bottom of the upper crust, because of the major temperature pre-intrusion of the host rocks. Different models testify the strong dependence from the temperature of the diffusion coefficients.

4.3 Second case study: Timescale and cooling of the Calabria continental lower crust inferred via garnet diffusion modelling: An example from the Sila Piccola Massif

A detailed structural and petrological study has been focused on the Sila Piccola Massif (Northern Calabria) to obtain new reliable constraints about the tectono-metamorphic history of the “Castagna Unit” (Dubois & Glangeaud, 1965; Dubois, 1976), by constraining the timescale of the metamorphic evolutionary stages. This unit represents a pervasive mylonitic horizon located within the Calabrian continental crust, consisting of greenschist to amphibolite facies rocks intruded by late-Hercynian granitoids. Structural investigations highlighted a pervasive mylonitic fabric that obliterated older metamorphic surfaces, locally preserved as relics in the low strain domains of the metapelite horizons. These relics of a pre-mylonitic cycle consist of the first generation of garnet, plagioclase, biotite, white mica and quartz in which garnet shows a *quasi*-absent crystal zoning. Based on different assemblages recognized in several rock microdomains, the mylonitic event consists of two metamorphic stages. Firstly, the syn-kinematic growth of the second generation of garnet, plagioclase, biotite, sillimanite and quartz (occurring in the pressure shadows of garnet porphyroclasts) suggests an early retrograde metamorphic stage developed under amphibolite facies conditions ($P = 5.8$ Kbar; $T = 630$ °C). Secondly, the syn-shearing crystal growth of chlorite, white mica, plagioclase and quartz (observed along the C-planes), indicates a late-retrograde metamorphic overprint under greenschist facies conditions ($P = 2-3$ Kbar; $T = 400-500$ °C) (Sacco, 2011). Finally, an asymmetrical folding involving the mylonitic foliation suggests a shallower deformation event probably ascribable to the staking stages of the Alpine-Appennine tectonic activity in the central Mediterranean area. Within this geological framework, a maximum timescale of ~ 5 Ma and a cooling rate of ~ 25 °C/Ma have been obtained by modelling garnet compositional relaxation of the chemical profiles along the outermost rims, amenable to the exhumation history of this portion of the southern European Variscan belt.

4.3.1 Introduction

This case study aims to reconstruct and interpret the tectono-metamorphic evolution of a portion of the Calabria crystalline basement known in the literature as Castagna Unit (Dubois & Glangeaud, 1965; Dubois, 1976). It is mainly composed of para- and orthogneiss rocks with minor micaschists, marble and amphibolite gneiss showing a pervasive mylonitic fabric. Currently, it represents one of the still little-known portions of basement within the Calabrian continental crust. Few data available in the geological literature suggest several assumptions for the metamorphic history of these rocks: (i) a poly-metamorphic history with *HP-LT* eo-Alpine/Alpine effects, responsible of the pervasive mylonitic-cataclastic fabric developed under greenschist facies conditions (Paglionico & Piccarreta, 1976); (ii) a polyphase pre-Alpine metamorphism occurred under greenschist to amphibolite facies conditions, overprinted by a widespread Alpine cataclastic-mylonitic fabric (Amodio Morelli et al., 1976); (iii) an Hercynian metamorphism with a locally *HP* Alpine overprint responsible of the production of thick mylonitic bands (Dietrich, 1988).

In this scenario, a multiscale and multidisciplinary approach was adopted here with the aim to depict the tectono-metamorphic history of the Castagna Unit, by allocating a timing of the mylonitic event.

In particular, a geological-structural mapping was realized to make an updated structural scheme of the investigated area. This step has been accompanied by a targeted sampling to identify significant parageneses used to reconstruct the tectono-metamorphic history of the Castagna Unit rocks.

Furthermore, detailed petrographic investigations and minero-chemical analyses were conducted to unravel the blasto-deformation relationships by evaluating the mineral compositional changes. These investigations were integrated with an innovative X-ray images analysis applied in conjunction of a thermodynamic modelling to constrain the PT conditions of the metamorphic evolutionary stages. Finally, a diffusion modelling of garnet compositional relaxation was applied to determine the timescale of the shearing event.

4.3.2 Geological Background

The Castagna Unit represents one of the continental crust-derived units widely cropping out in the northern CPO (Fig. 4.3).

In this case study, the focus is on the Sila Piccola Massif (SPM), that is the southernmost portion of the Sila Massif where the metamorphic rocks of the Castagna Unit are widely exposed. The SPM is located in the central-southern part of the northern Calabria and bounded by the Crati Valley to the northwest and by the Catanzaro trough to the south (Fig. 4.3). It is a stacked-nappe edifice mostly consisting of an Hercynian crystalline basement emplaced on the Tethyan ophiolitic units and Meso-Cenozoic sedimentary sequences of the Adria plate (Cirrincione et al., 2015). From the bottom to the top, this nappe structure can be subdivided in three main tectonic complexes, namely: the Apennine Complex (Perrone, 1996), the Liguride Complex (De Roeber, 1972; Lanzafame, et al., 1979; Spadea, 1980) and the Calabride Complex (Graeßner, et al., 2000; Cirrincione et al., 2015), each of them subdivided into several tectonic units (Ogniben, 1973).

The Apennine Complex (the “Panormide Complex” of Ogniben, 1973), cropping out in the southwestern sector of the SPM as a tectonic window of the “Bagni di Caronte” (Amodio Morelli et al., 1976), is located in the lower structural position. It is mainly composed by a Paleozoic phyllitic basement with early-Mesozoic carbonate sequences (Amodio Morelli et al., 1976; Lorenzoni & Zanettin Lorenzoni, 1983) and its origin, related to an African or European paleomargin, is still ambiguous (Alvarez, 1976; Dewey et al., 1989; Cello et al., 1990).

The Liguride Complex was initially divided in Upper and Lower Ophiolite Units (De Roeber, 1972; Lanzafame, et al., 1979; Spadea, 1980; Beccaluva et al., 1982; Guerrera et al., 1993; Cello et al., 1996; Rossetti et al., 2001). Afterwards, these Units have been grouped together due to their similar tectono-metamorphic evolution, as suggested by Liberi (2006). They consist of remnants of the neo-Tethyan oceanic crust (Piluso et al., 2000) showing evidence of an *HP-LT* metamorphic overprint (Cello et al., 1991).

Finally, in the uppermost structural position the Calabride Complex occur, which represents an entire Hercynian continental crust section (Graeßner et al., 2000;

Graeßner & Schenk, 2001) composed by a Paleozoic crystalline basement intruded by late-Hercynian granitoid rocks with a Mesozoic sedimentary cover (Messina et al., 1994; Piluso & Morten, 1999).

The significance and the paleogeographic position of the CPO remain a subject of contrasting hypothesis, variously interpreted as: a) fragment of the neo-Tethyan European continental margin (Ogniben, 1973; Dietrich, 1988; Dewey et al., 1989; Thomson, 1998); b) a portion of the African plate (Haccard et al., 1972; Alvarez, 1976; Amodio Morelli et al., 1976; Scandone, 1979); c) the basement and relative cover of a micro-continent formerly located between the two margins (Guerrera et al., 1993; Cello et al., 1996; Perrone, 1996; Critelli & Le Pera, 1998; Piluso & Morten, 2004); d) a result from the accretion of several crustal micro-plates (Vai, 1992). In a recent review paper, Cirrincione et al. (2015) regard the CPO a composite terrane as a result from the fusion of crustal blocks of different continental provenance. In this context, the northern Calabria sector constitutes a portion of the Adria paleomargin, whereas southern Calabria and NE-Sicily represent the relict of an accretionary wedge derived from the deformation of the European continental margin.

In this uncertain geological scenario, the Castagna Unit represents a pervasively mylonitized horizon located within the northern Calabride continental crust, sandwiched between the Bagni Unit (Amodio Morelli et al., 1976) and the Sila Unit (Dubois, 1976) (Fig. 4.16b).

The Bagni Unit consists of greenschist facies metapelite and metasandstone located at the base of the Calabride edifice but, actually, its geological significance is still discussed. Indeed, it is interpreted as the shallowest Paleozoic phyllitic unit in the Calabride Complex, showing an Alpine overprint (Amodio Morelli et al., 1976) responsible for *HP* lawsonite and Mg-riebeckite mineralogical association, or as remnants of the Tethyan oceanic coverage (Piluso, 1997; Piluso et al., 2000; Cirrincione et al., 2008).

The Sila Unit is structurally located at the top of the Calabride Complex and includes greenschist to amphibolites facies metamorphic rocks, Hercynian granitoids (Graeßner & Schenk, 2001) and relative sedimentary cover. In the Sila

Piccola area, it is represented by the high-grade Monte Gariglione “Alpine Crustal Slice” of [Amodio Morelli et al. \(1976\)](#) and [Colonna & Piccarreta \(1977\)](#).

In the intermediate structural position, the Castagna Unit consists of medium-high grade metamorphic rocks including paragneiss, augen gneiss, leucocratic orthogneiss and minor micaschist, marble and amphibolite gneiss, intruded by late-Hercynian granitoid rocks probably related to the Sila batholith emplacement ([Amodio Morelli et al., 1976](#)). In this view, mesostructural, petrographic and minerochemical investigations of this peculiar tectono-metamorphic unit are addressed in detail in the following sections.

4.3.3 Mesostructural features

Previous detailed structural investigations conducted along a NW-SE trending area in the SPM ([Fig. 4.16](#)) revealed a mylonitized horizon consisting, from the bottom to the top of the sequence, of minor micaschist, mostly orthogneiss and medium-fine grained amphibolite to greenschist facies metapelite layers, locally intercalated in the orthogneiss ([Fig. 4.16](#)).

The mesoscopic analysis highlighted several facies of orthogneiss that are widespread in the study area. Such rocks vary from weakly deformed biotite-rich augen gneiss, to two mica-bearing mylonitic augen gneiss and strongly mylonitic muscovite-rich leucogneiss (the “White Schist” described by [Cortese \(1895\)](#)). The metapelite outcrops consist of decimeter to meter thick bands of greyish medium-fine grained mylonitic paragneiss ([Sacco, 2011](#)), with a main mineralogical assemblage consisting of biotite, feldspar, quartz, chlorite, garnet, white mica and epidote.

The structural analysis highlighted a pervasive mylonitic fabric (S_m) defining the field foliation ([Fig. 4.17a-b](#)) and a well-developed stretching lineation (L_m), produced by a ductile deformation event which affects both metapelite and orthogneiss ([Sacco, 2011](#)). The S_m , averagely oriented NW-SE to SW-NE, obliterated previous metamorphic surfaces locally preserved as relics in the low strain domains of the metapelite horizons.

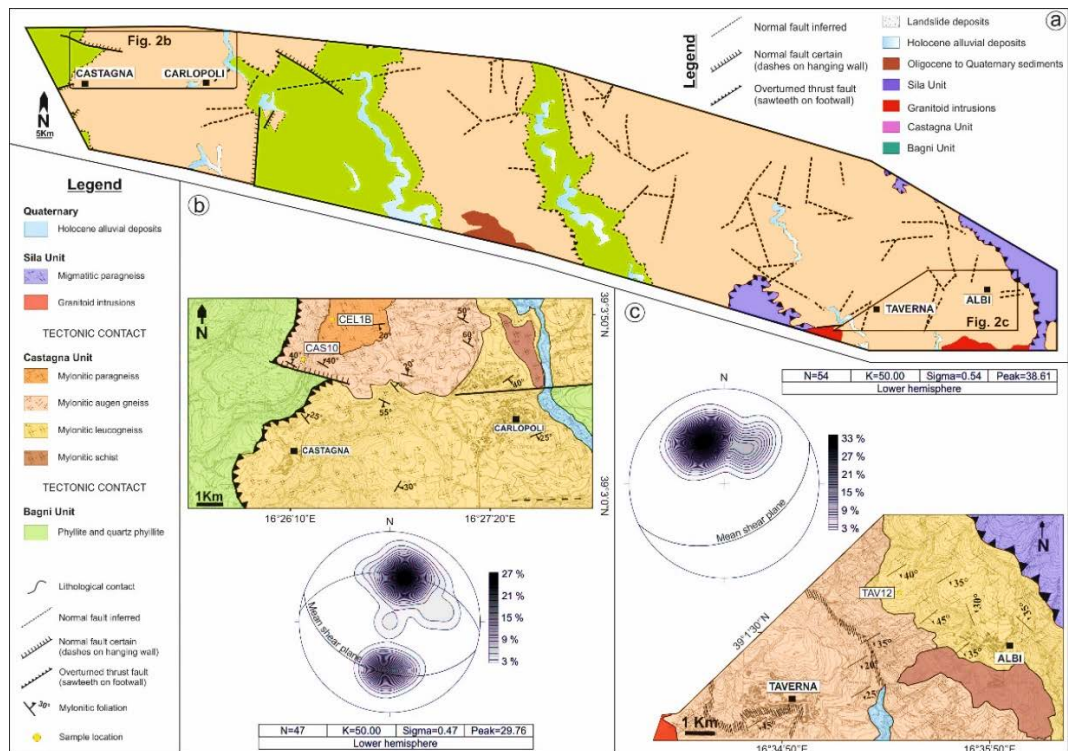


Fig. 4.16 – Geo-structural map of the crystalline basement of the Sila Piccola: (a) geological sketch map of the study area; (b) geo-structural map of the Sila Piccola near the Castagna and Carlopoli towns with samples location. Stereonet indicates the NNE-SSW trend of the field foliation; (c) geo-structural map of the Sila Piccola near the Taverna and Albi towns with samples location. Stereonet indicates the ESE-WNW trend of the field foliation (modified after Sacco, 2011).

The Lm, averagely oriented ESE-WNW to ENE-WSW, is marked by elongated quartz and feldspar crystals alignments (Sacco, 2011). In addition, at the outcrop and hand-sample scale several kinematic indicators, mostly represented by σ -type porphyroclasts, indicate a dextral top to the ESE sense of shear at the present-day geographic coordinates (Fig. 4.17c).

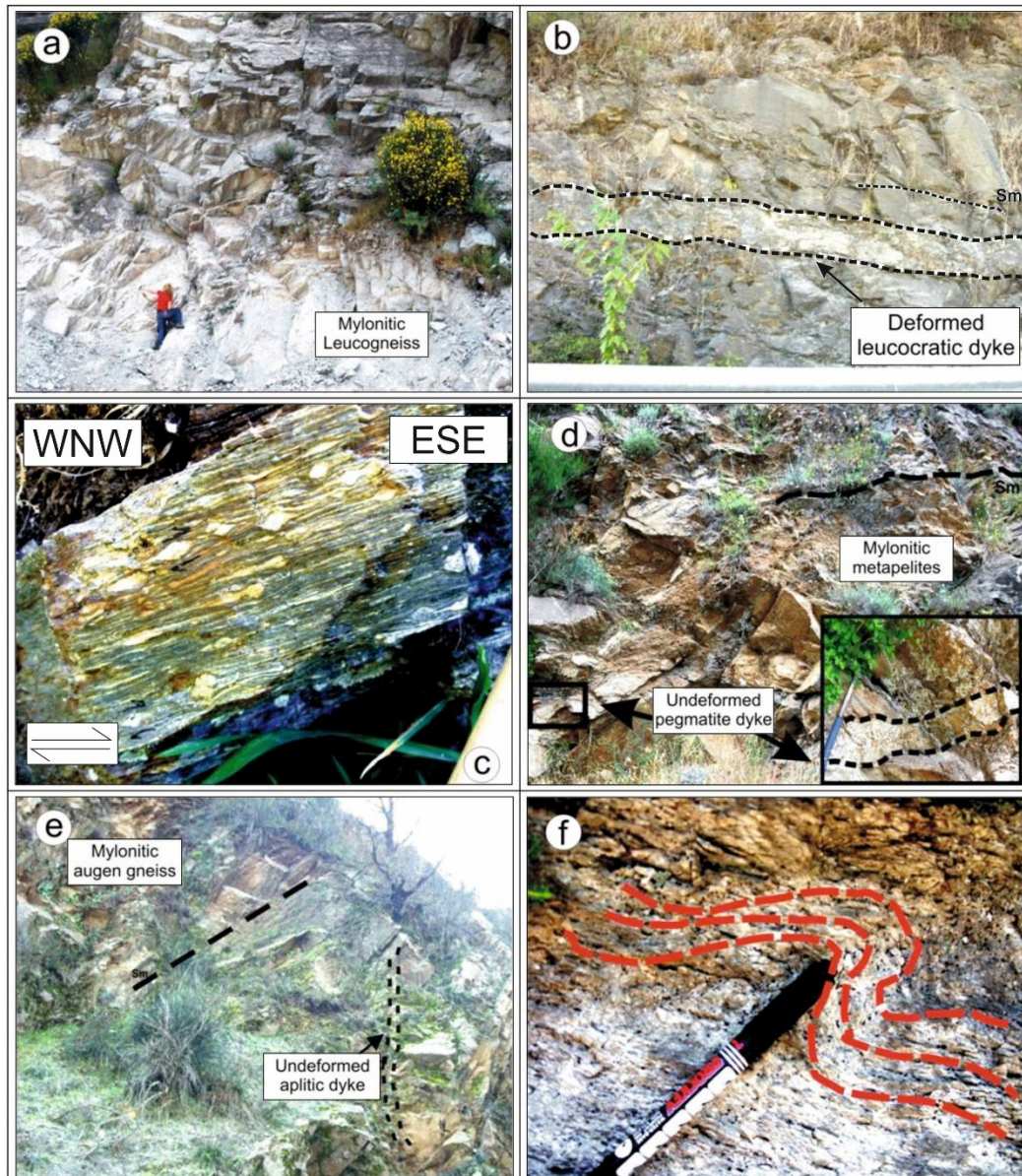


Fig. 4.17 - Mesostructural features in orthogneiss and metapelites of the Castagna Unit rocks: (a) mylonitic leucogneiss; (b) mylonitic paragneiss with a leucocratic dyke intrusion affected by the same shearing deformation; (c) kinematic indicators in an orthogneiss sample outlining a dextral top-to-the-ESE sense of shear; (d-e) pegmatitic-aplitic undeformed dikes cross-cutting mylonitic foliation (S_m) in both mylonitic metapelites and augen gneiss; (f) hand-specimen asymmetric folding of the mylonitic surface in orthogneiss (modified after Sacco, 2011).

Swarms of deformed leucocratic dykes (Fig. 4.17b) and sheared felsic calc-alkaline fine-grained porphyritic ones extensively occurs in the mylonitic leucogneiss.

Undeformed leucocratic pegmatitic-aplitic dykes crosscut the S_m in both metapelite and orthogneiss rocks, representing an important structural time-constraint on the age of the shearing event (Fig. 4.17d-e). Moreover, a W-SW verging asymmetrical folding involves, locally, the S_m in both metapelite and orthogneiss (Fig. 4.17f). This structure suggests a further deformation event

developing in a transitional ductile to brittle regime typical of a more superficial setting. All of these structural features are further characterized by a fractal repetition, as recognized by microscale investigations.

4.3.4 Petrography and mineral chemistry

4.3.4.1 *Methods*

Previous microprobe analyses (Sacco, 2011) were integrated with new ones (i.e., APPENDIX D1), performed by a Cameca SX-FIVE electron microprobe (EMP) equipped with four WDS spectrometers at the Camparis laboratory in Paris, under the following operating conditions: ~ 1 µm beam diameter, 15 kV accelerating voltage, and 10 nA beam current. Natural minerals and synthetic oxides were used as standards. Used mineral abbreviations are from Siivola & Schmid (2007), whereas mineral formulae were calculated using MINPET 2.02 software (Richard, 1995) on the basis of 12 oxygens and 8 cations for garnet, 8 oxygens for feldspars, 12 oxygens for white mica and 22 oxygens for biotite. Representative WDS analyses of garnet, biotite, white mica, plagioclase and K-feldspar, from metapelite and orthogneiss specimens are given in APPENDIX D1. The PAP correction method was applied to convert WDS intensities into wt % oxides. X-ray element maps were collected using a Tescan Vega LMU scanning electron microscope (SEM) equipped with an EDAX Neptune XM4-60 micro-analyser characterised by an ultra-thin Be window, at the Department of Biological, Geological and Environmental Sciences, University of Catania (Italy). Operating conditions were an accelerating potential of 15 kV and a beam current of 0.2 nA. Quantitative atomic concentrations and modal amounts of each mineral phase were obtained by processing the X-ray maps with the software program Q-XRMA (Ortolano et al., under review) developed at the Geoinformatics and Image Analysis Lab of the Biological, Geological and Environmental Sciences of Catania University.

4.3.4.2 *Petrographic description*

Petrographic, microstructural and mineral chemical analyses have been performed to reconstruct the tectono-metamorphic evolution of this portion of

the crystalline basement of the CPO, highlighting the sequence of the blasto-deformational relationships and textural features recorded in the Castagna Unit mylonitic rocks. Overall, 76 thin sections have been observed to choose representative samples of the main metamorphic events which affect this tectonic unit. In this view, 15 samples (para- and orthogneiss) have been selected for detailed microstructural and petrological studies.

Microscale analysis confirmed the pervasive mylonitic fabric already detected during previous mesostructural investigations (Sacco, 2011). The main mylonitic features recognized in thin section are depicted by S/C texture, core-mantle and strain shadow structures in feldspar porphyroclasts, oblique foliation in quartz microdomains, boudinaged feldspars and mica-fish textures as well (Fig. 4.18). As a consequence of the ductile deformation shearing event, pre-mylonitic structures has been obliterated totally. However, the low strain domains preserved in the metapelite samples. Textural analysis of kinematic indicators confirmed the top-to-the ESE sense of shear (Fig. 4.18a-d) observed at the outcrop scale, although microstructural elements locally define a contrasting top-to-the WNW sense of shear (Fig. 4.18e-g). This evidence has been recognized also by Sacco (2011) through the quartz *c*-axis pattern analyses of quartz-rich domains in strongly mylonitized orthogneiss samples. These quartz *c*-axis orientation patterns, developed during the mylonitic event and triggered by the effects of a combined sub-grain rotation and grain boundary migration recrystallization regime (Passchier & Trouw, 1996), permitted to constrain both kinematics and the temperature operating during the shearing deformation (Lister & Dornsiepen, 1982; Mainprice et al., 1986; Heillbronner & Tullis, 2006).

In particular, petrographic investigations highlighted a metamorphic evolution of the shearing episode characterized by an early-to-late syn-mylonitic retrograde

metamorphic overprint, developed from upper amphibolite to lower greenschist facies conditions, in both metapelite and orthogneiss horizons.

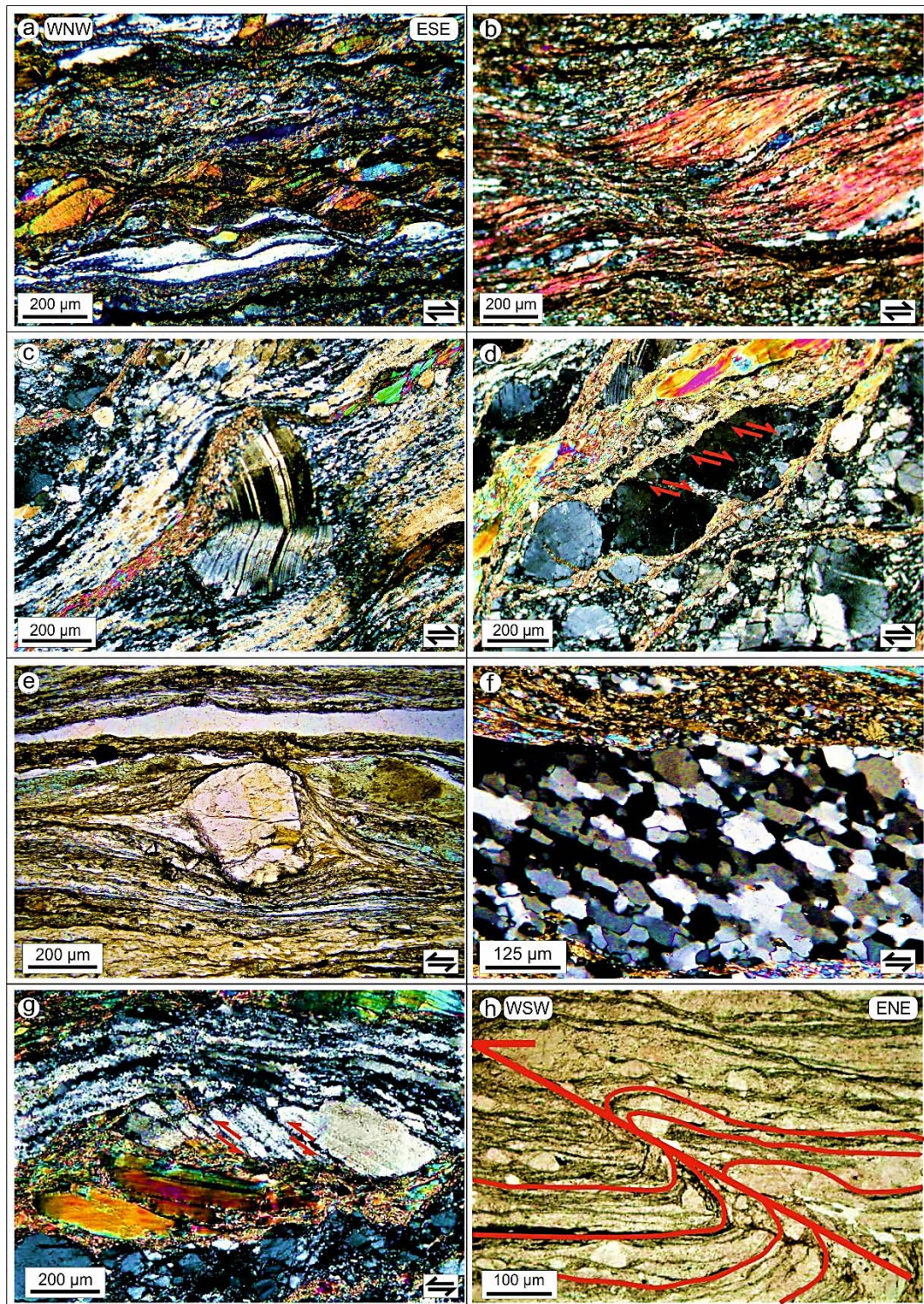


Fig. 4.18 - Observed microstructures representing two opposite sense of shear in both mylonitic para- and orthogneiss rocks: (a-d) – a) S-C-C' fabric in an augen gneiss, b) mica fish in a metapelite, c) asymmetric strain shadow and d) microboudin of plagioclase in a leucogneiss, indicating a dextral top-to-the ESE sense of shear; (e-g) – e) transitional to δ -type kinematic indicator, N//, f) oblique foliation in paragneiss and g) plagioclase domino-type structure in a leucogneiss, indicating an opposite sinistery top-to-WNW sense of shear; h) asymmetric folding of the mylonitic foliation (S_m), N// (modified after Sacco, 2011).

Moreover, microscopic observation highlighted also the existence of a further deformational event which folds the mylonitic surface, by producing an asymmetric millimetre-scale bending (Fig. 4.18h) with no associated blastesis. Based on these clues, a metapelite sample (i.e., CEL1B) consisting of one of the best preserved low strain domains within the pervasive mylonitic metapelite horizons has been considered suitable to describe the early stage of this evolution. Furthermore, garnets from this sample were used to model the potential compositional changes occurred due to diffusion for constraining the timescale of the retrograde metamorphic event.

4.3.4.3 Garnet-biotite-sillimanite paragneiss – CEL1B sample

Sample CEL1B is a coarse-medium grained paragneiss (Fig. 4.19a-b) showing a weakly developed mylonitic foliation. Mineral constituents are given by garnet, sillimanite, quartz, biotite, plagioclase, white mica, chlorite and epidote along with monazite and zircon as accessory phases. In particular, relicts of a pre-mylonitic metamorphic event can be recognized as an early mineralogical association consisting of oligoclase-andesine plagioclase (An_{27} to An_{32}), biotite ($X_{Fe} = 0.44-0.53$; $Ti/11ox = 0.10-0.13$), and quartz inclusions within the garnet porphyroclasts (Grt I) (Fig. 4.19c). The large idioblastic to sub-idioblastic garnet grains (sub-centimeter to centimeter) are mainly an almandine-pyropite solid solution with low contents of grossular and spessartine ($Alm_{73}Pyr_{20}Sps_3Grs_4$), showing homogeneous interiors and a flat compositional profile (Fig. 4.19d).

The subsequent metamorphic event recorded in these rocks suggests an early retrograde evolutionary stage (according to Grant & Weiblen, 1971; De Béthune et al., 1975) testified in the pressure shadows of garnet porphyroclasts by the syn-kinematic growth of a second generation of: plagioclase (An_{34-37}) (Fig. 4.19e), biotite ($X_{Fe} = 0.44-0.45$; $Ti/11ox = 0.07-0.12$) (Fig. 4.19f), sillimanite and quartz (Fig. 4.19a). This retrograde metamorphic event is marked by a tiny garnet overgrowth (Grt II) characterised by an increase in almandine and spessartine content ($Alm_{81}Pyr_{10}Sps_5Grs_5$) towards the rim of the homogeneous garnet crystals, whereas an opposite trend is recognized for the pyropite one (Fig. 4.19d).

These compositional trends are qualitatively visible in the X-ray elemental maps of the investigated thin section domain (Fig. 4.20).

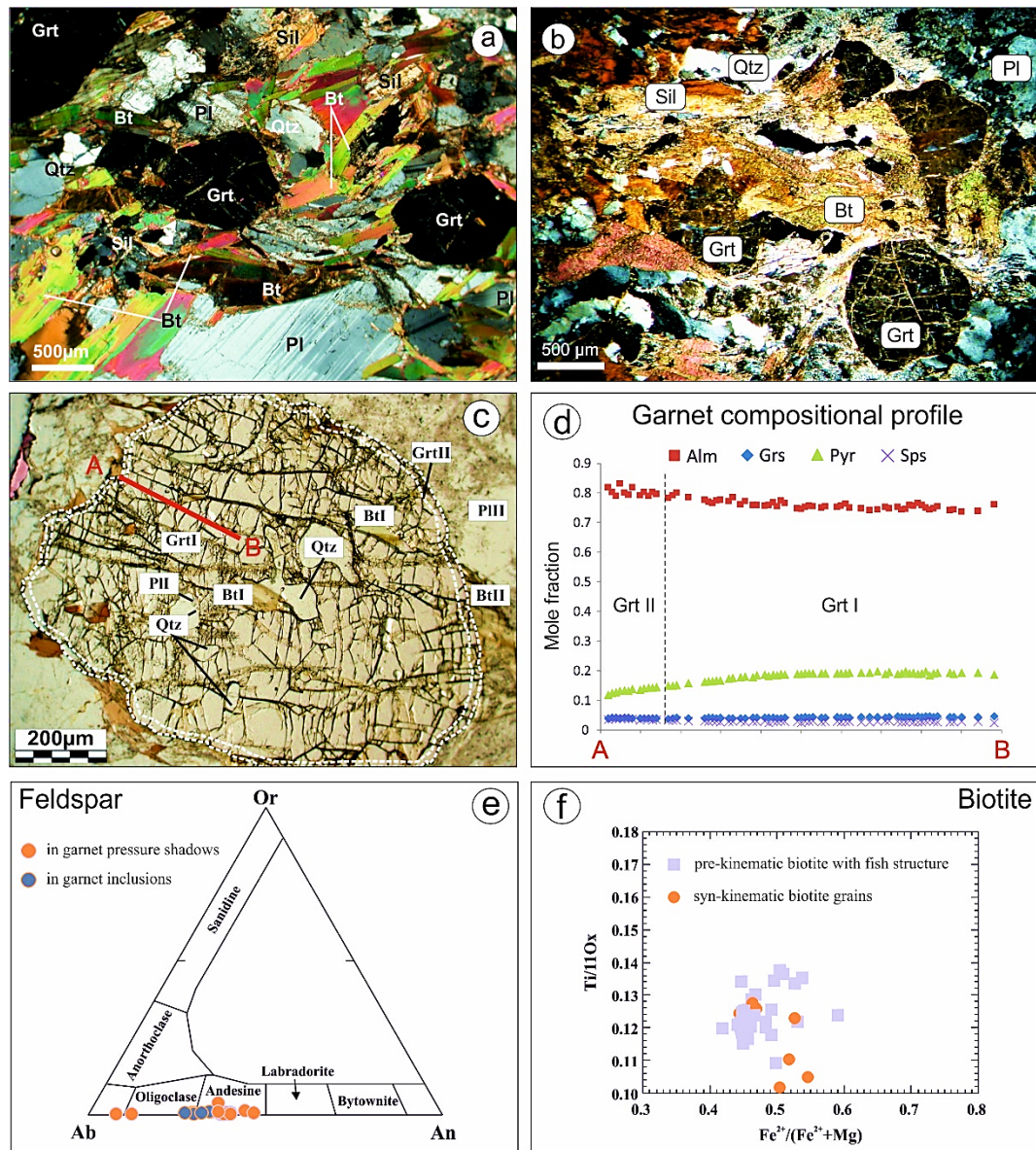


Fig. 4.19 - CEL1B sample: a, b) relict structures and parageneses observed in low strain domains; c) garnet porphyroblast with inclusions of pl, bt, and qtz, showing an Alm-rich rim in contact with pl_{II} and bt_{II}; d) garnet compositional profile.

Moreover, along mylonitic C-planes it was possible to observe an additional metamorphic overprint witnessed by the syn-shearing crystal growth of chlorite, white mica and quartz assemblage developed under greenschist facies conditions. Locally, lenticular epidote, chlorite and white mica aggregates are found arranged parallel to the mylonitic foliation, suggesting a likely total pseudomorphosis of the original garnet porphyroclasts.

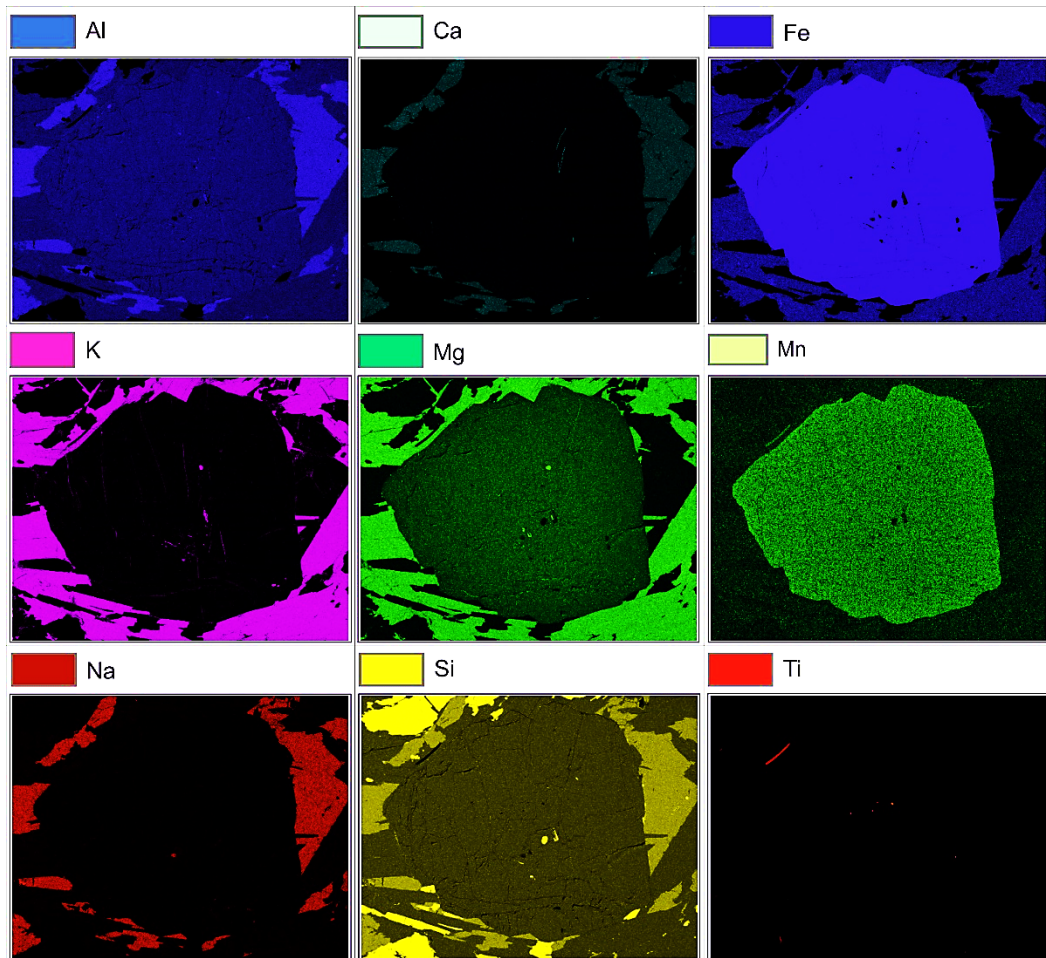


Fig. 4.20 - X-ray maps of the selected garnet domain from the CEL1B metapelite sample, showing a homogeneous interior (Grt I) rimmed by a thin garnet overgrowth (Grt II).

4.3.5 Image-assisted thermodynamic modelling

In order to unravel the *PT* conditions of the metamorphic events affecting the Castagna Unit rocks, a thermodynamic modeling approach was adopted. Notwithstanding the presence of pre-mylonitic relicts, it was not possible to obtain reliable information about the prograde history of the *PT* trajectory because of the strong equilibration established during the evolution of the ductile shear zone. For this reason, *PT* pseudosections allowed to constrain only the syn-mylonitic stage of the early retrograde metamorphic evolution affecting the investigated sector of the crystalline basement, by using the CEL1B specimen as the representative metapelite sample. *PT* pseudosections have been calculated for the CEL1B using the Perplex software packages (updated to November 2016, www.perplex.ethz.ch), taking care to bracket properly the effective reactant volumes describing the metamorphic equilibria. In this view, an image processing

of the X-ray elemental maps of the selected domain was used to quantify the effective bulk composition to be used in the pseudosection computation. Moreover, the fluid phase content (i.e., H₂O) was computed as well, with the aim to obtain an appropriate *PT* pseudosection able to give reliable compositional isopleth intersections of the retrograde paragenetic assemblage.

4.3.5.1 Quantitative image processing and thermobaric constraints

Thermodynamic modelling has been applied on the CEL1B to infer reliable *PT* conditions about the former stage of the retrograde metamorphic evolution recorded in these rocks. Pseudosection modelling approach is widely recognised as one of the suitable methods for obtaining thermobarometric information since it provides a framework to interpret both textural features and mineral compositions in terms of *PT* evolution (Powell & Holland, 1999), allowing geologically sensible results to be obtained. This approach requires the use of the bulk composition effectively in equilibrium during each stage of the porphyroblasts growth (e.g., Evans, 2004; Zuluaga et al., 2005; Zeh, 2006; Fiannacca et al., 2012; Ortolano et al., 2014a). However, the pervasive homogenizing effect observed in the studied garnet porphyroclasts triggered by diffusion mechanisms suggests that the system under examination is not in the overall equilibrium. This means that the XRF bulk-rock chemistry of this sample cannot be used in the pseudosection computation. For this reason, the effective bulk rock composition was calculated taking into account the textural equilibria between the syn-shear garnet porphyroclast rims and the mineralogical association in the matrix, consisting of low-Ti biotite, andesine-rich plagioclase, sillimanite and quartz. This step was granted by isolating the mineral modal percentages representative of the effective reactant volume (i.e., the syn-shear assemblage) through the Q-XRMA software and using a modified version of the spreadsheet of Ortolano et al. (2014a). The latter is used to compute the oxides amounts (expressed in weight percent) per each reactant mineral phase as a function of the relative modal percentages. In such a way, the bulk composition of the syn-shear volume was determined allowing the pseudosection to be constructed (Fig. 4.21). The latter has been computed by using: (i) a closed-system

behaviour, represented by the MnO, Na₂O, CaO, K₂O, FeO, MgO, Al₂O₃, SiO₂, H₂O (MnNCKFMASH) chemical system, assuming SiO₂ as a saturated thermodynamic component and H₂O as a saturated fluid phase component; (ii) the internally consistent thermodynamic database of [Holland & Powell \(1998\)](#) - updated by the same authors in [Holland & Powell \(2011\)](#); and (iii) the Compensated Redlich–Kwong fluid equation of state ([Holland & Powell 1998](#)).

Following the suggestions of [Evans \(2004\)](#) and [Cirriuncione et al. \(2008\)](#), pressure and temperature of the mylonitic event were constrained by using the intersection of at least three isopleths from different mineral compositions in equilibrium. As no significant intersections of the syn-shear assemblage have been obtained in the pseudosection, the amount of the fluid phase stored within the hydrous phases (i.e., biotite and white mica) involved in the metamorphic reactions, was constrained according to [Clemens & Vielzeuf \(1987\)](#). This condition was crucial for having a major control in defining the PT conditions experienced by the rocks, assuming the fluid phase was not in excess at high temperatures (T > 600 °C). As a consequence, an appropriate chemical system was derived to construct a new PT pseudosection representative of the reactant volume ([Fig. 4.22](#)).

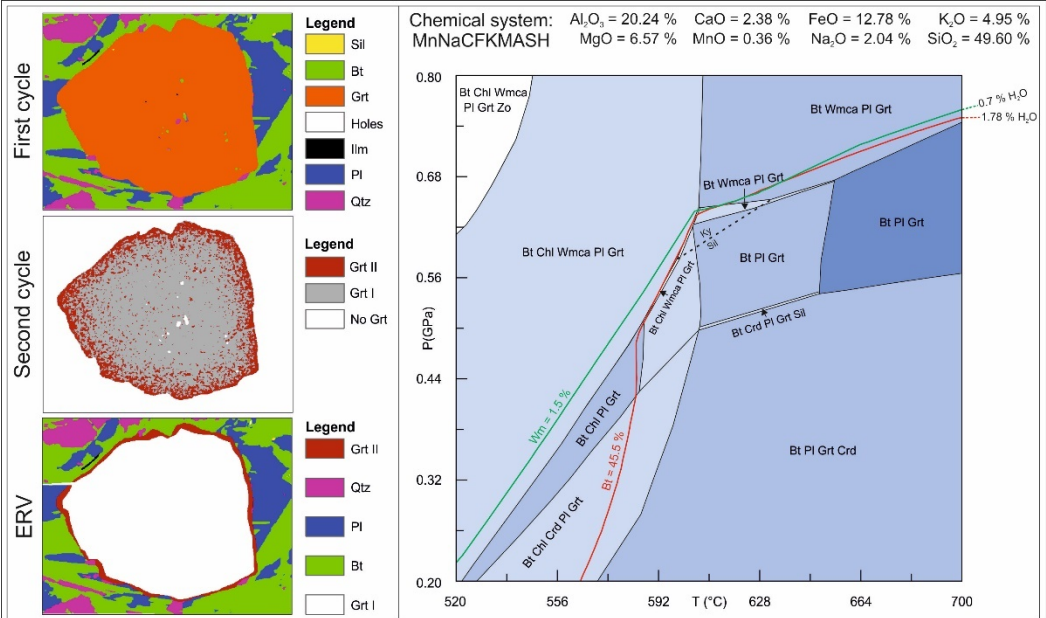


Fig. 4.21 - Definition of the effective reactant volume (ERV) by image analysis (left of the figure). On the right of the figure is shown the PT pseudosection computed by the approach of [Ortolano et al. \(2014a\)](#). Green and red isopleths show, respectively, the fluid content in white mica and biotite from which were constrained the fluid phase amounts.

In this case, a MnNCKFMASH closed-system (i.e., $\text{SiO}_2 = 49.17$, $\text{Al}_2\text{O}_3 = 20.10$, $\text{FeO} = 12.69$, $\text{MgO} = 6.55$, $\text{MnO} = 0.36$, $\text{CaO} = 2.21$, $\text{K}_2\text{O} = 4.92$, $\text{Na}_2\text{O} = 2.03$ and fixed $\text{H}_2\text{O} = 1.85$ wt % oxides), has been used as the bulk rock composition to describe the equilibrium among syn-mylonitic assemblage (i.e., garnet, plagioclase and biotite).

The meaningful compositional isopleth intersections obtained for the considered mineralogical phases improved the reliability of the chosen composition (Fig. 4.22). The intersections between garnet rim compositional isopleths (i.e., $\text{Grt II} = \text{Alm}_{69-71}\text{Pyr}_{17-18}\text{Sps}_{5-6}\text{Grs}_{5-6}$) and those of the plagioclase (i.e., $\text{Pl II} = \text{An}_{36-37}$) and biotite (i.e., $\text{Bt II} = (\text{Fe}/\text{Fe} + \text{Mg})_{44-47}$) in equilibrium (Fig. 4.22), allowed to obtain *PT* conditions of the earliest identified retrograde stage at $\sim 5.6 \pm 0.5$ Kbar and 630 ± 15 °C (Fig. 4.22). Such thermobaric estimates were used together with the garnet rim compositions as the input parameters in the diffusion modelling technique, to derive the timescale of the syn-shear metamorphic event.

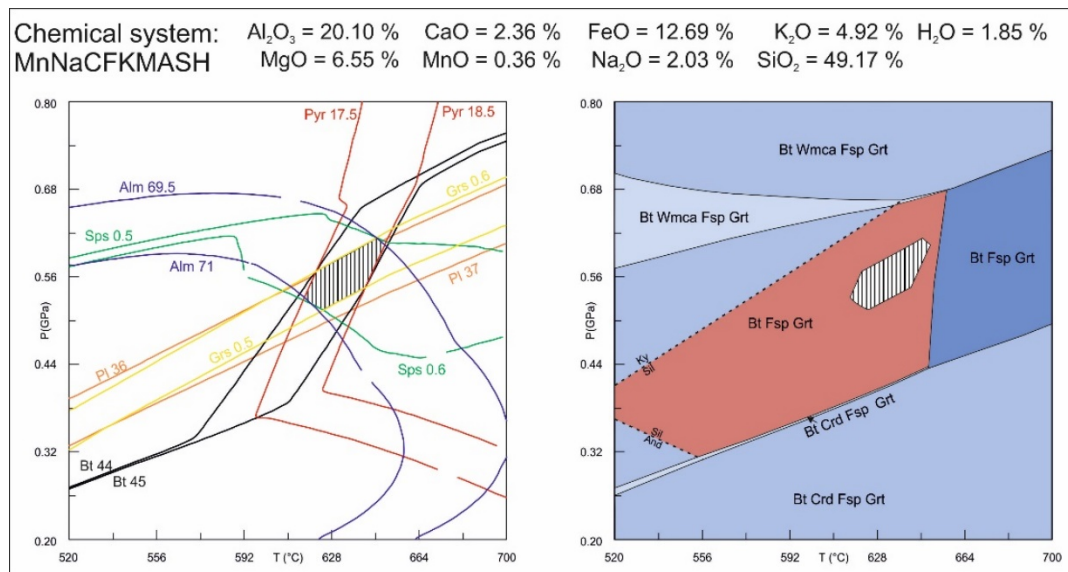


Fig. 4.22 – *PT* pseudosection of the syn-mylonitic assemblage for the CEL1B sample.

4.3.6 Diffusion modelling

Thermobaric constraints of the early retrograde stage were here used to compute diffusion coefficients for the investigated garnets. Since the main compositional variations observed between Grt I and Grt II (see Fig. 4.19) involves mainly iron and magnesium contents, garnet multicomponent diffusion and the diffusive

exchange with the surrounding matrix (i.e., biotite) were simplified in terms of an efficient interdiffusion (Chakraborty & Ganguly, 1992). In this perspective, an effective binary diffusion coefficient (i.e., $D(EB)_{FeMg}$) was computed according to Eq. 6, to model compositional changes in the garnet chemical profiles, by using the core compositions as the initial pre-diffusion condition and a semi-infinite VEC model as the boundary one. The semi-infinite condition is further justified since the modal abundance of biotite is not much larger compared to garnet, therefore the diffusive fluxes change the composition of both biotite and garnet. This condition explains why an infinite reservoir of biotite (Dodson, 1973) cannot be applied in defining the diffusion model.

As in the first case study (see section 4.2), also in this case a characteristic temperature of diffusion was used to correct the diffusion coefficients computation according to Eq. 21. The forward finite-difference numerical method described in section 3.4.2.3 was applied to solve the diffusion equation (i.e., Eq. 20), by using garnet diffusion coefficients data from Ganguly et al. (1998), taking into account their dependence from the composition and treating calcium as the dependent component. Both garnet and biotite were assumed to be homogeneous at the pre-diffusion condition, and linear cooling rates of 100, 30, 20 and 10 °C/Ma for a starting temperature of 630 °C (i.e., a characteristic temperature of 598.7 °C) and an end temperature of 500° C, were modelled.

Results of the diffusion model carried out with MATLAB scripting (Fig. 4.23) highlighted a retrograde evolution developed over a timescale of ~ 3-5 Ma, as shown from almandine and pyrope profiles if an initial flat chemical composition is assumed. Such a temporal interval defines a cooling rate of ~ 25 °C/Ma if the lower temperature of the late retrograde evolution (i.e., ~ 500 °C) is considered (Sacco, 2011). Model for grossular components gives back a longer timescale for the relaxation of compositional profiles (i.e., 10 Ma), probably due to the slow calcium cationic motion affected, in turn, by the interdiffusion treatment of the iron-magnesium chemical exchanges.

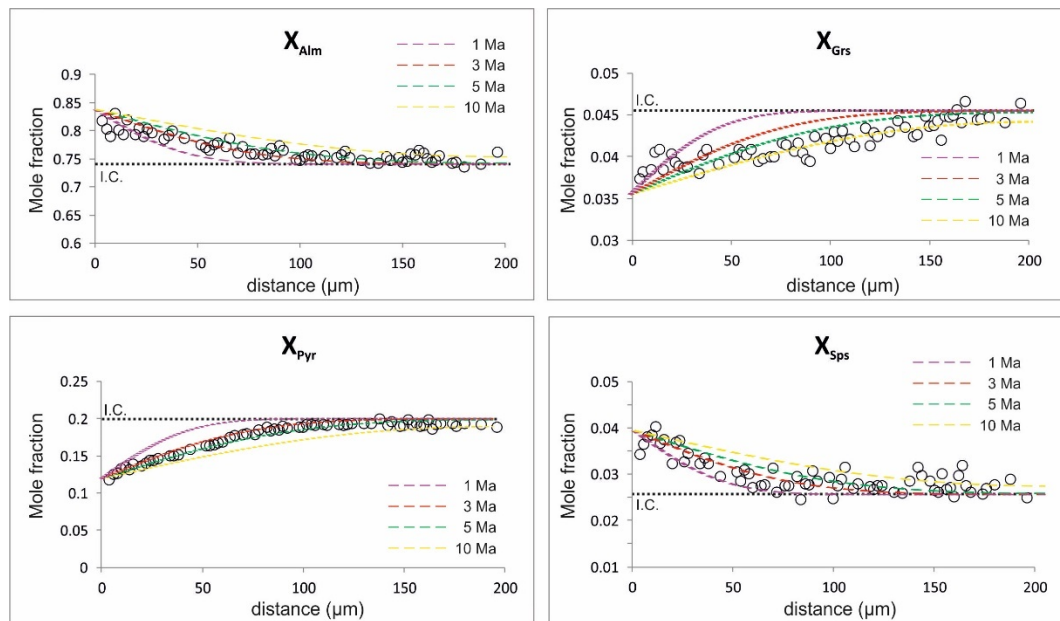


Fig. 4.23 - Diffusion model of the garnet retrograde zoning. X_{Grs} shows a longer timescale probable as a consequence of the slower calcium cationic movement.

4.3.7 Final remarks

A detailed structural study combined with petrographic, thermodynamic and diffusion investigations were focused on a portion of the crystalline basement of the Calabria-Peloritani Orogen, known in the literature as the Castagna Unit. This unit (Dubois & Glangeaud, 1965), cropping out in the overall northern Calabria, represents a pervasive mylonitized horizon located within the Calabride continental crust and consisting of amphibolite to greenschist facies rocks intruded by late-Hercynian granitoids.

Results from this study allowed to reconstruct the tectono-metamorphic evolution mainly related to the shearing deformational event affecting these rocks, providing new geological and geodynamic constraints.

In particular, previous field investigations highlighted a pervasive syn-mylonitic surface (Sm) (Fig. 4.17a) that obliterated older metamorphic ones, locally preserved as relics in the low strain domains of the metapelite horizons. Deformed leucocratic dykes (Fig. 4.17b) and felsic calc-alkaline porphyritic ones, probably related to the late-to-post collisional magmatic activity occurred during the extensional stage of the Hercynian Orogeny, are broadly widespread. Furthermore, not-deformed leucocratic pegmatitic-aplitic dykes probably linked

to the Sila batholith emplacement about 300-310 My (Graeßner et al., 2000) during the late-Hercynian magmatic activity, cross cut the mylonitic foliation in both metapelite and orthogneiss (Fig. 4.17d, e). This feature constitutes an important structural time-constraint on the age of the shearing event placing it to the last stages of the Hercynian tectonic activity.

Petrographic investigations carried out on Castagna Unit samples allowed to reconstruct a poly-metamorphic history supporting the hypothesis of a Variscan shear event (D2, Tab. 4.7) triggering the development of a pervasive mylonitic foliation (Sm) which erased the pre-mylonitic surface tracks. However, relicts of a pre-mylonitic cycle (D1, Tab. 4.7) testified by an assemblage made up of almandine-pyrope garnet, oligoclase-andesine plagioclase, biotite and quartz, were identified as low strain domains in metapelite horizons. However, the older pre-mylonitic paragenesis and the lack of crystal zoning in garnets were not useful in constraining step-by-step the prograde history and peak metamorphic conditions. Consequently, only the retrograde evolution of the entire metamorphic history has been unravelled.

Nevertheless, this pervasive homogenizing effect in garnet porphyroclasts, related to the intracrystalline diffusion mechanism (Bluckburn, 1969; Woodsworth, 1977; Caddick et al., 2010), was interpreted as a petrological feature enhancing a long residence time at *HT* conditions in the crust for the pre-mylonitic protholith. According to Caddick et al. (2010), this petrological feature suggests a long residence time at *HT* thermal regime (i.e., $T \geq 650$ °C), which must be greater than approximately 5 Ma to attenuate or obliterate the original growth zoning in garnet cores through intradiffusion mechanisms. This evidence supports the hypothesis of a pre-mylonitic protolith of a lower crust subsequently equilibrated under lower temperature.

Based on different assemblages recognised in several rock microdomains, the D2 event has been separated in two metamorphic stages. The first one is marked by a syn-kinematic growth of almandine-spessartine-rich garnet, andesine-rich plagioclase, biotite, sillimanite and quartz, observed in the pressure shadows of garnet porphyroclasts. Such an assemblage characterizes the low strain domains

of metapelites, indicating an early Variscan retrograde stage (M2a, Tab. 4.7) during which hydration reactions occur. Such reactions have been here interpreted as responsible of an equilibration of the protolith from higher to lower metamorphic grade under amphibolite facies conditions. The second one is recognized by a syn-shearing crystal growth of chlorite, phengite, albite and quartz observed along the C-planes in strongly mylonitic orthogneiss horizons. Such an assemblage likely derives from a late-Variscan retrograde metamorphic overprint (M2b, Tab. 4.7) developed under greenschist facies conditions. The thermal ranges of syn-shear crystallization (Stipp, 2002) is also confirmed by the occurrence of various quartz micro textures visible in differing rock domains (Sacco, 2011), which indicate various recrystallization conditions. Also, dislocation creep, as well as diffusion and recrystallization processes were responsible for the transitional ductile-to-brittle behavior of the feldspar porphyroclasts and development of core-mantle or bookshelf structures, suggesting a variation in temperature. Indeed, the former (core-mantle structures) were developed in medium-high temperature regime, whereas the latter (bookshelf structures) indicate a transition to brittle behavior due to a low- T thermal regime. In addition, the widespread presence of boudinaged feldspar porphyroclasts with pinch and swell structures (Fig. 4.18f), suggests that the shearing event operated under an extensional regime. This is also supported by felsic calc-alkaline dykes' intrusion in mylonitic leucogneiss affected by the same shearing deformation. Finally, the asymmetrical folding observed at the meso- and microscale (Fig. 4.17f and Fig. 4.18h) in both para- and orthogneiss involving the mylonitic foliation (S_m), suggests a shallower deformational event (D3, Tab. 4.7), probably ascribable to the stacking and thrusting stages of the Alpine-Appennine tectonic activity in the central Mediterranean area.

The PT pseudosections modelling performed in the low strained metapelite domains allowed reliable PT constraint specifically for the early retrograde stage of the metamorphic evolution. Such a result was achieved taking into account the textural equilibrium and compositional isopleth intersections among the narrow

retrograde rims of the homogenised garnets and the matrix minerals such as biotite and plagioclase, considering the effect of hydration reactions as well.

A reliable *PT* field (*P* mean of ~ 5.7 Kbar at *T* of ~ 630 °C) was constrained by isolating the effective reactant volume via image analysis of the elemental X-ray maps. This thermobaric constraint is consistent with the early stages of the retrograde metamorphic trajectory related to the shearing event at upper amphibolite facies conditions, whereas the subsequent pervasive mylonitic retrograde evolution has been constrained in the leucogneiss horizons at *T* = 500 °C (Sacco, 2011) by using conventional phengite barometer (Massonne & Schreyer, 1987).

Tab. 4.7 - Summary of the blasto-deformational events

Orogenic cycle		Variscan		Alpine	
Deformation event		D1	D2		D3
Metamorphic event		M1	M2 _a	M2 _b	
Crystallization event		Pre-Sm	Syn-Sm		
Crystallization phases	Quartz				No blastesis
	Garnet	<i>Grt_I</i>	<i>Grt_{II}</i>		
	Plagioclase	<i>Pl_I</i>	<i>Pl_{II}</i>	<i>Pl_{III}</i>	
	K-feldspar				
	Biotite	<i>Bt_I</i>	<i>Bt_{II}</i>		
	White mica	<i>Ms</i>		<i>Phg</i>	
	Chlorite				
	Sillimanite Epidote				
Metamorphic facies			Amphibolite	Greenschist	
P-T regime			LP-HT	LP-LT	
Microstructure		Garnet porphyroclasts and micafish textures	Shadow pressure	C-planes	Asymmetric fold

The diffusion model applied allowed to outline a maximum temporal estimates of about 5 Ma for the retrograde evolution, highlighting a slower exhumation with respect the shallower overlapping lithological units.

In this scenario, the “Castagna Unit” can be interpreted as an extensional late-to-post Hercynian shear zone, characterised by a slow cooling rate (i.e., ~ 25 °C/Ma) as a result of the deeper crustal position of the investigated rocks.

5. Conclusions

Innovative numerical petrology methods have been developed using several computer programming languages, to investigate chemical-physical properties of rocks at the microscale. These methods can help users to extract quantitative information from the final aspect of the metamorphic rocks, which often derives from the counterbalancing factors controlled by deformation vs. recovery processes, through a better quantification of the rock fabric parameters (e.g., grain and mineral size distribution) as well as by a better definition of the effective reactant volumes which took part during the different stages within the evolution of a given metamorphic rock.

In this perspective, a grain boundary detection toolbox (i.e., GSD) working on ArcGIS® software platform was created, via the Model Builder visual programming language, to draw grain boundaries and for creating polygon features in a GIS platform, by using thin section optical scans as input images. Such a tool allows users to obtain several pieces of information from the investigated samples such as grain surfaces and sizes displayed as derivative maps. The developed GSD toolbox has revealed to be a valuable asset for investigating the fabric characterising deformed rocks, especially those formed by many tiny grains, without resorting to the use of multiple images acquired at different optical orientations. Indeed, the tool permits to detect boundaries of all the grains having an area $< 0.01 \text{ mm}^2$ as well. This result represents a significant improvement in the quantitative recognition of the rock fabric parameters by the automatic digitization of optical images. Furthermore, the tool can help users to a priori select the appropriate grains where study the elements diffusion behaviour, if other conditions are satisfied (e.g., if mineral can be considered cut from its centre), because different grain sizes means different diffusive equilibration stages. Indeed, smaller grains change their core composition faster than the larger ones when diffusion proceeds, losing any information about the original growth chemical history. Therefore, studying the diffusive element behaviour on several grains with different grain sizes and compositions improves any thermobaric reconstruction as well as the timescale determination of geological events. These grain polygon maps have then been integrated with the mineralogical distribution map of the entire thin section, derived from the classification of μ -XRF elemental maps (Ortolano et al., 2014b). Such a result was obtained by the development of a new

toolbox (i.e., Min-GSD) which enhances the grain size distribution analysis by associating a unique mineral label to each polygon feature. This step has been achieved by using a spatial join operation which put together all the attributes information stored both in the grain polygon map and in the mineralogical distribution one. As a result of this integration, a new local geodatabase (i.e., a LIS) where each detected mineral grain is accompanied by geometrical and compositional data features was structured.

These mineral grain size data have been integrated, successively, with those of the mineral compositions, by improving a previous X-ray maps analyser (i.e., XRMA, [Ortolano et al., 2014b](#)) through the implementation of new lines of code (i.e., 4313 lines compared with the previous 2072) in Python computer language. This enhanced version (i.e., Q-XRMA) consists of an innovative multilinear regression technique that mirrors the stoichiometry-controlled natural interdependence of the elements within a specific mineral, able to calibrate X-ray maps per each classified mineral of selected thin section microdomains. Such a technique permits users to compute: (a) the elemental concentration within a single phase expressed in a.p.f.u; (b) maps of the end member fractions displaying the potential zoning patterns of solid solution mineral phases. To achieve this goal, control spot analyses (i.e., internal standards) performed with the same or another device are used to preserve the connection of each spot with the corresponding pixel in the map. Such a connection can be assured using a developed spreadsheets package (i.e., Q-XRMA coordinates conversion tool) which converts the analytical device coordinates into the ArcGIS® ones via relatively simple mathematical equations. As a result, the new implemented procedure permits user to extract quantitative chemical information in a few minutes without passing through additional laboratory analyses, providing, at the same time, some control indexes allowing testing the accuracy of the statistical models computed for specific elements. Moreover, several upgrades of the code have introduced the following improvements: (a) a better partition of the output results in specific folders referring to the used cycle, allowing an easier recognition of all files; (b) a saving of all the output files in database format tables potentially queryable; (c) the compatibility with 9.x and later versions of ArcGIS®; and, (d) the option of restarting a new round of analysis without exiting the program. In conclusion, this new GIS-based software can be usefully applied to obtain an assisted

semi-automated sequential image processing procedure applicable in many fields of petrological investigations. This procedure minimises, inter alia, the bias influence consequent to the spot location decision-making activity, highlighting, in turn, quantitative distribution maps able to unravel complex or hidden paragenetic equilibria of petrological interest.

The classification resulting from this innovative image analysis method of one or several microdomains per thin section, which are selected according to the potential sequence of recognized metamorphic equilibria, could be used to get a better definition of the effective bulk rock chemistries at the base of a more robust thermodynamic modelling. This definition could be achieved by the recognition of proper effective reactant volumes (i.e., the real reacting volumes of each recognised metamorphic equilibria), providing, in such a way, more reliable thermobaric constraints. These thermobaric constraints were here converted into *PT* maps by the development of an add-on (i.e., DCMC) of the previous tool (i.e., Q-XRMA), for creating maps of compositionally-dependent diffusion coefficients, by integrating diffusion data from the literature. As a result, a complete local information system (i.e., LIS) for the investigated mineral, involving data of composition, grain size, modal amounts and kinetic rates, was created and used for detailed investigation as the determination of the timescales of metamorphic events.

All of these methods mentioned above can be considered part of “**the *Petromatics***” discipline, here defined for the first time as “*the science which promotes an integrated multidisciplinary systematic approach to develop tools and techniques for detecting, handling, integrating, processing, analyzing, archiving and distributing textural-related spatial minerochemical data characterising rocks at the micro scale with continuity and in a digital format*”.

Furthermore, the quantification of the rock parameters at the microscale laid the groundwork for an innovative numerical petrological workflow here called Metamorphic Petrology Information System (MetPetIS). The latter is a new LIS able to store, manage and elaborate multidisciplinary and multiscale data collection from metamorphic basement rocks within a unique cyber-infrastructure. MetPetIS starts from the acquisition of high resolution optical thin section scans to extrapolate detailed grain

boundary maps, passing through the analysis of X-ray elemental maps of the entire thin section and specifically selected domains, ending with the definition of the kinetic parameters at the mineral scale of observation.

As an application, two case studies have been selected for testing the methodologies described above, with the aim to derive the timescale of specific metamorphic events. In particular, paragneisses from the Serre and Sila Massifs (Calabria, Italy) were investigated applying diffusion modelling, by creating LISs for millimetre almandine-rich garnets, whereas diffusion solvers were developed by coding scripts in MATLAB computer language.

In the first case study (i.e., the Serre Massif), innovative numerical petrology methods supported by image analysis were applied to model the *PT* conditions of the garnet growth stages and to constrain the timescale of the late Variscan static overgrowth phase. These purposes have been addressed by deriving quantitative maps able to extrapolate in turn the effective bulk compositions to be used in the pseudosection construction. A total of three pseudosection were calculated and the mineral isopleths intersections were carried out on a garnet micaschist sample (i.e., MA271). Thermobaric constraints permitted to reconstruct a *PT*-path that integrates and improves the previous one (i.e., [Angi et al., 2010](#)), which was affected by missing application of garnet fractionation techniques and, as a consequence, by the missing of specific reliable isopleth intersections for the peak metamorphic conditions. The new *PT* values were, then, used in conjunction with the garnet component compositions obtained by the Q-XRMA, for acquiring a suitable dataset of kinetic data to be used into the diffusion modelling. This modelling, was addressed via a finite-difference numerical solution to describe, with accuracy, the multicomponent diffusion typical of garnet. Results of modelled profiles displays a good fit between observed and predicted concentration values in the case of timescales ranging from 1 to 5 Ma for the Late-Variscan contact metamorphism. Such a result testifies relatively very fast heating/cooling rates (e.g., averagely from 40 °C/Ma to 150 °C/Ma) affecting the upper crustal rocks of the Serre Massif, resulting in a good agreement with the thermal model proposed by [Caggianelli et al. \(2000a\)](#), [Caggianelli & Prosser \(2002\)](#) and [Caggianelli et al. \(2007\)](#) for the same investigated region. As the strong dependence from temperature of the diffusion

coefficients, and the limit in detecting absolute values of temperature conditions, a timescale of 3 ± 2 Ma is constrained for the last metamorphic event affecting the bottom part of the upper crustal rocks of the Serre Massif, experiencing a probable faster heating/cooling rate from the lower crust of the same metamorphic basement.

In the second case study (i.e., the Sila Massif), numerical petrological techniques allowed to model (a) the *PT* conditions of the early retrograde stage experienced by the Sila rocks and (b) the garnet compositional variations occurred due to the triggering of diffusion phenomena. These goals were addressed through the quantification of the correct effective bulk composition supported by image analysis. The *PT* pseudosections modelling was performed for a sample from a low-strain domain of the mylonitic metapelites in order to obtain reliable *PT* constraints specifically for the early retrograde stage of the Variscan metamorphic evolution. Such a result was achieved taking into account the textural equilibrium and compositional isopleth intersections among the garnet retrograde rims and the matrix minerals such as biotite and plagioclase. A reliable *PT* field (*P* mean of ~ 5.7 Kbar at *T* of ~ 630 °C) was constrained by isolating the effective reactant volume via image analysis of the elemental X-ray maps. This thermobaric constraint is consistent with the early stages of the retrograde metamorphic trajectory related to the late-Variscan shearing event developed at upper amphibolite facies conditions. The diffusion models applied for the garnet components allowed to outline a temporal evolution of about 3-5 Ma for the retrograde evolution, highlighting a slower exhumation with respect to the shallower overlapping lithological units. However, a longer timescale (i.e., from 10 Ma to > 10 Ma) was defined by the grossular model as an effect of the slower motion of calcium cations involved in the volume diffusion in garnet. In conclusion, within this scenario the investigated Sila Massif rocks were characterised by a slow cooling rate (i.e., ~ 25 °C/Ma) as a result of a slower exhumation mechanism from deeper crustal position of the investigated rocks, probably connected with a transtensional activity of the strike-slip tectonics of the Eastern Variscan Shear Zone.

Acknowledgements

Of course, I'm not the man most likely to put black on white what people have represented for me. I like to think that I am a person to whom direct contact with others should never be missed. Perhaps for writing on a sheet I might be too prolific or too synthetic, failing in both cases to express what I really want. However, I will try to find a way out in this case. There are so many people I would like to thank for helping me grow professionally and humanly during this PhD period.

First of all, the most important thanks go to Professor Ortolano G. He was for me as mentor as a big brother, accompanying me to successes and failures, teaching me, at the same time, that from the greatest fears each of us can become invincible. I need him every one of the skills I've gained during the PhD, as well as just a term, has always been able to instill in me the curiosity that characterizes every person who is about to learn something new.

Heartfelt thanks go to Professor Cirrincione R., who has guided me in careful choices and has always been present by helping me with targeted goals, whenever I have had difficulties in the methodological approach followed. I think there are few people like him and with his foresight.

Special thanks go to Professor Fiannacca P., who with his loving words has been able to silence my moods, making me always feel in a safe harbor where I can not be afraid of anything. I have never met a person who knows how to measure determination, strength and sweetness the way she does, and that is why I am honored to have had her as a friend during this training course.

Affectionate thanks go to Eugenio F., thanks to whom I have learned to give the right value to the hard work and to Professor Punturo R., who can breathe tranquility and care with a simple smile.

To Cristina B., known by chance, but revealed to be a great friend to trust my insecurity and with which to enjoy the good results. For sure the sister I've never had.

To Marco V., a man of great value who is able to make you feel comfortable with a phrase, always present and available for everything in both the professional and the private. Certainly, the friend that everyone would like to have to go for a beer in the evening. I'm glad I met you.

Acknowledgment also goes to Professor Di Stefano A., for the constant support of the technical aspects associated with a PhD program and to have always been active in the training and growth of all PhD students.

All teachers in the Geopetrologica area, Antonino Pezzino, Eugenio Nicotra, Carmelo Ferlito, Renato Cristofolini, Paolo Mazzoleni, Germana Barone, Vittorio Scribano, Annalisa Tranchina, technical-scientific staff Elisabetta Giuffrida and Alfio Viola and PhD students, Marisa Giuffrida, Rachele Lombardo, Simona Raneri, Francesco Zuccarello, and

Salvatore Urso, are thanked for the auxiliary and constant availability provided on any occasion of dialogue and confrontation, both on the scientific and general level, and for the sincere friendship that has always been demonstrated.

Special thanks go to Professor Godard G. of the Institute de Physique du Globe de Paris, to have welcomed me in his structure, take time to teach me the basics of linear algebra and image analysis, accompanied by convivial moments in which I learned to know the history of Paris from one of the greatest acquaintances of our days.

Further thanks go to the Professors Chakraborty S. and Dohmen R. of the Ruhr Univesitat – Bochum, who have hosted me for two weeks to learn the basics of analytical and numerical diffusion modelling.

Other important thanks go to the illustrious professor Guzzetta, who represented to me a father figure from which to learn the basics for sound and rigorous scientific research, hanging on his every word the same way as a child hanging from those of a storyteller. I am honored to have met him on my way.

Reviews from Professors Daniele Castelli of the Univesity of Turin and Michele Zucali of the University of Milan are gratefully acknowledged for having improved the quality of the original manuscript and gave me many more occasions of discussion.

Finally, I want to thank Eleonora very much, for having come into my life in a disruptive way during this last year. For helping me grow and improve from every point of view, for encouraging me not to give up, backed up in times of crisis, and fundamentally, to never cease to believe in me and my abilities. To make me realize that there will never be a great man in life without having a big woman at his side. You are my star and I will make you shine.

Thanks to all of you, who have wanted to read this thesis.

References

- Acquafredda, P., Fornelli, A., Paglionico, A., & Piccarreta, G. (2006). Petrological evidence for crustal thickening and extension in the Serre granulite terrane (Calabria, southern Italy). *Geological Magazine*, *143*(2), 145-163.
- Acquafredda, P., Fornelli, A., Piccarreta, G., & Pascazio, A. (2008). Multi-stage dehydration–decompression in the metagabbros from the lower crustal rocks of the Serre (southern Calabria, Italy). *Geological Magazine*, *145*, 397-411.
- Ague, J. J., & Carlson, W. D. (2013). Metamorphism as Garnet Sees It: The kinetics of nucleation and growth equilibration, and diffusional relaxation. *Elements*, *9*, 439-445.
- Alvarez, W. (1976). A former continuation of the Alps. *Geological Society of American Bulletin*, *87*, 891-896.
- Amodio Morelli, L., Bonardi, G., Colonna, V., Dietrich, D., Giunta, G., Ippolito, F., . . . Zuppetta, A. (1976). L'Arco Calabro-Peloritano nell'orogene appenninico-maghrebide. *Memorie Società Geologica Italiana*, *17*, 1-60.
- Anderson, D. E., & Olimpio, J. C. (1977). Progressive homogenization of metamorphic gabbros, south morar, scotland: evidence for volume diffusion. *Canadian Mineralogist*, *15*, 205-216.
- Angì, G., Cirrincione, R., Fazio, E., Fiannacca, P., Ortolano, G., & Pezzino, A. (2010). Metamorphic evolution of preserved Hercynian crustal section in the Serre Massif (Calabria- Peloritani Orogen, southern Italy). *Lithos*, *115*, 1–4, 237-262.
- Atzori, P., Ferla, P., Paglionico, A., Piccarreta, G., & Rottura, A. (1984). Remnants of the Hercynian Orogen along the Calabrian-Peloritan Arc, southern Italy: a review. *Journal of the Geological Society of London*, *141*, 137-145.
- Beccaluva, L., Maciotta, G., & Spadea, P. (1982). Petrology and geodynamic significance of the Calabria-Lucania ophiolites. *Rendiconti della Società Italiana di Mineralogia e Petrografia*, *38*, 973-987.
- Beggan, C., & Hamilton, C. W. (2010). New image processing software for analyzing object size-frequency distributions, geometry, orientation, and spatial distribution. *Computers and Geosciences*, *36*, 539–549.
- Belfiore, C. M., Fichera, G. V., Ortolano, G., Pezzino, A., Visalli, R., & Zappalà, L. (2016). Image processing of the pozzolan reactions in Roman mortars via X-ray Map Analyser. *Microchemical Journal*, *125*, 242-253.
- Berger, A., Herwegh, M., Schwarz, J. O., & Putlitz, B. (2010). Quantitative analysis of crystal/grain sizes and their distributions in 2D and 3D. *Journal of Structural Geology*, *33*, 1751–1763.

- Bluckburn, W. H. (1969). Zoned and unzoned garnets from the Greenville gneisses around Gananoque, Ontario. *Canadian Mineralogist*, 9, 691-698.
- Bonardi, G., Compagnoni, R., Del Moro, A., Messina, A., & V., P. (1987). Riequilibrazioni tettonico metamorfiche alpine dell'Unita dell'Aspromonte, Calabria Meridionale. *Rendiconti della Società Italiana di Mineralogia e Petrologia*, 42, 301.
- Brady, J. B., & Cherniak, D. J. (2010). Diffusion in Minerals: An Overview of Published Experimental Diffusion Data. *Reviews in Mineralogy & Geochemistry*, 72, 1-22.
- Caddick, M. J., & Thompson, A. B. (2008). Quantifying the tectono-metamorphic evolution of pelitic rocks from a wide range of tectonic settings: Mineral compositions in equilibrium. *Contributions to Mineralogy and Petrology*, 156, 177-195.
- Caddick, M. J., Konopàsek, J., & Thompson, A. B. (2010). Preservation of garnet growth zoning and the duration of prograde metamorphism. *Journal of Petrology*, 51, 2327-2347.
- Caggianelli, A., & Prosser, G. (2002). Modelling the thermal perturbation of the continental crust after intraplate of thick granitoid sheets: a comparison with the crustal sections in Calabria (Italy). *Geological Magazine*, 139, 699-706.
- Caggianelli, A., Liotta, D., Prosser, G., & Ranalli, G. (2007). Pressure-temperature evolution of the late Hercynian Calabria continental crust: compatibility with post-collisional extensional tectonics. *Terra Nova*, 19, 502-514.
- Caggianelli, A., Prosser, G., & Del Moro, A. (2000a). Cooling and exhumation history of deep-seated and shallow level, late Hercynian granitoids from Calabria. *Geological Journal*, 35, 33-42.
- Caggianelli, A., Prosser, G., & Rottura, A. (2000b). Thermal history vs. fabric anisotropy in granitoids emplaced at different crustal levels: an example from Calabria, southern Italy. *Terra Nova*, 12, 109-16.
- Callister, W. D. (1985). *Materials Science and Engineering: An Introduction*. John Wiley & Sons, Inc.
- Carlson, W. D. (2006). Rates of Fe, Mg, Mn and Ca diffusion in garnet. *American Mineralogist*, 91, 1-11.
- Cashman, K. V., & Ferry, J. M. (1988). Crystal size distribution (CSD) in rocks and the kinetics and dynamics of crystallization III. Metamorphic crystallization. *Contribution to Mineralogy and Petrology*, 99, 401-415.
- Cella, F., Cirrincione, R., Critelli, S., Mazzoleni, P., Pezzino, A., Punturo, R., . . . Rapolla, A. (2004). Gravity modeling in fold-thrust belts: An example from the Peloritani Mountains, southern Italy. *International Geology Review*, 46, 1042-1050.

- Cello, G., Invernizzi, C., & Mazzoli, S. (1996). Structural signature of tectonic processes in the Calabrian Arc, southern Italy: Evidence from the oceanic-derived Diamante-Terranova Unit. *Tectonics*, *15*, 187-200.
- Cello, G., Lentini, F., & Tortorici, L. (1990). La struttura del settore calabro-lucano e suo significato nel quadro dell'evoluzione tettonica del sistema a thrust sudappenninico. *Studi Geologici Camerati*, 27-34.
- Cello, G., Morten, L., & De Francesco, A. M. (1991). The tectonic significance of the Diamante-Terranova unit (Calabria, southern Italy) in the Alpine evolution of the northern sector of the Calabrian Arc. *Bollettino della Società Geologica Italiana*, *110*, 685-694.
- Chakraborty, S. (2006). Diffusion modeling as a tool for constraining timescales of evolution of metamorphic rocks. *Mineralogy and Petrology*, *88*, 7-27.
- Chakraborty, S. (2008). Diffusion in solid silicates: a tool to track timescales of processes comes of age. *Annual Review of Earth and Planetary Sciences*, *36*, 153-190.
- Chakraborty, S., & Ganguly, J. (1991). Compositional zoning and cation diffusion in aluminosilicate garnets. In *Diffusion, atomic ordering and mass transport—selected problems in geochemistry* (Vol. 8). Ganguly, J.
- Chakraborty, S., & Ganguly, J. (1992). Cation diffusion in aluminosilicate garnets: experimental determination in spessartine-almandine diffusion couples, evaluation of effective binary diffusion coefficients, and application. *Contribution to Mineralogy and Petrology*, *111*, 74-86.
- Chakraborty, S., & Rubie, D. C. (1996). Mg tracer diffusion in aluminosilicate garnets at 750-850 °C, 1 atm and 1300 °C, 8.5 GPa. *Contribution to Mineralogy and Petrology*, *122*, 406-414.
- Cheng, A., & Cheng, D. T. (2005). Heritage and early history of the boundary element method. *Engineering Analysis with Boundary Elements*, *29*, 268-302.
- Christensen, J. N., Rosenfeld, J. L., & De Paulo, D. J. (1989). Rates of tectonometamorphic processes from rubidium and strontium isotopes in garnet. *Science*, *244*, 1465-1468.
- Chu, X., & Ague, J. J. (2015). Analysis of experimental data on divalent cation diffusion kinetics in aluminosilicate garnets with application to timescales of peak Barrovian metamorphism, Scotland. *Contribution to Mineralogy and Petrology*, *170*(25), 1-27. doi:DOI 10.1007/s00410-015-1175-y
- Cirriuncione, R., Fazio, E., Fiannacca, P., Ortolano, G., & Punturo, R. (2009). Microstructural investigation of naturally deformed leucogneiss from an alpine shear zone (Southern Calabria - Italy). *Pure and Applied Geophysics*, *166*, 5-7, 995-1010.

- Cirrinzione, R., Fazio, E., Fiannacca, P., Ortolano, G., Pezzino, A., & Punturo, R. (2015). The Calabria–Peloritani Orogen, a composite terrane in Central Mediterranean; its overall architecture and geodynamic significance for a pre-Alpine scenario around the Tethyan basin. *Periodico di Mineralogia*, 84(3B), 701-749.
- Cirrinzione, R., Fazio, E., Heilbronner, R., Kern, H., Mengel, K., Ortolano, G., . . . Punturo, R. (2010). Microstructure and elastic anisotropy of naturally deformed leucogneiss from a shear zone in Montalto (southern Calabria, Italy). *Geological Society London, Special Publication*, 332, 49-68.
- Cirrinzione, R., Fazio, E., Ortolano, G., Pezzino, A., & Punturo, R. (2012). Fault-related rocks as a tool for the comprehension of structural and metamorphic evolution of an accretionary wedge in a collisional belt (Peloritani Mountains, NE Sicily). *International Geology Review*, 54, 940-956.
- Cirrinzione, R., Ortolano, G., Pezzino, A., & Punturo, R. (2008). Poly-orogenic multi-stage metamorphic evolution inferred via P-T pseudosections: An example from Aspromonte Massif basement rocks (Southern Calabria, Italy). *Lithos*, 103, 466-502. doi:doi:10.1016/j.lithos.2007.11.001
- Clemens, J., & Vielzeuf, D. (1987) Constraints on melting and magma production in the crust. *Earth and Planetary Science Letters*, 86, 287-306.
- Colonna, V., & Piccarreta, G. (1976). Contributo alla conoscenza dell'unità di Castagna in Sila Piccola: rapporti tra micascisti, paragneiss e gneiss occhiadini. *Bollettino della Società Geologica Italiana*, 95, 39-48.
- Colonna, V., & Piccarreta, G. (1977). Carta Geologico-Petrografica delle zone comprese tra Serrastretta-Carlopoli-Gimigliano-Pianopoli (Sila Piccola, Calabria). *Allegato Sviluppo, Rivista della Cassa di Risparmio di Calabria e Lucania*, 9.
- Colonna, V., Lorenzoni, S., & Zanettin Lorenzoni, E. (1973). Sull'esistenza di due complessi metamorfici lungo il bordo sud-orientale del massiccio granitico delle Serre (Calabria). *Bollettino della Società Geologica Italiana*, 92, 841-860.
- Compagnoni, R., & Ferrando, S. (2010). Paleo-European crust of the Italian western Alps: Geological history of the Argentera Massif and comparison with Mont Blanc–Aiguilles Rouges and Maures. *Journal of the Virtual Explorer, Electronic Edition*, 36(3). doi:doi:10.3809/jvirtex.2009.00228
- Connolly, J. A. (1990a). Multivariable phase diagrams; an algorithm based on generalized thermodynamics. *American Journal of Science*, 290, 666-718.
- Connolly, J. A. (1990b). www.perplex.ethz.ch. Tratto da PerpleX Software: www.perplex.ethz.ch
- Connolly, J. A. (2005). Computation of phase equilibria by linear programming: a tool for geodynamic modeling and its application to subduction zone decarbonation. *Earth and Planetary Science Letter*, 236, 524-541.

- Connolly, J. A., & Petrini, K. (2002). An automated strategy for calculation of phase diagram sections and retrieval of rock properties as a function of physical conditions. *Journal of Metamorphic Geology*, 20, 697-708.
- Cooper, A. R. (1968). The use and limitation of the concept of an effective binary diffusion for multicomponent diffusion. In *Mass Transport in Oxides, Proc Symposium, US Dept of Commerce*.
- Cortese, E. (1895). Descrizione geologica della Calabria. *Memorie Descrittive della Carta Geologica d'Italia*, pp. 310.
- Cossio, R., & Borghi, A. (1998). PETROMAP: MS-DOS software package for quantitative processing of X-ray maps of zoned minerals. *Computers & Geosciences*, 24, 797–803.
- Cossio, R., Borghi, A., & Ruffini, R. (2002). Quantitative modal determination of geological samples based on X-ray multielemental map acquisition. *Microscopy and Microanalysis*, 8, 139–149.
- Costa, F., & Chakraborty, S. (2008). The effect of water on Si and O diffusion rates in olivine and their relation to transport properties and processes in the upper mantle. *Physics of the Earth and Planetary Interiors*, 166, 11-29.
- Costa, F., Dohmen, R., & Chakraborty, S. (2008). Timescales of magmatic processes from modeling the zoning patterns of crystals. *Reviews in Mineralogy and Geochemistry*, 69, 545–594.
- Coutelas, A., Godard, G., Blanc, P., & Person, A. (2004). Les mortiers hydrauliques: synthèse bibliographique et premiers résultats sur des mortiers de Gaule romaine. *Revue d'Archéométrie*, 28, 127–139.
- Crank, J. (1975). *The Mathematics of Diffusion*. Clarendon Press, Oxford.
- Critelli, S., & Le Pera, E. (1998). Post-Oligocene sediment-dispersal systems and unroofing history of the Calabrian microplate, Italy. *International Geology Review*, 40, 609-637.
- Cussler, E. L. (1997). *Diffusion: Mass Transfer in Fluid Systems*. Cambridge, England: Cambridge University Press.
- Dainelli, N., Bonechi, F., Spagnolo, M., & Canessa, A. (2010). *Cartografia numerica: Manuale pratico per l'utilizzo dei GIS*. Palermo: Dario Flaccovio.
- Dasgupta, S., Chakraborty, S., & Neogi, S. (2009). Petrology of an inverted Barrovian sequence of metapelites in Sikkim Himalaya, India: constraints on the tectonic inversion. *American Journal of Science*, 309, 43-84.
- Dasgupta, S., Ganguly, J., & Neogi, S. (2004). Inverted metamorphic sequence in the Sikkim Himalayas: crystallization history, P-T gradient and implications. *Journal of Metamorphic Geology*, 22, 395-412.

- Datch, E., & Proyer, A. (2002). Constraints on the duration of high-pressure metamorphism in the Tauren Window from diffusion modelling of discontinuous growth zones in eclogite garnet. *Journal of Metamorphic Geology*, 20, 769-780.
- De Andrade, V., Vidal, O., Lewin, E., O' Brien, P., & Agard, P. (2006). Quantification of electron microprobe compositional maps of rock thin sections: an optimized method and examples. *Journal of Metamorphic Geology*, 24, 655–668.
- De Béthune, S., Laduron, D., & Boquet, J. (1975). Diffusion process in resorbed garnet. *Contribution to Mineralogy and Petrology*, 50, 197-204.
- De Roever, E. W. (1972). Lawsonite-albite facies metamorphism near Fuscaldo, Calabria (Southern Italy), its geological significance and petrological aspects. *GUA Pap Geological Service*, 1, pp. 171.
- Del Moro, A., Fornelli, A., & Paglionico, A. (1994). K-feldspar megacrystic suite in the Serre (Southern Calabria–Italy). *Periodico di Mineralogia*, 63, 19-33.
- DeVasto, M. A., Czeck, D. M., & Bhattacharyya, P. (2012). Using image analysis and ArcGIS(R) to improve automatic grain boundary detection and quantify geological images. *Computers and Geosciences*, 49, 38-45.
- Dewey, J. F., Helman, M. L., Turco, E., Hutton, D. W., & Knott, S. D. (1989). Kinematic of the western Mediterranean. *Geological Society of London Special Publication*, 4, 265-283.
- Dietrich, D. (1988). Sense of overthrust shear in the alpine nappes of Calabria (Southern Italy). *Journal of Structural Geology*, 10(4), 373-381.
- Dodson, M. H. (1973). Closure temperatures in cooling geochronological and petrological systems. *Contribution to Mineralogy and Petrology*, 40, 259-274.
- Dodson, M. H. (1976). Kinetic processes and thermal cooling of slowly cooling solids. *Nature*, 259, 551-553.
- Dodson, M. H. (1986). Closure profiles in cooling systems. *Materials Science Forum*, 7, 145-154.
- Dohmen, R., & Chakraborty, S. (2003). Mechanism and kinetics of element and isotopic exchange mediated by a fluid phase. *American Mineralogist*, 88, 1251–1270.
- Dohmen, R., & Chakraborty, S. (2007). Fe-Mg diffusion in olivine II: point defect chemistry, change of diffusion mechanisms and a model for calculation of diffusion coefficients in natural olivine. *Physics and Chemistry of Minerals*, 34, 409-430.
- Dohmen, R., Becker, H. W., Meissner, E., Etzel, T., & Chakraborty, S. (2002). Production of silicate thin films using pulsed laser deposition (PLD) and applications to studies in mineral kinetics. *European Journal of Mineralogy*, 14, 1155-1568.

- Dubois, R. (1976). La suture calabro-apenninique Cretace-Eocene et l'ouverture Tyrrhénienne Neogene; étude pétrographique et structurale de la Calabre centrale. Thèse, Paris VI
- Dubois, R., & Glangeaud, L. (1965). Grandes structures, microstructures et sens des chevauchements de matériel cristallin à l'extrémité méridionale du massif de la Sila (Calabre centrale, Italie). *Bulletin de la Société géologique de France*, 7, 239-240.
- Duchene, S., Albarede, S., & Lardeaux, I. M. (1998). Mineral zoning and exhumation history in the Munchberg eclogites (Bohemia). *American Journal of Science*, 298, 30-59.
- Duchene, S., Lardeaux, J. M., & Albarede, F. (1997). Exhumation of eclogites: insights from depth-time path analysis. *Tectonophysics*, 280, 125-140.
- Ehlers, K., Powell, R., & Stüwe, K. (1994). Cooling rate histories from garnet + biotite equilibrium. *American Mineralogist*, 79, 737-744.
- Elliott, D. (1973). Diffusion Flow Laws in Metamorphic Rocks. *Geological Society of America Bulletin*, 84, 8, 2645-2664. doi:[https://doi.org/10.1130/0016-7606\(1973\)84<2645:DFLIMR>2.0.CO;2](https://doi.org/10.1130/0016-7606(1973)84<2645:DFLIMR>2.0.CO;2)
- Elphick, S. C., & Ganguly, J. L. (1985). Experimental determination of cation diffusivities in aluminosilicate garnets I. Experimental methods and interdiffusion data. *Contribution to Mineralogy and Petrology*, 90, 36-44.
- Evans, T. P. (2004). A method for calculating effective bulk composition modification due to crystal fractionation in garnet-bearing schists: implications for isopleths thermobarometry. *Journal of Metamorphic Geology*, 547-557.
- Faryad, S. W., & Chakraborty, S. (2005). Duration of Eo-Alpine metamorphic events obtained from multicomponent diffusion modeling of garnet: a case study from the Eastern Alps. *Contribution to Mineralogy and Petrology*, 150, 306-318.
- Fazio, E., Cirrincione, R., & Pezzino, A. (2008). Estimating P-T conditions of Alpine-type metamorphism using multistage garnet in the tectonic windows of the Cardeto area (southern Aspromonte Massif, Calabria). *Mineralogy and Petrology*, 93, 111-142.
- Ferla, P. (2000). A model of continental crustal evolution in the geological history of the Peloritani Mountains (Sicily). *Memorie della Società Geologica Italiana*, 55, 87-93.
- Fernando, G. W., Hauzenberger, C. A., Baumgartner, L. P., & Hofmeister, W. (2003). Modeling of retrograde diffusion zoning in garnet: evidence for slow cooling of granulites from Highland Complex of Sri Lanka. *Mineralogy and Petrology*, 78, 53-71.

- Festa, V., Caggianelli, A., Langone, A., & Prosser, G. (2013). Time–space relationships among structural and metamorphic aureoles related to granite emplacement: a case study from the Serre Massif (southern Italy). *Geological Magazine*, *150*, 441-454.
- Festa, V., Di Battista, P., Caggianelli, A., & Liotta, D. (2003). Exhumation and tilting of the late Hercynian continental crust in the Serre Massif (Southern Calabria-Italy). *Bollettino della Società Geologica Italiana*, *2*, 79-88.
- Festa, V., Messina, A., Paglionico, A., Piccarreta, G., & Rottura, A. (2004). Pre-Triassic history recorded in the Calabria-Peloritani segment of the Alpine chain, southern Italy. An overview. *Periodico di Mineralogia*, *73*(2), 57-71.
- Fiannacca, P., Cirrincione, R., Bonanno, F., & Carciotto, M. M. (2015). Source-inherited compositional diversity in granite batholiths: The geochemical message of Late Paleozoic intrusive magmatism in central Calabria (southern Italy). *Lithos*, *236-237*, 123-140.
- Fiannacca, P., Lo Pò, D., Ortolano, G., Cirrincione, R., & Pezzino, A. (2012). Thermodynamic modeling assisted by multivariate statistical image analysis as a tool for unraveling metamorphic P–T–d evolution: an example from ilmenite–garnet-bearing metapelite of the Peloritani Mountains, southern Italy. *Mineralogy and Petrology*, *106*, 151-171.
- Fiannacca, P., Ortolano, G., Pagano, M., Visalli, R., Cirrincione, R., & Zappalà, L. (2017 - in press). IG-Mapper: A new ArcGIS® toolbox for the geostatistics-based automated geochemical mapping of igneous rocks. *Chemical Geology*.
- Fiannacca, P., Williams, I. S., & Cirrincione, R. (2016). Timescales and mechanisms of batholith construction: Constraints from zircon oxygen isotopes and geochronology of the late Variscan Serre Batholith (Calabria, southern Italy). *Lithos*. doi:<http://dx.doi.org/10.1016/j.lithos.2016.06.011>
- Fick, A. (1855). Ueber Diffusion (On Diffusion). *Annalen der Physik und Chemie von J. C. Pogendorff*, *94*, 59-86.
- Florence, F. P., & Spear, F. S. (1993). Influence of reaction history and chemical diffusion on P-T calculations for staurolite schists from the Littleton formation, northwestern New Hampshire. *American Mineralogist*, *78*, 345-359.
- Fornelli, A., Caggianelli, A., Del Moro, A., Bargossi, G. M., Paglionico, A., Piccarreta, G., & Rottura, A. (1994). Petrology and evolution of the Central Serre granitoids (Southern Calabria–Italy). *Periodico di Mineralogia*, *63*, 53-70.
- Fornelli, A., Langone, A., Micheletti, F., & Piccarreta, G. (2011). Time and duration of Variscan high temperature metamorphic processes in the south European Variscides: Constraints from U-Pb chronology and trace element chemistry of zircon. *Mineralogy and Petrology*, *103*, 101-122.

- Fornelli, A., P. G., Acquafredda, P., Micheletti, F., & Paglionico, A. (2004). Multi-stage melting in the lower crust of the Serre (Southern Italy) Geochemical fractionation in migmatitic rocks from Serre granulitic terrane (Calabria, southern Italy). *Periodico di Mineralogia*, 73, 145-157.
- Fornelli, A., Piccarreta, G., Del Moro, A., & Acquafredda, P. (2002). Multi-stage melting in the lower crust of the Serre (Southern Italy). *Journal of Petrology*, 43(12), 2191-2217.
- Fourier, J. B. (1822). *Théorie analytique de la chaleur*. Chez Firmin Didot, père et fils.
- Freer, R., & Edwards, A. (1999). An experimental study of Ca-(Fe,Mg) interdiffusion in silicate garnets. *Contribution to Mineralogy and Petrology*, 134, 370-379.
- Friel, J. J., & Lyman, C. E. (2006). X-ray mapping in electron-beam instruments. *Microscopy and Microanalysis*, 12, 2–25.
- Gaidies, F., Abart, R., de Capitani, C., Schuster, R., Connolly, J. A., & Reusser, E. (2006). Characterization of polymetamorphism in the Austroalpine basement east of the Tauern Window using garnet isopleth thermobarometry. *Journal of Metamorphic Geology*, 24, 451-475.
- Ganguly, J. (1996). Constraint on the time scale of biotite-grade metamorphism during Acadian orogeny from a natural garnet-garnet diffusion couple. *American Mineralogist*, 81, 1208-12016.
- Ganguly, J. (2002). *Diffusion kinetics in minerals: Principles and applications to tectono-metamorphic processes*. (Vol. 4). Gramaccioli CM, Eötvös University Press, Budapest.
- Ganguly, J. (2010). Cation diffusion kinetics in aluminosilicate garnets and geological applications. *Reviews in Mineral and Geochemistry*, 72, 559-601.
- Ganguly, J., Cheng, W., & Chakraborty, S. (1998). Cation diffusion in aluminosilicate garnets: experimental determination in pyrope-almandine diffusion couples. *Contribution to Mineralogy and Petrology*, 131, 171-180.
- Ganguly, J., & Saxena, S. K. (1984). Mixing properties of aluminosilicate garnets: constraints from natural and experimental data, and applications to geothermobarometry. *American Mineralogist*, 69, 88-97.
- Ganguly, J., & Tirone, M. (1999). Diffusion closure temperature and age of a mineral with arbitrary extent of diffusion: theoretical formulation and applications. *Earth and Planetary Science*, 170, 131-140 (Erratum (2000) 180:223).
- Ganguly, J., Chakraborty, S., Sharp, T. G., & Rumble, D. (1996). Constraint on the time scale of biotite grade metamorphism during Acadian Orogeny from a natural garnet–garnet diffusion couple. *American Mineralogist*, 81, 1208-1216.

- Ganguly, J., Dasgupta, S., Cheng, W., & Neogi, S. (2000). Exhumation history of a section of the Sikkim Himalayas, India: records in the metamorphic mineral equilibria and compositional zoning of garnet. *Earth and Planetary Science Letter*, *183*, 471-486.
- Graeßner, T., & Schenk, V. (2001). An Exposed Hercynian Deep Crustal Section in the Sila Massif of Northern Calabria: Mineral Chemistry, Petrology and a P-T Path of Granulite-facies Metapelitic Migmatites and Metabasites. *Journal of Petrology*, *42*, 5, 931-961.
- Graeßner, T., Schenk, V., Brocker, M., & Metzger, K. (2000). Geochronological constraints on timing of granitoid magmatism, metamorphism and post-metamorphic cooling in the Hercynian crustal cross-section of Calabria. *Journal of Metamorphic Geology*, *18*, 409-421.
- Grant, J. A., & Weiblen, P. W. (1971). Retrograde zoning in garnet near the second sillimanite isograd. *American Journal of Science*, *270*, 281-296.
- Gu, Y. (2003). Automated scanning electron microscope based mineral liberation analysis: an introduction to JKMRC/FEI mineral liberation analyser. *Journal of Minerals and Materials Characterization and Engineering*, *2*, 33-41.
- Guerrera, F., Martin-Algarra, A., & Perrone, V. (1993). Late Oligocene-Miocene syn/late-orogenic successions in western and central Mediterranean chains from Betic Cordillera to Southern Apennine. *Terra Nova*, *5*, 525-544.
- Gueydan, F., Mehl, C., & Parra, T. (2005). Stress-strain rate history of a mid-crustal shear zone and the onset of brittle deformation inferred from quartz recrystallized grain size. In *Deformation Mechanisms, Rheology and Tectonics: from Minerals to the Lithosphere* (Vol. Special Publications, p. 127-142). Geological Society, London: Gapais, D., Brun, J.P., Cobbold, P.R.
- Haccard, D., Lorenz, C., & Grandjacquet, C. (1972). Essai sur l'évolution tectonogenetique de la liaison Alpes-apennines (de la Ligurie a la Calabre). *Memorie della Società Geologica Italiana*, *11*, 309-341.
- Hallett, B. W., & Spear, F. S. (2011). Insight into the Cooling of the Valhalla Complex, British Columbia. *Lithos*, *125*, 809-824.
- Handy, M. R. (1994). Flow laws for rocks containing two non-linear viscous phases; a phenomenological approach. *Journal of Structural Geology*, *16*, 3, 287-301.
- Hauzenberger, C. A., Robl, J., & Stüwe, K. (2005). Garnet zoning in high pressure granulite-facies metapelites, Mozambique belt, SE-Kenya: constraints on the cooling history. *European Journal of Mineralogy*, *17*, 43-55.
- Heillbronner, R., & Tullis, J. (2006). Evolution of c-axis pole figures and grain size during dynamic recrystallisation: Results from experimentally sheared quartzite. *Journal of Geophysical Research*, *111*.

- Hier-Majumder, S., Anderson, I. M., & Kohlstedt, D. L. (2005). Influence of protons on Fe-Mg interdiffusion in olivine. *Journal of Geophysical Research*, *110*. doi:doi:10.1029/2004JB003292
- Holland, T. J., & Powell, R. (1998). An internally consistent thermodynamic data set for phases of petrological interest. *Journal of Metamorphic Geology*, *16*, 309-343.
- Holland, T. J., & Powell, R. (2011). An improved and extended internally consistent thermodynamic dataset for phases of petrological interest, involving a new equation of state for solids. *Journal of Metamorphic Geology*, *29*, 333-383.
- Holland, T., Baker, J., & Powell, R. (1998). Mixing properties and activity-composition relationships of chlorites in the system MgO-FeO-Al₂O₃-SiO₂-H₂O. *European Journal of Mineralogy*, *10*, 395-406.
- Hosmer, D. W., & Lemeshow, S. (1989). *Applied logistic regression*. Wiley.
- Jackson, K. A. (2005). Thin-Film Deposition. In *Kinetic Processes: Crystal Growth, Diffusion, and Phase Transitions in Materials*. Wiley-VCH Verlag GmbH & Co. KGaA, Weinheim. doi:10.1002/3527603891.ch17
- Korolyuk, V. N., & Lepezin, G. G. (2008). Analysis of experimental data on the diffusion coefficients of Mg, Fe, Mn and Ca in garnets. *Russian Geology and Geophysics*, *49*, 557-569.
- Kress, V. C., & Ghiorso, M. S. (1993). Multicomponent diffusion in MgO-Al₂O₃-SiO₂ and CaO-MgO-Al₂O₃-SiO₂ melts. *Geochimica et Cosmochima Acta*, *57*, 4453-4466.
- Kress, V. C., & Ghiorso, M. S. (1995). Multicomponent diffusion in basaltic melts. *Geochimica et Cosmochima Acta*, *59*, 313-324.
- Lanari, P., Vidal, O., De Andrade, V., Dubacq, B., Lewin, E., Grosch, E., & Schwartz, S. (2014). XMapTools: a MATLAB®-based program for electron microprobe Xray image processing and geothermobarometry. *Computers & Geosciences*, *62*, 227-240.
- Langone, A., Caggianelli, A., Festa, V., & P. G. (2014). Time constraints on the building of the Serre 708 batholith: consequences for the thermal evolution of the Hercynian continental crust exposed in Calabria (southern Italy). *Journal of Geology*, *122*, 183-199.
- Lanzafame, G., Spadea, P., & Tortorici, L. (1979). Mesozoic ophiolites of northern Calabria and Lucanian Apenines(southern Italy). *Ofioliti*, *4*, 173-182.
- Lasaga, A. C. (1979). Multicomponent exchange and diffusion in silicates. *Geochimica et Cosmochima Acta*, *43*, 455-469.
- Lasaga, A. C. (1983). Geospeedometry: an extension of geothermometry. In *Saxena, S.K. (ed.): Kinetics and equilibrium in mineral reactions. Advances in Physical Geochemistry* (p. 81-114). Berlin: Springer-Verlag.

- Lasaga, A. C., Richardson, S. M., & Holland, H. D. (1977). The mathematics of cation diffusion and exchange between silicates minerals during retrograde metamorphism. In *Energetics of Geological Processes* (p. 353–88). New York: SK Saxena, S Bhattachanji, Springer-Verlag.
- Launeau, P., Cruden, A. R., & Bouchez, J. L. (1994). Mineral recognition in digital images of rocks; a new approach using multichannel classification. *Canadian Mineralogist*, 32, 919–933.
- Li, T., Yang, J. S., & Zhang, R. Y. (2008). Geochemical characteristics and UHP metamorphic age of the Hujialing garnet clinopyroxenite from the Sulu terrane, China and the bearing on its genesis. *International Geology Review*, 50, 48-60.
- Li, Y., Onasch, C. M., & Guo, Y. (2008). GIS-based detection of grain boundaries. *Journal of Structural Geology*, 30, 431-443.
- Liang, Y., Richter, F. M., & Chamberlin, L. (1997). Diffusion in silicate melts, III: empirical models for multicomponent diffusion. *Geochimica et Cosmochimica Acta*, 61, 5295-5312.
- Liberi, F., Morten, L., & Piluso, E. (2006). Geodynamic significance of ophiolites within the Calabrian Arc. *Island Arc*, 15, 26-43.
- Lister, G. S., & Dornsiepen, U. L. (1982). Fabric transitions in the Saxony granulite terrane. *Journal of Structural Geology*, 4, 81-92.
- Loomis, T. P. (1978a). Multicomponent diffusion in garnet: I. Formulation of isothermal models. *American Journal of Science*, 278, 1099-1118.
- Loomis, T. P. (1978b). Multicomponent diffusion in garnet: II. Comparison of models with natural data. *American Journal of Science*, 278, 1119-1137.
- Loomis, T. P., Ganguly, J., & Elphick, S. C. (1985). Experimental determination of cation diffusivities in aluminosilicate garnets. II. Multicomponent simulation and tracer diffusion coefficients. *Contribution to Mineralogy and Petrology*, 90, 45-51.
- Lorenzoni, S., & Zanettin Lorenzoni, E. (1983). Note illustrative della Carta Geologica della Sila alla scala 1:200.000. *Memorie della Società Geologica*, 36, 317-342.
- Maccarrone, E., Paglionico, A., Piccarreta, G., & Rottura, A. (1983). Granulite-amphibolite facies metasediments from the Serre (Calabria, Southern Italy): their protoliths and the processes controlling their chemistry. *Lithos*, 16, 95-111.
- Mainprice, D., Bouchez, J. L., Blumenfeld, P., & Tubia, J. M. (1986). Dominant c-slip in naturally deformed quartz: implications for dramatic plastic softening at high temperature. *Geology*, 14, 819-822.
- Marotta, A. M., & Spalla, M. I. (2007). Permian-Triassic high thermal regime in the Alps: Result of late Variscan collapse or continental rifting? Validation by numerical modeling. *Tectonics*, 26, 1-27. doi:doi:10.1029/2006TC002047

- Marquardt, D. W. (1980). A Critique of Some Ridge Regression Methods: Comment. *Journal of the American Statistical Association*, 75, 369, 87-91.
- Martínez-Martínez, J., Benavente, D., & García del Cura, M. A. (2007). Petrographic quantification of brecciated rocks by image analysis. Application to the interpretation of elastic wave velocities. *Engineering Geology*, 90, 41–54.
- Massonne, H. J., & Schreyer, W. (1987). Phengite geobarometry based on the limiting assemblage with K-feldspar, plogophite and quartz. *Contribution to Mineralogy and Petrology*, 96, 212-224.
- Matte, P. (2001). The Variscan collage and orogeny (480-290 Ma) and the tectonic definition of the Armorica microplate: A review. *Terra Nova*, 13(2), 122-128. doi:doi:10.1046/j. 1365-3121.2001.00327.x
- Mehrer, H. (2007). *Diffusion in Solids*. Springer.
- Messina, A., Russo, S., Borghi, A., Colonna, V., Compagnoni, R., Caggianelli, A., . . . Piccarreta, G. (1994). Il massiccio della Sila Settore Settentrionale dell'Arco Calabro Peloritano. *Bollettino della Società Geologica Italiana*, 113, 559-586.
- Micheletti, F., Barbey, P., Fornelli, A., Piccarreta, G., & Deloule, E. (2007). Latest Precambrian to Early Cambrian U–Pb zircon ages of augen gneisses from Calabria (Italy), with inference to the Alboran microplate in the evolution of the peri-Gondwana terranes. *International Journal of Earth Sciences*, 96, 843-860.
- Mungall, J. E., Romano, C., & Dingwell, D. B. (1998). Multicomponent diffusion in the molten system K₂O-Na₂OAl₂O₃-SiO₂-H₂O. *American Mineralogist*, 83, 685-699.
- Murphy, M., Alley, M., Demmel, J., Keutzer, K., Vasanawala, S. & Lustig, M. (2012). Fast ℓ_1 -SPIRiT Compressed Sensing Parallel Imaging MRI: Scalable Parallel Implementation and Clinically Feasible Runtime. *IEEE Transactions on Medical Imaging*, 31(6), 1250-1262.
- Neter, J., Kutner, M., Nachtsheim, C., & Wasserman, W. (1996). *Applied Linear Statistical Models*. New York: McGraw-Hill Companies, Inc.
- Newton, R. C., Charlu, T. V., & Kleppa, O. J. (1980). Thermochemistry of the high structural state plagioclases. *Geochemica et Cosmochimica Acta*, 44, 933-941.
- O'Brien, P. J. (1997). Garnet zoning and reaction textures in overprinted eclogites, Bohemian Massif, European Variscides: A record of their thermal history during exhumation. *Lithos*, 41, 119-133.
- Oakford, A., & Williams, P. (2011). The use and value of local information systems : A case study of the Milton Keynes intelligence (MKi) Observatory. *Aslib Proceedings*, 63, 5, 533-548. doi:DOI: 10.1108/00012531111165003
- Oelker, B., Altherr, R., & Paquin, J. (2003). Fast exhumation of the ultrahigh-pressure Alpe Arami garnet peridotite (Central Alps, Switzerland): constraints from

- geospeedometry and thermal modeling. *Journal of Metamorphic Geology*, 21, 395–402.
- Ogniben, L. (1973). Schema geologico della Calabria in base ai dati odierni. *Geologica Romana*, 12, 543-585.
- Onsager, L. (1945). Theories and problems of liquid diffusion. *Annals of the New York Academy of Sciences*, 46, 241–65.
- Ortolano, G., & Zappalà, L. (2012). Management and deployment of rock-analysis data from thin section to field-scale. *Rendiconti della Società Geologica Italiana*, 21, 726-728.
- Ortolano, G., Cirrincione, R., & Pezzino, A. (2005). PT evolution of Alpine metamorphism in the southern Aspromonte Massif (Calabria - Italy). *Schweizer Mineralogische und Petrographische Mitteilungen*, 85, 31-56.
- Ortolano, G., Cirrincione, R., Pezzino, A., & Puliatti, G. (2013). Geo-Petro-Structural study of the Palmi shear zone: Kinematic and rheological implications. *Rendiconti Online della Società Geologica Italiana*, 29, 126-129.
- Ortolano, G., Visalli, R., Cirrincione, R., & Rebay, G. (2014a). PT-path reconstruction via unravelling of peculiar zoning pattern in atoll shaped garnets via image assisted analysis: an example from the Santa Lucia del Mela garnet micaschists (Northeastern Sicily-Italy). *Periodico di Mineralogia*, 83, 2, 257-297.
- Ortolano, G., Visalli, R., Godard, G., & Cirrincione, R. (under review). Quantitative X-ray Map Analyser (Q-XRMA): A new GIS-based statistical approach for Mineral Image Analysis. *Computer and Geosciences*.
- Ortolano, G., Zappalà, L., & Mazzoleni, P. (2014b). X-ray Map Analyzer: a new ArcGIS® based tool for the quantitative statistical data handling of X-ray maps (Geo- and material-science applications). *Computers & Geosciences*, 72, 49–64.
- Padovano, M., Dorr, W., Elter, F. M., & Gerdes, A. (2014). The East Variscan Shear Zone: Geochronological constraints from the Capo Ferroarea (NE Sardinia, Italy). *Lithos*, 196-197, 27-41.
- Padovano, M., Elter, F. M., Pandeli, E., & Franceschelli, M. (2012). The East Variscan Shear Zone: New insights into its role in the Late Carboniferous collision in southern Europe. *International Geology Review*, 54(8), 957-970.
- Paglionico, A., & Piccarreta, G. (1976). Le unità del fiume Pomo e di Castagna nelle Serre settentrionali. *Bollettino della Società Geologica Italiana*, 95, 27-37.
- Passchier, C. W., & Trouw, R. A. (1996). *Microtectonics*. Berlin: Springer-Verlag.
- Pelletier, J. (2008). *Quantitative Modeling of Earth Surface Processes*. Cambridge University Press.

- Perchuk, A. L., Burchard, M., Schertl, H. P., Maresch, W. V., Gerya, T. V., Bernhardt, H. J., & Vidal, O. (2009). Diffusion of divalent cations in garnet: multi-couple experiments. *Contribution to Mineralogy and Petrology*, 157, 573-592.
- Perchuk, A., & Philippot, P. (1997). Rapid cooling and exhumation of eclogitic rocks from the great Caucasus, Russia. *Journal of Metamorphic Geology*, 15, 299-310.
- Perchuk, L. L., & Lavrent'yeva, I. V. (1990). "Experimental Study of Mineral Equilibria in the System Garnet-Orthopyroxene-Amphibole". *International Geology Review*, 5, 486-507.
- Perring, C. S., Barnes, S. J., Verrall, M., & Hill, R. E. (2004). using automated digital image analysis to provide quantitative petrographic data on olivine-phyric basalts. *Computers and Geosciences*, 30, 183-195.
- Perrone, V. (1996). Une nouvelle hypothèse sur la position paléogéographique et l'évolution tectonique des Unités de Verbicaro et de San Donato (region Calabro-Lucanienne; Italie): implications sur le limite Alpes-Appennines en Calabre. *Comptes Rendus de l'Académie des Sciences de Paris*, 322, 877-884.
- Pezzino, A. (1982). Confronti petrografici e strutturali tra i basamenti metamorfici delle unità inferiori dei Monti Peloritani (Sicilia). *Periodico di Mineralogia*, 1, 35-50.
- Piluso, E. (1997). Evoluzione tettonometamorfica dell'Unità di Polia-Copanello nel settore settentrionale della catena Costiera Tirrenica Calabrese. *PhD Thesis - Univerisità della Calabria*, pp. 232.
- Piluso, E., & Morten, L. (1999). Crust evolution from Variscan collapse to Tethyan opening inferred from the northern Calabria basement rocks, southern Italy. *Geophysical Research Abstracts*, 1(1), 1-67.
- Piluso, E., & Morten, L. (2004). Hercynian high temperature granulites and migmatites from the Catena Costiera, northern Calabria, southern Italy. *Periodico di Mineralogia*, 73, 159-172.
- Piluso, E., Cirrincione, R., & Morten, L. (2000). Ophiolites of the Calabrian Peloritan Arc and their relationships with the crystalline basement (Catena Costiera and Sila Piccola, Calabria, Southern Italy). *Ofioliti*, 25(2), 117-140.
- Powell, R., & Holland, T. (1999). Relating formulations of the thermodynamics of mineral solid solutions; activity modeling of pyroxenes, amphiboles, and micas. *American Mineralogist*, 84, 1-14.
- Richard, L. R. (1995). MinPet: Mineralogical and petrological data processing system, version 2.02. Québec, Canada: MinPet Geological Software.
- Richards, J. A. (1986). *Remote Sensing Digital Image Analysis: An Introduction*. Berlin: Springer-Verlag.

- Rossetti, F., Faccenna, C., Goffè, B., Patrick, M., Argentieri, A., Funiciello, R., & Mattei, M. (2001). Alpine structural and metamorphic signature of the Sila Piccola Massif nappe stack (Calabria, Italy): insights for the tectonic evolution of the Calabrian Arc. *Tectonics*, *20*, 112-133.
- Rottura, A. B., Del Moro, A., Maccarrone, E., Macera, P., Paglionico, A., Perrini, R., . . . Poli, G. (1990). Petrogenesis of contrasting Hercynian granitoids from the Calabrian Arc, Southern Italy. *Lithos*, *24*, 97-119.
- Sacco, V. (2011). Le miloniti dell'Unità di Castagna: Studio petrologico-strutturale e implicazioni geodinamiche. *PhD Thesis*, pp. 81. Catania, Sicilia, Italia.
- Sardini, P., Moreau, E., Sammartino, S., & Touchard, G. (1999). Primary mineral connectivity of polyphasic igneous rocks by high-quality digitisation and 2D image analysis. *Computers and Geosciences*, *25*, 599–608.
- Scandone, P. (1979). Origin of the Tyrrhenian Sea and Calabrian Arc. *Bollettino della Società Geologica Italiana*, *98*, 27-34.
- Schenk, V. (1980). U-Pb and Rb-Sr radiometric dates and their correlation with metamorphic events in the granulitic-facies basement of the Serra, Southern Calabria (Italy). *Contribution to Mineralogy and Petrology*, *73*, 23-38.
- Schenk, V. (1984). Petrology of felsic granulites, metapelites, metabasics, ultramafics and metacarbonates from southern Calabria (Italy): prograde metamorphism, uplift and cooling of a former lower crust. *Journal of Petrology*, *25*, 255-298.
- Schenk, V. (1989). P-T-t path of the lower crust in the Hercynian fold belt of southern Calabria. In *Evolution of metamorphic belts* (Vol. 43, p. 337-342). Geological Society of London. Special publication: Daly, J. S., Cliff, R. A., Yardley, B. W. D. (eds).
- Schwandt, C. S., Cygan, R. T., & Westrich, H. R. (1995). Mg self-diffusion in pyrope garnet. *American Mineralogist*, *80*, 483-490.
- Schwandt, C. S., Cygan, R. T., & Westrich, H. R. (1996). Ca self-diffusion in grossular garnet. *American Mineralogist*, *81*, 448-451.
- Shaw, D. (1973). *Atomic Diffusion in Semiconductors*. Plenum Press.
- Shewmon, P. (1989). *Diffusion in Solids, 2nd edition*. Warrendale, Pennsylvania, US: The Minerals, Metals and Materials Society.
- Siivola, J., & Schmid, R. A. (2007). *Systematic nomenclature for metamorphic rocks: List of mineral abbreviations. Recommendations by the IUGS Subcommission on the Systematics of Metamorphic Rocks*. Tratto da IUGS Subcommission on the Systematics: https://www.bgs.ac.uk/scmr/docs/papers/paper_12.pdf
- Smith, M. A., Scherer, E. E., & Mezger, K. (2013). Peak metamorphic temperatures from cation diffusion zoning in garnet. *Journal of Metamorphic Geology*, *31*, 339-358.

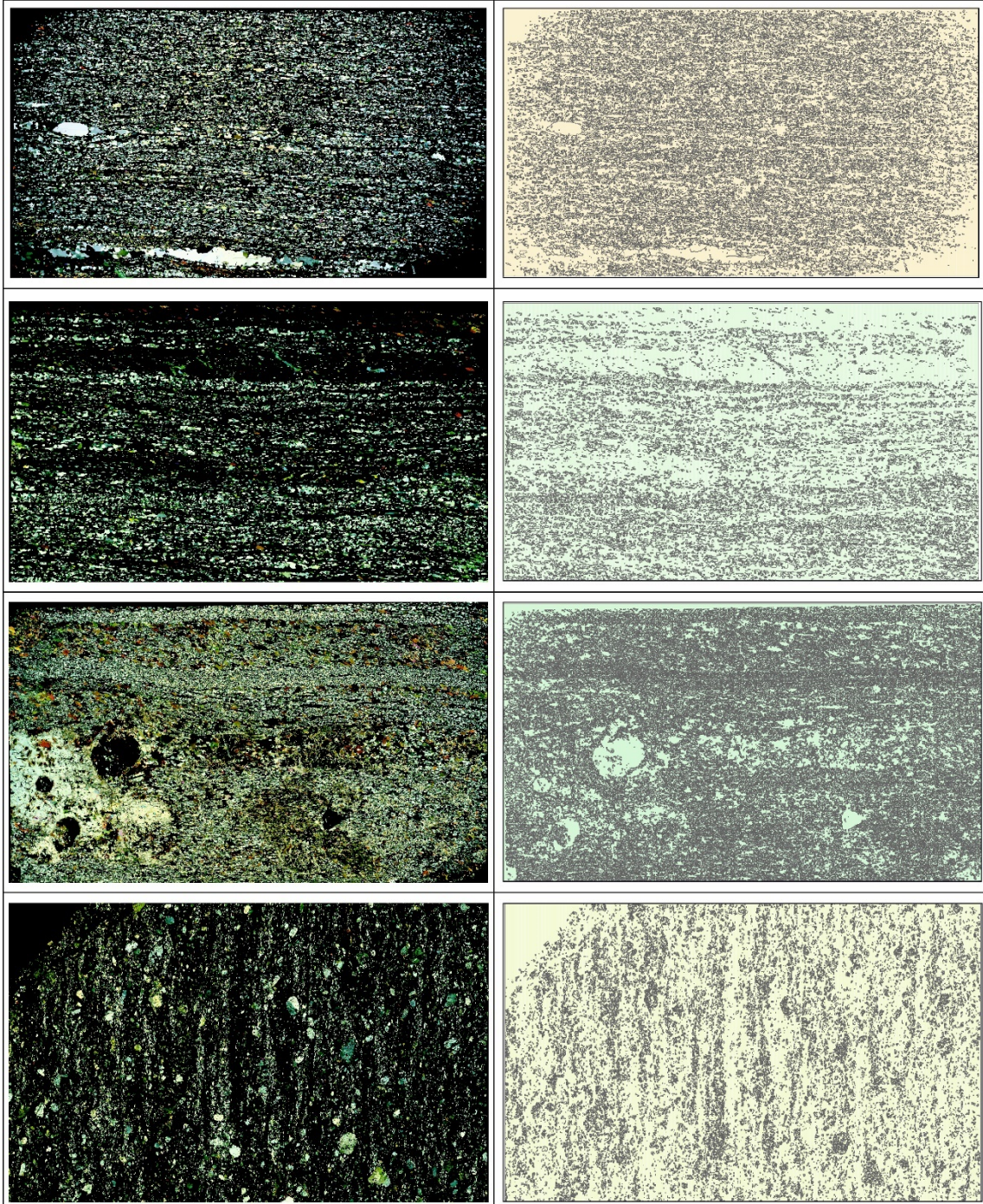
- Spadea, P. (1980). Contributo alla conoscenza dei metabasalti ofiolitici della Calabria Settentrionale e centrale e dell'Appennino Lucano. *Rendiconti della Società Italiana di Mineralogia e Petrografia*, 35, 251-276.
- Spear, F. S. (1988). Metamorphic fractional crystallization and internal metasomatism by diffusional homogenization of zoned garnets. *Contribution to Mineralogy and Petrology*, 99, 507-517.
- Spear, F. S. (1991). On the interpretation of peak metamorphic temperatures in light of garnet diffusion during cooling. *Journal of Metamorphic Geology*, 9, 379-388.
- Spear, F. S. (1993). *Metamorphic Phase Equilibria and Pressure – Temperature – Time Paths*. Washington, DC: Mineralogical Society of America.
- Spear, F. S. (2004). Fast cooling and exhumation of the Valhalla Metamorphic Core Complex. *International Geology Review*, 46, 193-209.
- Spear, F. S. (2014). The duration of near-peak metamorphism from diffusion modelling of garnet zoning. *Journal of Metamorphic Geology*, 32, 903-914. doi:doi:10.1111/jmg.12099.
- Spear, F. S., & Parrish, R. R. (1996). Petrology and cooling rates of the Valhalla Complex British Columbia, Canada. *Journal of Petrology*, 37, 733-765.
- Spear, F. S., & Peacock, S. M. (1989). Metamorphic pressure-temperature-time paths. *Short course in Geology*, 7, 0-102. Washinton, DC: American Geophysical Union.
- Spear, F. S., & Selverstone, J. (1983). Quantitative P-T paths from zoned minerals: Theory and tectonic applications. *Contributions to Mineralogy and Petrology*, 83, 348-357.
- Stalker, M. K., & Morral, J. E. (1990). Classification of concentration profiles in quaternary diffusion couples. *Acta Metallurgica et Materialia*, 38, 3, 439-447.
- Stipp, M. (2002). The eastern Tonale fault zone: A 'natural laboratory' for crystal plastic deformation of quartz over a temperature range from 250 to 700° C. *Journal of Structural Geology*, 24, 1861-1884.
- Storm, L. C., & Spear, F. S. (2005). Pressure, temperature and cooling rates of granulite facies migmatitic pelites from the southern Adirondack highlands, New York. *Journal of Metamorphic Geology*, 23, 107-130.
- Stüwe, K., & Ehlers, K. (1996). The qualitative zoning record of minerals. A method for determining the duration of metamorphic events? *Mineralogy and Petrology*, 56, 171-184.
- Tan, T. Y., & Gosele, U. (2005). Diffusion in Semiconductors. In *Diffusion in Condensed Matter – Methods, Materials, Models* (p. 165). Springer Verlag.

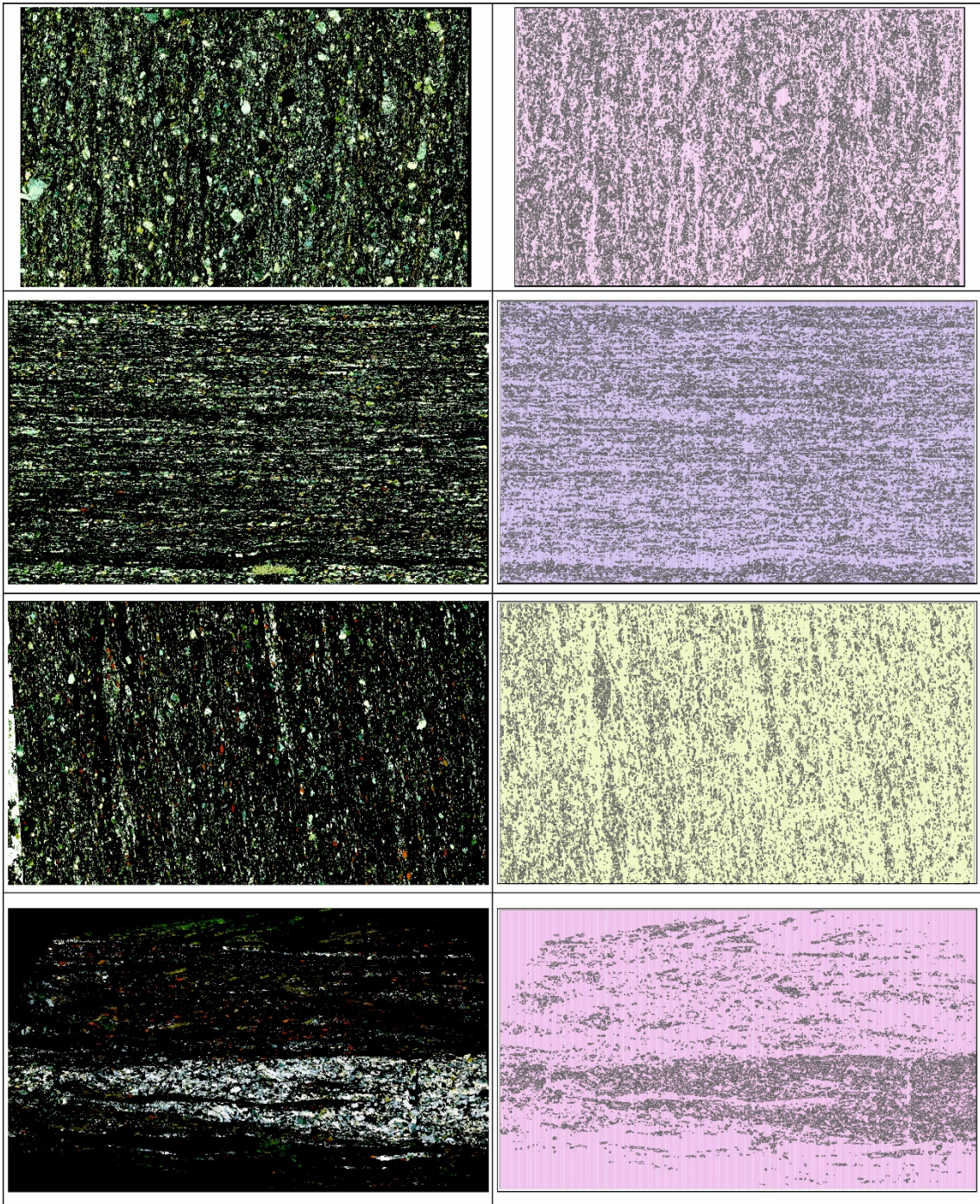
- Tarquini, S., & Favalli, M. (2010). A microscopic information system (MIS) for petrographic analysis. *Computers and Geosciences*, *36*, 665–674.
- Thomson, S. N. (1998). Assessing the nature of tectonic contacts using fission-tracks thermochronology: an example from the Calabrian arc, southern Italy. *Terra Nova*, *10*, 32-36.
- Tinkham, D. K., & Ghent, E. D. (2005). XRMapAnal: a program for analysis of quantitative X-ray maps. *American Mineralogist*, *90*, 737–744.
- Tirone, M., & Ganguly, J. (2010). Garnet compositions as recorders of P-T-t history of metamorphic rocks. *Gondwana Research*. doi:doi:10.1016/j.gr.2009.12.010
- Togami, S., Takano, M., & Kumazawa, M. (2000). An algorithm for the transformation of XRF images into mineral-distribution maps. *Canadian Mineralogist*, *38*, 1283–1294.
- Trial, A. F., & Spera, F. J. (1994). Measuring the multicomponent diffusion matrix: experimental design and data analysis for silicate melts. *Geochimica et Cosmochimica Acta*, *58*, 3769-3783.
- Tullis, J. (2002). Deformation of granitic rocks: Experimental studies and natural examples. *Reviews in Mineralogy and Geochemistry*, *51*.
- Vai, G. B. (1992). Il segmento Calabro-Peloritano dell'Orogene Ercinico. Disaggregazione palinspastica. *Bollettino della Società Geologica Italiana*, *111*, 109-121.
- Vidal, P. Æ.-P.-J. (2009). Diffusion of divalent cations in garnet: multi-couple experiments. *Contribution to Mineralogy and Petrology*.
- Von Raumer, J., Stampfli, G. M., & Bussy, F. (2003). Gondwana derived microcontinents - the constituents of the Variscan and Alpine collisional orogens. *Tectonophysics*, *365*, 7-22.
- Watson, E. B., & Baxter, E. F. (2007). Diffusion in solid-earth systems. *Earth and Planetary Science Letters*, *253*, 307–327.
- Willoughby, A. F. (1978). Atomic Diffusion in Semiconductors. *Reports on Progress in Physics*, *41*, 1665–1705.
- Woodsworth, G. J. (1977). Homogenization of zoned garnets from pelitic schists. *Canadian Mineralogist*, *15*, 230-242.
- Zappalà, L. (2014). Analisi ed implementazione di metodi geomatici per l'elaborazione di dati geopetrologici interoperabilità, geostatistica e classificazione di immagini multispettrali a raggi x. *PhD Thesis*. Catania, Sicilia, Italia.
- Zeh, A. (2006). Calculation of garnet fractionation in metamorphic rocks, with application to a flat-top, Y-rich garnet population from the Ruhla Crystalline Complex, Central Germany. *Journal of Petrology*, *47*, 2335–2356.

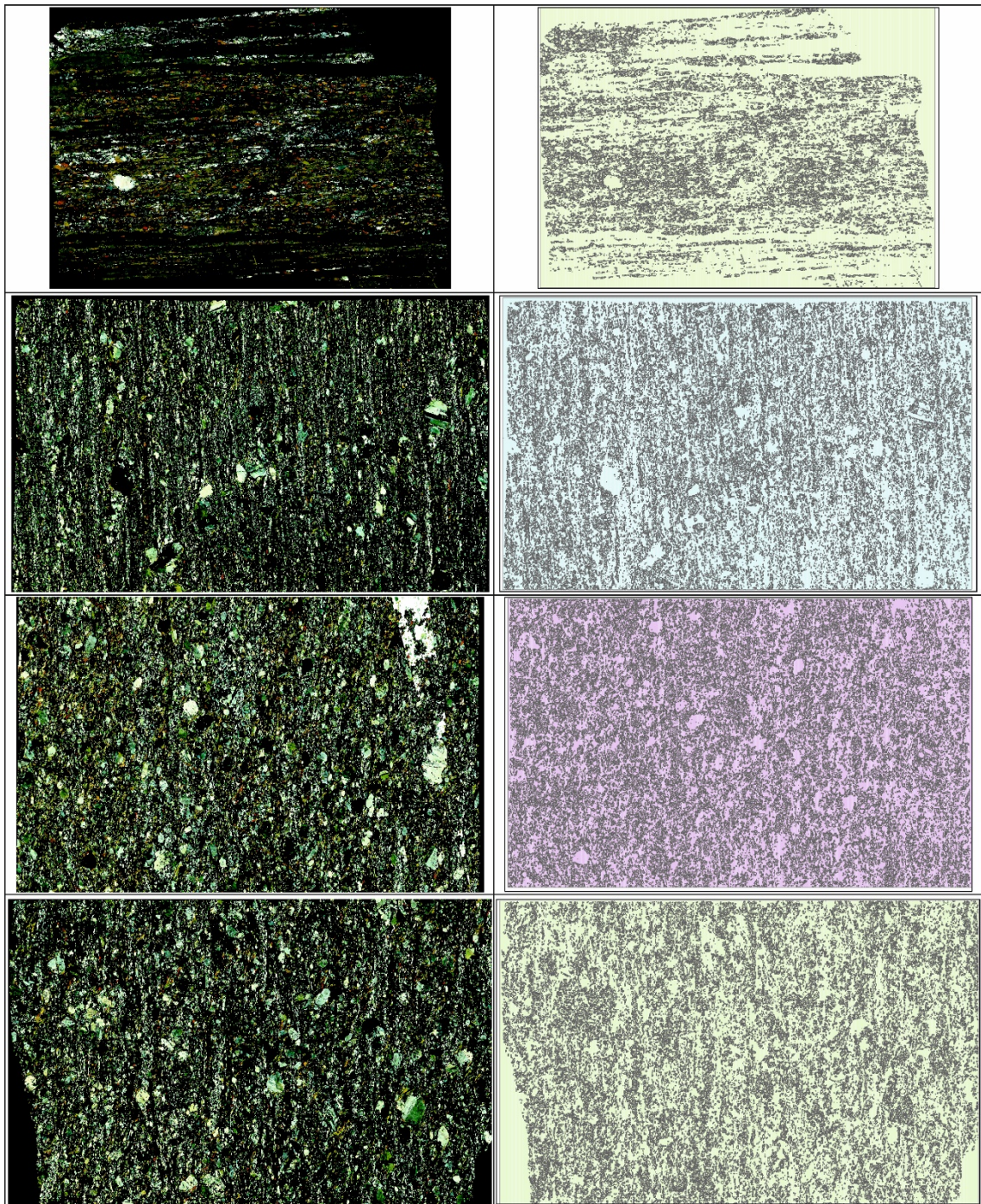
-
- Zhang, R. Y., Jahn, B. M., Chiu, J. G., Chu, H. Y., Chung, S. L., Li, T. F., & Lo, C. H. (2010). *Chemical Geology*, 276, 69-87.
- Zhang, Y. (1994). Reaction kinetics, geospeedometry, and relaxation theory. *Earth and Planetary Science Letter*, 122, 373-391.
- Zhang, Y. (2010). Diffusion in minerals and melts: Theoretical background. *Reviews in Mineralogy and Geochemistry*, 72, 5-59.
- Zuluaga, C. A., Stowell, H. H., & Tinkham, D. K. (2005). The effect of zoned garnet on metapelite pseudosection topology and calculated metamorphic P-T paths. *American Mineralogist*, 90, 1619-1628.

Appendices

APPENDIX A1 – Grain size detection of thin sections





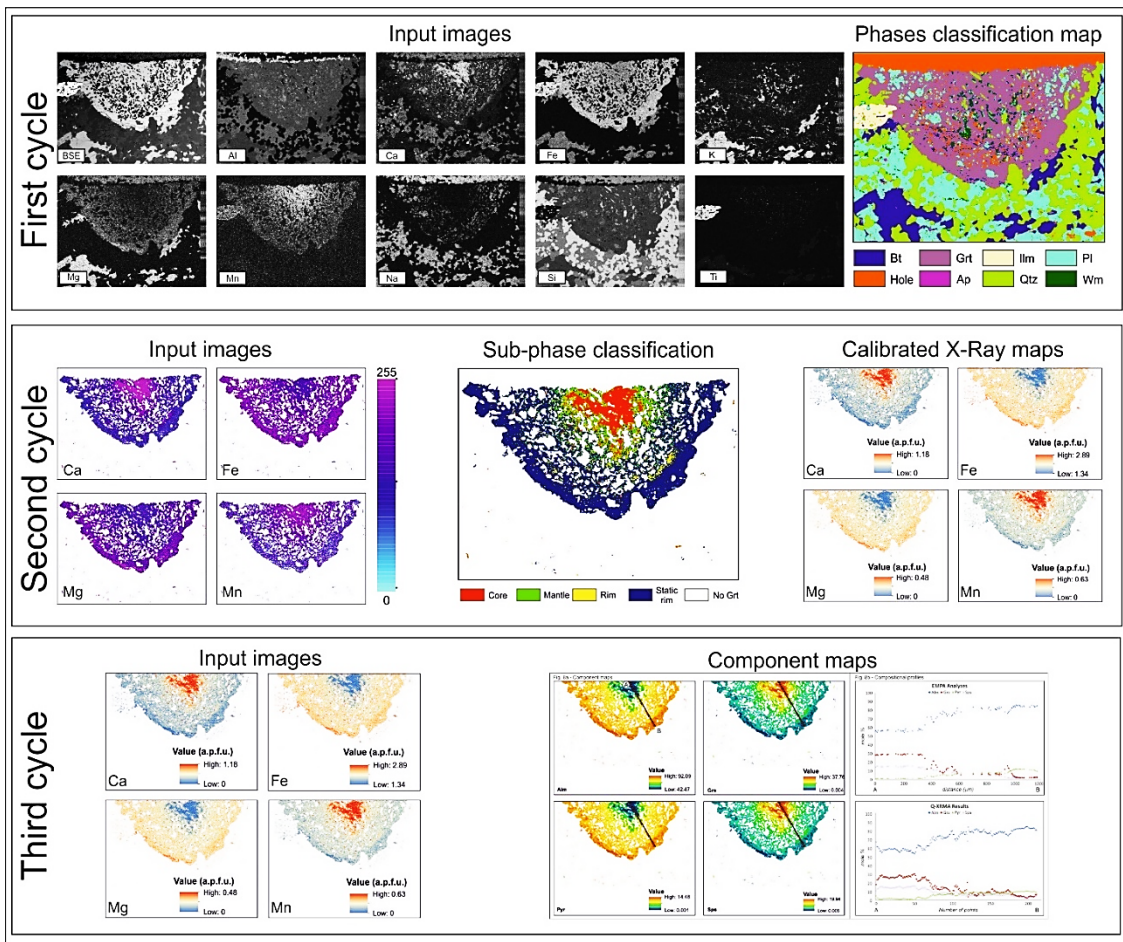


APPENDIX B1 – Quantitative X-ray Map Analyser User’s Guide

Q-XRMA - User’s Guide

Quantitative X-ray Map Analyser

GIS-based tool for the statistical handling of X-ray Maps



Summary

REQUIREMENT OF THE SYSTEM AND FORMER USER DEFINED SPECIFICATION.....	192
Installation procedure:	192
FIRST CYCLE	193
Pre-filtering phase	197
RGB synthesis and multivariate statistical analysis.....	199
SECOND CYCLE.....	206
Map algebra operation.....	207
Maximum Likelihood Classification of a mineral phase	207
Maps calibration	210
THIRD CYCLE	216
QUESTION AND ANSWERS	218

Requirement of the system and former user defined specification

This document provides an operative guide useful to perform Quantitative X-ray Map analysis using a Python script executable also from MS-DOS command prompt, largely based on ArcGIS® functions, without graphical user interface. The used ArcGIS® version (9.3 or later) should have ArcInfo license and support spatial analysis and data management extensions.

This application born to statistically handle several types of multispectral images such as the X-ray maps which represent a multidimensional illustration of the elemental distribution within a selected domain (Fig B1). The procedure provides three different cycles of analysis, each of them subdivided into several principal analytical steps, moreover, the second one provides also the possibility to predict the atomic concentration of a selected element within a specific classified mineral phase (Figs. B2-3). The aim of the first analytical cycle (First Cycle) is to analyse the entire selected domain, finalising the procedure by means of the classification of recognised mineral and non-mineral phases represented by means of arbitrary colours, useful to make, for instance, a mineral distribution map of selected domain. This first cycle is subdivided into two former steps of image processing consisting of a potential pre-filtering stage, followed by an RGB synthesis procedure and by the principal component analysis (PCA). The two latter steps of the first analytical cycle are characterised by the image classification procedure by means of a maximum likelihood classification (MLC) algorithm, successively potentially terminable with a post-filtering stage, useful to minimise the weight of the isolated pixel (Fig. B2). The second one (Second Cycle) consist of two sub-procedures (Fig. B3): i) the first one has the aim to deepen the analysis of a selected class, previously recognised, in order to classify further potential subdivisions, such as those responsible of mineral zonation; ii) the second one have the aim to predict the atomic concentration of the investigated element within a selected class by means a multilinear regression statistical approach. This analytical cycle is subdivided in a preliminary step of map algebra operation, aiming to the extraction of the selected classified class (e.g. a mineral phase) (Fig. B3). This is necessary to re-launch the multivariate statistical analytical step on a new X-ray maps array, representative just of the elemental distribution within a single detected phase. A latter stage of a maximum likelihood image classification followed by a potential post-filtering stage is also present in the final steps of this second cycle (Fig. B3).

Finally, the last cycle (Third Cycle) allows the user to compute some standard component maps for a set of common minerals or create its own component map by choosing single elements manually, through map algebra operations (Fig. B4).

The required software configuration provides the installation of ArcGIS® 9.3 or later accompanied by the presence of a 2.5 (for ArcGIS 9.3) or 2.7 (for ArcGIS 10.X) Python version.

Installation procedure:

Unzip “Q-XRMA.zip” in the root directory to obtain a path like “c:\ Q-XRMA\”.

Then it is necessary to copy and paste the pre-configured file “q_xrma.cfg” within the

prog directory as a function of the ArcGIS® version installed on the computer. As an alternative, the user may set the first part of configuration file q_xrma.cfg. Open it with a text-pad, thus edit the three parameters as a function of your ArcGIS® personal configuration, for instance, as follow:

```
#DOS Parameters
[DOS_info]
Dos_Shell_Cols=150
Dos_Shell_Lines=1000

#Path for ArcGis
[ARCGIS_info]
AGpath= C:/Program Files (x86)/ArcGIS/
Tbx_SA_path= C:/Program Files (x86)/ArcGIS/ArcToolbox/Toolboxes/Spatial Analyst
Tools.tbx
Tbx_DM_path=C:/Program Files (x86) /ArcGIS/ArcToolbox/Toolboxes/Data
Management Tools.tbx

#Path for data workspace
[XRMA_info]
DataPath=c:/Q-XRMA/data/
```

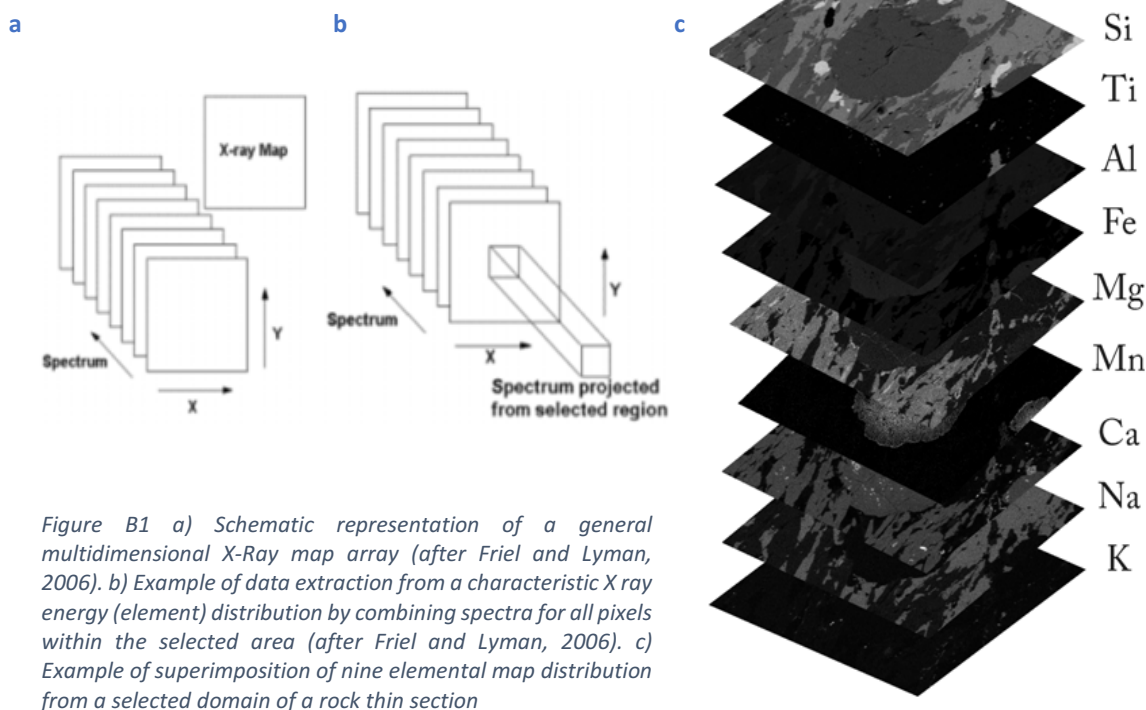


Figure B1 a) Schematic representation of a general multidimensional X-Ray map array (after Friel and Lyman, 2006). b) Example of data extraction from a characteristic X ray energy (element) distribution by combining spectra for all pixels within the selected area (after Friel and Lyman, 2006). c) Example of superimposition of nine elemental map distribution from a selected domain of a rock thin section

First Cycle

Before to begin, the user should create an input images workspace data path (Fig. B5). Thus, it is necessary to put X-ray maps in 8 bits “*.tif” format within “c:\Q-

XRMA\DataPath\MyWorkspace\input_img”, possibly after have renamed each image with the name of the specific element (e.g. Al.tif). Then open DOS cmd and digit:

1. “cd Python25”
2. “python c:\ Q-XRMA\prog\Q-XRMA.py”

In this way, the application starts recognising the operative system and the username.

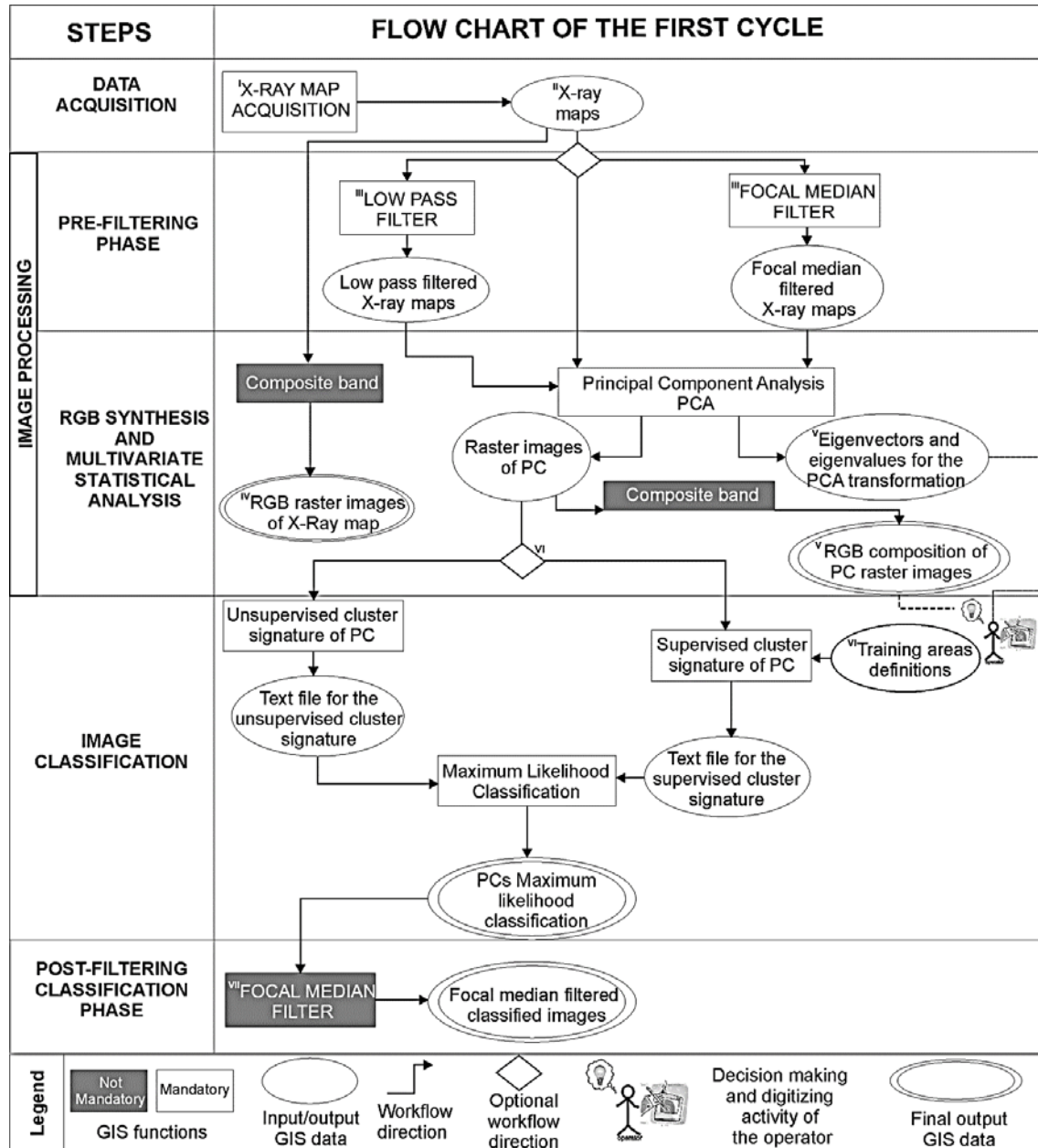


Figure B2 Flow chart of the first cycle of the geoprocessing procedure. Details of the procedure: I) SEM magnification has to be set in order to obtain a pixel dimension close to the double size of the beam radius of the used microprobe; II) the total number and dimension of the X-ray maps can be freely set; III) pre-classification filtering stage is an optional operation, useful for minimising the potential background noise of X-ray maps. A low-pass filter calculates the average value for a pixel centered around eight immediate neighbours. A focal median filter allows to replace the original pixel values calculated as the median of the pixel-values around a rectangular or circular perimeter of arbitrary dimension; IV) the procedure allows us optionally to compose all the possible RGB combinations with or without permutations of the original element channels; V) the analysis of the eigenvector matrix obtained from PCA transformation permits to easily analyze the variance of the multidimensional space represented by PCA analysis, allowing the operator to choose the best RGB combination for discrimination of the constituent phases; VI) after the decorrelation of the original X-ray maps and subsequent combination of the new PCs, it is possible to choose an unsupervised and/or supervised classification procedure. The first one is based upon an automated iso-cluster approach. The second one upon a semi-assisted procedure working by means of the definition of polygonal training areas digitized by the operator, characterised by an ascertained classification; VII) classified images can be successively filtered to enhance the segmentation.

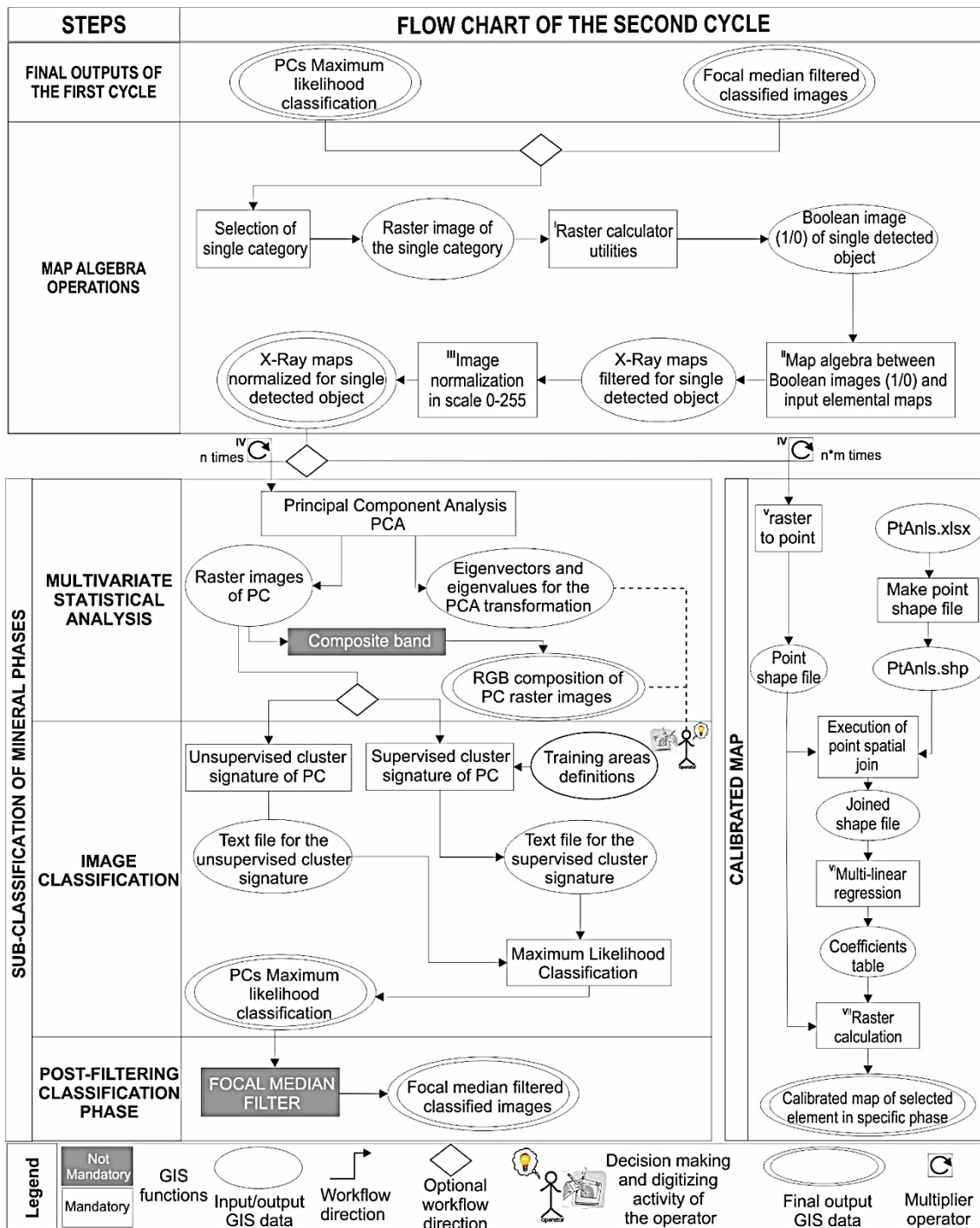


Figure B3 Flow chart of the second cycle of the geoprocessing procedure. Details of the procedure: I) the raster calculator utilities are a pixel-based tools package useful to manage raster images. These were here used for the calculation of a series of Boolean images (i.e. composed only of pixels with a value of one or zero) aiming to obtain new sets of the original X-ray maps filtered and normalized per detected class (e.g. mineral phase); II) the application of a multilinear regression algorithm between normalized image per detected class and laboratory control spot analyses to obtain new sets of calibrated X-ray maps. The procedure permits us to choose the type of primary X-ray maps (i.e. Original; Low Pass filtered; Focal median Filtered); III) the procedure can be potentially repeated n times for a second cycle of classification or $n*m$ times for the calibration procedure within the single mineral phase, where n is the number of phases classified in the first cycle, and m is the number of elements of the original X-ray map; IV) input data set for calibration provides the preliminary transformation of the original pixels to a point vector file containing as information the pixel value; V) multilinear regression calculates regression coefficients for the element investigated a table format file where store results.; VI) map algebra operation between coefficients calculated and the pixel intensity values of the original X-ray maps.

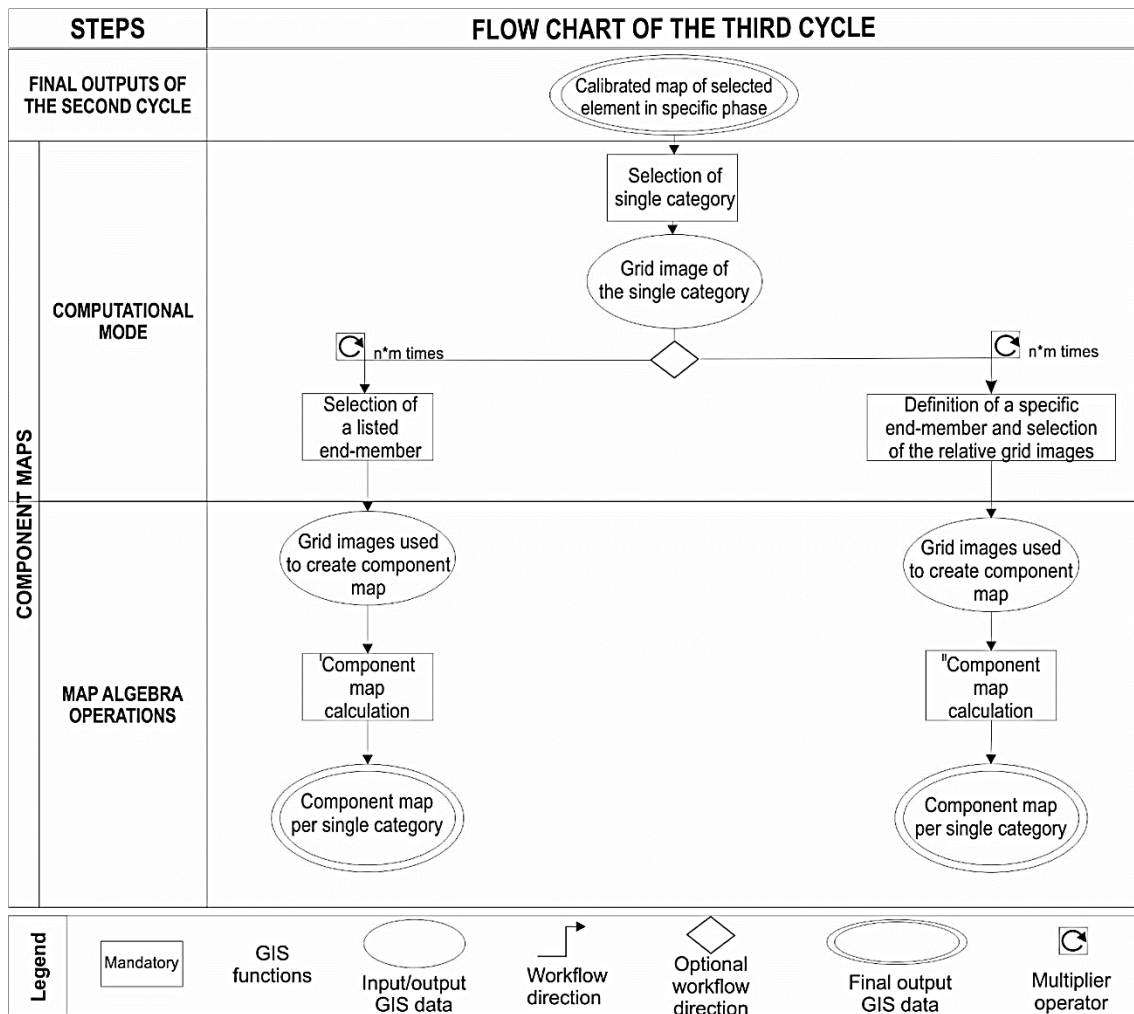


Figure B4 Flow chart of the third cycle of the geoprocessing procedure. Details of the procedure: I) the component map calculation specific for an end-member proposed by the tool per single detected class; II) the component map calculation characteristic for an end-member defined by the user by choosing specific calibrated X-Ray images.

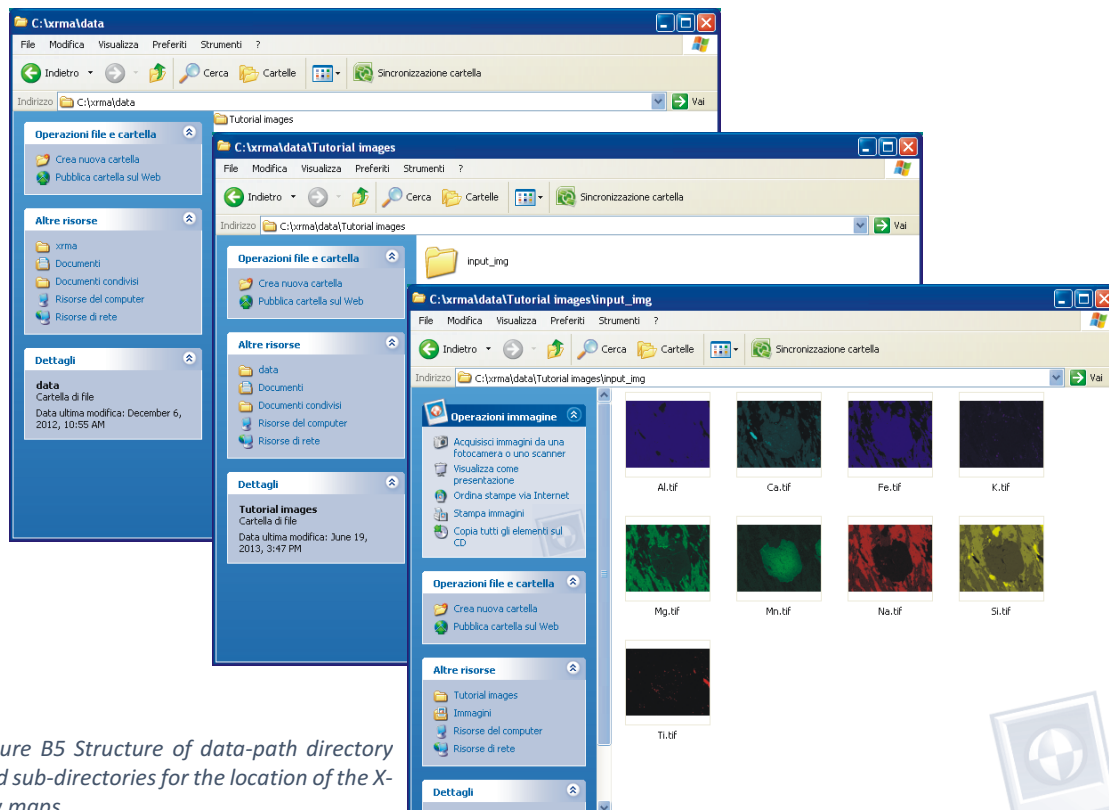


Figure B5 Structure of data-path directory and sub-directories for the location of the X-Ray maps

Then, begin to work and ask to set the workspace name to identify the user job or alternatively ask to create a new workspace (Fig. B6).

Pre-filtering phase

Following the procedure, once the user has located the images to analyse into subdirectory “c:\Q-XRMA\DataPath\MyWorkSpace\input_img”, he can choose which kind of filter or no-filter (default choice), it needs to be applied in order to reduce the potential instrumental noise, such as those recognizable in the EDS X-ray map (Fig. B7). The Low Pass Filter is applicable if the images appear very noisy. Alternatively, it is possible to apply a statistical filter such as Focal Median with the aim to reduce the weight of the isolated pixels.

In general, all the filtering procedures calculates new pixel-values centring, for instance, a specified 3 x 3 matrix (i.e. filter) over each input raster cell (i.e. pixel). As the filter is passed through each cell, the centre is assigned the sum of the products of the cell value and the corresponding operand in the 3 x 3 filter. The output raster cell at the centre of the filter is assigned a new pixel-value based on the following formula:

$$N = Z1*F1 + Z2*F2 + Z3*F3 + \dots + Z9*F9$$

Where N is the final matrix given by the new 3 x 3 matrix where each pixel is given by the product of the filter matrix Z with the original matrix F. When an input raster cell on the edge of the filter has a NoData value, the pixel-value of the cell is substituted for the missing values. On the edges of the raster, the filter lies partially outside the raster. When this occurs, the pixel-value of the cell at the centre of the filter is substituted for the missing values. In particular, a low pass filter smoothes the data by reducing local variation and removing noise calculating the average (mean) value for each 3 x 3 neighbourhood. The effect is that the high and low values within each neighbourhood will be averaged out, reducing the extreme values in the data.

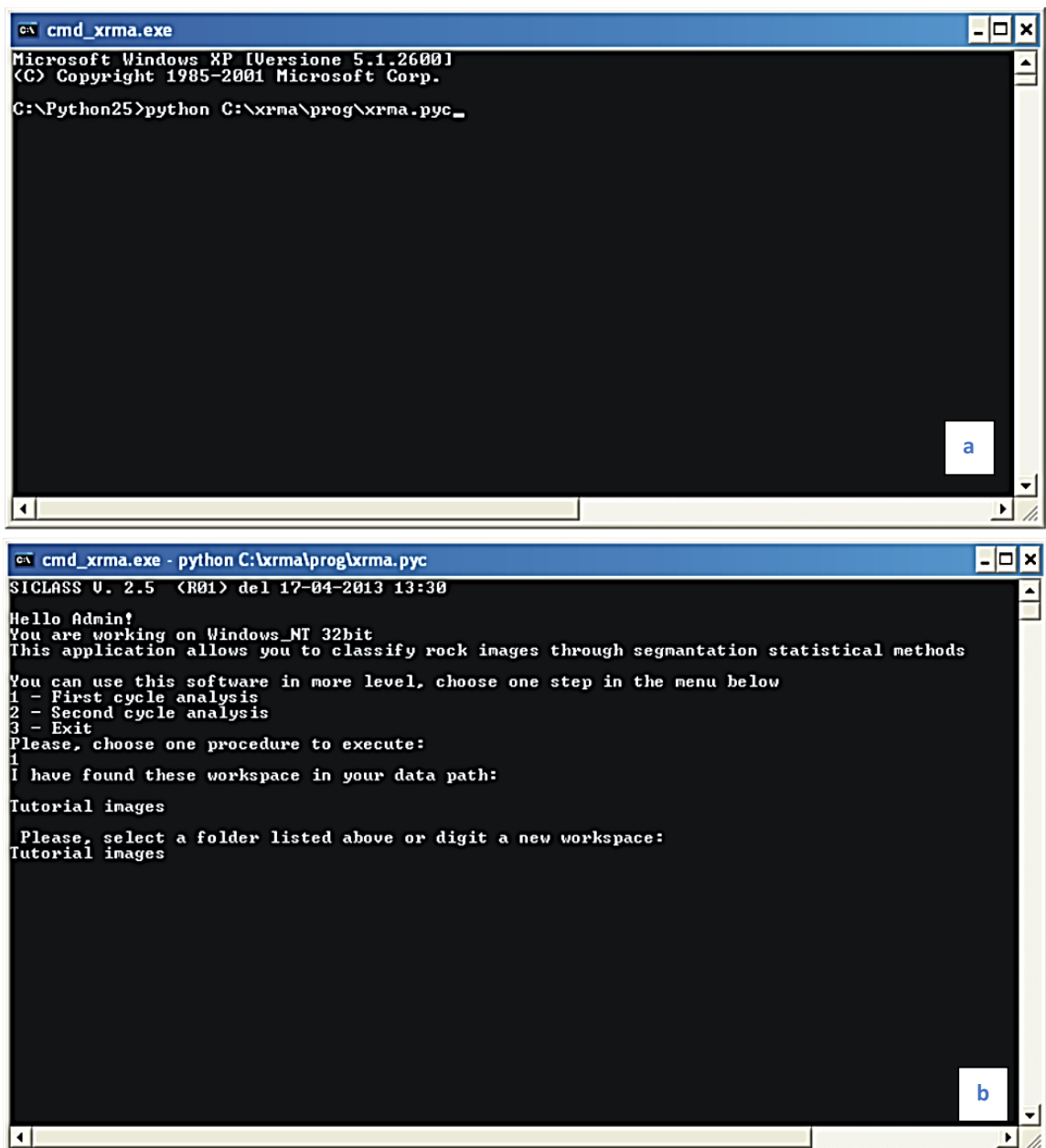
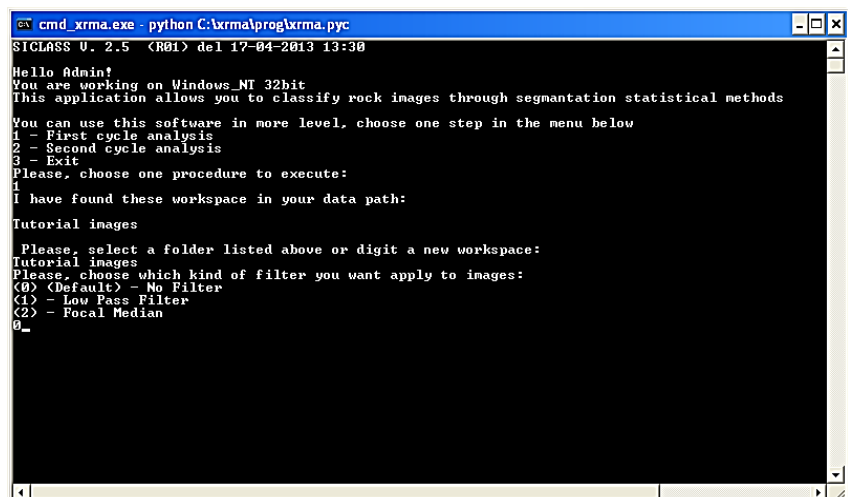


Figure B6 Example of the starting procedural steps of the script: a) starting instruction after opening of the DOS interface; b) choose of the data-path directory

Figure B7 List of the applicable filtering method



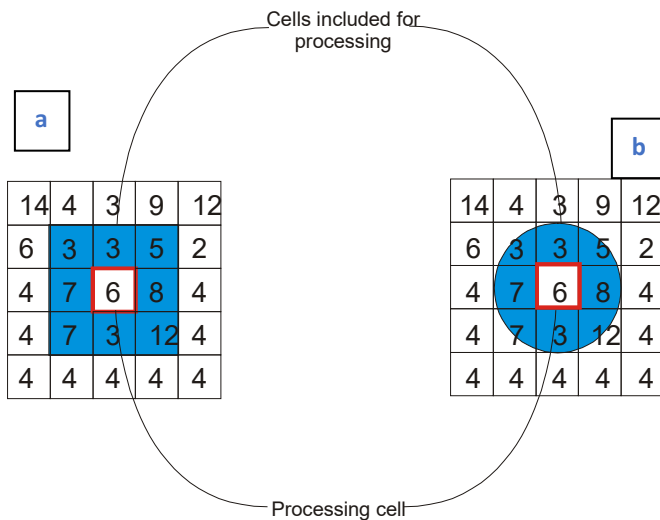


Figure B8 Schematic representation of the focal median principle used in the procedure: a) squared geometry with 3*3 cells per side; b) circled geometry with 3 cells of radius, any cells whose centre falls inside the radius of the circle will be included in processing neighbourhood

RGB synthesis and multivariate statistical analysis

The following operative function of the procedure (Fig. B2) provides the possibility to make the RGB composition of the original X-ray map array making several colour maps. These are used to display a single band raster per each available channel (i.e. one element per channel). In this way, each pixel value is associated with a colour, defined as a set of red, green, and blue (RGB) values (Fig. B9). Since each value has a distinct colour associated with it, it will always display the same way each time you open it in a program that can read a raster with a colour map. Colour maps are capable of handling up to 8-bit data per channel (i.e. 256 colours).

In our procedure, it is possible to choose no RGB composition or it is possible to do all the potential RGB composition following an automatic procedure consisting in a simple combination of the original channels without permutation or in a combination with all possible permutation (Fig. B10). In particular, the simple combination provides all the possible combination of the original images using each element just one time per channel, while combination with permutation provides all the possible combination with the permutation of the primary channels taking care to avoid the combination that use the same channel in two or three different primary colours. To this aim was implemented in python a recursive type algorithm which executes alternatively the two abovementioned functions, invoking in recursion the “Composite Band” function. Results will be automatically stored within the sub-directory: “c:\ Q- XRMA\DataPath\MyWorkSpace\1_FirCycle\out_img\xr_rgb_comb” or “c:\ Q- XRMA\DataPath\MyWorkSpace\1_FirCycle\out_img\xr_rgb_perm”, respectively.

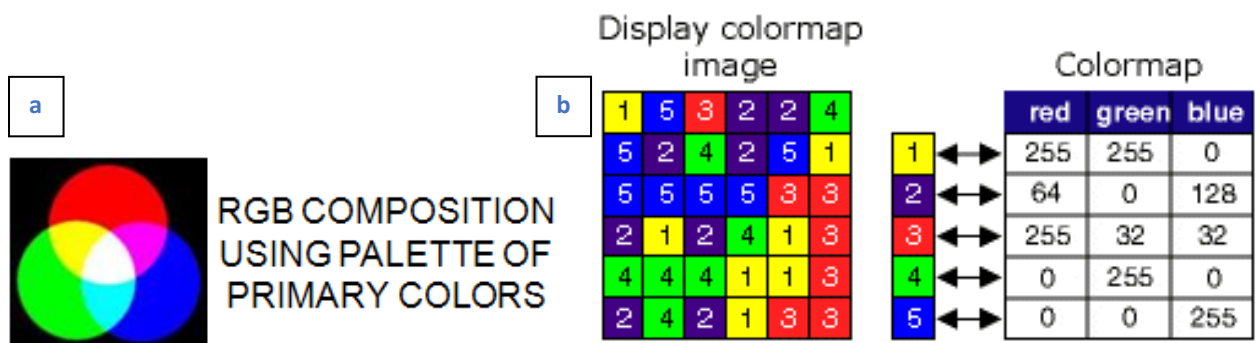


Figure B9 a) Schematic representation of the colour composition using primary colours and b) relative colour composition on a map (After ArcGIS tutorial)

Figure B10 List of the applicable RGB composition of the X-ray map array

```

cmd_xrma.exe - python C:\xrma\prog\xrma.py
X-RAY MAP ANALYZER U. 2.5 (R01) del 18-04-2013 17:30
Hello Admin!
You are working on Windows_NT 32bit
This application allows you to classify mineral phases by means of statistical data process of X-Ray Map
Please select one of the procedure listed below
1 - First cycle
2 - Second cycle
3 - Exit
Please, choose one procedure to execute:
1
I have found these workspace in your data path:
Tutorial images
Please, select a folder listed above or digit a new workspace:
Tutorial images
Please, choose which kind of filter you want apply to images:
(0) (Default) - No Filter
(1) - Low Pass Filter
(2) - Focal Median
0
No filter will be applied
Executing process, please wait....
Total images are: 9
Please, choose one of the operation listed below:
(0) Do not create composite band images of XRayMaps
(1) Create all combination of composite band images of XRayMaps (about 2 minutes wait)
(2) Create all permutation of composite band images of XRayMaps (about 10 minutes wait)
Digit your choice (First time you analyze specimen is not suggested choice (0)):

```

After this last optional operative function, the procedure provides a mandatory function consisting of the principal component analysis of the original set of X-ray map. The PCA is used to transform the data attributes of an original multiband raster, such as our X-ray map array, from the input multivariate attribute space to a new multivariate attribute space whose axes are rotated with respect to the original space (see Fig. B11 as a schematic example). The final result of a PCA is a new multiband raster with the same number of bands as the original raster (one band per axis in the new multivariate space), where the first principal component will have the greatest variance, the second will show the second most variance not described by the first, and so forth (Fig. B11). A further output of the PCA consists in the construction of the matrix of the eigenvalues and eigenvectors reported in the second row and one per column, respectively (see Table 1). This output can be visualized directly in the shell of the prompt (Fig. B12) or in “*.txt” form at the subdirectory: “c:\Q-XRMA\DataPath\MyWorkspace\1_FirCycle\pca\pca_report”. The columns represent the new axes of the multidimensional coordinate system expressed as vectors oriented respect to the previous primary elemental map. The eigenvalues expressed as the percentage of the total (see row 3 in Table 1), highlights as most of the information is concentrated, in the first three to five principal components. In our case, calculated results concentrate about the 96% of information within the first five principal components. The main reason to transform original data distribution displayed in the n-elemental space to a new multidimensional space represented by PCA is to compress data by eliminating redundancy, emphasize the variance within the bands of a raster, and make the data more interpretable (Fig. B13). This can aid the operator in recognizing the potential inter-dependence (e.g. the specific covariance) between elemental variability linked, for instance, with the recognition of the mineral phases (Table B1).

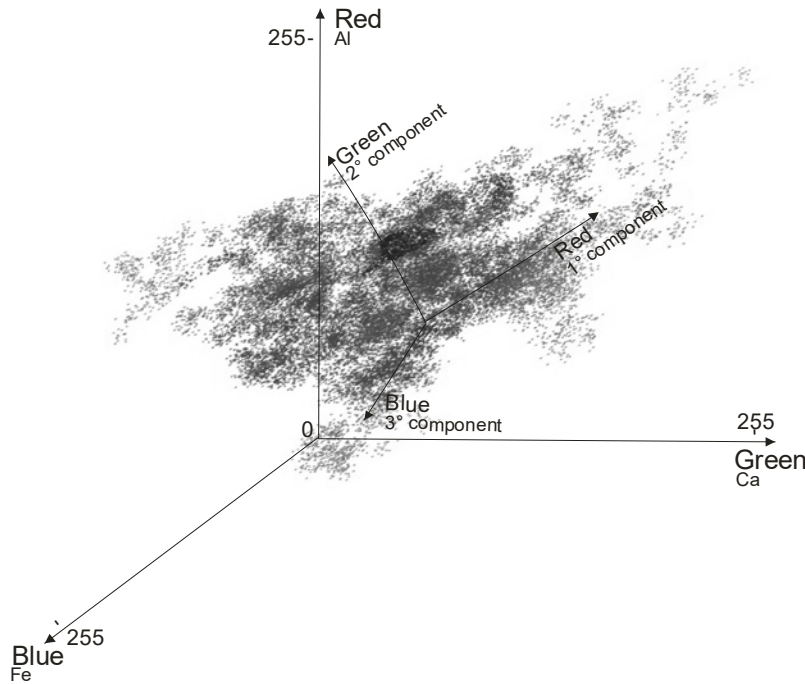


Figure B11 Example of schematic 3D representation of the decorrelation function known as principal component analysis, useful to re-project pixel values variability into a new coordinate system given by the axes of the principal components. This new coordinate system is able to minimize the redundancy (i.e. the superposition) of the original distribution, emphasizing class separability

```

Administrator: cmd_X-Ray_Map - python C:\xrma\prog\xrma.py
#
# Output raster(s):
# c:\xrma\data\XC02_1\pca\pca_
#
# COVARIANCE MATRIX
#
# Layer 1 2 3 4 5 6 7 8 9
#
# 1 251.38825 -95.95526 -42.82403 -5.15130 -67.64278 7.58302 102.63741 17.42342 -39.74739
# 2 -95.95526 332.88484 159.04396 6.13342 70.24043 20.43400 -162.14833 -369.77670 19.16644
# 3 -42.82403 159.04396 252.30149 4.76127 56.19442 35.15273 -167.56525 -380.60189 27.80159
# 4 -5.15130 6.13342 4.76127 10.11884 6.14789 -0.33847 -6.99778 -15.43286 1.01011
# 5 -67.64278 70.24043 56.18442 6.14789 118.39853 -0.53844 -62.09334 -123.39190 -5.45999
# 6 7.58302 20.43400 35.15273 -0.33847 -0.53844 13.96769 -22.23552 -51.71863 1.79274
# 7 102.63741 -162.14833 -167.56525 -6.99778 -62.09334 -22.23552 182.79166 244.14255 -17.06932
# 8 17.42342 -369.77670 -380.60189 -15.43286 -123.39190 -51.71863 244.14255 967.97512 -66.61902
# 9 -39.74739 19.16644 27.80159 1.01011 -5.45999 1.79274 -17.06932 -66.61902 82.99999
#
# CORRELATION MATRIX
#
# Layer 1 2 3 4 5 6 7 8 9
#
# 1 1.00000 -0.33170 -0.16687 -0.10214 -0.39208 0.12797 0.47880 0.03532 -0.27517
# 2 -0.33170 1.00000 0.54880 0.19568 -0.35381 0.29967 -0.65734 -0.65142 0.11531
# 3 -0.16687 0.54880 1.00000 0.09423 0.32461 0.59216 -0.78827 -0.77016 0.19212
# 4 -0.10214 0.19568 0.09423 1.00000 0.17762 0.32949 -0.16291 -0.15394 0.63485
# 5 -0.39208 0.35381 0.32461 0.17762 1.00000 -0.20966 -0.42288 -0.36449 -0.05508
# 6 0.12797 0.29967 0.59216 -0.02847 -0.20966 1.00000 -0.44805 -0.44472 0.05265
# 7 0.47880 -0.65734 -0.78827 -0.16291 -0.42288 -0.44805 1.00000 0.58041 -0.13858
# 8 0.03532 -0.65142 -0.77016 -0.15394 -0.36449 -0.44472 0.58041 1.00000 -0.23503
# 9 -0.27517 0.11531 0.19212 0.63485 -0.05508 0.05265 -0.13858 -0.23503 1.00000
#
# EIGENVALUES AND EIGENVECTORS
#
# Number of Input Layers 9
# Number of Principal Component Layers 9
#
# PC Layer 1 2 3 4 5 6 7 8 9
#
# Eigenvalues 1428.00556 344.83967 138.59033 115.68157 102.36745 42.61376 25.67704 9.38499 5.66524
#
# Eigenvectors
# Input Layer
# 1 0.08765 0.78185 0.23510 0.33410 0.12336 0.40632 -0.18532 -0.00258 -0.02681
# 2 -0.37219 -0.30133 0.81367 0.13562 -0.14712 0.19545 0.15836 0.03826 0.00180
# 3 -0.35784 -0.01600 -0.42558 0.54129 -0.01954 0.17605 0.58713 0.09479 -0.11182
# 4 -0.01368 -0.01099 -0.01066 -0.02668 0.03121 -0.00450 -0.13077 0.98592 0.09343
# 5 -0.12700 -0.21122 -0.07579 -0.26982 0.76820 0.48917 0.02861 -0.04657 0.16949
# 6 -0.04638 0.04079 -0.03408 0.16938 -0.10469 -0.08689 0.01273 -0.08328 0.96991
# 7 0.26795 0.32060 0.17324 -0.47562 -0.04029 -0.02610 0.74345 0.08851 0.07963
# 8 0.29277 -0.38183 0.07954 0.37509 -0.00487 0.25976 0.10396 0.03143 0.01521
# 9 -0.05769 -0.00152 -0.00156 -0.32911 -0.59920 0.07142 -0.11938 -0.01106 0.04491
#
# ['1' Al', '2' Ca', '3' Fe', '4' K', '5' Mg', '6' Mn', '7' Na', '8' Si', '9' Ti']
# Analyze matrix and select which image you need to include in your classification process
# Choose if you want select some PCA or include all: (S=Selected; 0=all)
    
```

Figure B12 Visualization of the calculated covariance and correlation matrix within the prompt of the procedure. These are at the base for the calculation of the eigenvalues and eigenvectors matrix, which report, one per column, the coordinates of the new rotated axes representing the principal components.

Table B1: Example of calculated eigenvectors and eigenvalues through the principal component analysis with relative elemental and mineral recognition per eigenvector

Principal Components	1 th	2 nd	3 rd	4 th	5 th	6 th	7 th	8 th	9 th
Eigenvalues	1428.0	344.83 9	138.590 33	115.6815 7	102.37	42.61376	25.677 0	9.385	5.665
Eigenvalues %	64.53	15.58	6.263	5.22	4.62	1.92	1.16	0.42	0.25
Element	Eigenvectors								
Al	0.0876	0.781 05	0.2351	0.3341	0.1233	0.40632	- 0.1853	-0.003	-0.027
Ca	-0.377	0.301 8	0.81367	0.13562	-0.147	0.1964	0.1583	0.0302	0.002
Fe	-0.358	-0.016	-0.42558	0.54129	-0.02	0.17605	0.5871	0.0947	-0.112
K	-0.014	0.010 9	-0.0106	-0.0266	0.0312	-0.0045	- 0.1307	0.9859	0.093
Mg	-0.127	0.211 2	-0.07579	-0.26902	0.7682	0.48917	0.0286	-0.046	0.169
Mn	-0.046	0.040 79	-0.03408	0.16938	-0.104	-0.08689	0.0127	-0.083	0.97
Na	0.2679	0.320 6	0.17324	-0.47562	-0.040	-0.0261	0.7434	0.0885	0.08
Si	0.7927	0.381 6	0.07854	0.37509	-0.004	0.25878	0.1039	0.0314	0.015
Ti	-0.058	0.061 5	-0.24156	-0.32911	-0.599	0.67142	- 0.1193	-0.011	0.045
Elemental brightness	Si-Na-Al	Al-Na-Mn	Ca-Al-Na-Si	Fe-Si-Al-Mn-Ca	Mg-Al	Ti-Mg-Al-Si-Ca-Fe	Na-Fe-Ca	K-Fe-Na	Mn-Mg
Mineral recognition	Qtz+Pl	Pl+Grt	Cc+Ap+Ttn	Grt-Qtz	Amph+Chl	Ilm+Chl+Ttn	Pl+FeOx	Wmca	Chl

Mineral phases can be recognised, indeed, because the pixel brightness in the new multidimensional space is due to the eigenvector orientation values ranging from -1 (pure black) to 1 (pure white) (Table B1) (Fig. B13). For instance, in the first principal component, the brightest value is given by Si, which accounts for 0.792, followed by Na (0.269) and Al (0.087) (Table 1) (Fig. B13b). In this case, is then reliable that the major contribution to the final brightness is given by those pixels representative for quartz and albite. The following second principal component is due instead by the fundamental elemental contribution of Al – Na – Mn, emphasizing the visualization of albite and garnet (Table B1) (Fig. B13b). This new graphical representation permits then to emphasize the maximum separability between recognisable classes, because most of the information can be directly visualized in the first three to five principal components. In this way, the RGB synthesis of three selected principal components is majorly informative than the variability expressed from a maximum of three elements per RGB synthesis, usable for the composition of the elemental channel (Fig. B13a).

In the following operative function, the prompt asks the user to produce or not a series of RGB combination of the new principal components.

Please, choose one of the operations listed below:

- (0) Do not create composite band images
- (1) Create automatically just one composite band image with PCA123
- (2) Create all combination of composite band images with all PCA (about 2 minutes wait)
- (3) Create all permutation of composite band images with all PCA (about 10 minutes wait)

The output results of this last operation can be visualized in *.tif format in the subdirectory

C:\Q-XRMA\DataPath\MyWorkSpace\1_FirCycle\out_img\rgb_comb
 or
 C:\Q-XRMA\DataPath\MyWorkSpace\1_FirCycle\out_img\rgb_perm
Image classification

First cycle procedure continues with the possibility to make the classification of all recognizable classes present in selected micro-domain. During this processing stage, the prompt asks the operator which kind of classification he wants to execute:

- “U” - Unsupervised Classification, without user interaction. In this case, the algorithm creates a signature file stored in: “C:\Q-XRMA\DataPath\MyWorkSpace\1_FirCycle\sign\isoclus1.gsg” based on an iso-cluster function useful to determine the characteristics of the natural groupings of cells in multidimensional attribute space.
- “S” - Supervised Classification, where the user has to prepare some training areas assisted by the visualization of the original X-ray map array and/or by the new principal components channels, finalized to a partial mineral pre-recognition. This training areas are then used by the signature function to prepare the “signature file” stored in the sub-directory: “C:\Q-XRMA\DataPath\MyWorkSpace\1_FirCycle\sign\signpca_cycle1.gsg”. This file is then used by the Maximum Likelihood Classification (MLC) algorithm, which assumes that each spectral class can be described by a multivariate normal distribution. Therefore, MLC takes advantage of both the mean vectors and the multivariate spreads of each class.

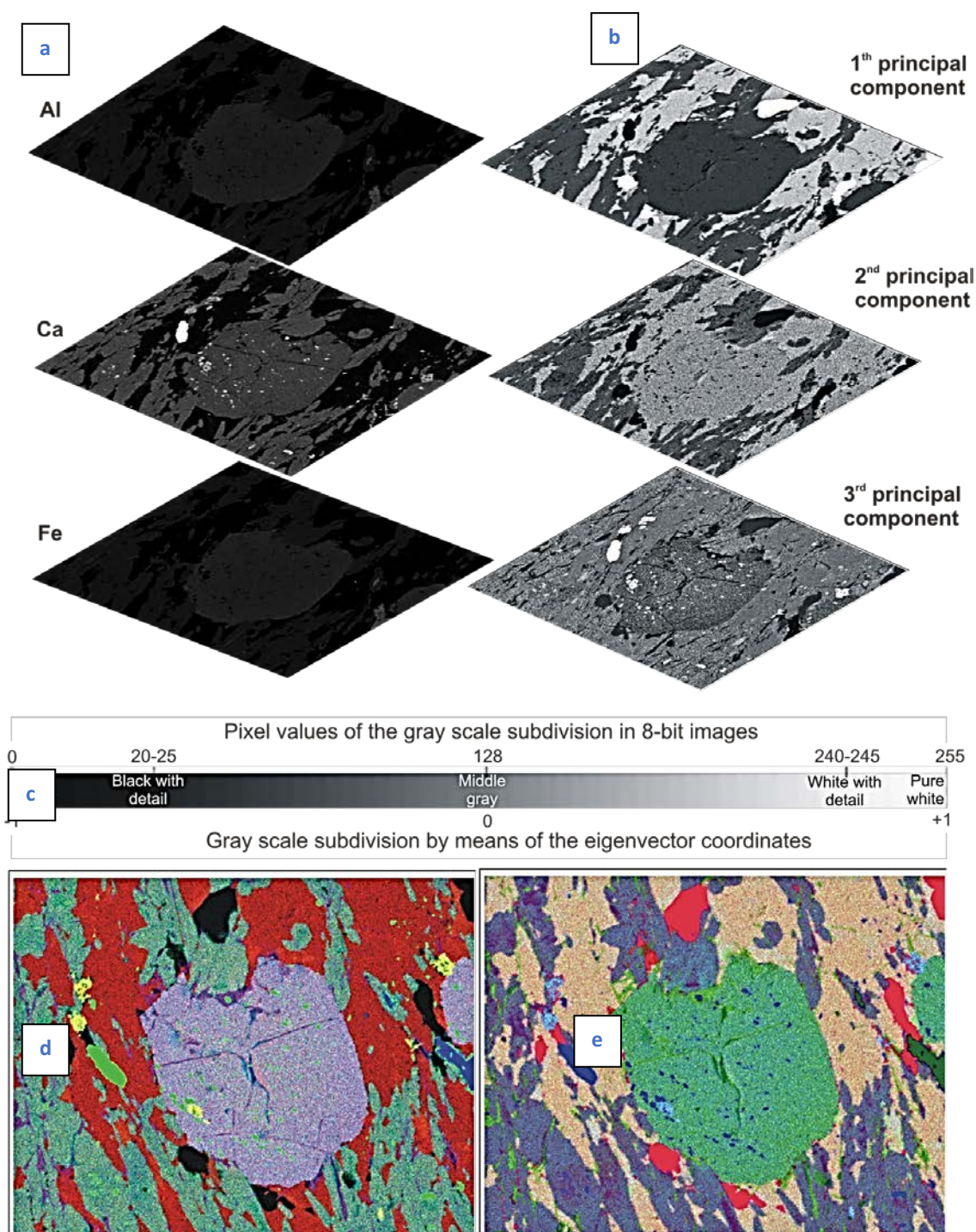


Figure B13: a) Superposition of three elemental channels expressed as gray-scale images; b) Superposition of the first three principal components calculated from the original Al, Ca, Fe, K, Mg, Mn, Na, Si, Ti X-ray maps array; c) Generic gray scale bar of 8-bit images. In the upper side the subdivision is expressed in the 0 (pure black) - 255 (pure white) classical range, in the lower side the subdivision is expressed in the range -1 (pure black) - +1 (pure white) as a function of the eigenvector coordinates of the specific principal component vector; d) RGB composition from Al-CA-Fe primary element map; e) RGB composition of the first three principal components calculated on the basis of the original nine elemental distribution map (i.e. Al, Ca, Fe, K, Mg, Mn, Na, Si, Ti)

```

Administratore cmd_X-Ray_Map - python C:\xrma\prog\xrma.pyc
Choose if you want select some PCA or include all: <S=Selected; A=All>
S
Do you want include PCA image n. 1 ? - Y/N
y
Do you want include PCA image n. 2 ? - Y/N
y
Do you want include PCA image n. 3 ? - Y/N
y
Do you want include PCA image n. 4 ? - Y/N
y
Do you want include PCA image n. 5 ? - Y/N
y
Do you want include PCA image n. 6 ? - Y/N
N
Do you want include PCA image n. 7 ? - Y/N
N
Do you want include PCA image n. 8 ? - Y/N
N
Do you want include PCA image n. 9 ? - Y/N
N

For <Supervised Classification> digit <S> else for <Unsupervised Classification> digit <U>
Please, digit how many phases you evaluate in your section: 7
...executing IsoCluster, please wait
Executing Maximum Likelihood Classification...
0.0
0.005
0.01
0.025
0.05
0.1
0.25
0.5
0.75
0.9
0.95
0.975
0.99
0.995
Choose one value of Reject Fraction as listed above or press Enter to accept Default: 0.005
Reject Fraction is: 0.005
EQUAL
SAMPLE
FILE
Choose one valid value of Priority as listed above or Press Enter to accept Default: SAMPLE
please wait ...

Unsupervised MLC successfully executed
Do you want apply a Focal Median Filter to Classified Image? Y = Yes; N = No - Y
For <Rectangle Area> digit <R> else for <Circle Area> digit <C> <Default = C>
Digit a number from 1 to 9 for radius. <Default = 2>
Do you want continue your analysis with Supervised Classification? Y/N
This is the first stage of your supervised analysis. Creating files and directories...
This is the first stage of your supervised analysis. Creating files and directories...
n. 0 areas detected
Training Areas Shape File already exists but is empty.
You have to design areas if you want run supervised classification, then press Enter or Ctrl+C for exit_

```

Figure B14 Visualization of the prompt interface reporting the selected choice of the principal components considered for the MLC, followed by the unsupervised classification procedural step characterised by the classification default options relatively to the reject factor (i.e. 0.005) and priority classification mode (i.e. SAMPLE). The following supervised classification mode allow to create the training areas.

If user digit “U”:

system performs an automatic classification of the selected X-ray map set, asking simple information to complete the cycle, such as the number of PC images to include in the calculation thread, the approximate number of expected classes of subdivisions (e.g. mineral phases), the rejected fraction of unclassified pixels, how a priori probabilities will be determined¹ (Fig. B14). The result of the unsupervised classification procedure will be then stored in the sub-directory “c:\Q-XRMA\DataPath\MyWorkspace\1_FirCycle\mlc\mlc_uns_pca”.

The output image of unsupervised MLC function can be successively filtered with a post classification focal median filter, with the potential aim to obtain a balanced image without the presence of noisy pixels. This last output can be found at the sub-directory

“c:\Q-XRMA\DataPath\MyWorkspace\1_FirCycle\mlc\mlc_uns_focal” (Fig. B15).

¹ When the EQUAL a priori option is specified, each cell is classified to the class to which it has the highest probability of being a member. By choosing the SAMPLE a priori option, the a priori probabilities assigned to all classes sampled in the input signature file will be proportional to the number of cells captured in each signature.

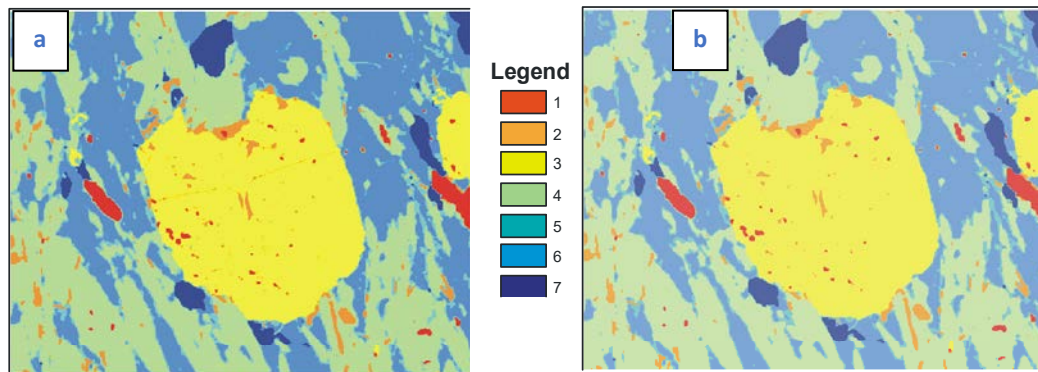


Figure B15 Unsupervised classification results: a) without focal median post-classification filtering; b) with focal median post-classification filtering

If user digit “S”:

system verifies if the directory “c:\Q-
XRMA\DataPath\MyWorkspace\1_FirCycle\input_vect” is empty or contains valid training areas files, so in this case continues his calculation. Otherwise (conversely), the system asks user to create training areas, remaining in standby operative mode (Fig. B14).

In order to create training areas, the user has to open ArcMap and edits “TrArea1.shp” placed in “c:\Q-
XRMA\DataPath\MyWorkspace\1_FirCycle\input_vect”. After this step, it is just necessary press enter to continue the procedure. At the end of this part of the procedure, the command prompt ultimate the supervised classification and obtain a classified image called mlc_1_sup. Also in this case the output image of MLC function can be filtered with a focal median post-processing filter, so it’s possible to obtain a balanced image without the presence of noisily pixels stored into sub-directory: “c:\Q-
XRMA\DataPath\MyWorkspace\1_FirCycle\mlc\mlc_sup_focal” (Fig. B16).

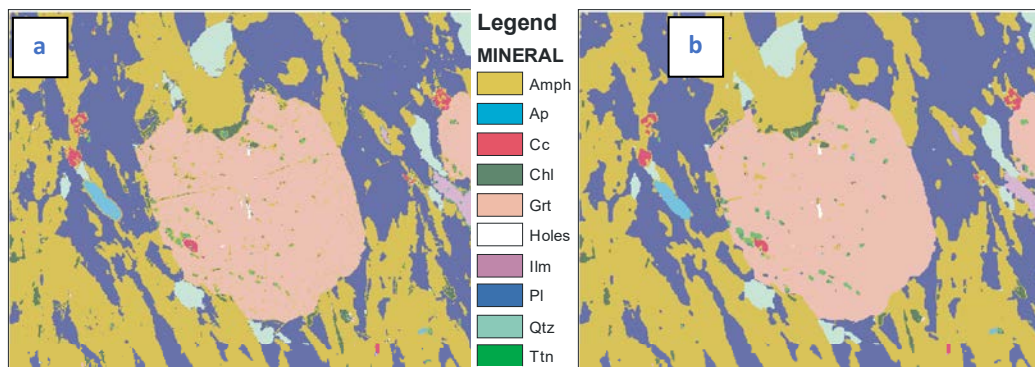


Figure B16 Supervised classification results: a) without focal median post-classification filtering; b) with focal median post-classification filtering

Second Cycle

In this case, the procedure allows the user to investigate within an arbitrarily selected phase recognised during the first cycle with more detail. At the end of the first cycle, it is indeed possible to use the results of the MLC, in order to select one or more phases to highlight for instance the potential existence of chemical gradient within a mineral phase,

such as mineral zonation. At the base of the second analytical cycle, there is the creation, via map algebra operations, of new sets of X-ray maps characteristics per single detected phase. After this preliminary operative step, the cycle proceeds with two distinct analytical possibilities. The first one (Maximum Likelihood Classification of a mineral phase) allows making the sub-classification of a selected mineral phase, while the second one (Maps calibration) calculates the atomic concentration of an element within a selected phase (Fig. B3). In this view, the procedure can be potentially repeated n times for the sub-classification procedure or $n*m$ times for the computation of the elemental atomic concentration expressed as atomic per formula unit (a.p.f.u.) within a single mineral phase, where n is the number of phases classified during the first cycle, while m is the number of the elements detected from the original X-ray maps.

Map algebra operation

This function provides a pixel-based raster calculation useful to obtain a series of new X-ray maps array per single detected object, aiming to focus on the subsequent operative steps, the pixels relatively to one single phase. After the selection of the workspace, the system creates a set of image files representing each chemical element in each mineral phase, applying a map algebra operation and then shows a list of the distinct mineral phases identified in the first cycle (Fig. B17). This procedure starts to calculate a series of Boolean images (i.e. composed only by pixel with the value of 1 or 0). These are useful to obtain the new sets of filtered X-ray maps, via the product between Boolean images per single detected class and the primary X-ray maps, (i.e. original, low pass filtered or focal median filtered) (Fig. B17). These last outputs are successively subjected to an operation of normalization to be sure each pixel has the real and not stretched intensity value in a scale of 0-255 values.

To do this, the prompt asks the user if prefer to make the new sets of X-rays maps per single detected mineral phase by means of the classes recognized during the maximum likelihood classification procedure or, those classes recognized by the focal median filtered classified image. After this operation, able to produce several sets of new X-ray maps as many as were the original ones (see e-p - element in phase sub-directory), it is possible to choose one phase per time, in order to investigate deeply about it, obtaining more details about potential inner chemical distribution.

Maximum Likelihood Classification of a mineral phase

After the choice of Maximum Likelihood Classification of a mineral phase (Fig. B18), the prompt asks to choose a specific phase where to execute again the principal component analysis on the specific X-ray map array representative for the single selected class (Fig. B18). The next step, is to apply the PCA function for those elements which potentially show the most variable elemental distribution recognizable in the selected class (e.g. Ca; Fe; Mg; Mn for garnet). Applying then the PCA function for those elements which potentially show the most variable elemental distribution recognizable in the selected class (e.g. Ca; Fe; Mg; Mn for Grt) (Fig. B19), will be possible to perform new images useful for a new maximum likelihood classification in the same manner produced

for the first cycle, but working just on the pixels of the single detected mineral phase (Fig. B20). It is worth noting that the percentage of the eigenvalue concentrated in the first principal component drastically rises up respect to the previous first cycle of analysis.

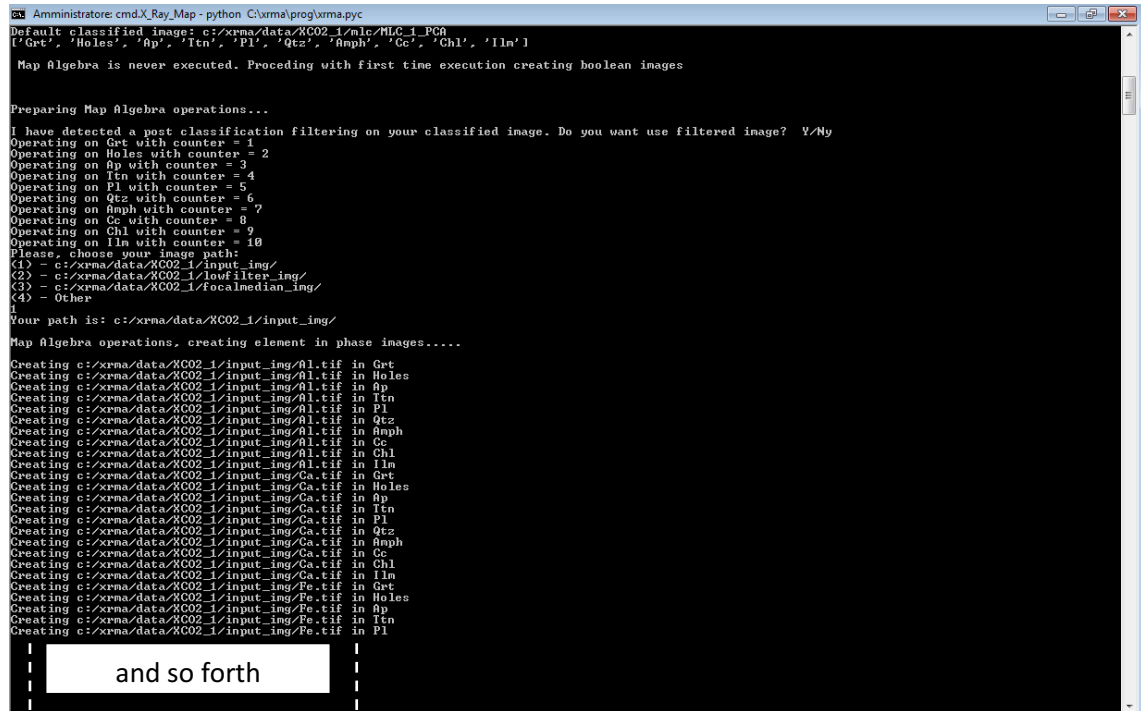


Figure B17 Visualization of the map algebra operation execute at the beginning of the second analytical stage

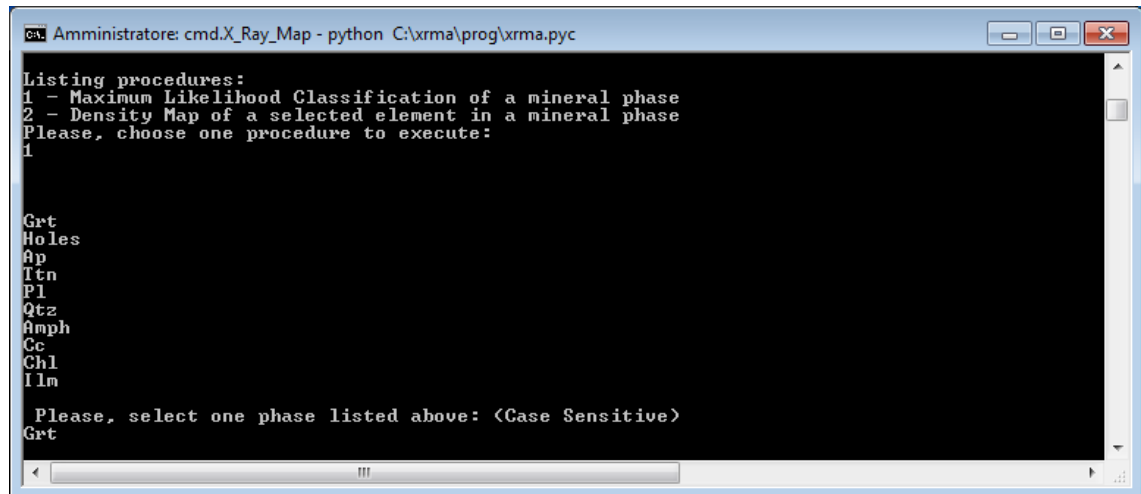


Figure B18 Choose of the sub-classification analytical procedure to be execute in the second cycle for garnet maximum likelihood classification

Similarly to the first cycle, user can choose if execute unsupervised or supervised classification. Nevertheless, commonly is better execute directly the supervised one, due to the easy possibility to depict the training areas editable within a new Training Areas file (TrArea2.shp) automatically stored inside the sub-folder: “c:\ Q- XRMA\DataPath\MyWorkspace\2_SecCycle\1_Classification\SelectedPhase\input_ve ct”. After editing and saved the new “*.shp” file, it is only necessary press enter to continue the procedure or restart Q-XRMA.pyc, choosing “Second Cycle”, if previously shut down the software. Yielded results, stored in the path “c:\ Q- XRMA\DataPath\MyWorkspace\2_SecCycle\1_Classification\SelectedPhase\mlc”, can be then post-classified with a focal median filtering stage to minimize the weight of isolated pixels. Obtained results can be opened in ArcGIS and exported in one of the most used raster formats (Fig. B21) as well as used to extrapolate quantitative results by means of ArcGIS functions (e.g. histograms of the volume percentages).

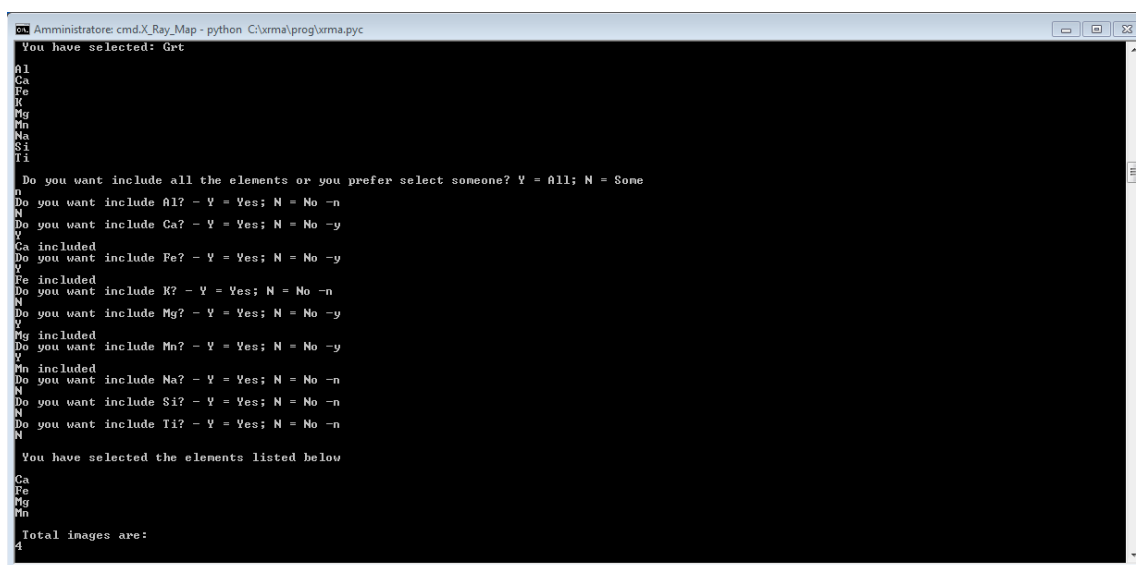


Figure B19 Choose of the elemental images to be included in the second cycle of principal component analysis for garnet

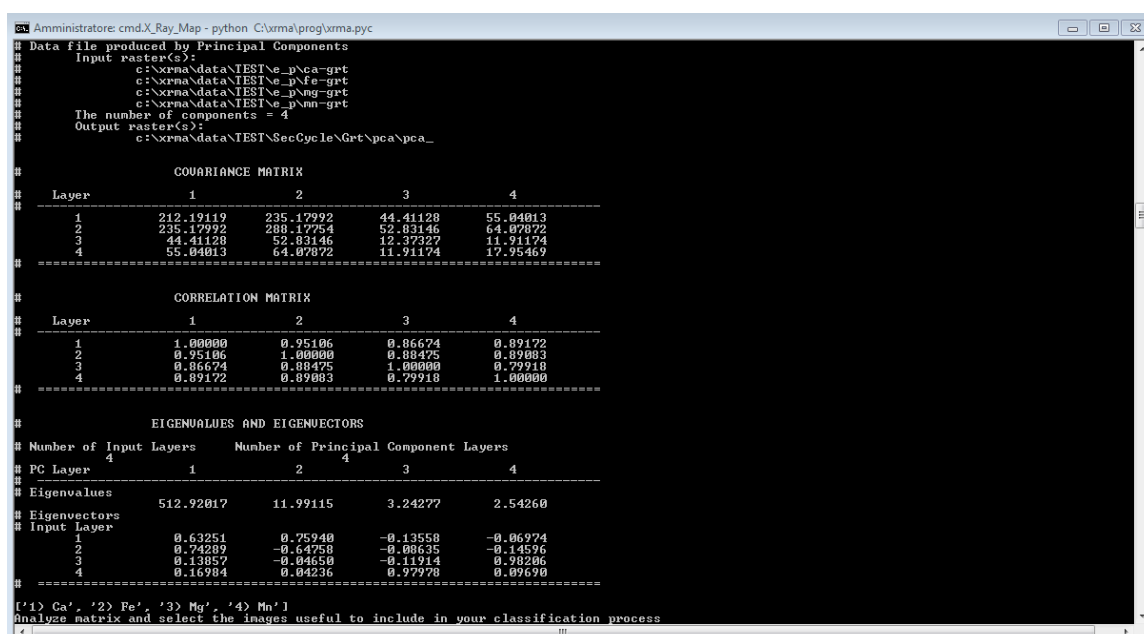


Figure B20 Principal component analysis of the selected elemental images within garnet

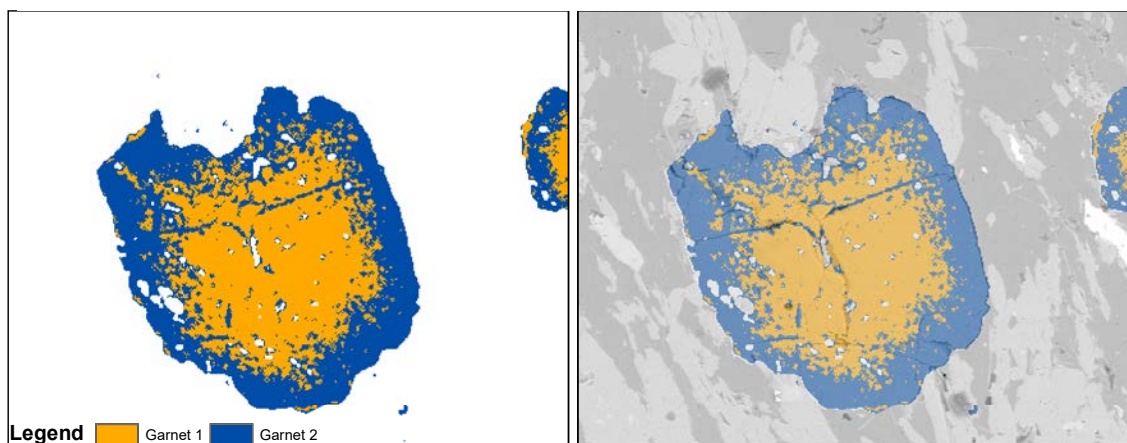


Figure B21 Supervised classification of the second analytical cycle for garnet, a) without and b) with superposition on BSE image

Maps calibration

The calibration procedure works for one single phase per time classified during the first cycle of analysis. Such analytical step applies a statistical approach based on a multilinear regression function. The choice of the multilinear regression algorithm has been done since considered the most suitable approach to take into account the natural compositional interdependence existing within each mineral phase due to its own stoichiometry. This choice was also useful to overcome the hindrances due to the potential different relationships (e.g. linear, exponential, logarithmic) existing between the element concentration and the correspondent pixel intensity.

The concentration-element/pixel-value relationship can be affected for instance: a) from the ab initio selection of the setting parameters of the used device; or b) using data carried out from different acquisition instruments. The use of a multilinear regression allows, indeed, to derive for each pixel the absolute concentration of an element (i.e. the dependent variable - DV) in a specific mineral phase, taking into account the weight of all of the other elements as well (i.e. the explanatory variables - EV). This in order to ensure the stoichiometry preservation.

Usually, one of the main issues in adopting a multilinear regression approach is in finding the correct explanatory variables helping to explain the potential interdependent variation of a parameter of interest. In order to answer this question, we selected as explanatory variables, the major elements constituting most of the common minerals (i.e. Al, Ca, Fe, K, Mg, Mn, Na, Si, Ti).

The calibration procedure is based on the application of the following interdependent multilinear regression equation:

$$[[C_i]] = \left[(\alpha_1 [[GV_i]]_0^{255}) + (\alpha_2 [[GV_j]]_0^{255}) + (\alpha_3 [[GV_k]]_0^{255}) \dots + (\alpha_n [[GV_n]]_0^{255}) \right] + \beta_i + \gamma_i$$

Where:

- i = the dependent variable representing the specific element to be predicted. It is a function of the explanatory variables;
- $j, k, l \dots n$ = the explanatory variables used to predict the dependent variable values;
- $[[C_i]]$ = the absolute concentration of the element i computed for each pixel;
- $\alpha_{1; 2; 3; \dots n}$ = the regression coefficients calculated between the measured concentration value of the elements stored in the control spot analysis, and the correspondent pixel intensity value of the original X-ray raster images at the same point;
- $[[GV_i]]_0^{255}; [[GV_j]]_0^{255} \dots [[GV_n]]_0^{255}$ = the pixel intensity values of the $i, j, k \dots n$, monochromatic elemental maps;
- β_i = the value of the intercept of the element i , that is the expected value of the dependent variable if all the independent (explanatory) variables are zero;
- γ_i = the random error for the element i , defined by the difference between the measured and predicted values.

The adopted calibration procedure also provides several statistical parameters, allowing to assess model performance and to evaluate the reliability of the predicted results. These can be summarized as follows:

- h) Regression coefficients: the coefficient calculated for each explanatory variable depicting the type of relationship (i.e. negative, positive or no relationship) between explanatory and dependent variables. In other words, to predict, for instance, Ca content in a plagioclase, it would be expected a negative relationship with the Na content. If during the calibration procedure an unexpected positive coefficient for the abovementioned relationship occurs, attention should be made before to proceed. In our procedure will be then computed 9 different regression coefficients, one per EVs;
- i) Probability: this parameter allows checking if every regression coefficient of the EVs is near or equaling to zero. The smaller probability value is, the smaller the possibility that the coefficient is equal to zero. This implies that those specific coefficients are important for the regression model. By contrast, EVs with coefficients showing high probability values should be removed from the regression equation. In our procedure, when the probability is lower than 0.01, an asterisk close to the value will appear on the regression report alerting as the coefficient of those specific EVs is consistent with the prediction model. Nevertheless, some explanatory variables could be considered good predictors as well from a theoretical point of view (e.g. for stoichiometry preservation), although showing regression coefficients with high probability values. This is statistically permitted, verifying the consistency of other test indexes (i.e. Joint F-Statistic and Joint Wald Statistic), highlighting the joint interdependence relationship between the regression coefficients;
- j) Variance inflation factor (VIF): the VIF is a check parameter that depicts the weight of the redundancy among the EVs. If the explanatory variables assume

VIF values larger than about 7.5, than the model is not good and the EVs should be removed from the regression model;

- k) *R-Squared and Corrected Akaike's information criterion (AICc)*: The R-Squared values are measures of model performance ranging from 0.0 to 1.0 and explaining the variation in the dependent variable. For instance, an R-Squared value of 0.8 means that the EVs explain 80 percent of the variation in the dependent variable. The AICc is used to compare different models performed about the same dependent variable (e.g. increasing or decreasing of control spot analysis). Comparing different calibration models, the model with a lower AICc is to be preferred;
- l) *Joint F-Statistic and Joint Wald Statistic*: These test indexes are used to verify the overall model statistical significance since they assess the interdependent coefficient relationships simultaneously. As a consequence, these tests measure the statistical meaning of the multilinear regression model even when one or more of the single coefficient results statistically meaningless (i.e. a probability value > 0.01), comparing the model with one EV with the multilinear regression model. When the results of these tests give values lower than 0.01, the applied multiple regression models can be considered reliable if the value associated with the Koenker (BP) statistic test (see below) is higher than 0.01.
- m) *The Koenker (BP) Statistic*: It is a test to determine whether the explanatory variables in the model have a consistent relationship to the dependent variable across the entire study area. If such a test shows a value lower than 0.01, the EVs vs. DV relationships are nonstationary or heteroscedastic (i.e. characterised by an anomalous value distribution).
- n) *The Jarque-Bera statistic*: It is a test to assess whether the residuals (i.e. the observed dependent variable values minus the predicted ones) are normally distributed according to a Gaussian distribution. When the result of this test gives a value lower than 0.01, the residuals are not normally distributed, indicating the occurrence of a probable bias, which can influence the reliability of the predictions. This could be due, for instance, to the presence of outliers in the control spot analyses. A possible solution could be the removal of the outliers and restart the procedure.

In order to preserve the interdependence relationship between the explanatory variables (i.e. selected major elements), the calibration procedure works for one phase per time previously classified and bracketed during the first cycle of analysis. To run the calibration procedure, all of the selected EVs are needed (i.e. Al, Ca, Fe, K, Mg, Mn, Na, Si, Ti X-ray maps) as well as two spreadsheets must be set (Figs. B22, B24). This operation has to be repeated whenever you wish to investigate a new mineralogical phase. The first spreadsheet (Fig. B22, i.e. Q-XRMA coordinate conversion tool) is useful to ensure the correct location of the control spot analyses within the map, converting the original device coordinates of each spot into the ArcGIS® coordinate system. Such a coordinate conversion spreadsheet can be used in two different cases: i) when X-ray maps and control spot analyses have been carried out with the same device (Fig. B22a); ii) when X-ray maps and control spot analyses have been carried out with different devices (Fig. B22b). In the first case, the device coordinates of the X-ray maps and their equivalents on ArcGIS® coordinate system are required as input information, together with the device

coordinates of each single control spot. The ArcGIS® XY coordinates can be easily obtained by using the extent information in the layer properties menu of the loaded map on the ArcGIS® project (Fig. B23). In the second case, it is necessary provide: i) the device XY coordinates of at least two control spot analyses and their equivalent on ArcGIS® coordinate system; ii) the matrix dimension of the X-ray maps; iii) the ArcGIS® coordinates of the X-ray maps; and iv) the device coordinates of each single control spot. Entering all the input values, the ArcGIS® XY coordinates are automatically calculated for each single control spot and then can be successively insert in the second spreadsheet (Fig. B24, i.e. PtAnls.xlsx).

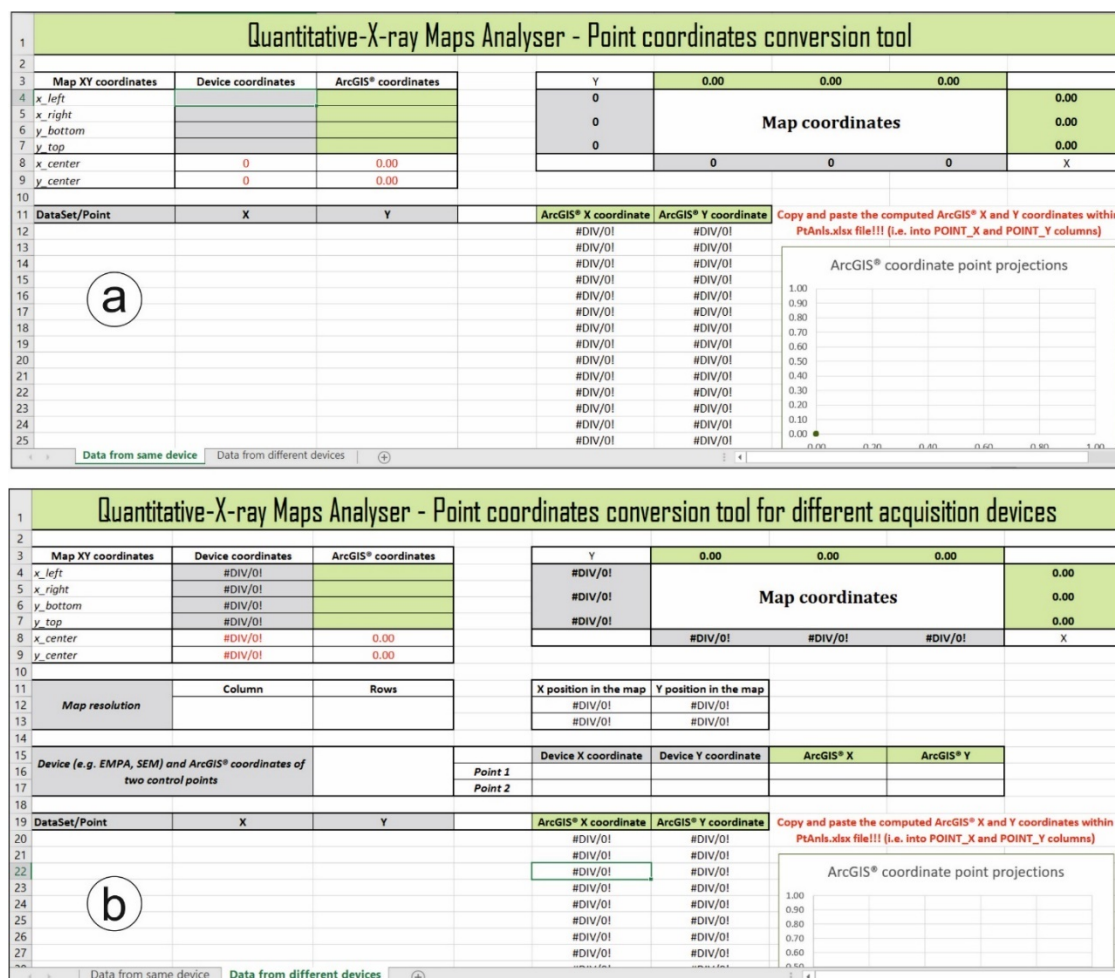


Figure B22 Point coordinates conversion spreadsheet used to automatically calculate the correct location of the control spot analyses converting the device coordinates into their equivalents on the ArcGIS® loaded maps.

The second spreadsheet contains every information about the sample location, mineral phase, sub-phase of the mineral investigated, number of analysis, chemical composition and the ArcGIS® XY coordinates. These coordinates are read by the software to automatically create a point shapefile subsequently required for the execution of the calibration steps.

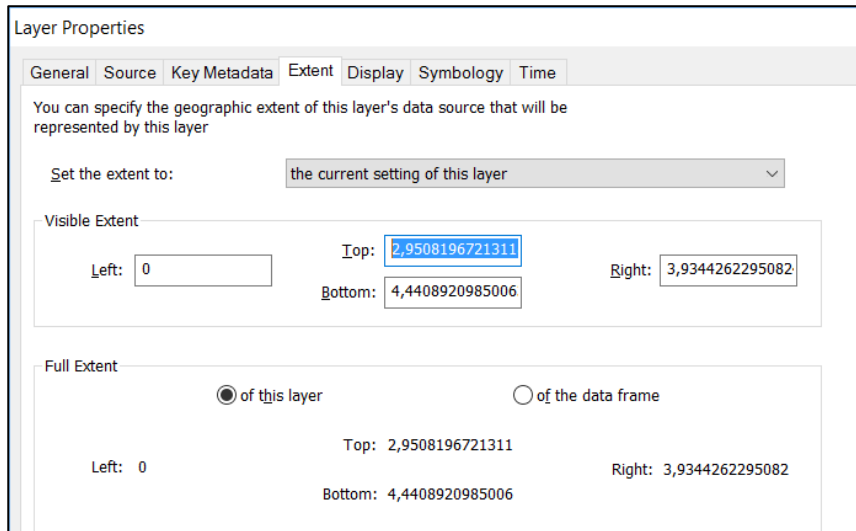


Figure B23 - Coordinates information for the loaded X-Ray map in the ArcGIS project to be used in the point coordinates conversion spreadsheet.

ID	ID_SAMPLE	LOCATION	MINERAL	SUB_PHASE	DOMAIN	ANALYSIS	POINT	AI	Ca	Fe	K	Mg	Mn	Na	P	Si	Ti	POINT_X	POINT_Y	
1	MA271	MPC	Grt I	IC	10	94	1		1,95	0,84	1,68	0,00	0,06	0,43	0,01	0,00	2,97	0,01	2,14	2,64
2	MA271	MPC	Grt I	IC	10	94	2		1,98	0,86	1,70	0,00	0,05	0,43	0,01	0,00	2,98	0,01	2,15	2,63
3	MA271	MPC	Grt I	IC	10	94	3		1,94	0,84	1,70	0,00	0,05	0,46	0,00	0,00	2,99	0,01	2,16	2,61
4	MA271	MPC	Grt I	IC	10	94	4		1,97	0,86	1,68	0,00	0,05	0,44	0,01	0,00	2,99	0,01	2,17	2,59
5	MA271	MPC	Grt I	IC	10	94	5		1,94	0,87	1,71	0,00	0,05	0,44	0,00	0,00	2,99	0,01	2,18	2,58
6	MA271	MPC	Grt I	IC	10	94	6		1,94	0,88	1,69	0,00	0,05	0,44	0,00	0,00	2,99	0,01	2,18	2,57
7	MA271	MPC	Grt I	IC	10	94	7		1,93	0,86	1,69	0,00	0,05	0,46	0,00	0,00	2,93	0,01	2,20	2,54
8	MA271	MPC	Grt I	IC	10	94	8		1,95	0,88	1,71	0,00	0,05	0,46	0,01	0,00	2,97	0,01	2,21	2,53
9	MA271	MPC	Grt I	IC	10	94	9		1,94	0,89	1,66	0,00	0,05	0,46	0,01	0,00	2,97	0,01	2,25	2,46
10	MA271	MPC	Grt I	IC	10	94	10		1,96	0,87	1,73	0,00	0,05	0,43	0,01	0,00	2,98	0,01	2,26	2,44
11	MA271	MPC	Grt I	IC	10	94	11		1,93	0,87	1,70	0,00	0,05	0,47	0,01	0,00	3,00	0,01	2,27	2,42
12	MA271	MPC	Grt I	IC	10	94	12		1,95	0,85	1,68	0,00	0,05	0,46	0,01	0,00	2,96	0,01	2,28	2,40
13	MA271	MPC	Grt I	IC	10	94	13		1,98	0,88	1,67	0,00	0,05	0,44	0,01	0,00	3,00	0,01	2,28	2,40
14	MA271	MPC	Grt I	IC	10	94	14		1,95	0,89	1,62	0,00	0,05	0,48	0,01	0,00	2,97	0,01	2,29	2,39
15	MA271	MPC	Grt I	IC	10	94	15		1,96	0,89	1,65	0,00	0,05	0,48	0,01	0,00	2,99	0,01	2,31	2,36
16	MA271	MPC	Grt I	IC	10	94	16		1,93	0,88	1,68	0,00	0,05	0,47	0,01	0,00	2,99	0,01	2,33	2,32
17	MA271	MPC	Grt I	IC	10	94	17		1,96	0,87	1,70	0,00	0,05	0,42	0,00	0,00	2,97	0,01	2,36	2,27
18	MA271	MPC	Grt I	IC	10	94	18		1,95	0,87	1,74	0,00	0,05	0,42	0,00	0,00	2,99	0,01	2,37	2,25
19	MA271	MPC	Grt I	IC	10	94	19		1,96	0,85	1,70	0,00	0,05	0,43	0,00	0,00	2,97	0,01	2,38	2,24
20	MA271	MPC	Grt I	IC	10	94	20		1,95	0,87	1,74	0,00	0,05	0,42	0,00	0,00	2,99	0,01	2,37	2,25
21	MA271	MPC	Grt I	MNT	10	94	21		1,94	0,36	2,16	0,01	0,13	0,39	0,01	0,00	2,97	0,01	2,40	2,20
22	MA271	MPC	Grt I	MNT	10	94	22		1,96	0,41	2,16	0,00	0,12	0,38	0,00	0,00	2,98	0,01	2,42	2,16
23	MA271	MPC	Grt I	MNT	10	94	23		1,95	0,50	2,11	0,00	0,13	0,32	0,00	0,00	2,97	0,01	2,44	2,12
24	MA271	MPC	Grt I	MNT	10	94	24		1,98	0,22	2,37	0,00	0,18	0,32	0,00	0,00	2,96	0,00	2,48	2,06
25	MA271	MPC	Grt I	MNT	10	94	25		1,96	0,27	2,31	0,00	0,17	0,32	0,00	0,00	2,96	0,01	2,49	2,04
26	MA271	MPC	Grt I	MNT	10	94	26		1,96	0,34	2,27	0,00	0,16	0,32	0,00	0,00	3,00	0,01	2,50	2,03
27	MA271	MPC	Grt I	MNT	10	94	27		1,94	0,38	2,20	0,00	0,14	0,30	0,01	0,00	2,94	0,00	2,50	2,03
28	MA271	MPC	Grt I	MNT	10	94	28		1,96	0,44	2,24	0,00	0,16	0,25	0,00	0,00	2,98	0,01	2,53	1,98
29	MA271	MPC	Grt I	MNT	10	94	29		1,95	0,31	2,30	0,01	0,19	0,26	0,01	0,00	3,00	0,01	2,53	1,97
30	MA271	MPC	Grt I	MNT	10	94	30		1,96	0,34	2,28	0,00	0,19	0,22	0,00	0,01	2,98	0,00	2,54	1,96
31	MA271	MPC	Grt I	MNT	10	94	31		1,94	0,23	2,46	0,00	0,21	0,20	0,00	0,00	3,01	0,00	2,55	1,94

Figure B24 – PtAnls.xlsx file used by the Python code to create an ArcGIS point shapefile. POINT_X and POINT_Y fields are filled with the data obtained by the specific conversion coordinates spreadsheet (Fig. B22)

In order to avoid unexpected calibration results, it is important verifying that the points created by the software are not located in correspondence of both border zones with other mineral phases and fractures. Otherwise, it is recommended removing these points by editing the abovementioned shape file (Fig. B25).

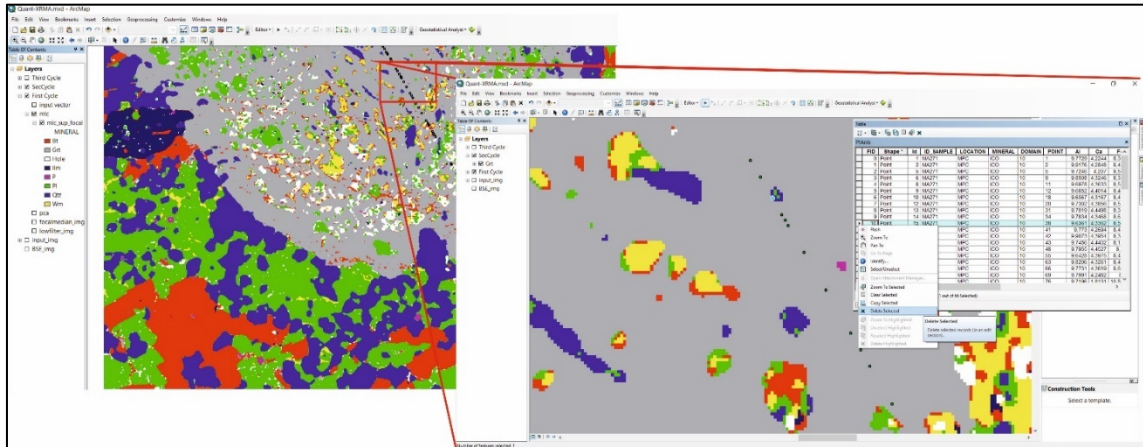


Figure B25 - Editing step of the ArcGIS shapefile to remove points near edge mineral zones.

Once the input files have been correctly set, the calibration of the X-ray maps can be performed. During the execution of the calibration procedure, the software verifies the statistical meaningful of each used calibration model, applying several statistical tests. As shown in the red areas of Fig. B26, reporting as an example the iron calibration within garnet, statistical test results (e.g. VIF, Joint F- and Wald Statistics, Koenker Statistic and Jarque-Bera) suggest that the applied calibration model can be considered reliable for the investigated dependent variable.

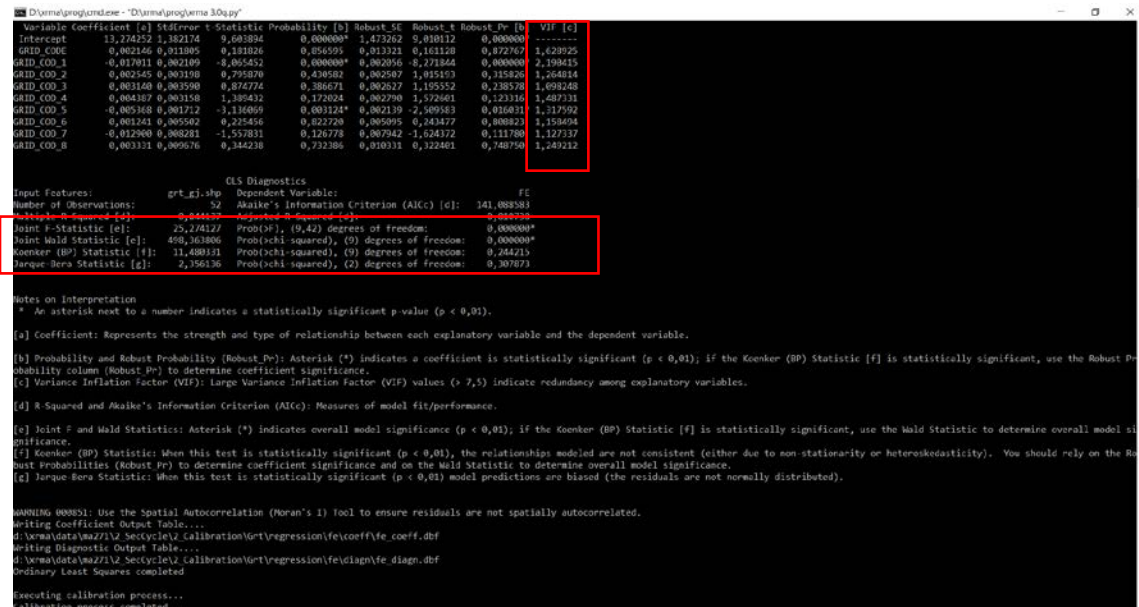


Figure B26 - Summary results of the calibration procedure using iron as a dependent variable. Test results (red areas) suggest that the applied statistical model can be considered reliable for the calibration.

The procedure creates a set of point shapefiles of the selected X-ray map array by a raster to point conversion function (Fig. B3) as well, that will be saved in: C:\Q-XRMA\DataPath\MyWorkspace\2_SecCycle\2_Calibration\SelectedPhase\chemical_analyses\. These files are containers of the chemical quantification per pixel of each single element, representing, at the same time, the chemical quarryable database format tables

specific for each investigated detected phase.

Each element calibration is followed by a regression report printed on the screen summarizing the results of the statistical tests. Such a report provides the user a fast way to check the reliability of its model (Fig. B26) and it will be saved in different tables within the main regression folder located in: C:\Q-XRMA\DataPath\MyWorkspace\2_SecCycle\2_Calibration\SelectedPhase\regression\. Once the calibration of the selected elements has ended, new calibrated X-ray maps are obtained and stored in: C:\Q-XRMA\data\MyWorkspace\2_SecCycle\e_p\calib (Fig. B27). These calibrated maps can be potentially used, in turn, as the input files of the third analytical cycle (Fig. B4) useful to derive mineral component maps.

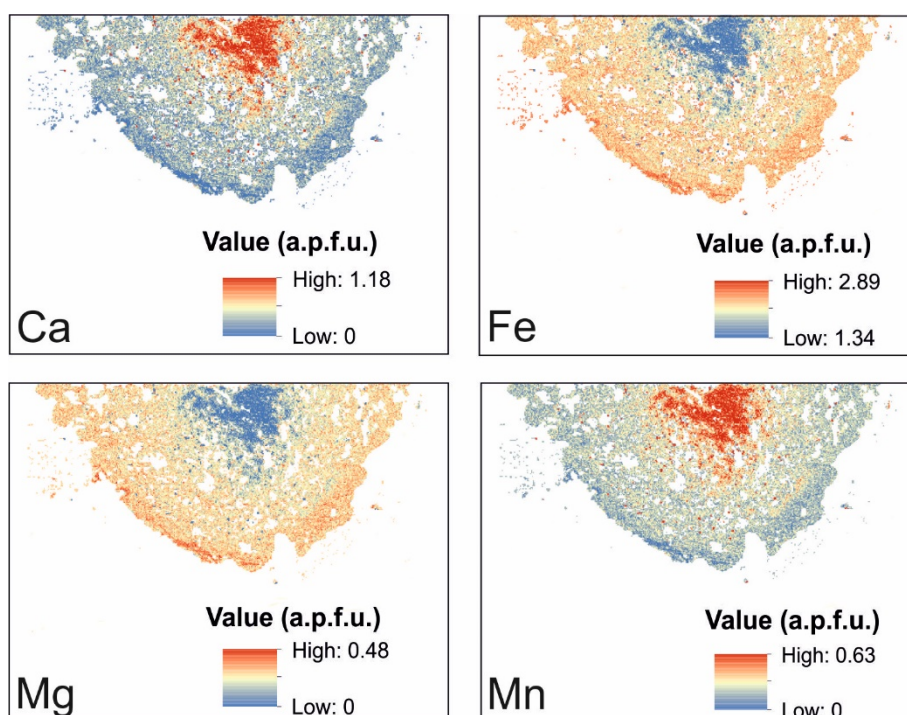


Figure B27 - Example of Ca, Fe, Mg and Mn calibrated images for a garnet.

Third Cycle

The third cycle of analysis (Fig. B4) is very simple to execute and it allows to combine the calibrated elemental maps, aiming to obtain maps of mineral components through two different computational modes. With the first one (blue area in Fig. B28) it is possible to automatically obtain different component maps defined for a set of common minerals, using as mask file a specific phase identified during the first analytical cycle (green area in Fig. B28). With the second one (red square in Fig. B28) it is possible to manually select which elements have to be used within a raster calculator for creating a specific component map for a mineral phase detected during the first cycle (green area in Fig. B28), by choosing “other” as the computational mode. In this last case, the user must define the name of the output map, the number of the elements to be used and the correct expression for deriving graphical outputs.

In both computational modes, the graphical outputs and the relative component concentration quantification per pixel are stored within database format tables potentially queryable for further purposes.


```

D:\xrma\prog\cmd.exe - "D:\xrma\prog\xrma 3.0q.py"
This application allows to classify mineral phases by means of statistical data process of X-Ray Map

Please select one of the procedure listed below
1 - First cycle
2 - Second cycle
3 - Third cycle
4 - Exit
Please, choose one procedure to execute:
3

This is the third round of your analysis
I have found these workspace in your data:
casc
INH239_M6
ha271
HA271_
HA271_10
HA271_EMG
H241_M1
Please, select a folder listed above or digit a new workspace (Case Sensitive):
Wrong workspace name. Please digit correct name as in list
Please, select a folder listed above or digit a new workspace (Case Sensitive):
ma271

grt
Jtz
Di
St
Sp
Alm
Prp
Hole
Please, choose one class detected in the 1st cycle listed above (Case Sensitive):
grt
You have selected Grt

1 - Alm, Grs, Pyr, Sps
2 - Pheng
3 - Ab, An
4 - Di, Hed
5 - Fo, Fa
6 - Other
Please, choose the corresponding number listed above for your component calculation:

```

Figure B28 - Third round of analysis to derive component maps. In the green area are listed the mineral phases identified during the first cycle of analysis. In the blue area are listed some end-member for common minerals. The red square highlight the manually computational mode.

As an example, in Fig. B29 are shown almandine, grossular, pyrope, spessartine and Fe/(Fe+Mg) component maps derived for a garnet microdomain.

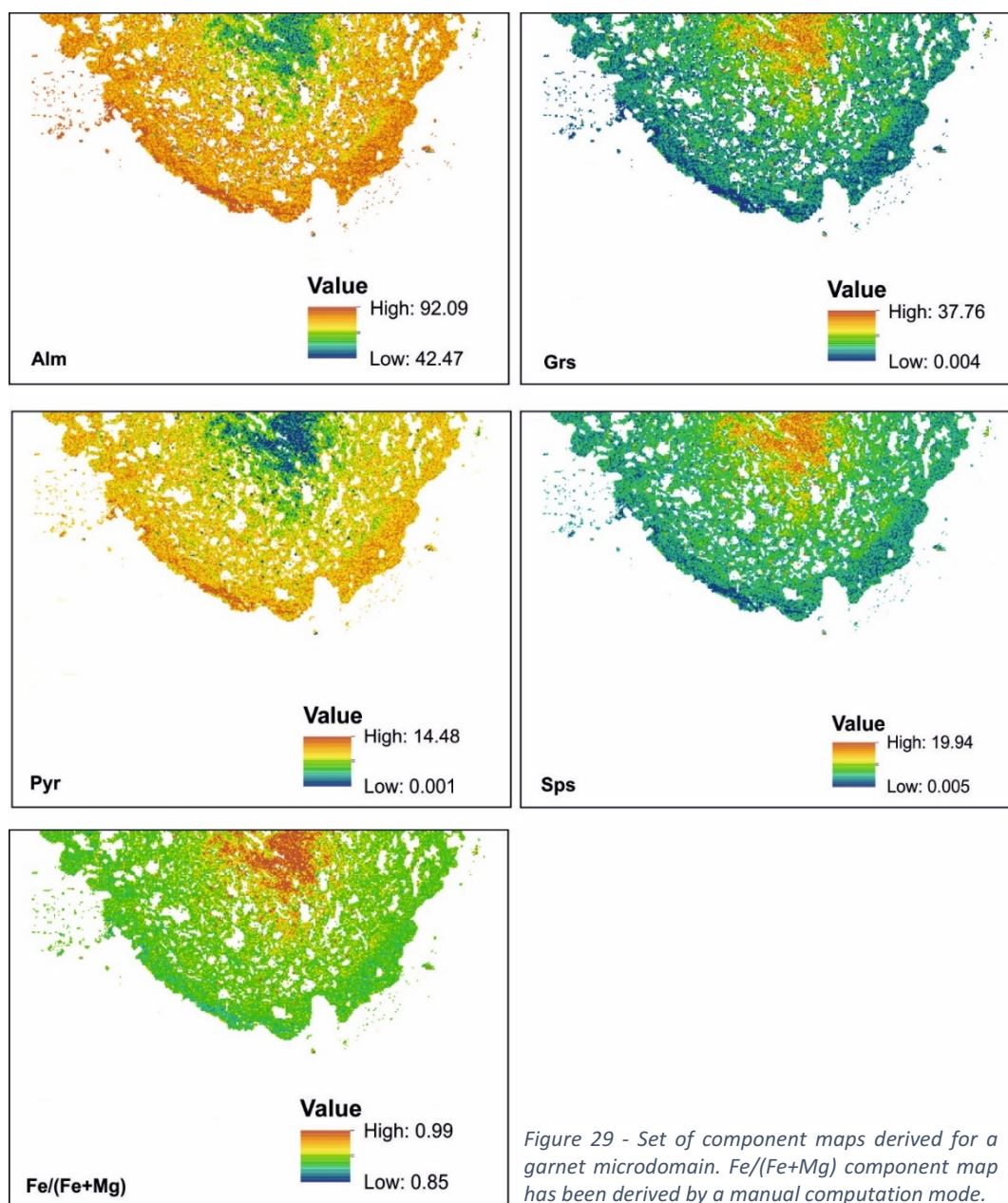


Figure 29 - Set of component maps derived for a garnet microdomain. Fe/(Fe+Mg) component map has been derived by a manual computation mode.

As the same for the calibration procedure, also for the component maps derivation there is a raster to point conversion operation allowing to obtain tables for the chemical quantification per pixel for each computed component. These quantification tables will be stored in: C:\Q-XRMA\MyDataPath\MyWorkspace\3_ThiCycle\MyPhase\c_m\chemical_analyses and subsequently used to investigate different chemical changes within the same phase, as shown in Fig. B30 for an example in garnet and plagioclase mineral phases.

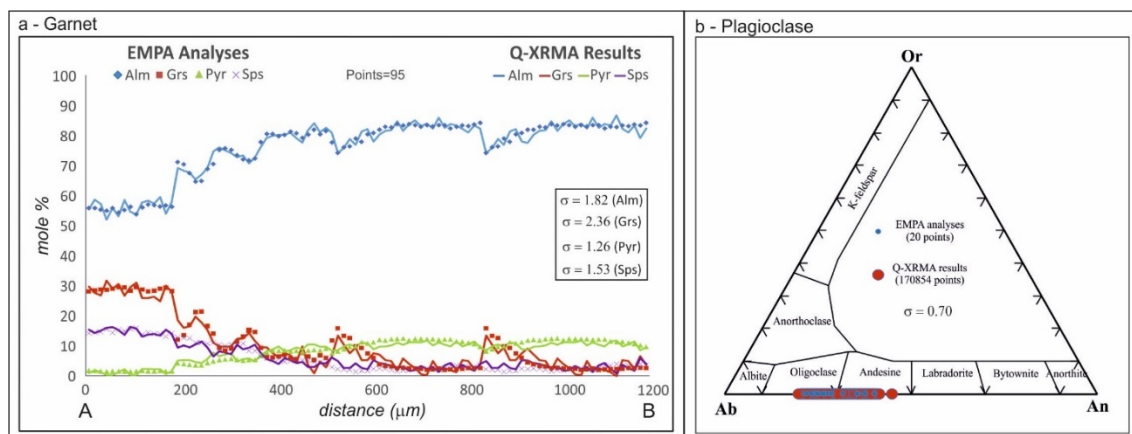


Figure B30 – Extraction of chemical analyses for garnet and plagioclase components compared with the control spot used for the calibration procedure.

Question and Answers

1. Why doesn't Q-XRMA run?

Try to check if your *AGpath*, *Tbx_SA_path* and *Tbx_DM_path* are correctly set into the *q_xrma.cfg* file, according to the ArcGIS® version installed on your personal computer. Also, check if your *DataPath* is the same of the workspace path.

2. Why Q-XRMA returns overwrite error?

Usually, this error is due to the execution of the file you want overwrite by another program (e.g. an open ArcGIS® project). Try to close all other open programs and restart the procedure.

3. Why doesn't PCA work during the first cycle of analysis?

Try to check if within the *input_img* folder there are files with “.aux” or “.aux.xml” extensions. If this is true, then delete them and restart the procedure.

4. Why ArcGIS® returns a database connection error with the *PtAnls.xlsx* file?

If you have an .xlsx file you want to use in ArcGIS® but do not have Excel 2007 installed, you will need to install the 2007 Office System Driver. It can be downloaded from the Microsoft Download Center. This is valid although you have a later Excel version installed.

APPENDIX B2 – EMP analyses of the investigated phases

TABLE B2 - GARNET MICROPROBE SPOT ANALYSES

SAMPLE	Analysis	POINT	Location	Mineral	SiO₂	TiO₂	Al₂O₃	Cr₂O₃
MA271	94	1	MPC	Grt	37.93	0.16	20.86	0
MA271	94	2	MPC	Grt	37.69	0.13	21.33	0
MA271	94	3	MPC	Grt	37.59	0.2	21.2	0
MA271	94	4	MPC	Grt	37.44	0.16	21.03	0
MA271	94	5	MPC	Grt	37.71	0.14	20.82	0
MA271	94	9	MPC	Grt	37.39	0.2	20.93	0
MA271	94	10	MPC	Grt	37.22	0.2	20.57	0
MA271	94	11	MPC	Grt	37.53	0.17	20.63	0
MA271	94	12	MPC	Grt	37.48	0.21	20.59	0
MA271	94	18	MPC	Grt	37.49	0.17	20.57	0
MA271	94	19	MPC	Grt	37.22	0.19	21.26	0
MA271	94	20	MPC	Grt	37.34	0.2	20.82	0
MA271	94	31	MPC	Grt	37.35	0.14	20.72	0
MA271	94	34	MPC	Grt	37.15	0.17	20.78	0
MA271	94	38	MPC	Grt	37.41	0.13	20.56	0
MA271	94	39	MPC	Grt	37.57	0.18	20.9	0
MA271	94	41	MPC	Grt	37.45	0.14	20.82	0
MA271	94	42	MPC	Grt	37.23	0.13	21.18	0
MA271	94	43	MPC	Grt	37.11	0.17	20.46	0
MA271	94	44	MPC	Grt	37.15	0.18	20.71	0
MA271	94	45	MPC	Grt	37.17	0.19	20.68	0
MA271	94	48	MPC	Grt	37.18	0.15	20.91	0
MA271	94	55	MPC	Grt	37.38	0.17	20.49	0
MA271	94	63	MPC	Grt	37.24	0.14	20.77	0
MA271	94	64	MPC	Grt	37.45	0.18	20.73	0
MA271	94	65	MPC	Grt	37.34	0.21	20.58	0
MA271	94	66	MPC	Grt	37.05	0.12	20.68	0
MA271	94	67	MPC	Grt	37.27	0.17	20.56	0
MA271	94	69	MPC	Grt	37.38	0.18	20.77	0
MA271	94	73	MPC	Grt	36.88	0.14	20.71	0
MA271	94	76	MPC	Grt	37.44	0.17	20.55	0
MA271	94	82	MPC	Grt	36.81	0.1	20.61	0
MA271	94	83	MPC	Grt	36.98	0.1	20.43	0
MA271	94	85	MPC	Grt	37.3	0.18	20.63	0
MA271	94	86	MPC	Grt	36.96	0.16	20.82	0
MA271	94	89	MPC	Grt	37.2	0.09	20.7	0
MA271	94	91	MPC	Grt	37.36	0.09	20.86	0
MA271	94	95	MPC	Grt	36.99	0.11	20.83	0
MA271	94	98	MPC	Grt	36.79	0.03	20.67	0
MA271	94	99	MPC	Grt	36.68	0.03	20.91	0
MA271	94	100	MPC	Grt	36.73	0.05	20.79	0
MA271	94	102	MPC	Grt	36.54	0.07	20.48	0
MA271	94	104	MPC	Grt	36.81	0.09	20.67	0
MA271	94	105	MPC	Grt	36.82	0.11	20.14	0
MA271	94	107	MPC	Grt	36.96	0.05	20.83	0
MA271	94	112	MPC	Grt	36.33	0.09	20.11	0

MA271	94	113	MPC	Grt	37.19	0.05	20.81	0
MA271	94	115	MPC	Grt	36.87	0.09	20.43	0
MA271	94	117	MPC	Grt	37.1	0.1	20.57	0
MA271	94	119	MPC	Grt	36.89	0.08	20.63	0
MA271	94	120	MPC	Grt	36.8	0.07	20.4	0
MA271	94	125	MPC	Grt	36.56	0.07	21.01	0
MA271	94	143	MPC	Grt	36.71	0.02	20.96	0
MA271	94	155	MPC	Grt	37.06	0.06	20.6	0
MA271	94	156	MPC	Grt	36.79	0.03	21	0
MA271	94	165	MPC	Grt	36.82	0.08	21.01	0
MA271	94	166	MPC	Grt	37.08	0.03	21.04	0
MA271	94	168	MPC	Grt	37.14	0.03	20.95	0
MA271	94	175	MPC	Grt	37.01	0.03	20.9	0
MA271	94	176	MPC	Grt	37.34	0.06	20.89	0
MA271	94	177	MPC	Grt	37.01	0.04	21.05	0
MA271	94	178	MPC	Grt	37.24	0.04	20.9	0
MA271	94	180	MPC	Grt	37.09	0.05	21.07	0
MA271	94	181	MPC	Grt	36.72	0.02	20.67	0
MA271	94	182	MPC	Grt	36.9	0.05	21.15	0
MA271	94	184	MPC	Grt	36.65	0.01	20.96	0
MA271	94	189	MPC	Grt	38.04	0.04	21.57	0
MA271	94	193	MPC	Grt	37.67	0.03	21.37	0
MA271	94	194	MPC	Grt	37.46	0.01	21.14	0
MA271	94	195	MPC	Grt	37.03	0.01	21.04	0
MA271	94	197	MPC	Grt	37.53	0.01	21.82	0
MA271	94	198	MPC	Grt	37.03	0	20.21	0
MA271	94	199	MPC	Grt	37.33	0.04	21.42	0
MA271	94	200	MPC	Grt	37.3	0	21.12	0
MA271	94	201	MPC	Grt	37.17	0.02	21.07	0
MA271	94	202	MPC	Grt	37.37	0	20.92	0
MA271	94	203	MPC	Grt	37.16	0.02	21.15	0
MA271	94	204	MPC	Grt	36.91	0	20.81	0
MA271	94	205	MPC	Grt	37.05	0	21.13	0
MA271	94	206	MPC	Grt	37.13	0	21.02	0
MA271	94	207	MPC	Grt	36.86	0	21.07	0
MA271	94	209	MPC	Grt	37.16	0.01	20.95	0
MA271	94	210	MPC	Grt	37.28	0.04	21.24	0
MA271	94	211	MPC	Grt	36.8	0.01	21.16	0
MA271	94	212	MPC	Grt	37.6	0.03	21.26	0
MA271	94	214	MPC	Grt	37.45	0	20.94	0
MA271	94	216	MPC	Grt	36.76	0	21.3	0
MA271	94	217	MPC	Grt	37.24	0	21.07	0
MA271	94	225	MPC	Grt	36.83	0.01	21.13	0
MA271	94	228	MPC	Grt	36.7	0	20.94	0
MA271	94	231	MPC	Grt	37.2	0.01	20.96	0
MA271	94	232	MPC	Grt	37.42	0.01	21.03	0
MA271	94	233	MPC	Grt	36.8	0.01	21.18	0
MA271	94	235	MPC	Grt	37.25	0	20.96	0
MA271	94	236	MPC	Grt	36.53	0	21.09	0

POINT	FeO	Fe ₂ O ₃	MnO	MgO	CaO	Na ₂ O	K ₂ O	Total	X
1	25.26	0	6.37	0.48	9.92	0.04	0	101.02	6390
2	25.71	0	6.5	0.44	10.14	0.03	0	101.97	6393.9
3	24.93	0	7	0.37	10.01	0.02	0	101.32	6397.8
4	24.55	0	6.96	0.43	10.14	0.01	0.01	100.73	6401.8
5	25.64	0	6.91	0.42	9.91	0.03	0.04	101.62	6405.7
9	25.11	0	6.54	0.41	10.11	0.04	0	100.73	6421.3
10	24.99	0	6.86	0.37	10.03	0.03	0.02	100.28	6425.3
11	25.65	0	6.46	0.41	10.21	0	0	101.06	6429.2
12	25.34	0	6.57	0.39	10.29	0.03	0.01	100.9	6433.1
18	25.42	0	6.83	0.42	10.11	0.03	0.01	101.05	6456.6
19	26	0	6.8	0.43	10.17	0.04	0.02	102.13	6460.5
20	25.79	0	6.89	0.4	10.32	0.04	0.03	101.84	6464.4
31	25.01	0	6.85	0.41	10.45	0.07	0	101	6507.5
34	25.86	0	6.35	0.42	10.16	0.04	0.05	100.97	6519.3
38	25.57	0	6.95	0.42	10.18	0.08	0	101.3	6535
39	25	0	6.25	0.43	10.04	0.05	0.01	100.41	6538.9
41	25.29	0	6.76	0.42	10	0.07	0.02	100.97	6546.7
42	25.18	0	6.59	0.43	10.33	0.04	0.01	101.11	6550.6
43	24.03	0	6.96	0.39	10.26	0.06	0	99.44	6554.6
44	25.43	0	6.63	0.4	10.34	0.03	0.01	100.86	6558.5
45	26.47	0	7	0.38	10.03	0.05	0	101.97	6562.4
48	24.76	0	7.11	0.41	10.45	0.08	0.03	101.08	6574.1
55	25.21	0	6.9	0.44	10.28	0.04	0	100.91	6601.6
63	25.27	0	6.12	0.44	10.06	0	0.01	100.07	6632.9
64	26.65	0	6.47	0.43	9.98	0.03	0.01	101.93	6636.8
65	25.95	0	6.2	0.42	9.95	0.01	0.03	100.69	6640.8
66	25.93	0	6.21	0.44	10.16	0.01	0.01	100.62	6644.7
67	25.9	0	5.84	0.41	10.27	0	0.03	100.45	6648.6
69	25.45	0	6.32	0.4	9.91	0.01	0	100.42	6656.4
73	28.04	0	5.23	0.66	8.57	0.07	0	100.3	6672.1
76	32.2	0	5.67	1.06	4.22	0.04	0.05	101.4	6683.9
82	32.07	0	5.58	1	4.72	0	0.01	100.89	6707.4
83	30.97	0	5.57	0.95	5.95	0	0	100.95	6711.3
85	29.69	0	4.93	0.91	7.51	0.07	0.04	101.26	6719.1
86	29.78	0	4.9	0.92	7.49	0.01	0	101.03	6723
89	31.58	0	4.79	1.1	5.82	0.03	0.05	101.35	6734.8
91	32.53	0	4.96	1.24	5	0	0	102.05	6742.6
95	34.15	0	4.64	1.35	3.28	0.02	0.03	101.38	6758.3
98	33.07	0	4.37	1.38	2.92	0	0	99.24	6770
99	35.33	0	4.78	1.52	2.56	0	0.03	101.84	6774
100	34.61	0	4.41	1.48	2.81	0.29	0	101.18	6777.9
102	34	0	4.58	1.44	3.15	0.01	0	100.26	6785.7
104	33.78	0	4.71	1.35	3.97	0.01	0.04	101.44	6793.6
105	32.2	0	4.41	1.18	4.33	0.04	0.03	99.27	6797.5
107	33.73	0	4.79	1.3	4.63	0.01	0.05	102.35	6805.3
112	32.04	0	3.61	1.31	5.2	0.03	0.03	98.76	6824.9
113	33.53	0	3.72	1.37	5.16	0	0.03	101.86	6828.8
115	34.05	0	3.73	1.61	3.63	0.04	0.06	100.5	6836.7

117	33.72	0	3.27	1.61	3.92	0	0	100.29	6844.5
119	35.12	0	2.9	1.68	3.24	0.02	0	100.56	6852.3
120	36.48	0	2.92	1.77	2.66	0	0.01	101.11	6856.2
125	34.04	0	2.67	1.91	1.84	0	0	98.09	6875.8
143	37.31	0	2.64	1.98	2.24	0	0.01	101.87	6946.4
155	36.84	0	2.35	2.12	2.17	0.04	0.01	101.25	6993.4
156	36.41	0	2.55	2.12	2.28	0	0	101.19	6997.3
165	36.57	0	2.1	2.16	2.43	0.02	0	101.18	7032.6
166	37.39	0	2.23	2.1	2.08	0.02	0.01	101.97	7036.5
168	35.5	0	2.24	2.1	1.94	0	0	99.91	7044.3
175	36.18	0	2.1	2.07	2.39	0.01	0.04	100.73	7071.7
176	36.22	0	2.29	2.04	2.34	0.03	0.01	101.21	7075.7
177	35.9	0	2.34	2.03	2.72	0.04	0.04	101.16	7079.6
178	37.26	0	2.35	2.16	2.31	0.03	0.02	102.31	7083.5
180	36.66	0	1.93	2.24	2.22	0	0	101.27	7091.3
181	37.11	0	2	2.16	1.86	0	0.01	100.55	7095.2
182	36.75	0	2.07	2.14	2.42	0.02	0.01	101.52	7099.2
184	36.97	0	1.72	2.28	2.07	0.02	0	100.67	7107
189	35.61	0	1.34	1.94	4.23	0.01	0.01	102.8	7126.6
193	34.75	0	1.02	2.12	5.68	0	0	102.63	7142.3
194	35.04	0	0.97	2.26	4.74	0.02	0	101.65	7146.2
195	35.35	0	0.92	2.44	4.45	0.01	0	101.25	7150.1
197	36.59	0	0.62	2.55	3.56	0.02	0.03	102.73	7157.9
198	34.84	0	0.78	2.78	3.23	0.06	0.01	98.93	7161.9
199	37.46	0	0.79	2.79	2.66	0.02	0.02	102.54	7165.8
200	37.44	0	1.08	2.85	2.15	0.02	0.02	101.98	7169.7
201	38.2	0	1.01	3.02	1.6	0.04	0.04	102.16	7173.6
202	37.62	0	1.13	3.04	1.39	0	0.01	101.48	7177.5
203	38.33	0	1.06	3	1.18	0	0	101.92	7181.4
204	37.18	0	0.93	3.07	1.1	0	0.02	100.02	7185.4
205	38.77	0	0.75	3.14	0.94	0	0.01	101.79	7189.3
206	38.47	0	0.86	3.17	0.95	0.01	0	101.61	7193.2
207	37.88	0	0.86	2.99	0.89	0.05	0	100.58	7197.1
209	38.64	0	1	3.13	0.88	0	0.03	101.8	7205
210	38.2	0	1.21	3.16	0.83	0.01	0.01	101.97	7208.9
211	38.27	0	1.16	3.1	0.74	0.01	0.02	101.28	7212.8
212	38.03	0	1.29	3.11	0.76	0.02	0	102.1	7216.7
214	37.55	0	0.93	3.04	0.87	0	0.01	100.77	7224.5
216	38.02	0	1.15	3.07	0.72	0	0.02	101.04	7232.4
217	37.64	0	1.61	3.08	0.75	0.02	0	101.4	7236.3
225	37.2	0	1.52	2.89	0.8	0	0	100.38	7267.6
228	38.15	0	1.8	2.85	0.84	0	0.01	101.29	7279.4
231	38.17	0	1.42	2.89	0.86	0.01	0	101.51	7291.1
232	37.53	0	1.52	2.79	0.91	0	0.03	101.23	7295.1
233	37.28	0	1.36	2.67	0.89	0.01	0.01	100.22	7299
235	37.98	0	1.79	2.59	0.96	0.03	0.01	101.56	7306.8
236	37.61	0	1.62	2.4	0.9	0	0.01	100.15	7310.7

POINT	Y	TSi	TAI	Sum_Z	Al ^{VI}	Fe ³	Ti	Cr	Sum_X
1	-39305	3.02	0	3.02	1.96	0	0.01	0	1.97
2	-39302	2.98	0	2.98	1.99	0	0.01	0	1.99
3	-39299	2.99	0	2.99	1.99	0	0.01	0	2
4	-39296	2.99	0	2.99	1.98	0	0.01	0	1.99
5	-39293	3	0	3	1.95	0	0.01	0	1.96
9	-39280	2.99	0	2.99	1.97	0	0.01	0	1.98
10	-39277	2.99	0	2.99	1.95	0	0.01	0	1.96
11	-39274	3	0	3	1.94	0	0.01	0	1.95
12	-39271	3	0	3	1.94	0	0.01	0	1.95
18	-39252	3	0	3	1.94	0	0.01	0	1.95
19	-39249	2.95	0	2.95	1.99	0	0.01	0	2
20	-39246	2.97	0	2.97	1.95	0	0.01	0	1.96
31	-39212	2.99	0	2.99	1.95	0	0.01	0	1.96
34	-39203	2.97	0	2.97	1.96	0	0.01	0	1.97
38	-39190	2.99	0	2.99	1.94	0	0.01	0	1.94
39	-39187	3.01	0	3.01	1.97	0	0.01	0	1.98
41	-39181	2.99	0	2.99	1.96	0	0.01	0	1.97
42	-39178	2.97	0	2.97	1.99	0	0.01	0	2
43	-39175	3	0	3	1.95	0	0.01	0	1.96
44	-39171	2.98	0	2.98	1.96	0	0.01	0	1.97
45	-39168	2.96	0	2.96	1.94	0	0.01	0	1.95
48	-39159	2.97	0	2.97	1.97	0	0.01	0	1.98
55	-39137	2.99	0	2.99	1.93	0	0.01	0	1.94
63	-39112	3	0	3	1.97	0	0.01	0	1.98
64	-39109	2.98	0	2.98	1.94	0	0.01	0	1.95
65	-39106	2.99	0	2.99	1.95	0	0.01	0	1.96
66	-39103	2.98	0	2.98	1.96	0	0.01	0	1.97
67	-39100	2.99	0	2.99	1.95	0	0.01	0	1.96
69	-39094	3	0	3	1.96	0	0.01	0	1.97
73	-39081	2.98	0	2.98	1.97	0	0.01	0	1.98
76	-39072	3.01	0	3.01	1.95	0	0.01	0	1.96
82	-39053	2.98	0	2.98	1.97	0	0.01	0	1.97
83	-39050	2.99	0	2.99	1.94	0	0.01	0	1.95
85	-39044	2.99	0	2.99	1.95	0	0.01	0	1.96
86	-39041	2.97	0	2.97	1.97	0	0.01	0	1.98
89	-39032	2.99	0	2.99	1.96	0	0.01	0	1.96
91	-39025	2.98	0	2.98	1.96	0	0.01	0	1.97
95	-39013	2.98	0	2.98	1.98	0	0.01	0	1.98
98	-39004	3.01	0	3.01	1.99	0	0	0	1.99
99	-39001	2.95	0	2.95	1.98	0	0	0	1.99
100	-38998	2.97	0	2.97	1.98	0	0	0	1.98
102	-38991	2.98	0	2.98	1.97	0	0	0	1.97
104	-38985	2.97	0	2.97	1.96	0	0.01	0	1.97
105	-38982	3.02	0	3.02	1.94	0	0.01	0	1.95
107	-38976	2.96	0	2.96	1.96	0	0	0	1.97
112	-38960	2.99	0	2.99	1.95	0	0.01	0	1.96
113	-38957	2.97	0	2.97	1.96	0	0	0	1.97
115	-38951	2.99	0	2.99	1.95	0	0.01	0	1.96
117	-38945	3	0	3	1.96	0	0.01	0	1.97

119	-38938	2.99	0	2.99	1.97	0	0	0	1.97
120	-38935	2.98	0	2.98	1.95	0	0	0	1.95
125	-38920	3.01	0	3.01	2.04	0	0	0	2.04
143	-38864	2.95	0	2.95	1.99	0	0	0	1.99
155	-38827	2.99	0	2.99	1.96	0	0	0	1.96
156	-38824	2.96	0	2.96	1.99	0	0	0	2
165	-38796	2.96	0	2.96	1.99	0	0	0	2
166	-38792	2.97	0	2.97	1.98	0	0	0	1.99
168	-38786	3.01	0	3.01	2	0	0	0	2
175	-38765	2.99	0	2.99	1.99	0	0	0	1.99
176	-38761	3	0	3	1.98	0	0	0	1.98
177	-38758	2.98	0	2.98	1.99	0	0	0	2
178	-38755	2.97	0	2.97	1.97	0	0	0	1.97
180	-38749	2.98	0	2.98	1.99	0	0	0	2
181	-38746	2.98	0	2.98	1.98	0	0	0	1.98
182	-38743	2.96	0	2.96	2	0	0	0	2
184	-38737	2.96	0	2.96	2	0	0	0	2
189	-38721	2.99	0	2.99	2	0	0	0	2
193	-38709	2.97	0	2.97	1.98	0	0	0	1.99
194	-38705	2.98	0	2.98	1.98	0	0	0	1.98
195	-38702	2.96	0	2.96	1.98	0	0	0	1.98
197	-38696	2.96	0	2.96	2.02	0	0	0	2.02
198	-38693	3.02	0	3.02	1.94	0	0	0	1.94
199	-38690	2.95	0	2.95	2	0	0	0	2
200	-38687	2.97	0	2.97	1.98	0	0	0	1.98
201	-38684	2.96	0	2.96	1.98	0	0	0	1.98
202	-38681	2.99	0	2.99	1.97	0	0	0	1.97
203	-38678	2.96	0	2.96	1.99	0	0	0	1.99
204	-38674	2.99	0	2.99	1.98	0	0	0	1.98
205	-38671	2.96	0	2.96	1.99	0	0	0	1.99
206	-38668	2.97	0	2.97	1.98	0	0	0	1.98
207	-38665	2.97	0	2.97	2	0	0	0	2
209	-38659	2.97	0	2.97	1.97	0	0	0	1.97
210	-38656	2.97	0	2.97	1.99	0	0	0	1.99
211	-38653	2.96	0	2.96	2	0	0	0	2
212	-38650	2.98	0	2.98	1.99	0	0	0	1.99
214	-38643	3.01	0	3.01	1.98	0	0	0	1.98
216	-38637	2.95	0	2.95	2.02	0	0	0	2.02
217	-38634	2.98	0	2.98	1.99	0	0	0	1.99
225	-38609	2.98	0	2.98	2.01	0	0	0	2.01
228	-38600	2.96	0	2.96	1.99	0	0	0	1.99
231	-38591	2.98	0	2.98	1.98	0	0	0	1.98
232	-38587	3	0	3	1.99	0	0	0	1.99
233	-38584	2.98	0	2.98	2.02	0	0	0	2.02
235	-38578	2.99	0	2.99	1.98	0	0	0	1.98
236	-38575	2.97	0	2.97	2.02	0	0	0	2.02

POINT	Fe ²	Mg	Mn	Ca	Na	K	Sum_Y	Sum_cat	O
1	1.68	0.06	0.43	0.85	0.01	0	3.02	8	12
2	1.7	0.05	0.44	0.86	0.01	0	3.05	8.02	12
3	1.66	0.04	0.47	0.85	0	0	3.03	8.01	12
4	1.64	0.05	0.47	0.87	0	0	3.03	8.01	12
5	1.7	0.05	0.46	0.84	0	0	3.07	8.02	12
9	1.68	0.05	0.44	0.87	0.01	0	3.04	8.02	12
10	1.68	0.04	0.47	0.86	0	0	3.06	8.02	12
11	1.71	0.05	0.44	0.87	0	0	3.07	8.02	12
12	1.69	0.05	0.44	0.88	0	0	3.07	8.02	12
18	1.7	0.05	0.46	0.87	0	0	3.08	8.03	12
19	1.72	0.05	0.46	0.86	0.01	0	3.1	8.05	12
20	1.71	0.05	0.46	0.88	0.01	0	3.11	8.05	12
31	1.67	0.05	0.46	0.89	0.01	0	3.09	8.04	12
34	1.73	0.05	0.43	0.87	0.01	0	3.09	8.04	12
38	1.71	0.05	0.47	0.87	0.01	0	3.11	8.04	12
39	1.67	0.05	0.42	0.86	0.01	0	3.01	8	12
41	1.69	0.05	0.46	0.86	0.01	0	3.06	8.03	12
42	1.68	0.05	0.44	0.88	0.01	0	3.06	8.03	12
43	1.63	0.05	0.48	0.89	0.01	0	3.05	8.02	12
44	1.7	0.05	0.45	0.89	0	0	3.09	8.04	12
45	1.76	0.04	0.47	0.86	0.01	0	3.14	8.06	12
48	1.65	0.05	0.48	0.89	0.01	0	3.09	8.04	12
55	1.69	0.05	0.47	0.88	0.01	0	3.1	8.03	12
63	1.7	0.05	0.42	0.87	0	0	3.04	8.01	12
64	1.77	0.05	0.44	0.85	0.01	0	3.11	8.04	12
65	1.74	0.05	0.42	0.86	0	0	3.07	8.02	12
66	1.74	0.05	0.42	0.87	0	0	3.09	8.04	12
67	1.74	0.05	0.4	0.88	0	0	3.07	8.02	12
69	1.71	0.05	0.43	0.85	0	0	3.04	8.01	12
73	1.89	0.08	0.36	0.74	0.01	0	3.08	8.03	12
76	2.16	0.13	0.39	0.36	0.01	0.01	3.05	8.01	12
82	2.17	0.12	0.38	0.41	0	0	3.08	8.03	12
83	2.09	0.11	0.38	0.51	0	0	3.1	8.04	12
85	1.99	0.11	0.33	0.64	0.01	0	3.09	8.04	12
86	2	0.11	0.33	0.64	0	0	3.09	8.04	12
89	2.12	0.13	0.33	0.5	0	0	3.09	8.03	12
91	2.17	0.15	0.33	0.43	0	0	3.08	8.03	12
95	2.3	0.16	0.32	0.28	0	0	3.07	8.03	12
98	2.26	0.17	0.3	0.26	0	0	2.99	7.99	12
99	2.38	0.18	0.33	0.22	0	0	3.11	8.05	12
100	2.34	0.18	0.3	0.24	0.05	0	3.11	8.06	12
102	2.32	0.17	0.32	0.27	0	0	3.08	8.03	12
104	2.28	0.16	0.32	0.34	0	0	3.11	8.05	12
105	2.2	0.14	0.31	0.38	0.01	0	3.04	8.01	12
107	2.26	0.16	0.32	0.4	0	0.01	3.14	8.06	12
112	2.21	0.16	0.25	0.46	0.01	0	3.08	8.03	12
113	2.24	0.16	0.25	0.44	0	0	3.1	8.04	12
115	2.31	0.19	0.26	0.32	0.01	0.01	3.09	8.03	12
117	2.28	0.19	0.22	0.34	0	0	3.04	8.01	12
119	2.38	0.2	0.2	0.28	0	0	3.06	8.02	12

120	2.47	0.21	0.2	0.23	0	0	3.12	8.04	12
125	2.34	0.23	0.19	0.16	0	0	2.92	7.97	12
143	2.51	0.24	0.18	0.19	0	0	3.12	8.06	12
155	2.48	0.25	0.16	0.19	0.01	0	3.09	8.04	12
156	2.45	0.25	0.17	0.2	0	0	3.08	8.04	12
165	2.46	0.26	0.14	0.21	0	0	3.08	8.04	12
166	2.5	0.25	0.15	0.18	0	0	3.09	8.04	12
168	2.4	0.25	0.15	0.17	0	0	2.98	7.99	12
175	2.44	0.25	0.14	0.21	0	0	3.05	8.02	12
176	2.43	0.24	0.16	0.2	0	0	3.04	8.01	12
177	2.41	0.24	0.16	0.23	0.01	0	3.06	8.03	12
178	2.49	0.26	0.16	0.2	0	0	3.11	8.05	12
180	2.46	0.27	0.13	0.19	0	0	3.05	8.02	12
181	2.52	0.26	0.14	0.16	0	0	3.08	8.03	12
182	2.47	0.26	0.14	0.21	0	0	3.07	8.04	12
184	2.5	0.27	0.12	0.18	0	0	3.07	8.04	12
189	2.34	0.23	0.09	0.36	0	0	3.02	8.01	12
193	2.29	0.25	0.07	0.48	0	0	3.08	8.04	12
194	2.33	0.27	0.07	0.4	0	0	3.07	8.03	12
195	2.36	0.29	0.06	0.38	0	0	3.1	8.05	12
197	2.41	0.3	0.04	0.3	0	0	3.06	8.04	12
198	2.37	0.34	0.05	0.28	0.01	0	3.06	8.02	12
199	2.48	0.33	0.05	0.23	0	0	3.09	8.05	12
200	2.49	0.34	0.07	0.18	0	0	3.09	8.04	12
201	2.54	0.36	0.07	0.14	0.01	0	3.12	8.05	12
202	2.51	0.36	0.08	0.12	0	0	3.07	8.03	12
203	2.56	0.36	0.07	0.1	0	0	3.09	8.04	12
204	2.52	0.37	0.06	0.1	0	0	3.05	8.02	12
205	2.59	0.37	0.05	0.08	0	0	3.1	8.05	12
206	2.57	0.38	0.06	0.08	0	0	3.09	8.04	12
207	2.55	0.36	0.06	0.08	0.01	0	3.06	8.03	12
209	2.58	0.37	0.07	0.08	0	0	3.1	8.04	12
210	2.54	0.37	0.08	0.07	0	0	3.07	8.03	12
211	2.57	0.37	0.08	0.06	0	0	3.09	8.04	12
212	2.52	0.37	0.09	0.06	0	0	3.05	8.02	12
214	2.52	0.36	0.06	0.07	0	0	3.02	8.01	12
216	2.55	0.37	0.08	0.06	0	0	3.06	8.04	12
217	2.52	0.37	0.11	0.06	0	0	3.06	8.03	12
225	2.51	0.35	0.1	0.07	0	0	3.03	8.02	12
228	2.57	0.34	0.12	0.07	0	0	3.11	8.05	12
231	2.56	0.34	0.1	0.07	0	0	3.07	8.03	12
232	2.51	0.33	0.1	0.08	0	0	3.03	8.01	12
233	2.52	0.32	0.09	0.08	0	0	3.02	8.01	12
235	2.54	0.31	0.12	0.08	0	0	3.06	8.03	12
236	2.55	0.29	0.11	0.08	0	0	3.04	8.02	12

POINT	Alm	Grs	Prp	Sps	XCa	XFe	XMg	Fe_Mg
1	55.8	28.07	1.88	14.24	0.28	0.56	0.02	0.97
2	55.81	28.19	1.71	14.3	0.28	0.56	0.02	0.97
3	54.79	28.17	1.44	15.59	0.28	0.55	0.01	0.97
4	54.13	28.63	1.7	15.54	0.29	0.54	0.02	0.97
5	55.64	27.54	1.64	15.18	0.28	0.56	0.02	0.97
9	55.28	28.51	1.62	14.59	0.29	0.55	0.02	0.97
10	54.98	28.26	1.47	15.29	0.28	0.55	0.01	0.97
11	55.76	28.44	1.58	14.22	0.28	0.56	0.02	0.97
12	55.25	28.74	1.52	14.49	0.29	0.55	0.02	0.97
18	55.21	28.14	1.64	15.02	0.28	0.55	0.02	0.97
19	55.7	27.91	1.63	14.75	0.28	0.56	0.02	0.97
20	55.2	28.31	1.54	14.94	0.28	0.55	0.02	0.97
31	54.27	29.06	1.6	15.06	0.29	0.54	0.02	0.97
34	56.15	28.26	1.63	13.97	0.28	0.56	0.02	0.97
38	55.11	28.1	1.62	15.17	0.28	0.55	0.02	0.97
39	55.61	28.62	1.69	14.07	0.29	0.56	0.02	0.97
41	55.33	28.04	1.65	14.99	0.28	0.55	0.02	0.97
42	54.91	28.87	1.67	14.55	0.29	0.55	0.02	0.97
43	53.51	29.27	1.53	15.69	0.29	0.54	0.02	0.97
44	55.17	28.73	1.53	14.57	0.29	0.55	0.02	0.97
45	56.23	27.29	1.43	15.06	0.27	0.56	0.01	0.98
48	53.73	29.07	1.57	15.63	0.29	0.54	0.02	0.97
55	54.63	28.53	1.7	15.14	0.29	0.55	0.02	0.97
63	55.97	28.55	1.74	13.73	0.29	0.56	0.02	0.97
64	57.01	27.34	1.63	14.02	0.27	0.57	0.02	0.97
65	56.75	27.89	1.62	13.73	0.28	0.57	0.02	0.97
66	56.35	28.28	1.7	13.68	0.28	0.56	0.02	0.97
67	56.68	28.79	1.58	12.95	0.29	0.57	0.02	0.97
69	56.23	28.04	1.59	14.14	0.28	0.56	0.02	0.97
73	61.64	24.14	2.57	11.65	0.24	0.62	0.03	0.96
76	71.16	11.94	4.19	12.7	0.12	0.71	0.04	0.94
82	70.41	13.26	3.91	12.42	0.13	0.7	0.04	0.95
83	67.43	16.61	3.67	12.29	0.17	0.67	0.04	0.95
85	64.65	20.95	3.53	10.88	0.21	0.65	0.04	0.95
86	64.78	20.87	3.56	10.79	0.21	0.65	0.04	0.95
89	68.87	16.27	4.28	10.58	0.16	0.69	0.04	0.94
91	70.46	13.88	4.79	10.87	0.14	0.7	0.05	0.94
95	75.12	9.24	5.3	10.34	0.09	0.75	0.05	0.93
98	75.67	8.56	5.64	10.13	0.09	0.76	0.06	0.93
99	76.53	7.1	5.89	10.48	0.07	0.77	0.06	0.93
100	76.39	7.95	5.8	9.85	0.08	0.76	0.06	0.93
102	75.17	8.91	5.66	10.26	0.09	0.75	0.06	0.93
104	73.35	11.04	5.24	10.36	0.11	0.73	0.05	0.93
105	72.67	12.52	4.73	10.08	0.13	0.73	0.05	0.94
107	72.02	12.66	4.95	10.37	0.13	0.72	0.05	0.94
112	71.71	14.91	5.21	8.18	0.15	0.72	0.05	0.93
113	72.34	14.26	5.26	8.13	0.14	0.72	0.05	0.93
115	75.11	10.25	6.31	8.32	0.1	0.75	0.06	0.92
117	75.07	11.17	6.38	7.38	0.11	0.75	0.06	0.92
119	77.71	9.17	6.63	6.49	0.09	0.78	0.07	0.92

120	79.3	7.41	6.87	6.42	0.07	0.79	0.07	0.92
125	80.08	5.54	8.02	6.36	0.06	0.8	0.08	0.91
143	80.43	6.19	7.62	5.76	0.06	0.8	0.08	0.91
155	80.47	6.07	8.25	5.21	0.06	0.8	0.08	0.91
156	79.69	6.4	8.26	5.65	0.06	0.8	0.08	0.91
165	80.09	6.8	8.44	4.67	0.07	0.8	0.08	0.9
166	81.19	5.78	8.13	4.9	0.06	0.81	0.08	0.91
168	80.68	5.66	8.49	5.16	0.06	0.81	0.08	0.9
175	80.29	6.79	8.2	4.73	0.07	0.8	0.08	0.91
176	80.19	6.64	8.04	5.13	0.07	0.8	0.08	0.91
177	79.13	7.69	7.97	5.21	0.08	0.79	0.08	0.91
178	80.22	6.36	8.28	5.13	0.06	0.8	0.08	0.91
180	80.65	6.25	8.79	4.31	0.06	0.81	0.09	0.9
181	81.82	5.24	8.47	4.46	0.05	0.82	0.08	0.91
182	80.29	6.77	8.35	4.58	0.07	0.8	0.08	0.91
184	81.4	5.84	8.94	3.82	0.06	0.81	0.09	0.9
189	77.67	11.82	7.55	2.97	0.12	0.78	0.08	0.91
193	74.2	15.53	8.06	2.22	0.16	0.74	0.08	0.9
194	75.97	13.17	8.74	2.12	0.13	0.76	0.09	0.9
195	76.32	12.3	9.37	2.01	0.12	0.76	0.09	0.89
197	78.97	9.85	9.82	1.36	0.1	0.79	0.1	0.89
198	77.9	9.27	11.06	1.77	0.09	0.78	0.11	0.88
199	80.32	7.3	10.66	1.72	0.07	0.8	0.11	0.88
200	80.76	5.94	10.95	2.35	0.06	0.81	0.11	0.88
201	81.9	4.39	11.52	2.18	0.04	0.82	0.12	0.88
202	81.85	3.87	11.79	2.49	0.04	0.82	0.12	0.87
203	82.84	3.27	11.57	2.33	0.03	0.83	0.12	0.88
204	82.61	3.14	12.17	2.08	0.03	0.83	0.12	0.87
205	83.67	2.59	12.09	1.65	0.03	0.84	0.12	0.87
206	83.26	2.64	12.23	1.88	0.03	0.83	0.12	0.87
207	83.77	2.53	11.78	1.92	0.03	0.84	0.12	0.88
209	83.35	2.44	12.02	2.2	0.02	0.83	0.12	0.87
210	82.84	2.3	12.19	2.66	0.02	0.83	0.12	0.87
211	83.35	2.07	12.01	2.57	0.02	0.83	0.12	0.87
212	82.93	2.12	12.1	2.85	0.02	0.83	0.12	0.87
214	83.43	2.46	12.02	2.08	0.02	0.83	0.12	0.87
216	83.41	2.03	12	2.56	0.02	0.83	0.12	0.87
217	82.33	2.1	12	3.57	0.02	0.82	0.12	0.87
225	82.83	2.27	11.47	3.43	0.02	0.83	0.11	0.88
228	82.7	2.34	11	3.96	0.02	0.83	0.11	0.88
231	83.25	2.4	11.23	3.13	0.02	0.83	0.11	0.88
232	83.03	2.58	10.98	3.41	0.03	0.83	0.11	0.88
233	83.65	2.57	10.68	3.09	0.03	0.84	0.11	0.89
235	83.24	2.68	10.1	3.98	0.03	0.83	0.1	0.89
236	84.18	2.57	9.58	3.67	0.03	0.84	0.1	0.9

Table B3 - Plagioclase microprobe spot analyses

Sample	Analysis	POINT	Location	Mineral	SiO2	TiO2	Al2O3	Fe2O3
MA271		1	MPC	Pl	62.47	0.01	23.82	0.00
MA271		2	MPC	Pl	61.80	0.01	24.39	0.00
MA271		3	MPC	Pl	61.87	0.00	24.33	0.00
MA271		4	MPC	Pl	63.35	0.00	23.08	0.00
MA271		5	MPC	Pl	62.30	0.03	23.97	0.00
MA271		6	MPC	Pl	61.55	0.00	24.61	0.00
MA271		7	MPC	Pl	61.83	0.01	24.37	0.00
MA271		8	MPC	Pl	62.39	0.06	23.90	0.00
MA271		9	MPC	Pl	60.23	0.00	25.73	0.00
MA271		10	MPC	Pl	60.36	0.01	25.62	0.00
MA271		11	MPC	Pl	60.44	0.01	25.55	0.00
MA271		12	MPC	Pl	61.38	0.08	24.76	0.00
MA271		13	MPC	Pl	61.56	0.05	24.60	0.00
MA271		14	MPC	Pl	62.93	0.00	23.44	0.00
MA271		15	MPC	Pl	63.44	0.02	23.01	0.00
MA271		16	MPC	Pl	61.79	0.00	24.40	0.00
MA271		17	MPC	Pl	62.43	0.04	23.87	0.00
MA271		18	MPC	Pl	61.43	0.04	24.71	0.00
MA271		19	MPC	Pl	61.97	0.05	24.25	0.00
MA271		20	MPC	Pl	62.94	0.00	23.43	0.00
FeO	MnO	MgO	BaO	CaO	Na2O	K2O	Total	X
0.21	0.02	0.00	0.00	4.47	9.09	0.01	100.12	3966.8
0.00	0.03	0.08	0.00	5.48	8.40	0.09	100.29	4047.0
0.00	0.07	0.00	0.00	5.55	8.58	0.00	100.41	4154.0
0.00	0.03	0.00	0.00	5.92	8.29	0.00	100.67	4225.4
0.00	0.02	0.00	0.00	6.92	7.73	0.01	100.98	5295.4
0.00	0.04	0.04	0.00	5.57	8.31	0.36	100.49	5429.1
0.00	0.00	0.01	0.00	5.79	8.39	0.11	100.51	5558.4
0.00	0.00	0.03	0.00	5.81	8.41	0.02	100.61	5692.2
0.00	0.03	0.04	0.00	5.59	8.40	0.10	100.12	5897.3
0.00	0.03	0.03	0.00	6.83	7.85	0.01	100.74	7123.3
0.00	0.00	0.04	0.00	5.29	8.50	0.33	100.16	7217.0
0.00	0.00	0.03	0.00	4.86	8.85	0.00	99.96	7324.0
0.00	0.01	0.00	0.00	5.47	8.40	0.07	100.16	7417.6
0.00	0.00	0.03	0.00	5.44	8.65	0.00	100.48	6998.5
0.00	0.00	0.09	0.00	5.45	8.54	0.07	100.61	7020.8
0.00	0.00	0.00	0.00	7.30	7.64	0.00	101.14	4983.3
0.00	0.01	0.00	0.00	6.63	7.89	0.00	100.87	8072.8
0.00	0.00	0.00	0.00	6.75	7.93	0.00	100.86	8393.7
0.00	0.01	0.00	0.00	7.39	7.41	0.08	101.17	8389.8
0.00	0.07	0.00	0.00	5.39	8.66	0.00	100.50	8383.8
Y	Si	Al	Fe3	Sum_Z	Ti	Fe2	Mn	Mg
-38490.1	2.76	1.24	0.00	4.00	0.00	0.01	0.00	0.00

-38496.3	2.73	1.27	0.00	4.00	0.00	0.01	0.00	0.01
-38496.3	2.73	1.27	0.00	4.00	0.00	0.00	0.00	0.00
-38510.6	2.80	1.20	0.00	4.00	0.00	0.01	0.00	0.00
-38365.0	2.75	1.25	0.00	4.00	0.00	0.01	0.00	0.00
-38340.4	2.72	1.28	0.00	4.00	0.00	0.00	0.00	0.00
-38328.1	2.73	1.27	0.00	4.00	0.00	0.00	0.00	0.00
-38311.6	2.76	1.24	0.00	4.00	0.00	0.00	0.00	0.00
-38229.6	2.66	1.34	0.00	4.00	0.00	0.01	0.00	0.00
-38301.4	2.67	1.33	0.00	4.00	0.00	0.00	0.00	0.00
-38241.9	2.67	1.33	0.00	4.00	0.00	0.00	0.00	0.00
-38252.2	2.71	1.29	0.00	4.00	0.00	0.01	0.00	0.00
-38258.3	2.72	1.28	0.00	4.00	0.00	0.02	0.00	0.00
-37971.1	2.78	1.22	0.00	4.00	0.00	0.00	0.00	0.00
-37938.3	2.80	1.20	0.00	4.00	0.00	0.00	0.00	0.01
-39119.9	2.73	1.27	0.00	4.00	0.00	0.00	0.00	0.00
-38988.9	2.76	1.24	0.00	4.00	0.00	0.01	0.00	0.00
-39165.9	2.71	1.29	0.00	4.00	0.00	0.00	0.00	0.00
-38922.8	2.74	1.26	0.00	4.00	0.00	0.01	0.00	0.00
-38966.9	2.78	1.22	0.00	4.00	0.00	0.00	0.00	0.00

Ba	Ca	Na	K	Sum_X	Cations	O	Ab	An
0.00	0.21	0.78	0.00	1.00	5.00	8	78.60	21.37
0.00	0.26	0.72	0.01	1.00	5.00	8	73.11	26.37
0.00	0.26	0.73	0.00	1.00	5.00	8	73.67	26.31
0.00	0.28	0.71	0.00	1.00	5.00	8	71.71	28.29
0.00	0.33	0.66	0.00	1.00	5.00	8	66.87	33.08
0.00	0.26	0.71	0.02	1.00	5.00	8	71.48	26.49
0.00	0.27	0.72	0.01	1.00	5.00	8	71.94	27.43
0.00	0.27	0.72	0.00	1.00	5.00	8	72.30	27.60
0.00	0.26	0.72	0.01	1.00	5.00	8	72.67	26.76
0.00	0.32	0.67	0.00	1.00	5.00	8	67.49	32.43
0.00	0.25	0.73	0.02	1.00	5.00	8	73.01	25.14
0.00	0.23	0.76	0.00	1.00	5.00	8	76.70	23.29
0.00	0.26	0.72	0.00	1.00	5.00	8	73.24	26.35
0.00	0.26	0.74	0.00	1.00	5.00	8	74.20	25.80
0.00	0.26	0.73	0.00	1.00	5.00	8	73.60	25.98
0.00	0.35	0.65	0.00	1.00	5.00	8	65.42	34.56
0.00	0.31	0.68	0.00	1.00	5.00	8	68.28	31.71
0.00	0.32	0.68	0.00	1.00	5.00	8	68.01	31.99
0.00	0.35	0.63	0.00	1.00	5.00	8	64.19	35.37
0.00	0.26	0.74	0.00	1.00	5.00	8	74.41	25.59

Or	XAn	XAlb	XOr
0.03	0.79	0.21	0.00
0.51	0.73	0.26	0.01
0.01	0.74	0.26	0.00
0.00	0.72	0.28	0.00

0.05	0.67	0.33	0.00
2.03	0.71	0.26	0.02
0.62	0.72	0.27	0.01
0.10	0.72	0.28	0.00
0.57	0.73	0.27	0.01
0.08	0.67	0.32	0.00
1.85	0.73	0.25	0.02
0.01	0.77	0.23	0.00
0.41	0.73	0.26	0.00
0.00	0.74	0.26	0.00
0.42	0.74	0.26	0.00
0.02	0.65	0.35	0.00
0.01	0.68	0.32	0.00
0.00	0.68	0.32	0.00
0.44	0.64	0.35	0.00
0.01	0.74	0.26	0.00

Table B4 - Biotite microprobe spot analyses

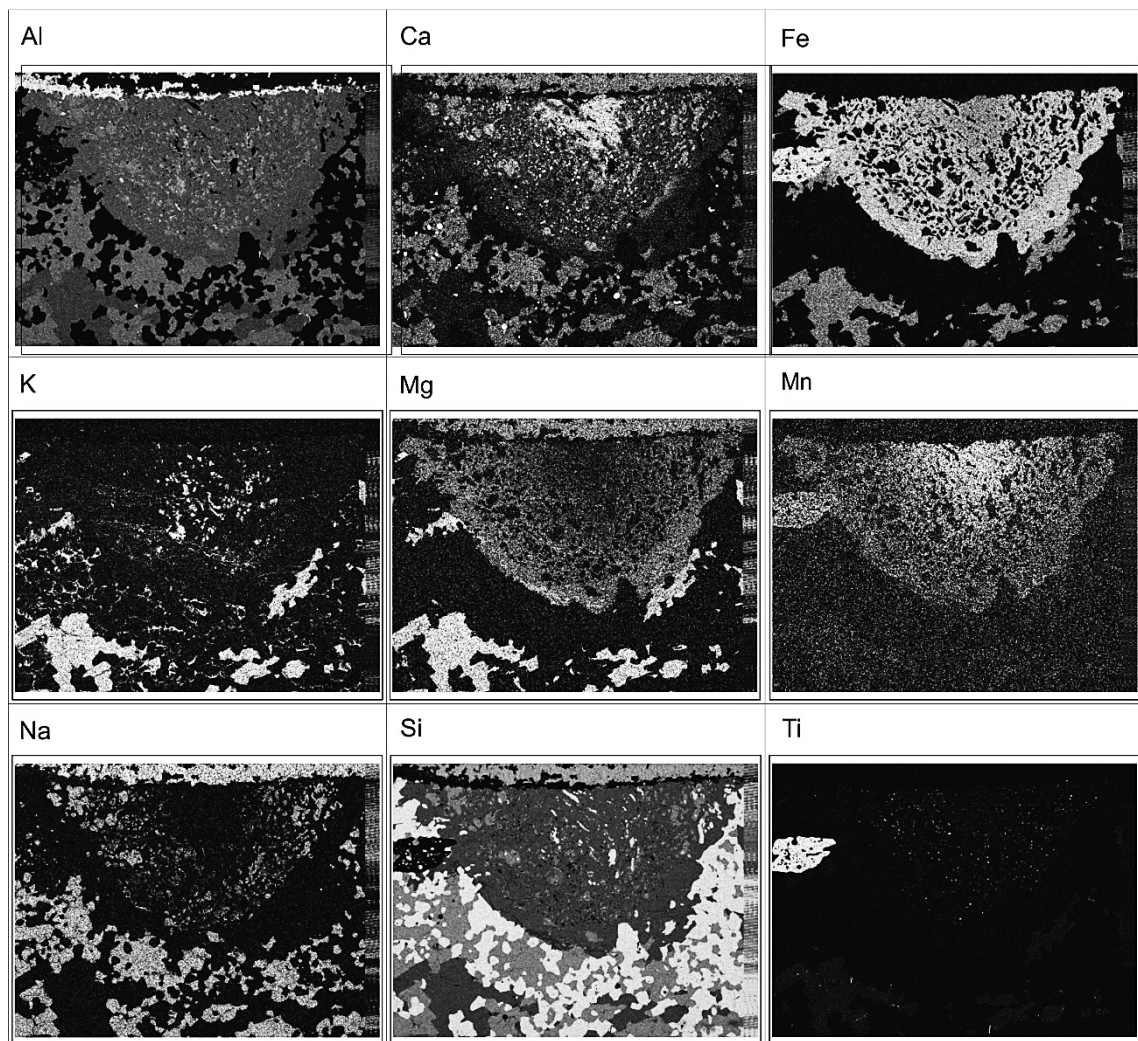
Sample	Analysis	POINT	Location	Mineral	SiO2	TiO2	Al2O3	Cr2O3
MA271		1	MPC	Bt	36.48	2.39	18.09	0.00
MA271		2	MPC	Bt	36.37	1.78	18.05	0.00
MA271		3	MPC	Bt	36.58	2.06	17.75	0.00
MA271		4	MPC	Bt	36.70	3.03	18.37	0.00
MA271		5	MPC	Bt	36.80	2.39	18.07	0.00
MA271		6	MPC	Bt	36.72	2.23	18.13	0.00
MA271		7	MPC	Bt	36.45	2.80	18.00	0.00
MA271		8	MPC	Bt	36.67	2.14	17.71	0.00
MA271		9	MPC	Bt	36.41	3.32	17.92	0.00
MA271		10	MPC	Bt	36.62	2.55	18.00	0.00
MA271		11	MPC	Bt	36.68	2.63	17.64	0.00
MA271		12	MPC	Bt	36.34	3.02	17.83	0.00
MA271		13	MPC	Bt	36.62	2.50	18.53	0.00
MA271		14	MPC	Bt	36.62	2.73	17.75	0.00
MA271		15	MPC	Bt	36.71	2.71	18.39	0.00
MA271		16	MPC	Bt	36.71	2.10	17.88	0.00
MA271		17	MPC	Bt	36.63	2.82	18.10	0.00
MA271		18	MPC	Bt	36.61	2.44	17.81	0.00
MA271		19	MPC	Bt	36.41	2.13	17.89	0.00
MA271		20	MPC	Bt	36.84	2.35	18.08	0.00
MA271		21	MPC	Bt	36.75	2.28	17.88	0.00
MA271		22	MPC	Bt	36.60	2.94	18.01	0.00
FeO	Fe2O3	MnO	MgO	BaO	CaO	Na2O	K2O	V2O5
24.26	0.00	0.03	9.00	0.00	0.00	0.17	9.55	0.00
23.35	0.00	0.03	8.99	0.00	0.04	0.00	9.52	0.00
23.10	0.00	0.03	8.40	0.00	0.03	0.00	9.09	0.00

23.43	0.00	0.00	7.71	0.00	0.02	0.31	9.35	0.00
23.54	0.00	0.03	8.00	0.00	0.02	0.14	9.34	0.00
24.19	0.00	0.00	8.29	0.00	0.04	0.29	9.51	0.00
23.11	0.00	0.03	9.17	0.00	0.00	0.07	9.24	0.00
23.29	0.00	0.00	7.55	0.00	0.04	0.13	9.22	0.00
23.77	0.00	0.00	8.01	0.00	0.05	0.00	9.11	0.00
23.53	0.00	0.00	7.98	0.00	0.04	0.14	9.32	0.00
23.35	0.00	0.03	7.29	0.00	0.02	0.06	9.60	0.00
23.66	0.00	0.07	8.06	0.00	0.04	0.00	9.27	0.00
23.94	0.00	0.04	7.70	0.00	0.00	0.00	9.40	0.00
23.62	0.00	0.03	8.56	0.00	0.05	0.00	8.97	0.00
24.15	0.00	0.00	8.38	0.00	0.02	0.30	9.43	0.00
23.52	0.00	0.00	8.04	0.00	0.02	0.13	9.61	0.00
23.71	0.00	0.03	7.46	0.00	0.02	0.06	9.36	0.00
23.92	0.00	0.00	8.50	0.00	0.05	0.06	9.21	0.00
24.18	0.00	0.04	7.48	0.00	0.02	0.00	9.42	0.00
24.12	0.00	0.05	7.49	0.00	0.04	0.00	9.67	0.00
23.82	0.00	0.03	7.15	0.00	0.04	0.06	9.26	0.00
23.28	0.00	0.00	7.54	0.00	0.02	0.23	9.77	0.00
Total	X	Y	Si	AlIV	AlVI	Ti	Fe3	Fe2
99.98	3987.4	-38214	2.72	1.28	0.32	0.13	0.00	1.51
98.14	4022.1	-38223	2.72	1.28	0.30	0.10	0.00	1.46
97.03	4091.6	-38244	2.73	1.27	0.29	0.12	0.00	1.44
98.91	4151.7	-38264	2.74	1.26	0.36	0.17	0.00	1.46
98.34	4223.9	-38284	2.75	1.25	0.34	0.13	0.00	1.47
99.42	4289.4	-38306	2.74	1.26	0.34	0.13	0.00	1.51
98.88	4337.5	-38327	2.72	1.28	0.30	0.16	0.00	1.44
96.74	6672.0	-38013	2.74	1.26	0.30	0.12	0.00	1.45
98.60	6703.2	-38024	2.72	1.28	0.29	0.19	0.00	1.48
98.19	6738.0	-38035	2.73	1.27	0.32	0.14	0.00	1.47
97.30	6776.5	-38045	2.74	1.26	0.29	0.15	0.00	1.46
98.29	6815.0	-38057	2.71	1.29	0.28	0.17	0.00	1.48
98.72	6860.8	-38064	2.73	1.27	0.36	0.14	0.00	1.49
98.33	7013.0	-38054	2.73	1.27	0.30	0.15	0.00	1.47
100.09	7064.3	-38074	2.74	1.26	0.36	0.15	0.00	1.51
98.02	7310.0	-38039	2.74	1.26	0.31	0.12	0.00	1.47
98.19	7372.3	-38055	2.73	1.27	0.33	0.16	0.00	1.48
98.61	7434.6	-38068	2.73	1.27	0.30	0.14	0.00	1.49
97.57	6496.0	-38120	2.72	1.28	0.29	0.12	0.00	1.51
98.64	6534.5	-38127	2.75	1.25	0.34	0.13	0.00	1.51
97.28	7315.5	-38454	2.74	1.26	0.32	0.13	0.00	1.49
98.38	7383.3	-38485	2.73	1.27	0.32	0.17	0.00	1.45
Cr	Mn	Mg	Ba	Ca	Na	K	Cations	O
0.00	0.00	1.00	0.00	0.00	0.02	0.91	7.90	11
0.00	0.00	1.00	0.00	0.00	0.00	0.91	7.77	11
0.00	0.00	0.93	0.00	0.00	0.00	0.87	7.65	11

0.00	0.00	0.86	0.00	0.00	0.04	0.89	7.78	11
0.00	0.00	0.89	0.00	0.00	0.02	0.89	7.74	11
0.00	0.00	0.92	0.00	0.00	0.04	0.91	7.85	11
0.00	0.00	1.02	0.00	0.00	0.01	0.88	7.82	11
0.00	0.00	0.84	0.00	0.00	0.02	0.88	7.61	11
0.00	0.00	0.89	0.00	0.00	0.00	0.87	7.73	11
0.00	0.00	0.89	0.00	0.00	0.02	0.89	7.73	11
0.00	0.00	0.81	0.00	0.00	0.01	0.91	7.63	11
0.00	0.00	0.90	0.00	0.00	0.00	0.88	7.72	11
0.00	0.00	0.86	0.00	0.00	0.00	0.89	7.75	11
0.00	0.00	0.95	0.00	0.00	0.00	0.85	7.74	11
0.00	0.00	0.93	0.00	0.00	0.04	0.90	7.89	11
0.00	0.00	0.90	0.00	0.00	0.02	0.92	7.73	11
0.00	0.00	0.83	0.00	0.00	0.01	0.89	7.70	11
0.00	0.00	0.95	0.00	0.00	0.01	0.88	7.77	11
0.00	0.00	0.83	0.00	0.00	0.00	0.90	7.66	11
0.00	0.00	0.83	0.00	0.00	0.00	0.92	7.74	11
0.00	0.00	0.80	0.00	0.00	0.01	0.88	7.62	11
0.00	0.00	0.84	0.00	0.00	0.03	0.93	7.74	11

Fe_FeMg	Mg_FeMg
0.60	0.40
0.59	0.41
0.61	0.39
0.63	0.37
0.62	0.38
0.62	0.38
0.59	0.41
0.63	0.37
0.62	0.38
0.62	0.38
0.64	0.36
0.62	0.38
0.64	0.36
0.61	0.39
0.62	0.38
0.62	0.38
0.64	0.36
0.61	0.39
0.64	0.36
0.64	0.36
0.65	0.35
0.63	0.37

APPENDIX B3 – X-ray maps of the studied example domain



APPENDIX B4 – Input control spot analysis

Table B5a - Garnet input chemical data (i.e. PtAnls.xlsx) used by Q-XRMA to make a point shape file.

Id	ID_SAMPLE	LOCATION	MINERAL	SUB_PHASE	DOMAIN	ANALYSIS	POINT	AI
1	MA271	MPC	Grt		10	94	1	1.95
2	MA271	MPC	Grt		10	94	2	1.98
3	MA271	MPC	Grt		10	94	3	1.98
4	MA271	MPC	Grt		10	94	4	1.97
5	MA271	MPC	Grt		10	94	5	1.94
6	MA271	MPC	Grt		10	94	9	1.97
7	MA271	MPC	Grt		10	94	10	1.95
8	MA271	MPC	Grt		10	94	11	1.94
9	MA271	MPC	Grt		10	94	12	1.94
10	MA271	MPC	Grt		10	94	18	1.93
11	MA271	MPC	Grt		10	94	19	1.98
12	MA271	MPC	Grt		10	94	20	1.95
13	MA271	MPC	Grt		10	94	31	1.94
14	MA271	MPC	Grt		10	94	34	1.96
15	MA271	MPC	Grt		10	94	38	1.93
16	MA271	MPC	Grt		10	94	39	1.97
17	MA271	MPC	Grt		10	94	41	1.95
18	MA271	MPC	Grt		10	94	42	1.98
19	MA271	MPC	Grt		10	94	43	1.95
20	MA271	MPC	Grt		10	94	44	1.95
21	MA271	MPC	Grt		10	94	45	1.94
22	MA271	MPC	Grt		10	94	48	1.96
23	MA271	MPC	Grt		10	94	55	1.93
24	MA271	MPC	Grt		10	94	63	1.96
25	MA271	MPC	Grt		10	94	64	1.94
26	MA271	MPC	Grt		10	94	65	1.94
27	MA271	MPC	Grt		10	94	66	1.95
28	MA271	MPC	Grt		10	94	67	1.94
29	MA271	MPC	Grt		10	94	69	1.96
30	MA271	MPC	Grt		10	94	73	1.96
31	MA271	MPC	Grt		10	94	76	1.94
32	MA271	MPC	Grt		10	94	82	1.96
33	MA271	MPC	Grt		10	94	83	1.94
34	MA271	MPC	Grt		10	94	85	1.94
35	MA271	MPC	Grt		10	94	86	1.97
36	MA271	MPC	Grt		10	94	89	1.95
37	MA271	MPC	Grt		10	94	91	1.95
38	MA271	MPC	Grt		10	94	95	1.97
39	MA271	MPC	Grt		10	94	98	1.99
40	MA271	MPC	Grt		10	94	99	1.98
41	MA271	MPC	Grt		10	94	100	1.97
42	MA271	MPC	Grt		10	94	102	1.96
43	MA271	MPC	Grt		10	94	104	1.96

44	MA271	MPC	Grt	10	94	105	1.94
45	MA271	MPC	Grt	10	94	107	1.95
46	MA271	MPC	Grt	10	94	112	1.95
47	MA271	MPC	Grt	10	94	113	1.96
48	MA271	MPC	Grt	10	94	115	1.95
49	MA271	MPC	Grt	10	94	117	1.96
50	MA271	MPC	Grt	10	94	119	1.97
51	MA271	MPC	Grt	10	94	120	1.94
52	MA271	MPC	Grt	10	94	125	2.04
53	MA271	MPC	Grt	10	94	143	1.98
54	MA271	MPC	Grt	10	94	155	1.95
55	MA271	MPC	Grt	10	94	156	1.99
56	MA271	MPC	Grt	10	94	165	1.99
57	MA271	MPC	Grt	10	94	166	1.98
58	MA271	MPC	Grt	10	94	168	2.00
59	MA271	MPC	Grt	10	94	175	1.98
60	MA271	MPC	Grt	10	94	176	1.97
61	MA271	MPC	Grt	10	94	177	1.99
62	MA271	MPC	Grt	10	94	178	1.96
63	MA271	MPC	Grt	10	94	180	1.99
64	MA271	MPC	Grt	10	94	181	1.97
65	MA271	MPC	Grt	10	94	182	2.00
66	MA271	MPC	Grt	10	94	184	1.99
67	MA271	MPC	Grt	10	94	189	2.00
68	MA271	MPC	Grt	10	94	193	1.98
69	MA271	MPC	Grt	10	94	194	1.97
70	MA271	MPC	Grt	10	94	195	1.98
71	MA271	MPC	Grt	10	94	197	2.02
72	MA271	MPC	Grt	10	94	198	1.94
73	MA271	MPC	Grt	10	94	199	1.99
74	MA271	MPC	Grt	10	94	200	1.97
75	MA271	MPC	Grt	10	94	201	1.97
76	MA271	MPC	Grt	10	94	202	1.97
77	MA271	MPC	Grt	10	94	203	1.98
78	MA271	MPC	Grt	10	94	204	1.98
79	MA271	MPC	Grt	10	94	205	1.98
80	MA271	MPC	Grt	10	94	206	1.98
81	MA271	MPC	Grt	10	94	207	2.00
82	MA271	MPC	Grt	10	94	209	1.97
83	MA271	MPC	Grt	10	94	210	1.99
84	MA271	MPC	Grt	10	94	211	2.00
85	MA271	MPC	Grt	10	94	212	1.99
86	MA271	MPC	Grt	10	94	214	1.98
87	MA271	MPC	Grt	10	94	216	2.01
88	MA271	MPC	Grt	10	94	217	1.98
89	MA271	MPC	Grt	10	94	225	2.01
90	MA271	MPC	Grt	10	94	228	1.98
91	MA271	MPC	Grt	10	94	231	1.97

92	MA271	MPC	Grt			10	94	232	1.98
93	MA271	MPC	Grt			10	94	233	2.02
94	MA271	MPC	Grt			10	94	235	1.98
95	MA271	MPC	Grt			10	94	236	2.02
Ca	Fe	K	Mg	Mn	Ti	Na	P	Si	Ti
0.84	1.68	0.00	0.06	0.43		0.01	0.00	3.01	0.01
0.86	1.70	0.00	0.05	0.43		0.01	0.00	2.97	0.01
0.85	1.65	0.00	0.04	0.47		0.00	0.00	2.98	0.01
0.87	1.64	0.00	0.05	0.47		0.00	0.00	2.98	0.01
0.84	1.70	0.00	0.05	0.46		0.00	0.00	2.99	0.01
0.86	1.68	0.00	0.05	0.44		0.01	0.00	2.99	0.01
0.86	1.68	0.00	0.04	0.47		0.00	0.00	2.99	0.01
0.87	1.71	0.00	0.05	0.44		0.00	0.00	2.99	0.01
0.88	1.69	0.00	0.05	0.44		0.00	0.00	2.99	0.01
0.86	1.69	0.00	0.05	0.46		0.00	0.00	2.99	0.01
0.86	1.71	0.00	0.05	0.45		0.01	0.00	2.93	0.01
0.88	1.71	0.00	0.05	0.46		0.01	0.00	2.96	0.01
0.89	1.66	0.00	0.05	0.46		0.01	0.00	2.97	0.01
0.87	1.73	0.00	0.05	0.43		0.01	0.00	2.97	0.01
0.87	1.70	0.00	0.05	0.47		0.01	0.00	2.98	0.01
0.86	1.67	0.00	0.05	0.42		0.01	0.00	3.00	0.01
0.85	1.68	0.00	0.05	0.46		0.01	0.00	2.98	0.01
0.88	1.67	0.00	0.05	0.44		0.01	0.00	2.96	0.01
0.89	1.62	0.00	0.05	0.48		0.01	0.00	3.00	0.01
0.88	1.70	0.00	0.05	0.45		0.00	0.00	2.97	0.01
0.85	1.76	0.00	0.04	0.47		0.01	0.00	2.95	0.01
0.89	1.65	0.00	0.05	0.48		0.01	0.00	2.96	0.01
0.88	1.68	0.00	0.05	0.47		0.01	0.00	2.99	0.01
0.87	1.70	0.00	0.05	0.42		0.00	0.00	2.99	0.01
0.85	1.77	0.00	0.05	0.43		0.01	0.00	2.97	0.01
0.85	1.74	0.00	0.05	0.42		0.00	0.00	2.99	0.01
0.87	1.74	0.00	0.05	0.42		0.00	0.00	2.97	0.01
0.88	1.74	0.00	0.05	0.40		0.00	0.00	2.99	0.01
0.85	1.70	0.00	0.05	0.43		0.00	0.00	2.99	0.01
0.74	1.89	0.00	0.08	0.36		0.01	0.00	2.97	0.01
0.36	2.16	0.01	0.13	0.39		0.01	0.00	3.00	0.01
0.41	2.16	0.00	0.12	0.38		0.00	0.00	2.97	0.01
0.51	2.09	0.00	0.11	0.38		0.00	0.00	2.98	0.01
0.64	1.98	0.00	0.11	0.33		0.01	0.00	2.98	0.01
0.64	2.00	0.00	0.11	0.33		0.00	0.00	2.96	0.01
0.50	2.11	0.00	0.13	0.32		0.00	0.00	2.98	0.01
0.43	2.16	0.00	0.15	0.33		0.00	0.00	2.97	0.01
0.28	2.29	0.00	0.16	0.32		0.00	0.00	2.97	0.01
0.26	2.26	0.00	0.17	0.30		0.00	0.00	3.00	0.00
0.22	2.37	0.00	0.18	0.32		0.00	0.00	2.95	0.00
0.24	2.33	0.00	0.18	0.30		0.05	0.00	2.96	0.00
0.27	2.31	0.00	0.17	0.32		0.00	0.00	2.97	0.00

0.34	2.27	0.00	0.16	0.32	0.00	0.00	2.96	0.01
0.38	2.20	0.00	0.14	0.30	0.01	0.00	3.00	0.01
0.39	2.25	0.01	0.15	0.32	0.00	0.00	2.94	0.00
0.46	2.20	0.00	0.16	0.25	0.01	0.01	2.98	0.01
0.44	2.24	0.00	0.16	0.25	0.00	0.00	2.96	0.00
0.31	2.30	0.01	0.19	0.26	0.01	0.00	2.98	0.01
0.34	2.28	0.00	0.19	0.22	0.00	0.01	3.00	0.01
0.28	2.37	0.00	0.20	0.20	0.00	0.00	2.98	0.00
0.23	2.46	0.00	0.21	0.20	0.00	0.00	2.97	0.00
0.16	2.34	0.00	0.24	0.19	0.00	0.00	3.01	0.00
0.19	2.50	0.00	0.24	0.18	0.00	0.00	2.94	0.00
0.19	2.47	0.00	0.25	0.16	0.01	0.00	2.98	0.00
0.20	2.44	0.00	0.25	0.17	0.00	0.00	2.95	0.00
0.21	2.46	0.00	0.26	0.14	0.00	0.00	2.96	0.00
0.18	2.50	0.00	0.25	0.15	0.00	0.00	2.96	0.00
0.17	2.40	0.00	0.25	0.15	0.00	0.00	3.01	0.00
0.21	2.44	0.00	0.25	0.14	0.00	0.00	2.98	0.00
0.20	2.43	0.00	0.24	0.16	0.00	0.00	2.99	0.00
0.23	2.41	0.00	0.24	0.16	0.01	0.00	2.97	0.00
0.20	2.48	0.00	0.26	0.16	0.00	0.00	2.96	0.00
0.19	2.46	0.00	0.27	0.13	0.00	0.00	2.97	0.00
0.16	2.51	0.00	0.26	0.14	0.00	0.00	2.97	0.00
0.21	2.46	0.00	0.26	0.14	0.00	0.00	2.95	0.00
0.18	2.49	0.00	0.27	0.12	0.00	0.00	2.96	0.00
0.36	2.34	0.00	0.23	0.09	0.00	0.00	2.99	0.00
0.48	2.28	0.00	0.25	0.07	0.00	0.00	2.96	0.00
0.40	2.32	0.00	0.27	0.06	0.00	0.00	2.97	0.00
0.38	2.36	0.00	0.29	0.06	0.00	0.00	2.95	0.00
0.30	2.40	0.00	0.30	0.04	0.00	0.01	2.94	0.00
0.28	2.37	0.00	0.34	0.05	0.01	0.00	3.01	0.00
0.22	2.47	0.00	0.33	0.05	0.00	0.00	2.95	0.00
0.18	2.48	0.00	0.34	0.07	0.00	0.00	2.96	0.00
0.14	2.54	0.00	0.36	0.07	0.01	0.00	2.95	0.00
0.12	2.51	0.00	0.36	0.08	0.00	0.00	2.98	0.00
0.10	2.55	0.00	0.36	0.07	0.00	0.00	2.96	0.00
0.10	2.51	0.00	0.37	0.06	0.00	0.00	2.98	0.00
0.08	2.58	0.00	0.37	0.05	0.00	0.00	2.95	0.00
0.08	2.57	0.00	0.38	0.06	0.00	0.00	2.96	0.00
0.08	2.55	0.00	0.36	0.06	0.01	0.00	2.96	0.00
0.08	2.58	0.00	0.37	0.07	0.00	0.00	2.96	0.00
0.07	2.54	0.00	0.37	0.08	0.00	0.00	2.96	0.00
0.06	2.56	0.00	0.37	0.08	0.00	0.00	2.95	0.00
0.06	2.52	0.00	0.37	0.09	0.00	0.00	2.98	0.00
0.07	2.52	0.00	0.36	0.06	0.00	0.00	3.00	0.00
0.06	2.55	0.00	0.37	0.08	0.00	0.00	2.94	0.00
0.06	2.51	0.00	0.37	0.11	0.00	0.00	2.97	0.00
0.07	2.51	0.00	0.35	0.10	0.00	0.00	2.97	0.00
0.07	2.56	0.00	0.34	0.12	0.00	0.01	2.94	0.00

0.07	2.55	0.00	0.34	0.10	0.00	0.00	2.97	0.00
0.08	2.51	0.00	0.33	0.10	0.00	0.01	2.99	0.00
0.08	2.52	0.00	0.32	0.09	0.00	0.00	2.97	0.00
0.08	2.54	0.00	0.31	0.12	0.00	0.00	2.98	0.00
0.08	2.55	0.00	0.29	0.11	0.00	0.00	2.96	0.00

POINT_X	POINT_Y
2.15	2.64
2.15	2.63
2.15	2.63
2.16	2.62
2.16	2.61
2.17	2.59
2.18	2.58
2.18	2.58
2.18	2.57
2.20	2.54
2.21	2.53
2.21	2.53
2.25	2.46
2.26	2.44
2.27	2.42
2.27	2.41
2.28	2.40
2.28	2.40
2.29	2.39
2.29	2.38
2.29	2.38
2.30	2.36
2.33	2.32
2.36	2.27
2.36	2.27
2.36	2.26
2.37	2.26
2.37	2.25
2.38	2.24
2.39	2.21
2.40	2.20
2.42	2.16
2.42	2.16
2.43	2.14
2.43	2.14
2.44	2.12
2.45	2.11
2.46	2.09
2.48	2.07
2.48	2.06
2.48	2.06

2.49	2.04
2.50	2.03
2.50	2.03
2.51	2.02
2.52	1.99
2.53	1.98
2.53	1.97
2.54	1.96
2.55	1.94
2.55	1.94
2.57	1.91
2.63	1.80
2.67	1.73
2.67	1.73
2.70	1.68
2.71	1.67
2.71	1.66
2.74	1.62
2.74	1.61
2.74	1.60
2.75	1.60
2.75	1.59
2.76	1.58
2.76	1.58
2.77	1.56
2.78	1.53
2.80	1.51
2.80	1.50
2.81	1.50
2.81	1.49
2.82	1.48
2.82	1.48
2.82	1.47
2.83	1.46
2.83	1.46
2.83	1.45
2.84	1.45
2.84	1.44
2.84	1.43
2.85	1.43
2.85	1.42
2.86	1.41
2.86	1.41
2.86	1.40
2.87	1.39
2.88	1.38
2.88	1.37
2.91	1.32

2.92	1.31
2.93	1.29
2.93	1.28
2.93	1.28
2.94	1.26
2.94	1.26

Table B6 - Plagioclase input chemical data (i.e. PtAnls.xlsx) used by Q-XRMA to make a point shape file.

Id	ID_SAMPLE	LOCATION	MINERAL	SUB_PHASE	DOMAIN	ANALYSIS	POINT	AI
1	MA271	MPC	PI		10		1	1.24
2	MA271	MPC	PI		10		2	1.27
3	MA271	MPC	PI		10		3	1.27
4	MA271	MPC	PI		10		4	1.20
5	MA271	MPC	PI		10		5	1.25
6	MA271	MPC	PI		10		6	1.28
7	MA271	MPC	PI		10		7	1.27
8	MA271	MPC	PI		10		8	1.24
9	MA271	MPC	PI		10		9	1.34
10	MA271	MPC	PI		10		10	1.33
11	MA271	MPC	PI		10		11	1.33
12	MA271	MPC	PI		10		12	1.29
13	MA271	MPC	PI		10		13	1.28
14	MA271	MPC	PI		10		14	1.22
15	MA271	MPC	PI		10		15	1.20
16	MA271	MPC	PI		10		16	1.27
17	MA271	MPC	PI		10		17	1.24
18	MA271	MPC	PI		10		18	1.29
19	MA271	MPC	PI		10		19	1.26
20	MA271	MPC	PI		10		20	1.22
Ca	Fe	K	Mg	Mn	Na	P	Si	Ti
0.21	0.01	0.00	0.00	0.00	0.78	0.00	2.76	0.00
0.26	0.01	0.01	0.01	0.00	0.72	0.00	2.73	0.00
0.26	0.00	0.00	0.00	0.00	0.73	0.00	2.73	0.00
0.28	0.01	0.00	0.00	0.00	0.71	0.00	2.80	0.00
0.33	0.01	0.00	0.00	0.00	0.66	0.00	2.75	0.00
0.26	0.00	0.02	0.00	0.00	0.71	0.00	2.72	0.00
0.27	0.00	0.01	0.00	0.00	0.72	0.00	2.73	0.00
0.27	0.00	0.00	0.00	0.00	0.72	0.00	2.76	0.00
0.26	0.01	0.01	0.00	0.00	0.72	0.00	2.66	0.00
0.32	0.00	0.00	0.00	0.00	0.67	0.00	2.67	0.00
0.25	0.00	0.02	0.00	0.00	0.73	0.00	2.67	0.00
0.23	0.01	0.00	0.00	0.00	0.76	0.00	2.71	0.00
0.26	0.02	0.00	0.00	0.00	0.72	0.00	2.72	0.00
0.26	0.00	0.00	0.00	0.00	0.74	0.00	2.78	0.00

0.26	0.00	0.00	0.01	0.00	0.73	0.00	2.80	0.00
0.35	0.00	0.00	0.00	0.00	0.65	0.00	2.73	0.00
0.31	0.01	0.00	0.00	0.00	0.68	0.00	2.76	0.00
0.32	0.00	0.00	0.00	0.00	0.68	0.00	2.71	0.00
0.35	0.01	0.00	0.00	0.00	0.63	0.00	2.74	0.00
0.26	0.00	0.00	0.00	0.00	0.74	0.00	2.78	0.00

POINT_X	POINT_Y
0.04	1.10
0.11	1.11
0.20	1.11
0.26	1.14
1.19	0.86
1.31	0.82
1.42	0.79
1.54	0.76
1.72	0.61
2.78	0.74
2.86	0.63
2.96	0.65
3.04	0.66
2.67	0.12
2.69	0.06
0.92	2.29
3.61	2.04
3.89	2.37
3.88	1.92
3.88	2.00

Table B7 - Biotite input chemical data (i.e. PtAnls.xlsx) used by Q-XRMA to make a point shape file.

Id	ID_SAMPLE	LOCATION	MINERAL	SUB_PHASE	DOMAIN	ANALYSIS	POINT	AI
1	MA271	MPC	Bt		10	95	1	1.59
2	MA271	MPC	Bt		10	95	2	1.59
3	MA271	MPC	Bt		10	95	3	1.56
4	MA271	MPC	Bt		10	95	4	1.62
5	MA271	MPC	Bt		10	95	5	1.59
6	MA271	MPC	Bt		10	95	6	1.60
7	MA271	MPC	Bt		10	95	7	1.58
8	MA271	MPC	Bt		10	95	8	1.56
9	MA271	MPC	Bt		10	95	9	1.58
10	MA271	MPC	Bt		10	95	10	1.58
11	MA271	MPC	Bt		10	95	11	1.55
12	MA271	MPC	Bt		10	95	12	1.57
13	MA271	MPC	Bt		10	95	13	1.63
14	MA271	MPC	Bt		10	95	14	1.56
15	MA271	MPC	Bt		10	95	15	1.62

16	MA271	MPC	Bt	10	95	16	1.57
17	MA271	MPC	Bt	10	95	17	1.59
18	MA271	MPC	Bt	10	95	18	1.57
19	MA271	MPC	Bt	10	95	19	1.57
20	MA271	MPC	Bt	10	95	20	1.59
21	MA271	MPC	Bt	10	95	21	1.57
22	MA271	MPC	Bt	10	95	22	1.58

Ca	Fe	K	Mg	Mn	Na	P	Si	Ti
0.00	1.51	0.91	1.00	0.00	0.02	0.00	2.72	0.13
0.00	1.46	0.91	1.00	0.00	0.00	0.00	2.72	0.10
0.00	1.44	0.87	0.93	0.00	0.00	0.00	2.73	0.12
0.00	1.46	0.89	0.86	0.00	0.04	0.00	2.74	0.17
0.00	1.47	0.89	0.89	0.00	0.02	0.00	2.75	0.13
0.00	1.51	0.91	0.92	0.00	0.04	0.00	2.74	0.13
0.00	1.44	0.88	1.02	0.00	0.01	0.00	2.72	0.16
0.00	1.45	0.88	0.84	0.00	0.02	0.00	2.74	0.12
0.00	1.48	0.87	0.89	0.00	0.00	0.00	2.72	0.19
0.00	1.47	0.89	0.89	0.00	0.02	0.00	2.73	0.14
0.00	1.46	0.91	0.81	0.00	0.01	0.00	2.74	0.15
0.00	1.48	0.88	0.90	0.00	0.00	0.00	2.71	0.17
0.00	1.49	0.89	0.86	0.00	0.00	0.00	2.73	0.14
0.00	1.47	0.85	0.95	0.00	0.00	0.00	2.73	0.15
0.00	1.51	0.90	0.93	0.00	0.04	0.00	2.74	0.15
0.00	1.47	0.92	0.90	0.00	0.02	0.00	2.74	0.12
0.00	1.48	0.89	0.83	0.00	0.01	0.00	2.73	0.16
0.00	1.49	0.88	0.95	0.00	0.01	0.00	2.73	0.14
0.00	1.51	0.90	0.83	0.00	0.00	0.00	2.72	0.12
0.00	1.51	0.92	0.83	0.00	0.00	0.00	2.75	0.13
0.00	1.49	0.88	0.80	0.00	0.01	0.00	2.74	0.13
0.00	1.45	0.93	0.84	0.00	0.03	0.00	2.73	0.17

POINT_X	POINT_Y
0.06	0.58
0.09	0.60
0.15	0.64
0.20	0.67
0.26	0.71
0.32	0.75
0.36	0.79
2.39	0.20
2.42	0.22
2.45	0.24
2.48	0.26
2.51	0.28
2.55	0.29
2.69	0.28
2.73	0.31

2.94	0.25
3.00	0.28
3.05	0.30
2.24	0.40
2.27	0.41
2.95	1.03
3.01	1.09

APPENDIX B5 – Summary report of the multilinear regressions

Table B8 - Summary of garnet calibration using input microprobe chemical data (red).

AI	Estimated	Residual	StdResid
1.95	1.95	0.00	0.11
1.98	1.95	0.03	1.84
1.98	1.96	0.03	1.48
1.97	1.95	0.03	1.58
1.94	1.95	0.00	-0.06
1.97	1.95	0.02	0.83
1.95	1.95	0.00	-0.11
1.94	1.94	-0.01	-0.29
1.94	1.95	-0.02	-0.86
1.93	1.95	-0.02	-0.83
1.98	1.96	0.02	1.07
1.95	1.94	0.00	0.11
1.94	1.95	-0.01	-0.48
1.96	1.94	0.01	0.65
1.93	1.96	-0.03	-1.64
1.97	1.95	0.02	1.06
1.95	1.95	0.00	-0.01
1.98	1.96	0.02	1.17
1.95	1.96	-0.01	-0.36
1.95	1.95	0.00	0.08
1.94	1.95	-0.01	-0.56
1.96	1.95	0.01	0.52
1.93	1.96	-0.03	-1.47
1.96	1.96	0.01	0.32
1.94	1.95	-0.02	-0.97
1.94	1.96	-0.01	-0.79
1.95	1.96	0.00	-0.14
1.94	1.95	-0.01	-0.41
1.96	1.95	0.01	0.80
1.96	1.96	0.01	0.33
1.94	1.96	-0.01	-0.64
1.96	1.97	-0.01	-0.47
1.94	1.97	-0.03	-1.76
1.94	1.96	-0.02	-1.30
1.97	1.96	0.00	0.10
1.95	1.97	-0.01	-0.80
1.95	1.97	-0.02	-0.91
1.97	1.97	0.00	0.00
1.99	1.97	0.02	1.07
1.98	1.96	0.01	0.81
1.97	1.97	0.01	0.29
1.96	1.98	-0.02	-0.91

1.96	1.96	0.00	-0.12
1.94	1.96	-0.03	-1.40
1.95	1.97	-0.01	-0.72
1.95	1.96	-0.02	-0.83
1.96	1.96	0.00	-0.25
1.95	1.96	-0.02	-0.98
1.96	1.97	-0.02	-0.84
1.97	1.97	0.00	-0.21
1.94	1.98	-0.04	-2.13
2.04	1.98	0.06	3.30
1.98	1.97	0.01	0.42
1.95	1.97	-0.02	-1.31
1.99	1.98	0.00	0.24
1.99	1.97	0.01	0.77
1.98	1.98	0.00	0.14
2.00	1.98	0.01	0.77
1.98	1.98	0.01	0.34
1.97	1.97	0.00	0.08
1.99	1.98	0.01	0.77
1.96	1.99	-0.03	-1.41
1.99	1.98	0.01	0.56
1.97	1.99	-0.02	-0.87
2.00	1.98	0.01	0.69
1.99	1.98	0.01	0.61
2.00	1.97	0.03	1.40
1.98	1.98	0.00	0.11
1.97	1.98	-0.01	-0.57
1.98	1.98	-0.01	-0.41
2.02	1.98	0.04	2.01
1.94	1.99	-0.05	-2.61
1.99	1.98	0.01	0.43
1.97	1.98	0.00	-0.22
1.97	1.97	0.00	-0.22
1.97	1.98	-0.01	-0.49
1.98	1.98	0.00	0.21
1.98	1.98	0.00	-0.09
1.98	1.98	0.00	0.19
1.98	1.98	-0.01	-0.33
2.00	1.98	0.01	0.71
1.97	1.98	-0.01	-0.75
1.99	1.99	0.00	-0.07
2.00	1.99	0.01	0.31
1.99	1.98	0.00	0.21
1.98	1.99	-0.01	-0.41
2.01	1.98	0.03	1.71
1.98	1.98	0.00	0.02
2.01	1.99	0.02	0.97
1.98	1.99	-0.01	-0.48

1.97	1.98	-0.01	-0.38
1.98	1.99	-0.01	-0.27
2.02	1.99	0.02	1.20
1.98	1.98	0.00	-0.08
2.02	1.98	0.03	1.80

Test indexes		Value
AI	AIC	-476.88
	AICc	-473.70
	R2	0.39
	AdjR2	0.32
	F-Stat	5.98
	F-Prob	0.00
	Wald	70.24
	Wald-Prob	0.00
	K(BP)	6.80
	K(BP)-Prob	0.66
	JB	5.11
	JB-Prob	0.08
	Sigma2	0.00

Ca	Estimated	Residual	StdResid
0.84	0.90	-0.05	-0.74
0.86	0.79	0.06	0.93
0.86	0.82	0.04	0.64
0.86	0.98	-0.11	-1.63
0.87	0.84	0.03	0.46
0.89	0.95	-0.06	-0.88
0.88	0.81	0.08	1.12
0.85	0.90	-0.04	-0.61
0.89	0.95	-0.06	-0.91
0.87	0.83	0.03	0.50
0.85	0.80	0.05	0.71
0.85	0.82	0.04	0.54
0.87	0.76	0.11	1.65
0.88	0.93	-0.04	-0.62
0.85	0.83	0.02	0.30
0.36	0.51	-0.14	-2.10
0.41	0.50	-0.09	-1.26
0.51	0.52	-0.01	-0.14
0.64	0.61	0.04	0.52
0.64	0.53	0.11	1.61
0.50	0.50	0.00	-0.05
0.43	0.35	0.08	1.16
0.28	0.27	0.02	0.23
0.26	0.31	-0.05	-0.72
0.27	0.34	-0.06	-0.89

0.34	0.37	-0.03	-0.41
0.39	0.37	0.03	0.40
0.46	0.43	0.03	0.43
0.44	0.36	0.08	1.18
0.28	0.27	0.01	0.08
0.19	0.22	-0.03	-0.46
0.19	0.19	-0.01	-0.10
0.20	0.20	0.00	-0.02
0.21	0.17	0.04	0.58
0.18	0.17	0.01	0.14
0.17	0.22	-0.05	-0.68
0.23	0.28	-0.04	-0.63
0.20	0.14	0.05	0.79
0.16	0.06	0.10	1.48
0.21	0.14	0.07	0.94
0.18	0.10	0.08	1.17
0.36	0.13	0.23	3.33
0.48	0.42	0.06	0.80
0.40	0.36	0.04	0.60
0.38	0.26	0.12	1.72
0.30	0.30	0.00	0.02
0.28	0.17	0.11	1.65
0.22	0.16	0.07	0.96
0.18	0.24	-0.06	-0.87
0.12	0.19	-0.07	-0.99
0.10	0.15	-0.04	-0.65
0.10	0.14	-0.05	-0.69
0.08	0.05	0.03	0.48
0.08	0.16	-0.08	-1.13
0.08	0.12	-0.04	-0.64
0.08	0.06	0.02	0.28
0.07	0.08	-0.01	-0.20
0.06	0.05	0.02	0.22
0.06	0.12	-0.06	-0.82
0.07	0.04	0.03	0.44
0.06	0.11	-0.04	-0.64
0.06	0.05	0.01	0.15
0.07	0.09	-0.02	-0.35
0.07	0.13	-0.06	-0.83
0.08	0.18	-0.11	-1.52
0.08	0.10	-0.02	-0.36
0.08	0.11	-0.04	-0.51
0.48	0.42	0.06	0.80
0.40	0.36	0.04	0.60
0.38	0.26	0.12	1.72
0.30	0.30	0.00	0.02
0.28	0.17	0.11	1.65
0.22	0.16	0.07	0.96

0.18	0.24	-0.06	-0.87
0.14	0.27	-0.14	-1.95
0.12	0.19	-0.07	-0.99
0.10	0.15	-0.04	-0.65
0.10	0.14	-0.05	-0.69
0.08	0.05	0.03	0.48
0.08	0.16	-0.08	-1.13
0.08	0.12	-0.04	-0.64
0.08	0.06	0.02	0.28
0.07	0.08	-0.01	-0.20
0.06	0.05	0.02	0.22
0.06	0.12	-0.06	-0.82
0.07	0.04	0.03	0.44
0.06	0.11	-0.04	-0.64
0.06	0.05	0.01	0.15
0.07	0.09	-0.02	-0.35
0.07	-0.01	0.08	1.19
0.07	0.13	-0.06	-0.83
0.08	0.18	-0.11	-1.52
0.08	0.10	-0.02	-0.36
0.08	0.19	-0.10	-1.50
0.08	0.11	-0.04	-0.51
Test indexes		Value	
Ca	AIC	-226.53	
	AICc	-223.35	
	R2	0.95	
	AdjR2	0.94	
	F-Stat	162.37	
	F-Prob	0.00	
	Wald	1958.39	
	Wald-Prob	0.00	
	K(BP)	11.14	
	K(BP)-Prob	0.27	
	JB	3.71	
	JB-Prob	0.16	
	Sigma2	0.00	

Fe	Estimated	Residual	StdResid
1.68	1.70	-0.02	-0.28
1.70	1.80	-0.10	-1.71
1.68	1.76	-0.08	-1.32
1.68	1.59	0.09	1.49
1.71	1.71	0.00	-0.05
1.66	1.63	0.03	0.55
1.70	1.80	-0.10	-1.70
1.76	1.68	0.08	1.39

1.65	1.65	0.00	-0.03
1.70	1.76	-0.07	-1.10
1.77	1.79	-0.02	-0.36
1.74	1.76	-0.02	-0.41
1.74	1.82	-0.08	-1.42
1.74	1.65	0.08	1.40
1.70	1.78	-0.07	-1.23
2.16	2.12	0.04	0.65
2.16	2.08	0.08	1.34
2.09	2.06	0.02	0.38
1.98	2.00	-0.02	-0.35
2.00	2.04	-0.04	-0.70
2.11	2.11	0.01	0.12
2.16	2.30	-0.14	-2.30
2.29	2.34	-0.05	-0.79
2.26	2.30	-0.05	-0.80
2.31	2.26	0.05	0.83
2.27	2.23	0.04	0.74
2.25	2.26	-0.01	-0.22
2.20	2.16	0.04	0.61
2.24	2.22	0.02	0.28
2.37	2.33	0.04	0.73
2.50	2.42	0.08	1.28
2.47	2.45	0.03	0.45
2.44	2.45	0.00	-0.08
2.46	2.47	-0.01	-0.19
2.50	2.48	0.02	0.27
2.40	2.41	-0.01	-0.09
2.41	2.38	0.03	0.45
2.48	2.50	-0.02	-0.28
2.51	2.57	-0.05	-0.88
2.46	2.48	-0.02	-0.36
2.49	2.53	-0.03	-0.56
2.34	2.48	-0.14	-2.39
2.28	2.26	0.02	0.39
2.32	2.31	0.01	0.18
2.36	2.41	-0.05	-0.88
2.40	2.35	0.05	0.89
2.37	2.48	-0.11	-1.92
2.47	2.51	-0.03	-0.59
2.48	2.39	0.09	1.51
2.51	2.46	0.05	0.85
2.55	2.51	0.04	0.74
2.51	2.50	0.01	0.14
2.58	2.59	0.00	-0.07
2.57	2.50	0.07	1.19
2.55	2.56	-0.01	-0.19
2.58	2.60	-0.03	-0.48

2.54	2.53	0.01	0.16
2.56	2.55	0.01	0.14
2.52	2.51	0.01	0.20
2.52	2.60	-0.08	-1.37
2.55	2.53	0.02	0.36
2.51	2.57	-0.05	-0.91
2.51	2.53	-0.02	-0.33
2.55	2.52	0.04	0.62
2.51	2.46	0.05	0.78
2.52	2.53	-0.02	-0.30
2.55	2.51	0.04	0.65
2.28	2.26	0.02	0.39
2.32	2.31	0.01	0.18
2.36	2.41	-0.05	-0.88
2.40	2.35	0.05	0.89
2.37	2.48	-0.11	-1.92
2.47	2.51	-0.03	-0.59
2.48	2.39	0.09	1.51
2.54	2.37	0.16	2.71
2.51	2.46	0.05	0.85
2.55	2.51	0.04	0.74
2.51	2.50	0.01	0.14
2.58	2.59	0.00	-0.07
2.57	2.50	0.07	1.19
2.55	2.56	-0.01	-0.19
2.58	2.60	-0.03	-0.48
2.54	2.53	0.01	0.16
2.56	2.55	0.01	0.14
2.52	2.51	0.01	0.20
2.52	2.60	-0.08	-1.37
2.55	2.53	0.02	0.36
2.51	2.57	-0.05	-0.91
2.51	2.53	-0.02	-0.33
2.56	2.65	-0.09	-1.57
2.55	2.52	0.04	0.62
2.51	2.46	0.05	0.78
2.52	2.53	-0.02	-0.30
2.54	2.42	0.12	2.00
2.55	2.51	0.04	0.65
Test indexes		Value	
Fe	AIC	-254.54	
	AICc	-251.36	
	R2	0.96	
	AdjR2	0.96	
	F-Stat	251.07	
	F-Prob	0.00	
	Wald	2519.67	

Wald-Prob	0.00
K(BP)	8.71
K(BP)-Prob	0.46
JB	0.61
JB-Prob	0.74
Sigma2	0.00

Mg	Estimated	Residual	StdResid
0.06	0.02	0.03	0.93
0.05	0.08	-0.03	-0.87
0.05	0.03	0.02	0.64
0.04	0.00	0.05	1.25
0.05	0.02	0.03	0.87
0.05	0.05	0.00	0.05
0.05	0.08	-0.03	-0.85
0.04	0.01	0.04	0.97
0.05	0.00	0.04	1.18
0.05	0.04	0.01	0.32
0.05	0.06	-0.01	-0.25
0.05	0.06	-0.01	-0.24
0.05	0.06	0.00	-0.10
0.05	0.01	0.04	1.16
0.05	0.05	0.00	0.05
0.13	0.19	-0.06	-1.63
0.12	0.15	-0.03	-0.86
0.11	0.15	-0.03	-0.91
0.11	0.14	-0.03	-0.96
0.11	0.13	-0.02	-0.64
0.13	0.17	-0.04	-1.06
0.15	0.25	-0.10	-2.71
0.16	0.22	-0.06	-1.64
0.17	0.23	-0.06	-1.70
0.17	0.23	-0.06	-1.55
0.16	0.14	0.02	0.62
0.15	0.16	0.00	-0.10
0.16	0.20	-0.04	-1.03
0.16	0.15	0.01	0.28
0.20	0.22	-0.01	-0.37
0.24	0.27	-0.03	-0.89
0.25	0.29	-0.03	-0.93
0.25	0.30	-0.05	-1.40
0.26	0.27	-0.01	-0.28
0.25	0.27	-0.02	-0.59
0.25	0.25	0.00	-0.05
0.24	0.28	-0.03	-0.94
0.26	0.31	-0.05	-1.42
0.26	0.31	-0.05	-1.39

0.26	0.31	-0.06	-1.61
0.27	0.31	-0.03	-0.90
0.23	0.29	-0.07	-1.81
0.25	0.24	0.00	0.14
0.27	0.29	-0.02	-0.49
0.29	0.32	-0.03	-0.95
0.30	0.32	-0.02	-0.52
0.34	0.35	-0.02	-0.50
0.33	0.33	0.00	-0.13
0.34	0.28	0.06	1.65
0.36	0.33	0.03	0.94
0.36	0.32	0.04	1.07
0.37	0.33	0.04	1.17
0.37	0.36	0.01	0.26
0.38	0.34	0.04	1.15
0.36	0.35	0.00	0.11
0.37	0.36	0.01	0.21
0.37	0.34	0.03	0.92
0.37	0.38	-0.01	-0.40
0.37	0.33	0.04	1.13
0.36	0.35	0.02	0.43
0.37	0.33	0.04	1.10
0.37	0.32	0.05	1.27
0.35	0.34	0.00	0.12
0.34	0.32	0.03	0.71
0.33	0.30	0.03	0.79
0.32	0.34	-0.02	-0.42
0.29	0.29	0.00	-0.12
0.25	0.24	0.00	0.14
0.27	0.29	-0.02	-0.49
0.29	0.32	-0.03	-0.95
0.30	0.32	-0.02	-0.52
0.34	0.35	-0.02	-0.50
0.33	0.33	0.00	-0.13
0.34	0.28	0.06	1.65
0.36	0.29	0.06	1.76
0.36	0.33	0.03	0.94
0.36	0.32	0.04	1.07
0.37	0.33	0.04	1.17
0.37	0.36	0.01	0.26
0.38	0.34	0.04	1.15
0.36	0.35	0.00	0.11
0.37	0.36	0.01	0.21
0.37	0.34	0.03	0.92
0.37	0.38	-0.01	-0.40
0.37	0.33	0.04	1.13
0.36	0.35	0.02	0.43
0.37	0.33	0.04	1.10

0.37	0.32	0.05	1.27
0.35	0.34	0.00	0.12
0.34	0.37	-0.03	-0.82
0.34	0.32	0.03	0.71
0.33	0.30	0.03	0.79
0.32	0.34	-0.02	-0.42
0.31	0.27	0.04	1.14
0.29	0.29	0.00	-0.12
Test indexes		Value	
Mg	AIC	-348.07	
	AICc	-344.89	
	R2	0.91	
	AdjR2	0.90	
	F-Stat	96.67	
	F-Prob	0.00	
	Wald	1437.46	
	Wald-Prob	0.00	
	K(BP)	14.39	
	K(BP)-Prob	0.11	
	JB	2.47	
	JB-Prob	0.29	
Sigma2	0.00		

Mn	Estimated	Residual	StdResid
0.43	0.45	-0.03	-0.59
0.43	0.40	0.04	0.82
0.44	0.47	-0.02	-0.53
0.47	0.49	-0.02	-0.53
0.44	0.49	-0.05	-1.13
0.46	0.44	0.02	0.52
0.45	0.39	0.06	1.34
0.47	0.49	-0.02	-0.45
0.48	0.47	0.01	0.20
0.42	0.42	0.00	-0.07
0.43	0.42	0.02	0.41
0.42	0.43	0.00	-0.10
0.42	0.42	0.00	0.06
0.40	0.47	-0.08	-1.68
0.43	0.42	0.01	0.29
0.39	0.25	0.13	2.96
0.38	0.32	0.06	1.31
0.38	0.32	0.06	1.35
0.33	0.31	0.02	0.51
0.33	0.35	-0.02	-0.42
0.32	0.28	0.04	0.93
0.33	0.18	0.15	3.39

0.32	0.25	0.07	1.56
0.30	0.23	0.07	1.66
0.32	0.22	0.09	2.09
0.32	0.33	-0.01	-0.21
0.32	0.29	0.04	0.85
0.25	0.27	-0.02	-0.48
0.25	0.33	-0.08	-1.78
0.20	0.24	-0.04	-0.87
0.18	0.15	0.03	0.68
0.16	0.14	0.02	0.55
0.17	0.11	0.06	1.41
0.14	0.17	-0.02	-0.50
0.15	0.15	0.00	-0.09
0.15	0.17	-0.01	-0.27
0.16	0.13	0.03	0.67
0.16	0.11	0.05	1.16
0.14	0.12	0.02	0.40
0.14	0.13	0.01	0.31
0.12	0.13	-0.01	-0.29
0.09	0.17	-0.08	-1.71
0.07	0.13	-0.07	-1.46
0.06	0.09	-0.02	-0.52
0.06	0.07	0.00	-0.09
0.04	0.09	-0.05	-1.19
0.05	0.05	0.00	0.05
0.05	0.06	0.00	-0.07
0.07	0.16	-0.08	-1.84
0.08	0.09	-0.01	-0.32
0.07	0.10	-0.03	-0.72
0.06	0.09	-0.03	-0.57
0.05	0.06	-0.01	-0.21
0.06	0.07	-0.02	-0.36
0.06	0.03	0.02	0.55
0.07	0.04	0.02	0.54
0.08	0.10	-0.02	-0.52
0.08	0.06	0.02	0.37
0.09	0.09	0.00	-0.01
0.06	0.04	0.02	0.41
0.08	0.10	-0.02	-0.51
0.11	0.13	-0.02	-0.45
0.10	0.08	0.02	0.48
0.10	0.10	0.00	-0.02
0.10	0.10	0.01	0.17
0.09	0.07	0.02	0.50
0.11	0.14	-0.03	-0.61
0.07	0.13	-0.07	-1.46
0.06	0.09	-0.02	-0.52
0.06	0.07	0.00	-0.09

0.04	0.09	-0.05	-1.19
0.05	0.05	0.00	0.05
0.05	0.06	0.00	-0.07
0.07	0.16	-0.08	-1.84
0.07	0.13	-0.06	-1.44
0.08	0.09	-0.01	-0.32
0.07	0.10	-0.03	-0.72
0.06	0.09	-0.03	-0.57
0.05	0.06	-0.01	-0.21
0.06	0.07	-0.02	-0.36
0.06	0.03	0.02	0.55
0.07	0.04	0.02	0.54
0.08	0.10	-0.02	-0.52
0.08	0.06	0.02	0.37
0.09	0.09	0.00	-0.01
0.06	0.04	0.02	0.41
0.08	0.10	-0.02	-0.51
0.11	0.13	-0.02	-0.45
0.10	0.08	0.02	0.48
0.12	0.04	0.08	1.86
0.10	0.10	0.00	-0.02
0.10	0.10	0.01	0.17
0.09	0.07	0.02	0.50
0.12	0.18	-0.06	-1.36
0.11	0.14	-0.03	-0.61
Test indexes		Value	
Mn	AIC	-308.56	
	AICc	-305.38	
	R2	0.91	
	AdjR2	0.90	
	F-Stat	97.65	
	F-Prob	0.00	
	Wald	1734.11	
	Wald-Prob	0.00	
	K(BP)	8.69	
	K(BP)-Prob	0.47	
	JB	17.29	
	JB-Prob	0.00	
	Sigma2	0.00	

Si	Estimated	Residual	StdResid
3.01	2.98	0.03	1.93
2.97	2.97	0.00	0.14
2.98	2.98	0.01	0.30
2.98	2.98	0.00	0.06
2.99	2.97	0.02	0.87

2.99	2.98	0.01	0.29
2.99	2.98	0.01	0.62
2.99	2.98	0.01	0.75
2.99	2.98	0.01	0.42
2.99	2.98	0.01	0.49
2.93	2.98	-0.04	-2.36
2.96	2.97	-0.01	-0.52
2.97	2.97	0.00	-0.26
2.97	2.98	-0.01	-0.58
2.98	2.98	-0.01	-0.50
3.00	2.99	0.01	0.57
2.98	2.98	0.00	0.12
2.96	2.98	-0.02	-1.37
3.00	2.98	0.02	1.16
2.97	2.97	-0.01	-0.31
2.95	2.98	-0.03	-1.68
2.96	2.97	-0.02	-0.96
2.99	2.98	0.01	0.44
2.99	2.98	0.00	0.27
2.97	2.98	-0.01	-0.71
2.99	2.98	0.01	0.47
2.97	2.98	-0.01	-0.67
2.99	2.98	0.00	0.25
2.99	2.98	0.01	0.78
2.97	2.98	-0.02	-0.91
3.00	2.97	0.03	1.95
2.97	2.98	-0.01	-0.34
2.98	2.98	0.00	-0.05
2.98	2.98	0.00	-0.10
2.96	2.98	-0.02	-0.95
2.98	2.97	0.01	0.49
2.97	2.97	0.00	0.22
2.97	2.97	-0.01	-0.33
3.00	2.97	0.04	2.02
2.95	2.97	-0.03	-1.44
2.96	2.97	-0.02	-0.88
2.97	2.97	0.00	-0.10
2.96	2.98	-0.02	-1.02
3.00	2.98	0.03	1.67
2.94	2.98	-0.04	-2.08
2.98	2.97	0.01	0.74
2.96	2.97	-0.01	-0.56
2.98	2.97	0.01	0.34
3.00	2.98	0.02	1.18
2.98	2.97	0.01	0.49
2.97	2.97	0.00	0.04
3.01	2.98	0.03	1.85
2.94	2.97	-0.03	-1.74

2.98	2.97	0.01	0.42
2.95	2.97	-0.02	-0.96
2.96	2.97	-0.02	-0.86
2.96	2.97	-0.01	-0.63
3.01	2.97	0.03	1.90
2.98	2.98	0.00	-0.15
2.99	2.98	0.01	0.83
2.97	2.97	0.00	-0.14
2.96	2.97	0.00	-0.18
2.97	2.99	-0.02	-1.01
2.97	2.97	0.01	0.29
2.95	2.96	-0.01	-0.48
2.96	2.96	-0.01	-0.37
2.99	2.97	0.02	1.26
2.96	2.98	-0.02	-0.96
2.97	2.97	0.00	0.01
2.95	2.96	-0.01	-0.59
2.94	2.96	-0.02	-1.21
3.01	2.96	0.05	2.68
2.95	2.97	-0.02	-1.27
2.96	2.97	-0.01	-0.41
2.95	2.96	-0.01	-0.69
2.98	2.97	0.02	0.88
2.96	2.96	-0.01	-0.49
2.98	2.97	0.02	0.92
2.95	2.96	-0.01	-0.50
2.96	2.96	0.00	-0.06
2.96	2.96	0.00	0.10
2.96	2.96	0.00	-0.06
2.96	2.96	0.00	-0.24
2.95	2.96	-0.01	-0.76
2.98	2.97	0.01	0.32
3.00	2.97	0.03	1.81
2.94	2.96	-0.02	-0.94
2.97	2.96	0.01	0.54
2.97	2.96	0.01	0.45
2.94	2.96	-0.02	-1.29
2.97	2.97	0.01	0.29
2.99	2.97	0.02	1.02
2.97	2.97	0.00	-0.09
2.98	2.97	0.01	0.53
2.96	2.97	-0.01	-0.43
Test indexes		Value	
Si	AIC	-486.98	
	AICc	-483.80	
	R2	0.16	
	AdjR2	0.07	

F-Stat	1.77
F-Prob	0.09
Wald	27.24
Wald-Prob	0.00
K(BP)	7.90
K(BP)-Prob	0.54
JB	1.42
JB-Prob	0.49
Sigma2	0.00

Table B9- Summary of plagioclase calibration using input macroprobe chemical data (red).

AI	Estimated	Residual	StdResid
1.26	1.25	0.01	0.60
1.28	1.29	-0.01	-0.69
1.32	1.32	0.00	0.06
1.20	1.21	-0.01	-1.04
1.23	1.22	0.00	0.26
1.29	1.28	0.01	0.59
1.28	1.29	-0.01	-0.77
1.24	1.24	0.00	0.30
1.38	1.37	0.01	1.09
1.35	1.34	0.01	1.04
1.30	1.30	-0.01	-0.40
1.33	1.34	-0.01	-0.79
1.25	1.25	0.00	-0.30
1.18	1.18	0.00	-0.09
1.20	1.20	0.00	-0.09
1.31	1.33	-0.02	-1.31
1.24	1.22	0.02	1.44
1.26	1.26	0.00	0.07
1.27	1.27	0.00	-0.02
1.25	1.25	0.00	0.06

	Test indexes	Value
AI	AIC	-108.33
	AICc	-75.33
	R2	0.97
	AdjR2	0.94
	F-Stat	32.49
	F-Prob	0.00
	Wald	396.04
	Wald-Prob	0.00
	K(BP)	9.23
	K(BP)-Prob	0.42
	JB	0.32

	JB-Prob	0.85
	Sigma2	0.00

Ca	Estimated	Residual	StdResid
0.21	0.20	0.01	0.72
0.26	0.25	0.00	0.21
0.24	0.24	-0.01	-0.67
0.23	0.23	0.00	0.53
0.31	0.31	0.00	-0.01
0.22	0.23	-0.01	-0.85
0.30	0.30	0.01	0.62
0.24	0.24	0.01	0.62
0.24	0.24	0.00	0.33
0.32	0.32	0.00	0.37
0.20	0.19	0.01	0.66
0.24	0.25	-0.01	-0.79
0.28	0.28	-0.01	-0.66
0.26	0.26	0.00	0.37
0.22	0.23	0.00	-0.52
0.32	0.32	0.00	0.26
0.29	0.30	0.00	-0.37
0.28	0.30	-0.02	-1.80
0.35	0.34	0.01	1.25
0.22	0.22	0.00	-0.26
Test indexes		Value	
Ca	AIC	-123.04	
	AICc	-90.04	
	R2	0.98	
	AdjR2	0.95	
	F-Stat	45.39	
	F-Prob	0.00	
	Wald	508.90	
	Wald-Prob	0.00	
	K(BP)	3.70	
	K(BP)-Prob	0.93	
	JB	1.26	
	JB-Prob	0.53	
	Sigma2	0.00	

K	Estimated	Residual	StdResid
0.000	0.000	0.000	0.022
0.005	0.004	0.000	0.747
0.000	0.000	0.000	-0.143
0.000	0.000	0.000	0.611
0.000	0.000	0.000	0.049
0.017	0.017	0.000	-0.596

0.007	0.006	0.001	1.294
0.001	0.000	0.000	0.706
0.005	0.004	0.001	1.326
0.001	0.001	0.000	-0.140
0.015	0.015	0.000	-0.187
0.000	0.001	-0.001	-1.712
0.004	0.005	0.000	-0.416
0.000	0.000	0.000	-0.345
0.004	0.004	0.000	-0.322
0.000	0.001	-0.001	-0.768
0.000	0.000	0.000	-0.539
0.000	0.000	0.000	-0.227
0.004	0.004	0.000	0.667
0.000	0.000	0.000	-0.027
Test indexes		Value	
K	AIC	-228.40	
	AICc	-195.40	
	R2	0.99	
	AdjR2	0.98	
	F-Stat	116.69	
	F-Prob	0.00	
	Wald	3684.98	
	Wald-Prob	0.00	
	K(BP)	10.77	
	K(BP)-Prob	0.29	
	JB	0.04	
	JB-Prob	0.98	
	Sigma2	0.00	

Na	Estimated	Residual	StdResid
0.77	0.77	0.00	0.08
0.71	0.71	0.00	0.05
0.67	0.69	-0.02	-0.70
0.59	0.58	0.01	0.31
0.63	0.63	0.01	0.24
0.60	0.62	-0.01	-0.51
0.79	0.77	0.02	0.71
0.64	0.67	-0.04	-1.29
0.65	0.67	-0.02	-0.81
0.67	0.68	-0.01	-0.47
0.58	0.57	0.01	0.37
0.79	0.74	0.05	1.75
0.77	0.79	-0.02	-0.68
0.75	0.75	0.01	0.26
0.64	0.63	0.01	0.27
0.61	0.61	0.00	0.05

0.63	0.65	-0.02	-0.69
0.60	0.62	-0.02	-0.59
0.63	0.60	0.03	0.98
0.63	0.62	0.02	0.67
Test indexes		Value	
Na	AIC	-78.45	
	AICc	-45.45	
	R2	0.92	
	AdjR2	0.84	
	F-Stat	12.16	
	F-Prob	0.00	
	Wald	201.18	
	Wald-Prob	0.00	
	K(BP)	7.52	
	K(BP)-Prob	0.58	
	JB	0.60	
	JB-Prob	0.74	
	Sigma2	0.00	

2.81	2.81	0.00	-0.12
2.75	2.76	-0.02	-0.51
2.85	2.85	0.01	0.19
2.79	2.76	0.03	0.74
2.70	2.72	-0.02	-0.46
2.74	2.75	-0.02	-0.51
2.75	2.71	0.04	1.22
2.76	2.81	-0.06	-1.65
2.75	2.76	-0.01	-0.32
2.70	2.69	0.01	0.19
2.60	2.60	0.00	-0.03
2.80	2.79	0.02	0.48
2.65	2.65	0.00	-0.10
2.68	2.70	-0.02	-0.61
2.81	2.75	0.06	1.61
2.81	2.81	0.00	0.09
2.76	2.75	0.01	0.33
2.66	2.69	-0.03	-0.94
2.75	2.75	0.01	0.15
2.84	2.84	0.01	0.26
Test indexes		Value	
Si	AIC	-70.08	
	AICc	-37.08	
	R2	0.86	
	AdjR2	0.74	
	F-Stat	6.92	
	F-Prob	0.00	

	Wald	677.92
	Wald-Prob	0.00
	K(BP)	9.58
	K(BP)-Prob	0.39
	JB	0.31
	JB-Prob	0.86
	Sigma2	0.00

Table B10 - Summary of biotite calibration using input macroprobe chemical data (red).

AI	Estimated	Residual	StdResid
1.59	1.59	0.00	-0.42
1.59	1.59	0.00	0.28
1.56	1.57	0.00	-0.56
1.62	1.61	0.00	0.43
1.59	1.59	0.00	0.31
1.60	1.60	0.00	-0.20
1.58	1.59	0.00	-0.37
1.56	1.56	0.00	0.42
1.58	1.58	-0.01	-0.96
1.58	1.57	0.01	2.15
1.55	1.55	0.00	0.22
1.57	1.57	0.00	-0.16
1.63	1.63	0.00	0.38
1.56	1.56	0.00	0.07
1.62	1.61	0.00	0.52
1.57	1.58	-0.01	-1.23
1.59	1.58	0.01	1.09
1.57	1.57	0.00	-0.26
1.57	1.57	0.00	0.09
1.59	1.59	0.00	0.09
1.57	1.58	0.00	-0.66
1.58	1.59	-0.01	-1.24

	Test indexes	Value
AI	AIC	-148.35
	AICc	-121.95
	R2	0.93
	AdjR2	0.88
	F-Stat	18.35
	F-Prob	0.00
	Wald	834.40
	Wald-Prob	0.00
	K(BP)	8.48
	K(BP)-Prob	0.49
	JB	3.78

	JB-Prob	0.15
	Sigma2	0.00

Fe	Estimated	Residual	StdResid
1.51	1.51	0.01	0.89
1.46	1.46	-0.01	-0.74
1.44	1.45	-0.01	-0.77
1.46	1.47	-0.01	-1.30
1.47	1.47	0.00	0.26
1.51	1.52	-0.01	-1.40
1.44	1.44	0.00	-0.13
1.45	1.45	0.00	0.31
1.48	1.48	0.00	0.29
1.47	1.46	0.01	1.03
1.46	1.47	-0.01	-1.07
1.48	1.48	0.00	-0.35
1.49	1.49	0.00	0.40
1.47	1.46	0.01	1.07
1.51	1.50	0.01	0.89
1.47	1.46	0.00	0.44
1.48	1.48	0.00	-0.01
1.49	1.50	-0.01	-0.69
1.51	1.51	0.00	0.46
1.51	1.50	0.00	0.12
1.49	1.48	0.01	0.79
1.45	1.46	0.00	-0.48
Test indexes		Value	
Fe	AIC	-135.65	
	AICc	-109.25	
	R2	0.91	
	AdjR2	0.84	
	F-Stat	12.94	
	F-Prob	0.00	
	Wald	290.50	
	Wald-Prob	0.00	
	K(BP)	8.91	
	K(BP)-Prob	0.45	
	JB	1.31	
	JB-Prob	0.52	
	Sigma2	0.00	

K	Estimated	Residual	StdResid
0.91	0.91	0.00	0.12
0.91	0.89	0.02	1.64
0.87	0.87	0.00	0.00
0.89	0.89	0.00	0.44

0.89	0.90	-0.01	-1.34
0.91	0.90	0.00	0.31
0.88	0.88	0.00	-0.24
0.88	0.89	-0.01	-1.04
0.87	0.87	0.00	0.00
0.89	0.90	-0.01	-1.15
0.91	0.90	0.02	1.53
0.88	0.89	0.00	-0.30
0.89	0.90	-0.01	-0.77
0.85	0.86	0.00	-0.14
0.90	0.90	0.00	-0.04
0.92	0.91	0.00	0.18
0.89	0.89	0.01	0.59
0.88	0.88	0.00	-0.28
0.90	0.90	-0.01	-0.73
0.92	0.92	0.00	0.05
0.88	0.88	0.01	0.49
0.93	0.92	0.01	0.71
Test indexes		Value	
K	AIC	-130.53	
	AICc	-104.13	
	R2	0.84	
	AdjR2	0.71	
	F-Stat	6.78	
	F-Prob	0.00	
	Wald	578.21	
	Wald-Prob	0.00	
	K(BP)	9.28	
	K(BP)-Prob	0.41	
	JB	0.37	
	JB-Prob	0.83	
	Sigma2	0.00	

Mg	Estimated	Residual	StdResid
1.00	0.99	0.01	0.86
1.00	1.01	-0.01	-0.40
0.93	0.93	0.00	0.27
0.86	0.85	0.00	0.18
0.89	0.89	0.00	-0.07
0.92	0.94	-0.01	-0.75
1.02	1.03	-0.01	-0.59
0.84	0.86	-0.02	-0.88
0.89	0.89	0.00	-0.17
0.89	0.90	-0.01	-0.73
0.81	0.82	-0.01	-0.49
0.90	0.88	0.01	0.84

0.86	0.86	0.00	0.01
0.95	0.95	0.00	0.09
0.93	0.94	-0.01	-0.38
0.90	0.86	0.03	1.95
0.83	0.84	-0.01	-0.48
0.95	0.92	0.03	1.52
0.83	0.84	-0.01	-0.51
0.83	0.85	-0.01	-0.88
0.80	0.79	0.00	0.08
0.84	0.83	0.01	0.51
Test indexes		Value	
Mg	AIC	-108.04	
	AICc	-81.64	
	R2	0.96	
	AdjR2	0.93	
	F-Stat	31.31	
	F-Prob	0.00	
	Wald	1250.42	
	Wald-Prob	0.00	
	K(BP)	5.97	
	K(BP)-Prob	0.74	
	JB	4.47	
JB-Prob	0.11		
Sigma2	0.00		

Si	Estimated	Residual	StdResid
2.72	2.72	0.00	0.54
2.72	2.72	0.00	-0.39
2.73	2.73	0.00	-0.88
2.74	2.74	0.00	0.11
2.75	2.74	0.00	0.56
2.74	2.74	0.00	-0.24
2.72	2.72	0.00	0.26
2.74	2.73	0.01	1.64
2.72	2.72	0.00	-0.57
2.73	2.73	0.00	0.49
2.74	2.74	0.00	0.70
2.71	2.71	0.00	-0.19
2.73	2.73	0.00	0.64
2.73	2.74	0.00	-0.38
2.74	2.74	0.00	0.39
2.74	2.75	-0.01	-1.47
2.73	2.74	0.00	-0.44
2.73	2.73	0.00	0.56
2.72	2.72	-0.01	-1.44
2.75	2.75	0.00	0.44

	2.74	2.74	0.00	0.49
	2.73	2.74	0.00	-0.83
	Test indexes		Value	
Si		AIC	-163.73	
		AICc	-137.33	
		R2	0.88	
		AdjR2	0.79	
		F-Stat	9.60	
		F-Prob	0.00	
		Wald	401.07	
		Wald-Prob	0.00	
		K(BP)	12.97	
		K(BP)-Prob	0.16	
		JB	0.19	
		JB-Prob	0.91	
		Sigma2	0.00	

Test indexes	Definition
AIC	Akaike's Information Criterion: A relative measure of performance used to compare models; the smaller AIC indicates the superior model.
AICc	Corrected Akaike's Information Criterion: second order correction for small sample sizes.
R2	R-Squared, Coefficient of Determination: The proportion of variation in the dependent variable that is explained by the model.
AdjR2	Adjusted R-Squared: R-Squared adjusted for model complexity (number of variables) as it relates to the data.
F-Stat	Joint F-Statistic Value: Used to assess overall model significance.
F-Prob	Joint F-Statistic Probability (p-value): The probability that none of the explanatory variables have an effect on the dependent variable.
Wald	Wald Statistic: Used to assess overall robust model significance.
Wald-Prob	Wald Statistic Probability (p-value): The computed probability, using robust standard errors, that none of the explanatory variables have an effect on the dependent variable.
K(BP)	Koenker's studentized Breusch-Pagan Statistic: Used to test the reliability of standard error values when heteroskedasticity (non-constant variance) is present.
K(BP)-Prob	Koenker (BP) Statistic Probability (p-value): The probability that heteroskedasticity (non-constant variance) has not made standard errors unreliable.
JB	Jarque-Bera Statistic: Used to determine whether the residuals deviate from a normal distribution.
JB-Prob	Jarque-Bera Probability (p-value): The probability that the residuals are normally distributed.
Sigma2	Sigma-Squared: OLS estimate of the variance of the error term (residuals).

APPENDIX B6 – EMP/Q-XRMA comparisons

Table B11 - Garnet component comparison profiles along the A-B transect of Fig. 2.27.

OBJECTID	Alm_EMPA	Grs_EMPA	Prp_EMPA	Sps_EMPA	Alm_Q-XRMA	Grs_Q-XRMA
1	55.80	28.07	1.88	14.24	55.37	29.74
2	55.81	28.47	1.72	14.44	58.63	27.69
3	55.28	28.74	1.63	14.71	57.14	26.80
4	54.98	28.68	1.49	15.53	51.96	31.70
5	55.76	29.00	1.61	14.50	55.88	28.99
6	54.27	29.57	1.63	15.33	53.09	30.62
7	55.17	29.40	1.57	14.90	58.44	26.71
8	56.23	28.35	1.48	15.64	54.55	29.51
9	53.74	29.59	1.60	15.91	53.75	31.05
10	55.97	28.75	1.75	13.83	57.70	25.90
11	57.01	28.16	1.68	14.44	58.31	25.90
12	56.75	28.37	1.65	13.97	57.33	26.38
13	56.35	28.99	1.74	14.02	59.48	24.84
14	56.68	29.31	1.61	13.19	53.92	30.07
15	56.23	28.23	1.60	14.24	57.79	28.01
16	71.16	12.05	4.23	12.82	69.06	18.57
17	70.41	13.55	4.00	12.68	68.20	16.01
18	67.43	17.07	3.77	12.63	67.54	16.45
19	64.65	21.33	3.59	11.07	65.36	19.74
20	64.78	21.36	3.64	11.04	66.89	17.70
21	68.87	16.60	4.36	10.79	68.95	15.36
22	70.46	14.15	4.89	11.09	74.68	11.07
23	75.12	9.36	5.38	10.48	75.97	9.84
24	75.67	8.49	5.59	10.04	74.92	9.74
25	75.16	9.11	5.79	10.48	74.10	9.87
26	73.35	11.36	5.40	10.66	72.64	12.38
27	72.02	13.12	5.13	10.74	73.38	12.46
28	71.71	15.19	5.31	8.34	70.59	14.33
29	72.34	14.64	5.41	8.35	72.55	11.73
30	77.70	9.31	6.73	6.59	76.14	9.48
31	80.43	6.39	7.88	5.95	79.08	9.48
32	80.47	6.20	8.44	5.32	79.80	7.52
33	79.69	6.52	8.41	5.75	80.07	6.21
34	80.09	6.93	8.61	4.75	80.19	7.52
35	81.19	5.90	8.31	5.00	80.78	6.86
36	80.68	5.61	8.41	5.11	79.02	4.59
37	79.13	7.77	8.06	5.27	77.52	9.80
38	80.22	6.53	8.51	5.27	81.70	3.59
39	81.82	5.35	8.65	4.56	83.99	0.98
40	80.29	6.90	8.51	4.67	81.05	4.89
41	81.40	5.95	9.10	3.89	82.41	2.93
42	77.67	11.83	7.56	2.97	80.78	6.49
43	74.20	15.87	8.25	2.27	74.10	13.44

44	75.97	13.37	8.88	2.15	75.74	10.49
45	76.32	12.62	9.62	2.06	78.76	7.52
46	78.97	9.94	9.92	1.37	76.80	9.45
47	77.90	9.37	11.18	1.79	81.31	5.23
48	80.32	7.47	10.91	1.76	82.03	5.23
49	80.76	6.07	11.19	2.40	77.85	7.52
50	81.84	3.95	12.01	2.54	80.13	7.17
51	82.84	3.34	11.83	2.38	81.49	5.23
52	82.60	3.17	12.30	2.11	81.70	4.90
53	83.67	2.66	12.41	1.69	84.64	1.95
54	83.26	2.70	12.53	1.92	81.43	5.86
55	83.76	2.56	11.92	1.94	83.66	3.93
56	83.35	2.50	12.34	2.25	84.97	2.61
57	82.84	2.34	12.41	2.70	82.95	0.65
58	83.34	2.12	12.28	2.62	83.88	0.33
59	82.93	2.14	12.22	2.88	82.30	4.92
60	83.42	2.47	12.06	2.09	85.81	1.97
61	83.40	2.06	12.19	2.60	82.41	2.61
62	82.33	2.13	12.17	3.62	83.71	1.96
63	82.82	2.29	11.55	3.45	83.22	1.31
64	83.24	2.44	11.45	3.19	82.08	5.25
65	83.03	2.59	11.03	3.42	80.92	4.93
66	83.65	2.57	10.69	3.09	83.22	2.30
67	84.17	2.59	9.65	3.70	82.30	3.61
68	74.20	15.87	8.25	2.27	74.10	13.44
69	75.97	13.37	8.88	2.15	75.74	10.49
70	76.32	12.62	9.62	2.06	78.76	7.52
71	78.97	9.94	9.92	1.37	76.80	9.45
72	77.90	9.37	11.18	1.79	81.31	5.23
73	80.32	7.47	10.91	1.76	82.03	5.23
74	80.76	6.07	11.19	2.40	77.85	7.52
75	81.90	4.51	11.86	2.25	77.45	9.12
76	81.84	3.95	12.01	2.54	80.13	7.17
77	82.84	3.34	11.83	2.38	81.49	5.23
78	82.60	3.17	12.30	2.11	81.70	4.90
79	83.67	2.66	12.41	1.69	84.64	1.95
80	83.26	2.70	12.53	1.92	81.43	5.86
81	83.76	2.56	11.92	1.94	83.66	3.93
82	83.35	2.50	12.34	2.25	84.97	2.61
83	82.84	2.34	12.41	2.70	82.95	0.65
84	83.34	2.12	12.28	2.62	83.88	0.33
85	82.93	2.14	12.22	2.88	82.30	4.92
86	83.42	2.47	12.06	2.09	85.81	1.97
87	83.40	2.06	12.19	2.60	82.41	2.61
88	82.33	2.13	12.17	3.62	83.71	1.96
89	82.82	2.29	11.55	3.45	83.22	1.31
90	82.70	2.41	11.31	4.07	86.60	0.00
91	83.24	2.44	11.45	3.19	82.08	5.25

92	83.03	2.59	11.03	3.42	80.92	4.93
93	83.65	2.57	10.69	3.09	83.22	2.30
94	83.24	2.72	10.24	4.03	79.08	6.54
95	84.17	2.59	9.65	3.70	82.30	3.61

Prp_Q- XRMA	Sps_Q- XRMA	Alm_Residuals	Grs_Residuals	Prp_Residuals	Sps_Residuals
0.98	15.36	0.43	-1.67	0.90	-1.12
1.95	14.33	-2.82	0.79	-0.23	0.11
1.31	15.03	-1.86	1.94	0.32	-0.32
0.33	16.01	3.02	-3.02	1.16	-0.49
0.33	16.29	-0.12	0.01	1.28	-1.79
1.30	15.31	1.18	-1.05	0.33	0.02
2.28	13.68	-3.27	2.69	-0.71	1.22
0.33	16.39	1.69	-1.16	1.15	-0.75
0.33	15.69	-0.01	-1.46	1.27	0.23
2.30	13.11	-1.73	2.85	-0.54	0.71
2.30	13.77	-1.30	2.26	-0.62	0.67
2.28	14.01	-0.58	1.99	-0.63	-0.04
2.29	13.40	-3.13	4.15	-0.54	0.62
0.65	15.36	2.76	-0.75	0.95	-2.17
1.63	14.01	-1.56	0.22	-0.03	0.23
5.21	9.45	2.11	-6.52	-0.98	3.37
5.23	10.13	2.21	-2.47	-1.23	2.55
5.26	9.54	-0.11	0.62	-1.49	3.09
4.61	10.53	-0.71	1.59	-1.01	0.55
4.26	11.48	-2.10	3.66	-0.62	-0.43
5.56	9.48	-0.09	1.24	-1.19	1.31
7.82	6.51	-4.22	3.08	-2.93	4.57
6.56	8.20	-0.86	-0.47	-1.18	2.29
7.14	7.79	0.75	-1.25	-1.55	2.25
7.57	7.24	1.07	-0.76	-1.78	3.24
4.89	10.42	0.71	-1.01	0.51	0.24
5.57	8.85	-1.36	0.66	-0.44	1.89
5.86	9.45	1.12	0.86	-0.56	-1.11
4.89	10.42	-0.21	2.92	0.52	-2.08
6.86	7.52	1.56	-0.17	-0.13	-0.92
8.17	5.56	1.34	-3.09	-0.29	0.39
8.82	4.90	0.66	-1.31	-0.39	0.42
9.80	3.92	-0.38	0.31	-1.39	1.83
8.17	5.88	-0.11	-0.58	0.44	-1.13
8.50	5.23	0.41	-0.96	-0.19	-0.23
9.51	4.26	1.67	1.02	-1.10	0.85
8.82	4.58	1.61	-2.03	-0.77	0.69
10.46	2.94	-1.48	2.94	-1.95	2.33
10.49	2.95	-2.17	4.37	-1.84	1.60
9.77	4.23	-0.75	2.01	-1.27	0.43
9.77	4.23	-1.01	3.01	-0.67	-0.34

8.44	6.17	-3.11	5.34	-0.88	-3.20
8.52	4.92	0.10	2.43	-0.28	-2.65
9.84	2.62	0.23	2.88	-0.96	-0.47
10.46	2.61	-2.44	5.10	-0.84	-0.55
9.77	4.23	2.17	0.49	0.15	-2.87
11.11	2.61	-3.41	4.14	0.07	-0.83
10.78	2.29	-1.71	2.24	0.13	-0.53
8.82	5.23	2.91	-1.45	2.36	-2.83
9.77	4.23	1.71	-3.22	2.24	-1.69
9.80	3.92	1.34	-1.89	2.03	-1.54
10.13	3.27	0.91	-1.73	2.17	-1.16
11.07	2.61	-0.97	0.71	1.33	-0.92
10.42	3.26	1.82	-3.16	2.11	-1.33
11.15	1.64	0.10	-1.38	0.77	0.30
11.11	1.96	-1.62	-0.11	1.23	0.29
11.11	3.27	-0.11	1.69	1.29	-0.56
11.76	2.29	-0.54	1.79	0.51	0.33
10.16	2.95	0.63	-2.78	2.06	-0.07
11.15	1.31	-2.38	0.50	0.91	0.78
10.42	3.58	0.99	-0.55	1.76	-0.98
9.80	4.25	-1.39	0.17	2.37	-0.63
11.44	2.29	-0.40	0.98	0.12	1.16
9.84	3.61	1.16	-2.80	1.61	-0.42
10.53	2.63	2.11	-2.34	0.51	0.79
11.48	1.64	0.43	0.28	-0.79	1.45
9.51	3.93	1.88	-1.02	0.14	-0.24
8.52	4.92	0.10	2.43	-0.28	-2.65
9.84	2.62	0.23	2.88	-0.96	-0.47
10.46	2.61	-2.44	5.10	-0.84	-0.55
9.77	4.23	2.17	0.49	0.15	-2.87
11.11	2.61	-3.41	4.14	0.07	-0.83
10.78	2.29	-1.71	2.24	0.13	-0.53
8.82	5.23	2.91	-1.45	2.36	-2.83
8.79	5.21	4.45	-4.61	3.06	-2.97
9.77	4.23	1.71	-3.22	2.24	-1.69
9.80	3.92	1.34	-1.89	2.03	-1.54
10.13	3.27	0.91	-1.73	2.17	-1.16
11.07	2.61	-0.97	0.71	1.33	-0.92
10.42	3.26	1.82	-3.16	2.11	-1.33
11.15	1.64	0.10	-1.38	0.77	0.30
11.11	1.96	-1.62	-0.11	1.23	0.29
11.11	3.27	-0.11	1.69	1.29	-0.56
11.76	2.29	-0.54	1.79	0.51	0.33
10.16	2.95	0.63	-2.78	2.06	-0.07
11.15	1.31	-2.38	0.50	0.91	0.78
10.42	3.58	0.99	-0.55	1.76	-0.98
9.80	4.25	-1.39	0.17	2.37	-0.63
11.44	2.29	-0.40	0.98	0.12	1.16

11.76	0.98	-3.90	2.41	-0.46	3.09
9.84	3.61	1.16	-2.80	1.61	-0.42
10.53	2.63	2.11	-2.34	0.51	0.79
11.48	1.64	0.43	0.28	-0.79	1.45
8.50	5.88	4.15	-3.82	1.75	-1.85
9.51	3.93	1.88	-1.02	0.14	-0.24

Table B12 - Plagioclase component comparison profiles measured at the same pixels.

OBJECTID	Ab_EMPA	An_EMPA	Ab_Q-XRMA	An_Q-XRMA	Ab_Residuals	An_Residuals
1	78.63	21.37	79.38	20.62	0.76	-0.76
2	73.49	26.51	73.96	26.04	0.47	-0.47
3	73.68	26.32	74.19	25.81	0.51	-0.51
4	71.71	28.29	71.60	28.40	-0.11	0.11
5	66.90	33.10	67.02	32.98	0.12	-0.12
6	72.96	27.04	72.94	27.06	-0.02	0.02
7	72.39	27.61	71.96	28.04	-0.43	0.43
8	72.37	27.63	73.63	26.37	1.25	-1.25
9	73.09	26.91	73.63	26.37	0.54	-0.54
10	67.55	32.45	68.00	32.00	0.45	-0.45
11	74.39	25.61	75.00	25.00	0.61	-0.61
12	76.71	23.29	74.75	25.25	-1.96	1.96
13	73.54	26.46	73.83	26.17	0.29	-0.29
14	74.20	25.80	74.26	25.74	0.05	-0.05
15	73.91	26.09	73.26	26.74	-0.66	0.66
16	65.44	34.56	65.59	34.41	0.16	-0.16
17	68.29	31.71	68.42	31.58	0.13	-0.13
18	68.01	31.99	67.39	32.61	-0.62	0.62
19	64.48	35.52	63.83	36.17	-0.65	0.65
20	74.41	25.59	73.81	26.19	-0.60	0.60

Table B13 - Biotite component comparison profiles measured at the same pixels.

OBJECTID	XFe_EMPA	XMg_EMPA	XFe_Q-XRMA	XMg_Q-XRMA	XFe_Residuals	XMg_Residuals
1	0.60	0.40	0.60	0.40	-0.002	-0.002
2	0.59	0.41	0.59	0.41	-0.002	0.002
3	0.61	0.39	0.61	0.39	0.002	-0.002
4	0.63	0.37	0.63	0.37	0.003	-0.003
5	0.62	0.38	0.62	0.38	0.000	0.000
6	0.62	0.38	0.62	0.38	-0.003	0.003
7	0.59	0.41	0.58	0.42	-0.003	0.003
8	0.63	0.37	0.63	0.37	-0.006	0.006
9	0.62	0.38	0.62	0.38	0.000	0.000
10	0.62	0.38	0.62	0.38	-0.005	0.005
11	0.64	0.36	0.64	0.36	-0.001	0.001
12	0.62	0.38	0.63	0.37	0.005	-0.005
13	0.64	0.36	0.63	0.37	-0.002	0.002
14	0.61	0.39	0.61	0.39	-0.002	0.002
15	0.62	0.38	0.61	0.39	-0.003	0.003
16	0.62	0.38	0.63	0.37	0.008	-0.008

17	0.64	0.36	0.64	0.36	-0.003	0.003
18	0.61	0.39	0.62	0.38	0.008	-0.008
19	0.64	0.36	0.64	0.36	-0.002	0.002
20	0.64	0.36	0.64	0.36	-0.005	0.005
21	0.65	0.35	0.65	0.35	0.001	-0.001
22	0.63	0.37	0.64	0.36	0.003	-0.003

APPENDIX C1 – EMP analyses of Serre Massif rocks

Table B14	Na	Mg	Al	Si	K	Ca	Ti	Cr
94 / 1 .	0.0289	0.2828	9.7729	15.0746	0	4.2244	0.0481	0.0047
94 / 2 .	0.0259	0.2594	9.9176	14.873	0	4.2848	0.0371	0.0025
94 / 3 .	0.0149	0.218	9.9127	14.9093	0.0011	4.2523	0.0585	0.0089
94 / 4 .	0.0056	0.2573	9.8742	14.9124	0.0059	4.3256	0.0472	0
94 / 5 .	0.0215	0.25	9.7246	14.9459	0.0223	4.207	0.0405	0.0012
94 / 6 .	0.073	0.2404	9.5636	14.8322	0.0151	4.257	0.3647	0
94 / 7 .	0.0521	0.3443	9.7949	15.0068	0.0565	3.5856	0.0602	0.0026
94 / 8 .	0.0311	0.2593	9.9672	15.0705	0.0078	3.7778	0.0587	0.001
94 / 9 .	0.0291	0.2455	9.8508	14.9339	0	4.3246	0.0613	0
94 / 10 .	0.0217	0.2243	9.7392	14.9541	0.0086	4.3161	0.0593	0.0036
94 / 11 .	0.0038	0.2418	9.6978	14.9669	0	4.3633	0.0497	0
94 / 12 .	0.0235	0.2326	9.6852	14.9605	0.0048	4.4014	0.0618	0.0015
94 / 13 .	0.074	0.2139	9.432	14.7265	0.0085	4.4493	0.4003	0.0057
94 / 14 .	0.1374	0.2505	9.8298	14.8297	0.0043	4.2831	0.0571	0.0074
94 / 15 .	0.0745	0.2297	9.8219	14.6957	0.0021	4.2232	0.0722	0.0074
94 / 16 .	0.1071	0.2269	9.7645	14.9349	0.0027	4.3258	0.0545	0.0129
94 / 17 .	0.1632	0.3867	10.088	14.5982	0.0503	3.7316	0.0393	0.0041
94 / 18 .	0.0234	0.2516	9.6567	14.9346	0.0059	4.3167	0.0511	0
94 / 19 .	0.0297	0.2512	9.877	14.6733	0.0095	4.2962	0.0558	0.0015
94 / 20 .	0.0271	0.2392	9.7302	14.8047	0.0154	4.3856	0.0603	0.0015
94 / 21 .	0.1377	0.2443	9.585	14.7951	0.0101	4.3593	0.1239	0
94 / 22 .	0.1763	0.2369	9.6375	14.582	0.0213	4.5935	0.129	0.0183
94 / 23 .	0.2236	0.2209	9.651	14.687	0.0396	4.4484	0.0839	0.007
94 / 24 .	0.0928	0.2534	9.7568	14.9398	0.0075	4.2907	0.0483	0.0063
94 / 25 .	0.0953	0.2367	9.8314	14.761	0.0266	4.3383	0.0435	0.003
94 / 26 .	0.1026	0.2323	9.6965	14.938	0.007	4.3994	0.0418	0.0039
94 / 27 .	0.1494	0.2407	9.7343	14.8833	0.0189	4.5095	0.0563	0
94 / 28 .	0.3053	0.238	9.8449	14.8493	0.013	4.3633	0.0566	0
94 / 29 .	0.1806	0.2144	9.3206	14.8002	0.0101	4.5831	0.4922	0
94 / 30 .	0.2976	0.2469	9.7323	14.6058	0.0724	4.4025	0.061	0.0115
94 / 31 .	0.0523	0.2453	9.7019	14.8377	0	4.4498	0.0409	0
94 / 32 .	0.0151	0.2203	9.3903	14.8391	0	4.5386	0.3171	0.008
94 / 33 .	0.0643	0.2476	9.8722	14.9757	0	4.1559	0.0623	0
94 / 34 .	0.0273	0.2501	9.7834	14.8364	0.023	4.3468	0.0506	0.0047
94 / 35 .	0.0679	0.2318	9.8148	14.8599	0.0209	4.2264	0.0541	0.0049
94 / 36 .	0.0981	0.2436	9.6477	14.9807	0.0198	4.2264	0.0524	0.0044
94 / 37 .	0.8411	0.2241	9.3499	14.9219	0.9391	4.6082	0.0324	0.0087
94 / 38 .	0.06	0.2502	9.6361	14.8776	0	4.3362	0.0402	0.0015
94 / 39 .	0.0356	0.2539	9.8438	15.0122	0.0054	4.299	0.0541	0.012
94 / 40 .	0.0198	0.2365	9.4986	14.9506	0.0011	4.3107	0.1983	0
94 / 41 .	0.0525	0.2506	9.773	14.9174	0.008	4.2694	0.0422	0
94 / 42 .	0.0326	0.2536	9.9073	14.7763	0.0032	4.3954	0.039	0.0061
94 / 43 .	0.0502	0.2329	9.7456	14.9954	0	4.4432	0.0526	0.0029
94 / 44 .	0.0235	0.2357	9.7473	14.8384	0.0048	4.4237	0.0535	0
94 / 45 .	0.0395	0.2229	9.6769	14.7628	0	4.2659	0.0582	0.0067

94 / 46 .	0.2603	0.2485	9.7438	14.8545	0.0259	4.413	0.0534	0.0097
94 / 47 .	0.0225	0.2447	9.7969	14.6406	0.0069	4.4682	0.0975	0.0108
94 / 48 .	0.0588	0.2403	9.7955	14.7824	0.0143	4.4527	0.0459	0
94 / 49 .	0.3429	0.2567	9.6705	14.8495	0.0321	4.3611	0.0589	0
94 / 50 .	0.5312	0.2637	9.5249	14.5876	0.2987	4.5029	0.0513	0.0106
94 / 51 .	0.1113	0.2431	9.7035	14.7567	0.0118	4.4183	0.0614	0.008
94 / 52 .	0.0744	0.2391	9.6901	14.9676	0.0188	4.3684	0.0571	0.0075
94 / 53 .	0.406	0.2302	9.1833	14.7923	0.0565	4.6612	0.5683	0
94 / 54 .	0.428	0.2421	9.5457	14.7302	0.4849	4.2568	0.1195	0
94 / 55 .	0.0272	0.2623	9.6428	14.9257	0	4.3975	0.0523	0.0073
94 / 56 .	0.0629	0.3665	9.983	14.5298	0.0032	3.7164	0.0588	0.0155
94 / 57 .	0.3394	1.663	11.2885	11.2318	0.2675	1.368	0.2622	0.0079
94 / 58 .	0.3115	0.7188	10.2852	12.7511	0.5077	2.4078	0.0711	0.0029
94 / 59 .	0.031	0.1547	7.4458	14.0405	0.0074	6.8923	3.0846	0.0032
94 / 60 .	0.0352	0.025	3.0954	12.9115	0.0115	10.7285	8.8578	0
94 / 61 .	0.0594	0.2191	9.4359	14.8937	0.0048	4.6769	0.3707	0.0074
94 / 62 .	0	0.2226	9.429	14.7316	0	4.5123	0.3118	0.0062
94 / 63 .	0.0028	0.2639	9.8206	14.942	0.007	4.3261	0.0432	0
94 / 64 .	0.0262	0.2527	9.6827	14.8448	0.0058	4.2376	0.0524	0.0017
94 / 65 .	0.0066	0.2483	9.7092	14.9468	0.0145	4.269	0.0636	0.0041
94 / 66 .	0.0104	0.2624	9.7731	14.8535	0.0054	4.3619	0.0373	0.0039
94 / 67 .	0.0009	0.242	9.7138	14.9438	0.015	4.4107	0.0517	0
94 / 68 .	0.0248	0.234	9.0162	14.672	0.0011	4.8348	0.9054	0.001
94 / 69 .	0.0056	0.241	9.7991	14.9632	0	4.2482	0.0532	0.0015
94 / 70 .	0.0065	0.2555	9.5604	14.8612	0.0032	4.3891	0.295	0.0003
94 / 71 .	0.0179	0.3273	9.6092	14.8679	0	4.2933	0.0482	0.0062
94 / 72 .	0.0366	0.3407	9.6284	14.8342	0.0154	4.1668	0.0604	0
94 / 73 .	0.0515	0.3942	9.822	14.838	0	3.6945	0.0416	0
94 / 74 .	0.1785	0.4782	8.6818	12.8666	0.099	2.8021	0.1947	0.0048
94 / 75 .	0.075	0.4735	10.0292	13.5089	0.0344	2.2505	0.0563	0
94 / 76 .	0.0291	0.6368	9.7196	15.0232	0.0275	1.8131	0.0512	0
94 / 77 .	0.0193	0.5847	10.105	14.8492	0.1232	2.3803	0.0339	0
94 / 78 .	0.1065	0.188	12.4981	14.8047	0.12	7.0365	0.013	0.003
94 / 79 .	0.1235	0.1475	15.3198	17.0528	4.6053	0.1654	0.005	0.0105
94 / 80 .	0.0953	0.6143	10.0217	15.2871	0.3166	1.2885	0.0322	0
94 / 81 .	0.0166	0.651	9.7707	14.6947	0.0124	1.7276	0.0322	0
94 / 82 .	0	0.6013	9.8015	14.8516	0.0032	2.0386	0.0301	0
94 / 83 .	0.001	0.5677	9.6939	14.8929	0.0011	2.5685	0.0307	0.005
94 / 84 .	0.0421	0.5525	9.6955	14.8613	0.071	2.9932	0.3265	0.007
94 / 85 .	0.0542	0.5403	9.6964	14.879	0.0182	3.2097	0.0528	0.0033
94 / 86 .	0.0096	0.5477	9.8309	14.8089	0	3.2149	0.0483	0.0013
94 / 87 .	0.0154	0.5869	9.4524	14.6014	0.0226	3.1642	0.5364	0
94 / 88 .	0.0722	0.2185	8.448	20.212	4.0584	0.8994	0.1506	0
94 / 89 .	0.0241	0.6567	9.7611	14.8855	0.0236	2.4973	0.0271	0
94 / 90 .	0.0482	1.0943	10.4348	14.3088	0.5767	1.4056	0.0376	0.003
94 / 91 .	0	0.7361	9.772	14.8495	0	2.1296	0.0274	0.0026
94 / 92 .	0.0039	0.7332	9.621	14.8356	0.0161	1.7703	0.1023	0.0051
94 / 93 .	0.0116	0.8107	9.9956	15.2726	0.2806	1.2714	0.0199	0.0022

94 / 94 .	0.1226	0.6339	10.7377	15.4735	0.7063	1.003	0.0033	0
94 / 95 .	0.0137	0.8089	9.8465	14.8377	0.0129	1.4092	0.0335	0.0121
94 / 96 .	0.004	0.8644	9.7296	14.4199	0.0049	1.217	0.325	0
94 / 97 .	0.0049	0.8605	9.8965	14.5829	0	1.1738	0.263	0.0157
94 / 98 .	0	0.8414	9.9413	15.0126	0	1.2771	0.0091	0.0005
94 / 99 .	0	0.9129	9.8983	14.7307	0.0151	1.1008	0.0085	0
94 / 100 .	0.2303	0.8862	9.8724	14.7973	0	1.2136	0.0166	0.0016
94 / 101 .	0.5134	0.3958	13.2356	17.2015	1.8027	0.4454	0	0
94 / 102 .	0.0089	0.8712	9.8091	14.8512	0	1.3703	0.0211	0
94 / 103 .	0.7109	0.7684	9.8669	15.4777	0.5942	1.1731	0.0133	0.0116
94 / 104 .	0.0068	0.8119	9.7942	14.7952	0.0194	1.7099	0.0276	0
94 / 105 .	0.0326	0.7157	9.6855	15.023	0.0164	1.8935	0.0352	0.0022
94 / 106 .	0	0.9383	9.5986	14.4276	0.0118	1.771	0.1771	0
94 / 107 .	0.0068	0.7722	9.7735	14.7156	0.0251	1.9739	0.0162	0
94 / 108 .	0.202	0.0676	8.567	22.2894	5.8753	0.2126	0.0102	0
94 / 109 .	0.1545	0.1144	8.0458	22.4063	6.8063	0.0732	0.0023	0
94 / 110 .	0	0.7089	9.6851	14.8882	0.148	2.4671	0.029	0.004
94 / 111 .	0.0536	2.629	10.4485	12.3891	0.3477	0.6005	0.0249	0
94 / 112 .	0.0276	0.7984	9.7261	14.908	0.0176	2.2854	0.0269	0.0036
94 / 113 .	0	0.8137	9.775	14.8196	0.0128	2.2035	0.0159	0
94 / 114 .	0.1402	0.8496	9.9347	14.9921	0.0336	1.9697	0.0203	0
94 / 115 .	0.0314	0.968	9.7315	14.9027	0.0304	1.571	0.0286	0
94 / 116 .	0.0154	0.7235	9.81	14.7428	0.0601	1.325	0.0217	0
94 / 117 .	0	0.9683	9.7905	14.9821	0.0011	1.6941	0.0303	0
94 / 118 .	0.0503	1.0454	9.879	14.5266	0.0854	1.4101	0.0392	0.0101
94 / 119 .	0.0167	1.0132	9.8276	14.9066	0	1.4008	0.0239	0.0086
94 / 120 .	0.003	1.0661	9.6996	14.8471	0.0071	1.1506	0.0219	0.008
94 / 121 .	0.7835	1.2145	18.3021	7.5952	0.5486	1.346	0.3526	0.0076
94 / 122 .	0.3193	0.2159	32.6345	4.6441	0.3578	0.4073	0.0448	0
94 / 123 .	0.5014	0.251	31.5318	4.8826	0.4119	0.4908	0.0944	0.0072
94 / 124 .	0.2593	1.0451	14.2903	13.0161	0.1666	0.7247	0.0485	0
94 / 125 .	0	1.175	10.1956	15.057	0	0.8104	0.0203	0
94 / 126 .	0.0134	0.8566	8.5163	17.0527	0.0239	0.6587	0.016	0.0115
94 / 127 .	0.0231	0.0219	0.6679	32.2343	0.0085	0.0326	0.0075	0.0019
94 / 128 .	0	0	0.0143	33.194	0	0.0134	0	0
94 / 129 .	0	0.008	0.025	33.1683	0.0034	0.0089	0.0081	0.0031
94 / 130 .	0.0073	0.0019	0.0247	33.1825	0.0078	0.0197	0.0047	0
94 / 131 .	2.0051	0.0063	3.7601	28.1781	0.1166	1.2062	0	0
94 / 132 .	4.7389	0	10.7545	19.8563	0.0287	3.1056	0	0
94 / 133 .	4.5757	0	10.8327	19.726	0.0349	3.0866	0.0107	0.0041
94 / 134 .	4.6988	0	10.8558	19.6937	0.0264	3.0819	0.004	0.0046
94 / 135 .	4.5859	0.0052	10.8826	19.7359	0.029	3.1613	0.0067	0
94 / 136 .	4.5576	0	10.8492	19.8469	0.0187	3.0751	0.0058	0
94 / 137 .	4.6014	0	10.855	19.7426	0.0173	3.0933	0.0017	0.0022
94 / 138 .	4.7032	0	10.9325	19.5238	0.0424	3.2023	0.0011	0
94 / 139 .	4.4077	0.0069	11.0156	19.6013	0.0604	3.1531	0.0137	0.0012
94 / 140 .	4.6644	0	10.9347	19.6587	0.0265	3.0306	0.0085	0.0021
94 / 141 .	0.365	0.0419	17.2402	16.9506	0.2023	0.1068	0.1297	0

94 / 142 .	0.156	0.7324	10.7921	15.4781	0.0982	0.8172	0.0217	0.0086
94 / 143 .	0	1.1852	9.8973	14.7068	0.0054	0.9614	0.0055	0.0037
94 / 144 .	0	1.1817	9.8378	15.1072	0	0.9042	0.0205	0.0005
94 / 145 .	0.821	1.1112	9.5817	15.3715	0.0139	0.8003	0.0145	0.0034
94 / 146 .	3.9224	0.0615	11.7353	18.5305	0.3862	0.2885	0.0071	0
94 / 147 .	1.5561	0.1684	14.934	18.6279	1.5279	0.0733	0	0.006
94 / 148 .	3.4429	0.0763	12.482	20.0567	1.5348	0.052	0.0132	0.001
94 / 149 .	6.4442	0.0418	8.5669	22.2931	0.0944	0.1823	0.0319	0
94 / 150 .	3.7052	0.0446	8.9544	14.075	0.0848	1.852	4.7522	0
94 / 151 .	4.3205	0	11.276	19.2978	0.0352	3.43	0.0093	0
94 / 152 .	3.7675	0.0054	12.2458	18.4491	0.0503	3.3502	0.0204	0.0027
94 / 153 .	2.1804	0.3092	10.6528	17.9778	0.0449	2.2725	0.0196	0.0159
94 / 154 .	0	1.2454	9.6205	14.9031	0.0075	1.0446	0.0371	0
94 / 155 .	0.0274	1.2696	9.7488	14.8826	0.0043	0.9337	0.0185	0.0031
94 / 156 .	0	1.266	9.9268	14.7561	0	0.9811	0.01	0
94 / 157 .	0.0285	1.2095	10.0596	14.5145	0.0202	0.9589	0.0217	0.0039
94 / 158 .	0.5262	0.0439	14.3935	19.0425	1.7396	0.0435	0.1857	0.0051
94 / 159 .	3.6266	2.0766	10.1567	19.5413	0.2199	0.0525	0.0129	0
94 / 160 .	7.3478	0.1587	8.1755	22.3461	0.075	0.0724	0.0024	0.0041
94 / 161 .	6.2395	0.0913	9.7238	21.5995	0.1078	0.034	0.0092	0.002
94 / 162 .	1.467	1.2254	13.9515	18.0087	0.5443	0.0451	0.0086	0
94 / 163 .	1.5417	0.2757	11.6402	21.0948	0.5368	0.1151	0.2665	0
94 / 164 .	0.0083	1.1373	7.5434	12.7299	0	0.7554	3.5556	0.0063
94 / 165 .	0.0127	1.2949	9.9433	14.7838	0	1.0434	0.0237	0.0013
94 / 166 .	0.0166	1.2504	9.8941	14.7967	0.0064	0.888	0.0095	0.0086
94 / 167 .	0.0127	1.2655	9.8157	14.5577	0.0133	0.904	0.0042	0.0063
94 / 168 .	0	1.2653	9.9943	15.0377	0.0016	0.8436	0.0105	0.0084
94 / 169 .	1.5255	0.6854	9.3137	17.7152	2.678	0.3866	0.0072	0.0154
94 / 170 .	5.0665	0.1867	10.6758	20.6749	1.0789	0.0921	0.0066	0
94 / 171 .	0.7526	0.3886	15.6511	18.3943	0.7921	0.0995	0.0183	0
94 / 172 .	1.1444	0.3505	20.8271	13.3702	0.89	0.3857	0.0361	0
94 / 173 .	3.111	0.0537	11.3065	21.552	0.2773	0.1238	0.0017	0
94 / 174 .	0.7765	1.1505	10.2087	15.2798	0.2404	0.7452	0.012	0
94 / 175 .	0.0078	1.245	9.9173	14.9031	0.0206	1.0298	0.0102	0.0023
94 / 176 .	0.0204	1.2182	9.8747	14.974	0.0032	1.0049	0.0181	0.0036
94 / 177 .	0.0272	1.2122	9.9474	14.8409	0.0189	1.1691	0.0124	0.0096
94 / 178 .	0.0243	1.2808	9.8011	14.8188	0.0118	0.983	0.0107	0
94 / 179 .	3.0068	1.1216	9.1823	16.1513	0.0563	0.6497	0.0076	0.0019
94 / 180 .	0	1.3392	9.9505	14.8605	0.0011	0.9523	0.0165	0.0023
94 / 181 .	0	1.3012	9.8608	14.8607	0.0049	0.8052	0.007	0.0115
94 / 182 .	0.0146	1.2799	9.9797	14.7732	0.0049	1.0382	0.0151	0.0024
94 / 183 .	0.0088	1.3309	9.8978	14.6691	0.0329	0.9923	0.024	0.0018
94 / 184 .	0.0138	1.3698	9.9641	14.7856	0	0.8948	0.0035	0.0217
94 / 185 .	0.2184	0.8448	12.3411	14.3499	0.1563	0.9782	0.0179	0
94 / 186 .	1.5492	1.4108	10.7382	15.4605	0.4183	0.4239	0.0023	0.0129
94 / 187 .	1.4456	0.8228	9.886	19.9756	2.787	0.0779	0.0032	0
94 / 188 .	0	1.359	9.8792	14.6611	0.0136	1.3969	0.0103	0
94 / 189 .	0.0066	1.1372	9.9857	14.9443	0.0074	1.78	0.0111	0.0002

94 / 190 .	0.0019	1.1574	9.6911	14.76	0.0138	2.1454	0.0043	0
94 / 191 .	0.0227	1.252	9.9829	14.5405	0.0495	1.9447	0.0199	0
94 / 192 .	0.0327	2.0717	6.2008	19.9658	0.0542	0.8018	0	0.0038
94 / 193 .	0	1.2408	9.893	14.7969	0	2.3888	0.0081	0.0102
94 / 194 .	0.0181	1.3363	9.8705	14.8394	0	2.0124	0.0033	0
94 / 195 .	0.0058	1.4472	9.8852	14.7623	0	1.899	0.0043	0.0008
94 / 196 .	0.0163	1.4769	9.921	14.6639	0	1.7908	0.0081	0.0029
94 / 197 .	0.0189	1.4931	10.0822	14.7182	0.0153	1.4957	0.0026	0
94 / 198 .	0.045	1.6826	9.6853	15.0571	0.0049	1.4093	0	0
94 / 199 .	0.0153	1.6419	9.9627	14.7318	0.009	1.1236	0.0131	0.0002
94 / 200 .	0.0164	1.6834	9.8733	14.7923	0.0107	0.9132	0.0006	0
94 / 201 .	0.027	1.7842	9.8519	14.7485	0.0219	0.679	0.0056	0.0055
94 / 202 .	0	1.8076	9.8343	14.9034	0.0027	0.5937	0	0
94 / 203 .	0.0029	1.7805	9.9158	14.7808	0	0.5031	0.0071	0
94 / 204 .	0	1.8507	9.9036	14.9083	0.0109	0.4768	0.001	0.0073
94 / 205 .	0	1.8669	9.9243	14.7614	0.0027	0.4004	0	0
94 / 206 .	0.0087	1.8853	9.8802	14.8109	0	0.4065	0	0
94 / 207 .	0.0352	1.793	9.9854	14.8236	0	0.3849	0	0.0094
94 / 208 .	0.0106	1.8402	10.1115	14.6374	0.0043	0.354	0	0
94 / 209 .	0	1.8576	9.8406	14.809	0.014	0.3763	0.002	0.0005
94 / 210 .	0.0097	1.8668	9.9323	14.795	0.0038	0.3526	0.0111	0.008
94 / 211 .	0.0068	1.8473	9.9825	14.7297	0.0103	0.3186	0.0018	0
94 / 212 .	0.0116	1.8392	9.9288	14.898	0	0.3216	0.0094	0.0101
94 / 213 .	1.3724	2.1649	14.6882	10.515	0.6077	0.6423	0.0318	0.0028
94 / 214 .	0	1.8151	9.8929	15.0113	0.0033	0.372	0	0.0047
94 / 215 .	0.0588	3.3069	11.1598	11.9756	0.1102	0.0535	0.0137	0.0146
94 / 216 .	0	1.8337	10.0557	14.7231	0.0087	0.3095	0.0006	0
94 / 217 .	0.0126	1.8313	9.9074	14.8608	0	0.3207	0	0.0069
94 / 218 .	0.04	2.1735	9.8291	14.4034	0.0518	0.2732	0	0
94 / 219 .	0.1581	4.6258	11.1257	11.1735	0.1317	0.0704	0.0118	0
94 / 220 .	0.044	1.5366	10.73	15.1267	0.0056	0.3354	0.0019	0
94 / 221 .	0.0275	1.8013	10.1517	14.618	0	0.3683	0	0
94 / 222 .	0.1121	3.8195	10.5411	11.9515	0.2353	0.0786	0.0076	0
94 / 223 .	0.0864	4.0454	11.6118	11.5583	0.2462	0.0501	0	0.0033
94 / 224 .	0.031	1.855	9.8057	14.5577	0	0.3669	0.0062	0
94 / 225 .	0	1.7385	10.0406	14.8518	0	0.3442	0.0031	0
94 / 226 .	0.0505	1.7887	10.0068	14.4178	0.0338	0.3317	0	0
94 / 227 .	0.0435	3.0192	10.2885	13.2925	0.2473	0.1698	0.0002	0.005
94 / 228 .	0	1.7015	9.8961	14.7115	0.0043	0.3625	0	0.0027
94 / 229 .	0.0551	2.8349	9.6239	13.4183	0.0923	0.342	0.0096	0
94 / 230 .	0.0275	3.9176	11.1807	11.6797	0.1977	0.0373	0	0
94 / 231 .	0.0039	1.7223	9.8741	14.8725	0	0.3674	0.0034	0.0013
94 / 232 .	0	1.6602	9.9105	14.9574	0.0135	0.39	0.0026	0
94 / 233 .	0.0098	1.608	10.0801	14.8569	0.0071	0.3868	0.0041	0.0095
94 / 234 .	0.0116	1.5549	9.9723	14.7098	0	0.3786	0	0
94 / 235 .	0.0244	1.5416	9.8768	14.8971	0.0038	0.4093	0.0008	0.01
94 / 236 .	0	1.4516	10.0756	14.8059	0.0027	0.3892	0	0.0075
94 / 237 .	0.0581	3.6401	9.2858	15.7136	0.0548	0.0137	0.0038	0

94 / 238 .	0.0418	0.0306	0.2982	32.6014	0.0091	0.0098	0.0014	0
94 / 239 .	0.0061	0.0005	0.0067	33.2385	0	0	0.0061	0
94 / 240 .	0.0218	0	0.0098	33.2549	0	0.0075	0.0037	0
94 / 241 .	0	0.0021	0.0027	33.2665	0.0082	0.0004	0.0039	0.0009
94 / 242 .	0.0048	0.0101	0.0062	33.2434	0.0005	0.0004	0.0064	0
94 / 243 .	0	0	0.0134	33.2334	0.0082	0.0044	0	0
94 / 244 .	0.0036	0	0.0049	33.2777	0.0072	0	0.0063	0.0087
94 / 245 .	0	0	0.0036	33.2569	0.0077	0	0.0082	0

Mn	Fe	F	P	Cl	Ni	O	Total	Sum_Cat
2.1432	8.3973	0	0.014	0	0	60.0091	100	15.0477
2.1735	8.4846	0	0.0031	0.0151	0	59.9233	100	15.2023
2.3536	8.2713	0	0.014	0.0112	0.0091	59.9652	100	15.0952
2.3484	8.1789	0.1076	0	0.0173	0.0365	59.883	100	15.1102
2.3185	8.5003	0	0.017	0.0223	0.0136	59.9153	100	15.2758
2.2738	8.4077	0	0	0.0103	0	59.9622	100	15.1789
2.4298	8.6211	0.0819	0.0241	0.0147	0	59.9255	100	14.9808
2.4335	8.3461	0	0	0	0	60.0469	100	14.8167
2.2138	8.3874	0	0	0.001	0	59.9525	100	15.1713
2.3362	8.3989	0	0	0.0062	0	59.9317	100	15.2755
2.1819	8.5551	0	0	0.0061	0.0046	59.9288	100	15.3421
2.2197	8.4608	0	0.0078	0.0174	0	59.923	100	15.3145
2.3162	8.4135	0.027	0.0216	0.0132	0	59.8984	100	15.3929
2.346	8.3636	0	0.0109	0.0092	0	59.8709	100	15.2432
2.2642	8.7201	0	0.0031	0.0041	0.0594	59.8224	100	15.4372
2.2982	8.3082	0.081	0.0031	0.0133	0	59.8668	100	15.1591
2.1621	8.9532	0.0266	0.0032	0.0321	0	59.7614	100	15.2336
2.3038	8.4703	0.107	0.0187	0	0	59.8602	100	15.3424
2.2709	8.5729	0.2373	0.0108	0	0	59.7139	100	15.3912
2.3151	8.5524	0	0	0	0.0136	59.8548	100	15.4923
2.3279	8.4312	0.2409	0.0186	0.0274	0	59.6986	100	15.3627
2.3679	8.319	0.2701	0	0.0163	0.055	59.5769	100	15.5173
2.4096	8.3434	0.2165	0.0141	0.0368	0	59.6181	100	15.4223
2.2465	8.4288	0	0	0.0388	0	59.8904	100	15.2194
2.3919	8.3628	0.0268	0.0248	0.0173	0.0137	59.827	100	15.3297
2.2349	8.445	0	0.0063	0	0	59.8923	100	15.3116
2.3068	8.199	0	0.0158	0.0258	0	59.8602	100	15.256
2.4877	7.9779	0.0276	0	0.0311	0	59.8052	100	15.0669
2.117	8.3042	0	0.0094	0.0653	0	59.903	100	15.2187
2.228	8.4753	0.2132	0	0.1484	0.0091	59.4961	100	15.3527
2.3067	8.3108	0.3477	0.0155	0.0041	0	59.6874	100	15.3126
2.2494	8.4355	0	0.0202	0	0.0274	59.9391	100	15.4438
2.3685	8.2826	0	0	0	0	59.9709	100	15.0546
2.1485	8.6378	0.0267	0	0	0	59.8647	100	15.3832
2.3663	8.4165	0.027	0.0125	0.0226	0	59.8744	100	15.241
2.2106	8.547	0	0.0188	0.0082	0.0322	59.9101	100	15.2276
1.8953	7.7579	0.0571	0.0049	0.0247	0	59.3345	100	14.4855

2.3418	8.5055	0	0.0218	0.0091	0.0547	59.8651	100	15.4337
2.114	8.3535	0.0536	0	0.0061	0	59.957	100	15.0204
2.2332	8.5473	0	0.0265	0	0.0137	59.9637	100	15.3277
2.282	8.4246	0	0.0125	0.0092	0.0457	59.9127	100	15.2266
2.2155	8.3583	0.1866	0.0202	0.0142	0	59.7917	100	15.2228
2.3812	8.1227	0	0.0142	0	0	59.9592	100	15.18
2.2425	8.4941	0.0268	0.0062	0	0.0366	59.867	100	15.396
2.3539	8.7918	0	0	0	0	59.8215	100	15.6345
2.3165	8.1961	0.0816	0	0.033	0	59.7636	100	15.1741
2.4063	8.4756	0	0.0093	0	0	59.8206	100	15.5948
2.3946	8.232	0.2151	0.0155	0.0081	0	59.7448	100	15.3196
2.1588	8.4067	0	0.019	0.0561	0.0233	59.7644	100	15.1833
2.2883	8.226	0	0.0159	0.3443	0.0188	59.3356	100	15.2809
2.3676	8.4984	0	0	0	0.0138	59.8062	100	15.5274
2.0884	8.5083	0.0805	0.0125	0	0.0046	59.8826	100	15.2042
2.0219	8.1781	0	0.0143	0.0332	0	59.8546	100	15.0914
1.9714	8.1548	0	0.0222	0.7775	0.0561	59.2109	100	14.6251
2.3341	8.4208	0	0.014	0.0214	0	59.8945	100	15.4147
2.2287	9.2542	0	0	0.0072	0	59.7738	100	15.5658
0.5899	14.3929	0.084	0.0454	0.0619	0.0173	58.3805	100	18.0138
1.4759	12.4001	0.052	0.0407	0.3848	0	58.5904	100	17.0026
1.4922	6.411	0.0303	0	0.0142	0	60.3929	100	14.9502
0.5716	2.0105	0.1879	0	0.0241	0	61.5408	100	13.3356
2.052	8.2571	0.0818	0	0.0103	0	59.931	100	15.2051
2.1492	8.69	0	0.0278	0	0.0182	59.9013	100	15.5741
2.0804	8.4807	0	0.0126	0.0031	0.0644	59.9532	100	15.1511
2.1723	8.835	0	0.0155	0	0	59.8733	100	15.4976
2.1016	8.6862	0	0.0125	0	0	59.9376	100	15.3051
2.1097	8.6921	0	0	0.0092	0	59.8811	100	15.4261
1.9844	8.6846	0	0.0016	0.001	0.0276	59.9228	100	15.3217
2.0162	8.1878	0	0.0016	0.0144	0.0602	60.0305	100	15.2728
2.1423	8.52	0.0535	0.011	0	0.023	59.9384	100	15.1515
1.9239	8.6086	0.1582	0	0.003	0.0498	59.8853	100	15.1771
1.8118	9.0138	0.21	0.0188	0	0.0092	59.7665	100	15.4462
2.134	8.6914	0.501	0	0	0	59.5909	100	15.3329
1.7825	9.4343	0	0	0.035	0.0415	59.8649	100	15.3055
1.4536	13.5759	0.1086	0.5492	0.0327	0	58.9742	100	18.3098
1.7569	11.879	0	0.3665	0.0646	0	59.5051	100	16.3599
1.9289	10.8053	0	0.0047	0.0082	0	59.9524	100	15.1841
1.6499	10.3224	0	0	0	0	59.9322	100	14.9373
0.4839	4.1932	0	0.0232	0.0701	0	60.4599	100	11.9016
0.1739	1.1468	0.0554	0.0169	0.026	0	61.1512	100	1.6336
1.768	10.4673	0.0486	0	0	0.0225	60.0378	100	14.1381
2.0077	11.2346	0.0246	0.0205	0.0113	0	59.7963	100	15.6209
1.9083	10.8215	0.05	0	0.029	0.0138	59.8509	100	15.3697
1.901	10.4279	0.0253	0.0032	0.0124	0	59.8695	100	15.4651
1.564	9.8522	0	0.0189	0.0206	0	59.9952	100	14.9619
1.6665	9.9044	0.1266	0.0109	0.0215	0.0091	59.807	100	15.3209

1.6617	9.9774	0	0.0063	0.0082	0	59.8849	100	15.4017
1.7111	9.9343	0	0	0.0226	0.0414	59.9112	100	15.3965
0.6477	3.87	0.2799	0.0111	0.0062	0	61.1259	100	5.6356
1.6236	10.5673	0.0249	0.011	0.0256	0.0046	59.8677	100	15.3449
1.1657	11.1827	0.1043	0.0137	0	0.0398	59.5846	100	14.8483
1.6682	10.8131	0.2202	0	0	0.0091	59.7721	100	15.347
1.6339	11.3958	0.0243	0	0	0	59.8584	100	15.5332
1.5506	10.6858	0.0247	0.008	0	0	60.0663	100	14.3185
1.3645	9.6951	0.0469	0.012	0	0	60.2012	100	12.6965
1.5773	11.4564	0.1208	0.019	0	0.0046	59.8474	100	15.2518
1.7533	11.8037	0.049	0	0	0.051	59.7781	100	15.6384
1.6255	11.6118	0.0244	0.0112	0.0031	0.0324	59.8944	100	15.2716
1.5107	11.2857	0.1718	0.0226	0	0	59.9273	100	14.9149
1.6247	11.8658	0	0.0016	0	0	59.8416	100	15.5042
1.5034	11.6605	0	0	0	0	59.8179	100	15.2637
0.4221	4.6	0	0.0188	0.0399	0	61.3247	100	5.8633
1.577	11.5569	0.0732	0.0048	0.0063	0	59.8501	100	15.3754
1.2761	10.0997	0.1761	0.0098	0	0.0142	59.8081	100	13.3173
1.6039	11.3566	0	0.0016	0	0.0184	59.8546	100	15.4823
1.5243	10.9891	0.0995	0.0161	0.0105	0.0606	59.8958	100	15.1226
1.4618	11.7855	0.1923	0.0189	0	0	59.6171	100	15.9566
1.6164	11.2292	0	0.0078	0.0031	0.0546	59.8057	100	15.5917
0.1046	0.8705	0	0.0163	0	0	61.7844	100	1.2553
0.0513	0.8387	0.0583	0	0.0051	0	61.4439	100	1.0776
1.4175	10.7947	0	0.0063	0.0051	0	59.846	100	15.3882
0.3996	14.2701	0.0496	0.0179	0.0304	0.0468	58.6923	100	17.8992
1.2546	10.9952	0	0.0371	0.0063	0	59.9132	100	15.3336
1.2561	11.1756	0.0964	0	0.0153	0.0137	59.8024	100	15.4489
1.112	10.9454	0	0.021	0.0105	0.014	59.9569	100	14.8767
1.2757	11.5099	0.0965	0.0111	0	0	59.8432	100	15.3246
1.3061	12.1615	0	0.0066	0.0032	0.0048	59.8192	100	15.5161
1.1191	11.388	0	0.0382	0.0125	0	59.976	100	15.1695
1.2006	11.9328	0.0994	0.0215	0.0238	0	59.6758	100	15.5889
0.992	11.8704	0	0.008	0.0125	0	59.9198	100	15.2764
0.9963	12.3102	0.0234	0.0064	0.0166	0	59.8437	100	15.5232
1.3454	9.5496	0.625	0.1343	0.378	0	57.8175	100	13.4555
0.027	0.7599	0.0904	0.0564	0.1616	0.0309	60.2501	100	1.4101
0.0706	1.3495	0	0.097	0.1556	0.0162	60.1399	100	2.1619
0.4008	10.0204	0	0	0	0.0297	59.9984	100	12.191
0.9312	11.7228	0	0	0	0	60.0876	100	14.6394
0.84	11.0691	0	0.1597	0.0104	0	60.7716	100	13.4244
0.0501	0.4809	0.2383	0.0193	0.0019	0.0369	66.1749	100	0.5855
0.0278	0.0908	0.1041	0.0014	0.0009	0.004	66.5491	100	0.132
0.0312	0.126	0.0259	0	0.0212	0	66.5708	100	0.1741
0.0139	0.0845	0.1043	0.0029	0	0	66.546	100	0.12
0.029	0.1319	0	0.0327	0.0048	0.0083	64.5208	100	1.3734
0	0.0831	0	0.0043	0.0009	0	61.4277	100	3.1887
0.0351	0.1112	0.2277	0	0.0082	0.0401	61.3069	100	3.2329

0	0.1019	0.1524	0.017	0	0.0443	61.3192	100	3.1838
0.0177	0.1025	0	0.0128	0.0009	0.0121	61.4473	100	3.2867
0.0175	0.1341	0	0	0.0009	0	61.4941	100	3.2267
0	0.1577	0	0.0255	0	0.0523	61.4509	100	3.251
0.0355	0.1617	0	0.0253	0.0882	0	61.284	100	3.3995
0	0.1726	0.0557	0.0356	0.0653	0	61.4109	100	3.3326
0.0252	0.2012	0	0.026	0.015	0	61.4071	100	3.257
0.0513	1.8357	0.235	0.1332	0.0351	0	62.6732	100	2.0357
0.949	10.5256	0	0.0197	0	0	60.4013	100	13.0242
0.8948	12.4989	0	0.0063	0	0	59.8348	100	15.5403
0.8906	11.9136	0.1652	0.008	0.0105	0.0186	59.9416	100	14.8901
0.8505	11.477	0	0.0344	0.0288	0	59.8919	100	14.239
0.0051	3.4831	0	0.2179	0.1467	0	61.2156	100	3.8382
0	0.7218	0.1075	0.0265	0.0131	0	62.2375	100	0.9635
0.0524	0.3635	0	0.003	0	0.0086	61.9136	100	0.5442
0.022	0.4556	0	0.0667	0.1023	0.0302	61.6684	100	0.7017
0.8047	4.685	0	0.1509	0.1468	0	60.7444	100	7.3863
0.0106	0.2117	0.0257	0	0.0249	0	61.3583	100	3.6523
0.0051	0.3064	0.2547	0.0445	0.326	0.0866	61.0854	100	3.6671
0.2481	4.8279	0.2201	0.0902	0.051	0.0478	61.0417	100	7.6577
0.6828	12.3962	0.2984	0.0047	0	0.032	59.7277	100	15.369
0.8005	12.3737	0.0923	0.0063	0	0	59.8392	100	15.3775
0.8659	12.2139	0.185	0	0	0.0229	59.7722	100	15.3269
0.7972	12.4796	0.0477	0.0164	0.0214	0.0713	59.7496	100	15.4452
0.0342	0.9939	0.3497	0.0756	0.0399	0.0174	62.5092	100	1.1155
0.0417	2.7468	0.1504	0.0466	0.0271	0	61.3008	100	4.9176
0.0314	0.4108	0	0	0.0083	0.008	61.3593	100	0.6733
0	0.433	0	0.0537	0.0337	0	61.6725	100	0.5583
0	2.3789	0.3794	0.0746	0.0632	0.025	61.8283	100	3.6494
0.0382	1.0991	0.2355	0.0645	0.1148	0.0329	62.9443	100	1.5281
1.5068	12.6767	0.0767	0	0	0.0139	59.9898	100	16.0762
0.7154	12.2812	0	0	0	0.0138	59.8867	100	15.3349
0.7525	12.4793	0	0	0.0133	0.0182	59.8664	100	15.3702
0.8402	12.6414	0.2944	0.0094	0	0.0453	59.5898	100	15.6511
0.7693	12.0211	0	0.0112	0.0083	0	60.0286	100	14.8993
0.3844	7.0718	0	0.034	0.0295	0	60.1534	100	8.5282
0	0.5438	0.2937	0.0173	0.0132	0.0177	61.3329	100	0.8226
0.0089	1.0205	0.0311	0.0474	0.0858	0	62.7099	100	1.5175
0.0581	1.2614	0.0362	0.0987	0.0959	0.0364	61.4093	100	2.0557
0.0182	0.5234	0.2872	0.043	0.1145	0	62.5878	100	0.7191
0.6591	10.9242	0	0.0264	0	0.0134	59.9637	100	13.479
0.7173	12.185	0	0	0	0.0322	59.9294	100	15.1771
0.7769	12.1462	0	0	0	0	59.9597	100	15.1462
0.793	12.0374	0.0465	0	0.0082	0	59.877	100	15.2117
0.7936	12.399	0	0.0063	0.0194	0	59.851	100	15.4564
0.6553	9.4931	0.1116	0	0	0.0086	59.5539	100	11.9197
0.6563	12.282	0	0.0048	0	0.0046	59.93	100	15.2298
0.6855	12.5625	0	0	0	0	59.9007	100	15.3544

0.7023	12.305	0	0	0	0	59.8848	100	15.3254
0.7839	12.3445	0	0.0222	0	0.0641	59.8277	100	15.4516
0.5861	12.4731	0	0	0	0	59.8875	100	15.3238
0.5629	10.2561	0	0.0388	0.0329	0.0146	60.1881	100	12.642
0.411	9.5181	0.0262	0.03	0.0425	0.0406	59.9155	100	11.7638
0.0112	3.442	0.0507	0.0409	0.0461	0.0259	61.385	100	4.3539
0.7365	12.0584	0.1639	0	0.0021	0	59.7191	100	15.5508
0.4472	11.7006	0	0	0	0.009	59.9706	100	15.065
0.5275	11.7851	0	0.0359	0	0.0498	59.8279	100	15.6154
0.2705	11.9697	0	0.1081	0.0011	0	59.8384	100	15.4369
0.1457	9.1261	0	0.0457	0.0103	0	61.5414	100	12.1453
0.341	11.4166	0	0.014	0.004	0	59.8867	100	15.3872
0.3241	11.609	0.0924	0.0063	0	0.0454	59.8429	100	15.2818
0.3104	11.7858	0	0.0189	0.0072	0.0091	59.8639	100	15.4424
0.2698	11.9745	0.0457	0.0047	0	0.0318	59.7936	100	15.512
0.2059	11.998	0.0675	0.0342	0.0081	0	59.8603	100	15.1927
0.2691	11.8477	0.0469	0.0194	0.0084	0	59.9243	100	15.2087
0.2642	12.3619	0	0.0109	0	0	59.8653	100	15.3916
0.3612	12.4154	0	0	0.0061	0.0726	59.8549	100	15.3732
0.338	12.6752	0	0.0189	0.002	0	59.8423	100	15.4764
0.3824	12.5471	0	0.0063	0.0072	0.0046	59.9107	100	15.3308
0.3578	12.7489	0	0.0047	0	0.0227	59.8757	100	15.3903
0.3168	12.5567	0	0.0112	0	0.0185	59.9381	100	15.201
0.2542	12.9171	0	0	0.0051	0.0091	59.8585	100	15.4386
0.2894	12.835	0	0.0032	0.0103	0	59.8705	100	15.4162
0.2918	12.7404	0	0.0192	0.0021	0	59.915	100	15.2101
0.3564	12.7579	0	0.022	0.0112	0.0408	59.8537	100	15.3085
0.3391	12.8765	0	0.0127	0	0	59.8718	100	15.4495
0.407	12.6787	0	0.0236	0	0.0091	59.9025	100	15.3051
0.3946	12.8104	0	0.0048	0.001	0.032	59.8602	100	15.3709
0.4332	12.6015	0	0.0063	0	0	59.9403	100	15.1955
0.267	11.0477	0	0.0867	0.1146	0	58.4588	100	14.1219
0.3144	12.5905	0	0.008	0.0052	0	59.9826	100	15.092
0.1006	14.3807	0.0483	0.0287	0	0.0052	58.7435	100	17.8417
0.3912	12.7368	0.1342	0	0	0	59.8065	100	15.2712
0.5444	12.5593	0	0.0238	0	0.0091	59.9237	100	15.2557
0.3708	13.1345	0	0.0502	0	0	59.6736	100	15.952
0.0769	14.2495	0.0496	0.0241	0.0157	0	58.2871	100	19.0226
0.3699	11.4874	0.2154	0.0075	0.0059	0.0043	60.1294	100	13.7293
0.4755	12.6757	0.0452	0.0032	0	0.0138	59.8198	100	15.3208
0.1732	14.4509	0.1258	0.0224	0	0	58.4819	100	18.5222
0.1061	13.6493	0.0491	0	0.0378	0	58.5563	100	17.8509
0.507	13.0533	0.1588	0.0016	0	0.0093	59.6475	100	15.7822
0.5189	12.5444	0	0.0064	0.0104	0.0046	59.9372	100	15.146
0.5205	13.0676	0.0688	0.0179	0.0265	0.0141	59.6553	100	15.7085
0.2829	13.238	0.2187	0.065	0.0149	0.0355	59.079	100	16.7099
0.6119	12.7908	0	0.0302	0.0176	0.0275	59.8432	100	15.4667
0.4564	13.9823	0	0.0419	0.0171	0.0202	59.106	100	17.6156

0.0936	14.1841	0.1964	0	0.0095	0	58.4758	100	18.2326
0.4793	12.7609	0	0	0	0.0091	59.9058	100	15.3299
0.5146	12.5468	0	0.0254	0.0113	0	59.9676	100	15.1116
0.4649	12.586	0	0.0176	0.0146	0	59.9546	100	15.0457
0.5035	13.008	0	0.0016	0	0.0135	59.8462	100	15.445
0.6068	12.7005	0	0.0079	0.0031	0	59.918	100	15.2582
0.5562	12.7477	0	0.0193	0.0042	0.0046	59.9354	100	15.1447
0.1406	10.8798	0	0.0298	0.0114	0	60.1686	100	14.6742
0	0.6336	0	0	0.0049	0.0084	66.3608	100	0.674
0	0.116	0	0	0.0074	0	66.6188	100	0.1165
0.0069	0.0483	0.0259	0	0	0.0079	66.6133	100	0.0627
0	0.0677	0	0	0.0111	0.0079	66.6285	100	0.0702
0.0344	0.0545	0	0	0.0202	0.0039	66.6151	100	0.0994
0.0173	0.0194	0.1557	0	0	0.0079	66.5401	100	0.0411
0	0.042	0	0	0.0138	0	66.6357	100	0.042
0	0.0486	0	0	0.0074	0.0397	66.6278	100	0.0486

Xca	Xfe	Xmg	Xmn	X	Y	Z	Comment
						-	Traversa Grt bordo - Grt nucleo della metà di
0.28	0.56	0.02	0.14	6390	39305	7	granato al bordo sezione
						-	Traversa Grt bordo - Grt nucleo della metà di
0.28	0.56	0.02	0.14	6394	39302	6	granato al bordo sezione
						-	Traversa Grt bordo - Grt nucleo della metà di
0.28	0.55	0.01	0.16	6398	39299	6	granato al bordo sezione
						-	Traversa Grt bordo - Grt nucleo della metà di
0.29	0.54	0.02	0.16	6402	39296	6	granato al bordo sezione
						-	Traversa Grt bordo - Grt nucleo della metà di
0.28	0.56	0.02	0.15	6406	39293	6	granato al bordo sezione
						-	Traversa Grt bordo - Grt nucleo della metà di
0.28	0.55	0.02	0.15	6410	39290	6	granato al bordo sezione
						-	Traversa Grt bordo - Grt nucleo della metà di
0.24	0.58	0.02	0.16	6414	39286	6	granato al bordo sezione
						-	Traversa Grt bordo - Grt nucleo della metà di
0.25	0.56	0.02	0.16	6417	39283	6	granato al bordo sezione
						-	Traversa Grt bordo - Grt nucleo della metà di
0.29	0.55	0.02	0.15	6421	39280	6	granato al bordo sezione
						-	Traversa Grt bordo - Grt nucleo della metà di
0.28	0.55	0.01	0.15	6425	39277	6	granato al bordo sezione
						-	Traversa Grt bordo - Grt nucleo della metà di
0.28	0.56	0.02	0.14	6429	39274	6	granato al bordo sezione
						-	Traversa Grt bordo - Grt nucleo della metà di
0.29	0.55	0.02	0.14	6433	39271	6	granato al bordo sezione
						-	Traversa Grt bordo - Grt nucleo della metà di
0.29	0.55	0.01	0.15	6437	39268	6	granato al bordo sezione
						-	Traversa Grt bordo - Grt nucleo della metà di
0.28	0.55	0.02	0.15	6441	39265	6	granato al bordo sezione
						-	Traversa Grt bordo - Grt nucleo della metà di
0.27	0.56	0.01	0.15	6445	39262	6	granato al bordo sezione

0.29	0.55	0.01	0.15	6449	39258	-	6	Traversa Grt bordo - Grt nucleo della metà di granato al bordo sezione
0.24	0.59	0.03	0.14	6453	39255	-	6	Traversa Grt bordo - Grt nucleo della metà di granato al bordo sezione
0.28	0.55	0.02	0.15	6457	39252	-	6	Traversa Grt bordo - Grt nucleo della metà di granato al bordo sezione
0.28	0.56	0.02	0.15	6461	39249	-	6	Traversa Grt bordo - Grt nucleo della metà di granato al bordo sezione
0.28	0.55	0.02	0.15	6464	39246	-	6	Traversa Grt bordo - Grt nucleo della metà di granato al bordo sezione
0.28	0.55	0.02	0.15	6468	39243	-	6	Traversa Grt bordo - Grt nucleo della metà di granato al bordo sezione
0.30	0.54	0.02	0.15	6472	39240	-	6	Traversa Grt bordo - Grt nucleo della metà di granato al bordo sezione
0.29	0.54	0.01	0.16	6476	39237	-	6	Traversa Grt bordo - Grt nucleo della metà di granato al bordo sezione
0.28	0.55	0.02	0.15	6480	39234	-	6	Traversa Grt bordo - Grt nucleo della metà di granato al bordo sezione
0.28	0.55	0.02	0.16	6484	39230	-	6	Traversa Grt bordo - Grt nucleo della metà di granato al bordo sezione
0.29	0.55	0.02	0.15	6488	39227	-	6	Traversa Grt bordo - Grt nucleo della metà di granato al bordo sezione
0.30	0.54	0.02	0.15	6492	39224	-	6	Traversa Grt bordo - Grt nucleo della metà di granato al bordo sezione
0.29	0.53	0.02	0.17	6496	39221	-	6	Traversa Grt bordo - Grt nucleo della metà di granato al bordo sezione
0.30	0.55	0.01	0.14	6500	39218	-	6	Traversa Grt bordo - Grt nucleo della metà di granato al bordo sezione
0.29	0.55	0.02	0.15	6504	39215	-	6	Traversa Grt bordo - Grt nucleo della metà di granato al bordo sezione
0.29	0.54	0.02	0.15	6508	39212	-	6	Traversa Grt bordo - Grt nucleo della metà di granato al bordo sezione
0.29	0.55	0.01	0.15	6512	39209	-	6	Traversa Grt bordo - Grt nucleo della metà di granato al bordo sezione
0.28	0.55	0.02	0.16	6515	39206	-	6	Traversa Grt bordo - Grt nucleo della metà di granato al bordo sezione
0.28	0.56	0.02	0.14	6519	39203	-	6	Traversa Grt bordo - Grt nucleo della metà di granato al bordo sezione
0.28	0.55	0.02	0.16	6523	39199	-	6	Traversa Grt bordo - Grt nucleo della metà di granato al bordo sezione
0.28	0.56	0.02	0.15	6527	39196	-	6	Traversa Grt bordo - Grt nucleo della metà di granato al bordo sezione
0.32	0.54	0.02	0.13	6531	39193	-	6	Traversa Grt bordo - Grt nucleo della metà di granato al bordo sezione
0.28	0.55	0.02	0.15	6535	39190	-	6	Traversa Grt bordo - Grt nucleo della metà di granato al bordo sezione
0.29	0.56	0.02	0.14	6539	39187	-	6	Traversa Grt bordo - Grt nucleo della metà di granato al bordo sezione
0.28	0.56	0.02	0.15	6543	39184	-	6	Traversa Grt bordo - Grt nucleo della metà di granato al bordo sezione

						-	Traversa Grt bordo - Grt nucleo della metà di
0.28	0.56	0.02	0.14	6645	39103	5	granato al bordo sezione
						-	Traversa Grt bordo - Grt nucleo della metà di
0.29	0.57	0.02	0.13	6649	39100	5	granato al bordo sezione
						-	Traversa Grt bordo - Grt nucleo della metà di
0.32	0.54	0.02	0.13	6653	39097	5	granato al bordo sezione
						-	Traversa Grt bordo - Grt nucleo della metà di
0.28	0.56	0.02	0.14	6656	39094	5	granato al bordo sezione
						-	Traversa Grt bordo - Grt nucleo della metà di
0.29	0.57	0.02	0.13	6660	39091	5	granato al bordo sezione
						-	Traversa Grt bordo - Grt nucleo della metà di
0.28	0.58	0.02	0.12	6664	39088	5	granato al bordo sezione
						-	Traversa Grt bordo - Grt nucleo della metà di
0.27	0.57	0.02	0.14	6668	39084	5	granato al bordo sezione
						-	Traversa Grt bordo - Grt nucleo della metà di
0.24	0.62	0.03	0.12	6672	39081	5	granato al bordo sezione
						-	Traversa Grt bordo - Grt nucleo della metà di
0.15	0.74	0.03	0.08	6676	39078	5	granato al bordo sezione
						-	Traversa Grt bordo - Grt nucleo della metà di
0.14	0.73	0.03	0.11	6680	39075	5	granato al bordo sezione
						-	Traversa Grt bordo - Grt nucleo della metà di
0.12	0.71	0.04	0.13	6684	39072	5	granato al bordo sezione
						-	Traversa Grt bordo - Grt nucleo della metà di
0.16	0.69	0.04	0.11	6688	39069	5	granato al bordo sezione
						-	Traversa Grt bordo - Grt nucleo della metà di
0.59	0.35	0.02	0.04	6692	39066	5	granato al bordo sezione
						-	Traversa Grt bordo - Grt nucleo della metà di
0.10	0.70	0.09	0.11	6696	39063	5	granato al bordo sezione
						-	Traversa Grt bordo - Grt nucleo della metà di
0.09	0.74	0.04	0.13	6700	39060	5	granato al bordo sezione
						-	Traversa Grt bordo - Grt nucleo della metà di
0.11	0.72	0.04	0.13	6703	39057	5	granato al bordo sezione
						-	Traversa Grt bordo - Grt nucleo della metà di
0.13	0.70	0.04	0.12	6707	39053	5	granato al bordo sezione
						-	Traversa Grt bordo - Grt nucleo della metà di
0.17	0.67	0.04	0.12	6711	39050	4	granato al bordo sezione
						-	Traversa Grt bordo - Grt nucleo della metà di
0.20	0.66	0.04	0.10	6715	39047	4	granato al bordo sezione
						-	Traversa Grt bordo - Grt nucleo della metà di
0.21	0.65	0.04	0.11	6719	39044	4	granato al bordo sezione
						-	Traversa Grt bordo - Grt nucleo della metà di
0.21	0.65	0.04	0.11	6723	39041	4	granato al bordo sezione
						-	Traversa Grt bordo - Grt nucleo della metà di
0.21	0.65	0.04	0.11	6727	39038	4	granato al bordo sezione
						-	Traversa Grt bordo - Grt nucleo della metà di
0.16	0.69	0.04	0.11	6731	39035	4	granato al bordo sezione
						-	Traversa Grt bordo - Grt nucleo della metà di
0.16	0.69	0.04	0.11	6735	39032	4	granato al bordo sezione
						-	Traversa Grt bordo - Grt nucleo della metà di
0.09	0.75	0.07	0.08	6739	39029	4	granato al bordo sezione

					-		Traversa Grt bordo - Grt nucleo della metà di
0.09	0.78	0.05	0.08	6841	38948	4	granato al bordo sezione
					-		Traversa Grt bordo - Grt nucleo della metà di
0.11	0.75	0.06	0.07	6845	38945	4	granato al bordo sezione
					-		Traversa Grt bordo - Grt nucleo della metà di
0.09	0.77	0.07	0.08	6848	38942	4	granato al bordo sezione
					-		Traversa Grt bordo - Grt nucleo della metà di
0.09	0.78	0.07	0.06	6852	38938	4	granato al bordo sezione
					-		Traversa Grt bordo - Grt nucleo della metà di
0.07	0.79	0.07	0.06	6856	38935	4	granato al bordo sezione
					-		Traversa Grt bordo - Grt nucleo della metà di
0.10	0.71	0.09	0.10	6860	38932	4	granato al bordo sezione
					-		Traversa Grt bordo - Grt nucleo della metà di
0.29	0.54	0.15	0.02	6864	38929	4	granato al bordo sezione
					-		Traversa Grt bordo - Grt nucleo della metà di
0.23	0.62	0.12	0.03	6868	38926	4	granato al bordo sezione
					-		Traversa Grt bordo - Grt nucleo della metà di
0.06	0.82	0.09	0.03	6872	38923	3	granato al bordo sezione
					-		Traversa Grt bordo - Grt nucleo della metà di
0.06	0.80	0.08	0.06	6876	38920	3	granato al bordo sezione
					-		Traversa Grt bordo - Grt nucleo della metà di
0.05	0.82	0.06	0.06	6880	38917	3	granato al bordo sezione
					-		Traversa Grt bordo - Grt nucleo della metà di
0.06	0.82	0.04	0.09	6884	38914	3	granato al bordo sezione
					-		Traversa Grt bordo - Grt nucleo della metà di
0.10	0.69	0.00	0.21	6888	38911	3	granato al bordo sezione
					-		Traversa Grt bordo - Grt nucleo della metà di
0.05	0.72	0.05	0.18	6892	38907	3	granato al bordo sezione
					-		Traversa Grt bordo - Grt nucleo della metà di
0.16	0.70	0.02	0.12	6895	38904	3	granato al bordo sezione
					-		Traversa Grt bordo - Grt nucleo della metà di
0.88	0.10	0.00	0.02	6899	38901	3	granato al bordo sezione
					-		Traversa Grt bordo - Grt nucleo della metà di
0.97	0.03	0.00	0.00	6903	38898	3	granato al bordo sezione
					-		Traversa Grt bordo - Grt nucleo della metà di
0.95	0.03	0.00	0.01	6907	38895	3	granato al bordo sezione
					-		Traversa Grt bordo - Grt nucleo della metà di
0.97	0.03	0.00	0.00	6911	38892	3	granato al bordo sezione
					-		Traversa Grt bordo - Grt nucleo della metà di
0.96	0.03	0.00	0.01	6915	38889	3	granato al bordo sezione
					-		Traversa Grt bordo - Grt nucleo della metà di
0.95	0.04	0.00	0.01	6919	38886	3	granato al bordo sezione
					-		Traversa Grt bordo - Grt nucleo della metà di
0.95	0.05	0.00	0.00	6923	38883	3	granato al bordo sezione
					-		Traversa Grt bordo - Grt nucleo della metà di
0.94	0.05	0.00	0.01	6927	38879	3	granato al bordo sezione
					-		Traversa Grt bordo - Grt nucleo della metà di
0.95	0.05	0.00	0.00	6931	38876	3	granato al bordo sezione
					-		Traversa Grt bordo - Grt nucleo della metà di
0.93	0.06	0.00	0.01	6935	38873	3	granato al bordo sezione

0.05	0.90	0.02	0.03	6939	38870	-	3	Traversa Grt bordo - Grt nucleo della metà di granato al bordo sezione
0.06	0.81	0.06	0.07	6942	38867	-	3	Traversa Grt bordo - Grt nucleo della metà di granato al bordo sezione
0.06	0.80	0.08	0.06	6946	38864	-	3	Traversa Grt bordo - Grt nucleo della metà di granato al bordo sezione
0.06	0.80	0.08	0.06	6950	38861	-	3	Traversa Grt bordo - Grt nucleo della metà di granato al bordo sezione
0.06	0.81	0.08	0.06	6954	38858	-	3	Traversa Grt bordo - Grt nucleo della metà di granato al bordo sezione
0.08	0.91	0.02	0.00	6958	38855	-	3	Traversa Grt bordo - Grt nucleo della metà di granato al bordo sezione
0.08	0.75	0.17	0.00	6962	38851	-	3	Traversa Grt bordo - Grt nucleo della metà di granato al bordo sezione
0.10	0.67	0.14	0.10	6966	38848	-	3	Traversa Grt bordo - Grt nucleo della metà di granato al bordo sezione
0.26	0.65	0.06	0.03	6970	38845	-	3	Traversa Grt bordo - Grt nucleo della metà di granato al bordo sezione
0.25	0.63	0.01	0.11	6974	38842	-	3	Traversa Grt bordo - Grt nucleo della metà di granato al bordo sezione
0.94	0.06	0.00	0.00	6978	38839	-	3	Traversa Grt bordo - Grt nucleo della metà di granato al bordo sezione
0.91	0.08	0.00	0.00	6982	38836	-	3	Traversa Grt bordo - Grt nucleo della metà di granato al bordo sezione
0.30	0.63	0.04	0.03	6986	38833	-	3	Traversa Grt bordo - Grt nucleo della metà di granato al bordo sezione
0.07	0.81	0.08	0.04	6990	38830	-	3	Traversa Grt bordo - Grt nucleo della metà di granato al bordo sezione
0.06	0.80	0.08	0.05	6993	38827	-	3	Traversa Grt bordo - Grt nucleo della metà di granato al bordo sezione
0.06	0.80	0.08	0.06	6997	38824	-	3	Traversa Grt bordo - Grt nucleo della metà di granato al bordo sezione
0.06	0.81	0.08	0.05	7001	38820	-	3	Traversa Grt bordo - Grt nucleo della metà di granato al bordo sezione
0.04	0.89	0.04	0.03	7005	38817	-	3	Traversa Grt bordo - Grt nucleo della metà di granato al bordo sezione
0.01	0.56	0.42	0.01	7009	38814	-	3	Traversa Grt bordo - Grt nucleo della metà di granato al bordo sezione
0.11	0.61	0.24	0.05	7013	38811	-	3	Traversa Grt bordo - Grt nucleo della metà di granato al bordo sezione
0.06	0.78	0.16	0.00	7017	38808	-	3	Traversa Grt bordo - Grt nucleo della metà di granato al bordo sezione
0.01	0.65	0.34	0.00	7021	38805	-	3	Traversa Grt bordo - Grt nucleo della metà di granato al bordo sezione
0.08	0.72	0.18	0.02	7025	38802	-	3	Traversa Grt bordo - Grt nucleo della metà di granato al bordo sezione
0.05	0.79	0.07	0.09	7029	38799	-	2	Traversa Grt bordo - Grt nucleo della metà di granato al bordo sezione
0.07	0.80	0.08	0.05	7033	38796	-	2	Traversa Grt bordo - Grt nucleo della metà di granato al bordo sezione

					-		Traversa Grt bordo - Grt nucleo della metà di
0.06	0.81	0.08	0.05	7037	38792	2	granato al bordo sezione
					-		Traversa Grt bordo - Grt nucleo della metà di
0.06	0.81	0.08	0.05	7040	38789	2	granato al bordo sezione
					-		Traversa Grt bordo - Grt nucleo della metà di
0.06	0.81	0.08	0.05	7044	38786	2	granato al bordo sezione
					-		Traversa Grt bordo - Grt nucleo della metà di
0.05	0.83	0.08	0.05	7048	38783	2	granato al bordo sezione
					-		Traversa Grt bordo - Grt nucleo della metà di
0.11	0.66	0.23	0.00	7052	38780	2	granato al bordo sezione
					-		Traversa Grt bordo - Grt nucleo della metà di
0.07	0.67	0.26	0.01	7056	38777	2	granato al bordo sezione
					-		Traversa Grt bordo - Grt nucleo della metà di
0.19	0.61	0.17	0.03	7060	38774	2	granato al bordo sezione
					-		Traversa Grt bordo - Grt nucleo della metà di
0.17	0.73	0.07	0.03	7064	38771	2	granato al bordo sezione
					-		Traversa Grt bordo - Grt nucleo della metà di
0.06	0.81	0.09	0.05	7068	38768	2	granato al bordo sezione
					-		Traversa Grt bordo - Grt nucleo della metà di
0.07	0.80	0.08	0.05	7072	38765	2	granato al bordo sezione
					-		Traversa Grt bordo - Grt nucleo della metà di
0.07	0.80	0.08	0.05	7076	38761	2	granato al bordo sezione
					-		Traversa Grt bordo - Grt nucleo della metà di
0.08	0.79	0.08	0.05	7080	38758	2	granato al bordo sezione
					-		Traversa Grt bordo - Grt nucleo della metà di
0.06	0.80	0.08	0.05	7084	38755	2	granato al bordo sezione
					-		Traversa Grt bordo - Grt nucleo della metà di
0.05	0.80	0.09	0.05	7087	38752	2	granato al bordo sezione
					-		Traversa Grt bordo - Grt nucleo della metà di
0.06	0.81	0.09	0.04	7091	38749	2	granato al bordo sezione
					-		Traversa Grt bordo - Grt nucleo della metà di
0.05	0.82	0.08	0.04	7095	38746	2	granato al bordo sezione
					-		Traversa Grt bordo - Grt nucleo della metà di
0.07	0.80	0.08	0.05	7099	38743	2	granato al bordo sezione
					-		Traversa Grt bordo - Grt nucleo della metà di
0.06	0.80	0.09	0.05	7103	38740	2	granato al bordo sezione
					-		Traversa Grt bordo - Grt nucleo della metà di
0.06	0.81	0.09	0.04	7107	38737	2	granato al bordo sezione
					-		Traversa Grt bordo - Grt nucleo della metà di
0.08	0.81	0.07	0.04	7111	38733	2	granato al bordo sezione
					-		Traversa Grt bordo - Grt nucleo della metà di
0.04	0.81	0.12	0.03	7115	38730	2	granato al bordo sezione
					-		Traversa Grt bordo - Grt nucleo della metà di
0.02	0.79	0.19	0.00	7119	38727	2	granato al bordo sezione
					-		Traversa Grt bordo - Grt nucleo della metà di
0.09	0.78	0.09	0.05	7123	38724	2	granato al bordo sezione
					-		Traversa Grt bordo - Grt nucleo della metà di
0.12	0.78	0.08	0.03	7127	38721	2	granato al bordo sezione
					-		Traversa Grt bordo - Grt nucleo della metà di
0.14	0.75	0.07	0.03	7131	38718	2	granato al bordo sezione

					-								Traversa Grt bordo - Grt nucleo della metà di
0.13	0.78	0.08	0.02	7134	38715	2							granato al bordo sezione
													Traversa Grt bordo - Grt nucleo della metà di
0.07	0.75	0.17	0.01	7138	38712	2							granato al bordo sezione
													Traversa Grt bordo - Grt nucleo della metà di
0.16	0.74	0.08	0.02	7142	38709	2							granato al bordo sezione
													Traversa Grt bordo - Grt nucleo della metà di
0.13	0.76	0.09	0.02	7146	38705	2							granato al bordo sezione
													Traversa Grt bordo - Grt nucleo della metà di
0.12	0.76	0.09	0.02	7150	38702	2							granato al bordo sezione
													Traversa Grt bordo - Grt nucleo della metà di
0.12	0.77	0.10	0.02	7154	38699	2							granato al bordo sezione
													Traversa Grt bordo - Grt nucleo della metà di
0.10	0.79	0.10	0.01	7158	38696	2							granato al bordo sezione
													Traversa Grt bordo - Grt nucleo della metà di
0.09	0.78	0.11	0.02	7162	38693	2							granato al bordo sezione
													Traversa Grt bordo - Grt nucleo della metà di
0.07	0.80	0.11	0.02	7166	38690	2							granato al bordo sezione
													Traversa Grt bordo - Grt nucleo della metà di
0.06	0.81	0.11	0.02	7170	38687	2							granato al bordo sezione
													Traversa Grt bordo - Grt nucleo della metà di
0.04	0.82	0.12	0.02	7174	38684	2							granato al bordo sezione
													Traversa Grt bordo - Grt nucleo della metà di
0.04	0.82	0.12	0.02	7178	38681	2							granato al bordo sezione
													Traversa Grt bordo - Grt nucleo della metà di
0.03	0.83	0.12	0.02	7181	38678	2							granato al bordo sezione
													Traversa Grt bordo - Grt nucleo della metà di
0.03	0.83	0.12	0.02	7185	38674	2							granato al bordo sezione
													Traversa Grt bordo - Grt nucleo della metà di
0.03	0.84	0.12	0.02	7189	38671	1							granato al bordo sezione
													Traversa Grt bordo - Grt nucleo della metà di
0.03	0.83	0.12	0.02	7193	38668	1							granato al bordo sezione
													Traversa Grt bordo - Grt nucleo della metà di
0.03	0.84	0.12	0.02	7197	38665	1							granato al bordo sezione
													Traversa Grt bordo - Grt nucleo della metà di
0.02	0.83	0.12	0.02	7201	38662	1							granato al bordo sezione
													Traversa Grt bordo - Grt nucleo della metà di
0.02	0.83	0.12	0.02	7205	38659	1							granato al bordo sezione
													Traversa Grt bordo - Grt nucleo della metà di
0.02	0.83	0.12	0.03	7209	38656	1							granato al bordo sezione
													Traversa Grt bordo - Grt nucleo della metà di
0.02	0.83	0.12	0.03	7213	38653	1							granato al bordo sezione
													Traversa Grt bordo - Grt nucleo della metà di
0.02	0.83	0.12	0.03	7217	38650	1							granato al bordo sezione
													Traversa Grt bordo - Grt nucleo della metà di
0.05	0.78	0.15	0.02	7221	38646	1							granato al bordo sezione
													Traversa Grt bordo - Grt nucleo della metà di
0.02	0.83	0.12	0.02	7225	38643	1							granato al bordo sezione
													Traversa Grt bordo - Grt nucleo della metà di
0.00	0.81	0.19	0.01	7229	38640	1							granato al bordo sezione

0.01	0.96	0.03	0.00	7330	38559	-	1	Traversa Grt bordo - Grt nucleo della metà di granato al bordo sezione
0.00	0.55	0.10	0.35	7334	38556	-	1	Traversa Grt bordo - Grt nucleo della metà di granato al bordo sezione
0.11	0.47	0.00	0.42	7338	38553	-	1	Traversa Grt bordo - Grt nucleo della metà di granato al bordo sezione
0.00	1.00	0.00	0.00	7342	38550	-	1	Traversa Grt bordo - Grt nucleo della metà di granato al bordo sezione
0.00	1.00	0.00	0.00	7346	38547	.		Traversa Grt bordo - Grt nucleo della metà di granato al bordo sezione

Distance (μ)	Mean Z	Point#	Date
0	14.9541	920	2016-02-28 20:33
5.1	15.1306	921	2016-02-28 20:36
10.05	15.0349	922	2016-02-28 20:39
15.03	14.9501	923	2016-02-28 20:41
20.03	15.1331	924	2016-02-28 20:44
25.02	14.9191	925	2016-02-28 20:47
30.02	14.6287	926	2016-02-28 20:49
35.02	15.2412	927	2016-02-28 20:52
40.01	14.9307	928	2016-02-28 20:55
45.01	14.9027	929	2016-02-28 20:58
50.01	15.0273	930	2016-02-28 21:00
55.01	14.9971	931	2016-02-28 21:03
60.01	15.2036	932	2016-02-28 21:06
65.01	15.0231	933	2016-02-28 21:08
70.01	15.1488	934	2016-02-28 21:11
75.01	14.8891	935	2016-02-28 21:14
80.01	14.8809	936	2016-02-28 21:16
85.01	15.0422	937	2016-02-28 21:19
90.01	15.2334	938	2016-02-28 21:22
95.01	15.1883	939	2016-02-28 21:25
100.01	15.0919	940	2016-02-28 21:27
105.01	15.0606	941	2016-02-28 21:30
110.01	14.9887	942	2016-02-28 21:33
115.01	14.9787	943	2016-02-28 21:36
120.01	15.095	944	2016-02-28 21:38
125.01	14.942	945	2016-02-28 21:41
130.01	14.7714	946	2016-02-28 21:44
135.01	14.6295	947	2016-02-28 21:46
140.01	14.9929	948	2016-02-28 21:49
145.01	15.0835	949	2016-02-28 21:52
150.01	15.0286	950	2016-02-28 21:55
155.01	15.1099	951	2016-02-28 21:57
160.01	14.5566	952	2016-02-28 22:00
165.01	15.0285	953	2016-02-28 22:03
170.01	14.9394	954	2016-02-28 22:05
175.01	14.9593	955	2016-02-28 22:08

180.01	13.9637	956	2016-02-28 22:11
185.01	15.1367	957	2016-02-28 22:13
190.01	14.8607	958	2016-02-28 22:16
195.01	15.0809	959	2016-02-28 22:19
200.01	15.0302	960	2016-02-28 22:22
205.02	15.0204	961	2016-02-28 22:24
210.02	14.7278	962	2016-02-28 22:27
215.02	15.033	963	2016-02-28 22:30
220.02	15.2629	964	2016-02-28 22:33
225.02	14.7778	965	2016-02-28 22:35
230.02	15.1807	966	2016-02-28 22:38
235.02	15.029	967	2016-02-28 22:41
240.02	14.6955	968	2016-02-28 22:43
245.02	14.6837	969	2016-02-28 22:46
250.02	15.0655	970	2016-02-28 22:49
255.02	14.8845	971	2016-02-28 22:52
260.02	14.6931	972	2016-02-28 22:54
265.02	14.6726	973	2016-02-28 22:57
270.02	15.021	974	2016-02-28 23:00
275.02	15.1647	975	2016-02-28 23:02
280.02	13.0397	976	2016-02-28 23:05
285.02	14.8725	977	2016-02-28 23:08
290.02	14.8425	978	2016-02-28 23:11
295.02	14.4449	979	2016-02-28 23:13
300.02	14.8609	980	2016-02-28 23:16
305.02	15.2612	981	2016-02-28 23:19
310.02	14.8812	982	2016-02-28 23:21
315.02	15.2237	983	2016-02-28 23:24
320.02	14.9847	984	2016-02-28 23:27
325.02	14.9791	985	2016-02-28 23:30
330.02	14.9471	986	2016-02-28 23:32
335.02	14.9435	987	2016-02-28 23:35
340.02	14.9244	988	2016-02-28 23:38
345.02	15.167	989	2016-02-28 23:40
350.02	15.0211	990	2016-02-28 23:43
355.02	15.0661	991	2016-02-28 23:46
360.02	15.0213	992	2016-02-28 23:49
365.02	14.5545	993	2016-02-28 23:51
370.02	14.8656	994	2016-02-28 23:54
375.02	15.3682	995	2016-02-28 23:57
380.02	15.0911	996	2016-02-28 23:59
385.02	12.9807	997	2016-02-29 0:02
390.02	11.2791	998	2016-02-29 0:05
395.02	15.3869	999	2016-02-29 0:08
400.02	15.5997	1000	2016-02-29 0:10
405.02	15.3295	1001	2016-02-29 0:13
410.03	15.2714	1002	2016-02-29 0:16
415.02	15.0854	1003	2016-02-29 0:18

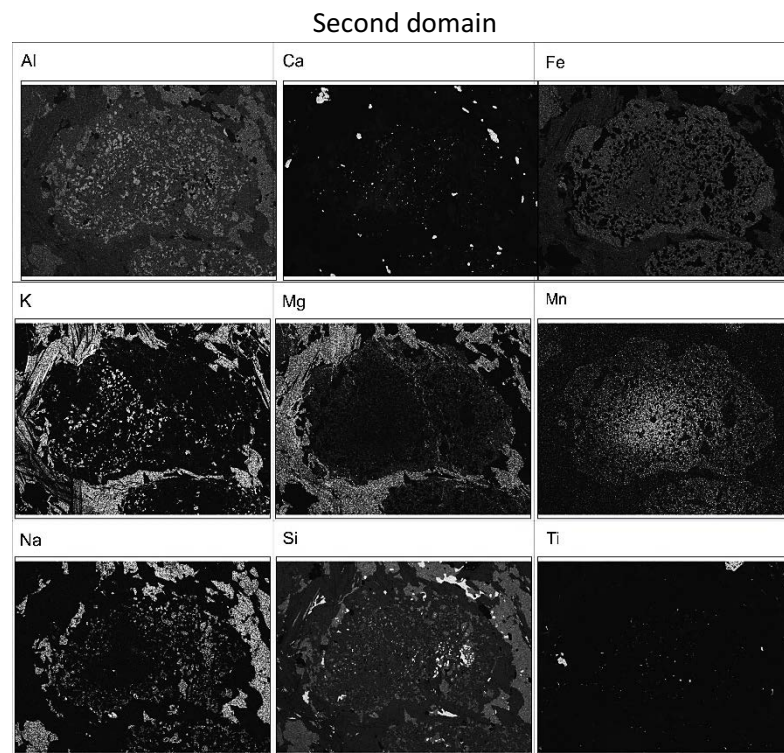
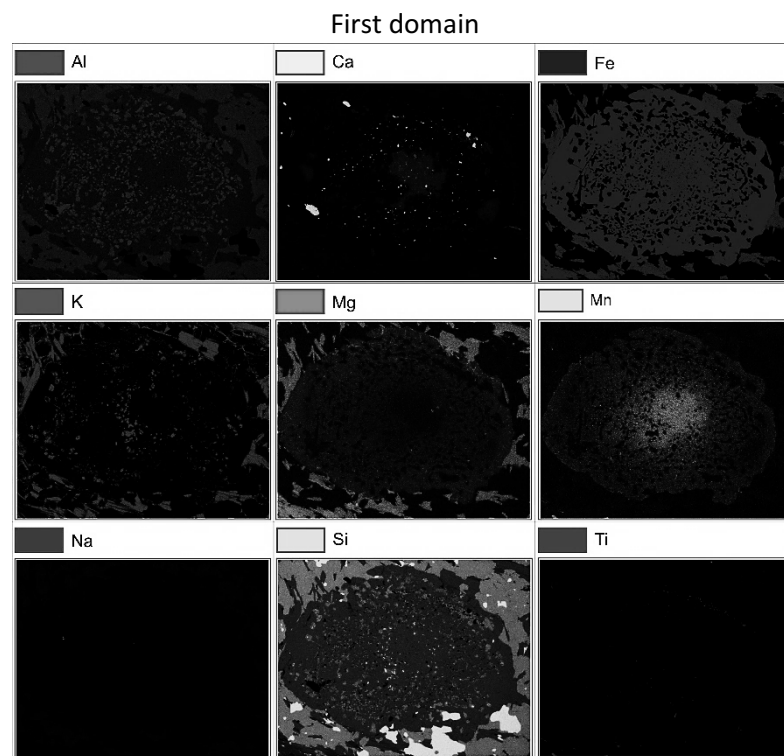
420.02	15.2086	1004	2016-02-29 0:21
425.03	15.1641	1005	2016-02-29 0:24
430.02	15.2537	1006	2016-02-29 0:27
435.02	12.4077	1007	2016-02-29 0:29
440.03	15.3013	1008	2016-02-29 0:32
445.03	14.0462	1009	2016-02-29 0:35
450.03	15.4587	1010	2016-02-29 0:38
455.02	15.5881	1011	2016-02-29 0:40
460.03	14.9387	1012	2016-02-29 0:43
465.03	15.4126	1013	2016-02-29 0:46
470.02	15.4391	1014	2016-02-29 0:48
475.02	15.5218	1015	2016-02-29 0:51
480.03	15.418	1016	2016-02-29 0:54
485.03	15.0266	1017	2016-02-29 0:57
490.02	15.5631	1018	2016-02-29 0:59
495.03	15.3857	1019	2016-02-29 1:02
500.03	11.3211	1020	2016-02-29 1:05
505.03	15.2658	1021	2016-02-29 1:07
510.02	14.3391	1022	2016-02-29 1:10
515.03	15.4402	1023	2016-02-29 1:13
520.03	15.0669	1024	2016-02-29 1:16
525.03	15.6517	1025	2016-02-29 1:18
530.03	15.6066	1026	2016-02-29 1:21
535.03	11.8148	1027	2016-02-29 1:24
540.03	11.3019	1028	2016-02-29 1:26
545.03	15.3966	1029	2016-02-29 1:29
550.03	14.1703	1030	2016-02-29 1:32
555.03	14.9146	1031	2016-02-29 1:35
560.03	15.4269	1032	2016-02-29 1:37
565.03	14.8192	1033	2016-02-29 1:40
570.03	15.2436	1034	2016-02-29 1:43
575.03	14.976	1035	2016-02-29 1:46
580.03	15.1558	1036	2016-02-29 1:48
585.03	14.7781	1037	2016-02-29 1:51
590.03	15.2572	1038	2016-02-29 1:54
595.03	15.4397	1039	2016-02-29 1:56
600.03	5.1359	1040	2016-02-29 1:59
605.03	8.7824	1041	2016-02-29 2:02
610.03	5.7652	1042	2016-02-29 2:05
615.03	15.3655	1043	2016-02-29 2:07
620.03	14.7515	1044	2016-02-29 2:10
625.03	14.7778	1045	2016-02-29 2:13
630.03	10.8273	1046	2016-02-29 2:15
635.03	10.9166	1047	2016-02-29 2:18
640.03	10.9909	1048	2016-02-29 2:21
645.03	10.8942	1049	2016-02-29 2:24
650.03	10.7659	1050	2016-02-29 2:26
655.04	11.2765	1051	2016-02-29 2:29

660.03	11.5101	1052	2016-02-29 2:32
665.03	11.425	1053	2016-02-29 2:34
670.03	11.3806	1054	2016-02-29 2:37
675.04	11.4855	1055	2016-02-29 2:40
680.03	11.4677	1056	2016-02-29 2:43
685.03	10.2823	1057	2016-02-29 2:45
690.03	10.4955	1058	2016-02-29 2:48
695.04	11.2346	1059	2016-02-29 2:51
700.03	9.604	1060	2016-02-29 2:53
705.03	15.3602	1061	2016-02-29 2:56
710.04	15.547	1062	2016-02-29 2:59
715.04	15.0469	1063	2016-02-29 3:02
720.04	14.57	1064	2016-02-29 3:04
725.03	8.5756	1065	2016-02-29 3:07
730.04	10.4531	1066	2016-02-29 3:10
735.04	10.5356	1067	2016-02-29 3:12
740.03	8.7848	1068	2016-02-29 3:15
745.04	12.0648	1069	2016-02-29 3:18
750.04	11.4849	1070	2016-02-29 3:21
755.04	8.1472	1071	2016-02-29 3:23
760.04	11.6396	1072	2016-02-29 3:26
765.04	15.428	1073	2016-02-29 3:29
770.04	15.4041	1074	2016-02-29 3:31
775.04	15.3923	1075	2016-02-29 3:34
780.04	14.9516	1076	2016-02-29 3:37
785.04	10.7698	1077	2016-02-29 3:40
790.04	11.1903	1078	2016-02-29 3:42
795.04	10.9677	1079	2016-02-29 3:45
800.04	10.2439	1080	2016-02-29 3:48
805.04	9.6819	1081	2016-02-29 3:51
810.04	8.4556	1082	2016-02-29 3:53
815.04	16.5278	1083	2016-02-29 3:56
820.04	15.3546	1084	2016-02-29 3:59
825.04	15.5338	1085	2016-02-29 4:02
830.04	15.7308	1086	2016-02-29 4:04
835.04	15.0832	1087	2016-02-29 4:07
840.04	11.1891	1088	2016-02-29 4:10
845.04	10.1918	1089	2016-02-29 4:12
850.04	8.9887	1090	2016-02-29 4:15
855.04	7.7121	1091	2016-02-29 4:18
860.04	8.5023	1092	2016-02-29 4:21
865.04	15.0478	1093	2016-02-29 4:23
870.04	15.2751	1094	2016-02-29 4:26
875.04	15.3239	1095	2016-02-29 4:29
880.04	15.3187	1096	2016-02-29 4:31
885.04	15.5675	1097	2016-02-29 4:34
890.04	14.8951	1098	2016-02-29 4:37
895.04	15.3383	1099	2016-02-29 4:40

900.04	15.2975	1100	2016-02-29 4:42
905.04	15.3968	1101	2016-02-29 4:45
910.05	15.4694	1102	2016-02-29 4:48
915.04	15.2814	1103	2016-02-29 4:50
920.04	13.6219	1104	2016-02-29 4:53
925.05	12.6493	1105	2016-02-29 4:56
930.04	12.2158	1106	2016-02-29 4:59
935.04	15.2362	1107	2016-02-29 5:01
940.04	15.4426	1108	2016-02-29 5:04
945.05	15.5007	1109	2016-02-29 5:07
950.05	14.926	1110	2016-02-29 5:10
955.04	12.5438	1111	2016-02-29 5:12
960.05	15.3809	1112	2016-02-29 5:15
965.05	15.2776	1113	2016-02-29 5:18
970.05	15.219	1114	2016-02-29 5:21
975.04	15.3686	1115	2016-02-29 5:23
980.05	15.4386	1116	2016-02-29 5:26
985.05	14.8221	1117	2016-02-29 5:29
990.05	15.467	1118	2016-02-29 5:31
995.04	15.4538	1119	2016-02-29 5:34
1000.05	15.4757	1120	2016-02-29 5:37
1005.05	15.3328	1121	2016-02-29 5:40
1010.05	15.4518	1122	2016-02-29 5:42
1015.05	15.1029	1123	2016-02-29 5:45
1020.05	15.4297	1124	2016-02-29 5:48
1025.05	15.3839	1125	2016-02-29 5:50
1030.05	15.2123	1126	2016-02-29 5:53
1035.05	15.4906	1127	2016-02-29 5:56
1040.05	15.4375	1128	2016-02-29 5:59
1045.05	15.44	1129	2016-02-29 6:01
1050.05	15.3695	1130	2016-02-29 6:04
1055.05	15.4276	1131	2016-02-29 6:07
1060.05	9.6296	1132	2016-02-29 6:10
1065.05	15.1972	1133	2016-02-29 6:12
1070.05	13.989	1134	2016-02-29 6:15
1075.05	15.2963	1135	2016-02-29 6:18
1080.05	15.3497	1136	2016-02-29 6:20
1085.05	15.1716	1137	2016-02-29 6:23
1090.05	13.4604	1138	2016-02-29 6:26
1095.05	15.6281	1139	2016-02-29 6:29
1100.05	15.2263	1140	2016-02-29 6:31
1105.05	13.4797	1141	2016-02-29 6:34
1110.05	13.5924	1142	2016-02-29 6:37
1115.05	15.2617	1143	2016-02-29 6:39
1120.05	15.1743	1144	2016-02-29 6:42
1125.06	15.1154	1145	2016-02-29 6:45
1130.05	13.99	1146	2016-02-29 6:48
1135.05	15.44	1147	2016-02-29 6:50

1140.06	14.4025	1148	2016-02-29 6:53
1145.06	13.6582	1149	2016-02-29 6:56
1150.05	15.3981	1150	2016-02-29 6:58
1155.05	15.3151	1151	2016-02-29 7:01
1160.06	15.1637	1152	2016-02-29 7:04
1165.06	15.7178	1153	2016-02-29 7:07
1170.05	15.4282	1154	2016-02-29 7:09
1175.05	15.2206	1155	2016-02-29 7:12
1180.06	13.0792	1156	2016-02-29 7:15
1185.06	10.6604	1157	2016-02-29 7:17
1190.05	10.9979	1158	2016-02-29 7:20
1195.06	10.9736	1159	2016-02-29 7:23
1200.06	10.9669	1160	2016-02-29 7:26
1205.06	11.0378	1161	2016-02-29 7:28
1210.06	10.9193	1162	2016-02-29 7:31
1215.06	10.9447	1163	2016-02-29 7:34
1220.06	10.9221	1164	2016-02-29 7:36

APPENDIX C2 – X-ray maps of garnet microdomains from Serre Massif rocks



Third domain as in APPENDIX B3

APPENDIX C3 – XRF composition

Table B15 - Bulk rock chemistry (wt%)

Sample	SiO ₂	TiO ₂	Al ₂ O ₃	FeO	MgO	MnO	CaO	Na ₂ O	K ₂ O	TOTAL
MA271	60.86	0	16.07	12.26	2.48	0.2	2.98	2.88	2.27	100

APPENDIX C4 – Sample locations

Table B16 - Sample location* and schematic minero-textural features of the investigated samples

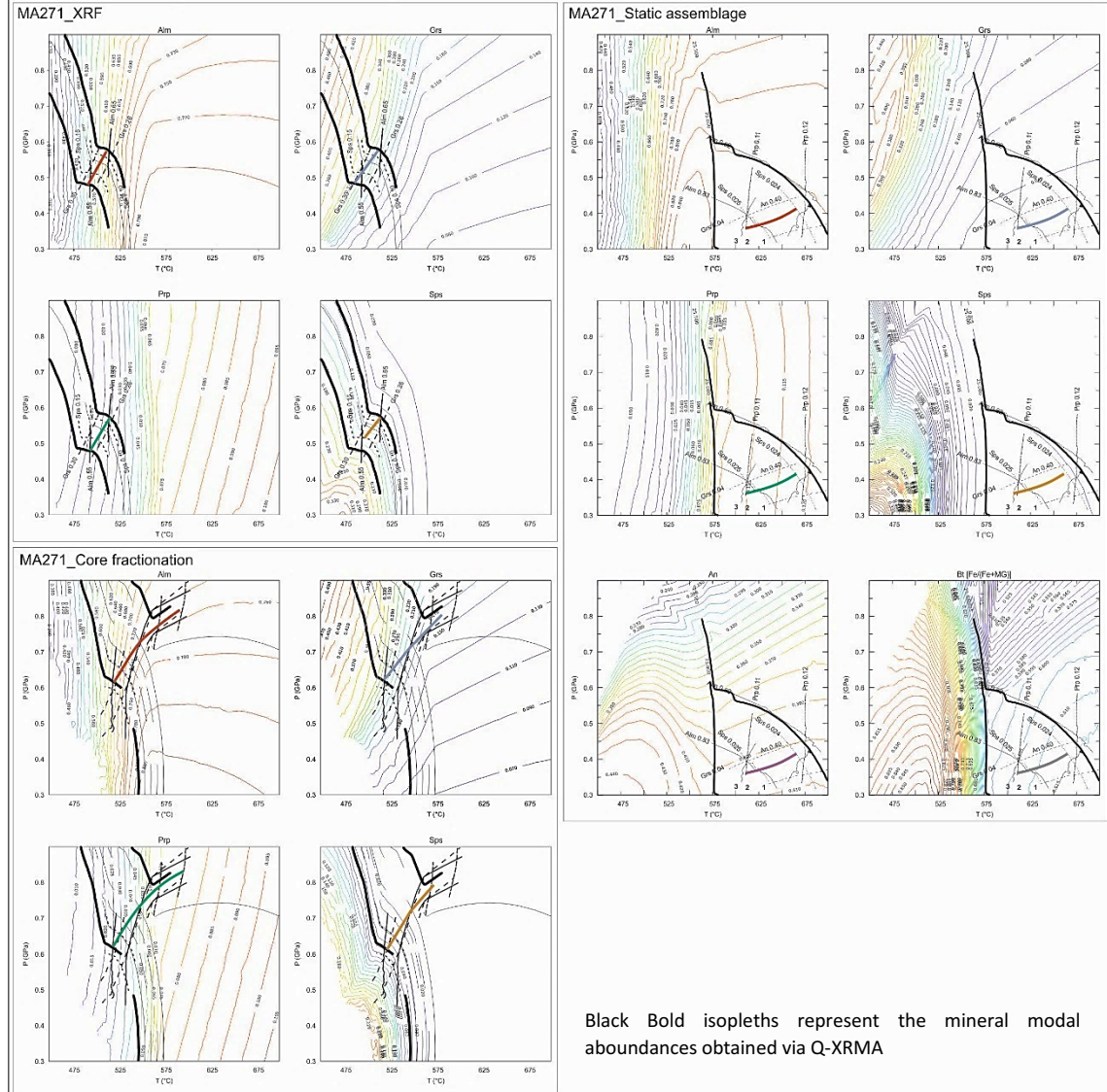
Sample	LAT	LONG
AR221	38°21'74"	16°20'13"
GR155	38°22'13"	16°16'01"
GR157	38°22'6"	16°15'57"
GR159	38°22'33"	16°16'03"
GR164	38°22'21"	16°15'11"
GR166	38°22'30"	16°15'02"
MA271	38°22'76"	16°12'72"
MA272	38°22'08"	16°17'49"
MA600	38°22'10"	16°17'47"
MAR178	38°22'37"	16°17'52"
MAR179	38°28'16"	16°26'32"
MAR199	38°27'58"	16°25'55"
PA248	38°28'10"	16°25'37"
PA249	38°28'19"	16°25'14"
PA250	38°23'43"	16°20'58"
PA251	38°23'50"	16°20'47"
PC218	38°23'49"	16°20'26"
PC219	38°24'17"	16°21'30"
PC220	38°24'11"	16°21'31"
PE236	38°24'06"	16°21'26"
PE237	38°24'12"	16°21'24"
PE238	38°27'44"	16°25'20"
PE239	38°27'42"	16°25'17"
PI103	38°27'39"	16°25'16"
PI104	38°27'40"	16°25'13"
PI105	38°27'42"	16°25'14"
PI106	38°26'58"	16°24'49"
PI107	38°23'54"	16°21'22"
PI108	38°23'05"	16°21'11"
PO115	38°23'30"	16°23'04"
PO138	38°23'35"	16°22'31"
SC226	38°23'16"	16°23'13"
SC227	38°23'23"	16°22'51"
SC228	38°22'08"	16°17'49"
SC229	38°22'10"	16°17'47"

*GPS coordinates: World Geodetic System 84 (WGS84).

Major minerals in decreasing order of abundance: **bold style**; minor minerals (<1 vol.%): *italics*; heavy and ore minerals: (brackets).

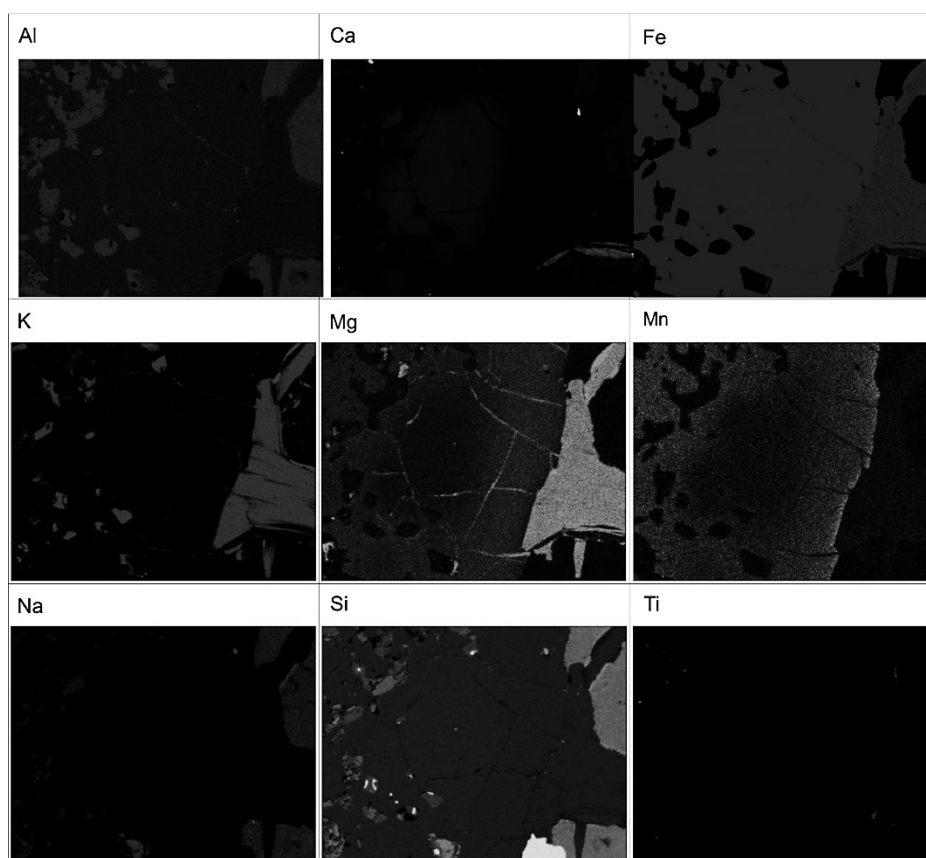
APPENDIX C5 – Isopleth intersections

Fig. C3 - Perplex Mineral Isopleths



Black Bold isopleths represent the mineral modal abundances obtained via Q-XRMA

APPENDIX C6 – X-ray maps of a zoom in a garnet rim



APPENDIX C7 – Sequence of calculation adopted in the MATLAB scripts

Script sequence executed in MATLAB® to model diffusion on garnet

0. Calculate the new temperature as $T_{ch} = 0.95 * T_{peak}$ where T_{peak} is the temperature at peak temperature conditions.
1. Calculate $D(T, X)$ and D_{max} between the element of the D-matrix using the mantle composition and the starting T .
2. Calculate the time step as $\Delta t = R\Delta x^2/D_{max}$ where D_{max} is the largest component of the D matrix.
3. Calculate the new composition for each grid point. The gradient at each interior grid point is calculated as $(C_{i+1} - C_{i-1})/\Delta x$ (i refers to the grid point) and matrix-multiplied by the 3-by-3 diffusion matrix and the scalar x^2 . The gradient of the core is zero. D_{max} is recalculated here and stored for later.
4. Calculate the change in concentration as $C = C + \Delta C$. The core composition is calculated as $\Delta C = 6D\Delta t(C_2 - C_1)/\Delta x^2$ (see Crank, J. (1975), eq. 8.39, pg. 149). Finally, X_{Ca} is calculated for each grid point as $1 - (X_{Fe} + X_{Mn} + X_{Mn})$ and the sequence restarts at step 1.

APPENDIX D1 – EMP analyses of Sila Piccola rocks

Table D1	Na	Mg	Si	Al	K	Ca	Cr	Fe
2 / 1 .	0.1748	1.4091	14.7666	10.2607	0.1529	0.626	0.01	12.1917
2 / 2 .	0.0152	1.6537	14.7231	9.9451	0.0126	0.6198	0.0024	12.6662
2 / 3 .	0.0101	1.7656	15.0131	9.8705	0.0069	0.5968	0.0172	12.2527
2 / 4 .	0.0191	1.8792	14.9651	9.968	0.0061	0.6358	0.0012	12.0206
2 / 5 .	0.0281	1.895	14.969	10.0683	0.0023	0.6252	0.0199	11.823
2 / 6 .	0.0243	1.9833	14.7479	9.83	0.0034	0.5736	0.0259	12.4073
2 / 7 .	0	2.0194	14.8958	9.9515	0	0.6068	0	11.9872
2 / 8 .	0.009	1.9609	15.0037	9.9549	0	0.6131	0	11.8906
2 / 9 .	0.0202	2.0715	14.738	9.92	0.0004	0.5737	0.026	12.2399
2 / 10 .	0	2.0383	14.7903	10.0576	0.0111	0.5945	0.037	11.9185
2 / 11 .	0.0302	2.0453	14.97	9.9955	0.0027	0.6028	0.0225	11.8668
2 / 12 .	0.004	2.0898	14.8202	9.9916	0	0.5873	0.016	12.0278
2 / 13 .	0.0261	2.1496	14.8279	10.0506	0.0131	0.5826	0.0149	11.8074
2 / 14 .	0.0222	2.1529	14.8683	9.9414	0.0012	0.5782	0.0161	12.0136
2 / 15 .	0.001	2.1813	14.8253	10.0083	0.0004	0.5806	0	11.9237
2 / 16 .	0	2.2148	14.993	10.1169	0.0145	0.5801	0.0292	11.5499
2 / 17 .	0.0372	2.2334	14.6558	10.1866	0	0.5836	0.0062	11.933
2 / 18 .	0.0331	2.25	14.8766	10.0863	0.0093	0.5685	0	11.7433
2 / 19 .	0	2.239	14.8368	10.0008	0.0131	0.602	0	11.8518
2 / 20 .	0.011	2.266	14.8794	9.8643	0.0038	0.6119	0.0025	11.9757
2 / 21 .	0	2.3306	14.6669	10.0942	0.0069	0.6217	0.0233	11.8281
2 / 22 .	0.031	2.3468	14.8246	9.9985	0.0073	0.5897	0	11.6744
2 / 23 .	0.0259	2.3763	14.7924	10.0686	0	0.5859	0.0025	11.7593
2 / 24 .	0.2684	2.3507	14.7691	9.937	0.0302	0.6412	0	11.7082
2 / 25 .	0.2069	2.3774	14.835	10.1483	0.0699	0.637	0.0176	11.3985
2 / 26 .	0.006	2.4235	14.6883	9.9973	0.0122	0.6141	0.0025	11.8947
2 / 27 .	0.034	2.4448	14.8818	10.0243	0.0031	0.5969	0.005	11.6136
2 / 28 .	0.0149	2.4546	14.9931	9.9821	0.0008	0.6126	0	11.528
2 / 29 .	0.018	2.4679	14.8076	10.1791	0.0093	0.6061	0.0326	11.4478
2 / 30 .	0.0229	2.5066	14.941	9.9234	0.0031	0.6023	0	11.6044
2 / 31 .	0.0199	2.5154	14.8461	10.0287	0.0008	0.6118	0	11.6388
2 / 32 .	0.0228	2.5922	15.0202	10.0551	0.0043	0.6226	0.02	11.1662
2 / 33 .	0	2.6133	14.8955	9.9603	0.007	0.5897	0.01	11.5551
2 / 34 .	0	2.6455	14.7808	9.9313	0	0.5944	0	11.7606
2 / 35 .	0.0167	2.6414	14.6947	10.053	0.0027	0.6301	0	11.6594
2 / 36 .	0.0207	2.6616	14.8656	10.0403	0	0.5984	0.0149	11.3884
2 / 37 .	0.0266	2.6866	14.9172	9.9036	0.0023	0.5977	0	11.5495
2 / 38 .	0.0272	2.6521	14.7829	9.9169	0.0083	0.6022	0.0109	11.6415
2 / 39 .	0.0168	2.6763	14.8627	10.0825	0	0.6231	0.005	11.3647
2 / 40 .	0.0254	2.7594	14.7906	10.1026	0	0.6201	0.0234	11.3482
2 / 41 .	0.0294	2.7434	14.6559	10.0048	0.0083	0.6207	0.0123	11.6066
2 / 42 .	0.0168	2.8105	14.822	10.0346	0.0038	0.6086	0	11.3184
2 / 43 .	0.0029	2.7402	14.8755	10.0525	0.0027	0.6235	0.0086	11.3664
2 / 44 .	0.0266	2.7856	14.8893	9.8625	0.0054	0.6047	0.0025	11.4939
2 / 45 .	0.033	2.7506	14.8359	10.1024	0.0095	0.5938	0.0232	11.2984

2 / 46 .	0	2.8336	14.7634	9.918	0.0053	0.589	0.0037	11.5673
2 / 47 .	0.0186	2.7942	14.8254	9.9193	0.0072	0.6337	0.0111	11.4456
2 / 48 .	0.0276	2.7935	14.7221	9.9479	0.0061	0.5987	0.0209	11.662
2 / 49 .	0.0732	2.8893	14.8437	10.2813	0.6951	0.516	0.0156	10.5824
2 / 50 .	0.0128	2.8158	14.89	9.9894	0.0092	0.6317	0	11.2083
2 / 51 .	0.0402	2.8153	14.907	10.0852	0.0376	0.6139	0	11.177
2 / 52 .	0	2.865	14.811	9.9866	0.0053	0.6425	0.0332	11.2673
2 / 53 .	0.0167	2.8748	14.9438	9.8319	0.0111	0.6262	0.0012	11.3381
2 / 54 .	0.0157	2.8585	14.8585	9.9299	0.0011	0.6438	0.0186	11.2917
2 / 55 .	0.0738	2.8449	14.6413	10.0337	0.0271	0.6365	0.0062	11.4872
2 / 56 .	0	2.8761	14.9017	10.0039	0.0089	0.6295	0.0037	11.2222
2 / 57 .	0.0157	2.8563	14.7808	10.0624	0.0034	0.6163	0.031	11.2974
2 / 58 .	0.0297	2.9335	14.6982	9.9875	0.0069	0.6379	0	11.3685
2 / 59 .	0.0353	2.9266	14.594	10.0283	0.0046	0.6377	0.0344	11.5284
2 / 60 .	0.0363	2.8739	14.752	10.098	0.0038	0.6491	0.031	11.2501
2 / 61 .	0.0444	2.8587	14.9045	9.9172	0.0042	0.6184	0.0062	11.3162
2 / 62 .	0.0118	2.8769	14.8087	9.9305	0.0076	0.6407	0	11.4196
2 / 63 .	0.0187	2.8835	14.8931	9.9403	0.0046	0.6349	0.0311	11.2401
2 / 64 .	0.1284	2.6959	15.4946	11.1082	1.2819	0.3195	0.0355	8.5065
2 / 65 .	0.1288	2.7363	15.6352	11.1571	1.4253	0.397	0	8.0384
2 / 66 .	0	2.8904	14.9404	9.981	0	0.643	0	11.1899
2 / 67 .	0.0197	2.8704	15.0459	10.0498	0.0008	0.6403	0.005	10.9169
2 / 68 .	0.0049	2.8943	14.955	9.9967	0	0.6628	0	11.1225
2 / 69 .	0.0227	2.8222	14.9832	10.1508	0	0.6575	0	10.9467
2 / 70 .	0.0186	2.9752	14.8447	10.0174	0.0019	0.6504	0.0236	11.1143
2 / 71 .	0.0393	2.9481	14.963	10.0781	0	0.6494	0.005	10.882
2 / 72 .	0.0079	2.8448	14.8575	9.9447	0.0019	0.6338	0.0099	11.2735
2 / 73 .	0.0099	2.9317	14.8207	10.0484	0	0.6383	0	11.1879
2 / 74 .	0.0354	2.8908	14.7523	9.8637	0.0046	0.6376	0.0123	11.502
2 / 75 .	0.0913	2.8244	14.7619	10.0642	0.0226	0.6695	0.0285	11.2369
2 / 76 .	0.0195	2.8587	14.8969	10.0563	0	0.653	0.0099	11.1484
2 / 77 .	0.0344	2.9564	14.8035	10.0638	0	0.6541	0.0162	11.1486
2 / 78 .	0.0029	2.8697	14.7546	10.0173	0.0076	0.663	0	11.3551
2 / 79 .	0.0089	2.8867	14.8032	9.988	0	0.6274	0.0162	11.322
2 / 80 .	0.1018	2.8317	14.7357	9.9371	0.0246	0.6704	0.0137	11.4282
2 / 81 .	0.0283	2.8552	14.814	9.9705	0.0038	0.6682	0.016	11.3645
2 / 82 .	0.0267	2.9536	14.854	9.9183	0.0185	0.6725	0.0037	11.2131
2 / 83 .	0.0532	2.7744	14.9294	9.9732	0	0.6826	0.0075	11.1261
2 / 84 .	0.0128	2.8674	14.899	9.9786	0.0146	0.66	0.0149	11.1821
2 / 85 .	0.0099	2.8848	14.8527	9.9283	0.0031	0.6971	0.0199	11.2953
2 / 86 .	0.0216	2.8731	14.7386	9.9962	0	0.6877	0.0049	11.357
2 / 87 .	0.0108	2.8802	14.7649	9.8118	0.0046	0.6236	0	11.623
2 / 88 .	0.0059	2.8897	14.8704	10.1057	0	0.6641	0.005	11.1044
2 / 89 .	0.0079	2.8402	14.9123	10.0518	0.0027	0.6669	0.0025	11.1457
2 / 90 .	0.0108	2.8874	14.7379	10.0891	0.0042	0.6586	0.0161	11.2784
2 / 91 .	0.0206	2.891	14.9363	10.0322	0.0046	0.6707	0	11.0296
2 / 92 .	0.0049	2.8046	14.688	10.0259	0.0094	0.6757	0	11.4621
2 / 93 .	0.0363	2.8788	14.9955	10.0564	0.0058	0.7144	0.02	10.8827

2 / 94 .	0	2.9183	14.785	9.8847	0	0.6626	0.025	11.3818
2 / 95 .	0.001	2.8796	14.8994	10.0539	0	0.6601	0.0252	11.0807
2 / 96 .	0.0396	2.4893	14.6578	9.9326	0.0396	0.6937	0	11.9018
2 / 97 .	0.0499	2.3662	14.8916	10.4091	0.2384	0.6223	0	11.0359
2 / 98 .	0.0089	2.739	14.8191	10.1009	0.0154	0.6687	0.0261	11.2502
2 / 99 .	0.0366	2.8102	14.8116	9.983	0	0.6937	0.0062	11.392

Mn	Ti	O	Total	Sum_Cat	XCa	XFe	XMg	XMn
0.5095	0.0198	59.879	100	14.7363	0.04248	0.827324	0.095621	0.034574
0.5979	0	59.8157	100	15.5376	0.03989	0.815197	0.106432	0.038481
0.5123	0	59.9678	100	15.1274	0.039452	0.809967	0.116715	0.033866
0.5461	0	59.9653	100	15.0817	0.042157	0.797032	0.124601	0.036209
0.5703	0	59.999	100	14.9135	0.041922	0.792772	0.127066	0.038241
0.5734	0	59.831	100	15.5376	0.036917	0.798534	0.127645	0.036904
0.6035	0	59.9358	100	15.2169	0.039877	0.787756	0.132708	0.03966
0.5502	0.0196	59.9981	100	15.0148	0.040833	0.791925	0.130598	0.036644
0.5598	0	59.8504	100	15.4449	0.037145	0.792488	0.134122	0.036245
0.5978	0.0259	59.929	100	15.1491	0.039243	0.786746	0.134549	0.039461
0.483	0	59.9813	100	14.9979	0.040192	0.791231	0.136372	0.032205
0.5522	0	59.911	100	15.2571	0.038494	0.788341	0.136972	0.036193
0.5581	0.0328	59.9369	100	15.0977	0.038589	0.782066	0.142379	0.036966
0.4883	0	59.9177	100	15.233	0.037957	0.788656	0.141331	0.032055
0.5158	0.0328	59.9308	100	15.2014	0.038194	0.784382	0.143493	0.033931
0.4722	0	60.0294	100	14.817	0.039151	0.779503	0.149477	0.031869
0.4778	0.0131	59.8733	100	15.2278	0.038325	0.783633	0.146666	0.031377
0.4837	0	59.9493	100	15.0455	0.037785	0.780519	0.149546	0.032149
0.502	0.0262	59.9284	100	15.1948	0.039619	0.779991	0.147353	0.033038
0.4827	0	59.9027	100	15.3363	0.039899	0.780873	0.147754	0.031474
0.509	0.0388	59.8805	100	15.2894	0.040662	0.773614	0.152432	0.033291
0.537	0.0589	59.9318	100	15.1479	0.038929	0.770694	0.154926	0.03545
0.4424	0.0261	59.9205	100	15.1639	0.038638	0.77548	0.156708	0.029175
0.4911	0.0066	59.7974	100	15.1912	0.042209	0.770723	0.154741	0.032328
0.4098	0.0066	59.893	100	14.8227	0.042975	0.768989	0.160389	0.027647
0.4539	0.0453	59.8622	100	15.3862	0.039912	0.773076	0.157511	0.0295
0.4574	0	59.939	100	15.1127	0.039497	0.768466	0.161771	0.030266
0.4258	0	59.9882	100	15.021	0.040783	0.767459	0.163411	0.028347
0.4619	0.0132	59.9565	100	14.9837	0.040451	0.764017	0.164706	0.030827
0.4515	0	59.9449	100	15.1648	0.039717	0.765219	0.165291	0.029773
0.4039	0.0065	59.9283	100	15.1699	0.04033	0.76723	0.165815	0.026625
0.4549	0.0132	60.0287	100	14.8359	0.041966	0.752647	0.174725	0.030662
0.4108	0.0131	59.9452	100	15.1689	0.038876	0.761763	0.17228	0.027082
0.414	0	59.8732	100	15.4145	0.038561	0.762957	0.171624	0.026858
0.4463	0	59.8558	100	15.3772	0.040976	0.758226	0.171774	0.029023
0.4686	0	59.9414	100	15.117	0.039585	0.753351	0.176067	0.030998
0.3893	0	59.9273	100	15.2231	0.039263	0.758683	0.176482	0.025573
0.417	0.051	59.89	100	15.3128	0.039327	0.760246	0.173195	0.027232
0.41	0.0066	59.9523	100	15.0741	0.041336	0.753922	0.177543	0.027199

0.4099	0	59.9204	100	15.1376	0.040964	0.74967	0.182288	0.027078
0.4185	0.0516	59.8485	100	15.3892	0.040333	0.754204	0.178268	0.027194
0.4415	0.0196	59.9243	100	15.179	0.040095	0.745662	0.185157	0.029086
0.3663	0.0065	59.9549	100	15.0964	0.041301	0.752921	0.181513	0.024264
0.4169	0.0065	59.9062	100	15.3011	0.03952	0.751181	0.182052	0.027246
0.4146	0	59.9387	100	15.0574	0.039436	0.750355	0.182674	0.027535
0.4589	0	59.8608	100	15.4488	0.038126	0.748751	0.183419	0.029705
0.4269	0.0194	59.8985	100	15.3004	0.041417	0.748059	0.182623	0.027901
0.3763	0	59.8448	100	15.4305	0.0388	0.755776	0.181038	0.024387
0.2994	0	59.804	100	14.2871	0.036116	0.740696	0.202231	0.020956
0.4377	0.0456	59.9596	100	15.0935	0.041852	0.742591	0.186557	0.028999
0.3684	0	59.9554	100	14.9746	0.040996	0.746397	0.188005	0.024602
0.4121	0.0452	59.9317	100	15.1869	0.042306	0.741909	0.188649	0.027135
0.4329	0	59.9233	100	15.272	0.041003	0.742411	0.18824	0.028346
0.47	0	59.9121	100	15.264	0.042178	0.73976	0.187271	0.030791
0.4342	0.0065	59.8086	100	15.4028	0.041324	0.745786	0.1847	0.02819
0.4036	0	59.9505	100	15.1314	0.041602	0.74165	0.190075	0.026673
0.4178	0.0065	59.9122	100	15.1878	0.040579	0.743847	0.188065	0.027509
0.4615	0.0262	59.8499	100	15.4014	0.041418	0.738147	0.19047	0.029965
0.3694	0.0258	59.8156	100	15.4621	0.041243	0.745591	0.189276	0.023891
0.4075	0	59.8982	100	15.1806	0.042759	0.741084	0.189314	0.026843
0.3994	0.0065	59.9242	100	15.1927	0.040704	0.744845	0.188163	0.026289
0.4123	0.0065	59.8854	100	15.3495	0.041741	0.743972	0.187426	0.026861
0.4103	0.0065	59.9369	100	15.1688	0.041856	0.741001	0.190094	0.027049
0.1852	0.0425	60.2019	100	11.7071	0.027291	0.72661	0.230279	0.015819
0.2316	0.0213	60.229	100	11.4033	0.034814	0.704919	0.239957	0.02031
0.3898	0	59.9655	100	15.1131	0.042546	0.740411	0.191251	0.025792
0.4099	0.0066	60.0348	100	14.8375	0.043154	0.735764	0.193456	0.027626
0.3882	0	59.9755	100	15.0678	0.043988	0.738164	0.192085	0.025764
0.3933	0	60.0236	100	14.8197	0.044367	0.738659	0.190436	0.026539
0.4264	0	59.9275	100	15.1663	0.042885	0.732829	0.196172	0.028115
0.413	0.0198	60.0023	100	14.8925	0.043606	0.730703	0.197959	0.027732
0.4718	0.0261	59.928	100	15.2239	0.041632	0.740513	0.186864	0.030991
0.4432	0	59.92	100	15.2011	0.04199	0.735993	0.192861	0.029156
0.4468	0.0129	59.8416	100	15.4772	0.041196	0.743158	0.186778	0.028868
0.4249	0	59.8757	100	15.1557	0.044175	0.741431	0.186359	0.028036
0.3973	0	59.9601	100	15.0574	0.043367	0.740393	0.189853	0.026386
0.3903	0.0131	59.9197	100	15.1494	0.043177	0.73591	0.19515	0.025763
0.4508	0	59.879	100	15.3386	0.043224	0.740296	0.18709	0.02939
0.3983	0.0327	59.9167	100	15.2344	0.041183	0.743186	0.189486	0.026145
0.4037	0.0196	59.8337	100	15.334	0.04372	0.745285	0.184668	0.026327
0.3743	0.0065	59.8988	100	15.2622	0.043781	0.744617	0.187077	0.024525
0.4434	0	59.8962	100	15.2826	0.044004	0.733717	0.193266	0.029013
0.4776	0.0197	59.9564	100	15.0607	0.045323	0.738751	0.184215	0.031712
0.4099	0.0131	59.9476	100	15.1194	0.043653	0.739586	0.18965	0.027111
0.389	0.0065	59.9135	100	15.2662	0.045663	0.739889	0.188966	0.025481
0.4078	0.0325	59.8805	100	15.3256	0.044873	0.741048	0.187471	0.026609
0.4495	0	59.8315	100	15.5763	0.040035	0.746198	0.184909	0.028858

0.3834	0.0066	59.9647	100	15.0416	0.044151	0.738246	0.192114	0.025489
0.4029	0	59.9671	100	15.0557	0.044296	0.740298	0.188646	0.026761
0.4161	0.0065	59.8948	100	15.2405	0.043214	0.740028	0.189456	0.027302
0.4155	0.0197	59.9797	100	15.0068	0.044693	0.734973	0.192646	0.027687
0.3958	0.0578	59.8758	100	15.3382	0.044053	0.747291	0.182851	0.025805
0.4037	0	60.0064	100	14.8796	0.048012	0.731384	0.193473	0.027131
0.453	0.0131	59.8765	100	15.4157	0.042982	0.738325	0.189307	0.029386
0.4309	0	59.9692	100	15.0513	0.043857	0.736196	0.191319	0.028629
0.4229	0.0204	59.8025	100	15.5077	0.044733	0.767477	0.16052	0.02727
0.4105	0	59.976	100	14.4349	0.043111	0.764529	0.163922	0.028438
0.4168	0.0131	59.9418	100	15.0747	0.044359	0.746297	0.181695	0.027649
0.3728	0	59.894	100	15.2687	0.045433	0.746102	0.18405	0.024416

X	Y	Z	Distance (μ)	Mean Z	Point#	Date
8128	23158	249	0	15	2	2016-04-13 11:06
8128	23160	249	2	15	3	2016-04-13 11:08
8129	23162	249	4	15	4	2016-04-13 11:10
8129	23164	249	6	15	5	2016-04-13 11:11
8129	23166	249	8	15	6	2016-04-13 11:13
8130	23168	249	10	15	7	2016-04-13 11:15
8130	23170	249	12	15	8	2016-04-13 11:16
8130	23172	249	14	15	9	2016-04-13 11:18
8130	23174	249	16	15	10	2016-04-13 11:20
8131	23176	249	18	15	11	2016-04-13 11:21
8131	23178	249	20	15	12	2016-04-13 11:23
8131	23180	249	22	15	13	2016-04-13 11:25
8132	23182	249	24	15	14	2016-04-13 11:26
8132	23184	249	26	15	15	2016-04-13 11:28
8132	23186	249	28	15	16	2016-04-13 11:29
8133	23188	249	30	15	17	2016-04-13 11:31
8133	23190	249	32	15	18	2016-04-13 11:33
8133	23192	249	34	15	19	2016-04-13 11:34
8134	23194	249	36	15	20	2016-04-13 11:36
8134	23196	249	38	15	21	2016-04-13 11:38
8134	23198	249	40	15	22	2016-04-13 11:39
8134	23200	249	42	15	23	2016-04-13 11:41
8135	23202	249	44	15	24	2016-04-13 11:43
8135	23204	249	46	15	25	2016-04-13 11:44
8135	23206	249	48	15	26	2016-04-13 11:46
8136	23208	249	50	15	27	2016-04-13 11:47
8136	23210	249	52	15	28	2016-04-13 11:49
8136	23212	249	54	15	29	2016-04-13 11:51
8137	23213	249	56	15	30	2016-04-13 11:52
8137	23215	249	58	15	31	2016-04-13 11:54

8137	23217	249	60	15	32	2016-04-13 11:56
8138	23219	249	62	15	33	2016-04-13 11:57
8138	23221	249	64	15	34	2016-04-13 11:59
8138	23223	250	66	15	35	2016-04-13 12:01
8138	23225	250	68	15	36	2016-04-13 12:02
8139	23227	250	70	15	37	2016-04-13 12:04
8139	23229	250	72	15	38	2016-04-13 12:06
8139	23231	250	74	15	39	2016-04-13 12:07
8140	23233	250	76	15	40	2016-04-13 12:09
8140	23235	250	78	15	41	2016-04-13 12:11
8140	23237	250	80	15	42	2016-04-13 12:12
8141	23239	250	82	15	43	2016-04-13 12:14
8141	23241	250	84	15	44	2016-04-13 12:15
8141	23243	250	86	15	45	2016-04-13 12:17
8142	23245	250	88	15	46	2016-04-13 12:19
8142	23247	250	90	15	47	2016-04-13 12:20
8142	23249	250	92	15	48	2016-04-13 12:22
8142	23251	250	94	15	49	2016-04-13 12:24
8143	23253	250	96	14	50	2016-04-13 12:25
8143	23255	250	98	15	51	2016-04-13 12:27
8143	23257	250	100	15	52	2016-04-13 12:29
8144	23259	250	102	15	53	2016-04-13 12:30
8144	23261	250	104	15	54	2016-04-13 12:32
8144	23263	250	106	15	55	2016-04-13 12:33
8145	23265	250	108	15	56	2016-04-13 12:35
8145	23267	250	110	15	57	2016-04-13 12:37
8145	23269	250	112	15	58	2016-04-13 12:38
8145	23271	250	114	15	59	2016-04-13 12:40
8146	23273	250	116	15	60	2016-04-13 12:42
8146	23275	250	118	15	61	2016-04-13 12:43
8146	23277	250	120	15	62	2016-04-13 12:45
8147	23279	250	122	15	63	2016-04-13 12:47
8147	23281	250	124	15	64	2016-04-13 12:48
8147	23283	250	126	13	65	2016-04-13 12:50
8148	23285	250	128	13	66	2016-04-13 12:52
8148	23287	250	130	15	67	2016-04-13 12:53
8148	23289	251	132	15	68	2016-04-13 12:55
8149	23291	251	134	15	69	2016-04-13 12:57
8149	23293	251	136	15	70	2016-04-13 12:58
8149	23295	251	138	15	71	2016-04-13 13:00
8149	23297	251	140	15	72	2016-04-13 13:01
8150	23299	251	142	15	73	2016-04-13 13:03
8150	23301	251	144	15	74	2016-04-13 13:05

8150	23303	251	146	15	75	2016-04-13 13:06
8151	23305	251	148	15	76	2016-04-13 13:08
8151	23307	251	150	15	77	2016-04-13 13:10
8151	23309	251	152	15	78	2016-04-13 13:11
8152	23310	251	154	15	79	2016-04-13 13:13
8152	23312	251	156	15	80	2016-04-13 13:15
8152	23314	251	158	15	81	2016-04-13 13:16
8153	23316	251	160	15	82	2016-04-13 13:18
8153	23318	251	162	15	83	2016-04-13 13:19
8153	23320	251	164	15	84	2016-04-13 13:21
8153	23322	251	166	15	85	2016-04-13 13:23
8154	23324	251	168	15	86	2016-04-13 13:24
8154	23326	251	170	15	87	2016-04-13 13:26
8154	23328	251	172	15	88	2016-04-13 13:28
8155	23330	251	174	15	89	2016-04-13 13:29
8155	23332	251	176	15	90	2016-04-13 13:31
8155	23334	251	178	15	91	2016-04-13 13:33
8156	23336	251	180	15	92	2016-04-13 13:34
8156	23338	251	182	15	93	2016-04-13 13:36
8156	23340	251	184	15	94	2016-04-13 13:37
8157	23342	251	186	15	95	2016-04-13 13:39
8157	23344	251	188	15	96	2016-04-13 13:41
8157	23346	251	190	15	97	2016-04-13 13:42
8157	23348	251	192	15	98	2016-04-13 13:44
8158	23350	251	194	15	99	2016-04-13 13:46
8158	23352	252	196	15	100	2016-04-13 13:47